

Carlo Rainieri · Giovanni Fabbrocino

---

# Operational Modal Analysis of Civil Engineering Structures

An Introduction and Guide for  
Applications

---

# Operational Modal Analysis of Civil Engineering Structures



---

Carlo Rainieri • Giovanni Fabbrocino

# Operational Modal Analysis of Civil Engineering Structures

An Introduction and Guide  
for Applications



Springer

Carlo Rainieri  
Department of Biosciences  
and Territory, Structural  
and Geotechnical Dynamics Lab  
University of Molise  
Termoli, Italy

Giovanni Fabbrocino  
Department of Biosciences  
and Territory, Structural  
and Geotechnical Dynamics Lab  
University of Molise  
Termoli, Italy

ISBN 978-1-4939-0766-3

ISBN 978-1-4939-0767-0 (eBook)

DOI 10.1007/978-1-4939-0767-0

Springer New York Heidelberg Dordrecht London

Library of Congress Control Number: 2014934330

© Springer Science+Business Media New York 2014

This work is subject to copyright. All rights are reserved by the Publisher, whether the whole or part of the material is concerned, specifically the rights of translation, reprinting, reuse of illustrations, recitation, broadcasting, reproduction on microfilms or in any other physical way, and transmission or information storage and retrieval, electronic adaptation, computer software, or by similar or dissimilar methodology now known or hereafter developed. Exempted from this legal reservation are brief excerpts in connection with reviews or scholarly analysis or material supplied specifically for the purpose of being entered and executed on a computer system, for exclusive use by the purchaser of the work. Duplication of this publication or parts thereof is permitted only under the provisions of the Copyright Law of the Publisher's location, in its current version, and permission for use must always be obtained from Springer. Permissions for use may be obtained through RightsLink at the Copyright Clearance Center. Violations are liable to prosecution under the respective Copyright Law.

The use of general descriptive names, registered names, trademarks, service marks, etc. in this publication does not imply, even in the absence of a specific statement, that such names are exempt from the relevant protective laws and regulations and therefore free for general use.

While the advice and information in this book are believed to be true and accurate at the date of publication, neither the authors nor the editors nor the publisher can accept any legal responsibility for any errors or omissions that may be made. The publisher makes no warranty, express or implied, with respect to the material contained herein.

Printed on acid-free paper

Springer is part of Springer Science+Business Media ([www.springer.com](http://www.springer.com))

*To our families*



---

## Preface

Operational Modal Analysis is the testing procedure yielding experimental estimates of the modal parameters from measurements of the structural response only.

This book reports relevant information and established research results about Operational Modal Analysis in a unified framework. Most of the material in the book is currently disseminated throughout several books and journal papers. An effort has been made to organize this material in a book entirely focused on Operational Modal Analysis. The different aspects of output-only modal testing, from test design to post-processing of results, are analyzed. The book is intended to provide a fundamental theoretical and applicative resource for professional engineers and researchers involved in modal testing of civil structures.

It has been conceived as a guide through the most relevant theoretical and practical concepts in view of the development of a customized system for output-only modal testing based on programmable hardware. The illustrated essential theory provides a general framework to acquire the ability and understanding of the techniques. On the other hand, the large attention devoted to the implementation details provides a valuable stimulus in approaching the study. The applicative perspective makes learning easy and the book suitable for a wide range of readers. In order to simplify the practical implementation of concepts and methods, the use of LabVIEW for software and system development is recommended, because it is characterized by an advantageous learning curve. Moreover, it is very powerful and versatile, making possible the integration of measurements and data processing in a single platform.

Under this premise, it is possible to understand the choice of focusing the attention on implementation details rather than heavy mathematical proofs. The mathematics is kept as simple as each topic allows; most of the equations are functional to the prompt implementation of algorithms and methods by the reader. The basic software accompanying the book is oriented to fit the needs of both the modal analysts on one hand, and undergraduate/graduate students, researchers and developers on the other hand. The latters, in fact, are usually interested in writing their own code for further developments or business opportunities, and the accompanying software serves as a reference. Test engineers, instead, can find here the tools and the fundamental information to promptly start the modal tests and properly interpret the results.

The material is presented at a level suitable for upper-level undergraduate or post-graduate students and professional engineers. In fact, all the material in the book and the organization of the topics are based on the courses given by the authors at undergraduate and graduate students of the University of Molise and the University of Naples Federico II as well as the field experience made in the context of the spin-off company S2X s.r.l. An attempt has been made to produce a self-contained book, with basics of structural dynamics and modal analysis as the only prerequisite to understand most of the presented material. Sufficient details are given in the chapters to cover the necessary multidisciplinary skills that are required to the modal analyst. Several references are also provided at the end of each chapter for the reader who is interested in more details about the various topics.

A number of explanatory applications will help the reader in gaining confidence with the concepts and understanding the potential of output-only modal testing. Most of the analyzed case studies are applications to real structures. This circumstance permits to highlight issues and challenges of output-only modal testing that are often encountered in the practice.

The last part of the book is focused on automated Operational Modal Analysis, providing an outlook on its promising applicative perspectives in the field of vibration-based Structural Health Monitoring. An overview of the latest developments in the field of automated Operational Modal Analysis is presented. It basically represents a particular viewpoint about the matter, since a wide consensus in the definition of the “best methods” for automated output-only modal identification has not been reached, yet. However, the analysis of the main issues related to automation, together with the attention devoted throughout the book to relevant aspects of data acquisition and storage (including storage in MySQL relational databases), aims at linking the material in this book with the wider area of civil Structural Health Monitoring, that is currently a very active research field.

Since this is a new book, instructors, students, and professional engineers are invited to write us ([carlo.rainieri@unimol.it](mailto:carlo.rainieri@unimol.it), [giovanni.fabbrocino@unimol.it](mailto:giovanni.fabbrocino@unimol.it)) if they have questions, suggestions, or if they identify errors or relevant issues.

We thank you in advance for the time you will spend for this.

Termoli, Italy

Carlo Rainieri  
Giovanni Fabbrocino

---

# Contents

<b>1</b>	<b>Introduction . . . . .</b>	<b>1</b>
1.1	Operational Modal Analysis: A New Discipline? . . . . .	1
1.2	Preliminary Concepts . . . . .	3
1.3	Fundamental Principle and Applications of OMA . . . . .	8
1.4	Organization of the Book . . . . .	10
1.5	A Platform for Measurement Execution and Data Processing . . . . .	12
1.5.1	Generalities . . . . .	12
1.5.2	VIs and Toolkits for Data Processing and System Identification . . . . .	15
1.5.3	Recurrent Structures for Software Development . . . . .	16
	References . . . . .	20
<b>2</b>	<b>Mathematical Tools for Random Data Analysis . . . . .</b>	<b>23</b>
2.1	Complex Numbers, Euler's Identities, and Fourier Transform . . . . .	23
2.2	Stationary Random Data and Processes . . . . .	28
2.2.1	Basic Concepts . . . . .	28
2.2.2	Fundamental Notions of Probability Theory . . . . .	29
2.2.3	Correlation Functions . . . . .	35
2.2.4	Spectral Density Functions . . . . .	38
2.2.5	Errors in Spectral Density Estimates and Requirements for Total Record Length in OMA . . . . .	44
2.3	Matrix Algebra and Inverse Problems . . . . .	46
2.3.1	Fundamentals of Matrix Algebra . . . . .	46
2.3.2	Inverse Problems: Error Norms and Least Squares Solutions . . . . .	49
2.4	Applications . . . . .	53
2.4.1	Operations with Complex Numbers . . . . .	53
2.4.2	Fourier Transform . . . . .	53
2.4.3	Statistics . . . . .	54
2.4.4	Probability Density Functions . . . . .	54
2.4.5	Auto- and Cross-Correlation Functions . . . . .	55
2.4.6	Auto-Correlation of Gaussian Noise . . . . .	55

2.4.7	Auto-Power Spectral Density Function . . . . .	56
2.4.8	Singular Value Decomposition . . . . .	56
References	. . . . .	57
<b>3</b>	<b>Data Acquisition</b> . . . . .	59
3.1	Selection of the Measurement Scheme . . . . .	59
3.2	Transducers . . . . .	62
3.3	Data Acquisition Systems . . . . .	70
3.4	Wired vs. Wireless . . . . .	73
3.5	Sensor Installation . . . . .	75
3.6	Sampling, Filtering, and Decimation . . . . .	81
3.7	Data Validation and Pretreatment . . . . .	84
3.8	Applications . . . . .	90
3.8.1	Aliasing . . . . .	90
3.8.2	Mode Shape Merging . . . . .	90
3.8.3	Filtering and Decimation . . . . .	91
3.8.4	Hardware Selection and Data Acquisition (Storage on File) . . . . .	91
3.8.5	Data Storage (MySQL Database) . . . . .	99
3.8.6	Data Pretreatment . . . . .	100
References	. . . . .	101
<b>4</b>	<b>Output-only Modal Identification</b> . . . . .	103
4.1	Fundamental Assumptions in OMA . . . . .	103
4.2	Structural Dynamics Models . . . . .	105
4.2.1	Frequency Response and Impulse Response . . . . .	105
4.2.2	State-Space Models . . . . .	109
4.2.3	ARMA Models . . . . .	117
4.2.4	Fraction Polynomial Models . . . . .	120
4.2.5	The Unified Matrix Polynomial Approach to Modal Analysis . . . . .	123
4.3	Classification of OMA Techniques . . . . .	126
4.4	Frequency Domain Methods . . . . .	127
4.4.1	The Basic Frequency Domain (Peak-Picking) Method . . . . .	127
4.4.2	The Frequency Domain Decomposition Method . . . . .	130
4.4.3	Frequency Domain Parametric Methods for OMA . . . . .	133
4.5	Time Domain Methods . . . . .	146
4.5.1	NExT-Type Procedures . . . . .	146
4.5.2	AR- and ARMA-Type Methods . . . . .	151
4.5.3	Stochastic Subspace Identification . . . . .	153
4.5.4	Second Order Blind Identification . . . . .	166
4.6	Other Methods for OMA . . . . .	173
4.6.1	Transmissibility Functions . . . . .	174
4.6.2	The Random Decrement Technique . . . . .	175

---

4.7	Some Remarks About OMA Methods . . . . .	177
4.8	Post-Processing of Modal Parameter Estimates . . . . .	179
4.8.1	Analysis of Mode Shape Estimates . . . . .	179
4.8.2	Quality Checks and Comparisons . . . . .	185
4.9	Stabilization Diagrams for Parametric OMA Methods . . . . .	191
4.10	Applications . . . . .	195
4.10.1	Basic Frequency Domain . . . . .	195
4.10.2	Frequency Domain Decomposition . . . . .	199
4.10.3	Least Squares Complex Frequency . . . . .	201
4.10.4	Stochastic Subspace Identification . . . . .	203
4.10.5	Second Order Blind Identification . . . . .	205
4.10.6	Influence of Sensor Layout . . . . .	206
	References . . . . .	206
<b>5</b>	<b>Applications . . . . .</b>	<b>211</b>
5.1	Assessing the Adequacy of the Measurement Chain . . . . .	211
5.2	Damping Estimation . . . . .	215
5.3	Correlation Between Numerical and Experimental Modal Property Estimates . . . . .	221
5.3.1	Preliminary Geometric and Structural Survey . . . . .	223
5.3.2	Output-Only Modal Identification . . . . .	225
5.3.3	Finite Element Modeling . . . . .	228
5.3.4	Tuning of Selected Model Parameters . . . . .	231
5.4	Mass Normalized Mode Shapes . . . . .	237
5.5	The Excitation System: Identification of Spurious Frequencies . . . . .	243
5.6	Development of Predictive Correlations . . . . .	257
	References . . . . .	263
<b>6</b>	<b>Automated OMA . . . . .</b>	<b>267</b>
6.1	Statement of the Problem . . . . .	267
6.2	Automated OMA in Frequency Domain: LEONIDA . . . . .	268
6.2.1	Objectives . . . . .	268
6.2.2	Principles and Implementation . . . . .	271
6.2.3	Comparison with Other Frequency Domain Algorithms . . . . .	276
6.2.4	Explanatory Applications . . . . .	279
6.3	Automated OMA by Hybrid Method: ARES . . . . .	285
6.3.1	Algorithm . . . . .	285
6.3.2	Validation and Application . . . . .	289
6.4	Automated Modal Tracking: AFDD-T . . . . .	293
6.4.1	Objectives . . . . .	293
6.4.2	Principles and Implementation . . . . .	294
6.4.3	Validation and Application . . . . .	300
6.5	Automated OMA and Vibration-Based Monitoring . . . . .	307
	References . . . . .	313
<b>Index . . . . .</b>		<b>315</b>



---

## List of Abbreviations

AC	Alternate current
ADC	Analog digital converter
ADO	ActiveX Data Object
AFDD-T	Automated frequency domain decomposition-tracking
AMUSE	Algorithm for multiple unknown signal extraction
AR	Auto regressive
ARES	Automated modal parameter extraction system
ARMA	Auto-regressive moving average
ARMAV	Auto-regressive moving average vector
BFD	Basic frequency domain
BMID	Blind modal identification
BR	Balanced realization
BSS	Blind source separation
CMRR	Common mode rejection ratio
COMAC	Coordinate modal assurance criterion
Cov-SSI	Covariance-driven stochastic subspace identification
CPU	Central processing unit
CVA	Canonical variate analysis
DC	Direct current
DD-SSI	Data-driven stochastic subspace identification
DDT	Dynamic data type
DFT	Discrete Fourier transform
DOF	Degree of freedom
DR	Dynamic range
DSN	Data source name
ECOMAC	Enhanced coordinate modal assurance criterion
EFDD	Enhanced frequency domain decomposition
EMA	Experimental modal analysis
ERA	Eigensystem realization algorithm
EVD	Eigenvalue decomposition
FDD	Frequency domain decomposition
FE	Finite element
FEM	Finite element model
FFT	Fast Fourier transform

FIR	Finite impulse response (filter)
FOH	First-order hold
FRF	Frequency response function
FSDD	Frequency spatial domain decomposition
ICA	Independent component analysis
IEPE	Integrated electronics piezoelectric
IIR	Infinite impulse response (filter)
IMAC	International Modal Analysis Conference
IOMAC	International Operational Modal Analysis Conference
IRF	Impulse response function
ISMA	International Conference on Noise and Vibration Engineering
ITD	Ibrahim time domain
IV	Instrumental variable
JAD	Joint approximate diagonalization
LMFD	Left matrix fraction description
LR	Lower residual (term)
LSB	Least significant bit
LSCE	Least squares complex exponential
LSCF	Least squares complex frequency
LSFD	Least squares frequency domain
LTI	Linear time invariant
MA	Moving average
MAC	Modal assurance criterion
MAX	Measurement and automation explorer
MDOF	Multi-degree of freedom
MFD	Matrix fraction description
MIMO	Multiple input multiple output
MISO	Multiple input single output
MLE	Maximum likelihood estimator
MOF	Modal overlap factor
MPC	Modal phase collinearity
MPD	Mean phase deviation
MSF	Modal scale factor
NExT	Natural excitation techniques
NMD	Normalized modal difference
ODBC	Open database connectivity
ODS	Operational deflection shape
OMA	Operational modal analysis
p-LSCF	Poly-reference least squares complex frequency
PC	Principal component
PCA	Principal component analysis
PEM	Prediction error method
PMR	Participating mass ratio
PSD	Power spectral density
r.c.	Reinforced concrete

RD	Random decrement
RMFD	Right matrix fraction description
rms	Root mean square
SDOF	Single degree of freedom
SERP	Stationary and ergodic random process
SHM	Structural health monitoring
SIMO	Single input multiple output
SISO	Single input single output
SNR	Signal-to-noise ratio
SOBI	Second-order blind identification
SRP	Stationary random process
SSI	Stochastic subspace identification
SVD	Singular value decomposition
UMPA	Unified matrix polynomial approach
UPC	Unweighted principal component
UR	Upper residual (term)
VI	Virtual instrument
ZOH	Zero order hold



---

## List of Symbols

$\text{dB}$	Decibel
$h(\tau)$	IRF
$H(\omega)$	FRF
$[\cdot]$	Matrix
$\langle \cdot \rangle$	Row vector
$\{\cdot\}$	Column vector
$i$	Imaginary unit/number of block rows
$f_s$	Sampling frequency
$T$	Period/duration
$N$	Number of samples
$*$	Complex conjugate
$H$	Hermitian adjoint
$T$	Transpose
$+$	Pseudoinverse
$N_{\text{DOF}}$	Number of DOFs
$N_m$	Number of modes
$\lambda$	Continuous-time pole/eigenvalue
$\mu$	Discrete-time pole/mean
$\varepsilon$	Error
$n$	Order of state space model or polynomial model
$p$	Order of AR/ARMA model/number of time lags in SOBI
$l$	Number of output time series
$\hat{\cdot}$	Estimated quantity
$\gamma_{xy}^2(\omega)$	Coherence function
$\Delta f$	Frequency resolution
$\Delta f_n$	Relative scatter between natural frequency estimates
$\Delta t$	Sampling interval
$t_k$	Discrete time instant
$Re(\cdot)$	Real part of a complex number
$Im(\cdot)$	Imaginary part of a complex number
$\ \cdot\ $	L2-norm
$ [\cdot] $	Determinant
$adj([\cdot])$	Adjoint matrix
$f_{d,r}$	Damped frequency

---

$\omega_{d,r}$	Damped circular frequency
$f_r$	Natural frequency
$\omega_r$	Natural circular frequency
$\xi_r$	Damping ratio
$\sigma_r$	Real part of the pole associated to the r-th mode
$sgn(\cdot)$	Signum function
$n_b$	Number of data segments
$S_{YY}(\omega)$	Two-sided output power spectrum
$S_{YY}^+(\omega)$	Positive power spectrum
$G_{YY}(\omega)$	One-sided output power spectrum
$R_{yy}(\tau)$	Output correlation function
$C_{yy}(\tau)$	Output covariance function
$T_{ij}^d(\omega)$	Transmissibility function
$D_{yy}(\tau)$	RD signature
$p_r(t)$	Modal coordinate
$\alpha_j$	Mode shape scaling factor
$N_f$	Number of frequency lines
$\Omega_f$	Generalized transform variable at discrete frequency $\omega_f$
$z_f$	$z$ -domain polynomial basis function at discrete frequency $\omega_f$
$tr(\cdot)$	Trace
$\otimes$	Kronecker product
$\ell(\cdot)$	Cost function
$n_\alpha$	AR order of ARMA model
$n_\gamma$	MA order of ARMA model
$N_c$	Dimension of matrix coefficient
$\sigma^2$	Variance
$t$	Threshold to stop JAD
$\{\psi\}$	Mass normalized mode shape/eigenvector
$\{\phi\}$	Unscaled mode shape
$\{y(t)\}$	Displacement response in time domain/measured output
$\{f(t)\}$	Forcing vector
$\{\gamma_r\}$	Operational reference vector
$\{s(t)\}$	State vector/source
$\{z(t)\}$	Whitened data
$\{s_k\}$	Discrete-time state vector
$\{u_k\}$	Sampled input
$\{y_k\}$	Sampled output
$\{w_k\}$	Vector of process noise in state-space models
$\{v_k\}$	Vector of measurement noise in state-space models
$\{e_k\}$	Innovation
$\{u_1\}$	First singular vector
$\{\theta\}$	Unknown polynomial coefficients in LSCF
$\{\theta_{N_k}\}$	k-th vector of the numerator coefficients in LSCF
$\{\theta_d\}$	Vector of the denominator coefficients in LSCF

---

$\{\hat{s}_k\}$	Kalman state estimate at time $t_k$
$\{n(t)\}$	Additive noise
$\{x(t)\}$	Signal part of the observed data in SOBI
$[M]$	Mass matrix
$[C]$	Damping matrix
$[K]$	Stiffness matrix
$[Z(\omega)]$	Dynamic stiffness matrix
$[R_r]$	Residue matrix
$[A_c]$	State matrix (continuous time)
$[B_c]$	Input influence matrix (continuous time)
$[C_a]$	Output location matrix (acceleration)
$[C_v]$	Output location matrix (velocity)
$[C_d]$	Output location matrix (displacement)
$[C_c]$	Output influence matrix (continuous time)
$[D_c]$	Direct transmission matrix (continuous time)
$[A]$	Discrete-time state matrix/mixing matrix
$[B]$	Discrete-time input matrix
$[C]$	Discrete-time output matrix
$[D]$	Discrete-time direct transmission matrix
$\begin{bmatrix} [Q^{ww}] & [S^{wv}] \\ [S^{vw}]^T & [R^{vv}] \end{bmatrix}$	Covariance matrices of process noise and measurement noise
$[R_i]$	Output covariance matrix at time lag $i$
$[\Sigma]$	State covariance matrix/diagonal matrix of singular values
$[G]$	Next state-output covariance matrix
$[K_k]$	Non-steady state Kalman gain
$[P_k]$	Covariance of the Kalman state estimates in non-steady state
$[J]$	Jacobian matrix
$[\theta]$	Matrix of the unknown parameters in p-LSCF
$[\beta_o]$	Matrix of the unknown numerator coefficients for output o in p-LSCF
$[\alpha]$	Matrix of the unknown denominator coefficients in p-LSCF
$[H_{i j}]$	Hankel matrix (subfixes i and j denote the time instants of the first and the last entry in the first column of the matrix)
$[P]$	Kalman state covariance matrix in steady-state
$[\alpha_i]$	Matrix of the AR coefficients
$[\gamma_i]$	Matrix of the MA coefficients
$[O_i]$	Observability matrix
$[\Phi]$	Modal matrix
$[U]$	Matrix of the left singular vectors/demixing matrix in SOBI
$[V]$	Matrix of the right singular vectors
$[T_{i j}]$	Block Toeplitz matrix whose entries on the first row are correlations evaluated at time lags from i to j
$[\Gamma_i]$	Reversed controllability matrix
$[U_1]$	Matrix of the left singular vectors corresponding to nonzero singular values

$[V_1]$	Matrix of the right singular vectors corresponding to nonzero singular values
$[\Sigma_1]$	Submatrix of $[\Sigma]$ holding the nonzero singular values
$[\hat{S}_i]$	Kalman filter state sequence
$[Y_p]$	Matrix of the past outputs
$[Y_f]$	Matrix of the future outputs
$[Y_p^+]$	Matrix of the past outputs with one block row added
$[Y_f^-]$	Matrix of the future outputs with one block row removed
$[\Pi_E]$	Orthogonal projection on the row space of $[E]$
$[P_i]$	Projection matrix
$[O_i^\uparrow]$	Observability matrix with the last $l$ rows deleted
$[O_i^\downarrow]$	Observability matrix with the first $l$ rows deleted
$[\rho_w], [\rho_v]$	Kalman filter residuals
$[W]$	Whitening matrix in SOBI

---

## 1.1 Operational Modal Analysis: A New Discipline?

The use of experimental tests to gain knowledge about the dynamic response of civil structures is a well-established practice. In particular, the experimental identification of the modal parameters can be dated back to the middle of the Twentieth Century (Ewins 2000). Assuming that the dynamic behavior of the structure can be expressed as a combination of modes, each one characterized by a set of parameters (natural frequency, damping ratio, mode shape) whose values depend on geometry, material properties, and boundary conditions, Experimental Modal Analysis (EMA) identifies those parameters from measurements of the applied force and the vibration response.

In the last decades the principles of system identification and the experimental estimation of the modal parameters have provided innovative tools for the understanding and control of vibrations, the optimization of design, and the assessment of performance and health state of structures. In fact, even if the Finite Element (FE) method and the fast progress in computing technologies have made excellent analysis tools available to the technical community, the development of new high-performance materials and the increasing complexity of structures have required powerful tools to support and validate the numerical analyses. In this context the experimental identification of the modal properties definitely supports the engineers to get more physical insight about the dynamic behavior of the structure and to discriminate between the errors due to discretization and those due to simplified or even wrong modeling assumptions. Moreover, since the vibration response originates from the modes, which are inherent properties of the structure, forces exciting the structure at resonant frequencies yield large vibration responses that can result in discomfort or even damage. Regular identification of modal parameters and analysis of their variation can support the assessment of structural performance and integrity.

Since the origin of EMA, testing equipment and data processing algorithms have significantly evolved. EMA is currently a well-established field, based on a sound

theoretical background. An extensive illustration of EMA techniques can be found in a number of books (Ewins 2000, Heylen et al. 1998, Maia et al. 1997) widely adopted as references by the scientific and technical community.

EMA has been applied in different fields, such as automotive engineering, aerospace engineering, industrial machinery, and civil engineering. The identification of the modal parameters by EMA techniques becomes more challenging in the case of civil engineering structures because of their large size and low frequency range. The application of controlled and measurable excitation is often a complex task that requires expensive and heavy devices. For this reason the community of civil engineers has more recently focused the attention on the opportunities provided by *Operational Modal Analysis* (OMA). OMA can be defined as the modal testing procedure that allows the experimental estimation of the modal parameters of the structure from measurements of the vibration response only. The idea behind OMA is to take advantage of the natural and freely available excitation due to ambient forces and operational loads (wind, traffic, micro-tremors, etc.) to replace the artificial excitation. So, they are no more considered as disturbance but, on the contrary, they make possible the dynamic identification of large civil structures. Since OMA requires only measurements of the dynamic response of the structure in operational conditions, when it is subjected to the ambient excitation, it is also known under different names, such as ambient vibration modal identification or output-only modal analysis.

Over the years, OMA has evolved as an autonomous discipline. However, most of the OMA methods have been derived from EMA procedures, so they share a common theoretical background with input–output procedures. The main difference is in the formulation of the input, which is known in EMA while it is random and not measured in OMA. Thus, while EMA procedures are developed in a deterministic framework, OMA methods can be seen as their stochastic counterpart.

In the civil engineering field, OMA is very attractive because tests are cheap and fast, and they do not interfere with the normal use of the structure. Moreover, the identified modal parameters are representative of the actual behavior of the structure in its operational conditions, since they refer to levels of vibration actually present in the structure and not to artificially generated vibrations. On the other hand, the low amplitude of vibrations in operational conditions requires very sensitive, low-noise sensors and a high performance measurement chain. Additional limitations come from the assumption about the input, as mentioned, for instance, in Sect. 1.3. Nevertheless, it represents an attractive alternative to input–output modal analysis and it shares with EMA most of the fields of application of modal identification results. In some cases, such as testing of historical structures (where it reduces the invasiveness of tests and the risk of damage) or vibration-based health assessment and monitoring (where the replacement of the artificial excitation with ambient vibrations makes it especially suitable for automation), OMA outperforms EMA, and this justifies its increasing popularity in the civil engineering community.

Research findings and several successful applications of OMA in different fields are documented in a number of Journals and proceedings of international conferences such as the annual IMAC conference (<http://www.sem.org/CONF-IMAC-TOP.asp>) organized by the Society of Experimental Mechanics, or the

biannual ISMA conference (<http://www.isma-isaac.be>) in Leuven (Belgium). The large research activity in the field, focused on both the theoretical basis and the applications of OMA, has motivated the creation, in 2005, of an international conference entirely focused on OMA, the International Operational Modal Analysis Conference (IOMAC). Even if some tutorial and overview papers about OMA have been published over the years, books aimed at explaining the basics of OMA testing to a wide audience are still missing. The present book is intended as a guide through the most relevant theoretical and practical aspects of OMA. It provides an extensive description and discussion about OMA, with the details for software implementation of the most popular data processing methods. Moreover, it provides criteria for the selection of the measurement chain and illustrates how a customized measurement system can be developed by means of programmable hardware. A number of explanatory examples and an outlook on the perspectives of OMA in the field of Structural Health Monitoring (SHM) will help the reader in better understanding the concepts and potentialities of OMA.

Several relevant references are included at the end of each chapter. They provide an overview, albeit partial and subjective, of the scientific literature about OMA. The reader interested in more details about specific topics can find in the list of references a valid support to extend the information reported in the book.

The larger attention devoted to the implementation details with respect to theoretical background and analytical derivations is motivated by the wide variety of potential readers the book is meant to. They include students and academicians who could be interested in developing their own software and systems for study and research purposes. Thus, the focus on implementation details provides a valuable stimulus in approaching the study of OMA. On the other hand, the illustration of relevant aspects of the theoretical background of OMA provides a general framework to acquire the ability and understanding of the techniques. The book is useful also for the nonspecialist or manager to get an insight into the matter, its opportunities, and limitations, and to go beyond that bizarre feeling of a “mysterious black box.”

The additional material accompanying the book (datasets, software) helps the reader in familiarizing with OMA, while the modal analyst can find the tools and the fundamental information to promptly start the modal tests and properly interpret the results. The basic software accompanying the book can also serve to test a number of OMA methods in view of the choice among the different commercial software packages available on the market. Theory, algorithms, and implementation details have been organized by defining some milestones in learning and always with the application in mind. The applicative perspective makes learning easy and the book suitable for a wide range of readers.

---

## 1.2 Preliminary Concepts

A preliminary, brief discussion about signals and systems is definitely useful to clarify the general context of application of the concepts illustrated in this book and to set some nomenclature. The summarized notions about signals, systems, and

structural dynamics indirectly define the required cultural background to approach the study of OMA. The interested reader can refer to the literature for more details and a more systematic analysis of the herein-reported concepts (see, for instance, Chopra 2000, Ewins 2000, Bendat and Piersol 2000).

A *signal* is any physical quantity varying with respect to one or more independent variables and associated to information of interest. A *system* converts an input signal into an output signal. Mapping the response to a given stimulus reveals important information about the system. For instance, the analysis of swinging of a building (output signal) under wind load (input signal) makes possible the identification of the dynamic characteristics of the building.

Typical engineering problems are in the form of *forward problems*. For instance, they aim at estimating the response of a known system to a given input. However, attention is herein focused on *inverse problems*, where the output is known but either the input or the system characteristics are unknown. In particular, attention is focused on the identification of the characteristics of the system when the output signal is known (and some assumptions are made about the input).

The term *noise* refers to any undesired signal superimposed on the signal of interest. The amount of noise in a signal is quantified by the signal-to-noise ratio (SNR), expressed in dB as follows:

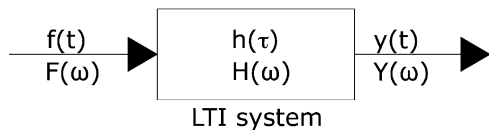
$$SNR = 20\log\left(\frac{A_s}{A_n}\right) \quad (1.1)$$

where  $A_s$  and  $A_n$  denote the signal amplitude and the noise amplitude (expressed in the same units), respectively. When the SNR is low, the signal of interest can become indistinguishable. Thus, appropriate data acquisition strategies must be adopted to minimize the level of noise that inevitably affects measurements (Chap. 3).

Complex signals may be decomposed into elemental signals. Examples of elemental signals are the impulse and the sinusoid. When the signal is decomposed into scaled and shifted impulses, a time domain analysis takes place; if, instead, the signal is decomposed into scaled sinusoids of different frequency, analysis is carried out in the frequency domain. It is always possible to convert a signal from one domain to the other, so the final choice is usually dictated by considerations about computational efficiency, ease of data interpretation, and noise reduction techniques.

The dynamic behavior of physical systems is often described by defining an ideal *constant-parameter linear system* (also known as linear time-invariant—LTI—system, Fig. 1.1). A system is characterized by constant parameters if all its fundamental properties are invariant with respect to time. Moreover, it shows a linear mapping between input and output if the response characteristics are additive and homogeneous. As a result, the response of the system to a linear combination of given inputs equals the same linear combination of the system responses to the individual, separately analyzed inputs. The constant-parameter assumption is reasonably valid for several physical systems encountered in the practice. However, its validity depends on the extension of the considered time interval. For large

**Fig. 1.1** Schematic illustration of LTI system



observation periods it could be not realistic. This is the case, for instance, of structures subjected to continual vibrations, where fatigue damage can cause a change in the stiffness of the structure. The time intervals of practical interests for the output-only modal testing are such that it is possible to consider the structure as time invariant. The validity of the linearity assumption for real structures depends not only on the characteristics of the structure, but also on the magnitude of the input. Physical systems typically show nonlinear response characteristics when the magnitude of the applied load is large. Moreover, nonlinearities are often not associated to abrupt changes in the response; the presence of a transition makes the problem even more complex. However, for the applications of our interest, the response of many structures can be reasonably assumed to be linear, since ambient excitation yields small amplitude vibrations.

From a general point of view, the dynamics of a civil structure, like any mechanical system, can be described in terms of its mass, stiffness, and damping properties, or in terms of its vibration properties (natural frequencies, damping ratios, and mode shapes) or in terms of its response to a standard excitation.

The first approach is usually adopted when a FE model of the structure is set.

The dynamic properties of structures describe their free vibration response (when no force or acceleration is applied) or, in other words, the ways in which they “naturally” vibrate. In fact, under certain assumptions, the dynamic response of the structure can be decomposed into a set of vibration modes, each one with a characteristic deflected shape of its own: the mode shape. The corresponding natural frequency and damping ratio govern the motion of the structure according to one of these shapes. Natural frequencies and mode shapes can be obtained from the mass and stiffness properties of the structure through the solution of an eigenproblem. Under the assumption of proportional viscous damping, the modes of the damped structure coincide with those of the undamped structure. Thus, it is possible to compute the real eigenvalues and eigenvectors (associated with the natural frequencies and the mode shapes) of the system without damping and, in a second stage, apply a correction to the modal responses to account for the effect of damping.

It is worth pointing out that, while the eigenfrequencies of undamped or proportionally damped systems are univocally determined, the eigenvectors are not. In fact, the eigenproblem leaves the scaling factor undetermined. However, it affects only the amplitude, while the shape (that is to say, the relative values of the components of the mode shape vector) remains unchanged. For this reason, conventional scaling procedures are usually adopted to normalize the mode shape vectors. A frequently adopted scaling scheme is based on the orthogonality of natural modes with respect to the mass and stiffness matrices of the structure. The pre- and post-multiplication of those matrices by the modal matrix  $[\Phi]$ ,

which collects the mode shape vectors in columns, yield the following diagonal matrices:

$$[\Phi]^T [M] [\Phi] = \begin{bmatrix} & & \\ & \ddots & \\ & & m_r & \\ & & & \ddots \end{bmatrix} \quad (1.2)$$

$$[\Phi]^T [K] [\Phi] = \begin{bmatrix} & & \\ & \ddots & \\ & & k_r & \\ & & & \ddots \end{bmatrix} \quad (1.3)$$

Thus, it is possible to normalize the mode shape vectors in a way that the matrix of (1.2) equals the identity matrix. According to this scaling scheme, the elements on the main diagonal of the matrix of (1.3) correspond to the eigenvalues. The relationship between the mass normalized mode shape  $\{\psi_r\}$  and the unscaled one  $\{\phi_r\}$  for the r-th mode is:

$$\{\psi_r\} = \frac{1}{\sqrt{m_r}} \{\phi_r\} \quad (1.4)$$

where:

$$m_r = \{\phi_r\}^T [M] \{\phi_r\} \quad (1.5)$$

is also called *modal mass*.

In the more general case of nonproportional viscous damping, the free vibration solution is determined from a complex eigenproblem. The obtained eigenvalues as well as the corresponding complex-valued eigenvectors are in complex conjugate pairs. In practical applications of OMA, real-valued mode shapes are typically identified, but complex mode shapes are sometimes estimated, too. Complex mode shape vectors can be the result of nonproportional damping or other causes, so it is important to recognize whether they are physical or not. More details are reported in Chap. 4.

Other descriptors of the dynamics of constant-parameter linear systems are defined in terms of their response to “standard” excitations. When the excitation is represented by a unit impulse input, the dynamics of the system can be described by its *impulse response function* (IRF). When the excitation is a unit-amplitude sinusoidal force applied at every frequency in a given range, another descriptor is obtained: it is the so-called *frequency response function* (FRF) defined over the considered range of frequency. As with the modal parameters, FRFs and IRFs are univocally determined from the mass, damping, and stiffness properties of the structure. Moreover, they can also be expressed in terms of modal parameters (Chap. 4). Even if each conversion from one model to

the other is theoretically reversible (for instance, it is possible to compute the modal properties from the mass, stiffness, and damping matrices, and vice versa), in the case of experimental investigations only a limited subset of points of the structure are measured, and not all the modes are identified. The incomplete information has serious consequences on the possibility to reconstruct the mass, damping, and stiffness matrices from the results of modal testing.

Consider for simplicity a *Single Degree of Freedom* (SDOF) system, that is to say a system whose dynamic response is described by a single displacement parameter, as opposed to *Multi Degree of Freedom* (MDOF) systems, where the displaced positions of all masses with respect to their initial configuration are described by a number of independent displacement parameters (degrees of freedom—DOFs). The following concepts can be easily extended to general MDOF systems by appropriate matrix notation. For any arbitrary input  $f(t)$ , the output of the SDOF system is given by the following convolution integral of the IRF  $h(\tau)$  with the input:

$$y(t) = \int_0^{\infty} h(\tau)f(t - \tau)d\tau. \quad (1.6)$$

The lower limit of integration is zero since the LTI system has been assumed to be *physically realizable (causal)*, that is to say, it responds only to past inputs. The assumption of causality, in fact, implies that:

$$h(\tau) = 0 \quad \forall \tau < 0. \quad (1.7)$$

A LTI system is also *stable* if every bounded input function  $f(t)$  produces a bounded output  $y(t)$ .

Alternatively, a physically realizable and stable LTI system can be described by the FRF  $H(\omega)$ . The convolution integral of (1.6) reduces to a simple multiplication when it is expressed in terms of the FRF and the Fourier transforms of the input— $F(\omega)$ —and the output— $Y(\omega)$ —(see also Chap. 2):

$$Y(\omega) = H(\omega)F(\omega). \quad (1.8)$$

A LTI system cannot cause any frequency translation. It can only modify the amplitude and phase of the applied input. Its FRF is a function of the sole frequency, while it is not function of either time or system excitation.

From the experimental point of view, FRFs are estimated by forced vibration tests. Depending on the number of applied inputs and the number of measured outputs, four types of testing scheme can be identified: Single Input Single Output (SISO), Single Input Multiple Output (SIMO), Multiple Input Single Output (MISO), Multiple Input Multiple Output (MIMO). The output-only modal tests, which represent the subject of this book, are always of the MIMO type because of the assumptions about the input (see also Chap. 4).

### 1.3 Fundamental Principle and Applications of OMA

OMA aims at estimating the dynamic properties of LTI systems from records of their dynamic response only. Thus, the unknown environmental and operational loads play a fundamental role in testing and in the subsequent modal analysis. If, on one hand, the environmental excitation is advantageous when large civil structures are tested, on the other hand data acquisition and, above all, data processing require supplemental attention to carry out successful output-only modal tests. In fact, since the input is unmeasured, some characteristics of the excitation can be erroneously confused with dynamic properties of the structure under test. Moreover, since the test engineer has no control on the applied excitation, the identification of closely spaced modes can be a more difficult task with respect to EMA. Specific actions and functional checks are needed to ensure that good quality information about closely spaced modes can be extracted from the measured data. For instance, this objective can be achieved by ensuring a sufficient amount of independent information in the data. In Chapter 4 it is shown that the output power spectral density (PSD) matrix can be expressed in terms of the FRF matrix of the structure and the input PSD matrix (4.12). As a consequence, its rank (defining the number of independent rows or columns in the matrix) cannot be larger than the rank of the individual matrices appearing in the product. This implies that closely spaced modes cannot be estimated if the rank of the input PSD matrix is equal to one. This happens when only one input is present, or the inputs are fully correlated. It can be also the case when free decay data are used for output-only modal identification. In fact, in this case multiple sets of initial conditions are needed to handle closely spaced modes, since multi-output measurements with respect to a single set of initial conditions are equivalent to a SIMO scheme (Zhang et al. 2005).

Rank deficiency over a limited frequency band in the proximity of the considered closely spaced modes can partially hide the actual physical properties of the structure (for instance, by revealing only one of the modes, or a combination of the two modes). Thus, a proper design of sensor layout and a preliminary evaluation of the sources of excitation acting on the structure in its operational conditions play a primary role in ensuring the possibility to obtain high quality information from modal testing. As a general rule, a large number of sensors allow maximizing the rank of the FRF matrix, while several uncorrelated inputs ensure the maximization of the rank of the input PSD matrix. On the contrary, correlated inputs or input applied in a single point limit the rank of the input PSD matrix; sensors placed in nodes of the mode shapes or multiple sensors measuring the same DOF (thus, adding no new independent information) limit the rank of the FRF matrix. Some recommendations for the definition of sensor layout for recurrent typologies of civil structures are reported in Chap. 3. About the input, moving loads acting on the structure or environmental loads, such as wind and traffic, force the rank of the input PSD matrix to values larger than one.

Despite of the differences in terms of excitation, output-only modal testing consists of the same three basic steps encountered in classical input–output testing:

- Planning and execution of tests: this step concerns the definition of the experimental setup (measurement chain, sensor layout, attachment of sensors, cable paths, etc.) and the data acquisition parameters (duration of records, sampling frequency).
- Data processing and identification of the modal parameters: this step concerns the validation and pre-treatment (filtering, decimation, etc.) of the acquired data, some signal processing operations (for instance, for the computation of correlation functions, PSD functions, random decrement functions, transmissibility functions, etc.), and the estimation of the modal parameters.
- Validation of the modal parameter estimates.

The estimated modal parameters are usually not the final objective of the test. In fact, they are often used as input or reference for a number of applications. Model updating (Friswell and Mottershead 1995, Ewins 2000) is probably the most common. The modal parameter estimates provided by FE models are often not fully reliable, due to inaccuracies related to discretization and model setting. As a result, the numerical model is typically not representative of the actual dynamic behavior of the structure and a correction is needed to make it more adherent to the experimental observations. The correction is based on the evaluation of the correlation between experimental and numerical estimates of the modal properties and on a guided refinement of the model, so that, after the update, it can more reliably predict the dynamic behavior of the structure. The validation or, eventually, the calibration of the model ensure a more accurate prediction of the structural response to complex excitations and a more reliable evaluation of the effects of hazardous natural or manmade events. Another typical application of the updated model is damage detection (see, for instance, Teughels and De Roeck 2004).

The identified modal parameters are sometimes used for troubleshooting. A typical example consists in the assessment of the cause of excessive vibrations. In this case, the estimated modal parameters can be used also for sensitivity analyses (Ewins 2000) and structural modification. In fact, they allow predicting the effects of structural modifications and evaluating a variety of solutions for the vibration problem without incurring in the high costs usually associated to actual interventions. Assuming that the structural modifications are sufficiently small, a linear sensitivity analysis makes possible the identification of the most sensitive parts of the structure for the application of the structural modification and the solution of the vibration problem.

A relevant field of application of the identified modal parameters is damage detection and SHM. Vibration-based damage detection relies on the changes in the dynamic properties of the structure caused by damage. Thus, given reference estimates of the modal parameters of the structure in healthy conditions, the integrity of the structure can be assessed, in principle, by comparing the subsequent modal parameter estimates with the reference ones. The vibration-based damage assessment of structures has received a considerable attention in the last few decades, with the development of methods not only to detect the presence of

damage, but also to localize and quantify it. An extensive review about these techniques is available in the literature (Doebling et al. 1996, Sohn et al. 2003, Farrar and Worden 2013). The main drawback of damage detection techniques based on the analysis of the changes in the estimated modal properties is related to the influence of boundary conditions and operational and environmental factors on the estimates. Such an influence can produce changes in the modal parameter estimates that are of the same order of magnitude as those due to damage. However, in recent years a number of techniques able to remove the influence of environmental factors on modal parameter estimates have been developed (see, for instance, Deraemaeker et al. 2008, Magalhaes et al. 2012), thus raising a renewed interest towards vibration-based damage detection. Another relevant limitation to the extensive application of these damage detection techniques was the lack of fully automated procedures for the estimation of the modal parameters of the monitored structure. This issue has determined large research efforts in the last few years to develop reliable and robust automated OMA techniques. This topic is extensively discussed in Chap. 6.

An application of modal parameter estimates somehow related to vibration-based SHM and to inherent limitations of OMA techniques is represented by the estimation of the modal masses or, equivalently, the scaling factors of mode shapes. In fact, since the input is not measured, only unscaled mode shapes can be obtained from operational modal testing. For this reason, specific techniques for the estimation of the scaling factors, based on the application of known structural modifications, have been developed. This topic is discussed in Chap. 5. The estimation of the scaling factors makes possible, among the rest, the reconstruction of the FRF matrix from the experimental results and the application of a specific class of damage detection techniques (see, for instance, Doebling et al. 1998, Pandey and Biswas 1994).

Additional applications concern load identification. In this case, the known modal parameters are used to solve an inverse problem for the identification of the unknown forces that produced a given measured response (Parloo et al. 2003).

---

## 1.4 Organization of the Book

The wide range of applications and the increasing demand for output-only modal testing in the current civil engineering practice justify the increasing attention and the large research efforts in the field of OMA observed in the last decade. The present book has been conceived and prepared in order to transfer the OMA concepts from academy to practice and foster the attraction of young students and researchers to this discipline. For this reason, it is organized in clearly defined learning steps covering the required interdisciplinary notions to train a thorough and effective modal analyst. The topics discussed in the book encompass the fundamental theoretical notions, the criteria for proper measurement execution, and the methods and criteria for an appropriate and detailed data analysis. The integration of those three components is the key for a full exploitation of the potentialities of OMA. The importance of mixing

all the necessary theoretical and practical skills for a successful modal testing can be easily realized by recognizing, for instance, that a well-trained test engineer must be able to quickly identify anomalies in the measurements and the corresponding possible technical solutions (they sometimes simply consist in the replacement of a faulty connector or in the relocation of one or more sensors). This is possible only if the modal analyst has a sound theoretical basis.

The balance between theoretical and practical aspects of OMA is highlighted by the content of the different chapters. In Chapter 2 the basic notions of random processes and inverse problems are reported. Chapter 3 is focused on the issues related to measurement execution. Chapter 4 discusses the main models of the dynamic behavior of structures, how these models are applied in the context of OMA, the similarities and differences about different OMA methods, and the procedures for post-processing and validation of experimental results.

In the illustration of the fundamental analysis tools (Chap. 2) and the theoretical basis of OMA methods (Chap. 4), heavy mathematical derivations are avoided to focus the attention on the concepts and their practical implications. The attention to the applicative aspects is remarked by the detailed presentation of the algorithms and implementation details of popular OMA methods and by the applications proposed at the end of the next three chapters. The latter, in particular, are aimed at the prompt practical verification of the previously discussed theoretical notions, thus providing a valuable motivation to learning. In most of the proposed applications the reader has two options: he can develop his own systems and software according to the reported algorithms and tutorials, or he can use the basic software accompanying the book. The two options are conceived to fulfill the needs of both academicians and technicians.

Guidelines for the application in the field of the concepts and notions reported in the first chapters can be obtained from the analysis of the case studies discussed in Chap. 5. Finally, Chapter 6 extensively analyzes the latest developments in the field of OMA concerning the automated identification of the modal parameters. At the end of the last two chapters no applications are proposed. The reason is that Chap. 5 already has a practical character, while the topic discussed in Chap. 6 (automated OMA) is very recent. Thus, Chapter 6 basically reports the viewpoint of the authors about the matter, since a wide consensus in the definition of the “best methods” for automated output-only modal identification has not been reached, yet.

At the end of these preliminary notes and before the introduction of the recommended platform for the implementation of the systems and procedures discussed in this book, it is worth remarking two additional aspects concerning the illustration of the topics. The adopted approach consists in making the various topics “as simple as possible but not simpler”. For this reason, heavy mathematical derivations are avoided, providing all the necessary references for the reader interested in more details; however, the mathematical description of concepts and algorithms has been retained to ensure an autonomous learning basis and simplify their practical implementation. The mathematical description of models and methods is also functional to the understanding of the common characters behind different OMA methods. Starting from a number of investigations reported in the

literature, the unifying mathematical framework of the different OMA methods is presented to highlight the similarities, in terms of theoretical background and analysis tools, behind apparently unrelated procedures. Among the unifying concepts of OMA, that of *spatial* (or modal) *filtering* needs to be mentioned for its implications in a number of (both manual and automated) OMA procedures. It consists in the isolation of the contribution of a mode based on the estimate of the corresponding shape. This type of filtering can be applied in the frequency domain as well as in the time domain and it requires a number of measurement channels not lower than the number of active modes in the investigated frequency range. The isolated modal response simplifies the estimation of the corresponding modal parameters. Applications of this concept can be found in Chaps. 4 and 6.

The second and last remark concerns the detailed discussion reported in Chap. 3 about different aspects of measurement execution. Only if the quality of data acquisition is satisfactory the success of the output-only modal identification is guaranteed. On the contrary, there is no data processing method able to solve the problems due to poor data acquisition. In other words, only if the measurement chain is able to resolve the structural response in operational conditions the physical information is present in the data and it can be extracted. Filtering, averaging, and other data processing tools provide a valuable support to put in evidence this information, but they are totally ineffective when the physical information is buried in noise due to an inappropriate choice of the measurement chain. The signal must be improved at the lowest level by careful design of test setup, adequate choice of electronics, and proper isolation. In summary, a good modal analysis always starts from good measurements. Be aware of it!

---

## 1.5 A Platform for Measurement Execution and Data Processing

### 1.5.1 Generalities

The choice of the programming language for software implementation is always personal and depends on the background and skills of the user. The algorithms and systems described in the book can be easily implemented with any programming language where advanced mathematical and data processing tools are available and it is possible to manage the communication with the measurement hardware for data acquisition. Based on the authors' experience, this book recommends the use of LabVIEW ([www.ni.com/labview](http://www.ni.com/labview)) because this was originally developed with the objective of integrating measurement and data processing in a single platform. It is characterized by an advantageous learning curve, which allows a fast and easy development of systems and software, but it is also very powerful and versatile. In fact, advanced functions and analysis tools are available and it makes possible the communication with a large number of commercial devices. An overview of relevant aspects about programming in LabVIEW is given in this section, since all the proposed applications are discussed assuming LabVIEW

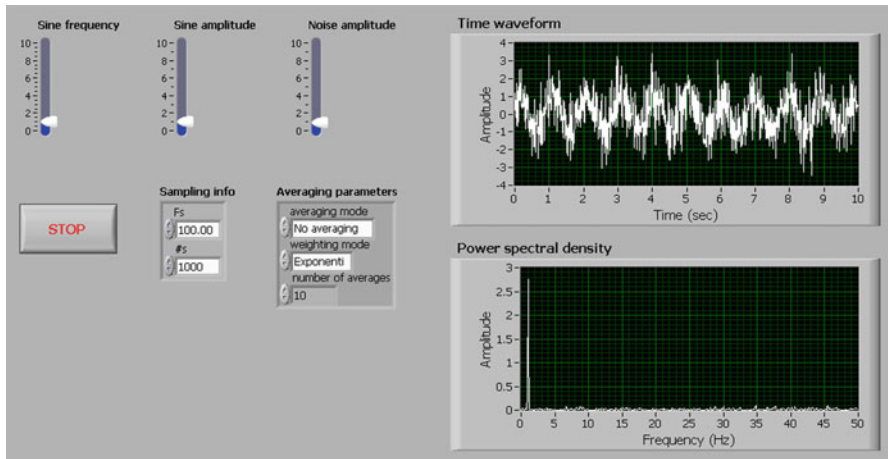


**Fig. 1.2** Front panel

as the common platform for system and software implementation. The choice of the platform for measurement execution and data processing can obviously be different but, for practical reasons, it is impossible to provide a tutorial for every programming language. Nevertheless, since the algorithms are general, any other choice is possible for their implementation, provided that the reader carries out the appropriate language translations.

LabVIEW programs are called Virtual Instruments, or VIs, because their appearance and operation imitate physical instruments, such as oscilloscopes and multimeters. LabVIEW contains a wide set of tools to acquire, analyze, display, and store data, as well as for code troubleshooting (National Instruments 2005a). Programming in LabVIEW requires the design and implementation of a user interface, or Front Panel (Fig. 1.2), with controls and indicators, which are the interactive input and output terminals of the VI, respectively. Figure 1.2 shows a simple VI to analyze the variations of a signal and its spectrum for different amplitudes of its components, a sinusoid and a random signal. The user can interactively set the parameters of the signals by means of the controls.

Several types of controls and indicators are available. Examples of controls are knobs, push buttons, dials, and other input mechanisms. Controls simulate instrument input mechanisms and supply data to the block diagram (Fig. 1.3) of the VI. Examples of indicators are graphs, LEDs, and other output displays. Indicators simulate instrument output mechanisms and display the data acquired or generated by the block diagram. Controls and indicators can handle different types of variables; it is possible to distinguish:

- Numeric controls and indicators, such as slides and knobs, graphs, charts.
- Boolean controls and indicators, such as buttons and switches.
- String, path, array, cluster, enumerated type controls... each one associated to a certain type of data.

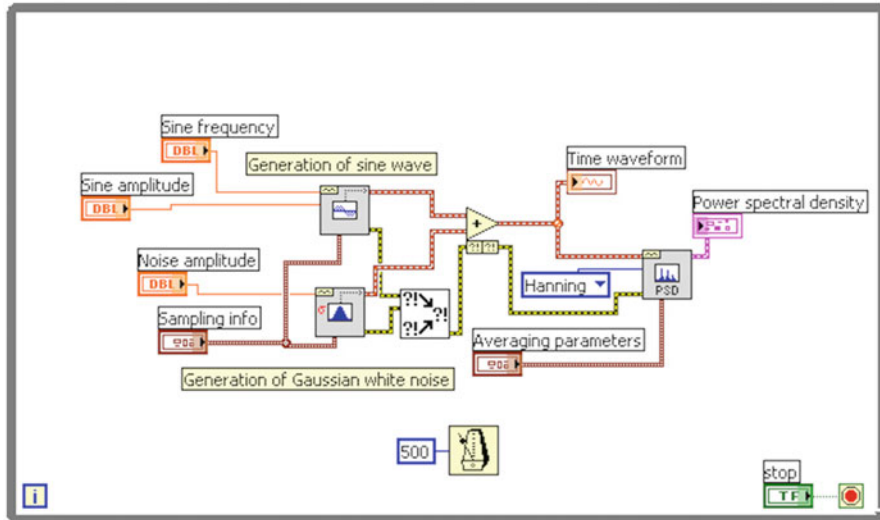


**Fig. 1.3** Block diagram

The management of the user interface is based on the related code developed in the block diagram by using VIs and structures to get the control of the Front Panel objects. Objects in the block diagram include terminals and nodes. Block diagrams are built by connecting the objects with wires. The color and symbol of each terminal indicate the data type of the corresponding control or indicator. Constants are terminals that supply given data values to the block diagram.

An example of code is reported in Fig. 1.3, which shows the block diagram associated to the Front Panel of Fig. 1.2. In this simple example, the management of the user interface is based on a While Loop. The user sets the values of the controls in the Front Panel and they are continuously acquired and sent to the VIs for signal generation. The outputs of these VIs are then combined (added) and used to compute the spectrum of the signal.

LabVIEW can also be used to communicate with hardware such as data acquisition, vision, and motion control devices, as well as GPIB, PXI, VXI, RS232, and RS485 equipment. It can be both National Instruments and third party hardware. Hardware configuration is carried out through a specific interface that is illustrated in Chap. 3 in the context of the proposed application for the development of a dynamic data acquisition system based on programmable hardware.

LabVIEW adopts a dataflow model for the running VIs. A block diagram node executes when it receives all the required inputs. When a node executes, it produces output data that are passed to the next node in the dataflow path. The movement of data through the nodes determines the execution order of the VIs and structures on the block diagram. The main difference between LabVIEW and other programming languages is indeed in the dataflow model. Text-based programming languages typically respond to a control flow model of program execution. In control flow,



**Fig. 1.4** VIs for output-only modal identification (included in the Time Series Analysis Tools)

the sequential order of program elements determines the execution order of the program. In LabVIEW the flow of data rather than the sequential order of commands determines the execution order of block diagram elements. Therefore, it is possible to create block diagrams that have simultaneous operations.

Dataflow execution makes memory management easier than the control flow model of execution. In LabVIEW the user typically does not allocate memory for variables or assign values to them. On the contrary, he defines a block diagram with wires that represent the transition of data. When a VI generates new data, it automatically allocates the memory for those data. When the VI no longer uses the data, LabVIEW de-allocates the associated memory. When new data are added to an array or a string, LabVIEW allocates sufficient additional memory to manage the new data.

### 1.5.2 VIs and Toolkits for Data Processing and System Identification

Many output-only modal identification techniques require the preliminary computation of spectra and correlation functions. Advanced VIs for their estimation from the acquired time series are available in the Signal Processing Palette in LabVIEW. Additional advanced tools for vibration analysis are also available as LabVIEW add-ons, such as the Sound and Vibration Toolkit and the Time Series Analysis Tools in the Advanced Signal processing Toolkit.

The Time Series Analysis Tools, in particular, include several statistical tools of interest for random data analysis. Moreover, they include also some VIs for the output-only modal parameter identification based on polynomial models, state-space models, and least squares estimators (Fig. 1.4). In particular, tools for the estimation of autoregressive (AR) and autoregressive moving average (ARMA) models are available.

A brief introduction about these tools is herein reported for the reader interested in applying such models. However, as discussed in Chap. 4, AR and ARMA models did not reach a level of robustness adequate for the application in the context of OMA of civil engineering structures.

AR and ARMA models allow predicting (even if in the presence of a prediction error) the current value of a time series based on a number of past values. These models can also be used to describe LTI systems and to extract the modal parameters (Chap. 4). From a general point of view, the estimation of AR and ARMA models requires an appropriate selection of the order of the polynomial. It is obvious that the higher the model order, the better the model fits the time series, because a high-order

model has more degrees of freedom. However, an overestimated order can introduce spurious artifacts not related to the physics of the observed system. As a result, a number of criteria for selection of the order have been developed over the years. They take into account the model-fitting error associated to a certain choice of the order but they also incorporate a penalty when the order increases. Many of those criteria (Akaike's Information Criterion, Bayesian Information Criterion, Final Prediction Error Criterion, Minimal Description Length Criterion, Phi Criterion), differing only for the way the penalty is evaluated, are available in the Time Series Analysis Tools of the Advanced Signal Processing Toolkit. More details about the VIs in the Toolkit and their applications can be found in the related user manual (National Instruments 2005b).

The additional toolkits can simplify the implementation of the algorithms discussed in this book, but they are not critical and their use can be avoided with no large penalties. In fact, all the necessary tools for the implementation of OMA algorithms are already present in LabVIEW. They include, among the others, linear algebra tools, tools for probability and statistics, curve fitting tools, tools for polynomial analysis, tools for filtering and signal processing. In the application of these tools, the analysis of the related documentation, such as the LabVIEW Analysis Concepts (National Instruments 2004), is recommended to avoid possible mistakes in the interpretation of input settings, outputs, and mode of operation. Moreover, the analysis of the above mentioned documentation might disclose functionalities that cannot be immediately recognized by the user.

### 1.5.3 Recurrent Structures for Software Development

An effective software development in LabVIEW starts from the implementation of a main VI and several subVIs organized in a hierarchical structure (Fig. 1.5). Each subVI has to perform specific and usually very limited tasks. This approach to software implementation based on the definition of a VI hierarchy is recommended to take advantage of the opportunities of dataflow and to make the code understandable to third parties or after long time. Moreover, even in the presence of a well-defined sequence of operations, it is advantageous to make use of structures for the management of the interactions with the user. The simplest example is represented by the While Loop structure presented in Sect. 1.5.1. Shift registers (Fig. 1.6) are typically used to preserve data between subsequent iterations. In other words, shift registers allow sending values from previous iterations to the next.

Loops are not the only possibility to manage user interaction. There are also other, more advanced structures that can fit specific needs, such as the management of parallel operations (for instance, data acquisition and data processing) or the execution of some operations depending on given conditions. They are also available in the form of design patterns. *Design patterns* are standard templates for software implementation that have been developed over the years by the LabVIEW community. Since they represent solutions to common problems in software implementation, they can be profitably used as the basis to develop a large number of applications.

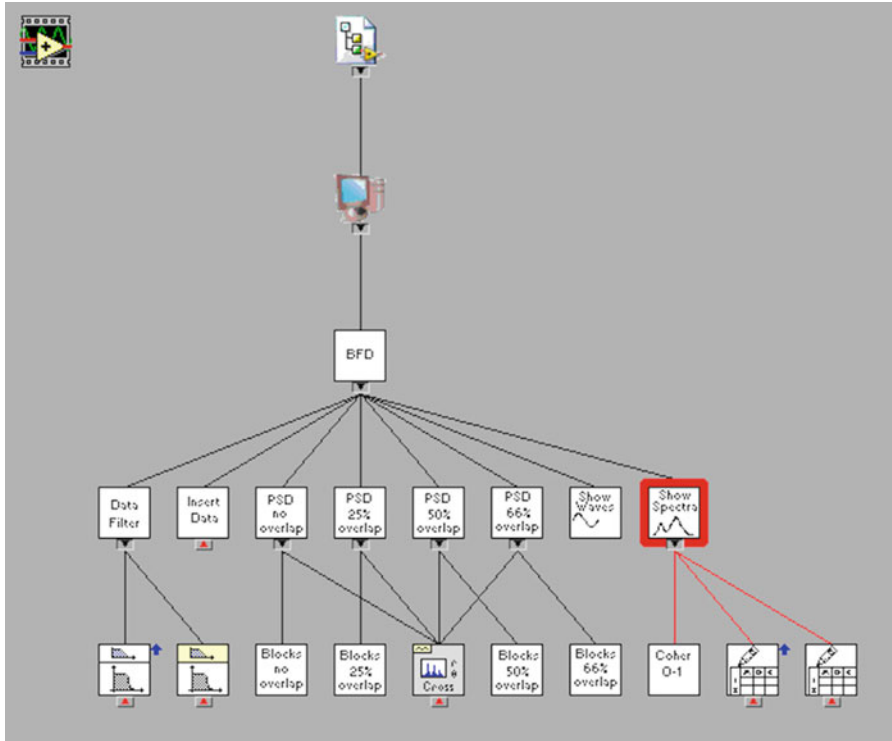


**Fig. 1.5** Sample VI hierarchy

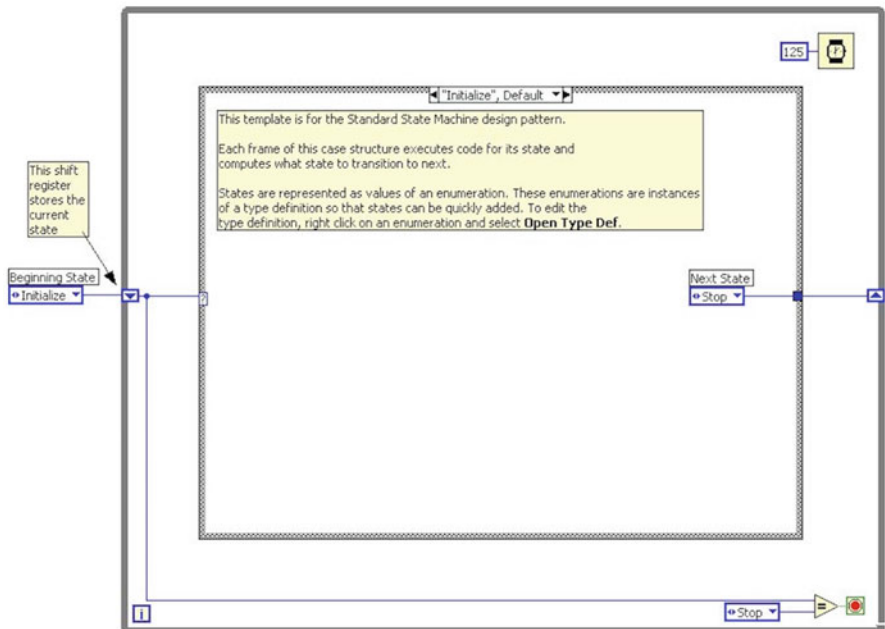


**Fig. 1.6** State machine

The *State Machine* (Fig. 1.6) is one of these fundamental architectures. It allows the execution of different sections of code (states) in an order that can be determined in several different ways. Thus, it can be used to implement complex decision-making algorithms represented by flowcharts.

State Machines are used in applications where distinguishable states exist. An initialization phase is sometimes needed. State Machines perform a specific action for each state in the diagram. Each state can lead to one or multiple states, or end the process. The user input or results of computations in the running state determine the next state. This is the reason why they are commonly adopted to manage the user interactions. Different user inputs lead to different processing segments. Each of these segments represents one of the states in the State Machine.

Since each state in a State Machine carries out a specific action and calls the next state, this architecture requires the definition of some conditions. Thus, the common elements in a State Machine architecture are: the While Loop, which continually executes the various states, the Case Structure, containing the code associated to a certain state, the shift register and the transition code, which determines the next state in the sequence (Fig. 1.6).

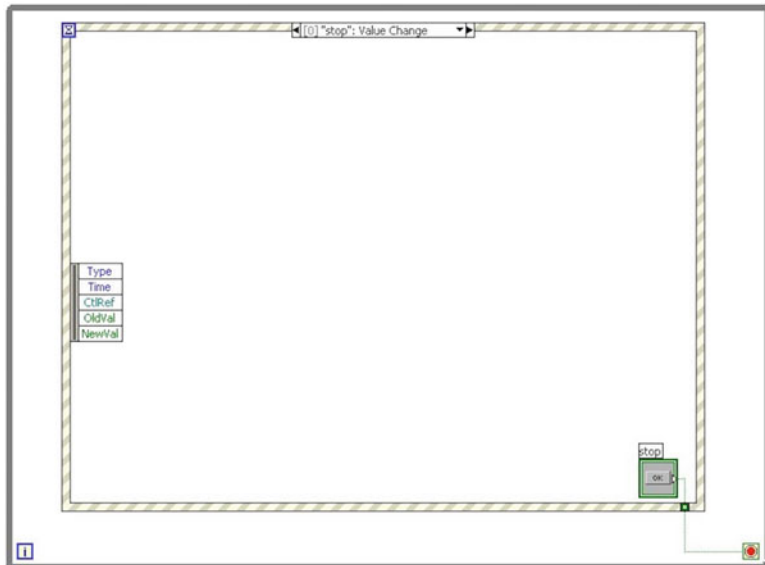
Another design pattern commonly used to interact with user input via the front panel is the *Event structure*.

Events are caused by actions of the user (for instance, a click of the mouse). In this case the execution of the code is governed by the occurring events. In an event-driven program, the program first waits for events to occur, responds to those events, then returns to waiting for the next event. How the program responds depends on the code implemented for that specific event. The order in which an event-driven program executes depends on which events occur and on the order in which those events occur. While the program waits for the next event, it frees up CPU resources that might be used to perform other processing tasks.

In LabVIEW, the Event structure (Fig. 1.7) allows handling events in an application. Multiple cases can be added to the Event structure and configured to handle one or more events. Configuration of the events is easy. It is sufficient to right-click the Event structure border and select Edit Events Handled by This Case from the shortcut menu. The Edit Events dialog box appears (Fig. 1.8) and it is possible to configure the event.

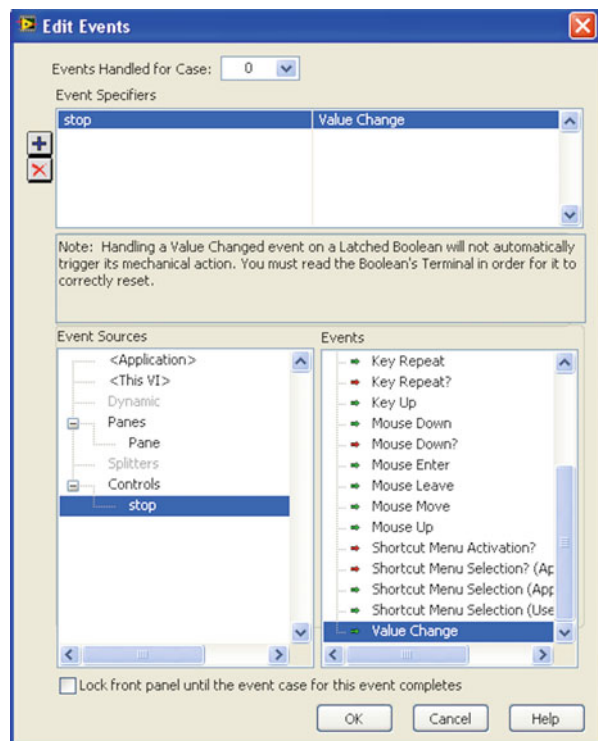
The Event structure waits until an event happens, then it executes the VI in the case associated to that event. Using the Event structure minimizes the CPU usage because the VI does not continually poll the Front Panel for changes, as in the case of the While Loop structure. In contrast to polling, the Event structure does not lose user events. In fact, events are stored in a queue and processed in the order in which they occur.

The execution of parallel operations is slightly more complex and requires specific structures. The *Producer/Consumer architecture* (Fig. 1.9) is a commonly adopted design pattern for the development of data acquisition and data logging systems. It consists of two parallel loops, where the first loop produces data and the other consumes those data. Data queues are used to communicate data between the loops. The queues ensure data buffering between producer and consumer loops.



**Fig. 1.7** Event structure

**Fig. 1.8** The edit events dialog box



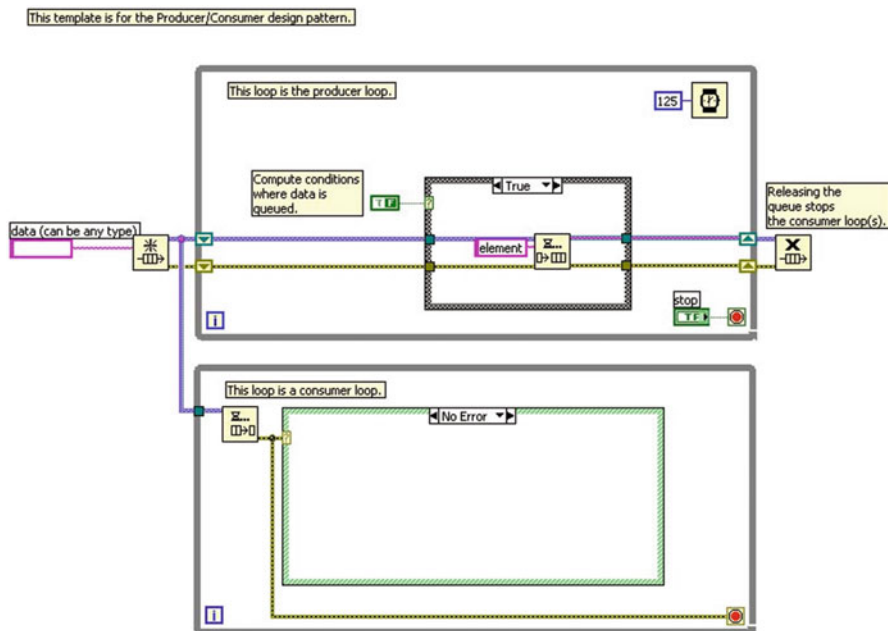


**Fig. 1.9** Producer/consumer

The typical use of the Producer/Consumer pattern is for applications acquiring multiple sets of data to be processed in order and in parallel (that is to say, with no influence of the consumer on the producer cycle). In fact, since data are queued, the Producer/Consumer pattern gives the possibility to handle multiple processes at the same time while iterating at individual rates. The buffered communication makes this architecture very effective for data acquisition. In fact, it is possible to develop an application carrying out data acquisition and data processing at the same time. The first cycle performs data acquisition while the second processes the data at an eventually lower speed.

The use of the previously described structures and design patterns is recommended for many of the applications proposed at the end of the next chapters. More details and sample applications of design patterns are available on the Internet (zone.ni.com) and in the LabVIEW Context Help.

## References

- Bendat JS, Piersol AG (2000) Random data: analysis and measurement procedures, 3rd edn. Wiley, New York
- Chopra AK (2000) Dynamics of structures—theory and applications to earthquake engineering, 2nd edn. Prentice Hall, Upper Saddle River, NJ
- Deraemaeker A, Reynders E, De Roeck G, Kullaa J (2008) Vibration-based structural health monitoring using output-only measurements under changing environment. *Mech Syst Signal Proc* 22:34–56

- Doebling SW, Farrar CR, Prime MB, Shevitz DW (1996) Damage identification and health monitoring of structural and mechanical systems from changes in their vibration characteristics: a literature review, Technical Report LA-13070-MS, UC-900. Los Alamos National Laboratory, New Mexico
- Doebling SW, Farrar CR, Prime MB (1998) A summary review of vibration-based damage identification methods. *Shock Vib Dig* 30(2):91–105
- Ewins DJ (2000) Modal testing: theory, practice and application, 2nd edn. Research Studies Press Ltd., Baldock
- Farrar CR, Worden K (2013) Structural health monitoring: a machine learning perspective. Wiley, Chichester
- Friswell MI, Mottershead JE (1995) Finite element model updating in structural dynamics. Kluwer, Dordrecht
- Heylen W, Lammens S, Sas P (1998) Modal analysis theory and testing. Katholieke Universiteit Leuven, Leuven
- Magalhaes F, Cunha A, Caetano E (2012) Vibration based structural health monitoring of an arch bridge: from automated OMA to damage detection. *Mech Syst Signal Proces* 28:212–228
- Maia NMM, Silva JMM, He J, Lieven NAJ, Lin RM, Skingle GW, To W-M, Urueira APV (1997) Theoretical and experimental modal analysis. Research Studies Press, Taunton
- National Instruments (2004) LabVIEW analysis concepts. National Instruments Corporation, Austin
- National Instruments (2005a) LabVIEW fundamentals. National Instruments Corporation, Austin
- National Instruments (2005b) LabVIEW advanced signal processing toolkit—time series analysis tools user manual. National Instruments Corporation, Austin
- Pandey AK, Biswas M (1994) Damage detection in structures using changes in flexibility. *J Sound Vib* 169:3–17
- Parloo E, Verboven P, Guillaume P, Van Overmeire M (2003) Force identification by means of in-operation modal models. *J Sound Vib* 262:161–173
- Sohn H, Farrar CR, Hemez FM, Shunk DD, Stinemates DW, Nadler BR (2003) A review of structural health monitoring literature: 1996–2001. Technical Report LA-13976-MS, UC-900, Los Alamos National Laboratory, New Mexico
- Teughels A, De Roeck G (2004) Structural damage identification of the highway bridge Z24 by FE model updating. *J Sound Vib* 278:589–610
- Zhang L, Brincker R, Andersen P (2005) An overview of operational modal analysis: major development and issues. In: Proc 1st International Operational Modal Analysis Conference, Copenhagen

## 2.1 Complex Numbers, Euler's Identities, and Fourier Transform

Sinusoidal signals are frequently used in signal processing and system analysis. In fact, sines and cosines are orthogonal functions and form a base for the analysis of signals. Moreover, they are eigenfunctions for LTI systems. However, in order to simplify operations and mathematical manipulations, sinusoidal signals are often expressed by complex numbers and exponential functions.

Consider a sinusoidal function characterized by amplitude  $M > 0$ , frequency  $\omega$  and phase angle  $\varphi$ :

$$y(t) = M \cos(\omega \cdot t - \varphi) \quad (2.1)$$

Taking advantage of the Euler's formulas:

$$e^{iX} = \cos(X) + i \cdot \sin(X) \quad (2.2)$$

$$e^{-iX} = \cos(X) - i \cdot \sin(X) \quad (2.3)$$

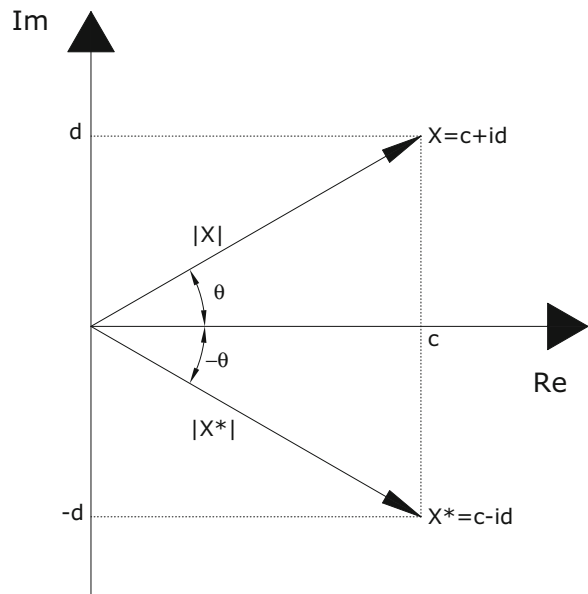
$$\cos(X) = \frac{e^{iX} + e^{-iX}}{2} \quad (2.4)$$

$$\sin(X) = \frac{e^{iX} - e^{-iX}}{2i} \quad (2.5)$$

where  $i$  is the imaginary unit ( $i^2 = -1$ ),  $y(t)$  can be rewritten in terms of complex exponentials:

$$y(t) = \frac{M}{2} e^{i(\omega \cdot t - \varphi)} + \frac{M}{2} e^{-i(\omega \cdot t - \varphi)} \quad (2.6)$$

**Fig. 2.1** Graphical representation of a complex number and its conjugate



The representation in terms of complex numbers and exponential functions has several advantages. First of all, the representation in terms of exponential functions simplifies computations and analytical derivations. In fact, they convert product into sum (2.7) and power into product (2.8), and the derivative of an exponential function is the function itself multiplied by a factor (2.9).

$$e^a \cdot e^b = e^{a+b} \quad (2.7)$$

$$(e^a)^b = e^{a \cdot b} \quad (2.8)$$

$$\frac{d(e^a)}{db} = \frac{da}{db} e^a \quad (2.9)$$

Moreover, the graphical representation of complex numbers  $c + id$  in rectangular (2.10) and polar coordinates (2.11) gives different opportunities to analyze the data and recover the information they hold. In Fig. 2.1 the complex number  $c + id$  and its conjugate  $c - id$  are represented in the complex plane. Taking into account the relation ((2.10) and (2.11)) between the amplitude ( $r$ ) and phase ( $\theta$ ) in polar coordinates on one hand and the real ( $c$ ) and imaginary ( $d$ ) part in rectangular coordinates on the other, it can be noted that the complex conjugate has the same amplitude of the original complex number but opposite phase.

$$(c, d) = (r \cos \theta, r \sin \theta) \quad (2.10)$$

$$(r, \theta) = \left( \sqrt{c^2 + d^2}, \arctan \frac{d}{c} \right) \quad (2.11)$$

On the other hand, algebraic operations with complex numbers lead to operations with real numbers taking into account that  $i^2 = -1$ , treating complex number as polynomials and multiplying numerator and denominator by the complex conjugate of the denominator in the division:

$$(c + id) + (e + if) = (c + e) + i(d + f) \quad (2.12)$$

$$(c + id) \cdot (e + if) = (c \cdot e - d \cdot f) + i(c \cdot f + d \cdot e) \quad (2.13)$$

$$\frac{(c + id)}{(e + if)} = \frac{(c + id)(e - if)}{(e + if)(e - if)} = \frac{(c + id)(e - if)}{e^2 + f^2} \quad (2.14)$$

Operations with complex numbers satisfy the commutative, associative, and distributive rules.

The idea behind the Fourier analysis is that any signal can be decomposed as a linear combination of sinusoidal functions at different frequencies. This can be understood by taking into account the relation between sinusoidal functions and complex exponentials and that both are orthogonal functions, that is to say, they fulfill the following general conditions ((2.15) and (2.16)):

$$\int_a^b f_u(t) f_v^*(t) dt = 0, \quad u \neq v \quad (2.15)$$

$$\int_a^b f_u(t) f_v^*(t) dt \neq 0 < \infty, \quad u = v \quad (2.16)$$

where  $f_u$  and  $f_v$  are complex valued functions and the superscript \* means complex conjugate. In particular, this type of decomposition, originally developed for periodical functions, can be extended to nonperiodic functions, such as transients and random signals, by assuming that they are periodic functions with period equal to the duration  $T$  of the signal. For a nonperiodic signal  $x(t)$ , the (forward) Fourier transform (*analysis equation*: (2.17)) and the inverse Fourier transform (*synthesis equation*: (2.18)) are given by:

$$X(f) = \int_{-\infty}^{+\infty} x(t) e^{-i2\pi ft} dt \quad (2.17)$$

$$x(t) = \int_{-\infty}^{+\infty} X(f) e^{i2\pi ft} df. \quad (2.18)$$

Thus, (2.17) shows that any signal  $x(t)$  can be decomposed in a sum (represented by the integral) of sinusoidal functions (recall the Euler's formula relating complex exponentials and sinusoidal functions, (2.2) and (2.3)). In practical applications,

when the signal  $x(t)$  is recorded and analyzed by means of digital equipment, it is represented by a sequence of values at discrete equidistant time instants. As a consequence, only discrete time and frequency representations are considered, and the expression of the Fourier transform has to be changed accordingly.

First of all, when dealing with discrete signals it is worth noting that the *sampling interval*  $\Delta t$  is the inverse of the *sampling frequency*  $f_s$  (representing the rate by which the analog signal is sampled and digitized):

$$\Delta t = \frac{1}{f_s}. \quad (2.19)$$

In order to properly resolve the signal,  $f_s$  has to be selected so that it is at least twice the highest frequency  $f_{\max}$  in the time signal:

$$f_s \geq 2f_{\max}. \quad (2.20)$$

Moreover, the following “uncertainty principle” holds:

$$\Delta f = \frac{1}{N\Delta t} \quad (2.21)$$

In the presence of a finite number  $N$  of samples, the frequency resolution  $\Delta f$  can only be improved at the expense of the resolution in time  $\Delta t$ , and vice versa. As a consequence, for a given sampling frequency, a small frequency spacing  $\Delta f$  is always the result of a long measuring time  $T$  (large number of samples  $N$ ):

$$T = N\Delta t \quad (2.22)$$

Assuming that the signal  $x(t)$  has been sampled at  $N$  equally spaced time instants and that the time spacing  $\Delta t$  has been properly selected (it satisfies the Shannon’s theorem (2.20)), the obtained discrete signal is given by:

$$x_n = x(n\Delta t) \quad n = 0, 1, 2, \dots, N - 1. \quad (2.23)$$

Taking into account the uncertainty principle expressed by (2.21), the discrete frequency values for the computation of  $X(f)$  are given by:

$$f_k = \frac{k}{T} = \frac{k}{N\Delta t} \quad k = 0, 1, 2, \dots, N - 1 \quad (2.24)$$

and the Fourier coefficients at these discrete frequencies are given by:

$$X_k = \sum_{n=0}^{N-1} x_n e^{-j\frac{2\pi kn}{N}} \quad k = 0, 1, 2, \dots, N - 1. \quad (2.25)$$

The  $X_k$  coefficients are complex numbers and the function defined in (2.25) is often referred to as the *Discrete Fourier Transform* (DFT). Its evaluation requires  $N^2$  operations. As a consequence, in an attempt to reduce the number of operations, the *Fast Fourier Transform* (FFT) algorithm has been developed (Cooley and Tukey 1965). Provided that the number of data points equals a power of 2, the number of operations is reduced to  $N \cdot \log_2 N$ . The inverse DFT is given by:

$$x_n = \frac{1}{N} \sum_{k=0}^{N-1} X_k e^{\frac{i2\pi kn}{N}} \quad n = 0, 1, 2, \dots, N - 1 \quad (2.26)$$

The coefficient  $X_0$  captures the static component of the signal (DC offset). The magnitude of the Fourier coefficient  $X_k$  relates to the magnitude of the sinusoid of frequency  $f_k$  that is contained in the signal with phase  $\theta_k$ :

$$|X_k| = \sqrt{[\operatorname{Re}(X_k)]^2 + [\operatorname{Im}(X_k)]^2} \quad (2.27)$$

$$\theta_k = \arctan\left(\frac{\operatorname{Im}(X_k)}{\operatorname{Re}(X_k)}\right) \quad (2.28)$$

The Fourier transform is a fundamental tool in signal analysis, and it has the following important properties:

- Linearity: given two discrete signals  $x(t)$  and  $y(t)$ , the Fourier transform of any linear combination of the signals is given by the same linear combination of the transformed signals  $X(f)$  and  $Y(f)$ ;
- Time shift: if  $X(f)$  is the Fourier transform of  $x(t)$ , then  $X(f)e^{-i2\pi f t_0}$  is the Fourier transform of  $x(t-t_0)$ ;
- Integration and differentiation: integrating in the time domain corresponds to dividing by  $i2\pi f$  in the frequency domain, differentiating in the time domain to multiplying by  $i2\pi f$  in the frequency domain;
- Convolution: convolution in time domain corresponds to a multiplication in the frequency domain, and vice versa; for instance, the Fourier transform of the following convolution integral:

$$a(t) = \int_{-\infty}^{+\infty} b(\tau) \cdot c(t - \tau) d\tau = b(t)^* c(t) \quad (2.29)$$

is given by:

$$A(f) = B(f) \cdot C(f) \quad (2.30)$$

These last two properties are some of the major reasons for the extensive use of the Fourier transform in signal processing, since complex calculations are transformed into simple multiplications.

## 2.2 Stationary Random Data and Processes

### 2.2.1 Basic Concepts

The observed data representing a physical phenomenon can sometimes be described by an explicit mathematical relationship: in such a case, data are deterministic. The observed free vibration response of a SDOF system under a set of initial conditions is an example of deterministic data, since it is governed by an explicit mathematical expression depending on the mass and stiffness properties of the system. On the contrary, random data cannot be described by explicit mathematical relationships (the exact value at a certain time instant cannot be predicted) and they must be described in probabilistic terms.

A *random* (or *stochastic*) *process* is the collection of all possible physical realizations of the random phenomenon. A *sample function* is a single time history representing the random phenomenon and, as such, is one of its physical realizations. A *sample record* is a sample function observed over a finite time interval; as such, it can be thought as the observed result of a single experiment. In the following, attention is focused on Stationary Random Processes (SRP) and, above all, on the particular category of Stationary and Ergodic Random Processes (SERP).

A collection of sample functions (also called *ensemble*) is needed to characterize a random process. Said  $x_k(t)$  the  $k$ -th function in the ensemble, at a certain time instant  $\bar{t}$  the mean value of the random process can be computed from the instantaneous values of each function in the ensemble at that time as follows:

$$\mu_x(\bar{t}) = \lim_{K \rightarrow \infty} \frac{1}{K} \sum_{k=1}^K x_k(\bar{t}). \quad (2.31)$$

In a similar way the autocorrelation function can be computed by taking the ensemble average of the product of instantaneous values at time instants  $\bar{t}$  and  $\bar{t} + \tau$ :

$$R_{xx}(\bar{t}, \bar{t} + \tau) = \lim_{K \rightarrow \infty} \frac{1}{K} \sum_{k=1}^K x_k(\bar{t})x_k(\bar{t} + \tau). \quad (2.32)$$

Whenever the quantities expressed by (2.31) and (2.32) do not vary when the considered time instant  $\bar{t}$  varies, the random process is said to be (weakly) stationary. For *weakly stationary random processes*, the mean value is independent of the time  $\bar{t}$  and the autocorrelation depends only on the time lag  $\tau$ :

$$\mu_x(\bar{t}) = \mu_x \quad (2.33)$$

$$R_{xx}(\bar{t}, \bar{t} + \tau) = R_{xx}(\tau). \quad (2.34)$$

In the following sections the basic descriptive properties for stationary random records (probability density functions, auto- and cross-correlation functions, auto- and cross-spectral density functions, coherence functions) are briefly discussed,

focusing the attention in particular on ergodic processes. The above-mentioned descriptive properties are, in fact, primary tools of signal analysis. They are commonly used to prepare the data for most OMA techniques.

### 2.2.2 Fundamental Notions of Probability Theory

A preliminary classification of data is based on their probability density function.

For a given random variable  $x$ , the random outcome of the  $k$ -th experiment is a real number and it can be indicated as  $x_k$ . The *probability distribution function*  $P(x)$  provides, for any given value  $x$ , the probability that the  $k$ -th realization of the random variable is not larger than  $x$ :

$$P(x) = \text{prob}[x_k \leq x] \quad (2.35)$$

Moreover, whenever the random variable assumes a continuous range of values, the *probability density function* is defined as follows:

$$p(x) = \lim_{\Delta x \rightarrow 0} \frac{\text{prob}[x < x_k \leq x + \Delta x]}{\Delta x} \quad (2.36)$$

The probability density function and the probability distribution function show the following properties:

$$p(x) \geq 0 \quad (2.37)$$

$$\int_{-\infty}^{+\infty} p(x) dx = 1 \quad (2.38)$$

$$P(x) = \int_{-\infty}^x p(\zeta) d\zeta \quad (2.39)$$

$$P(a) \leq P(b) \quad \text{if } a \leq b \quad (2.40)$$

$$P(-\infty) = 0, \quad P(+\infty) = 1 \quad (2.41)$$

In a similar way, in the presence of two random variables  $x$  and  $y$ , it is possible to define the *joint probability distribution function*:

$$P(x, y) = \text{prob}[x_k \leq x \text{ and } y_k \leq y] \quad (2.42)$$

and the *joint probability density function*:

$$p(x, y) = \lim_{\substack{\Delta x \rightarrow 0 \\ \Delta y \rightarrow 0}} \frac{\text{prob}[x < x_k \leq x + \Delta x \text{ and } y < y_k \leq y + \Delta y]}{\Delta x \Delta y} \quad (2.43)$$

The probability density functions of the individual random variables can be obtained from the joint probability density function as follows:

$$p(x) = \int_{-\infty}^{+\infty} p(x,y)dy \quad (2.44)$$

$$p(y) = \int_{-\infty}^{+\infty} p(x,y)dx \quad (2.45)$$

If the following condition holds:

$$p(x,y) = p(x)p(y) \quad (2.46)$$

the two random variables are *statistically independent*; for statistically independent variables it also follows that:

$$P(x,y) = P(x)P(y) \quad (2.47)$$

When a random variable assumes values in the range  $(-\infty, +\infty)$ , its mean value (or expected value) can be computed from the product of each value with its probability of occurrence as follows:

$$E[x_k] = \int_{-\infty}^{+\infty} xp(x)dx = \mu_x. \quad (2.48)$$

In a similar way it is possible to define the *mean square value* as:

$$E[x_k^2] = \int_{-\infty}^{+\infty} x^2 p(x)dx = \psi_x^2 \quad (2.49)$$

and the *variance*:

$$E[(x_k - \mu_x)^2] = \int_{-\infty}^{+\infty} (x - \mu_x)^2 p(x)dx = \psi_x^2 - \mu_x^2 = \sigma_x^2. \quad (2.50)$$

By definition, the *standard deviation*  $\sigma_x$  is the positive square root of the variance, and it is measured in the same units as the mean value.

The covariance function of two random variables is defined as:

$$C_{xy} = E[(x_k - \mu_x)(y_k - \mu_y)] = \int_{-\infty}^{+\infty} \int_{-\infty}^{+\infty} (x_k - \mu_x)(y_k - \mu_y) p(x,y) dx dy. \quad (2.51)$$

Taking into account that the following relation exists between the covariance of the two random variables and their respective standard deviations:

$$|C_{xy}| \leq \sigma_x \sigma_y \quad (2.52)$$

the *correlation coefficient* can be defined as:

$$\rho_{xy} = \frac{C_{xy}}{\sigma_x \sigma_y}. \quad (2.53)$$

It assumes values in the range  $[-1, +1]$ . When it is zero, the two random variables are *uncorrelated*. It is worth noting that, while independent random variables are also uncorrelated, uncorrelated variables are not necessarily independent. However, it is possible to show that, for physically important situations involving two or more normally distributed random variables, being mutually uncorrelated does imply independence (Bendat and Piersol 2000).

Relevant distributions for the analysis of data in view of modal identification are the sine wave distribution and the Gaussian (or normal) distribution.

When a random variable follows a Gaussian distribution, its probability density function is given by:

$$p(x) = \frac{1}{\sigma_x \sqrt{2\pi}} e^{-\frac{(x-\mu_x)^2}{2\sigma_x^2}} \quad (2.54)$$

while its probability distribution function is:

$$P(x) = \frac{1}{\sigma_x \sqrt{2\pi}} \int_{-\infty}^x e^{-\frac{(\zeta-\mu_x)^2}{2\sigma_x^2}} d\zeta \quad (2.55)$$

with  $\mu_x$  and  $\sigma_x$  denoting the mean value and the standard deviation of the random variable, respectively. The Gaussian probability density and distribution functions are often expressed in terms of the standardized variable  $z$ , characterized by zero mean and unit variance:

$$z = \frac{x - \mu_x}{\sigma_x} \quad (2.56)$$

for convenience of plotting and applications. The Gaussian probability density and distribution functions in standardized form are given by:

$$p(z) = \frac{1}{\sqrt{2\pi}} e^{-\frac{z^2}{2}} \quad (2.57)$$

$$P(z) = \frac{1}{\sqrt{2\pi}} \int_{-\infty}^x e^{-\frac{\zeta^2}{2}} d\zeta \quad (2.58)$$

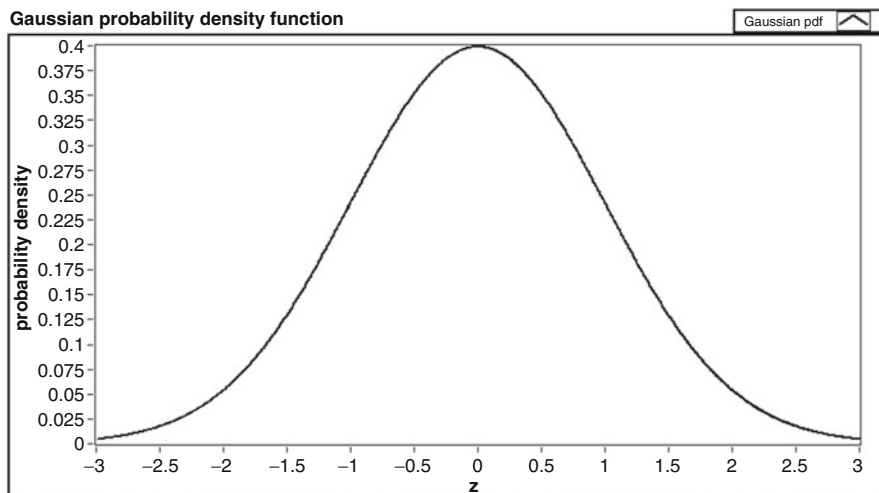


**Fig. 2.2** Gaussian probability density function

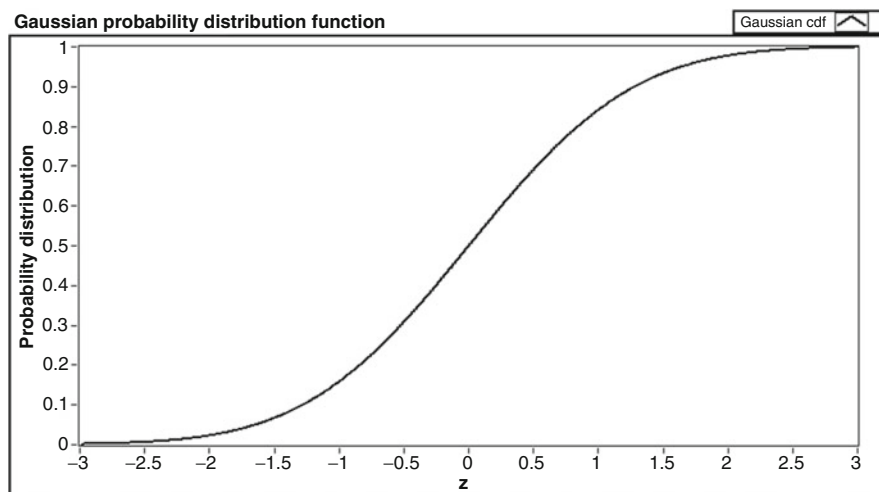


**Fig. 2.3** Gaussian probability distribution function

Figures 2.2 and 2.3 show the plots of (2.57) and (2.58).

The importance of the Gaussian distribution in physical problems can be partially addressed to the central limit theorem (Papoulis 1991). It states that, given  $K$  mutually independent random variables, whatever their (eventually different) distributions, their sum is a normally distributed random variable when  $K \rightarrow \infty$ .

A sine wave characterized by given amplitude  $A$  and frequency  $f_0$  can be considered a random variable when its initial phase angle is a random variable.

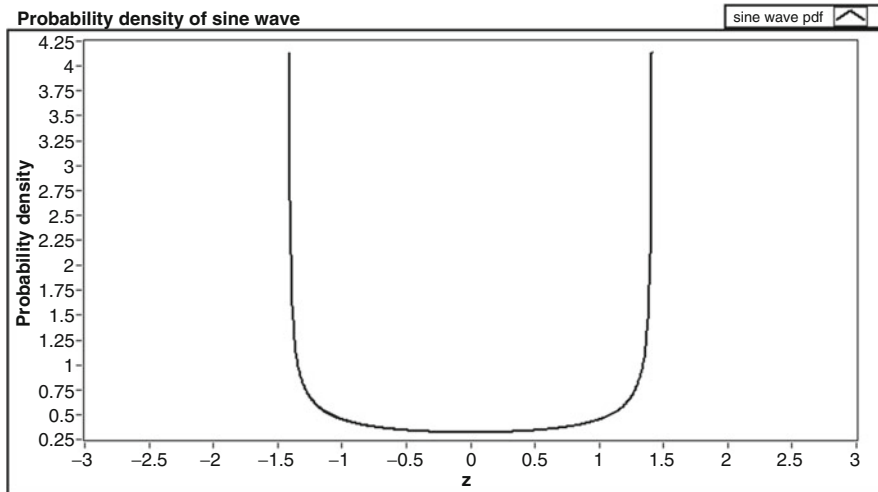


**Fig. 2.4** Probability density function of a sine wave

Assuming that the latter is characterized by a uniform probability density function in the range  $[0, 2\pi]$ , the sine wave probability density function is given by:

$$p(x) = \frac{1}{\pi\sqrt{A^2 - x^2}}, \quad |x| < A \quad (2.59)$$

while its mean value and variance are:

$$\mu_x = 0, \quad \sigma_x^2 = \frac{A^2}{2}. \quad (2.60)$$

The plot of the probability density function of the sine wave is shown in Fig. 2.4.

If a Gaussian noise  $n(t)$  (with zero mean and  $\sigma_n^2$  variance) is added to the above mentioned sine wave:

$$g(t) = A \sin(2\pi f_0 t + \theta) + n(t) \quad (2.61)$$

it is possible to demonstrate (Bendat and Piersol 2000) that the standardized probability density function has the following expression:

$$p(z) = \frac{1}{\pi\sigma_n} \int_0^\pi \frac{1}{\sqrt{2\pi}} e^{-\frac{1}{2}\left(\frac{z-A\cos\zeta}{\sigma_n}\right)^2} d\zeta \quad (2.62)$$

and its shape depends on the following variance ratio:

$$R = \frac{\sigma_s^2}{\sigma_n^2} = \frac{A^2}{2\sigma_n^2}. \quad (2.63)$$

The estimation of probability density functions from recorded data and the analysis of their shape provide an effective mean for the identification of spurious harmonics superimposed to the stochastic response of the structure under test, as shown in Chap. 5.

It is worth noting that, when dealing with finite records of the structural response, an exact knowledge of parameters, such as mean and variance, and, therefore, of probability density functions is generally not available. Only estimates based on finite datasets can be obtained. Thus, it is desirable to get high quality estimates from the available data. They can be obtained through an opportune choice of the estimator. Since different estimators exist for the same quantity, the choice should be oriented towards estimators that are:

- Unbiased: the expected value of the estimator is equal to the parameter being established;
- Efficient: the mean square error of the estimator is smaller than for other possible estimators;
- Consistent: the estimator approaches the parameter under estimation with a probability approaching unity as the sample size increases.

Thus, even if a different choice is possible, the unbiased estimators for the mean and variance given by:

$$\hat{\mu}_x = \frac{1}{N} \sum_{i=1}^N x_i \quad (2.64)$$

$$\hat{\sigma}_x^2 = \frac{1}{N-1} \sum_{i=1}^N (x_i - \hat{\mu}_x)^2 \quad (2.65)$$

are adopted in the following; the hat (^) indicates that the quantities in (2.64) and (2.65) are estimates of the true mean and variance based on a finite number of samples.

The probability density function of a record can be estimated by dividing the full range of data into a number of intervals characterized by the same (narrow) width. For instance, assuming that [a, b] is the full range of data values, it can be divided into K intervals characterized by the equal width W:

$$W = \frac{b-a}{K} \quad (2.66)$$

Then, the number  $N_k$  of data values falling into the k-th interval  $[d_{k-1}, d_k]$ :

$$d_{k-1} = a + (k-1)W, \quad d_k = a + kW \quad (2.67)$$

provide the following estimate of the probability density function:

$$\hat{p}(x) = \frac{N_k}{NW}. \quad (2.68)$$

Note that the first interval includes all values not larger than  $a$ , while the last interval includes all values strictly larger than  $b$ . Moreover:

$$\sum_{k=0}^{K+1} N_k = N. \quad (2.69)$$

The output of this procedure can be represented in the form of a sequence of sample probability density estimates in accordance with (2.68):

$$\hat{p}_k = \left( \frac{N_k}{N} \right) \left( \frac{K}{b-a} \right) \quad k = 1, 2, \dots, K \quad (2.70)$$

Alternatively, it can be either represented in the form of a histogram, which is simply the sequence of the values of  $N_k$  without changes, or expressed in terms of the sample percentage  $N_k/N$  of data in each interval.

### 2.2.3 Correlation Functions

Correlation functions play a primary role in output-only modal identification. In fact, under the assumption of stationary and random response of the structure, the second-order statistics of the response carry all the physical information.

Given the sample functions  $x_k(t)$  and  $y_k(t)$  of two stationary random processes, the mean values, independent of  $t$ , are given by:

$$\mu_x = E[x_k(t)] = \int_{-\infty}^{+\infty} xp(x)dx \quad (2.71)$$

$$\mu_y = E[y_k(t)] = \int_{-\infty}^{+\infty} yp(y)dy \quad (2.72)$$

in agreement with (2.48). The assumption of stationary random processes yields covariance functions that are also independent of  $t$ :

$$C_{xx}(\tau) = E[(x_k(t) - \mu_x)(x_k(t + \tau) - \mu_x)] \quad (2.73)$$

$$C_{yy}(\tau) = E[(y_k(t) - \mu_y)(y_k(t + \tau) - \mu_y)] \quad (2.74)$$

$$C_{xy}(\tau) = E[(x_k(t) - \mu_x)(y_k(t + \tau) - \mu_y)] \quad (2.75)$$

If the mean values are both equal to zero, the covariance functions coincide with the correlation functions:

$$R_{xx}(\tau) = E[x_k(t)x_k(t + \tau)] \quad (2.76)$$

$$R_{yy}(\tau) = E[y_k(t)y_k(t+\tau)] \quad (2.77)$$

$$R_{xy}(\tau) = E[x_k(t)y_k(t+\tau)]. \quad (2.78)$$

The quantities  $R_{xx}$  and  $R_{yy}$  are called *auto-correlation* functions of  $x_k(t)$  and  $y_k(t)$ , respectively;  $R_{xy}$  is called *cross-correlation* function between  $x_k(t)$  and  $y_k(t)$ .

When the mean values are not zero, covariance functions and correlation functions are related by the following equations:

$$C_{xx}(\tau) = R_{xx}(\tau) - \mu_x^2 \quad (2.79)$$

$$C_{yy}(\tau) = R_{yy}(\tau) - \mu_y^2 \quad (2.80)$$

$$C_{xy}(\tau) = R_{xy}(\tau) - \mu_x\mu_y. \quad (2.81)$$

Taking into account that two stationary random processes are uncorrelated if  $C_{xy}(\tau) = 0$  for all  $\tau$  (2.53) and that this implies  $R_{xy}(\tau) = \mu_x\mu_y$  for all  $\tau$  (2.81), if  $\mu_x$  or  $\mu_y$  equals zero the two processes are uncorrelated when  $R_{xy}(\tau) = 0$  for all  $\tau$ .

Taking into account that the cross-correlation function and the cross-covariance function are bounded by the following inequalities:

$$|C_{xy}(\tau)|^2 \leq C_{xx}(0)C_{yy}(0) \quad (2.82)$$

$$|R_{xy}(\tau)|^2 \leq R_{xx}(0)R_{yy}(0) \quad (2.83)$$

and noting that:

$$|C_{xx}(\tau)| \leq C_{xx}(0) \quad (2.84)$$

$$|R_{xx}(\tau)| \leq R_{xx}(0) \quad (2.85)$$

it follows that the maximum values of the auto-correlation and auto-covariance functions occur at  $\tau = 0$ ; they correspond to the mean square value and variance of the data, respectively:

$$R_{xx}(0) = E[x_k^2(t)], \quad C_{xx}(0) = \sigma_x^2. \quad (2.86)$$

When the mean values and covariance (correlation) functions of the considered stationary random processes can be directly computed by means of time averages on an arbitrary pair of sample records instead of computing ensemble averages, the two stationary random processes are said to be *weakly ergodic*. In other words, in the presence of two ergodic processes, the statistical properties of weakly stationary random processes can be determined from the analysis of a pair of sample records only, without the need of collecting a large amount of data. As a consequence, in the

presence of two ergodic processes, the mean values of the individual sample functions can be computed by a time average as follows:

$$\mu_x(k) = \lim_{T \rightarrow \infty} \frac{1}{T} \int_0^T x_k(t) dt = \mu_x \quad (2.87)$$

$$\mu_y(k) = \lim_{T \rightarrow \infty} \frac{1}{T} \int_0^T y_k(t) dt = \mu_y. \quad (2.88)$$

The index  $k$  denotes that the  $k$ -th sample function has been chosen for the computation of the mean value: since the processes are ergodic, the results are independent of this choice ( $\mu_x(k) = \mu_x$ ,  $\mu_y(k) = \mu_y$ ). It is worth pointing out that the mean values are also independent of the time  $t$ .

In a similar way, auto- and cross-covariance functions can be computed directly from the  $k$ -th sample function as follows:

$$\begin{aligned} C_{xx}(\tau, k) &= \lim_{T \rightarrow \infty} \frac{1}{T} \int_0^T [x_k(t) - \mu_x] [x_k(t + \tau) - \mu_x] dt = \\ &= R_{xx}(\tau, k) - \mu_x^2 \end{aligned} \quad (2.89)$$

$$\begin{aligned} C_{yy}(\tau, k) &= \lim_{T \rightarrow \infty} \frac{1}{T} \int_0^T [y_k(t) - \mu_y] [y_k(t + \tau) - \mu_y] dt = \\ &= R_{yy}(\tau, k) - \mu_y^2 \end{aligned} \quad (2.90)$$

$$\begin{aligned} C_{xy}(\tau, k) &= \lim_{T \rightarrow \infty} \frac{1}{T} \int_0^T [x_k(t) - \mu_x] [y_k(t + \tau) - \mu_y] dt = \\ &= R_{xy}(\tau, k) - \mu_x \mu_y \end{aligned} \quad (2.91)$$

and, the processes being ergodic, the results are independent of the chosen function ( $C_{xx}(\tau, k) = C_{xx}(\tau)$ ,  $C_{yy}(\tau, k) = C_{yy}(\tau)$ ,  $C_{xy}(\tau, k) = C_{xy}(\tau)$ ).

It is worth pointing out that only stationary random processes can be ergodic. When a stationary process is also ergodic, the generic sample function is representative of all others so that the first- and second-order properties of the process can be computed from an individual sample function by means of time averages. With stationary and ergodic processes, the auto- and cross-correlation functions are given by the following expressions:

$$R_{xx}(\tau) = \lim_{T \rightarrow \infty} \frac{1}{T} \int_0^T x(t)x(t + \tau) dt \quad (2.92)$$

$$R_{yy}(\tau) = \lim_{T \rightarrow \infty} \frac{1}{T} \int_0^T y(t)y(t + \tau) dt \quad (2.93)$$

$$R_{xy}(\tau) = \lim_{T \rightarrow \infty} \frac{1}{T} \int_0^T x(t)y(t + \tau) dt. \quad (2.94)$$

Ergodic random processes are definitely an important class of random processes. Since the time-averaged mean value and correlation function are equal to the ensemble-averaged mean and correlation function respectively, a single sample function is sufficient to compute those quantities instead of a collection of sample functions. In practical applications stationary random processes are usually ergodic. From a general point of view, a random process is ergodic if the following sufficient conditions are fulfilled:

- The random process is weakly stationary and the time averages  $\mu_x(k)$  and  $C_{xx}(\tau, k)$  ((2.87) and (2.89)) are the same for all sample functions;
- The auto-covariance function fulfills the following condition:

$$\frac{1}{T} \int_{-T}^T |C_{xx}(\tau)| d\tau \rightarrow 0 \quad \text{for } T \rightarrow \infty. \quad (2.95)$$

In practical applications, individual time history records are referred to as stationary if the properties computed over short time intervals do not significantly vary from one interval to the next. In other words, eventual variations are limited to statistical sampling variations only. Since a sample record obtained from an ergodic process is stationary, verification of stationarity of the individual records justifies the assumption of stationarity and ergodicity for the random process from which the sample record is obtained. Tests for stationarity of data (Bendat and Piersol 2000) are advisable before processing.

From a sample record, the correlation function can be estimated either through direct computation or by means of FFT procedures. The latter approach is faster than the former but suffers some drawbacks related to the underlying periodic assumption of the DFT. If the direct estimation of the autocorrelation is considered, it is given by:

$$\hat{R}_{xx}(r\Delta t) = \frac{1}{N-r} \sum_{n=1}^{N-r} x_n x_{n+r} \quad r = 0, 1, 2, \dots, m \quad (2.96)$$

for a stationary record with zero mean ( $\mu = 0$ ) and uniformly sampled data at  $\Delta t$ . Thus, (2.96) provides an unbiased estimate of the auto-correlation function at the time delay  $r\Delta t$ , where  $r$  is also called the lag number and  $m$  denotes the maximum lag.

## 2.2.4 Spectral Density Functions

Given a pair of sample records  $x_k(t)$  and  $y_k(t)$  of finite duration  $T$  from stationary random processes, their Fourier transforms (which exist as a consequence of the finite duration of the signals) are:

$$X_k(f, T) = \int_0^T x_k(t) e^{-i2\pi ft} dt \quad (2.97)$$

$$Y_k(f, T) = \int_0^T y_k(t) e^{-i2\pi ft} dt \quad (2.98)$$

and the *two-sided auto- and cross-spectral density functions* are defined as follows:

$$S_{xx}(f) = \lim_{T \rightarrow \infty} E \left[ \frac{1}{T} X_k^*(f, T) X_k(f, T) \right] \quad (2.99)$$

$$S_{yy}(f) = \lim_{T \rightarrow \infty} E \left[ \frac{1}{T} Y_k^*(f, T) Y_k(f, T) \right] \quad (2.100)$$

$$S_{xy}(f) = \lim_{T \rightarrow \infty} E \left[ \frac{1}{T} X_k^*(f, T) Y_k(f, T) \right] \quad (2.101)$$

where  $*$  denotes complex conjugate. Two-sided means that  $S(f)$  is defined for  $f$  in the range  $(-\infty, +\infty)$ ; the expected value operation is working over the ensemble index  $k$ . The *one-sided auto- and cross-spectral density functions*, with  $f$  varying in the range  $(0, +\infty)$ , are given by:

$$G_{xx}(f) = 2S_{xx}(f) = 2 \lim_{T \rightarrow \infty} \frac{1}{T} E \left[ |X_k(f, T)|^2 \right] \quad 0 < f < +\infty \quad (2.102)$$

$$G_{yy}(f) = 2S_{yy}(f) = 2 \lim_{T \rightarrow \infty} \frac{1}{T} E \left[ |Y_k(f, T)|^2 \right] \quad 0 < f < +\infty \quad (2.103)$$

$$G_{xy}(f) = 2S_{xy}(f) = 2 \lim_{T \rightarrow \infty} \frac{1}{T} E \left[ X_k^*(f, T) Y_k(f, T) \right] \quad 0 < f < +\infty \quad (2.104)$$

The two-sided spectral density functions are more commonly adopted in theoretical derivations and mathematical calculations, while the one-sided spectral density functions are typically used in the applications. In particular, in practical applications the one-sided spectral density functions are always the result of Fourier transforms of records of finite length ( $T < \infty$ ) and of averaging of a finite number of ensemble elements.

Before analyzing the computation of PSDs in practice, it is interesting to note that PSDs and correlation functions are Fourier transform pairs. Assuming that mean values have been removed from the sample records and that the integrals of the absolute values of the correlation functions are finite (this is always true for finite record lengths), that is to say:

$$\int_{-\infty}^{+\infty} |R(\tau)| d\tau < \infty \quad (2.105)$$

the two-sided spectral density functions are the Fourier transforms of the correlation functions:

$$S_{xx}(f) = \int_{-\infty}^{+\infty} R_{xx}(\tau) e^{-i2\pi f\tau} d\tau \quad (2.106)$$

$$S_{yy}(f) = \int_{-\infty}^{+\infty} R_{yy}(\tau) e^{-i2\pi f\tau} d\tau \quad (2.107)$$

$$S_{xy}(f) = \int_{-\infty}^{+\infty} R_{xy}(\tau) e^{-i2\pi f\tau} d\tau \quad (2.108)$$

Equations (2.106)–(2.108) are also called the *Wiener-Khinchin relations* in honor of the mathematicians that first proved that correlations and spectral densities are Fourier transform pairs. The auto-spectral density functions are real-valued functions, while the cross-spectral density functions are complex-valued. In terms of one-sided spectral density functions, the correspondence with the correlation functions is given by:

$$G_{xx}(f) = 4 \int_0^{\infty} R_{xx}(\tau) \cos(2\pi f \tau) d\tau \quad (2.109)$$

$$G_{yy}(f) = 4 \int_0^{\infty} R_{yy}(\tau) \cos(2\pi f \tau) d\tau \quad (2.110)$$

$$G_{xy}(f) = 2 \int_{-\infty}^{+\infty} R_{xy}(\tau) e^{-i2\pi f\tau} d\tau = C_{xy}(f) - iQ_{xy}(f) \quad (2.111)$$

where  $C_{xy}(f)$  is called the *coincident spectral density function* (co-spectrum) and  $Q_{xy}(f)$  is the *quadrature spectral density function* (quad-spectrum). The one-sided cross-spectral density function can be also expressed in complex polar notation as follows:

$$G_{xy}(f) = |G_{xy}(f)| e^{-i\theta_{xy}(f)} \quad 0 < f < \infty \quad (2.112)$$

where the magnitude and phase are given by:

$$|G_{xy}(f)| = \sqrt{C_{xy}^2(f) + Q_{xy}^2(f)} \quad (2.113)$$

$$\theta_{xy}(f) = \arctan \frac{Q_{xy}(f)}{C_{xy}(f)}. \quad (2.114)$$

Taking into account that the cross-spectral density function is bounded by the cross-spectrum inequality:

$$|G_{xy}(f)|^2 \leq G_{xx}(f)G_{yy}(f) \quad (2.115)$$

it is possible to define the *coherence function* as follows:

$$\gamma_{xy}^2(f) = \frac{|G_{xy}(f)|^2}{G_{xx}(f)G_{yy}(f)} = \frac{|S_{xy}(f)|^2}{S_{xx}(f)S_{yy}(f)} \quad (2.116)$$

where:

$$0 \leq \gamma_{xy}^2(f) \leq 1 \quad \forall f. \quad (2.117)$$

Note that the conversion from two-sided to one-sided spectral density functions doubles the amplitude ( $|S_{xy}(f)| = |G_{xy}(f)|/2$ ) while preserving the phase.

It is worth pointing out two important properties of Gaussian random processes for practical applications. First, it can be shown (Bendat and Piersol 2000) that if a Gaussian process undergoes a linear transformation, the output is still a Gaussian process. Moreover, given a sample record of an ergodic Gaussian random process with zero mean, it can be shown (Bendat and Piersol 2000) that the Gaussian probability density function  $p(x)$ :

$$p(x) = \frac{1}{\sigma_x \sqrt{2\pi}} e^{-\frac{x^2}{2\sigma_x^2}} \quad (2.118)$$

is completely determined by the knowledge of the auto-spectral density function. In fact, taking into account that (Bendat and Piersol 2000):

$$\sigma_x^2 = \int_{-\infty}^{+\infty} x^2 p(x) dx \approx \int_0^{\infty} G_{xx}(f) df, \quad (2.119)$$

$G_{xx}(f)$  alone determines  $\sigma_x$ . As a consequence, spectral density functions (and their Fourier transform pairs, the correlation functions) play a fundamental role in the analysis of random data, since they contain the information of interest.

In practical applications, PSDs can be obtained by computing the correlation functions first and then Fourier transforming them. This approach is known as the Blackman-Tukey procedure. Another approach, known as the *Welch procedure*, is, instead, based on the direct computation of the FFT of the records and the estimation of the PSDs in agreement with (2.102)–(2.104). The Welch procedure is less computational demanding than the Blackman-Tukey method, but it requires some operations on the signal in order to improve the quality of the estimates.

According to (2.102)–(2.104), the one-sided auto-spectral density function can be estimated by dividing a record into  $n_d$  contiguous segments, each of length  $T = N\Delta t$ , Fourier transforming each segment and then computing the auto-spectral

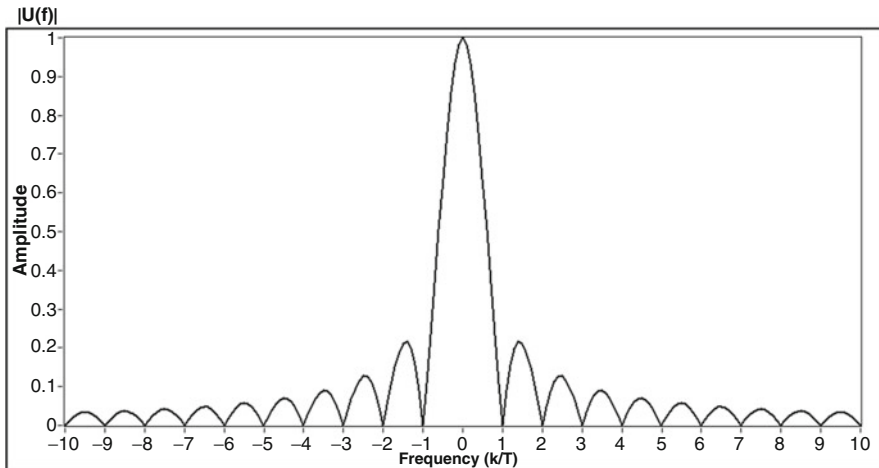


**Fig. 2.5** DFT of a rectangular window: amplitude

density through an ensemble averaging operation over the  $n_d$  subsets of data as follows:

$$\hat{G}_{xx}(f) = \frac{2}{n_d N \Delta t} \sum_{i=1}^{n_d} |X_i(f)|^2. \quad (2.120)$$

The number of data values  $N$  in each segment is often called the *block size* for the computation of each FFT; it determines the frequency resolution of the resulting estimates. The number of averages  $n_d$ , instead, determines the random error of the estimates, as discussed in Sect. 2.2.5.

Even if the direct computation via FFT of the spectral density function is advantageous from a computational point of view, specific strategies are required to eliminate the errors originating from the fact that the estimates are based on records of finite length. A sample record  $x(t)$  can be interpreted as an unlimited record  $v(t)$  multiplied by a rectangular time window  $u(t)$ :

$$x(t) = u(t) v(t) \quad u(t) = \begin{cases} 1 & 0 \leq t \leq T \\ 0 & \text{elsewhere} \end{cases}. \quad (2.121)$$

As a consequence, the Fourier transform of  $x(t)$  is given by the convolution of the Fourier transforms of  $u(t)$  and  $v(t)$ . The Fourier transform of a rectangular signal is basically a sinc function (Fig. 2.5) with side lobes characterized by a fairly large amplitude with respect to the main lobe (the amplitude difference is just  $-13$  dB). The large side lobes of  $|U(f)|$  allow the energy at a certain frequency to spread to nearby frequencies, causing large amplitude errors. This phenomenon is also known as *leakage* and it may introduce significant distortions in the estimated spectra, in particular in the presence of data characterized by narrow bandwidth. However, it does not happen when the analyzed data are periodic with a period equal to the record

length. In such a case, in fact, the discrete frequency values, equally spaced at  $\Delta f = 1/T$ , coincide with zeros of the spectral window in the frequency domain with the only exception of the frequency line in the main lobe. The result is an exact reproduction of the correct spectrum. Thus, in order to suppress the leakage problem, data are made periodic by tapering them by an appropriate time window, which eliminates the discontinuities at the beginning and end of the analyzed record. There are different options for the choice of the window (Heylen et al. 1998). Here, the most commonly employed window is introduced. It is the full cosine tapering window, also known as *Hanning window*, which is given by:

$$u_{\text{Hanning}}(t) = \begin{cases} 1 - \cos^2\left(\frac{\pi t}{T}\right) & 0 \leq t \leq T \\ 0 & \text{elsewhere} \end{cases} \quad (2.122)$$

The highest side lobe level of the Hanning window is 32 dB below the main lobe. Thus, leakage is minimized. However, the use of the Hanning window to compute spectral density estimates by Fourier transform techniques implies a loss factor of 3/8:

$$\frac{\int_0^T u_{\text{Hanning}}^2(t) dt}{\int_0^T u^2(t) dt} = \frac{3}{8}. \quad (2.123)$$

As a consequence, a rescaling is needed to obtain spectral density estimates characterized by the correct magnitude.

It is worth noting that time history tapering by the Hanning window for leakage suppression also increases the half power bandwidth of the main lobe. Such an increase, in the order of about 60 %, may affect damping estimates (see also Chap. 5). In order to avoid the increase in the half power bandwidth, the length of each segment has to be increased until each FFT provides the same bandwidth with tapering that would have occurred without it. For a given number of averages  $n_d$  and, therefore, a given random error, the increase in the length of the tapered segments implies an increase in the total record length. If data are limited, an increase in the length of the tapered segments is possible at the expenses of the number of averages  $n_d$ . In this case, however, the resulting PSD estimates are characterized by an increased variability. A possible countermeasure to increase  $n_d$  in the presence of limited data consists in dividing the total record into partially overlapping segments.

The estimated auto- and cross-spectral densities can be assembled into a 3D matrix where one dimension is represented by the discrete frequency values at which the spectral densities are estimated. For a given value of frequency, the resulting matrix has dimensions depending on the number of sample records considered in the analysis, and it is a Hermitian matrix (see also Sect. 2.3.1) with real-valued terms on the main diagonal, and off diagonal terms which are complex conjugate of each other.

## 2.2.5 Errors in Spectral Density Estimates and Requirements for Total Record Length in OMA

In Sect. 2.2.2 the definition of unbiased estimator has been reported. Attention is herein focused on the errors affecting the estimates. In fact, a recommended length of the records for OMA applications can be obtained from the analysis of errors in spectral density estimates.

From a general point of view, the repetition of a certain experiment leads to a number of estimates  $\hat{x}$  of the quantity of interest  $x$ . When the expected value of the estimates over the  $K$  experiments is equal to the true value  $x$ , the estimate  $\hat{x}$  is unbiased. On the contrary, when there is a scatter between expected value of the estimates and true value, it is possible to define the bias  $b[\hat{x}]$  of the estimate:

$$b[\hat{x}] = E[\hat{x}] - x. \quad (2.124)$$

The *bias error* is a systematic error occurring with the same magnitude and in the same direction when measurements are repeated under the same conditions.

The variance of the estimate:

$$Var[\hat{x}] = E[(\hat{x} - E[\hat{x}])^2] \quad (2.125)$$

describes the *random error*, namely the not systematic error occurring in different directions and with different magnitude when measurements are repeated under the same conditions.

The *mean square error*:

$$mse[\hat{x}] = E[(\hat{x} - x)^2] = Var[\hat{x}] + (b[\hat{x}])^2 \quad (2.126)$$

provides a measure of the total estimation error. It is equivalent to the variance when the bias is zero or negligible. It also leads to the definition of *normalized rms error* of the estimate:

$$\epsilon[\hat{x}] = \frac{\sqrt{E[(\hat{x} - x)^2]}}{x}. \quad (2.127)$$

In practical applications the normalized rms error should be as small as possible to ensure that the estimates are close to the true value. Estimates characterized by large bias error and small random error are precise but not accurate; estimates characterized by small bias error and large random error are accurate but not precise. Since the bias error can be removed when identified while the random error cannot, for the first type of estimates the mean square error can be potentially reduced.

When the estimation of auto PSDs is considered, it can be shown (Bendat and Piersol 2000) that, in the case of normally distributed data, the random portion of

the normalized rms error of an estimate is a function only of the total record length and of the frequency resolution:

$$\epsilon_r^2 = \frac{1}{T_r \Delta f}. \quad (2.128)$$

Simple manipulations of (2.128) lead to a suggested value of the total record length for OMA applications as a function of the fundamental period of the structure under investigation. In fact, as previously mentioned, the random error depends on the number of averages  $n_d$ . It can be shown (Bendat and Piersol 2000) that the required number of averages to get an assigned random error in the estimation of the auto-spectral densities can be obtained by (2.129):

$$n_d = \frac{1}{\epsilon_r^2}. \quad (2.129)$$

A relatively small normalized random error:

$$\epsilon_r = \frac{1}{\sqrt{n_d}} \leq 0.10 \quad (2.130)$$

is associated to a number of averages:

$$n_d \geq 100. \quad (2.131)$$

On the other hand, a negligible bias error, in the order of 2 %, can be obtained by choosing (Bendat and Piersol 2000):

$$\Delta f = \frac{1}{T} = \frac{B_r}{4} = \frac{2\xi_n \omega_n}{4} \quad (2.132)$$

where  $B_r$  is the half power bandwidth at the natural frequency  $\omega_n$ ,  $\xi_n$  is the associated damping ratio, while  $T$  is the length of the i-th data segment. The relation between the total record length  $T_r$  and the length  $T$  of the i-th data segment is:

$$T_r = n_d T \Rightarrow T = \frac{T_r}{n_d}. \quad (2.133)$$

Taking into account the relation between natural circular frequency and natural period of a mode and that the fundamental mode is characterized by the longest natural period, the substitution of (2.133) into (2.132) yields the following expression:

$$T_r = \frac{n_d}{\pi \xi_1} T_1 \quad (2.134)$$

relating the total record length to the fundamental period of the structure under investigation. Assuming  $n_d = 100$  and a typical value for the damping ratio—for instance, about 1.5 % for reinforced concrete (r.c.) structures in operational conditions—a suggested value for the total record length is about 1,000–2,000 times the natural period of the fundamental mode of the structure, in agreement with similar suggestions reported in the literature (Cantieni 2004).

Taking into account the assumptions under the formula given in (2.134), the suggested value for the total record length minimizes the random error  $\varepsilon_r$  and suppresses the leakage (since a very small value for the bias error  $\varepsilon_b$  has been set).

## 2.3 Matrix Algebra and Inverse Problems

### 2.3.1 Fundamentals of Matrix Algebra

Most OMA methods are based on fitting of an assumed mathematical model to the measured data. In such a case, the ultimate task is to determine the unknown modal parameters of the system from the measured response of the structure under certain assumptions about the input. This is an example of inverse problem. The solution of inverse problems is based on matrix algebra, including methods for matrix decomposition.

Matrix algebra plays a relevant role also in the case of those OMA methods that extract the modal parameters without assumptions about the system that produced the measured data. Thus, a review of basics of matrix algebra and of some methods for the solution of inverse problems is helpful to understand the mathematical background of the OMA methods described in Chap. 4.

Consider the generic matrix:

$$[A] = \begin{bmatrix} a_{1,1} & \dots & a_{1,M} \\ \dots & a_{i,j} & \dots \\ a_{L,1} & \dots & a_{L,M} \end{bmatrix} \quad (2.135)$$

of dimensions  $L \times M$ . Its generic element is  $a_{i,j}$ , where the index  $i = 1, \dots, L$  refers to the row number while the index  $j = 1, \dots, M$  refers to the column number. In accordance with the usual starting point of counters in LabVIEW, a more convenient notation is  $i = 0, \dots, L-1$  and  $j = 0, \dots, M-1$ . The matrix  $[A]$  can be *real-valued* or *complex valued*, depending if its elements are real or complex numbers. When the matrix dimensions are equal ( $L = M$ ), the matrix is said to be a *square matrix*. For a square matrix, the *trace* is the sum of the elements in the main diagonal. If all the off-diagonal elements in a square matrix are zero while all the elements in the main diagonal are equal to one, the obtained matrix is the *identity matrix*  $[\mathbb{I}]$ .

It is worth noting that, while addition and scalar multiplication are element-wise operations with matrices, the matrix multiplication is based on the dot product of row and column vectors, as expressed by (2.136). This provides the generic element

of the product matrix in terms of the elements in the i-th row and j-th column of the two matrices in the product:

$$[C] = [A][B], \quad c_{ij} = \sum_k a_{i,k} b_{k,j} \quad (2.136)$$

Switching of columns and rows of a certain matrix  $[A]$  provides the *transpose* matrix  $[A]^T$ . When a square matrix coincides with its transpose, it is said to be *symmetric*. If the matrix  $[A]$  is complex-valued, its Hermitian adjoint  $[A]^H$  is obtained by transposing the matrix  $[A]^*$  whose elements are the complex conjugates of the individual elements of the original matrix  $[A]$ . A square matrix identical to its Hermitian adjoint is said to be *Hermitian*; real-valued symmetric matrices are a special case of Hermitian matrices.

The *inverse*  $[A]^{-1}$  of the matrix  $[A]$  is such that  $[A]^{-1}[A] = [I]$ . A determinant equal to zero characterizes a *singular* (noninvertible) matrix. On the contrary, if the determinant is nonzero, the matrix is invertible (or *nonsingular*). The matrix  $[A]$  is *orthogonal* if its inverse and its transpose coincide:  $[A]^{-1} = [A]^T$  (its rows and columns are, therefore, orthonormal vectors, that is to say, orthogonal unit vectors). If  $[A]$  is complex-valued, it is a *unitary* matrix if its Hermitian adjoint and its inverse coincide:  $[A]^{-1} = [A]^H$ . The following relations hold:

$$([A][B])^{-1} = [B]^{-1}[A]^{-1} \quad (2.137)$$

$$([A][B])^T = [B]^T[A]^T \quad (2.138)$$

$$([A][B])^H = [B]^H[A]^H \quad (2.139)$$

$$\left( [A]^{-1} \right)^T = \left( [A]^T \right)^{-1}. \quad (2.140)$$

The *rank*  $r([A])$  of a matrix  $[A]$  is given by the number of independent rows or columns in  $[A]$ . By definition, a row (column) in a matrix is linearly independent if it cannot be computed as a linear combination of the other rows (columns). If the rank of an  $L \times L$  matrix  $[A]$  is  $r([A]) = S$ , with  $S < L$ , then there exists a submatrix of  $[A]$  with dimensions  $S \times S$  and nonzero determinant.

When the matrix  $[A]$  acts as a linear operator transforming a certain vector  $\{x\}$  into a new vector  $\{y\}$ :

$$\{y\} = [A]\{x\} \quad (2.141)$$

if the  $L \times L$  matrix  $[A]$  is noninvertible, there are vectors  $\{x\}$  providing:

$$\{y\} = [A]\{x\} = \{0\}. \quad (2.142)$$

Those vectors define a subspace of  $\{x\}$  called the *null space*. As a consequence, not all the space of  $\{y\}$  can be reached from  $\{x\}$ ; the *range* of  $[A]$  defines the subset of the space of  $\{y\}$ , which can be reached through the transformation defined in (2.141). The dimension of the range coincides with the rank of  $[A]$ , and the sum of the dimensions of the null space and the range equals the dimension  $L$  of the matrix. If the matrix  $[A]$  is invertible:

$$\{y\} = [A]\{x\} = \{0\} \Leftrightarrow \{x\} = \{0\} \quad (2.143)$$

and the dimension of the null space is zero.

Whenever the vector  $\{y\}$  (2.141) can be computed via the matrix multiplication  $[A]\{x\}$ , and via the scalar product  $\lambda\{x\}$ ,  $\lambda$  is defined an *eigenvalue* of  $[A]$  and  $\{x\}$  is the corresponding *eigenvector*. The eigenvalues are obtained as a solution of the characteristic equation:

$$\det([A] - \lambda[I]) = 0 \quad (2.144)$$

and the corresponding eigenvectors are computed by replacing the obtained eigenvalues  $\lambda_k$  into (2.145):

$$([A] - \lambda_k[I])\{x_k\} = \{0\}. \quad (2.145)$$

If the matrix  $[A]$  is Hermitian or symmetric, the eigenvectors corresponding to distinct eigenvalues are orthogonal (their dot product is zero); its eigenvalues are real. If the symmetric matrix  $[A]$  is positive-definite (2.146):

$$\{x\}^T [A]\{x\} > 0 \quad \forall \{x\} \neq \{0\} \quad (2.146)$$

the eigenvalues are real and positive and the matrix  $[A]$  is invertible.

When dealing with systems of equations, the matrix inversion can be more effectively implemented by decomposing the matrix into factors. There are different types of matrix decomposition methods. The *eigenvalue decomposition* (EVD) provides an expression for the invertible square matrix  $[A]$  as a product of three matrices:

$$[A] = [X][\Lambda][X]^{-1} \quad (2.147)$$

where the columns of  $[X]$  are the eigenvectors of  $[A]$  while  $[\Lambda]$  is a diagonal matrix containing the corresponding eigenvalues of  $[A]$ . Taking advantage of the eigenvalue decomposition of  $[A]$  and of (2.137), the inverse of  $[A]$  can be obtained as:

$$[A]^{-1} = \left( [X][\Lambda][X]^{-1} \right)^{-1} = [X][\Lambda]^{-1}[X]^{-1}. \quad (2.148)$$

The elements in  $[\Lambda]^{-1}$  are the inverse of the eigenvalues of  $[A]$ . Note that, whenever the matrix  $[A]$  is also symmetric, the matrix  $[X]$  is orthogonal.

The *Singular Value Decomposition* (SVD) can be considered an extension of the EVD to rectangular matrices. The SVD of a real-valued matrix  $[A]$  of dimensions  $L \times M$ , with  $L \geq M$  and  $r([A]) \leq M$ , is given by:

$$[A] = [U][\Sigma][V]^T \quad (2.149)$$

where  $[\Sigma]$  of dimensions  $L \times M$  is a rectangular diagonal matrix containing the singular values, arranged in descending order; in particular, the first  $r$  singular values are positive, while the remaining singular values  $\sigma_{r+1}, \dots, \sigma_M$  are all equal to zero.  $[U]$  and  $[V]$  are orthogonal matrices of dimensions  $L \times L$  and  $M \times M$ , respectively. The column vectors  $\{u_1, \dots, u_r\}$  of  $[U]$  span the range of  $[A]$ , while the vectors  $\{v_{r+1}, \dots, v_M\}$  span the null space of  $[A]$ . If  $[A]$  is a complex-valued matrix, the SVD is generalized by replacing the transpose with the Hermitian operator.

The SVD has many applications in signal processing and for the solution of inverse problems, including the computation of pseudo-inverse, least squares fitting of data, matrix approximation and rank determination. In the common case in which  $[A]$  is a square, real-valued matrix,  $[\Sigma]$  can be interpreted as a scaling matrix, while  $[U]$  and  $[V]^T$  can be regarded as rotation matrices; thus, the SVD can be also interpreted as a sequence of three geometrical transformations, namely a rotation, a scaling, and another rotation. The SVD is also used for the computation of the *Moore-Penrose pseudoinverse* of a matrix. For instance, the pseudo-inverse of the matrix  $[A]$  is given by:

$$[A]^+ = [V][\Sigma]^+[U]^T \quad (2.150)$$

where  $[\Sigma]^+$  is the pseudoinverse of  $[\Sigma]$ , obtained by replacing every nonzero diagonal entry by its reciprocal and transposing the resulting matrix. Note that the product  $[A][A]^+$  usually does not provide the identity matrix. The pseudoinverse  $[A]^+$ , instead, satisfies the following property:  $[A][A]^+[A] = [A]$ .

Other decomposition methods (LQ decomposition, RQ decomposition) for square matrices result in the conversion of the matrix  $[A]$  into a product of an orthogonal matrix  $[Q]$  and an upper  $[R]$  or lower  $[L]$  triangular matrix. The Cholesky factorization, instead, is a decomposition of a real-valued, symmetric, and positive-definite matrix into the product of a lower triangular matrix and its transpose. Further details about matrix algebra and decompositions can be found elsewhere (Golub and Van Loan 1989).

### 2.3.2 Inverse Problems: Error Norms and Least Squares Solutions

A frequent approach in OMA is the fitting of a hypothesized model to the measurements in order to extract the unknown modal parameters. The approach

to fitting depends on the selected model. For the sake of clarity, in this section the main concepts are illustrated with reference to a very simple and general polynomial function:

$$y(x) = c_0 + c_1x + c_2x^2 + \dots + c_{L-1}x^{L-1} \quad (2.151)$$

No specific references are made to the theoretical background of OMA at this stage, but the application of these concepts in different contexts is straightforward and it will become clearer when the theory of some OMA methods is reviewed in Chap. 4.

Assuming that  $M$  measurements have been carried out, the  $L$  unknown model parameters ( $c_0, c_1, \dots, c_{L-1}$ ) can be determined from the following set of  $M$  equations:

$$\begin{aligned} y_1 &= c_0 + c_1x_1 + c_2x_1^2 + \dots + c_{L-1}x_1^{L-1} \\ &\quad \dots \\ y_i &= c_0 + c_1x_i + c_2x_i^2 + \dots + c_{L-1}x_i^{L-1} \\ &\quad \dots \\ y_M &= c_0 + c_1x_M + c_2x_M^2 + \dots + c_{L-1}x_M^{L-1} \end{aligned} \quad (2.152)$$

which can be rearranged in matrix form as:

$$\{y\} = \begin{Bmatrix} y_1 \\ \dots \\ y_i \\ \dots \\ y_M \end{Bmatrix} = \begin{bmatrix} 1 & x_1 & x_1^2 & \dots & x_1^{L-1} \\ \dots & \dots & \dots & \dots & \dots \\ 1 & x_i & x_i^2 & \dots & x_i^{L-1} \\ \dots & \dots & \dots & \dots & \dots \\ 1 & x_M & x_M^2 & \dots & x_M^{L-1} \end{bmatrix} \begin{Bmatrix} c_0 \\ \dots \\ c_i \\ \dots \\ c_{L-1} \end{Bmatrix} = [M]\{c\}. \quad (2.153)$$

Note that the setting of the problem in matrix form does not require a linear functional relation between  $y$  and  $x$ . A linear combination of basis functions of  $x$  is also appropriate. In general, there are more measurements than unknowns ( $M > L$ ), so that an overdetermined set of equations is defined, and measurements are noisy. It is worth pointing out that the problem is definitely underdetermined when the number of unknowns  $L$  exceeds the number of equations  $M$ . In this case the inverse problem cannot lead to a unique solution and additional information has to be provided or the number of unknowns has to be reduced. On the contrary, when  $M > L$  the problem may actually be overdetermined, but it can be also even-determined or underdetermined, depending on the eventual presence of interrelated measurements which do not provide additional information. Thus, the rank of the matrix in (2.153) actually determines if the problem is overdetermined or underdetermined. However, in practical applications, the sole determination of the rank of a matrix can be misleading due to the presence of measurement noise. For instance, the rank of the following matrix:

$$\begin{bmatrix} 1 & 0 \\ 1 & 10^{-8} \end{bmatrix} \quad (2.154)$$

is 2 but the second row can be considered linearly dependent on the first row from the practical point of view, since it does not provide a significant contribution of information to the solution of the inverse problem. In similar conditions the SVD of the matrix can provide more valuable information about the type of inverse problem. In fact, the *condition number*  $\kappa$ , defined as the ratio between the maximum and minimum absolute values of singular values, can be computed to assess if the matrix is noninvertible ( $\kappa = \infty$ ), ill-conditioned ( $\kappa$  very large) or invertible (small  $\kappa$ ). Since the small singular values in ill-conditioned problems magnify the errors, considering only the subset of the largest singular values can reduce their effect. The selection of the number of singular values to be retained is usually based on sorting of the singular values and identification of jumps; in the absence of jumps, a selection ensuring numerical stability is carried out.

Assuming that a curve fitting the measured data has been found and the functional relation between  $y$  and  $x$  in (2.151) has been established, there will be an error (or *residual*) associated to the  $i$ -th measurement. It can be computed as difference between the predicted ( $y_{i,pred}$ ) and the measured ( $y_{i,meas}$ ) value of  $y$ :

$$\varepsilon_i = y_{i,meas} - y_{i,pred} \quad (2.155)$$

Thus, the objective of the analysis is the estimation of the unknown coefficients ( $c_0, c_1, \dots, c_{L-1}$ ) from the measured data in a way able to minimize the sum of the residuals when all measurements are taken into account.

Different definitions for the residuals can be adopted, taking into account that the selected error definition has an influence on the estimation of the unknown parameters. For instance, when the data are characterized by the presence of very large and very small values in the same set, the computation of the residuals according to (2.155) biases the inversion towards the largest values. As an alternative, one of the following definitions of residual can be considered:

$$\varepsilon_i = \frac{y_{i,meas} - y_{i,pred}}{y_{i,pred}} \quad (\text{proportional error}) \quad (2.156)$$

$$\varepsilon_i = \log(y_{i,meas}) - \log(y_{i,pred}) \quad (\text{log difference}) \quad (2.157)$$

Additional error definitions can be found in the literature (see, for instance, Santamarina and Fratta 2005).

A global evaluation of the quality of the fit can be obtained from the computation of the norm of the vector of residuals  $\{\varepsilon\}$ :

$$\{\varepsilon\} = \begin{Bmatrix} \varepsilon_1 \\ \dots \\ \varepsilon_i \\ \dots \\ \varepsilon_M \end{Bmatrix} \quad (2.158)$$

The generic *n-norm* is given by:

$$L_n = \sqrt[n]{\sum_i |\epsilon_i|^n}. \quad (2.159)$$

The order of the norm is related to the weight placed on the larger errors: the higher the order of the norm, the higher the weight of the larger errors. Three notable norms are:

$$L_1 = \sum_i |\epsilon_i| \quad (2.160)$$

$$L_2 = \sqrt{\sum_i |\epsilon_i|^2} = \sqrt{\{\epsilon\}^T \{\epsilon\}} \quad (2.161)$$

$$L_\infty = \max(|\epsilon_1|, \dots, |\epsilon_i|, \dots, |\epsilon_M|). \quad (2.162)$$

The  $L_1$  norm provides a robust solution, since it is not sensitive to a few large errors in the data; the  $L_2$  norm is compatible with additive Gaussian noise present in the data; the  $L_\infty$  norm considers only the largest error and, as a consequence, is the most sensitive to errors in the data.

Based on the previous definitions, the least squares solution of the inverse problem can be defined as the set of values of the coefficients ( $c_0, c_1, \dots, c_{L-1}$ ) that minimizes the  $L_2$  norm of the vector of residuals. Thus, setting the derivative of this  $L_2$  norm with respect to  $\{c\}$  equal to zero, under the assumption that  $[M]^T [M]$  is invertible the least squares solution provides the following estimate of the model parameters:

$$\{c\} = \left( [M]^T [M] \right)^{-1} [M]^T \{y_{meas}\} = [M]^+ \{y_{meas}\}. \quad (2.163)$$

The *least squares method* is a standard approach to the approximate solution of overdetermined systems. However, it works well when the uncertainties affect the dependent variable. If substantial uncertainties affect also the independent variable, the total least square approach has to be adopted. It is able to take into account the observational errors on both dependent and independent variables. The mathematical details of the method are out of the scope of the book, and the interested reader can refer to (Golub and Van Loan 1989) for more details. However, it is worth recalling the geometrical interpretation of the total least squares method in comparison with the least squares approach. In fact, when the independent variable is error-free, the residual represents the distance between the observed data point and the fitted curve along the  $y$  direction. On the contrary, in total least squares, when both variables are measured in the same units and the errors on both variables are the same, the residual represents the shortest distance between the data point and the fitted curve. Thus, the residual vector is orthogonal to the tangent of the curve.

## 2.4 Applications

### 2.4.1 Operations with Complex Numbers

*Task.* Create a calculator to carry out the following operations with complex numbers:

- Get real part and imaginary part of a complex number;
- Get amplitude and phase of a complex number;
- Compute complex conjugate of a complex number;
- Compute sum, product, and division between two complex numbers;
- Compute amplitude and phase of  $1 + 0i$  and  $0 + 1i$ ;
- Compute:  $(1 + 0i) + (0 + 1i)$ ,  $(1 + 0i) * (0 + 1i)$ ,  $(1 + 0i)/(0 + 1i)$ ;  $(1 + 1i) + (1 - 1i)$ ,  $(1 + 1i) * (1 - 1i)$ ,  $(1 + 1i)/(1 - 1i)$ .

*Suggestions.* This is a very simple example to get confidence with the LabVIEW environment and with basic operations with complex numbers. In the design of the user interface on the Front Panel, place controls and indicators and set in their properties a complex representation of the data (right click on the control/indicator, then select “Representation” and “Complex Double CDB”). Then, write the code in the Block Diagram (CTRL+E to open it from the Front Panel). Algebraic operators are in the Functions Palette under “Programming – Numeric”; the operations on complex numbers are under “Programming – Numeric – Complex.” Appropriately connect controls and indicators. Use the While Loop structure under “Programming – Structures” to develop a simple, interactive user interface. It is possible to define the timing in the execution of the cycles by means of the “Wait Until Next ms Multiple.vi” in “Programming – Timing.”

*Sample code.* Refer to “Complex values – calculator.vi” in the folder “Chapter 2” of the disk accompanying the book.

### 2.4.2 Fourier Transform

*Task.* Compute the DFT of the following signals:

- Sine wave at frequency  $f = 3$  Hz,
- Sine wave at frequency  $f = 6$  Hz,
- Constant signal,
- Combinations of the previous signals,

and analyze how the magnitude and phase spectra change when:

- The windowed signal is periodic (for instance, when  $N$  is a multiple of 100),
- The windowed signal is not periodic (truncated),
- The length of the signal is doubled.

Consider a sampling interval  $\Delta t$  equal to 0.01 s, which implies a sampling frequency  $f_s = 100$  Hz  $\gg f_{\max} = 6$  Hz.

*Suggestions.* In the design of the user interface on the Front Panel, place a control to input the number of data points  $N$ ; place three “Waveform Graph” controls (it is in

the Controls Palette under “Modern – Graph”) to show the signal in time domain and the amplitude and phase spectra in frequency domain. In the Block Diagram place the “Sine.vi” (it can be found in the Functions Palette under “Mathematics – Elementary – Trigonometric”); use a “For Loop” structure (it can be found in the Functions Palette under “Programming – Structures”) to generate signals of the desired length. Transform the obtained arrays of Double into Waveform type of data by wiring the sampling interval and the array of values of the signal to the “Build Waveform.vi” (it can be found in the Functions Palette under “Programming – Waveform”). Compute the Fourier Transform of the signals by means of “SVT FFT Spectrum (Mag-Phase).vi” (“Addons – Sound & Vibration – Frequency Analysis – Baseband FFT”). Appropriately connect controls and indicators. Use the While Loop structure under “Programming – Structures” to develop a simple, interactive user interface. It is possible to define the timing in the execution of the cycles by means of the “Wait Until Next ms Multiple.vi” in “Programming – Timing.”

*Sample code.* Refer to “FFT mag-phase.vi” in the folder “Chapter 2” of the disk accompanying the book.

### 2.4.3 Statistics

*Task.* Compute mode, mean, maximum and minimum value, standard deviation, and variance of the data in “Data for statistics and histogram.txt” in the folder “Chapter 2\Statistics” of the disk accompanying the book. Use the data to plot a histogram. Pay attention to the obtained results for different values of the number of intervals.

*Suggestions.* Use the “Read from Spreadsheet File.vi” to load the data from file. Maximum and minimum value in the data can be identified by means of the “Array Max & Min.vi” under “Programming – Array.” Mean, standard deviation, and variance can be computed by means of the “Std Deviation and Variance.vi” under “Mathematics – Probability and Statistics.” In the same palette there are “Mode.vi” and “Histogram.vi,” which can be used to compute the mode and plot the histogram. Place a “XY Graph” on the Front Panel to plot the resulting histogram.

*Sample code.* Refer to “Statistics and histogram.vi” in the folder “Chapter 2\Statistics” of the disk accompanying the book.

### 2.4.4 Probability Density Functions

*Task.* Plot the standardized probability density function of a sine wave in noise (2.62) for different values of the variance ratio defined in (2.63).

*Suggestions.* Use the “For Loop” to set the vector of values of the standardized variable  $z$  where the probability density function will be computed. Compute the variance of the Gaussian noise from the values of the variance ratio. Use a

“For Loop” to compute the values of the function in the integral at the selected values of  $z$ . Use the “Numeric Integration.vi” under “Mathematics – Integration & Differentiation” to compute the integral. Put the arrays of the values of  $z$  and  $p(z)$  into a cluster (use the “Bundle.vi” under “Programming – Cluster & Variant”), create an array of the plots of  $p(z)$  and show them in a “XY graph” on the Front Panel.

*Sample code.* Refer to “Sine wave in Gaussian noise.vi” in the folder “Chapter 2” of the disk accompanying the book.

#### 2.4.5 Auto- and Cross-Correlation Functions

*Task.* Compute and plot all the possible auto- and cross-correlation functions from the data in “Sample record 12 channels – sampling frequency 10 Hz.txt” in the folder “Chapter 2Correlation” of the disk accompanying the book. Data in the file are organized in columns: the first column gives the time; the next 12 columns report the data for each of the 12 time histories.

*Suggestions.* Use the “Read from Spreadsheet File.vi” to load the data from file. Compute the auto-correlation functions associated to the 12 time series and the cross-correlation between couples of records. Use the formula (2.96) for the direct estimation of correlation functions, eventually organizing the data into matrices and taking advantage of the matrix product. Organize the resulting data into a 3D matrix so that one of its dimensions is associated to the time lag, and at a certain time lag a square matrix of dimensions  $12 \times 12$  is obtained. Use the “While Loop” to create a user-interface for the selection of one of the auto- or cross-correlation functions from the matrix. Plot the data into a “Waveform Graph” placed on the Front Panel.

*Sample code.* Refer to “Correlation function.vi” in the folder “Chapter 2Correlation” of the disk accompanying the book.

#### 2.4.6 Auto-Correlation of Gaussian Noise

*Task.* Generate a Gaussian white noise, compute its mean, variance, and standard deviation, and plot its autocorrelation function. Use the “AutoCorrelation.vi” under “Signal Processing – Signal Operation.”

*Suggestions.* Use the “Gaussian white noise.vi” under “Signal Processing – Signal Generation” to generate the data. Use the “While Loop” structure to create a user-interface for the selection of the parameters (number of samples and standard deviation of simulated data) for data generation. Place the appropriate controls for such parameters on the Front Panel. Use the “AutoCorrelation.vi” under “Signal

Processing – Signal Operation” to compute the auto-correlation function. Plot the data into a “Waveform Graph” placed on the Front Panel.

*Sample code.* Refer to “Statistics and auto-correlation of Gaussian noise.vi” in the folder “Chapter 2” of the disk accompanying the book.

### 2.4.7 Auto-Power Spectral Density Function

*Task.* Compute (according to the Welch procedure) and plot the auto-spectral density functions of the data in “Sample record 12 channels – sampling frequency 10 Hz.txt” (see Sect. 2.4.5). Divide the time series into a user-selectable number of segments; consider a 50 % overlap of the data segments. Analyze the effects of windowing and number of segments on the resulting spectra and the frequency resolution.

*Suggestions.* Create a SubVI that, given a time history, the number of segments and the sampling frequency, provides an array of waveform data, where each waveform consists of a (partially overlapping) data segment, and the number of data segments  $n_d$ . Take advantage of the “For Loop” structure to divide the total record into  $n_d$  segments. In the main VI, use the “Read from Spreadsheet File.vi” to load the data from file. Compute the sampling frequency from the sampling interval. Select one time history in the dataset and send it to the previously mentioned SubVI to divide it into partially overlapping segments. Use the “For Loop” structure and the “SVT Power Spectral Density.vi” under “Addons – Sound & Vibration – Frequency Analysis – Baseband FFT” to compute the averaged PSDs. Plot the results into a “Waveform Graph” placed on the Front Panel. Use the “While Loop” structure to create a user-interface for the selection of the time histories and the analysis parameters.

*Sample code.* Refer to “Averaged PSD.vi” and “Overlap 0.5.vi” in the folder “Chapter 2PSD and overlap” of the disk accompanying the book.

### 2.4.8 Singular Value Decomposition

*Task.* Create a matrix  $[A]$  of dimensions  $8 \times 8$  and whose entries are random numbers. Create a constant matrix  $[B]$  of dimensions  $8 \times 8$  and rank  $r([B]) = 6$ . Compute the matrices  $[A] + [B]$  and  $[A][B]$ . For each of the previously mentioned matrices compute the SVD, plot the obtained singular values after they have been normalized with respect to the largest one, compute the condition number.

*Suggestions.* Use the “Random number (0-1).vi” under “Programming – Numeric” and two “For Loop” structures inside each other to create  $[A]$ . The matrix multiplication can be carried out by the “ $A \times B.vi$ ” under “Mathematics – Linear Algebra.”

The SVD can be carried out by the “SVD Decomposition.vi” under “Mathematics – Linear Algebra.”

*Sample code.* Refer to “SVD and rank of a matrix.vi” in the folder “Chapter 2” of the disk accompanying the book.

---

## References

- Bendat JS, Piersol AG (2000) Random data: analysis and measurement procedures, 3rd edn. Wiley, New York, NY
- Cantieni R (2004) Experimental methods used in system identification of civil engineering structures. In: Proc 2nd Workshop Problemi di vibrazioni nelle strutture civili e nelle costruzioni meccaniche, Perugia
- Cooley JW, Tukey JW (1965) An algorithm for the machine calculation of complex Fourier series. Math Comp 19:297–301
- Golub GH, Van Loan CF (1989) Matrix computations. John Hopkins University Press, Baltimore, MD
- Heylen W, Lammens S, Sas P (1998) Modal analysis theory and testing. Katholieke Universiteit Leuven, Leuven
- Papoulis A (1991) Probability, random variables, and stochastic processes, 3rd edn. McGraw-Hill, New York, NY
- Santamarina JC, Fratta D (2005) Discrete signals and inverse problems: an introduction for engineers and scientists. Wiley, Chichester

## 3.1 Selection of the Measurement Scheme

High-quality measurements represent the first fundamental step for a successful modal identification. Any OMA method is ineffective if measurements are totally corrupted by noise. Poor measurements can be the result of an incorrect choice of sensors or measurement hardware, but they can also be due to incorrect wiring. In fact, for a given choice of the measurement hardware and sensors, different measurement schemes can often be adopted. The choice of the most appropriate cabling scheme and the adoption of the related specifications for the entire analog signal path play a primary role in the collection of high-quality data. Nowadays versatile data acquisition systems are available on the market, allowing different wiring configurations. If such schemes can slavishly be implemented in the case of commercial systems, attention is needed whenever sensors and data acquisition systems do not come from the same manufacturer or programmable hardware is used to develop an own measurement system. In both cases the proper wiring is usually in the full responsibility of the user.

A detailed analysis of cabling schemes and noise control techniques is out of the scope of the book (refer to Ott 1988, and Barnes 1987 for more details), but their rough illustration can still provide useful guidelines to avoid common errors in measurement execution. The herein reported suggestions cannot replace a detailed analysis of documents and specifications accompanying sensors and measurement systems for the definition of the appropriate wiring scheme, but they can definitely support the inexperienced user in the selection of the measurement chain and scheme.

The main components in a modal analysis test are the structure under investigation, a number of motion transducers, a data acquisition device, and a data processing system for the extraction of the modal information from recorded data.

About the transducers, the function of any sensor is the conversion of a physical quantity into an electrical one, typically voltage. Then, the electrical signal in the form of voltage is transferred to the data acquisition hardware for digitization.

Sensors can, therefore, be interpreted as voltage signal sources. Since a voltage signal represents a measure of the electrical potential difference between two points, the selection of the reference point has a primary influence on voltage measurements. As a consequence, sensors can be classified as grounded signal sources and floating signal sources depending on the adopted reference in voltage measurements.

The measurement reference point for *grounded* (or *ground-referenced*) *signal sources* is represented by the ground of the building power system. Thus, the sensor is already connected to a common ground point with the data acquisition device, assuming that this is plugged into the same power system as the signal source. It is worth noting that, even if two grounded signal sources are connected to the same building power system, the reference potential can be slightly different. The different ground potential in different points of the same power system has to be taken into account in the choice of the cabling scheme. In fact, if grounded signal sources are incorrectly wired, the differences in the ground potential can corrupt the measurements, as it will be clarified next.

When none of the terminals of the source is referred to the building ground system, there is no absolute reference for the voltage signal. A sensor characterized by an isolated ground reference point is referred to as *floating* (or *nonreferenced*) *signal source*. In the case of floating signal sources, the ground of the measurement device is used to establish a reference for the signal and prevent excessive drift.

A similar classification can be adopted for the measurement devices. In fact, in a *single-ended* (or *grounded*, or *ground-referenced*) *measurement system*, voltage measurements are referred to the ground, while in a *differential* (or *nonreferenced*) *measurement system* none of the terminals are tied to a ground reference. Variants are the *nonreferenced single-ended systems*, where the potential at the reference point can be different from the ground potential, and the *pseudo-differential systems*, which combine some characteristics of differential and single-ended systems. In fact, both the positive and negative input terminals are wired in pseudo-differential systems, like in the differential ones; however, the negative input is also connected to the system ground through relatively small impedance. This provides some isolation between the ground of the sensors and that of the measurement device.

The above-mentioned different measurement schemes are characterized by different capabilities in rejecting certain types of noise sources. Thus, the final choice depends on the required level of immunity to these noise sources, taking into account that certain combinations of signal sources and measurement device are particularly vulnerable to measurement errors as an effect of the disturbance. In this section common-mode voltage and ground-loop current are analyzed. Additional noise sources, such as the noise picked up from the environment or the noise due to inappropriate termination of the cable shield, will be discussed in Sect. 3.4.

When a differential measurement device is considered, in the ideal case it responds only to the potential difference between the noninverting (+) and the inverting (−) terminal. Thus, the voltage value, with respect to the ground, that is present at both terminals is completely rejected. Such a voltage is referred to as *common-mode voltage*. The capability of actual devices of rejecting common-mode

voltage is limited and described by the following parameters: the common-mode voltage range and the *common-mode rejection ratio* (CMRR). The CMRR is a measure of the ability of an instrument to reject interference from a common-mode signal. It is usually expressed in dB. The CMRR basically describes the ability of a differential measurement system to reject noise common to both inputs: the higher the CMRR, the better the circuitry can extract differential signals in the presence of common-mode noise. The *common-mode voltage range*, instead, defines limits for the voltage swing on each input with respect to the measurement system ground. Violation of this constraint results in measurement errors and even in damage to the data acquisition device. For this reason some device manufacturers provide an equation which limits the sum of common-mode voltage, bias voltage of the sensor and full-scale voltage of the sensor. This sum must be in the predefined voltage range to ensure that the data acquisition device can be used with the selected sensors.

The quality of measurements with differential systems primarily depends on their capability of rejecting common-mode voltage, since unwanted noise is often present in this form. Typical sources of common-mode voltage noise are 50/60 Hz signals from power lines, power supply ripple, or electromagnetic fields.

Differential measurement devices are the best choice in the presence of grounded signal sources. In fact, if a grounded sensor is connected to a single-ended measurement device, the electrical potential difference between the ground of the signal source and that of the measurement system induces a current, which is called *ground-loop current*. Ground-loop induced noise may have both AC and DC components. As a consequence, both noise and offset errors are introduced in the measurements. Such noisy measurements often show the power line frequency component. The signal degradation due to ground-loop effects can be tolerated only in the presence of signals characterized by a high voltage level and low impedance wires between signal sources and measurement device.

In the presence of floating signal sources, single-ended measurement systems can be confidently used since no ground-loop is created. Floating signal sources can also be measured by differential systems, provided that the common-mode voltage range of the measurement device is respected. When floating signal sources are acquired by differential systems, bias resistors connecting the two leads with the measurement system ground are usually adopted to anchor the voltage level of the source to a certain reference and prevent erratic or saturated readings.

In general terms, differential measurement systems probably represent the favorite choice in many cases, since they are able to reject ground-loop induced errors and also the noise picked up from the environment up to a certain degree. On the other hand, single-ended measurement systems do not provide common-mode voltage rejection and are susceptible of ground-loop problems but they may represent a valid alternative when a large number of channels are required. In fact, in this case only a single analog input channel is required. Thus, single-ended devices provide twice the number of channels with respect to the equivalent differential systems. If the magnitude of the induced errors is smaller than the required accuracy of the data, single-ended measurement devices can be adopted.

Commercial solutions available on the market sometimes permit the selection of both single ended and differential configurations by simple settings of sensors and data acquisition hardware. Following the configuration and wiring instructions, the quality of data is usually preserved even in the presence of fairly long cables. More attention is needed, instead, when sensors and data acquisition hardware do not come from the same manufacturer. In this case, compatibility has to be checked, and additional caution is needed to prevent unintentional introduction of noise. For instance, ground connections have to be carefully planned to avoid ground-loops, in particular if PC-based data acquisition systems and separate mains power supply for the sensors are used.

In vibration measurements by programmable hardware the pseudo-differential configuration is sometimes adopted. Similarly with differential devices, pseudo-differential systems provide common-mode voltage rejection. However, while differential systems provide both AC and DC common-mode rejection, pseudo-differential devices provide only DC common-mode voltage rejection. Even in the presence of such a limitation in terms of common-mode voltage rejection, pseudo-differential systems may represent a valid alternative for dynamic data acquisition. In fact, the isolation between sensor ground and measurement device ground allows minimizing ground-loop effects when grounded signal sources are used. In summary, pseudo-differential measurements can be recommended for floating signal sources and can eventually be used also for grounded signal sources; however, differential systems provide more common-mode voltage rejection. Differential systems are recommended for grounded signal sources; floating sources can be measured too, but additional connections to ground by means of bias resistors are needed to prevent signal drifts beyond the common-mode range.

---

### **3.2 Transducers**

The role of transducers is the translation of physical quantities into electrical signals. For instance, motion transducers convert displacement, velocity, or acceleration into an electrical quantity (typically, voltage) that is proportional to the magnitude of the considered physical quantity. Different types of sensors are available to measure the dynamic response of civil structures. In this section attention is mainly focused on (both piezoelectric and force-balance) accelerometers, even if different types of sensors, such as electromagnetic sensors (seismograph, geophone), can also be adopted in output-only modal testing.

In piezoelectric sensors the conversion of the mechanical quantity into an electrical quantity is obtained by taking advantage of the piezoelectric property of some natural (quartz) or man-made (polycrystalline ceramics, such as barium titanate) materials. As a consequence of piezoelectricity, when a force is applied to the crystal, negative and positive ions accumulate onto the opposite surfaces of the crystal. The amount of accumulated charge is directly proportional to the applied force. In piezoelectric accelerometers a mass is coupled to the crystal.

When an input acceleration is applied at the base of the accelerometer, the inertia force associated to the mass causes a deformation of the crystal. The piezoelectric material generates an electric charge proportional to its deformation.

The electrical charge on piezoelectric crystals can be induced by compression, shear, or flexural deformation. Each method offers advantages and drawbacks. Thus, piezoelectric accelerometers are alternatively built according to one of these methods by choosing the most appropriate for the considered application. In compression mode the seismic mass applies a compressive force on the piezoelectric crystal mounted on a rigid base. This method leads to a high-frequency range but it is susceptible to thermal transient effects because the crystal is in contact with the base of the housing. Moreover, any deformation of the base is transmitted to the crystal, which provides erratic readings not associated to the acceleration. For these reasons, compressive design of piezoelectric accelerometers is being more and more replaced by shear and flexural design. Accelerometers based on the shear method show the best overall performance. In this case the crystal is clamped between a center post and the outer mass: the larger the attached mass, the larger the shear force applied to the crystal for a given acceleration. These accelerometers work well over a high-frequency range and do not suffer strain or thermal transient effects, since the crystal is not in direct contact with the base. Flexural design leads to very high output signals because the crystal is subjected to high stress levels. The bending of the crystal can be the result of inertia forces associated to the sole mass of the crystal, but additional weight can be added to the crystal to enhance bending. This type of accelerometers shows a limited frequency range in comparison with the previous ones, and they are more prone to damage if exposed to excessive shock or vibration. Accelerometers based on flexural design are typically well suited for low frequency, low vibration amplitude applications such as modal testing of structures.

The charge collected by electrodes on the piezoelectric crystal is transmitted to a signal conditioner, which converts the electric charge into voltage. A remote signal conditioner characterizes charge mode sensors. On the contrary, a built-in signal conditioner characterizes the so-called Integrated Electronics Piezo-Electric (IEPE) accelerometers (also known as voltage mode accelerometers). In the presence of a built-in signal conditioner, the signal cable carries also the required power supply. As a consequence, the signal is high-pass filtered to remove the frequencies close to DC. The (built-in or remote) signal conditioner output is a voltage signal available for display, recording, and analysis. Nowadays IEPE accelerometers (Fig. 3.1) are replacing charge mode sensors since they offer a number of advantages, such as simplified operation, lower cost, resolution virtually unaffected by cable type and length (long cables can be used without increase in noise, loss of resolution, or signal attenuation).

From a mechanical point of view, a piezoelectric accelerometer is equivalent to a SDOF system characterized by an oscillating mass subjected to an input ground motion; the spring and the dashpot of the SDOF system are represented by the piezoelectric material. As a consequence, some characteristics of piezoelectric

**Fig. 3.1** IEPE accelerometers (by PCB Piezotronics Inc.)

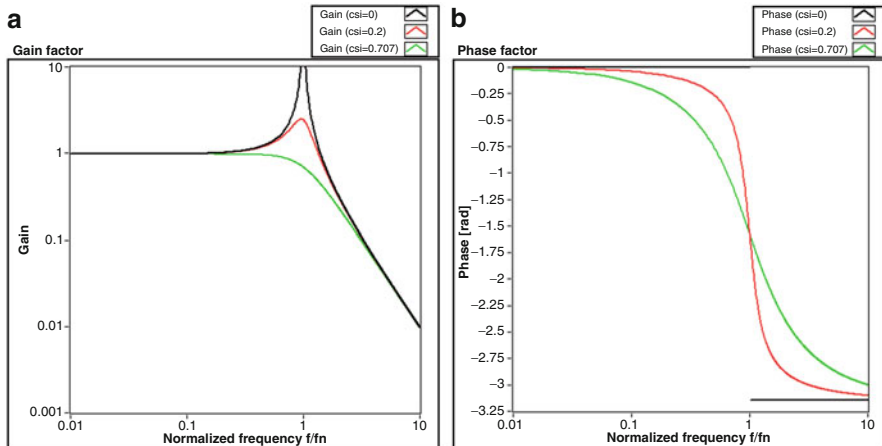


**Fig. 3.2** Sample FRFs of piezoelectric accelerometers for different damping values: amplitude (a) and phase (b)

accelerometers can be obtained from the analysis of the FRF of the system, relating the input acceleration and the output voltage (Fig. 3.2).

In terms of amplitude, the widest frequency range with uniform gain is associated to a damping ratio of 0.707. For this reason, some accelerometers are designed with added damping in order to maximize their frequency range. This is mainly the case of large accelerometers, characterized by low values of the first natural frequency. From a general point of view, independently of the damping ratio, the gain factor is basically uniform for frequencies up to 20 % of the undamped natural frequency of the sensor. Thus, it may happen that no specific design in terms of damping is carried out by the manufacturer, and the useful frequency range of the sensor is simply up to 20 % of its natural frequency.

**Fig. 3.3** Force balance accelerometers  
(by Kinematics Inc.)



In terms of phase, a damping ratio equal to 0.707 leads to a phase function, which is basically linear over the frequency range where the frequency response amplitude is flat. The linear phase function induces only a time delay and, as a consequence, it does not distort the time history. On the contrary, deviations from the damping value of 0.707 lead to a phase distortion in the measured structural response. However, in these cases the sensor can be used in a frequency range up to 20 % of its natural frequency without distortion of the measured structural response. In fact, in this frequency range the phase is zero. It is worth noting that the fundamental natural frequency of the sensor also depends on how it is mounted. In fact, as it will be clarified in Sect. 3.5, when the attachment of the sensor to the structure is not rigid, the natural frequency of the accelerometer can be lower than the value declared by the manufacturer and referred to rigid mounting. As a consequence, a narrower frequency range is obtained.

Force-balance accelerometers (Fig. 3.3) are based on a capacitor with moving plates and a control system creating a restoring force when a minute displacement of the plates occurs as an effect of the applied input ground motion. At rest the two moving capacitor plates (also referred to as “the moving mass”) are symmetrical to the fixed central plate and no voltage is generated. Acceleration causes the capacitive sensor plates to move with respect to the fixed central plate. This displacement results in an unbalanced signal. This error signal is manipulated in order to create a DC error term. The feedback loop compensates for this error signal by creating a magnetic restoring force to balance the capacitor plates back to their original equilibrium position. The current traveling through the coil is thus directly proportional to the applied acceleration.

Force balance accelerometers can measure also static forces, so their bandwidth starts from DC. The upper bound of the frequency range is, instead, limited to a few hundred Hz. Thus, a narrower frequency range typically characterizes force balance accelerometers with respect even to the large seismic piezoelectric accelerometers, but it still fulfills the requirements of testing and monitoring of civil structures. An example of frequency response of force balance accelerometers is illustrated in Fig. 3.4.

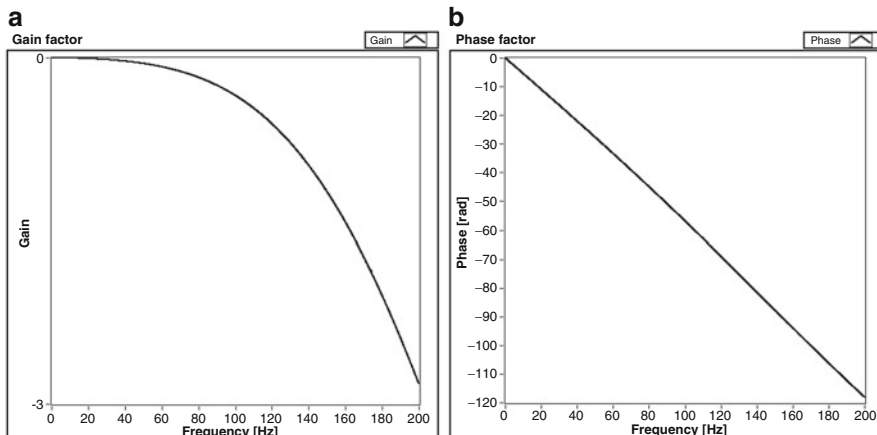


**Fig. 3.4** Gain (a) and phase (b) of the typical frequency response of force balance accelerometers

In recent years geophones have been adopted in a number of OMA tests (Brincker et al. 2005, Schmidt 2007). These sensors provide velocity measurements and they do not need power supply. In fact, the signal is produced by the relative movement of the coil (representing the oscillating mass) with respect to a magnet attached to the base of the sensor. Geophones are robust high-performance sensors, in particular with respect to sensor self noise; however, they are characterized by poor performance at low frequencies. Some proposals for digital correction of the output signal in order to overcome these limitations can be found in the literature (Brincker et al. 2005, Barzilai 2000).

When accelerometers are used for ambient vibration testing of civil structures, the low amplitude of motion and the limited frequency range of the structure under test orient the choice towards high-sensitivity accelerometers such as those used for seismic networks. However, frequency band and sensitivity are not the only parameters to be taken into account. Sensor specifications must be carefully analyzed in order to properly select and use the sensors for a specific application. In particular, it is worth noting that some sensor characteristics, such as dynamic range or sensitivity, might be frequency dependent. Thus, a sensor might show better specifications in a certain frequency band and worse specifications elsewhere. This circumstance must be taken into account in the choice of a sensor.

Independently of the type of sensor, the output voltage signal is proportional to the measured physical quantity through a constant, the *sensitivity* of the sensor. Sensitivity is usually given as the gain of the sensor (for example, 10 V/g) and it is in some way related to the smallest signal that can be resolved. In fact, the sensitivity of a sensor is defined as the minimum input of physical parameter that will create a detectable output change. However, the smallest detectable signal is also limited by the noise generated in the electronics. From a general point of view, a high gain should be preferred since an amplified signal minimizes the noise effects associated to the transmission over cables. Besides, it is important to verify

that the maximum sensor output has a level fitting the recorder maximum input so that the sensor dynamic range is optimally used.

The *dynamic range*  $DR_s$  of a sensor (often expressed in dB) is the ratio between the largest and the smallest signal it can measure:

$$DR_s = 10 \log \left( \frac{V_{\max,s}}{V_{n,s}} \right)^2 \quad (3.1)$$

In (3.1)  $V_{\max,s}$  and  $V_{n,s}$  represent the maximum voltage signal and the noise floor of the sensor, respectively. The noise floor typically depends on frequency and it is expressed in  $V/\sqrt{\text{Hz}}$ . Thus, it has to be squared and integrated over the considered frequency range in order to compute the value of  $DR_s$ . Nowadays, the best accelerometers have a dynamic range higher than 150 dB. However, the dynamic range of the total measurement chain depends also on the dynamic range of the digitizer. As a consequence, a dynamic range in the order of 120–140 dB is also suitable since it fits well the dynamic range of the average 24 bit digitizers.

*Sensor resolution* represents the smallest incremental change of physical quantity that leads to a detectable change in the sensor output. It is usually expressed in absolute terms or as a percentage of the *full-scale range*. This provides the minimum and maximum values of the physical quantity that can be measured by the sensor. Some accelerometers are characterized by user-selectable full-scale range.

An ideal sensor should behave linearly, but a certain deviation from linearity is always present. Such deviation should be as limited as possible and it is expressed by the percentage of nonlinearity. Accelerometers with good performance typically show a *nonlinearity* lower than 1 %.

The *cross axis sensitivity* of a sensor quantifies its sensitivity to motion perpendicular to the main axis. Accelerometers for modal testing typically show a low transverse sensitivity, in the order of 2 % or less.

Readings from accelerometers are often characterized by a certain offset. The *offset error* is defined as the output of the sensor at zero input. Some accelerometers permit the minimization of the offset error through a mechanical intervention.

*Settling time* of piezoelectric accelerometers is another parameter to be taken into account during measurements. It represents the time needed by the sensor to reach a stable output once power is supplied to the sensor. In other words, after power is supplied, it is the amount of time to wait before starting recording in order to get stable measurements.

*Sensor self noise* plays a primary role in determining the capability of the sensor to properly resolve the structural response. In fact, if the signal to be recorded is very small, it may drown in the electronic noise of the sensor. Reliable information about or quantification of sensor self noise is, therefore, fundamental in the presence of very weak ambient excitation or in the case of very massive low-rise structures.

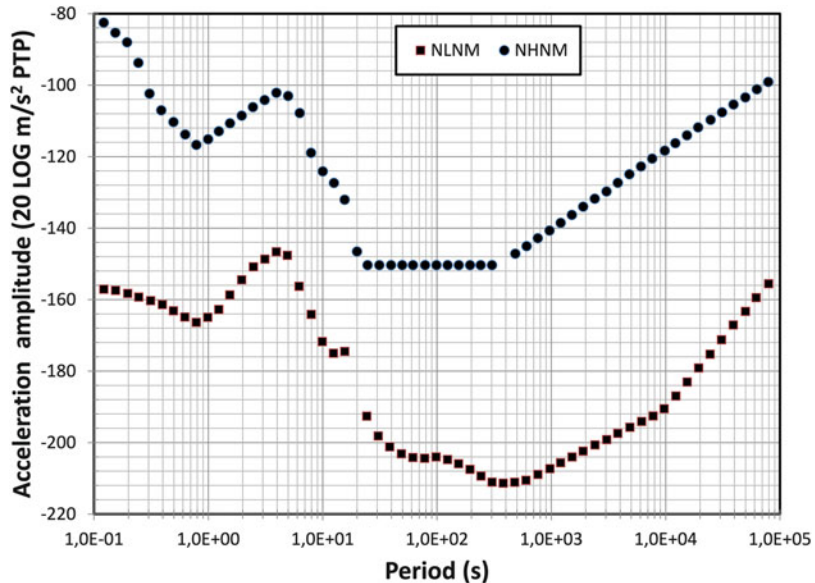


**Fig. 3.5** Peterson's noise models: New Low Noise Model (NLNM), New High Noise Model (NHHNM)

Methods to estimate the noise floor of sensors are described in Brincker and Larsen (2007). An approach is based on the isolation of the sensor from any vibration (for instance, by a seismic isolation chamber). When two or more sensors are available, an alternative approach is based on measurements carried out in the same location. In this case only one physical signal is present (the ambient vibration signal), and the SVD of the PSD matrix makes possible the simultaneous estimation of signal spectrum and noise floor of sensors.

Comparing the noise floor of the sensors with reference models of the seismic background noise can be useful to check their effectiveness for ambient vibration measurements. Even if such models were developed to deal with seismic background noise, Peterson's noise curves (Peterson 1993) represent a valuable tool to assess the performance of a sensor in the presence of very low levels of vibration. In fact, seismic micro-tremors represent low-amplitude vibrations of the ground due to artificial and natural noise sources. Starting from ground acceleration PSDs determined for noisy and quiet periods at 75 worldwide distributed digital stations and averaging the spectra of the three quietest and the three noisiest independent records, Peterson has derived two curves (Fig. 3.5) which represent upper and lower bounds of the typical PSDs of the observed ambient noise. In very quiet conditions, the sensor is able to properly resolve the seismic background noise if its noise floor is below the Peterson's low noise model. Otherwise, the sensor output signal is just electronic noise. Thus, the Peterson's curves are extremely useful as a reference for assessing the quality of seismic stations, for predicting the detectability of small

signals, and for the design of seismic sensors. By definition, the low noise model represents a conservative estimate of the expected level of micro-tremor excitation. Man-made activities, site amplification, and other factors influence the actual micro-tremor input so that almost all sites have a noise level above the Peterson's low-noise model, often by a large factor. The Peterson's low-noise model summarizes the lowest observed vertical seismic noise levels throughout the seismic frequency band. Peterson's investigations have also shown that the minimum level of horizontal acceleration is similar or slightly higher. As a consequence, the Peterson's low-noise model can be considered representative of both the vertical and horizontal minimum vibration levels.

The expected level of vibration of a structure in operational conditions is definitely higher than the seismic background noise, at least as an effect of site and structural amplifications. As a consequence, a sensor that accomplishes the Peterson's low-noise model is also effective for OMA tests. Taking into account the structural amplification at resonance and the Peterson's low-noise model, a sensor for OMA test in very quiet environment has to be characterized by a noise floor in the order of  $-140$  dB or better in the frequency range  $0.1\text{--}100$  Hz.

Both piezoelectric and force balance seismic accelerometers are very effective in measuring the response of civil structures in operational conditions. Each type of sensor has advantages and limitations. For instance, piezoelectric accelerometers are easy to install and are characterized by a good frequency response (large bandwidth), but they are also characterized by fragile sensing elements and by some limitations in measuring low-frequency components; moreover, the coaxial cable typically adopted to link the sensors with the data acquisition hardware is more prone to pick up noise from the environment with respect to the cables (made by individually shielded twisted pairs) adopted for force balance accelerometers (see also Sect. 3.4). On the other hand, force balance sensors have a low-noise floor and they are able to measure very low-frequency signals and even the DC component. However, the upper bound of their bandwidth is much lower than the upper frequency limit of piezoelectric sensors. Moreover, they suffer DC drifts and are characterized by expensive and heavy cabling. Electromagnetic sensors can sometimes be used for OMA tests taking advantage of their low-noise floor and of the cheap and noise robust cabling made by a single shielded twisted pair. However, the bad response at low frequencies limits their use in many civil engineering applications.

It is worth noting that the final choice of the sensors is always the result of a number of factors. In this book the use of seismic (piezoelectric or force balance) accelerometers is recommended because of their high performance in measuring low-amplitude ambient vibrations. However, the test engineer has to be aware that the market offers a large variety of sensors, characterized by a range of specifications and prices: thus, the final choice must take into account different factors, such as the final objective of measurements, the expected amplitude of the motion to be measured, the characteristics of the sensors in relation to those of the data acquisition hardware and of the tested structure, and, the last but not the least, the available budget.

### 3.3 Data Acquisition Systems

Data acquisition systems perform the conversion of the analog signals coming from the sensors into digital signals, which can be stored into a digital medium and analyzed by software. A large variety of systems for data acquisition are available on the market. They show different characteristics, configurations, and price, and the choice is made even more difficult when the available budget is not the sole constraint. In fact, additional factors influencing the choice are portability, the experience of the analyst, and the degree of compatibility with third-party hardware and software. A rough distinction can be made between dedicated solutions offered by specialized vendors (Fig. 3.6a) and customizable solutions based on programmable hardware (Fig. 3.6b). The first class of equipment is usually characterized by a steep learning curve, so that basic knowledge about signal acquisition and limited time to get confidence with the system are sufficient to carry out the first tests; however, these systems are accompanied by proprietary software for configuration and control of the measurement process and typically suffer for limited versatility. On the other hand, the solutions based on programmable hardware require more time, deeper theoretical knowledge, and larger efforts by the user to begin field



**Fig. 3.6** Dynamic data acquisition system by Kinematics Inc. (a) and programmable hardware by National Instruments™ (b)

tests. In fact, the user has in charge the duty of selecting the hardware components and developing the data acquisition software. However, the main advantages with these solutions are the lower price and the higher versatility. In both cases, the analysis of the main characteristics of analog-to-digital converters (ADCs) is helpful in order to properly select, among different solutions, the system that better fits the user's needs.

An ADC is a device that converts the continuous signal coming from the sensors into a sequence of digital numbers representing the amplitude of the signal. The conversion is based on the discretization of time (sampling) and signal amplitude (quantization). Quantization necessarily introduces a small amount of error, since the continuous amplitude of the signal is approximated by a finite number of discrete values. However, the quantization error is usually negligible with respect, for instance, to measurement noise. It can become significant only in the case of poor resolution.

The *resolution* of an ADC can be defined as the smallest step that can be detected. This is related to one change of the Least Significant Bit (LSB). For high dynamic range digitizers, the order of magnitude of resolution is about  $1 \mu\text{V}$ . The number of bits of an ADC is sometimes also referred to as resolution. However, most ADCs have an internal noise higher than one count: in this case, the number of noise free bits, rather than the total bit number, yields the effective resolution.

The *noise level* is related to the number of bits occupied by noise when the input is zero. Only the last two bits are typically corrupted by noise in good quality 24-bit digitizers.

The *dynamic range* is defined as the ratio between the largest and the smallest value the ADC can acquire without significant distortion. It is usually expressed in dB. Taking into account that the lowest bits often contain only noise, the dynamic range is also defined as the ratio between the largest input voltage and the noise level of the digitizer. This number may be dependent on the sampling frequency. Good digitizers currently have a dynamic range higher than 100 dB.

An example is helpful to illustrate the previous concepts. Consider an ADC characterized by a number of bits equal to  $N_{bit}$ . Assume that the maximum and minimum input voltage have the same absolute value; in other words, the input voltage varies between  $\pm V_{max, ADC}$  (for instance,  $\pm 5 \text{ V}$ ). The available number of discrete amplitude values is  $N = 2^{N_{bit}}$ . As a consequence, the nominal value of the ADC resolution is:

$$\Delta V_{ADC} = \frac{2V_{max, ADC}}{N} = \frac{2V_{max, ADC}}{2^{N_{bit}}} = V_{max, ADC} 2^{1-N_{bit}}. \quad (3.2)$$

Since the noise floor  $V_{n, ADC}$  of the ADC is usually larger than  $\Delta V_{ADC}$ , the least significant bits are given by (3.3):

$$2^{LSB} = \frac{V_{n, ADC}}{\Delta V_{ADC}} \quad (3.3)$$

and, as a consequence, the number of effective bits  $N_{bit, eff}$  is:

$$N_{bit, eff} = N_{bit} - LSB. \quad (3.4)$$

The dynamic range of the ADC can be computed from the number of effective bits as:

$$DR_{ADC} = 20 \log \left( \frac{V_{max, ADC}}{V_{n, ADC}} \right) = 20 \log (2^{N_{bit, eff} - 1}) \approx 6(N_{bit, eff} - 1). \quad (3.5)$$

Thus, a dynamic range of about 120 dB corresponds to 21 effective bits and vice versa. It is worth noting that the dynamic range of the complete measurement system depends also on the dynamic range of the sensors. For this reason, maximum input and noise floor of data acquisition system and sensors have to match.

The *sampling rate* is the number of samples acquired per second. The maximum sampling rate of the ADC defines the largest *frequency range* that can be investigated. For the majority of applications of OMA in civil engineering, a maximum sampling rate of 100 Hz or 200 Hz is satisfactory. Moreover, when large structures characterized by a high content of low-frequency modes are tested, the data acquisition system, like the sensors, has to be able to measure low-frequency components. In these conditions a frequency range starting from DC is required.

The *absolute accuracy* is a measure of all error sources. It is defined as the difference between the input voltage and the voltage representing the output. Ideally, this error should be  $\pm LSB/2$  (the quantization error, that is to say the error only due to the digitization steps).

*Conversion time*, that is to say the minimum time required for a complete conversion, is defined only for converters based on a sample-and-hold architecture. However, the sigma-delta architecture is currently preferred for 24-bit ADCs because of its higher performance; because of the different architecture, based on a continuous signal tracking, the conversion interval is not important for sigma-delta ADCs. Without describing sigma-delta converters in details, it is worth noting that their high performance is basically obtained by sampling the input signal at a frequency much higher than the desired data rate. The samples then pass through a filter which expands the data to 24 bits, rejects signal components higher than the Nyquist frequency associated to the desired sampling frequency, and digitally resamples the data at the chosen data rate. In general, the built-in anti-aliasing filters automatically adjust themselves (see Sect. 3.6 for more details about aliasing). The combination of analog and digital filtering provides a very accurate representation of the signal.

If several channels are available in the same digitizer, a signal recorded in one channel may be seen in another channel. This phenomenon is referred to as *cross talk*. The amount of cross talk is expressed in dB and means how much lower the level in a channel is in the neighboring channels. A good quality 24-bit digitizer has 120 dB of damping or better. Cheap multichannel digitizers, instead, usually use a single ADC and an analog multiplexer, which connects different inputs sequentially

to the ADC input. This limits the cross talk separation since analog multiplexers have limited performance. For high-quality measurements, solutions with one digitizer per channel are therefore recommended.

*Nonlinearity* is related to how two different signals at the input are intermodulated (so that the amplitude of a signal depends on the other) at the output. It is expressed as a percentage of the full scale. This is usually not a problem with modern sigma-delta converters.

The *offset* represents the DC level of the output when the input is zero. Some offset is always present, due to the ADC or the connected devices, but it can often be minimized. It is worth noting that any offset limits the dynamic range, since the ADC will reach its maximum value (positive or negative) for smaller input values than its nominal full scale.

Additional characteristics influencing the choice of the solutions for data acquisition are versatility and robustness. For instance, systems allowing the selection of different measurement schemes (single ended and differential) or acquisition of signals from sensors of different type are definitely more attractive. Portability, low power consumption and possibility of battery operation, robustness in varying environmental conditions also play a primary role in the choice of the equipment for field testing. Finally, distributed measurements by modular instruments are becoming more and more attractive thanks to the possibility to use the same device to carry out tests with either a few or a large number of measurement channels. This characteristic is particularly attractive in testing large or complex structures, when pretests or local tests with a reduced number of sensors and global measurements with a large number of channels have to be carried out on the same structure in a limited amount of time.

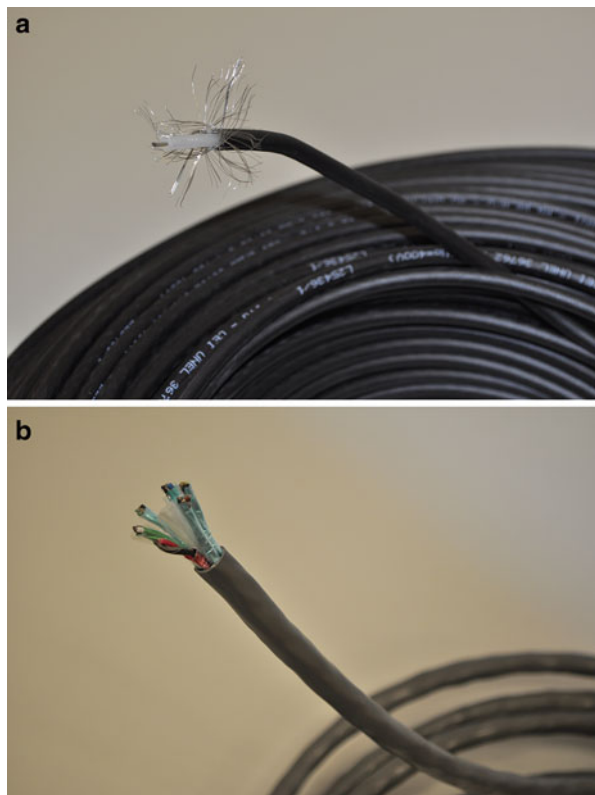
---

### 3.4 Wired vs. Wireless

The last decade has been characterized by large efforts in the development of wireless sensor networks for structural testing and health monitoring. The first commercially available wireless sensor platform, originally developed at the University of California-Berkeley, appeared in 1999. Since then, this technology has experienced a rapid development and an increasing interest of the scientific and professional community in this field. The commercial success is mainly due to the low cost and the possibility to combine different sensors in the same wireless node. More details can be found elsewhere (Lynch and Loh 2006).

Even if a number of wireless sensing solutions are currently available, offering attractive advantages such as the reduction of costs and installation time associated to the use of cables, they have not fully replaced wired systems. The main advantage of wired systems over wireless sensor network is in the time synchronization of the channels. Simultaneous sampling, in fact, ensures the phase coherence among all the measurement channels, preventing errors in the computation of cross-correlation and cross-spectral density functions. Time synchronization in wireless sensor networks requires specific solutions while it represents an ordinary task

**Fig. 3.7** Coaxial cable (a) and cable consisting of multiple individually shielded twisted pairs (b)



when a single data acquisition system and wired sensors are adopted. In wireless sensor networks, each node has an ADC of its own. As a consequence, time synchronization of the different ADCs requires an external time base providing a time reference. A possible solution for time synchronization of distributed ADCs is represented by GPS. Whenever a GPS signal is available, wireless sensor networks can be adopted.

The choice of the type of cable and the connection with the terminals also influence the quality of measurements. The following types of cables are typically used to carry the analog signals from the sensors to the data acquisition system:

- Coaxial cables (Fig. 3.7a)
- Cables consisting of a single shielded twisted pair
- Cables consisting of multiple twisted pairs with common shield
- Cables consisting of multiple individually shielded twisted pairs (Fig. 3.7b)

Coaxial cables (typically used for piezoelectric accelerometers) are very cheap but they are the most vulnerable to electrical noise exposure; cables consisting of multiple individually shielded twisted pairs (typically used for force balance accelerometers) are heavy and expensive but they are the least prone to pick up noise from the environment.

The connection of the wires with the terminals represents another critical aspect, since a poor connection fosters the introduction of electrical noise. In this perspective, particular attention has to be focused on proper shield termination, avoiding ground current flows through the shield. This is possible by connecting the shield to the ground only at one end. Instructions for cable assembly provided by sensor and data acquisition system manufacturers have to be carefully fulfilled.

Even when ground loops are avoided, there is always a certain amount of noise picked up from the environment. Some rules of thumb can help to minimize these effects. For instance, mobile phones must be switched off during tests, and cables and data acquisition systems must be placed as far as possible from sources of electromagnetic noise, including the computer screen. Moreover, dangling wires must be avoided. Cables must be clamped during tests because their motion can cause triboelectric effects. In simple words, the charge generated on the dielectric within the cable can lead to changes in the magnetic field if the dielectric does not maintain contact with the cable conductors, thus generating errors in the measurements.

If the measurement scheme has been appropriately defined, and installation and measurements are properly carried out, the collected data will be of good quality and ready for the analysis. During data processing, techniques for noise reduction can be adopted to further improve the quality of the obtained modal identification results. However, it is worth emphasizing that there is no substitute to good measurements. The acquired signal must carry the physical information together with a certain amount of noise in order to successfully apply OMA techniques. Signal processing techniques and advanced modal analysis techniques have no effects if the recorded signal consists of noise only.

---

### 3.5 Sensor Installation

Sensor layout and attachment method influence the identifiability of the modal properties of the structure under test. In particular, while the attachment method might have an influence on the extension of the investigated frequency range, the possibility to observe different and sometimes closely spaced modes depends on sensor layout (as mentioned also in Chap. 1).

Accelerometers can be mounted by a variety of methods, including magnet, adhesive, and stud or screwed bolt. The main drawback when using stud or screwed bolt is the higher difficulty in moving the sensors in different positions of the structure. However, a stiff connection ensures that the useful frequency range of the accelerometer is not limited by the mounting method. In fact, the connection between sensor and structure acts like a spring, leading to a spring-mass system with the sensor itself. As a consequence, a reduction in the stiffness of the connection narrows the useful frequency range of the accelerometer by a reduction of its upper limit. The connection by stud or screwed bolt usually ensures a very stiff connection. However, a smooth flat surface of the structure at the desired sensor locations is also required to avoid a reduction of the upper frequency limit.

In fact, the prepared surface allows the sensor to be installed normally to it and with a very stiff contact between sensor and structure. On the contrary, a rough surface can lead to misalignments or poor contact, causing a loss of stiffness of the connection and the corresponding reduction of the frequency range. From a general point of view, the choice of the attachment method depends on different parameters, such as accessibility of the selected sensor positions, structural surface, expected amplitude of vibration and frequency range, portability, and surface type and conditions.

Sensor location mainly influences the observability of the structural modes. One of the reasons which may require to move the sensors from one location to another is their installation in correspondence or very close to nodes of the structural mode shapes. In similar cases the data collected by those sensors do not provide effective information for the identification of some of the structural modes (specifically, those modes whose nodes correspond to the position of the sensors). In fact, as already mentioned in Chap. 1, sensor placed at nodal points limits the rank of the FRF matrix. Another reason to move the sensors could be the identification of distinct resonances associated to very similar mode shape estimates as a result of poor spatial resolution of measurements and unfortunate choice of sensor layout.

The choice of the sensor layout depends on the number of available sensors, the needed information about the mode shapes, which may lead to different requirements in terms of spatial density of the sensors, and the objectives of the modal identification test. In the literature several studies aimed at the optimization of sensor location are available (see, for instance, Papadimitriou and Lombaert 2012, Cyrille 2012, Marano et al. 2011). However, the results obtained from the application of those methods depend on the adopted criteria and optimization techniques, leading to different possible layouts. Thus, those techniques can support the definition of the test layout but a careful planning by the test engineer and a certain amount of physical insight still play a relevant role in the definition of layouts able to maximize the observability of the modes and the amount of information provided by the sensors. Nevertheless, it is possible to define the minimum number of sensors that have to be installed to identify at least the fundamental modes of a structure. In fact, assuming that at least a couple of closely spaced modes exists and that the measurement noise limits the identifiability of some modes, in particular in the case of weakly excited structures, the fundamental modes can be identified by appropriate installation of at least 6–8 sensors. “Appropriate installation” means that the adopted sensor layout ensures the observability of modes of different type (for instance, translational and torsional modes) and does not limit the rank of the FRF matrix (for instance, installation of sensors in very close points has to be avoided since the information they provide is basically the same). When some a priori information about the mode shapes is available, an effective sensor layout can be obtained by installing the sensors in a set of points where all the modes of interest are well represented (that is to say, those modes show fairly large modal displacements at the selected locations). Even if the sensor layout varies from structure to structure and it can also be refined during the test if the measurements do not appear satisfactory at a first preliminary analysis, some

**Fig. 3.8** Recurrent sensor layout for buildings and tower-like structures

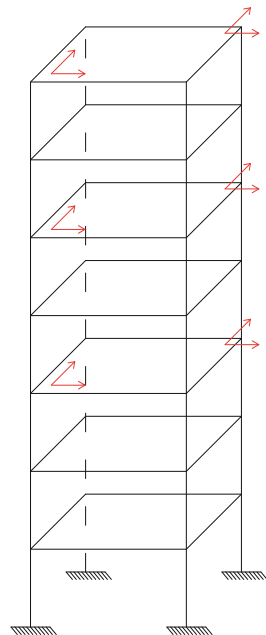
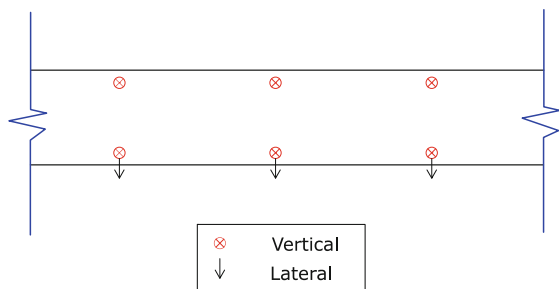


**Fig. 3.9** Recurrent sensor layout for bridge spans



recurrent schemes for sensor placement can be identified. They are shown in Fig. 3.8 for buildings and tower-like structures, and in Fig. 3.9 for bridges.

Under the assumption of rigid floors in building-like structures, at least three sensors have to be installed on a floor. In order to ensure the observability of both translational and torsional modes, the sensors have to be installed in two orthogonal directions and in opposite corners of each instrumented floor. Installing the sensors on, at least, two distinct floors allows, in principle, the identification of some higher modes, too. When the tested structure is a bridge, both vertical and horizontal components of acceleration have to be measured in order to ensure the identification of both horizontal and vertical bending modes. Moreover, installation of couples of sensors measuring the vertical component of acceleration at the same abscissa along the main axis of the bridge but in symmetrical points with respect to it ensures the observability of torsional modes.

The previously suggested layouts represent only crude guidelines for the installation of the sensors. The actual test layout has to be defined taking into account all the previously discussed issues and the characteristics of the tested structure. In some cases the objective of the tests can be the investigation of the dynamic response of selected portions of a structure, such as the cables in cable-stayed bridges or steel rods in ancient vaults. When similar lightweight structural components are tested, it is important to ensure that the attached accelerometers have a minimum influence on the vibratory behavior of the tested system. In particular, the added mass represented by wires and sensors has to be as limited as possible. Taking into account that the weight of the sensor typically increases with its sensitivity, the influence of the added mass on the dynamic response has to be carefully evaluated if high sensitivity accelerometers are going to be used. If a significant influence of the added mass on the dynamic response is expected, alternative solutions have to be adopted. They can range from the replacement of the heavy high-sensitivity accelerometers with lighter accelerometers at the expenses of a reduction in sensitivity, up to the adoption of wireless sensor networks.

In some cases the number of available sensors is not sufficient to obtain the desired spatial resolution for the mode shape estimates. For instance, assume that the mode shapes have to be estimated in  $M$  points and the number of available sensors is  $N_s < M$ . The estimation of the mode shapes in all the  $M$  points, therefore, requires the execution of multiple tests in order to cover all the points of interest. Assuming that  $T$  tests have to be carried out,  $T$  datasets are obtained. However, the mode shape estimates obtained from each dataset cannot simply be glued together to obtain the mode shape estimate in the desired  $M$  locations. In fact, as mentioned in Chap. 1, the excitation is not measured in OMA and, as a consequence, the obtained mode shape estimates cannot be scaled in order to fulfill the property of orthogonality with respect to the mass matrix. Only un-scaled mode shape estimates can be obtained, and the scaling factor between mass-normalized mode shapes and un-scaled mode shapes can vary from test to test. In these conditions the only possibility to merge the different partial mode shape estimates is to carry out multiple tests where a number of sensors  $N_{ref}$  (called *reference sensors*) remain in the same position during all tests and the other  $N_{rov}$  sensors (called *roving sensors*) are moved until the structural response is measured at all the desired  $M$  locations. The mode shape estimates obtained from each dataset can be then divided in two parts:  $N_{ref}$  components are defined over the set of points common to all tests, while the remaining  $N_{rov}$  components are defined over non-overlapping sets of points. The  $N_{ref}$  components of the estimated mode shape obtained from the  $i$ -th test are related to the  $N_{ref}$  components obtained from the first dataset in the same locations through a scaling constant:

$$\left\{ \phi_{ref,1}^k \right\} = \alpha_{1,i}^k \left\{ \phi_{ref,i}^k \right\} \quad (3.6)$$

where  $\{\phi_{ref,1}^k\}$  and  $\{\phi_{ref,i}^k\}$  are the portions of the  $k$ -th mode shape estimated from the first and  $i$ -th dataset at the  $N_{ref}$  reference points, respectively. Assuming  $N_{ref} \geq 3$ ,

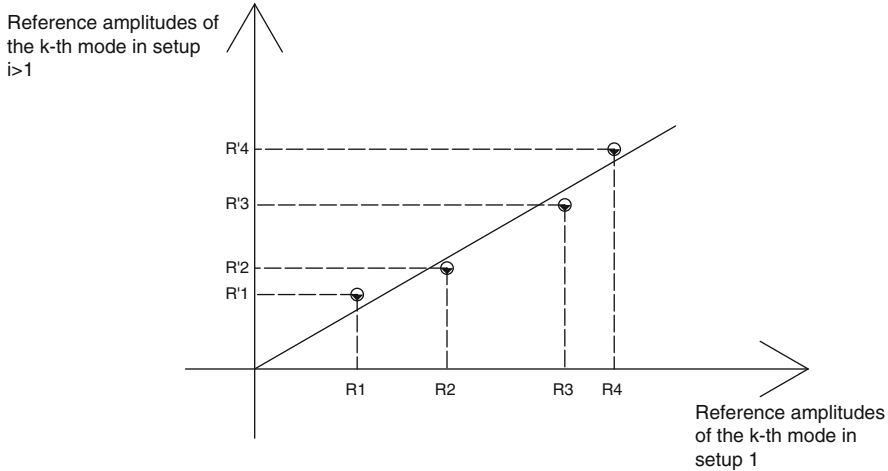


**Fig. 3.10** Determination of the scaling factor of mode shapes in multi-setup measurements

the scaling factor is easily determined by solving a least squares problem (Fig. 3.10); the resulting scaling factors are finally used to merge the different portions into the total mode shape vector:

$$\{\phi^k\} = \left\{ \begin{array}{l} \{\phi_{ref,1}^k\} \\ \{\phi_{rov,1}^k\} \\ \alpha_{1,2}^k \{\phi_{rov,2}^k\} \\ \dots \\ \alpha_{1,i}^k \{\phi_{rov,i}^k\} \\ \dots \\ \alpha_{1,T-1}^k \{\phi_{rov,T-1}^k\} \end{array} \right\}. \quad (3.7)$$

It is worth noting that, if the  $k$ -th mode shape vector is characterized by small components in the reference points, noise can heavily affect the resulting value of the scaling factor. Thus, the use of a fairly large number of reference sensors is recommended in order to ensure the availability of a number of reasonably large mode shape components for all the modes. Additional details and more advanced procedures to merge mode shape estimates from different setups can be found in the literature (Reynders et al. 2009, Dohler et al. 2010a, Dohler et al. 2010b).

The previous discussions highlight the importance of an accurate design of the test. A final suggestion can be given for those situations where the number of sensors is not a limiting factor but there is the need for an improvement of the SNR (this could be the case of very weak excitation, so that, even if the sensors are able

to properly resolve the small amplitude vibrations, the peaks of mode resonances are not so far from the noise level). In these conditions, if sensors are installed in couples, so that the two sensors in the same couple measure the same physical signal  $s(t)$  (that is, the two sensors are located in the same point and measure the same component of acceleration):

$$y_1(t) = s(t) + n_1(t), \quad (3.8)$$

$$y_2(t) = s(t) + n_2(t), \quad (3.9)$$

assuming that each sensor has its own inherent noise:

$$n_1(t) \neq n_2(t), \quad (3.10)$$

and that signal and noise for each sensor as well as the noise components of the two sensors in the couple are uncorrelated:

$$E[s(t)n_1(t - \tau)] = 0 \quad (3.11)$$

$$E[s(t)n_2(t - \tau)] = 0 \quad (3.12)$$

$$E[n_1(t)n_2(t - \tau)] = 0 \quad (3.13)$$

simple mathematical manipulations allow to recognize that the cross-correlation between  $y_1(t)$  and  $y_2(t)$  is:

$$R_{y_i y_j}(\tau) = E[s(t)s(t - \tau)] + \delta_{ij}E[n_i(t)n_j(t - \tau)] \quad i, j = 1, 2. \quad (3.14)$$

As a consequence, the cross-correlation (or equivalently the cross-spectrum) between the two channels extracts the signal from the noise of the sensors and can be used to improve the signal-to-noise ratio when it is poor with only one sensor.

In a similar way, it is possible to compute the auto-correlation (auto-spectrum) of the signal difference  $y_1(t) - y_2(t)$  and show that it is a measure of the sum of the noises in the two sensors:

$$R_{y_1 - y_2, y_1 - y_2}(\tau) = R_{n_1, n_1}(\tau) + R_{n_2, n_2}(\tau) \quad (3.15)$$

while the auto-correlation of the sum of the signals,  $y_1(t) + y_2(t)$ , amplifies the signal with respect to the noise:

$$R_{y_1 + y_2, y_1 + y_2}(\tau) = 4R_{s, s}(\tau) + R_{n_1, n_1}(\tau) + R_{n_2, n_2}(\tau). \quad (3.16)$$

The installation of couples of sensors in the same position obviously does not overcome the limits of the sensors. If the single sensor is not able to measure the structural response, no physical information is included in the data but they are just noise. However, if the sensors are properly selected, so that they are able to resolve the structural response, this sensor layout can improve the SNR of the collected data.

## 3.6 Sampling, Filtering, and Decimation

The definition of the value of the sampling frequency represents one of the most important settings in dynamic tests. It is always a compromise between the need for an accurate representation of the signal in digital form and the available (eventually large, but always limited) memory and hard disk space for data storage and analysis. Thus, very long observation periods may require lower values of the sampling frequency to avoid overburdening. However, the sampling frequency cannot be set too low, because it determines the frequency range that can be investigated. As a consequence, it has to be set depending on the maximum frequency of the structure under test.

Assuming that the expected value of the maximum frequency is 20 Hz, the sampling frequency has to be set in a way able to observe this maximum frequency. The Shannon's theorem (2.20) states that the sampling frequency has to be at least twice the highest frequency contained in the time signal. In the present example, a sampling frequency larger than 40 Hz is needed, so that the upper bound of the observable frequency range (the so-called *Nyquist frequency*  $f_N = f_s/2$ ) is higher than 20 Hz.

Figure 3.11 shows the effect of an inadequate selection of the sampling rate that causes an erroneous reconstruction of the waveform after digitization of the continuous signal with a high-frequency signal appearing as a low-frequency one. Thus, a typical problem of digital signal analysis caused by the discrete sampling of continuous signals is the so-called *aliasing*. Aliasing originates from the discretization of the continuous signal when the signal is sampled too slowly and, as a consequence of this under-sampling, higher frequencies than the Nyquist

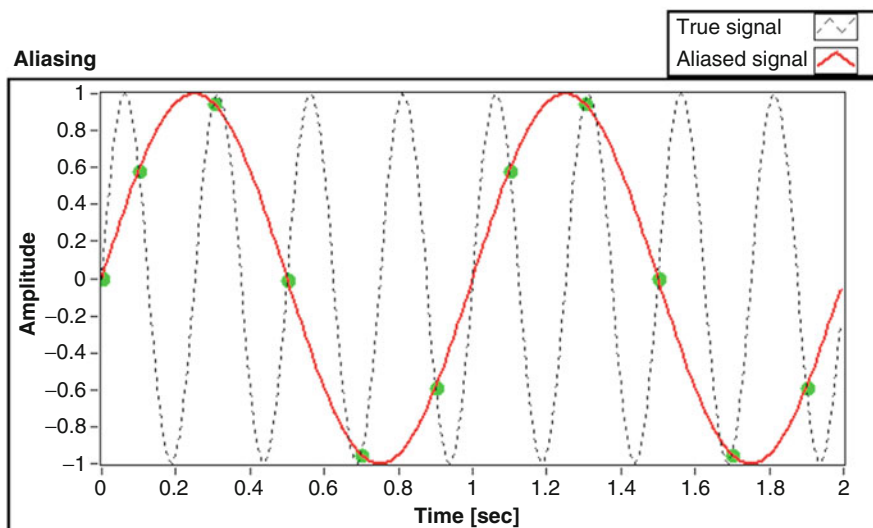


**Fig. 3.11** Aliasing

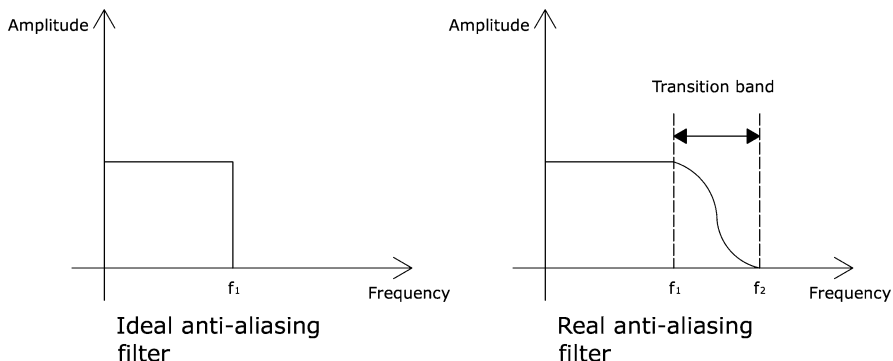


**Fig. 3.12** Ideal and real anti-aliasing filter

frequency are reflected in the observed frequency range causing amplitude and frequency errors in the spectrum of the signal.

For instance, assume that the analog signal includes the power line frequency  $f_{PL} = 50 \text{ Hz} > f_N$ ; in the absence of any countermeasure, when the analog signal is sampled at  $f_s = 40 \text{ Hz}$ , the frequency  $f_{PL}$  will be aliased and it will appear as a frequency component of the signal at 10 Hz. In fact, the alias frequency is given by the absolute value of the difference between the closest integer multiple of the sampling frequency and the input frequency. In the present case:  $|f_s - f_{PL}| = |40 - 50| \text{ Hz} = 10 \text{ Hz}$ . This alias frequency cannot be distinguished from actual low-frequency components in the signal. Effective countermeasures are, therefore, needed to prevent distortions in the computation of the spectrum of the digital signal.

The only method to avoid aliasing is the removal of all frequency components in the analog signal that are above the Nyquist frequency before the analog-to-digital conversion. An analog low-pass filter applied before this conversion allows restricting the frequency range of the original analog signal. Such an analog filter with sharp cut-off is usually referred to as the *anti-aliasing filter*. The presence of an analog anti-aliasing filter before the ADC is a critical requirement in the selection of the data acquisition system, since it only can minimize aliasing. It is worth pointing out that an ideal anti-aliasing filter passes all the frequencies below and removes all the frequencies above the cut-off frequency of the filter, but it is not physically realizable. Thus, real anti-aliasing filters always have a transition band, which causes a gradual attenuation of the input frequencies (Fig. 3.12). Thus, the frequencies in the transition band can still cause aliasing.

Taking into account that no low-pass filter has an infinitely sharp roll-off, the filter is often set at 80 % of the Nyquist frequency (40 % of the sampling frequency) or even less, depending on the roll-off rate of the filter itself. Thus, the portion of the spectrum close to the Nyquist frequency is inevitably distorted and should be disregarded. In other words, due to the existence of this finite transition band in the analog anti-aliasing filter, the sampling frequency has to be set higher than

twice the maximum frequency in the signal. In the previous sample case, assuming that the filter is set at 80 % of the Nyquist frequency so that it cuts off all frequencies above  $f_N$  and the transition band is  $[0.8f_N, f_N]$ , the frequency component at 20 Hz can be properly measured by setting  $f_s > 50$  Hz.

Unwanted frequency components can still be present in the acquired data. Digital filters can reject them. In Chap. 2 the modification of the signal in time domain by windowing has been discussed. Like the windows, the filters modify the signal but they act in frequency domain. They are usually classified as low-pass, high-pass, band-pass, and band-stop, depending on the frequency range of the signal that the filter is intended to pass from the input to the output with no attenuation. In particular, a low-pass filter excludes all frequencies above the cut-off frequency of the filter, while a high-pass filter excludes the frequencies below the cut-off frequency; a band-pass filter excludes all frequencies outside its frequency band, while a band-stop filter excludes the frequencies inside the filter band. Since the real filters have certain roll-off features outside the design frequency limits, the extension of the transition band and some effects on magnitude and phase of the signal have to be taken into account in the applications of digital filters.

An ideal low-pass filter removes all frequency components above the cut-off frequency. Moreover, it is characterized by a linear phase shift with frequency. The linear phase implies that the signal components at all frequencies are delayed by a constant time. As a consequence, the overall shape of the signal is preserved. However, the transfer functions of real filters only approximate the characteristics of ideal filters. A real filter can show a *ripple* (that is to say, an uneven variation of the gain with frequency) in the pass-band, a transition band outside the filter limits, and finite attenuation and ripple in the stop-band. Real filters can also show some nonlinearity in their phase response, causing a distortion of the shape of the signal. Thus, *center frequency* (the frequency where the filter causes a  $-3$  dB attenuation) and *roll-off rate* of the filter play a primary role in the choice of the filter, together with the presence of ripple in the pass-band (often present in high order filters) and phase nonlinearity.

Two types of digital filters exist, the so-called *Finite Impulse Response* (FIR) filters, characterized by a finite impulse response, and the *Infinite Impulse Response* (IIR) filters, whose impulse response exists indefinitely. The main difference is that the output of FIR filters depends only on the current and past input values, while the output of IIR filters depends also on the past output values.

IIR filters have an ARMA structure (see also Chap. 4). They provide a fairly sharp roll-off with a limited number of coefficients. Thus, the main advantage in using IIR filters is that they require fewer coefficients than FIR filters to carry out similar filtering operations. As a consequence, they are less computational demanding. However, they often show nonlinear phase and ripples.

FIR filters are also referred to as moving average filters. Their main advantage consists in a linear phase response, which makes them ideal for applications where the information about the phase has to be preserved. Unlike IIR filters, FIR filters are also always stable.

It is worth pointing out once again that only analog filters can definitely ensure that aliasing has not occurred. Alias frequencies cannot be recognized after the signal has been sampled, and this makes digital filters ineffective for their removal.

When records of the structural response are filtered to remove unwanted frequency components before modal parameter extraction, it is important to take into account the errors on amplitude and phase induced by filters. However, if the same filtering operation is applied to all measurement channels in the dataset, it does not negatively affect the estimation of the mode shapes.

In the context of modal identification, high-pass filters are often used to remove frequencies close to DC, while low-pass filters are used to exclude high-frequency components in view of decimation. The acquired signals are often sampled at a higher frequency than needed for the analysis. *Decimation* (or down-sampling) is therefore used to resample the acquired signals to a lower sampling frequency. This task cannot be accomplished simply by removing a certain number of samples depending on the adopted decimation factor (for instance, one in every two samples if the decimation factor is equal to 2). In fact, aliasing may occur due to the presence of frequency components between the original Nyquist frequency and the new value after decimation. These frequency components above the new Nyquist frequency have to be removed before decimation by applying a low-pass filter. Low-pass filtering ensures that the decimated data are not affected by aliasing.

---

### 3.7 Data Validation and Pretreatment

Validation of the collected data is recommended before they are analyzed and the modal parameters estimated. The validation step is definitely feasible in the case of offline data processing, while it is usually omitted in automated OMA. It consists in the careful inspection of the time histories and, in particular, of their distribution to identify common anomalies in the data. A usual assumption in data processing is that data are stationary, with Gaussian distribution and no periodicities. Simple considerations about the physical mechanisms that produced the data are often sufficient to assess if the data can be considered stationary. For instance, this is the case when data are generated by time-invariant phenomena (both the structure and the loading). However, OMA methods are robust even in the presence of slightly nonstationary data; on the contrary, application of OMA to large transients, such as those associated to earthquake loading, leads to unpredictable and often erroneous results. If data are collected under conditions that do not permit an assumption of stationarity based on physical considerations, specific investigations based, for instance, on the reverse arrangements test (Bendat and Piersol 2000) can be carried out.

Periodic signals in otherwise random data lead to sharp peaks in the auto-spectrum that can be confused with narrow-band resonances. Some techniques for the identification of periodic components in random data will be illustrated in Chap. 5.

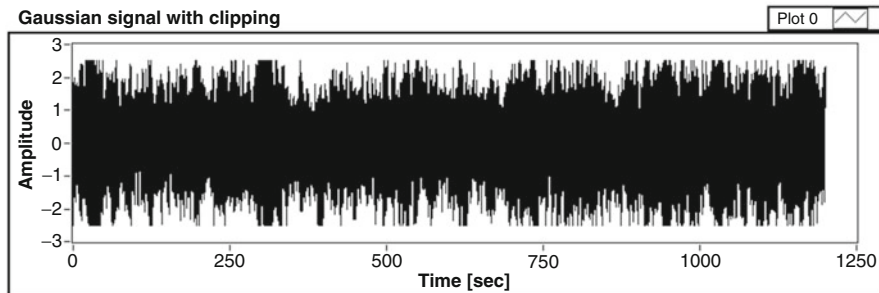


**Fig. 3.13** Random signal affected by clipping

Even if specific tests, such as the chi-square goodness-of-fit test, can be carried out (Bendat and Piersol 2000), an easy check for normality consists in the comparison between the estimated probability density function of the data and the theoretical normal distribution. This is especially true in the case of sufficiently long records, such as those typically adopted in OMA tests. Deviations from normality can also provide information about the presence of certain anomalies in the data.

Different anomalies can affect the raw data. One of the most common is signal *clipping*, which occurs when the signal saturates the ADC. Clipping may be two-sided, thus revealing improper matching between sensor output and ADC input, or one-sided, usually caused by excessive offset. It can be easily recognized by a visual inspection of the time series (Fig. 3.13) or by the analysis of the probability density function of the data (Fig. 3.14). It is worth noting that low-pass filtering typically obscures clipping, making its identification impossible. Thus, digital filtering has to be applied after data validation.

Improper matching between sensor output and ADC input can also lead to *excessive instrumentation noise*. This happens if the input signal from the sensor has a very low voltage with respect to the maximum allowed input voltage of the ADC. As a consequence, it occupies only a limited number of the available bits of the ADC. Since the least significant bits are occupied by noise, it is clear that the capabilities of the ADC are poorly exploited, and the resulting data are characterized by a low SNR. An excessive instrumentation noise can be detected through the inspection of the auto-spectrum of the signal, since the resonances appear nearly buried in noise (Fig. 3.15). In extreme cases, the signal is so small that it is totally obscured by the digital noise of the ADC. *Excessive digital noise* can be easily identified by visual inspection of the time series. In fact, the signal appears as a sequence of well-defined steps (Fig. 3.16). In these cases the measurement chain is definitely inadequate and it has to be replaced.

*Intermittent noise spikes* may sometimes appear in the measured time histories (Fig. 3.17). They can be the result of actual physical events, but malfunctioning of the measurement chain (for instance, a defective connector or shielded cable when subjected to vibration) might also cause them.

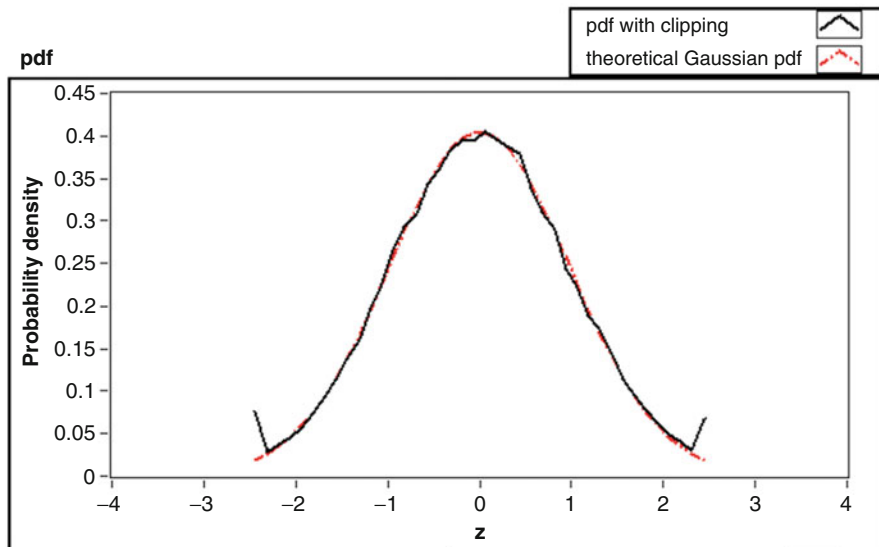


**Fig. 3.14** Probability density function of a random signal affected by clipping

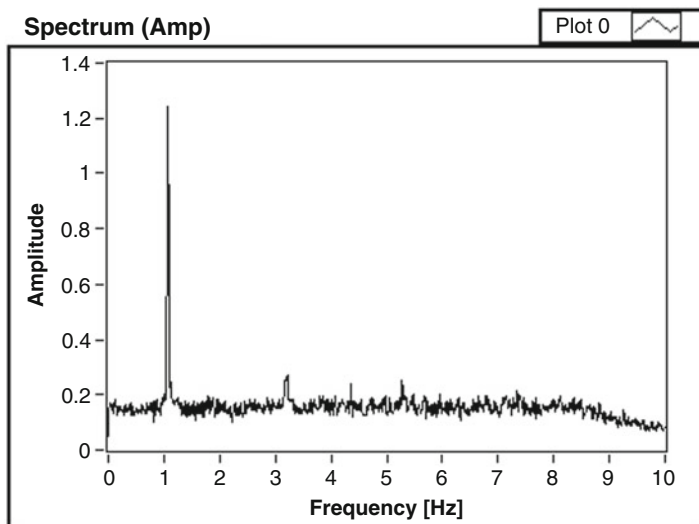


**Fig. 3.15** Spectrum of a signal affected by excessive noise

Detection of noise spikes can take advantage of probability density analysis. In fact, the noise spikes make the tails of the probability density function too thick (Fig. 3.18) in comparison with the theoretical normal distribution. Moreover, since intermittent noise spikes appear like very short pulses, thus approximating delta

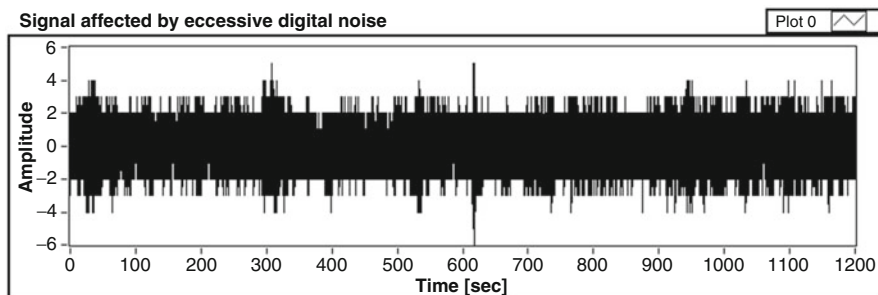


**Fig. 3.16** Time history characterized by excessive digital noise

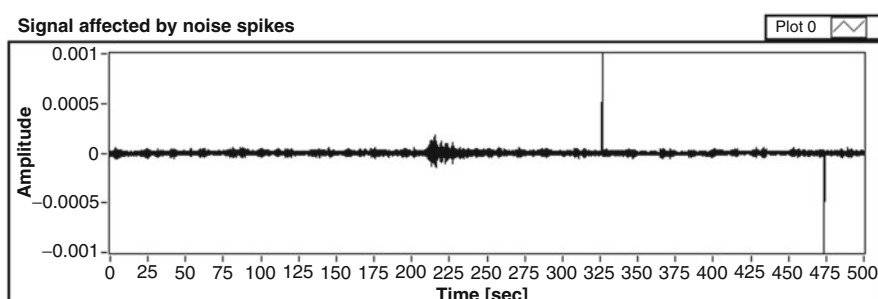


**Fig. 3.17** Random signal with noise spikes

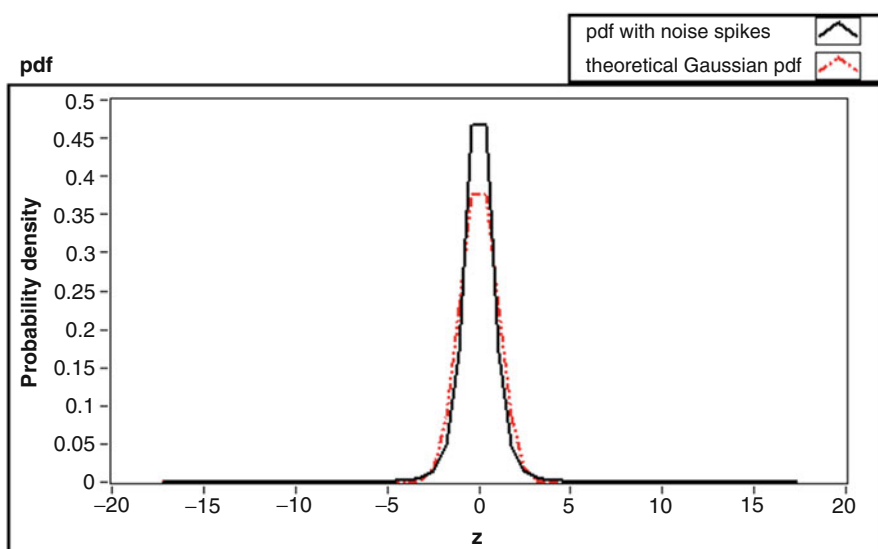


**Fig. 3.18** Probability density function of a random signal with noise spikes

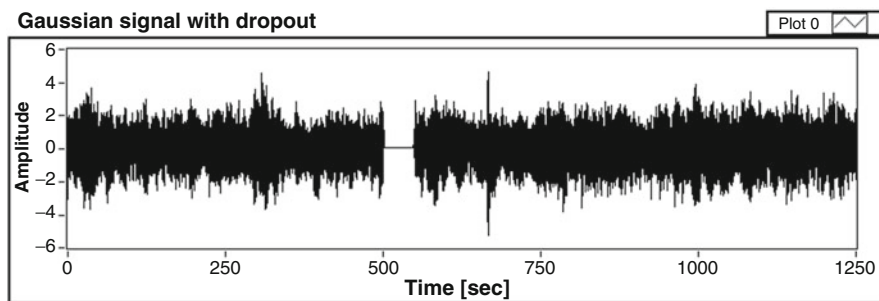


**Fig. 3.19** Temporary dropout in random signal

functions (whose spectral density is flat), intermittent noise spikes will tend to flatten the auto-spectrum of the data. In the extreme case, the effect of intermittent noise spikes, as for the excessive instrumentation noise, is a burying of resonances in noise so that the auto-spectrum is similar to that of white noise.

Electric power distribution systems radiate electromagnetic energy at the power line frequency (50 or 60 Hz, depending on the Country). This energy is commonly picked up by the data acquisition system. *Power line pickup* mainly occurs in the presence of ground loop or break in the shielding. Power line pickup appears as a sine wave at the power line frequency. It usually does not distort the information in the signal and it causes saturation only in extreme cases. Power line pickup can be detected by one of the techniques for identification of spurious harmonics, or by the analysis of the probability density function, which looks like that of sine wave in Gaussian noise (Chap. 2).

Malfunction of sensors or data acquisition system may cause temporary or permanent *dropouts* of the signals, that is to say, the signal suddenly diminishes into the instrumentation noise floor for no apparent reason. Signal dropouts may be due, for instance, to malfunction in the transmission or to loss of power. They can be easily recognized by visual inspection of the time series (Fig. 3.19) or the associated probability density functions (Fig. 3.20). Ignoring signal dropouts leads to major distortions of correlation and spectral density functions and, as a consequence, to serious errors in the analysis of data.

*Offsets* and *spurious trends* are sometimes present in the time series. Assuming that the mean value of the data is known to be zero (this is the case of structures subjected to null net acceleration, such as civil structures), the offset can easily be removed by subtracting the mean value to the corresponding time series.

Trends in the data can be detected by visual inspection. In general, they may be physically meaningful if the signal has a time-varying mean value and the measurement system frequency range goes to DC. However, trends are very often spurious and they may occur for a number of reasons. In most cases, they are induced by temperature. Spurious trends lead to a magnification of the low-frequency components in the auto-spectrum of the signal. In particular, the frequencies below  $1/T_r$  are affected, where  $T_r$  is the total record length. These frequencies are typically well below the frequency range of interest. Thus, a correction of the time

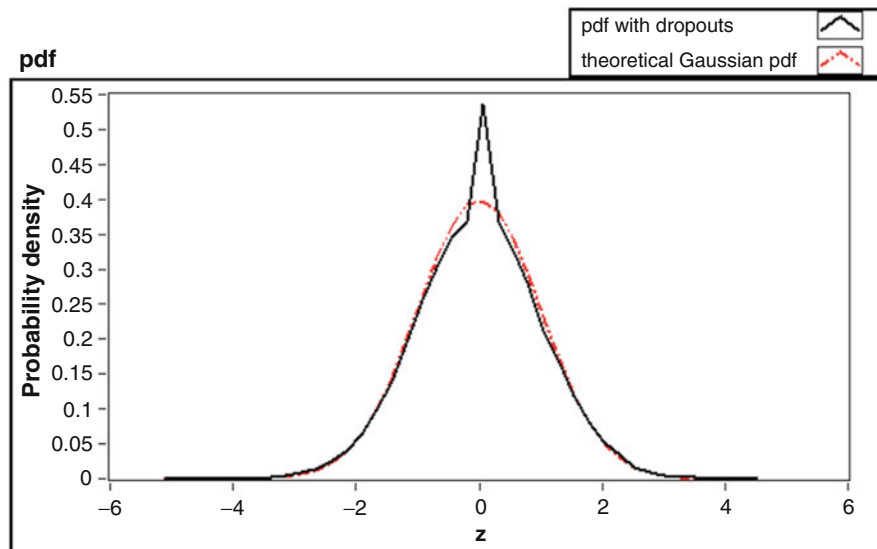


**Fig. 3.20** Probability density function of random signal with dropouts

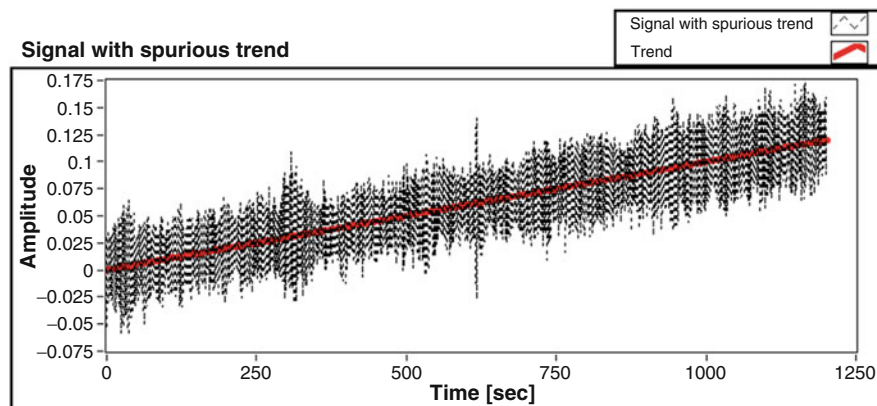


**Fig. 3.21** Removal of spurious linear trend in a random signal

series for removal of spurious trends usually does not affect the analysis results but, on the contrary, it prevents a misinterpretation of the data. Two methods can be adopted to remove spurious trends from the datasets. Whenever low-frequency information in the data has to be preserved down to the minimum frequency  $1/T_r$ , regression analysis represents the best method for removal of spurious trends. It consists in fitting a low-order polynomial to the data using least squares procedures (Chap. 2). Then, the values of the polynomial are subtracted from the time history. Removal of a linear trend is schematically illustrated in Fig. 3.21.

More complex trends can also be removed, but they require fitting of polynomials of order larger than 1. However, the use of polynomials of order not larger than 3 is recommended (Bendat and Piersol 2000), in order to avoid removal of actual low-frequency information in the data together with the spurious trend. If the low-frequency components below  $10/T_r$  are not of interest, spurious trends can be removed by high-pass filtering. This is usually the case when the total time histories are divided into blocks for the computation of ensemble-averaged spectra, since the frequency resolution adopted in spectrum computation is typically larger than  $10/T_r$ .

## 3.8 Applications

### 3.8.1 Aliasing

*Task.* Plot three sine waves characterized by the following values of frequency:  $f_1 = 1$  Hz,  $f_2 = 4$  Hz, and  $f_3 = 6$  Hz, respectively. Compare the results obtained by adopting the following values for the sampling frequency:  $f_{s,1} = 5$  Hz and  $f_{s,2} = 100$  Hz. The three sine waves will appear identical when  $f_s = f_{s,1}$ .

*Suggestions.* Set a 5 s duration for the signals. Use a “For Loop” structure to generate the time instants for the computation of the sine functions. Convert the frequencies of the sine waves in radians and compute the values of the functions at the previously defined time instants:  $g(t) = \sin(2\pi f_i t)$ . Use the “Build Waveform.vi” under “Programming – Waveform” to define the waveform associated to each sine wave. Use the “Waveform Graph” to plot the sine waves. A “While Loop” structure can be helpful to interactively set the value of the sampling frequency and analyze the corresponding results.

*Sample code.* Refer to “Aliasing.vi” in the folder “Chapter 3” of the disk accompanying the book.

### 3.8.2 Mode Shape Merging

*Task.* Mode shapes for the three fundamental modes of a steel cable obtained from two different test setups are reported in two files (“Setup 1 mode shapes.txt” and “Setup 2 mode shapes.txt”) in the “Chapter 3Mode shape merging” folder of the disk accompanying the book. The reference channels for the two setups are reported in “Reference channels for mode shape merging.txt” in the same folder. For each of the three mode shapes determine the scale factor for merging.

*Suggestions.* Load the mode shapes from file. Use the “Index Array.vi” under “Programming – Array” to select the mode shape components corresponding to the reference channels. Note that “0” (and not 1) denotes the first vector component

in LabVIEW. Compute the scale factors by solving a least square problem (see Chap. 2) for the unknown scale factor associated to the i-th mode shape.

*Sample code.* Refer to “Mode shape merging.vi” in the folder “Chapter 3\Mode shape merging” of the disk accompanying the book.

### 3.8.3 Filtering and Decimation

*Task.* Develop software for offline filtering and decimation. Apply it to the dataset “Sample record 12 channels – sampling frequency 100 Hz.txt” in the folder “Chapter 3\Filtering and decimation” of the disk accompanying the book. The time histories are organized in columns. The first column provides the time. Resample the data in order to obtain a new sampling frequency of 20 Hz.

*Suggestions.* Load the data from file. The original sampling frequency (100 Hz) can easily be computed as the inverse of the difference between two subsequent time instants. Use a “While Loop” structure to manage input from the user interface. Input will concern the selection of the type and order of the filter and its frequency limits, and the setting of the decimation factor. Eventually, take advantage of the Property Node (right click on the control and select “Create – Property Node”) of the controls to disable some controls as a function of the selected type of filter (for instance, the upper frequency limit control can be disabled if a high-pass filter is selected). Select one of the filters under “Signal Processing – Filters”. Pass the input data to the selected VI for filtering. Use a “For Loop” structure to pass the individual time histories to the VI for filtering. Use the “TSA Resampling.vi” under “Addons – Time Series Analysis – Preprocessing” to resample the filtered time histories. Use the new sampling frequency and a “For Loop” structure to update the column of time. Save into the same file the new column of time and the decimated time histories. Pay attention to the selection of frequency limits and type of the filter when the datasets are going to be decimated. An inappropriate selection may cause aliasing.

*Sample code.* Refer to “Filtering and decimation.vi” in the folder “Chapter 3\Filtering and decimation” of the disk accompanying the book.

### 3.8.4 Hardware Selection and Data Acquisition (Storage on File)

*Task.* Develop a low-cost data acquisition system for dynamic measurements based on programmable hardware.

*Suggestions.* Programmable hardware can be a valuable low-cost solution for data acquisition in the field of OMA. The present tutorial describes the practical application of the basic concepts about the measurement hardware outlined in the

chapter, up to the development of a simple and low-cost system for output-only modal tests.

A simple and cheap data acquisition system can easily be developed starting from the appropriate choice of sensors and programmable hardware. Taking into account that the possibility to properly resolve the structural response to ambient vibrations depends on the performance of the different components of the measurement chain and their combination, a compromise between cost and performance of hardware components could be necessary. In this framework, the development of a low-cost measurement system, adequate for a number of applications and useful to gain confidence with dynamic measurements and output-only modal tests, can rely on IEPE accelerometers and National Instruments™ Compact DAQ device, and the implementation of a software in LabVIEW environment for measurement system management and data acquisition.

As an example, IEPE seismic accelerometers with the following characteristics:  $\pm 0.5g$  full-scale range,  $10 \text{ V/g}$  sensitivity,  $0.15\text{--}1,000 \text{ Hz}$  bandwidth, resolution lower than  $1E-5 \text{ g}$ , and low noise, nonlinearity, and transverse sensitivity, show good performance for a number of practical applications at an affordable cost. In order to check the compatibility between sensors and measurement hardware, the following data about the sensors have also to be inspected: excitation voltage and current, output bias voltage. For instance, assume that the excitation voltage required by the sensors is in the range  $18\text{--}30 \text{ V DC}$ , the excitation current is in the range  $2\text{--}20 \text{ mA}$ , and the output bias voltage is in the range  $8\text{--}12 \text{ V DC}$ .

The development of a low-cost solution for acquisition of acceleration data can take advantage of NI9234 modules, gathered into a Compact DAQ chassis and linked via USB to a PC. Either ground-referenced or floating sensors can be used, since the system is based on a pseudodifferential configuration. A 24-bit ADC of the sigma-delta type (with analog prefiltering) characterizes the modules. The internal master timebase  $f_M$  is about  $13 \text{ MHz}$  while the data rate for sampling is in the range  $1.652\text{--}51.2 \text{ kHz}$ . Equation (3.17) provides the available data rates:

$$f_s = \frac{f_M}{(256)(n)} \quad n = 1, 2, \dots, 31 \quad (3.17)$$

For instance, for  $n=25$  the sampling frequency is equal to  $2,048 \text{ Hz}$ . This formula has to be implemented into the software for management of data acquisition and measurement hardware to automatically provide the available sampling rates to the user.

The input coupling is user-selectable and it can be either AC or DC. The AC cut-off frequency is  $0.5 \text{ Hz}$  at  $-3 \text{ dB}$ : as a consequence, the selection of AC coupling makes the recorder not suitable for very flexible structures, even if the adopted sensors have a frequency range with a suitable lower bound. AC coupling can be advantageous in some applications, but the limitations in terms of frequency range have to be taken into account. For flexible structures DC coupling is recommended. By the way, AC coupling can be used for a number of applications with confidence.

The modules provide adequate excitation voltage (19 V) and current (2.1 mA) for IEPE accelerometers, as demonstrated by the comparison with the previously mentioned sensor requirements.

The input range is  $\pm 5$  V and it exactly matches the maximum amplitude of voltage signals coming from the sensors. Moreover, the full-scale voltage of the sensor and its output bias voltage, together with the common mode voltage range of the module, must comply with an allowable voltage range defined in the specifications of the input module. The common mode voltage range is  $\pm 2$  V. The allowable voltage range of the module is 0–19 V. According to the characteristics of the adopted sensors and data acquisition modules, in the worst case the sum of the common mode voltage range, output bias voltage, and full-scale voltage equals 19 V. Thus, the modules are adequate to acquire the data coming from the selected IEPE sensors.

CMRR is 47 dB (typical) while crosstalk value is  $-110$  dB. The modules ensure simultaneous sampling. The built-in anti-aliasing filters automatically adjust themselves according to the specified data rate. The dynamic range is also fairly good (102 dB). The link between accelerometers and recorder can be made by RG-58/U low-impedance coaxial cables.

After the selection of sensors and data acquisition modules, the measurement system has to be completed by the implementation of the management and data acquisition software.

The first step concerns the configuration of the data acquisition modules in the Measurement & Automation Explorer (MAX). If the drivers are properly installed and the measurement hardware is connected with the PC, the modules appear under “Devices and Interfaces” on the left of the window (Fig. 3.22).

The development of the software can be initiated even if the hardware components are not available, but the measurement device has to be simulated. Assuming that this is the case and that the software is intended to manage a USB 9234 module, this can be simulated by the following procedure:

- Right-click “Devices and Interfaces”;
- Select “Create New”;
- Select “Simulated NI-DAQmx Device or Modular Instrument”;
- Select “NI USB-9234”;
- When the simulated device appears under “Devices and Interfaces”, open the “Test Panel” (Fig. 3.23) to check the functionality of the device and set some parameters, such as input coupling and power supply.

Once the hardware has been configured, some measurement parameters have to be set in MAX. The expert user can set these parameters also by software. However, this tutorial illustrates only the simplest and fastest method to carry out measurements by means of programmable hardware. The interested reader can find more details in the extensive documentation about data acquisition by LabVIEW. In order to set measurement parameters such as sensitivity and full-scale range, a measurement task has to be configured according to the following procedure:

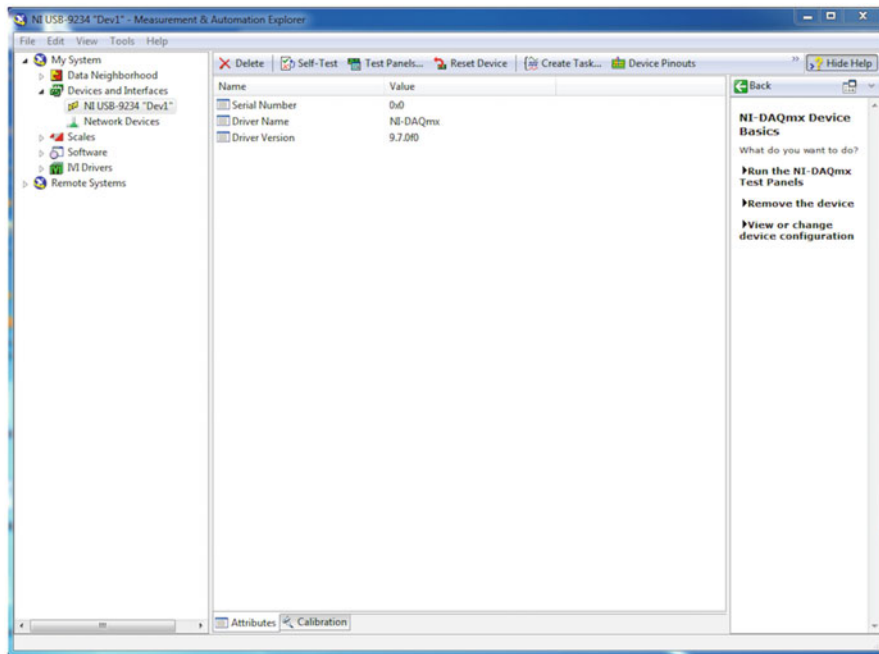


Fig. 3.22 MAX interface

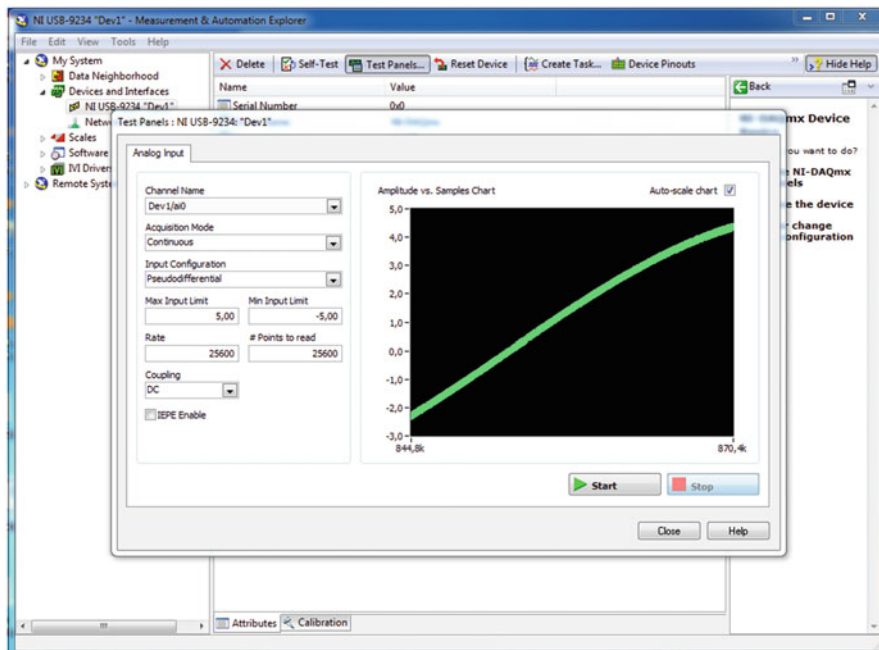
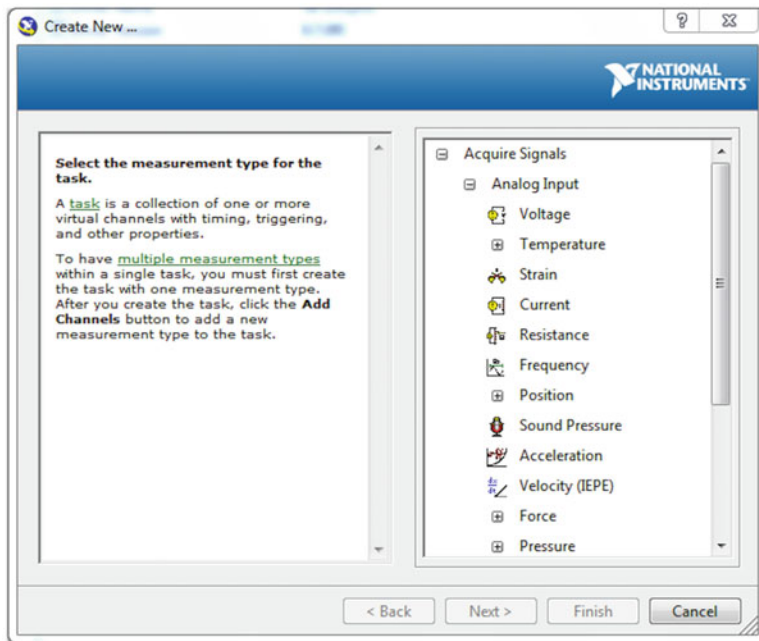
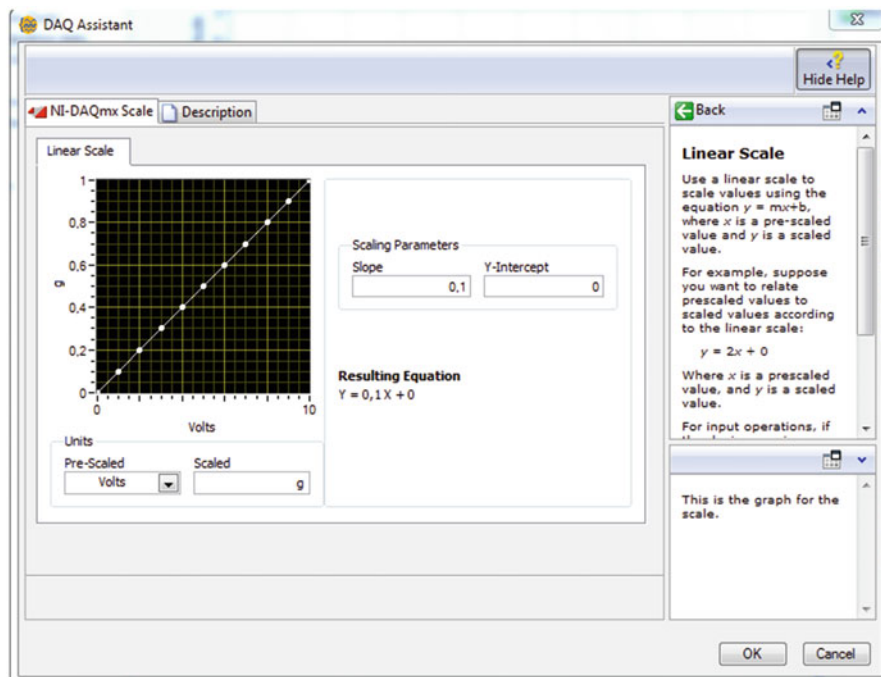


Fig. 3.23 Test panel



**Fig. 3.24** Configuration of the task for data acquisition

- Right-click on “NI-DAQmx Tasks” under “Data Neighborhood” in MAX (left of the window) and select “Create New NI-DAQmx Task...”;
- Select “Acquire Signals – Analog Input – Voltage” (Fig. 3.24);
- Choose the name of the task, for instance “Acceleration data”;
- Select the physical channels you are going to use; for instance, select all the available channels (denoted as ai0, ..., ai3) and click “Finish”;
- For each channel, use the sensitivity of the sensor connected at that channel to convert voltage into acceleration; a scale has to be defined;
- Under “Custom Scaling” select “Create New – Linear” and enter the name for the scale, for instance “Acceleration”;
- Set the value of “Slope” under “Scaling Parameters” equal to the inverse of the sensitivity; the “Scaled” unit depends on the units of measurement of the sensitivity: if it is expressed in V/g (as in the present case), the scaled unit is g (Fig. 3.25);
- Selecting “Acceleration” under “Custom Scaling”, it is possible to set the full-scale range in g; since the full-scale range of the selected accelerometers is  $\pm 0.5g$ , the “Max” and “Min” values under “Signal Input Range” have to be set equal to 0.5 and -0.5, respectively (Fig. 3.26);
- The measurement scheme can be selected under “Terminal Configuration”;



**Fig. 3.25** Setting of sensor sensitivity

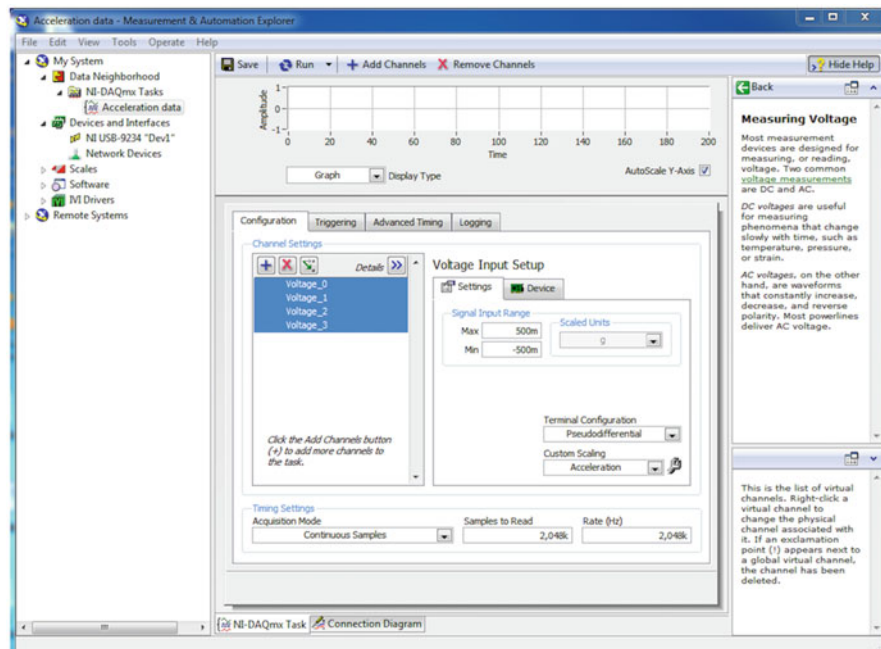


**Fig. 3.26** Setting of sensor full-scale range

- The “Acquisition Mode” is also selectable; the available choices are: “1 sample”, “N samples”, “Continuous samples”; in the present case, “Continuous samples” is adopted;
- Click the “Save” button.

The configuration of the data acquisition modules in MAX is now completed and it is possible to start with the implementation of the software in LabVIEW.

In practical applications it is useful to inspect the spectra of the signals during data acquisition, so that it is possible to assess the quality of the acquired data and identify predominant frequency components in the signals. Thus, adoption of a Producer-Consumer architecture is recommended in the development of the data acquisition software. The Producer cycle is devoted to the acquisition of raw data from the measurement modules, while the spectra are directly computed in the Consumer cycle from data segments coming from the Producer. Data storage is carried out in the Consumer cycle, too.

The simplest and quickest way to set the data acquisition parameters of your measurement system is to use the “DAQ Assistant.vi”. As an alternative, the expert user can take advantage of the higher versatility of the DAQmx – Data Acquisition VIs at the expense of an increase in the programming efforts. Assuming that the “DAQ Assistant.vi” is used, it must be placed in the Producer cycle. When setting the sample rate, refer to the manual of the measurement modules for the allowable values. In the present case, suppose to adopt a sampling frequency of 2,048 Hz. This value is usually much too high for practical applications in civil engineering. Thus, data have to be filtered and decimated. This can be done on-line or off-line. In the first case, a VI for filtering and decimation has to be implemented and it has to follow the “DAQ Assistant.vi”. Data coming from the DAQ Assistant are of the “dynamic data type” (DDT, denoted by a blue wire). Use “From DDT” under “Express – Signal Manipulation” to convert dynamic data in any other type of data (for instance, waveform data). The filtered and decimated time histories can be then queued and sent to the Consumer cycle. If the time histories are going to be filtered and decimated off-line, output data coming from the DAQ Assistant are directly queued, eventually after the conversion of the type of data. The DAQ Assistant allows the selection of the physical channels (use the “Add Channel” button on the left of the window; Fig. 3.27) and the setting of parameters such as sensitivity and full-scale range, on the analogy with the MAX.

Use a “Waveform Chart” (under “Modern – Graph” in the Controls Palette) to show on the screen the raw data passed to the Consumer cycle. Use the “SVT Cross Spectrum (Mag-Phase).vi” to compute ensemble averaged auto- and cross-power spectra (Fig. 3.28).

On-line data processing and visualization are two relevant tasks of the Consumer cycle, but it has to ensure also data storage through a continuous streaming of data on disk. The simplest method to carry out the data streaming on disk is to use the “Write To Measurement File.vi” under “Express – Output”. It has to be connected with the data coming from the Producer. A Boolean control has to be used to enable/disable data storage. The “Write To Measurement File.vi” allows a number of settings, such as name of the file, delimiter, and so on. However, the most

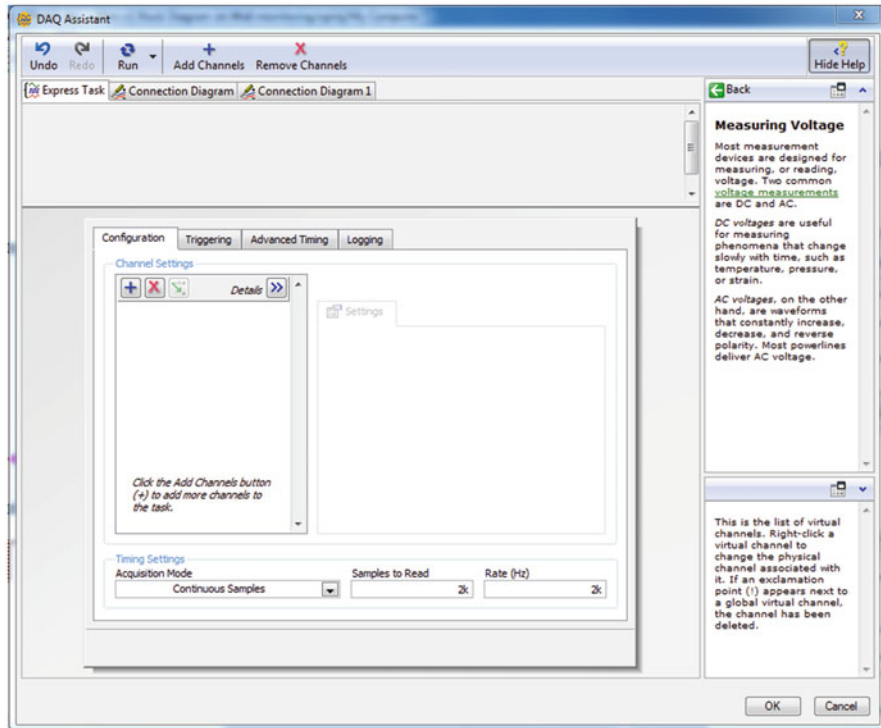


**Fig. 3.27** DAQ Assistant

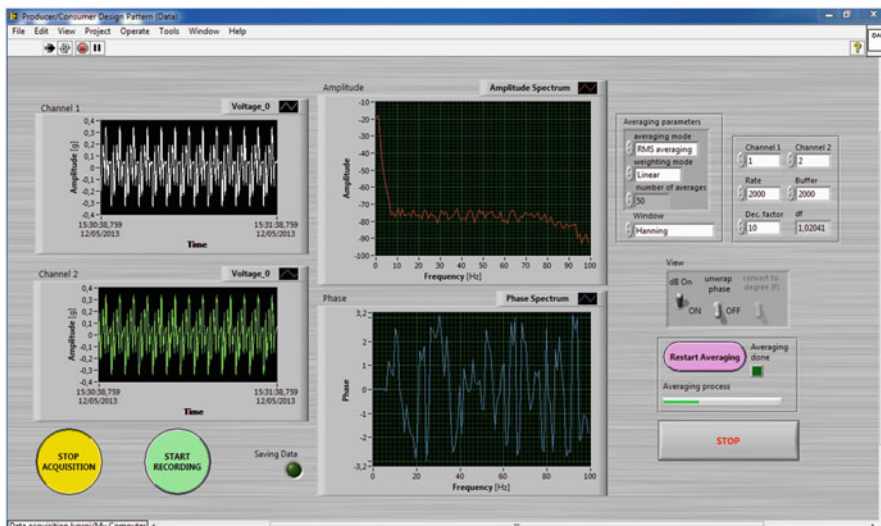


**Fig. 3.28** Example of user interface of the data acquisition software

important setting concerns the file format. The available options are text file and binary file. Use the text file to make the data available to other users or applications; use the binary file to handle large amount of data and optimize the access time (this is the case, for instance, when data are not resampled so that long records at high sampling rate are stored on file).

*Sample code.* Refer to “Data acquisition.lvproj” in the folder “Chapter 3\Data acquisition” of the disk accompanying the book.

### 3.8.5 Data Storage (MySQL Database)

*Task.* Create a MySQL database for data storage and develop software to read and write data in a table of the database.

*Suggestions.* MySQL relational databases represent a profitable alternative for data storage and management with respect to files, in particular when large amounts of data have to be handled. MySQL is a free alternative to other databases. It can be downloaded from [www.mysql.com](http://www.mysql.com).

After the installation, enter the Query Browser and create your database for data storage. It may include one or more tables. As an example, use the following command line:

“create database vibrations;”

to create a database and assign it the name “vibrations”. Then type:

“use vibrations;”

to select the database. Finally, create a table where data are going to be stored. For instance, the following command line:

“create table vibrationdata(id INT(10) NOT NULL AUTO\_INCREMENT, a1  
FLOAT(2,8), a2 FLOAT(2,8), a3 FLOAT(2,8), a4 FLOAT(2,8), PRIMARY  
KEY(id));”

creates the table “vibrationdata” where “id” is an integer counter associated to the record, “a1”, “a2”, “a3”, and “a4” represent the four measurement channels and the associated data are of the floating type with two integer and six decimal positions. “id” is also the primary key, that is to say the code univocally associated to each record in the database. More details about MySQL syntax and commands can be found on the website and in several technical publications.

The communication between LabVIEW and the created database requires the configuration of the “data source name” (DSN) of the database. Open “Control Panel – Administration tools – Data sources (ODBC)” in the operating system and click on the “Add” button. Select the MySQL ODBC driver and configure it. In the field “Data Source Name” insert the name LabVIEW will use to access the database, for instance “measurements”. In the field “Server” write “localhost” if the software developed in LabVIEW and the database are on the same computer, otherwise insert the IP number of the PC hosting the MySQL database and set the “Port” number under “Connect Options” (it is typically set equal to 3306). Insert the username and password set during the installation of MySQL in the corresponding

fields. Now, the database “vibrations” should appear in the list “Database”, and clicking the “Test” button a window appears reporting the message of successful connection.

The configuration of the DSN allows the execution of queries by LabVIEW. In the development of the software it is possible to take advantage of the “Database Connectivity Toolkit” where a number of VIs to communicate and operate with the database are available. An alternative for more expert LabVIEW developers is the communication with the database by means of the ActiveX technology and the ActiveX Data Objects (ADO). In this case, use the “Automation Open.vi” under “Connectivity – ActiveX” to start a connection with the ADODB.\_Connection library, and then use properties and methods of ADOs to execute the query. In particular, use the method “Open” to open the communication with the database by providing DSN, UserID, and Password as strings. Use the method “Execute” to execute a query passed as a string. If you are reading data from the database, use the method “getstring” applied to “Recordset” to get the data from the database in the form of string. Finally, close the references to “Recordset” and the database by the method “Close”. If you are writing data in the database, they have to be converted into string and sent by the appropriate query, for instance:

```
“insert into vibrations.vibrationdata set a1 = value1, a2 = value2, a3 = value3,  
a4 = value4;”
```

replacing “value1, . . . , value4” with the acceleration data coming from the data acquisition system. If you are reading data from the database, they are in the form of string and they have to be manipulated and converted into the most appropriate type of data. A sample query to read data from the database is:

```
“select * from vibrations.vibrationdata limit 10”
```

If the software has been properly developed, no errors appear when reading or writing the data.

*Sample code.* In the folder “Chapter 3\Communication with MySQL database” of the disk accompanying the book there are the files “Write MySQL DB.vi” and “Read MySQL DB.vi”. In the first, four sine waves are generated (sampling frequency equal to 100 Hz) and the values at each time instant are used to create the query to write the data in the database. The query is then passed to the subVI called “Query to write.vi” which communicates with the database and executes the query. The simulated data of the four sine waves can be replaced by measured data by combining this VI with the software developed in Sect. 3.8.4.

The “Read MySQL DB.vi” opens the communication with the database, gets the data, converts them from string to numbers, and closes the communication with the database.

### 3.8.6 Data Pretreatment

*Task.* Develop a software for data pretreatment (mean and spurious trend removal) and validation.

*Suggestions.* The software has to execute distinct actions:

- Offset removal,
- Removal of spurious trends,
- Computation of the probability density function of time histories for validation purposes.

Thus, a state machine architecture can be adopted. As mentioned in Chap. 1, a state machine architecture is based on the execution of distinct actions, each one associated to a specific condition in a case structure. Data are passed among the states by the shift register on the external While Loop. In order to move from one state to another, the possible states have to be listed into a control of the enumerated type (“Enum” under “Modern – Ring & Enum” of the Controls Palette). Place the Enum control on the Front Panel, select it and click on “Edit – Customize Control”. A new window appears, showing only the Enum control. On top of this window, click on the “Control” button and select “Type Def.”. Right-click on the control and select “Edit Items” to add the name of the states to the list (for instance, “remove average”, “detrend”, “data validation”, and “end”). Save and rename the Enum control, and use it to move from one state to another in the state machine architecture. Create a startup VI to load the data (from file or database) and pass them to the first state (“remove average”), where the offset associated to each time history is removed. A SubVI can do offset removal. After offset removal, pass the data to the next state, which removes spurious trends, by appropriately setting the value of the previously defined Enum control. Removal of spurious trends can be done by a specific SubVI, which appears on the screen when called and closes afterwards (place the SubVI in the case structure, right-click its icon, and select “SubVI Node Setup”; select “Show front panel when called” and “Close afterwards if originally closed”). Removal of spurious trends is carried out in the SubVI by passing the individual time histories to “TSA Detrend.vi” (under “Addons – Time Series Analysis – Preprocessing”) and defining the polynomial order. A While Loop structure can be adopted to manage user interactions via controls on the Front Panel. When the SubVI for trend removal closes, its outputs are the preprocessed data and a new value of the Enum control, which passes the data to the next state (“data validation”). In the “Data validation.vi” data are standardized and the probability density function associated to each time history can be plotted to detect anomalies such as clipping, drop-out, and so on. Use a Boolean control and a case structure to eventually remove corrupted time histories. Use a While Loop structure to manage user interactions. After the validation, the Enum control is set equal to “end” and the preprocessed data are ready to be saved.

*Sample code.* Refer to “Data pretreatment.lvproj” in the folder “Chapter 3\Data pretreatment” of the disk accompanying the book.

## References

- Barnes JR (1987) Electronic system design: interference and noise control techniques. Prentice Hall, Inc., Englewood Cliffs, NJ
- Barzilai A (2000) Improving a geophone to produce an affordable broadband seismometer. PhD Dissertation, Stanford University
- Bendat JS, Piersol AG (2000) Random data: analysis and measurement procedures, 3rd edn. Wiley, New York, NY
- Brincker R, Larsen JA (2007) Obtaining and estimating low noise floors in vibration sensors. In: Proc XXV International Modal Analysis Conference, Orlando, FL
- Brincker R, Lagö TL, Andersen P, Ventura CE (2005) Improving the classical geophone sensor element by digital correction. In: Proc XXIII International Modal Analysis Conference, Kissimmee, FL
- Cyrille S (2012) Sensor placement for modal identification. *Mech Syst Signal Process* 27:461–470. doi:[10.1016/j.y.mssp.2011.07.022](https://doi.org/10.1016/j.y.mssp.2011.07.022)
- Dohler M, Andersen P, Mevel L (2010) Data merging for multi-setup operational modal analysis with data-driven SSI. In: Proc XXVIII International Modal Analysis Conference, Jan 31–Feb 4, 2010, Jacksonville, FL
- Dohler M, Reynders E, Magalhaes F, Mevel L, De Roeck G, Cunha A (2010) Pre- and post-identification merging for multi-setup OMA with covariance-driven SSI. In: Proc XXVIII International Modal Analysis Conference, Jan 31–Feb 4, 2010, Jacksonville, FL
- Lynch JP, Loh KJ (2006) A summary review of wireless sensors and sensor networks for Structural Health Monitoring. *Shock Vib Dig* 38:91–128. doi:[10.1177/0583102406061499](https://doi.org/10.1177/0583102406061499)
- Marano GC, Monti G, Quaranta G (2011) Comparison of different optimum criteria for sensor placement in lattice towers. *Struct Design Tall Spec Build* 20:1048–1056. doi:[10.1002/tal.605](https://doi.org/10.1002/tal.605)
- Ott HW (1988) Noise reduction techniques in electronic systems, 2nd edn. Wiley, New York, NY
- Papadimitriou C, Lombaert G (2012) The effect of prediction error correlation on optimal sensor placement in structural dynamics. *Mech Syst Signal Process* 28:105–127. doi:[10.1016/j.y.mssp.2011.05.019](https://doi.org/10.1016/j.y.mssp.2011.05.019)
- Peterson J (1993) Observations and modeling of seismic background noise. U.S. Geological Survey Open-File Report 93-322
- Reynders E, Magalhaes F, De Roeck G, Cunha A (2009) Merging strategies for multi-setup operational modal analysis: application to the Luiz I steel arch bridge. In: Proc XXVII International Modal Analysis Conference, Orlando, FL
- Schmidt T (2007). Dynamic behavior of twin bell towers. In: Brincker R and Moller N (eds) Proc 2nd International Operational Modal Analysis Conference, April 30–May 2, 2007, Copenhagen

## 4.1 Fundamental Assumptions in OMA

The expression Operational Modal Analysis means the class of modal identification methods based on response measurements only. This discipline has been systematized in the last two decades but early applications can be traced back to the beginning of modal testing in the 1960s. At that time output-only modal identification was referred to as ambient vibration testing. The first applications of OMA were mainly based on the analysis of PSDs and the identification of *Operational Deflection Shapes* (ODSs). An ODS represents the deflection of a structure at a particular frequency under a generic input and it is usually the result of the contribution of different modes. However, under certain assumptions, which are going to be illustrated in Sect. 4.4.1, ODSs are a close estimate of the actual mode shapes. In the 1990s a number of methods working in time domain were developed and applied in combination with correlation functions, leading to the so-called Natural Excitation Techniques (NExT) for output-only modal testing. In the same period the use of ARMA models for modal parameter estimation, first suggested in the late 1970s, started spreading. An increasing number of applications appeared in the literature but output-only modal identification was not fully developed and widely accepted as a reliable source of information, yet. However, at the end of the 1990s new effective output-only modal identification techniques, such as the Frequency Domain Decomposition (FDD) and the Stochastic Subspace Identification (SSI), became available, overcoming the limitations of the previous techniques in dealing with closely spaced modes and noise. Nowadays, OMA is a widely accepted tool for modal identification, with several successful applications in civil engineering (bridges, buildings, pedestrian bridges, historical structures, offshore platforms, wind turbines, dams, stadia), mechanical and industrial engineering (ships, trucks, car bodies, engines, rotating machineries), aerospace engineering (in-flight modal identification of aircrafts and shuttles, studies about flutter).

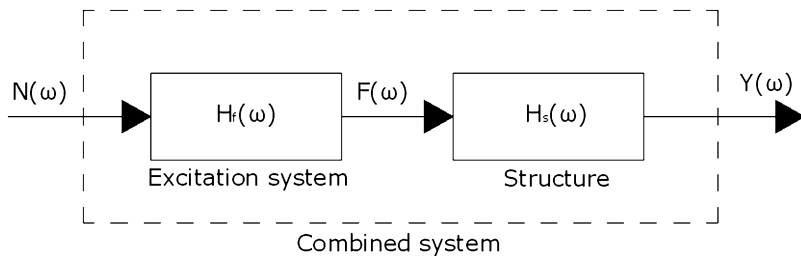


**Fig. 4.1** The combined system

OMA is based on the following assumptions:

- *Linearity* (the response of the system to a given combination of inputs is equal to the same combination of the corresponding outputs),
- *Stationarity* (the dynamic characteristics of the structure do not change over time, so that the coefficients of the differential equations governing the dynamic response of the structure are independent of time),
- *Observability* (the sensor layout has been properly designed to observe the modes of interest, avoiding, for instance, nodal points).

Moreover, unlike traditional modal testing where the input is controlled, OMA is based on the dynamic response of the structure under test to noncontrollable and immeasurable loadings such as environmental and operational loads (traffic, wind, microtremors, and so on). As a consequence, some assumptions about the input are needed. If the structure is excited by white noise, that is to say, the input spectrum is constant, all modes are equally excited and the output spectrum contains full information about the structure. However, this is rarely the case, since the excitation has a spectral distribution of its own. Modes are, therefore, weighted by the spectral distribution of the input and both the properties of the input and the modal parameters of the structure are observed in the response. Additionally, noise and eventual spurious harmonics due to rotating equipment are observed in the response. Thus, in the general case, the structure is assumed to be excited by unknown forces that are the output of the so-called excitation system loaded by white noise (Fig. 4.1). Under this assumption, the measured response can be interpreted as the output of the combined system, made by the excitation system and the structure under test in series, to a stationary, zero mean, Gaussian white noise.

Since the excitation system and the structure under test are in series, the FRF of the combined system is the product their respective FRFs:

$$H_c(\omega) = H_f(\omega)H_s(\omega) \quad (4.1)$$

where  $H_c(\omega)$ ,  $H_f(\omega)$ , and  $H_s(\omega)$  are the FRFs of the combined system, the excitation system, and the structure under test, respectively. In fact, for each subsystem, output and input are related by the following equations:

$$F(\omega) = H_f(\omega)N(\omega) \quad (4.2)$$

$$Y(\omega) = H_s(\omega)F(\omega) \quad (4.3)$$

where  $N(\omega)$ ,  $F(\omega)$ , and  $Y(\omega)$  denote the Fourier transforms of the white noise input to the excitation system, the excitation system output, and the structure output, respectively. In this context, the measured response includes information about the excitation system and the structure under test but the modal parameters of the structure are preserved and identifiable, and the characteristics of the excitation system have no influence on the accuracy of modal parameter estimates (Ibrahim et al. 1996). The discrimination between structural modes and properties of the excitation system is possible since the structural system has a narrowband response and time invariant properties, while the excitation system has a broadband response and it may have either time varying or time invariant properties. The estimation of the modal model (Sect. 4.2.1) of the structure gives the opportunity to estimate also the unknown forces, according to (4.3).

The assumption of *broadband excitation* ensures that all the structural modes in the frequency range of interest are excited. Assuming that the combined system is excited by a random input, the second order statistics of the response carry all the physical information about the system (Chap. 2) and play a fundamental role in output-only modal identification. The focus on second order statistics is justified by the central limit theorem. In fact, the structural response is approximately Gaussian in most cases, no matter of the distributions of the (independent) input loads, which are often not Gaussian. The spatial distribution of the input also affects the performance of OMA methods, in particular in the presence of closely spaced modes (Herlufsen et al. 2005). A distribution of random in time and space inputs provides better modal identification results (Herlufsen et al. 2005). In fact, the identification of closely spaced modes requires that the rank of the excitation PSD matrix is larger than 1 and, therefore, multiple uncorrelated inputs are applied (Chap. 1). The presence of measurement noise and spurious harmonics in response measurements requires appropriate data processing to eventually mitigate their effects and discriminate them from actual structural modes.

## 4.2 Structural Dynamics Models

### 4.2.1 Frequency Response and Impulse Response

The dynamic behavior of a structure can be represented either by a set of differential equations in time domain, or by a set of algebraic equations in frequency domain. Equations of motion are traditionally expressed in time domain, thus obtaining, for a general MDOF system, the following set of linear, second order differential equations expressed in matrix form:

$$[M]\{\ddot{y}(t)\} + [C]\{\dot{y}(t)\} + [K]\{y(t)\} = \{f(t)\} \quad (4.4)$$

where  $\{\ddot{y}(t)\}$ ,  $\{\dot{y}(t)\}$  and  $\{y(t)\}$  are the vectors of acceleration, velocity, and displacement, respectively;  $[M]$ ,  $[C]$ , and  $[K]$  denote the mass, damping, and stiffness matrices;  $\{f(t)\}$  is the forcing vector. This matrix equation is written for a linear, time invariant ( $[M]$ ,  $[C]$  and  $[K]$  are constant), observable system with viscous damping. It describes the dynamics of the  $N_{DOF}$  discrete DOFs of the structure and it is usually referred to as the spatial model. The definition of the spatial model (of mass, stiffness, and damping properties) is the first step in theoretical analyses and it usually requires a large number of DOFs (some order of magnitude larger than the number of DOFs required for an accurate experimental model) in order to adequately describe the dynamic behavior of the structure. Equations of motion, which are coupled in this formulation, can be decoupled under the assumption of proportional damping by solving an eigenproblem. As a result, the complete solution is obtained by superposition of eigensolutions. This is a standard formulation of the dynamic problem reported in several structural dynamics and modal analysis books (Chopra 2000, Ewins 2000, Heylen et al. 1998).

The matrix differential equation of (4.4) becomes a set of linear algebraic equations by applying the Fourier transform and its properties (Chap. 2):

$$(-\omega^2[M] + i\omega[C] + [K])\{Y(\omega)\} = \{F(\omega)\} \quad (4.5)$$

where  $\{Y(\omega)\}$  and  $\{F(\omega)\}$  are the Fourier transforms of  $\{y(t)\}$  and  $\{f(t)\}$ , respectively;  $i$  is the imaginary unit (Chap. 2). A linear time-invariant system can be, therefore, represented through its FRF, which is given by the ratio between the Fourier transforms of the output and the input. Equation (4.5) can be rewritten as:

$$[Z(\omega)]\{Y(\omega)\} = \{F(\omega)\} \quad (4.6)$$

by adopting the following position:

$$-\omega^2[M] + i\omega[C] + [K] = [Z(\omega)]. \quad (4.7)$$

According to its definition, the FRF is therefore given by:

$$[H(\omega)] = [Z(\omega)]^{-1} = \frac{adj([Z(\omega)])}{|Z(\omega)|} \quad (4.8)$$

with  $adj([Z(\omega)])$  and  $|Z(\omega)|$  the adjoint matrix and the determinant of the dynamic stiffness matrix  $[Z(\omega)]$ , respectively; the FRF matrix carries all the information about the inertial, elastic, and energy dissipating properties of the structure ((4.7) and (4.8)). The FRF can be also expressed in terms of modal parameters through a partial fraction expansion as (refer to Ewins 2000, and Heylen et al. 1998 for more details):

$$[H(\omega)] = \sum_{r=1}^{N_m} \frac{[R_r]}{i\omega - \lambda_r} + \frac{[R_r]^*}{i\omega - \lambda_r^*} = \sum_{r=1}^{N_m} \frac{Q_r \{\phi_r\} \{\phi_r\}^T}{i\omega - \lambda_r} + \frac{Q_r^* \{\phi_r\}^* \{\phi_r\}^{*T}}{i\omega - \lambda_r^*} \quad (4.9)$$

where  $N_m$  denotes the number of modes,  $\{\phi_r\}$  is the mode shape,  $Q_r$  holds the information about the modal scaling factor, and  $\lambda_r = \sigma_r + i\omega_{d,r}$  is the pole of the  $r$ -th mode holding the information about damped frequency  $f_{d,r} = \omega_{d,r}/(2\pi)$  and damping ratio  $\xi_r = -\sigma_r/\sqrt{\sigma_r^2 + \omega_{d,r}^2}$  of the  $r$ -th mode. The structure of the FRF matrix expressed by (4.9) highlights some useful results for modal analysis. First of all, (4.9) shows that each mode gives a contribution to the response of the system at any frequency. Thus, it is impossible to excite only one mode of a structure by means of a single frequency sine wave (Richardson and Schwarz 2003). However, near a resonance this summation can be approximated by the term related to the corresponding mode. Moreover, (4.9) shows that every element of the FRF matrix has the same denominator. Thus, the eigenvalues (poles) of the system are given by the common denominator and they can be estimated either from any individual FRF or from multiple FRFs measured on the same structure. The selected approach leads to the classification of modal analysis techniques as local or global, respectively. The residue matrix  $[R_r]$ , which is a complex-valued matrix basically given by an outer product of the mode shape vector with itself (Heylen et al. 1998):

$$[R_r] = Q_r \{\phi_r\} \{\phi_r\}^T \quad (4.10)$$

holds the information about mode shapes.

The relation between input and output through the FRF matrix:

$$\{Y(\omega)\} = [H(\omega)] \{F(\omega)\} \quad (4.11)$$

can be manipulated to obtain a fundamental equation of OMA. In fact, taking into account the definition of PSD and the properties of transpose (Chap. 2), the product  $\{Y(\omega)\}^* \{Y(\omega)\}^T$  can be computed and the following relation between PSD matrix of the output and FRF matrix can be obtained:

$$[S_{YY}(\omega)] = [H(\omega)]^* [S_{FF}(\omega)] [H(\omega)]^T. \quad (4.12)$$

Assuming that the PSD matrix of the input is constant (as reported in Sect. 4.1, in OMA the input to the combined system is a stationary, zero mean Gaussian white noise), the output PSD matrix carries the same information and can be expressed in pole-residue form as the FRF matrix:

$$[S_{YY}(\omega)] = \sum_{r=1}^{N_m} \frac{\{\phi_r\} \{\gamma_r\}^T}{i\omega - \lambda_r} + \frac{\{\phi_r\}^* \{\gamma_r\}^H}{i\omega - \lambda_r^*} + \frac{\{\gamma_r\} \{\phi_r\}^T}{-i\omega - \lambda_r} + \frac{\{\gamma_r\}^* \{\phi_r\}^H}{-i\omega - \lambda_r^*} \quad (4.13)$$

where  $\{\gamma_r\}$  is the operational reference vector associated to the  $r$ -th mode: it corresponds to the modal participation vector  $Q_r \{\phi_r\}^T$  appearing in the pole-residue form of the FRF matrix but, unlike this, it depends on all the modal parameters of the system, the input locations, and the input correlation matrix (Peeters 2000).

In (4.13) the poles hold the information about natural frequencies and damping ratios, while the residues hold the information about the mode shapes. However, since the input is not measured, only un-scaled mode shapes can be obtained. Equation (4.13) clearly shows that, for each mode, the output PSD provides four poles in complex conjugate pairs ( $\lambda_r, \lambda_r^*, -\lambda_r, -\lambda_r^*$ ).

Taking into account that FRF and IRF on one hand, and spectral density functions and correlation functions on the other hand are Fourier transform pairs, similar analogies are possible between IRFs and correlation functions in the framework of OMA. In fact, in time domain the dynamic response of a structure to a generic input is determined by the IRF, whose mathematical expression:

$$[h(t)] = \sum_{r=1}^{N_m} ([R_r] e^{\lambda_r t} + [R_r]^* e^{\lambda_r^* t}) \quad (4.14)$$

shows evident analogies with the mathematical structure of the FRF reported in (4.9). The poles hold the information about natural frequencies and damping ratios, while the information about the mode shapes is in the  $[R_r]$  matrices.

In the output-only case and under the same assumptions about the input as above, it is possible to show (James et al. 1992, James et al. 1995) that also the correlation function can be expressed as a sum of complex exponentials:

$$[R_{yy}(\tau)] = \begin{cases} \sum_{r=1}^{N_m} (\{\phi_r\} \{\gamma_r\}^T e^{\lambda_r \tau} + \{\phi_r\}^* \{\gamma_r\}^H e^{\lambda_r^* \tau}) & \tau \geq 0 \\ \sum_{r=1}^{N_m} (\{\gamma_r\} \{\phi_r\}^T e^{-\lambda_r |\tau|} + \{\gamma_r\}^* \{\phi_r\}^H e^{-\lambda_r^* |\tau|}) & \tau < 0 \end{cases}. \quad (4.15)$$

The poles  $\lambda_r$  provide the natural frequencies and damping ratios, while the information about the mode shapes is in the residue matrices. As with the PSD matrix, only un-scaled mode shapes can be obtained from output-only modal identification based on correlation functions. It is interesting to note that the causal part (positive lags) of the correlation functions contains the stable poles ( $\sigma < 0$ ) while the noncausal part (negative lags) contains the unstable poles ( $\sigma > 0$ ).

Time domain modal identification methods usually identify the modal parameters from the causal part only, thus reducing the total number of poles by a factor 2. Moreover, since the modal decomposition of the causal part of the correlation functions and that of IRFs are very similar, modal parameter estimators traditionally used in the context of input-output modal analysis can be applied also in the context of OMA.

A similar reduction of the number of poles is sometimes carried out also in frequency domain. In fact, the so-called *positive power spectra* are sometimes preferentially adopted in practical applications—for instance, to enhance numerical conditioning in the poly-reference Least Squares Complex Frequency (p-LSCF) method-.

The order  $n = 2N_m$  of the positive power spectra is the same as that of the FRF and contains all the necessary information about the structure. The positive power spectra are defined as the DFT of the correlation functions at positive time lags only:

$$[S_{YY}^+(\omega)] = DFT\left([R_{yy}(\tau)]|_{\tau \geq 0}\right). \quad (4.16)$$

It is worth noting that the positive power spectra are different from the one-sided spectra (Chap. 2). More details about positive power spectra and their role in output-only modal identification are reported in Sects. 4.2.4, 4.4.3.2 and 4.9.

### 4.2.2 State-Space Models

State space-models are used to convert the second order problem, governed by the differential equation of motion expressed in matrix form in (4.4) into two first order problems, defined by the so-called state equation and observation equation.

The state equation can be obtained from (4.4) by some mathematical manipulations. When the forcing vector  $\{f(t)\}$  is factorized into the matrix  $[\bar{B}]$ , which defines the location of inputs, and the vector  $\{u(t)\}$  describing the time variation, (4.4) can be rewritten as follows:

$$[M]\{\ddot{y}(t)\} + [C]\{\dot{y}(t)\} + [K]\{y(t)\} = [\bar{B}]\{u(t)\} \quad (4.17)$$

or, equivalently:

$$\{\ddot{y}(t)\} + [M]^{-1}[C]\{\dot{y}(t)\} + [M]^{-1}[K]\{y(t)\} = [M]^{-1}[\bar{B}]\{u(t)\}. \quad (4.18)$$

The definition of the *state vector*:

$$\{s(t)\} = \begin{Bmatrix} \{\dot{y}(t)\} \\ \{y(t)\} \end{Bmatrix} \quad (4.19)$$

and its substitution in the set of equations consisting of (4.18) and the following identity:

$$[M]\{\dot{y}(t)\} = [M]\{\ddot{y}(t)\} \quad (4.20)$$

yield:

$$\{\dot{s}(t)\} = \begin{bmatrix} -[M]^{-1}[C] & -[M]^{-1}[K] \\ [I] & [0] \end{bmatrix} \{s(t)\} + \begin{bmatrix} [M]^{-1}[\bar{B}] \\ [0] \end{bmatrix} \{u(t)\}. \quad (4.21)$$

From (4.21) the *state matrix*  $[A_c]$  and the *input influence matrix*  $[B_c]$  can be defined as follows:

$$[A_c] = \begin{bmatrix} -[M]^{-1}[C] & -[M]^{-1}[K] \\ [I] & [0] \end{bmatrix}, \quad (4.22)$$

$$[B_c] = \begin{bmatrix} [M]^{-1}[\bar{B}] \\ [0] \end{bmatrix}, \quad (4.23)$$

and the *state equation* can be written as:

$$\{\dot{s}(t)\} = [A_c]\{s(t)\} + [B_c]\{u(t)\} \quad (4.24)$$

where the subscript  $c$  denotes continuous time.

In the most general case, the observation equation can be written as:

$$\{y_l(t)\} = [C_a]\{\ddot{y}(t)\} + [C_v]\{\dot{y}(t)\} + [C_d]\{y(t)\} \quad (4.25)$$

under the assumption that measurements of the structural response are taken at  $l$  locations and the sensors are accelerometers, velocimeters, and displacement transducers;  $\{y_l(t)\}$  is the vector of the measured outputs,  $[C_a]$ ,  $[C_v]$  and  $[C_d]$  are the output location matrices for acceleration, velocity, and displacement, respectively. In the following, the index  $l$  in  $\{y_l(t)\}$  will be dropped wherever  $\{y_l(t)\}$  cannot be confused with the vector of displacements  $\{y(t)\}$ . It is worth emphasizing that, while a real structure is characterized by an infinite number of DOFs (which becomes a finite but large number in the lumped mass models usually set for numerical analyses), in a practical vibration test this number decreases down to a few dozens or even less. Substitution of the expression for  $\{\ddot{y}(t)\}$  obtained from (4.18) into (4.25) yields the following equation:

$$\begin{aligned} \{y_l(t)\} &= \left( [C_v] - [C_a][M]^{-1}[C] \right) \{\dot{y}(t)\} \\ &\quad + \left( [C_d] - [C_a][M]^{-1}[K] \right) \{y(t)\} . \\ &\quad + \left( [C_a][M]^{-1}[\bar{B}] \right) \{u(t)\} \end{aligned} \quad (4.26)$$

The *observation equation*:

$$\{y(t)\} = [C_c]\{s(t)\} + [D_c]\{u(t)\} \quad (4.27)$$

provides the vector of the measured outputs as a function of the state and the input; it is obtained from (4.26), taking into account the definition of state vector (4.19), with the following positions:

$$[C_c] = \begin{bmatrix} [C_v] - [C_a][M]^{-1}[C] & [C_d] - [C_a][M]^{-1}[K] \end{bmatrix}, \quad (4.28)$$

$$[D_c] = [C_a][M]^{-1}[\bar{B}]. \quad (4.29)$$

$[C_c]$  is the *output influence matrix*,  $[D_c]$  is the *direct transmission matrix*. The direct transmission matrix disappears if no accelerometers are used for output measurements. The physical sense of this matrix is related to the circumstance that a step change in the input  $\{u(t)\}$  causes a step change in the acceleration response.

The state equation (4.24) and the observation equation (4.27) define the *continuous-time state-space model*. An important characteristic of this model is the existence of an infinite number of equivalent state-space representations for a given system: each one is referred to as a *realization*. As a consequence, the experimental test allows establishing only one of these infinite realizations. Application of a similarity transformation proves the multiplicity of realizations. In fact, said  $[T]$  an arbitrary nonsingular square matrix, substitution of:

$$\{s(t)\} = [T]\{z(t)\} \quad (4.30)$$

into the equations of the continuous-time state-space model yields:

$$\{\dot{z}(t)\} = [T]^{-1}[A_c][T]\{z(t)\} + [T]^{-1}[B_c]\{u(t)\} \quad (4.31)$$

$$\{y(t)\} = [C_c][T]\{z(t)\} + [D_c]\{u(t)\} \quad (4.32)$$

Comparisons of (4.31) with (4.24) and of (4.32) with (4.27) show that the matrices  $[T]^{-1}[A_c][T]$ ,  $[T]^{-1}[B_c]$ ,  $[C_c][T]$  and  $[D_c]$  describe the same relationships as the matrices  $[A_c]$ ,  $[B_c]$ ,  $[C_c]$  and  $[D_c]$ . Moreover, since the state matrices of any couple of realizations are related by a similarity transformation, the eigenvalues (carrying the information about the modal parameters of the system) are preserved.

Taking into account that experimental tests yield measurements taken at discrete time instants while (4.24) and (4.27) are expressed in continuous time, the continuous-time state-space model has to be converted to discrete time. For a given sampling period  $\Delta t$ , the continuous-time equations can be discretized and solved at all discrete time instants  $t_k = k\Delta t$ ,  $k \in \mathbb{N}$ . An assumption about the behavior of the time-dependent variables between two samples has to be made to this aim. For instance, the Zero Order Hold (ZOH) assumption states that the input is piecewise constant over the sampling period. Under this assumption the continuous-time state-space model can be converted to the *discrete-time state-space model*:

$$\{s_{k+1}\} = [A]\{s_k\} + [B]\{u_k\} \quad (4.33)$$

$$\{y_k\} = [C]\{s_k\} + [D]\{u_k\} \quad (4.34)$$

where  $\{s_k\} = \{s(k\Delta t)\}$  is the *discrete-time state vector* yielding the sampled displacements and velocities;  $\{u_k\}$  and  $\{y_k\}$  are the *sampled input* and *sampled output*, respectively;  $[A]$  is the *discrete state matrix*,  $[B]$  is the *discrete input*

matrix,  $[C]$  is the *discrete output matrix* and  $[D]$  is the direct transmission matrix. The relations between continuous-time matrices and the corresponding discrete time matrices are:

$$[A] = e^{[A_c] \Delta t} \quad (4.35)$$

$$[B] = ([A] - [I])[A_c]^{-1}[B_c] \quad (4.36)$$

$$[C] = [C_c] \quad (4.37)$$

$$[D] = [D_c] \quad (4.38)$$

Thus, the ZOH sampling does not influence these last two matrices. As an alternative, assuming a piecewise linear behavior between two subsequent samples—First Order Hold (FOH) assumption—different, more complex relations between continuous-time and discrete-time state-space matrices can be derived (see, for instance, Franklin et al. 2006). Mathematical derivation of (4.33) and (4.34) and of the relations between continuous-time and discrete-time matrices is beyond the scope of the present book. The interested reader can refer to the literature (Juang 1994) for more details.

The model expressed by (4.33) and (4.34) is a deterministic model since the system is driven by a deterministic input only. Stochastic components must be necessarily included in order to describe actual measurement data. When stochastic components are included in the model, the following *discrete-time combined deterministic-stochastic state-space model* is obtained:

$$\{s_{k+1}\} = [A]\{s_k\} + [B]\{u_k\} + \{w_k\} \quad (4.39)$$

$$\{y_k\} = [C]\{s_k\} + [D]\{u_k\} + \{v_k\} \quad (4.40)$$

where  $\{w_k\}$  is the *process noise* due to disturbances and model inaccuracies, while  $\{v_k\}$  is the *measurement noise* due to sensor inaccuracies. The state equation models the dynamic behavior of the system; the observation equation defines that part of the dynamic response of the system that can be observed in the output of the model.

In the context of OMA, structures are excited by immeasurable inputs. Since the information about the input  $\{u_k\}$  is not available, the measured system response  $\{y_k\}$  is generated only by the two stochastic processes  $\{w_k\}$  and  $\{v_k\}$ , and the following *discrete-time stochastic state-space model* is obtained:

$$\{s_{k+1}\} = [A]\{s_k\} + \{w_k\} \quad (4.41)$$

$$\{y_k\} = [C]\{s_k\} + \{v_k\}. \quad (4.42)$$

In the absence of  $\{u_k\}$ , its role is implicitly modeled by process noise and measurement noise. In particular, the process noise becomes the input that drives

the dynamics of the system, while the measurement noise accounts for the direct disturbance of the response of the system. Thus, when a stochastic state-space model is adopted, the objective is the determination of the order  $n$  of the unknown system and of a realization of the matrices  $[A]$  and  $[C]$  (up to within a similarity transformation) from a large number of measurements of the output  $\{y_k\}$  generated by the system itself. The state matrix  $[A]$  transforms the current state of the system  $\{s_k\}$  in the next state  $\{s_{k+1}\}$ , while the product of the observation matrix  $[C]$  with the state vector provides the observable part of the dynamics of the system. More precisely, the response vector  $\{y_k\}$  is given by the observable part of the state plus the measurement noise. The process noise and the measurement noise are both immeasurable. They are assumed to be zero mean, stationary white noise processes with covariance matrices given by:

$$E \left[ \begin{Bmatrix} \{w_p\} \\ \{v_p\} \end{Bmatrix} \left\langle \begin{Bmatrix} \{w_q\}^T & \{v_q\}^T \end{Bmatrix} \right\rangle \right] = \begin{cases} \begin{bmatrix} [Q^{ww}] & [S^{wv}] \\ [S^{wv}]^T & [R^{vv}] \end{bmatrix} & p = q \\ [0] & p \neq q \end{cases} \quad (4.43)$$

where  $p$  and  $q$  are two arbitrary time instants. The estimation of the matrices  $[Q^{ww}]$ ,  $[R^{vv}]$  and  $[S^{wv}]$  is also part of the identification process. The assumption of white noise for  $\{w_k\}$  and  $\{v_k\}$  is fundamental in the proof of SSI methods (see Van Overschee and De Moor 1996 for more details). Thus, if the unmeasured input includes some dominant frequency components, they appear as poles of the state matrix  $[A]$  together with the eigenvalues of the system. This is equivalent to the identification of the dynamic properties of both the structure under investigation and the excitation system forming the combined system (driven by stationary, zero mean Gaussian white noise as input) that is the generally assumed objective of identification in OMA.

In agreement with the stochastic framework of OMA, the system response in the state-space model is represented by a zero mean Gaussian process. The output covariance matrices are given by:

$$[R_i] = E[\{y_{k+i}\}\{y_k\}^T] \quad (4.44)$$

and they carry all the information to describe the process. A *covariance equivalent model* can be then defined as the estimated state-space model characterized by correct covariance and, therefore, able to describe the statistical properties of the system response. The estimator producing this model is referred to as an optimal estimator.

The state  $\{s_k\}$  is also a zero mean Gaussian process described by its covariance (which is independent of the time instant  $k$ ):

$$[\Sigma] = E[\{s_k\}\{s_k\}^T] \quad (4.45)$$

and it is uncorrelated with the process noise and the measurement noise:

$$E[\{s_k\}\{w_k\}^T] = [0] \quad (4.46)$$

$$E[\{s_k\}\{v_k\}^T] = [0]. \quad (4.47)$$

Taking into account the previous assumptions about the noise terms, the system response and the state, mathematical manipulations of the state-space equations ((4.41) and (4.42)) lead to the following fundamental relations:

$$[\Sigma] = [A][\Sigma][A]^T + [Q^{ww}] \quad (4.48)$$

$$[R_0] = [C][\Sigma][C]^T + [R^{vv}] \quad (4.49)$$

$$[G] = [A][\Sigma][C]^T + [S^{vw}] \quad (4.50)$$

$$[R_i] = [C][A]^{i-1}[G] \quad (4.51)$$

where:

$$[G] = E[\{s_{k+1}\}\{y_k\}^T] \quad (4.52)$$

is the *next state-output covariance matrix* (covariance between the response of the system  $\{y_k\}$  and the updated state vector  $\{s_{k+1}\}$ ). The last property expressed by (4.51) is very important. In fact, since the output covariance sequence  $[R_i]$  can be directly estimated from the measured data (4.44), its decomposition according to (4.51) permits the estimation of the state-space matrices and the solution of the system identification problem.

The stochastic state-space model in (4.41) and (4.42) can be expressed in an alternative form through the introduction of the so-called Kalman filter. Without going into the details (the interested reader can refer to Juang 1994 for a more detailed discussion about the Kalman filter and the related mathematical derivations), the so-called forward innovation model is briefly illustrated below.

For a given time instant  $t_k$ , suppose that the system matrices  $[A]$ ,  $[C]$ ,  $[Q^{ww}]$ ,  $[R^{vv}]$ ,  $[S^{vw}]$  and all previous measurements  $[Y^{k-1}]$  are known:

$$[Y^{k-1}] = [\{y_0\}, \{y_1\}, \dots, \{y_{k-1}\}]^T. \quad (4.53)$$

A classical estimation problem concerns the ability to optimally predict the response measurements. Thus, an *optimal predictor* can be defined as the one minimizing the error between the predicted and measured response. The system response can be optimally predicted if an optimal predictor of the states is available. The quality of the predictor of the states is quantified by the *state prediction error*:

$$\{\varepsilon_k\} = \{s_k\} - \{\hat{s}_k\}, \quad (4.54)$$

which represents the part of  $\{s_k\}$  that cannot be predicted by the one-step-ahead predictor of the state vector  $\{\hat{s}_k\}$ . This is defined as the conditional mean of  $\{s_k\}$  given all previous measurements:

$$\{\hat{s}_k\} = E[\{s_k\}|[Y^{k-1}]]. \quad (4.55)$$

In a similar way it is possible to define the *innovation*:

$$\{e_k\} = \{y_k\} - \{\hat{y}_k\} \quad (4.56)$$

as the part of the measured response  $\{y_k\}$  that cannot be predicted by the one-step-ahead predictor  $\{\hat{y}_k\}$ . This is defined as the conditional mean of  $\{y_k\}$  given all previous measurements:

$$\{\hat{y}_k\} = E[\{y_k\}|[Y^{k-1}]] = E[(C\{s_k\} + \{v_k\})|[Y^{k-1}]] = [C]\{\hat{s}_k\} \quad (4.57)$$

The last part of (4.57) is obtained by taking into account (4.42) and assuming no correlation between the measurement noise  $\{v_k\}$  at instant  $t_k$  and the previous measurements  $[Y^{k-1}]$ . Since  $\{y_k\}$  is assumed zero mean and Gaussian distributed,  $\{e_k\}$  is a zero mean Gaussian white noise process.

The Kalman filter for linear and time-invariant systems relates the predictors given by (4.55) and (4.57) as follows:

$$\{\hat{s}_{k+1}\} = [A]\{\hat{s}_k\} + [K_k]\{e_k\} \quad (4.58)$$

$$\{e_k\} = \{y_k\} - [C]\{\hat{s}_k\}. \quad (4.59)$$

The matrix  $[K_k]$  is referred to as *nonsteady state Kalman gain*. Given the initial state estimate  $\{\hat{s}_0\} = \{0\}$ , the initial covariance of the state estimate  $[P_0] = E[\{\hat{s}_0\}\{\hat{s}_0\}^T] = [0]$  and the output measurements  $[Y^{k-1}]$ , the nonsteady-state Kalman state estimate at time  $t_k$  can be obtained from the following recursive formulas providing the Kalman state estimate, the Kalman gain, and the Kalman state covariance, respectively:

$$\{\hat{s}_k\} = [A]\{\hat{s}_{k-1}\} + [K_{k-1}](\{y_{k-1}\} - [C]\{\hat{s}_{k-1}\}) \quad (4.60)$$

$$[K_{k-1}] = \left( [G] - [A][P_{k-1}][C]^T \right) \left( [R_0] - [C][P_{k-1}][C]^T \right)^{-1} \quad (4.61)$$

$$\begin{aligned} [P_k] &= [A][P_{k-1}][A]^T + \\ &\quad \left( [G] - [A][P_{k-1}][C]^T \right) \left( [R_0] - [C][P_{k-1}][C]^T \right)^{-1} \left( [G] - [A][P_{k-1}][C]^T \right)^T \end{aligned} \quad (4.62)$$

Equation (4.62) is also known as the *Riccati equation*. The Kalman filter provides the state estimate  $\{\hat{s}_k\}$  at instant  $t_k$  given the previous state estimate  $\{\hat{s}_{k-1}\}$  and the measurements  $\{y_{k-1}\}$ . Obtained the Kalman state covariance matrix  $[P_k]$  as a solution of the Riccati equation:

$$[P_k] = E[\{\hat{s}_k\}\{\hat{s}_k\}^T] \quad (4.63)$$

the covariance of the innovation can be computed, taking into account (4.59), as:

$$E[\{e_k\}\{e_k\}^T] = [R_0] - [C][P_k][C]^T. \quad (4.64)$$

When the measurements are Gaussian distributed, the Kalman filter provides an optimal prediction of the states. It is worth pointing out that the Kalman state covariance is not steady at startup, since the Kalman filter experiences a transient phase. However, under certain assumptions about the state matrix ([A] is stable, that is to say the real parts of all its eigenvalues are negative), the steady state is quickly reached and the state covariance matrix and the Kalman gain become constant (independent of time:  $[P_k] = [P]$  and  $[K_k] = [K]$ ). In steady-state:

$$\{\hat{s}_{k+1}\} = [A]\{\hat{s}_k\} + [K]\{e_k\} \quad (4.65)$$

$$\{e_k\} = \{y_k\} - [C]\{\hat{s}_k\}. \quad (4.66)$$

The steady-state Kalman gain [K] is obtained by finding the solution [P] of the algebraic Riccati equation:

$$[P] = [A][P][A]^T + \left( [G] - [A][P][C]^T \right) \left( [R_0] - [C][P][C]^T \right)^{-1} \left( [G] - [A][P][C]^T \right)^T \quad (4.67)$$

and substituting it into the following equation:

$$[K] = \left( [G] - [A][P][C]^T \right) \left( [R_0] - [C][P][C]^T \right)^{-1}. \quad (4.68)$$

Then, the covariance matrix of the innovation can be computed:

$$E[\{e_k\}\{e_k\}^T] = [R_0] - [C][P][C]^T. \quad (4.69)$$

Rearranging (4.66), the *forward innovation model* is obtained:

$$\{\hat{s}_{k+1}\} = [A]\{\hat{s}_k\} + [K]\{e_k\} \quad (4.70)$$

$$\{y_k\} = [C]\{\hat{s}_k\} + \{e_k\}. \quad (4.71)$$

Comparison of the forward innovation model with the state-space model given by (4.41) and (4.42) shows that in the forward innovation model the prediction of the state replaces the state vector and the two processes  $\{w_k\}$  and  $\{v_k\}$  are converted into a single process, the innovation.

The closed form solution for the Kalman gain given by the Riccati equation makes the Kalman filter very attractive. However, in the context of dynamic identification the system matrices [A], [C],  $[Q^{ww}]$ ,  $[R^{vv}]$ ,  $[S^{wv}]$  are not known.

Thus, the state sequence has to be determined directly from the output data through geometric manipulations without solving the Riccati equation. The Data-Driven Stochastic Subspace Identification (DD-SSI) method allows the estimation of the states directly from the experimental data by applying robust numerical techniques, such as SVD and QR decomposition (see Sect. 4.5.3.2 for more details).

### 4.2.3 ARMA Models

The equation of motion of a randomly excited linear time-invariant system can be also written as follows:

$$[M]\{\ddot{y}(t)\} + [C]\{\dot{y}(t)\} + [K]\{y(t)\} = \{w(t)\} \quad (4.72)$$

where  $\{w(t)\}$  is a continuous-time, zero mean Gaussian white noise. It is possible to show (Andersen et al. 1996, Andersen 1997) that this system can be also described by a discrete-time Auto-Regressive Moving Average Vector (ARMAV) model (the ARMA model is referred to as an ARMA vector model to point out its multivariate character) by approximating the differential operator with finite differences over a finite time step  $\Delta t$ .

Historically, ARMAV models have been used for the estimation of the modal parameters of civil structures. Due to a number of shortcomings (in particular for systems with many outputs and many modes, where the large set of parameters to be estimated leads to large computational burden and convergence problems), stochastic state-space models have progressively replaced them in the context of modal identification. However, the basics of ARMA models and their relation with state-space models are herein briefly illustrated for the sake of completeness.

In order to explain how modal parameters can be extracted from an ARMA model, assume that a continuous-time system is observed at discrete time instants  $k$  with a sampling interval  $\Delta t$ . The discretization is based on the covariance equivalence technique (Bartlett 1946, Pandit and Wu 1983). Since the input on the structure is not available (it is immeasurable), the equivalent discrete-time system can be obtained only by requiring that the covariance function of its response to a Gaussian white noise input is coincident at all discrete time lags with that of the continuous-time system. This implies that the first and second order moments of the response of the discretized model are equal to the first and second order moments of the response of the continuous-time system at all the considered discrete time instants. Under the assumption that the response of the system is Gaussian distributed, the covariance equivalent model is the most accurate approximated model, since it is exact at all discrete time lags. The generalization of this approach to multivariate second order systems is illustrated elsewhere (Andersen et al. 1996). When the dynamic response of the system is driven by the Gaussian white noise  $\{w(t)\}$  but there are also some disturbances (process and measurement noise), the latter have also to be taken into account by the equivalent

discrete-time model. In the presence of such disturbances, an ARMAV( $n_\alpha$ ,  $n_\gamma$ ) model has the form:

$$\begin{aligned} \{y_k\} + [\alpha_1]\{y_{k-1}\} + \dots + [\alpha_{n_\alpha}]\{y_{k-n_\alpha}\} \\ = \{e_k\} + [\gamma_1]\{e_{k-1}\} + \dots + [\gamma_{n_\gamma}]\{e_{k-n_\gamma}\} \end{aligned} \quad (4.73)$$

where, as in the case of the state-space model,  $\{y_k\}$  is the vector of the output at the time instant  $t_k$ , and  $\{e_k\}$  is the innovation and it is a zero mean Gaussian white noise. The left-hand side of (4.73) is the Auto-Regressive (AR) part, while the right-hand side is the Moving Average (MA) part. The matrices  $[\alpha_i]$  contain the AR parameters, while the matrices  $[\gamma_i]$  contain the MA parameters;  $n_\alpha$  and  $n_\gamma$  represent the AR and MA order of the model, respectively.

It is possible to show (see, for instance, Andersen 1997, Andersen and Brincker 1999) that a covariance equivalent ARMAV model can be converted into a forward innovation state space model, and vice versa. Let us consider a minimal realization of the state-space model of (4.70) and (4.71). A *minimal realization* corresponds to the minimal state space dimension ensuring that all modes are appropriately excited and observed in the output. In fact, if the order of the state-space model is too large, the model will contain redundant information; on the contrary, if the state-space dimension is too small, a certain amount of information about the modeled system will be lost. More details about the mathematical conditions to obtain a minimal realization can be found elsewhere (see, for instance, Kailath 1980). Said  $n$  the order of the minimal realization of the considered forward innovation model and  $l$  the number of outputs, if the ratio  $n/l = p$  is an integer value it is possible to show that, independently of the specific realization, an ARMAV( $p$ ,  $p$ ) model is equivalent to the considered forward innovation model (Andersen 1997).

The conversion of an ARMAV model into a state-space representation requires the selection of a specific realization. A realization, which can be easily constructed from the AR and MA matrices and is well conditioned (so that it is numerically efficient when implemented into a system identification software), must be adopted. The so-called *observability canonical state-space realization* is usually adopted in this case (Andersen 1997). It is given by:

$$[A] = \begin{bmatrix} [0] & [I] & [0] & \dots & [0] \\ [0] & [0] & [I] & \ddots & [0] \\ \vdots & \ddots & \ddots & \ddots & \vdots \\ [0] & [0] & [0] & \ddots & [I] \\ -[\alpha_p] & -[\alpha_{p-1}] & -[\alpha_{p-2}] & \cdots & -[\alpha_1] \end{bmatrix} \quad (4.74)$$

$$[K] = \begin{bmatrix} [I] & [0] & [0] & \cdots & [0] \\ [\alpha_1] & [I] & [0] & \ddots & [0] \\ \vdots & \ddots & \ddots & \ddots & \vdots \\ [\alpha_{p-2}] & [\alpha_{p-3}] & [\alpha_{p-4}] & \ddots & [0] \\ [\alpha_{p-1}] & [\alpha_{p-2}] & [\alpha_{p-3}] & \cdots & [I] \end{bmatrix} \begin{bmatrix} [\gamma_1] - [\alpha_1] \\ [\gamma_2] - [\alpha_2] \\ \vdots \\ [\gamma_{p-1}] - [\alpha_{p-1}] \\ [\gamma_p] - [\alpha_p] \end{bmatrix} \quad (4.75)$$

$$[C] = \begin{bmatrix} [I] & [0] & [0] & \cdots & [0] \end{bmatrix}. \quad (4.76)$$

When the state matrix  $[A]$  is expressed in the form of (4.74), it is also known as the *companion matrix* for the auto-regressive matrix polynomial. The EVD of the companion matrix provides the modal parameters of the system:

$$[A] = [\Psi][M][\Psi]^{-1} \quad (4.77)$$

where the columns  $\{\psi_m\}$  of  $[\Psi]$  are the pl eigenvectors of  $[A]$ , while the corresponding pl eigenvalues  $\mu_m$  are collected in the diagonal matrix  $[M]$ . The eigenvectors are a combination of mode shapes  $\{\phi_m\}$  and eigenvalues  $\mu_m$ :

$$[\Psi] = \begin{bmatrix} \{\phi_1\} & \cdots & \{\phi_{pl}\} \\ \mu_1\{\phi_1\} & \cdots & \mu_{pl}\{\phi_{pl}\} \\ \vdots & \cdots & \vdots \\ \mu_1^{p-1}\{\phi_1\} & \cdots & \mu_{pl}^{p-1}\{\phi_{pl}\} \end{bmatrix}. \quad (4.78)$$

Thus, taking into account (4.76), the mode shapes of the system can be obtained as:

$$\{\phi_m\} = [C]\{\psi_m\} \quad (4.79)$$

while natural frequencies and damping ratios of the continuous-time system are obtained from the eigenvalues, after their conversion from discrete-time to continuous-time taking into account (4.35):

$$\lambda_m = \frac{\ln(\mu_m)}{\Delta t}, \quad \lambda_m = -\xi_m \omega_m \pm i \omega_m \sqrt{1 - \xi_m^2} \quad (4.80)$$

where  $m = 1, \dots, pl$  is the index denoting the generic pole. If the modes are under-damped (this is the case of the structural systems considered in this book), the poles appear in complex conjugate pairs (4.80) and the number of modes  $N_m$  is half the order  $pl$  of the system. The modal properties of the structure are obtained by the EVD of the companion matrix, holding only the AR coefficient matrices. Thus, the MA coefficient matrices do not influence them, and the possibility to use AR models for modal parameter estimation has been investigated (Pandit 1991). However, an AR model of order  $p$  is not an equivalent representation of the previously mentioned minimal realization of the forward innovation model.

The use of AR instead of ARMA models can be justified if the AR model order goes to infinity. In fact, it can be shown that an AR model with infinite order is theoretically equivalent to an ARMA model of finite order. However, for very large values of the order of the AR model many spurious poles are introduced and they have to be separated from the true system poles.

#### 4.2.4 Fraction Polynomial Models

The FRF matrix can be expressed not only in pole-residue form (4.9) but also using a *Matrix Fraction Description* (MFD), that is to say, a ratio of two matrix polynomials. In particular, both a Left MFD (LMFD):

$$[H(\omega)] = [A_L(\omega)]^{-1} [B_L(\omega)] \quad (4.81)$$

and a Right MFD (RMFD):

$$[H(\omega)] = [B_R(\omega)][A_R(\omega)]^{-1} \quad (4.82)$$

can be adopted. The *common-denominator model* (also known as scalar matrix fraction model) of the FRF represents a special case of MFD where the numerator is a matrix polynomial while the denominator is a polynomial characterized by scalar coefficients:

$$[H(\omega)] = \frac{[B(\omega)]}{[A(\omega)]} = \frac{\sum_{j=0}^n [\beta_j(\omega)] \Omega^j(\omega)}{\sum_{j=0}^n \alpha_j \Omega^j(\omega)} \quad (4.83)$$

where  $\Omega(\omega)$  is the *polynomial basis function*. Comparison of (4.83) and (4.9) leads to recognize that the denominator holds the information about the poles of the structure, while the numerator holds the information about the mode shapes. When a common-denominator model is considered, the poles are obtained as roots of the denominator polynomial; in the case of MFD, the poles are obtained as solutions of a generalized eigenvalue problem (Sect. 4.4.3).

When an MFD is adopted, the size ( $N_c \times N_c$ ) of the matrix coefficients  $[A_j]$  (with  $N_c$  depending on the number of inputs or outputs according to the selected description) and the order  $n$  of the matrix polynomial determine the number of modes that can be identified in accordance with the following relation:

$$N_c \cdot n = 2N_m. \quad (4.84)$$

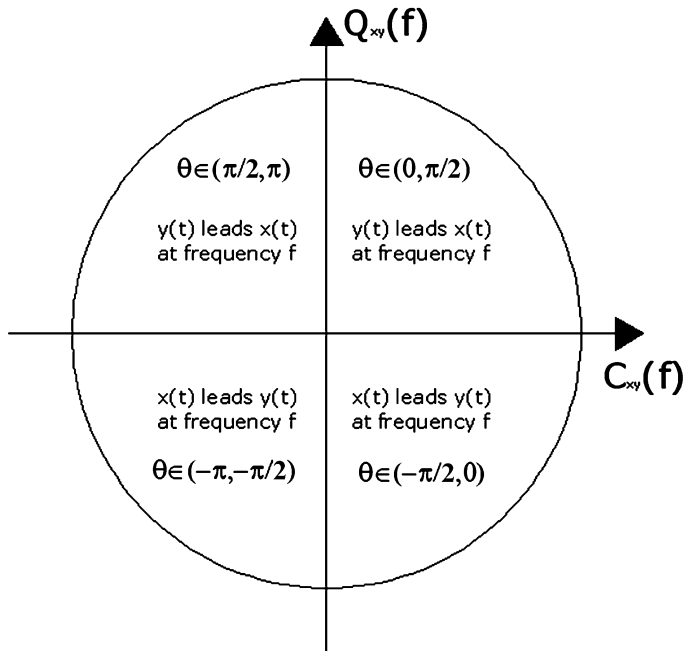


**Fig. 4.2** 4-quadrant symmetry of cross-power spectra

Based on this relation, a low order model with large matrix coefficients can be expanded to a high order matrix polynomial with smaller matrix coefficients in order to identify  $N_m$  modes in the presence of a reduced number of inputs or outputs (low  $N_c$ ). A polynomial of order  $2N_m$  with scalar coefficients represents the limit of this expansion.

In the OMA framework, MFD is applied to power spectra instead of FRFs. As mentioned in Sect. 4.2.1, positive power spectra are also sometimes adopted to improve numerical conditioning (see also Sects. 4.4.3.2 and 4.9). In fact, power spectra show a 4-quadrant symmetry and, therefore, they provide four poles in complex conjugate pairs for each mode. Poles characterized by negative real part are denoted as *stable poles*, while *unstable poles* are characterized by positive real part. The 4-quadrant symmetry (Fig. 4.2) requires doubling the order with respect to FRFs to identify a certain number of modes  $N_m$ , and this may result in worse numerical conditioning. Thus, the estimation of positive power spectra, resulting in a prior separation of stable and unstable poles, improves the numerical conditioning and this simplifies the identification of the structural modes by the p-LSCF estimator (Sect. 4.9). Processing positive power spectra could have a detrimental effect on the accuracy and reliability of mode shape estimates. However, the procedure for their computation is illustrated below for the sake of completeness.

The computation of positive power spectra (see also Cauberghe 2004) is based on the procedure for the estimation of unbiased correlation functions via FFT

(Bendat and Piersol 2000). The Wiener-Khinchin relations between correlation and spectral density functions have been introduced in Chap. 2. Those relations make possible the computation of correlation functions as inverse Fourier transforms of spectral density functions, and the computation of spectral density functions as Fourier transforms of correlation functions. However, as a consequence of the periodic assumption of the finite Fourier transform, the correlation functions obtained by this procedure appear as if they were computed from periodic functions. As a result, the value of the correlation function at the generic time lag  $\tau$  is a combination of two terms,  $\hat{R}_{yy}(\tau)$  and  $\hat{R}_{yy}(T - \tau)$ . In particular, it is possible to show that the following equation holds (Bendat and Piersol 2000):

$$\begin{aligned}\hat{S}_{YY}(f) &= \frac{1}{T} \int_0^T \tau \hat{R}_{yy}(T - \tau) e^{-i2\pi f \tau} d\tau + \frac{1}{T} \int_0^T (T - \tau) \hat{R}_{yy}(\tau) e^{-i2\pi f \tau} d\tau \\ &= \int_0^T \hat{R}_c(\tau) e^{-i2\pi f \tau} d\tau\end{aligned}\quad (4.85)$$

where:

$$\hat{R}_c(\tau) = \frac{(T - \tau)}{T} \hat{R}_{yy}(\tau) + \frac{\tau}{T} \hat{R}_{yy}(T - \tau) \quad (4.86)$$

is the *circular correlation function*, whose expression in discrete time becomes:

$$\hat{R}_c(r\Delta t) = \frac{(N - r)}{N} \hat{R}_{yy}(r\Delta t) + \frac{r}{N} \hat{R}_{yy}[(N - r)\Delta t]. \quad (4.87)$$

A procedure to separate the two contributions consists in adding  $N$  zeroes to the original  $N$  data values so that the first half of the correlation function estimate shows the correlation function values for the positive lags (the causal part of the correlation function which contains the stable poles) and the second half of the estimate shows the correlation function values for the negative lags (the noncausal part of the correlation function which contains the unstable poles). Equation (4.88) gives the two portions of the correlation function obtained by adding  $N$  zeroes:

$$\hat{R}_s(r\Delta t) = \begin{cases} \frac{(N - r)}{N} \hat{R}_{yy}(r\Delta t) & r = 0, \dots, N - 1 \\ \frac{(r - N)}{N} \hat{R}_{yy}[(2N - r)\Delta t] & r = N, \dots, 2N - 1 \end{cases} \quad (4.88)$$

where the subscript  $s$  is referred to the separation of the two contributions. Thus, the causal part of the unbiased correlation function estimate is:

$$\hat{R}_{yy}(r\Delta t) = \frac{N}{N - r} \hat{R}_s(r\Delta t) \quad r = 0, \dots, N - 1. \quad (4.89)$$

The above discussion leads to the following procedure for the computation of positive power spectra:

- Divide the record of the structural response into  $n_b$  independent (no overlap) blocks of  $N$  samples, where the number of samples  $N$  in each block has to be larger than the maximum lag number of interest  $m$ :  $N \geq m$ ;
- Extend each block with additional  $N$  zeroes;
- Use the extended blocks to compute the power spectra according to the Welch procedure;
- Compute the inverse Fourier transform and consider only the first  $m$  samples for  $m < N$ , or discard the second half of the obtained correlation function if  $m = N$ ; rescale the values of the obtained correlation function by  $N/(N - r)$ . For  $m = N$ , since the tail of the correlation function is affected by high noise levels, an exponential window can be applied to reduce the effect of leakage and the influence of the higher lags characterized by larger variance; however, this requires a correction of the damping values obtained from modal identification: said  $\beta$  the factor determining the ratio between the amplitude at the last time lag and the initial amplitude of the exponential window, the damping associated to the  $r$ -th pole  $\lambda_r$  can be corrected taking into account that  $\lambda_r^{corrected} = \lambda_r^{estimated} + \beta$  (Verboven 2002, Heylen et al. 1998); a suggested value for  $\beta$  is such that the amplitude at the last time lag of the window is 0.1 % of its initial amplitude (Verboven 2002);
- The positive power spectra are finally obtained by Fourier transform of the retained portion of the causal part of the correlation function.

The positive power spectra show a 2-quadrant symmetry and, therefore, the same order  $n = 2N_m$  of FRFs. As a consequence, only one pair of complex conjugate poles is present in the data for each mode. The relation between power spectra and positive power spectra is (Peeters and Van der Auweraer 2005):

$$[S_{YY}(\omega)] = [S_{YY}^+(\omega)] + [S_{YY}^+(\omega)]^H. \quad (4.90)$$

#### 4.2.5 The Unified Matrix Polynomial Approach to Modal Analysis

A number of input–output modal identification techniques have been developed over the years according to the theoretical expressions of FRF or IRF. Different physically based models and different mathematical manipulations produced a number of different methods. However, it has been shown (Allemang and Brown 1998) that those apparently unrelated procedures could be treated according to a unified approach. Such an approach is herein summarized because it can be easily extended to OMA. It is useful to highlight the similarities and differences among the various modal identification methods, whose correlation is stronger than it appears at a first insight.

The original approach starts from the polynomial model historically used for the FRF; assuming that the response to the input applied at location q is measured at location p, the related FRF can be expressed as follows:

$$H_{pq}(\omega) = \frac{Y_p(\omega)}{F_q(\omega)} = \frac{\beta_n(i\omega)^n + \beta_{n-1}(i\omega)^{n-1} + \dots + \beta_1(i\omega)^1 + \beta_0(i\omega)^0}{\alpha_m(i\omega)^m + \alpha_{m-1}(i\omega)^{m-1} + \dots + \alpha_1(i\omega)^1 + \alpha_0(i\omega)^0} \quad (4.91)$$

or:

$$H_{pq}(\omega) = \frac{Y_p(\omega)}{F_q(\omega)} = \frac{\sum_{k=0}^n \beta_k(i\omega)^k}{\sum_{h=0}^m \alpha_h(i\omega)^h}. \quad (4.92)$$

Equation (4.92) can be rewritten in order to obtain the following linear equation in the unknown  $\alpha_h$  and  $\beta_k$  terms:

$$\sum_{h=0}^m \alpha_h(i\omega)^h Y_p(\omega) = \sum_{k=0}^n \beta_k(i\omega)^k F_q(\omega). \quad (4.93)$$

For a general MIMO case, (4.93) is expressed in matrix form as follows:

$$\sum_{h=0}^m \left( [\alpha_h](i\omega)^h \right) \{Y(\omega)\} = \sum_{k=0}^n \left( [\beta_k](i\omega)^k \right) \{F(\omega)\} \quad (4.94)$$

or:

$$\sum_{h=0}^m \left( [\alpha_h](i\omega)^h \right) [H(\omega)] = \sum_{k=0}^n \left( [\beta_k](i\omega)^k \right). \quad (4.95)$$

A similar expression can be derived in the time domain where, in terms of sampled data, the time domain matrix polynomial results from a set of finite difference equations (Allemand and Brown 1998):

$$\sum_{h=0}^m [\alpha_h] \{y_{i-h}\} = \sum_{k=0}^n [\beta_k] \{f_{i-k}\} \quad (4.96)$$

This model corresponds to an ARMA(m, n) model (compare (4.96) with (4.73)). If only free decay or IRF data are considered, (4.96) can be further simplified since the forcing function can be set equal to zero and the  $[\beta_k]$  coefficients can be eliminated (Allemand and Brown 1998):

$$\sum_{h=0}^m [\alpha_h] \{y_{i-h}\} = \{0\}. \quad (4.97)$$

The number of roots is given by the product of the order of the polynomial by the number of measurement locations, as for the classical ARMA models.

Comparison of (4.94) and (4.96) leads to recognize that the time and frequency domain models can be expressed in terms of functionally similar matrix polynomial models. Since the ARMA terminology is traditionally related to the time domain, the Unified Matrix Polynomial Approach (UMPA) terminology has been proposed (Allemand and Brown 1998) in order to describe the common polynomial structure characterizing the various modal identification methods in either time or frequency domain. Following the original discussion, the same nomenclature for the coefficient matrices has been used in both time and frequency domain in order to point out the similarities. However, the coefficient matrices in the frequency domain are different from those in the time domain. Moreover, while the characteristic matrix polynomial equation in frequency domain can be expressed in the same domain, for time domain methods it is expressed in the  $z$ -domain and the roots  $z_r$  in this domain have to be converted in the continuous-time domain (4.80). Once the matrices  $[\alpha_h]$  have been found, the modal parameters can be estimated according to the previously described approach (Sect. 4.2.3) based on the construction of the companion matrix.

The extension of UMPA to the output-only case is immediate if FRFs and IRFs are replaced by spectral density functions and correlation functions into (4.95) and (4.97), respectively. Thus, the development of UMPA allowed gathering a number of time domain and frequency domain algorithms in a unified framework, pointing out the relations among different modal identification algorithms beyond their mathematical model (time domain, frequency domain, state-space, AR, ARMA). Nonparametric methods can be seen as zero order models where only the spatial information related to the sensor position is used and data are processed at a single frequency line at a time.

Even if the unifying characteristic of different OMA methods, represented by the matrix polynomial structure, has been remarked, for historical reasons OMA methods are illustrated in the next sections according to the usual classification based on the adopted model and domain of implementation. For instance, the methods based on the analysis of correlation functions, such as Least Squares Complex Exponential (LSCE), Ibrahim Time Domain (ITD), Eigensystem Realization Algorithm (ERA), and Instrumental Variable (IV), will be discussed in different contexts in spite of the previously described common formulation. Similarly, time domain methods based on the analysis of raw data, such as DD-SSI and Prediction Error Method (PEM), will be separately analyzed according to the state-space and ARMA formulation, respectively. The separate discussion follows the historical development of the methods and it is helpful to point out the main differences among them that are mainly related to the role played by noise. Moreover, the separate discussion allows pointing out a specific difference between state-space and ARMA models. In fact, in the state-space representation the internal structure of the system is described, while ARMA models simply map the input-output behavior of the system. For this reason, a state-space model is also referred to as an internal representation of a system, while the ARMA model as an external representation.

### 4.3 Classification of OMA Techniques

Most OMA techniques are derived from traditional input–output modal identification procedures, but refer to a different mathematical framework. In fact, OMA is developed in a stochastic framework and it is based on the analysis of random signals (Chap. 2). OMA techniques are always of the multiple input type. Thus, classification of OMA methods according to the number of inputs (single input, multiple input), as in the case of input–output modal analysis, is not applicable.

Different criteria may apply for the classification of OMA methods. Each criterion points out a specific aspect common to different analysis methods and it is helpful to guide the user towards the choice of the favorite or most appropriate analysis method, depending on the advantages and limitations related to specific assumptions and data processing procedures.

A first distinction is between *parametric* and *nonparametric methods*. If a model is fitted to data, the technique is referred to as parametric. These procedures are more complex and computational demanding with respect to the nonparametric ones. However, they usually show better performance with respect to the faster and easy-to-use nonparametric techniques. Nonparametric techniques, on the other hand, are particularly useful during field tests to get a quick insight about effectiveness of measurements and results of dynamic identification. In the class of parametric models, a further distinction is made between low order and high order models. A *low order model* is used for those cases where the number of physical coordinates is greater than the number of measurable eigenvalues. On the contrary, a *high order model* is usually adopted when the system is under-sampled in the spatial domain.

Another distinction is between *SDOF* and *MDOF methods*, depending on the assumption about the number of modes determining the structural response in a given bandwidth. If only one mode is dominant, it is possible to assume that the structural response in that frequency range depends only on that mode and its parameters can be separately determined. SDOF methods are based on this assumption. They are very fast and characterized by low computational burden, but the SDOF assumption is a reasonable approximation only if the modes of the structure are well separated. In the presence of closely spaced or even coincident modes, MDOF methods have to be adopted in order to properly identify the different modes contributing to the overall structural response.

Modal frequencies and damping ratios are independent of the output location and they can be estimated on a local basis, that is to say, from the separate analysis of the individual response time histories. In this case, each analyzed time history can provide a slightly different estimate of the same modal parameter: as a result, a set of *local estimates* is obtained. On the contrary, if data processing affects all response measurements at the same time, *global estimates* for the modal parameters are obtained. A further distinction is between *one-stage* and *two-stage methods*. In the first case, natural frequencies, damping ratios, and mode shapes are estimated at the same time; in the second case, instead, selected parameters (for instance, natural frequencies and damping ratios) are estimated first, while the remaining

parameters (for instance, the mode shapes) are estimated in a second data processing step based on the modal estimates obtained in the first stage of analysis.

A classical distinction is based on the domain of implementation. OMA methods based on the analysis of response time histories or correlation functions are referred to as *time domain methods*. Methods based on spectral density functions are, instead, referred to as *frequency domain methods*. This distinction may look like artificial, since they simply consider different representations of the same signal (in fact, it is always possible to transform the signal from one domain to the other). However, when parametric methods are considered, the selection between time and frequency domain can be relevant in practical applications since different mechanisms of noise rejection and quality of numerical conditioning characterize the two classes of methods.

Time domain methods are usually better conditioned than the frequency domain counterparts. This is mainly related to the effect of the powers of frequencies in frequency domain equations; numerical conditioning has been recently improved through the adoption of polynomial basis functions formulated in the  $z$ -domain (see also Sect. 4.4.3 for more details).

The adopted strategy to deal with noisy measurements represents another discriminating aspect between time domain and frequency domain methods. Time domain methods are usually more suitable to handle noisy data, and they can avoid some signal processing errors, such as leakage. Time domain methods take advantage of the SVD to reject noise or, as in the case of ARMA models, they try to model also the noise. However, in this latter case a higher model order is required to fit noise effects and, as a consequence, a lot of additional spurious poles appear. Averaging is, instead, the strategy adopted by frequency domain methods to deal with noisy measurements (see also Chap. 2).

Among the parametric time domain methods a further distinction is between *covariance-driven* and *data-driven methods*. The former require a preprocessing step to estimate the correlation functions from response measurements; the latter, instead, directly process the raw data.

---

## 4.4 Frequency Domain Methods

### 4.4.1 The Basic Frequency Domain (Peak-Picking) Method

The most undemanding method for output-only modal parameter identification is the Basic Frequency Domain (BFD) method, also known as the Peak-Picking method. It is based on the computation of auto- and cross-spectra and it has been widely used in the past for modal identification purposes (see, for instance, Felber 1993 for its application in civil engineering). The name of the method comes from the fact that the modes are identified by picking the peaks in the PSD plots.

The BFD technique can be classified as a SDOF method for OMA. In fact, it is based on the assumption that, around a resonance, only one mode is dominant. As a consequence, the pole-residue form of the output PSD matrix (4.13) can be

approximated by the contribution of the dominant mode only. For instance, if only the  $r$ -th mode is dominant, the structural response is approximately equal to the modal response:

$$\{y(t)\} \approx \{\phi_r\} p_r(t) \quad (4.98)$$

where  $p_r(t)$  is the modal coordinate related to the  $r$ -th mode. As a consequence, the correlation functions are approximately given by:

$$[R_{yy}(\tau)] = E\left[\{y(t + \tau)\}\{y(t)\}^T\right] = R_{p_r p_r}(\tau) \{\phi_r\} \{\phi_r\}^T \quad (4.99)$$

where:

$$R_{p_r p_r}(\tau) = E[p_r(t + \tau)p_r(t)] \quad (4.100)$$

is the modal auto-correlation function, and the spectral density matrix is given by:

$$[G_{YY}(\omega)] = G_{P_r P_r}(\omega) \{\phi_r\} \{\phi_r\}^H \quad (4.101)$$

where  $G_{P_r P_r}(\omega)$  is the auto-spectral density function of the modal coordinate. It is clear from (4.101) that in this case the PSD matrix is of rank one. Thus, at resonance any column of the PSD matrix can be considered as an estimate of the corresponding mode shape, up to a scaling factor (the input being unmeasured).

From a practical point of view, the trace of the PSD matrix (the sum of the auto-spectra) at each discrete frequency value is computed first to identify the peaks corresponding to structural resonances. Then, the mode shapes associated to the identified frequencies are obtained from one of the columns of the PSD matrix. A reference sensor for the computation of the cross-spectral densities with all other measurement channels has to be selected. The reference sensor has to be selected so that most of the modes can be observed. As a consequence, sensors close to nodes of the mode shapes cannot be adopted as reference sensors. The ideal choice for the reference sensor makes possible the identification of all the modes through the computation a single column of the PSD matrix (the column made by the cross-spectral densities between the selected reference sensor and all other sensors). However, depending on the geometry of the structure and the adopted sensor layout, a single reference sensor could be insufficient to identify all the modes and at least a couple of reference sensors with different orientation have to be adopted. For instance, in the case of a building-like structure characterized by two bending modes in two orthogonal directions— $x$  and  $y$ —and sensors parallel to these directions, the selection of a sensor measuring along  $x$  as reference permits the identification of the bending modes in the  $x$  direction and eventually torsional modes, but it is inadequate to identify the bending modes in the  $y$  direction. These can be observed only through the selection of an additional reference sensor measuring along  $y$ .

The inspection of the coherence functions (Chap. 2) between couples of channels also supports the identification of the actual modes of the structure (Fig. 4.3).

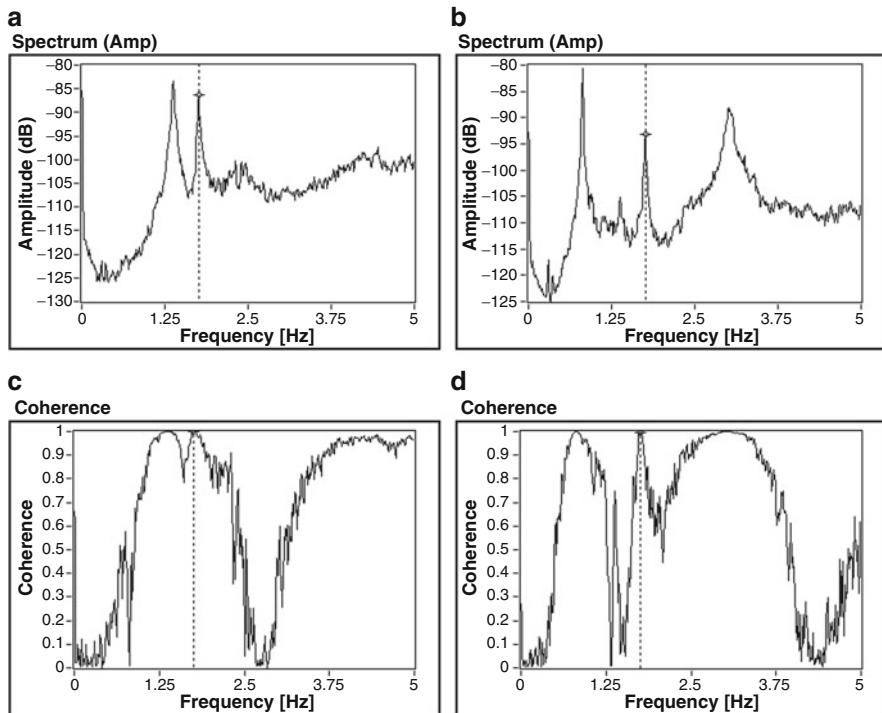


**Fig. 4.3** Auto-power spectra of two reference channels in orthogonal directions (**a**, **b**) and coherence functions with channels in the same directions of the references (**c**, **d**); note that the torsional mode (marked in the plots) yields high coherence with both the reference channels

In fact, in correspondence of a resonant frequency, the coherence function is close to 1 because of the high signal-to-noise ratio at that frequency. This characteristic is helpful in the discrimination between real eigenfrequencies and peaks due to disturbances. Moreover, the coherence function can support the identification of the nature of a mode. For instance, assume that the structure under investigation shows two bending modes in two orthogonal directions—*x* and *y*—and a torsional mode in a certain frequency range. When the torsional mode is considered, the coherence function shows a value close to 1 if either the two channels are in the same direction or in two orthogonal directions. On the contrary, bending modes are associated to low values of the coherence when it is computed for two orthogonal sensors. The combination of information from spectra and coherence functions, therefore, makes possible the identification of structural modes. This procedure sometimes makes possible the identification even of closely spaced modes. However, the success of the identification process heavily depends on the geometry of the structure and the skill of the analyst. The results of modal identification suffer a certain degree of subjectivity also in the case of noisy measurements, when the peaks in the spectra are not clear.

The BFD method provides local estimates of the modal properties. Moreover, the accuracy of the estimated eigenfrequencies depends on the frequency resolution of the spectra. A fine frequency resolution is fundamental to obtain good natural frequency estimates.

In principle, the BFD should be applied to evaluate natural frequencies and mode shapes only. The half-power bandwidth method is sometimes applied to get damping estimates from the spectra. However, a number of studies have shown that they are not accurate (see, for instance, Peeters 2000, Rainieri et al. 2010).

In summary, the BFD technique is effective when damping is low and modes are well separated. If these conditions are violated it may lead to erroneous results. In fact, the method identifies ODSs instead of the actual mode shapes, and they are generally a combination of all mode shapes; they are good approximations of the actual mode shapes if only one mode is dominant at the considered frequencies. In the case of closely spaced modes, the respective contributions are significant and the ODS is the superposition of multiple modes. Despite of these drawbacks, the method is very simple and undemanding from a computational point of view. Thus, it is a basic but useful analysis tool for the analyst, in particular during field tests, to get a quick insight about effectiveness of measurements and results of dynamic identification.

#### 4.4.2 The Frequency Domain Decomposition Method

The introduction of the FDD technique (Brincker et al. 2001) has overcome the previously discussed drawbacks of the BFD method concerning the identification of closely spaced modes. This method was originally applied to FRFs and known as Complex Mode Indicator Function (CMIF) to point out its ability to detect multiple roots and, therefore, the possibility to count the number of dominant modes at a certain frequency (Shih et al. 1988). The method has been then systematized for the use with response spectrum data.

A theoretical proof of the method is based on the modal expansion of the structural response:

$$\{y(t)\} = [\Phi]\{p(t)\} \quad (4.102)$$

where  $[\Phi]$  is the modal matrix and  $\{p(t)\}$  the vector of modal coordinates. From (4.102) the correlation matrix of the responses can be computed:

$$[R_{yy}(\tau)] = E\left[\{y(t + \tau)\}\{y(t)\}^T\right] = [\Phi][R_{pp}(\tau)][\Phi]^T \quad (4.103)$$

The PSD matrix can be obtained from (4.103) by taking the Fourier transform:

$$[G_{YY}(\omega)] = [\Phi][G_{PP}(\omega)][\Phi]^H \quad (4.104)$$

The PSD matrix of the modal coordinates is diagonal if they are uncorrelated. A similar decomposition is obtained in the case of uncorrelated excitation forces characterized by a flat spectral density function (Brincker and Zhang 2009).

Taking into account that the SVD of the PSD matrix at a certain frequency  $\omega$  leads to the following factorization:

$$[G_{YY}(\omega)] = [U][\Sigma][V]^H \quad (4.105)$$

where  $[U]$  and  $[V]$  are the unitary matrices holding the left and right singular vectors and  $[\Sigma]$  is the matrix of singular values (arranged in descending order), for a Hermitian and positive definite matrix, such as the PSD matrix, it follows that  $[U] = [V]$  and the decomposition of (4.105) can be rewritten as:

$$[G_{YY}(\omega)] = [U][\Sigma][U]^H. \quad (4.106)$$

The comparison between (4.104) and (4.106) suggests that it is possible to identify a one-to-one relationship between singular vectors and mode shapes; moreover, the singular values are related to the modal responses and they can be used to define the spectra of equivalent SDOF systems characterized by the same modal parameters as the modes contributing to the response of the MDOF system under investigation. Since the SVD provides the singular values arranged in descending order, near a resonance the first singular value contains the information about the dominant mode at that frequency. Moreover, since the number of nonzero elements in  $[\Sigma]$  equals the rank of the PSD matrix at the considered frequency, this property can be used to identify closely spaced or even coincident modes. In fact, the number of dominant singular values (defining the rank of the output PSD matrix) at a certain frequency equals the number of modes that give a significant contribution to the structural response at that particular frequency. Assuming that only one mode is dominant at the frequency  $\omega$ , and that the selected frequency is associated to the peak of resonance of the  $k$ -th mode, the PSD matrix approximates to a rank one matrix with only one term on the right side of (4.106):

$$[G_{YY}(\omega)] = \sigma_1 \{u_1\} \{u_1\}^H, \quad \omega \rightarrow \omega_k. \quad (4.107)$$

In such a case, the first singular vector  $\{u_1\}$  represents an estimate of the mode shape of the  $k$ -th mode:

$$\{\hat{\phi}_k\} = \{u_1(\omega_k)\} \quad (4.108)$$

and the corresponding singular value  $\sigma_1$  belongs to the auto PSD function of the equivalent SDOF system corresponding to the mode of interest. The equivalent SDOF PSD function is identified as the set of singular values around a peak of the singular value plots (Fig. 4.4) that are characterized by similar singular vectors. In the enhanced version of the method, the so-called Enhanced Frequency Domain Decomposition (EFDD) (Brincker et al. 2001, Gade et al. 2005), this SDOF PSD function is used to estimate also the modal damping ratio. The comparison of the

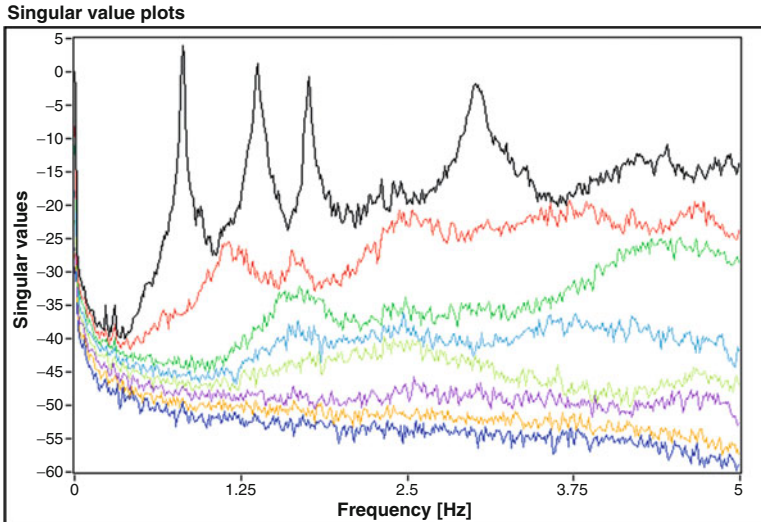


**Fig. 4.4** Sample singular value plots

mode shape estimate  $\{\hat{\phi}_k\}$  at the peak with the singular vectors associated to the frequency lines around the peak leads to the identification of the singular values whose singular vectors show a correlation with  $\{\hat{\phi}_k\}$  higher than a user-defined threshold, the so-called *MAC Rejection Level*. Such singular values define the equivalent SDOF PSD function. The *Modal Assurance Criterion* (MAC) is used as a measure of the correlation between two modal vectors (see also Sect. 4.8.2.2 for more details about the MAC index); it is given by (Allemang and Brown 1982):

$$MAC(\{u_j\}, \{\hat{\phi}_k\}) = \frac{\left| \{u_j\}^H \{\hat{\phi}_k\} \right|^2}{\left( \{u_j\}^H \{u_j\} \right) \left( \{\hat{\phi}_k\}^H \{\hat{\phi}_k\} \right)} \quad (4.109)$$

where  $\{u_j\}$  is the generic singular vector in the vicinity of the peak in the singular value plots corresponding to the  $k$ -th mode.

By definition, the MAC is a number in the range  $[0, 1]$ ; it is equal to zero when the vectors under comparison are orthogonal, and equal to 1 when the vectors differ by a scale factor only. A typically adopted value of the MAC Rejection Level is about 0.8. The identified equivalent SDOF PSD function is used to evaluate the modal damping ratio, and to get estimates of the natural frequency independent of the frequency resolution of the spectra. The inverse Fourier transform of the equivalent SDOF PSD function yields an approximated correlation function of the equivalent SDOF system. Thus, an estimate of the modal damping ratio is obtained in the time domain through a linear regression on the logarithmic decrement. In a similar way, an estimate of the natural frequency independent of the frequency resolution can be obtained through a linear regression on the zero crossing times of the equivalent SDOF system correlation function, eventually taking into account that damped  $f_{d,k}$  and undamped

natural frequency  $f_k$  (which are very similar at low values of the modal damping ratio  $\xi_k$ ) are related as follows:

$$f_{d,k} = f_k \sqrt{1 - \xi_k^2}. \quad (4.110)$$

The FDD method permits the identification of closely spaced modes. However, it is worth pointing out that in this case the mode shape estimates could be biased. In fact, since the SVD forces the singular vectors to be orthogonal, if the experimental mode shapes are also orthogonal the obtained estimates are unbiased. On the contrary, if the mode shapes are not orthogonal, the mode shape estimates for the closely spaced modes are biased and the bias mainly affects the weak mode, while the mode shape estimate for the dominant mode is still good. The bias depends on the difference between the first and second singular value: the larger this difference, the smaller the error. Thus, the mode shape estimates should be obtained from singular vectors at frequencies characterized by the largest difference between the first and second singular value. In the presence of closely spaced modes, this frequency might be different from the frequency of the peak.

In the literature it is possible to find variants to the above-described classical implementation of the FDD/EFDD method (Jacobsen et al. 2008, Rodrigues et al. 2004). In particular, an alternative implementation of FDD based on EVD instead of SVD is also available (Brincker and Zhang 2009). Among the FDD variants, it is worth mentioning the so-called Frequency-Spatial Domain Decomposition (FSDD), where spatial filtering is adopted to enhance the estimation of modal frequencies and damping ratios. The *spatial filtering*, also known as coherent averaging, is a method for data condensation based on a dot product of the data with a weighting vector. Information in the data that is not coherent with the weighting vectors is averaged out of the data. Typical spatial filtering procedures are based on the use of data coming from sensors located in a local area of the system in order to enhance local modes, or on the use of mode shape estimates as weighting functions to enhance particular modes. The spatial filtering belongs to the class of the so-called condensation algorithms together with least squares and transformations (such as SVD). The FSDD makes use of mode shape estimates computed via SVD of the output PSD matrix to enhance PSDs. The use of a mode shape estimate (provided by FDD) as weighting vector leads to an enhanced PSD, which approximates the PSD of a SDOF system. As a consequence, a SDOF curve fitter may be profitably used to estimate the natural frequency and the damping ratio of the considered mode. More details about FSDD can be found elsewhere (Zhang et al. 2005a).

#### 4.4.3 Frequency Domain Parametric Methods for OMA

Frequency domain parametric modal identification methods are based on either fraction polynomial models or the modal (pole-residue) model. Modal identification methods based on the modal model, such as the Least Squares Frequency

Domain (LSFD) estimator, have an historical relevance but they are not in wide use. In fact, when an estimate of the pole is not available, the LSFD method leads to a nonlinear least squares problem that needs for an optimization algorithm to be solved and good starting values to reduce the iterations. As a consequence, the LSFD estimator is used only to obtain global estimates of the mode shapes in combination with other methods providing the poles.

The methods based on MFD are basically curve-fitting techniques based on the minimization of an equation error between the measured and the predicted PSD matrix. For instance, the equation error for a common-denominator model is given by:

$$\varepsilon_{YY}(\omega_f) = \hat{G}_{YY}(\omega_f) - \frac{B_{YY}(\omega_f, \{\theta\})}{A(\omega_f, \{\theta\})} \quad (4.111)$$

where  $\hat{G}_{YY}(\omega_f)$  is the measured value of the spectrum at the frequency line f for a generic couple of measurement channels;  $B_{YY}$  and  $A$  are the numerator and denominator polynomials, respectively; the polynomial coefficients  $\{\theta\}$  are the parameters to be estimated. In order to identify the parameters  $\{\theta\}$ , a cost function is defined as the sum of squares of the Frobenius norms of the errors at all frequency lines:

$$\ell(\{\theta\}) = \sum_{f=1}^{N_f} \|[\varepsilon(\omega_f)]\|_F^2 \quad (4.112)$$

where  $\varepsilon_{YY}(\omega_f)$  is the generic element of  $[\varepsilon(\omega_f)]$ .

The cost function has a nonlinear expression in the unknown parameters. Thus, iterative algorithms, such as the Gauss-Newton approach, have to be applied. However, they typically suffer problems of convergence, local minima, and computational burden. Moreover, since the solution is sensitive to the initial value, good starting values are required. Maximum Likelihood Estimators (MLEs) are based on this approach. In order to find good initial values for the application of the MLE, some approaches to linearize the cost function have been introduced. As a consequence, sub-optimal initial values of the parameters are obtained as a solution of a linear least squares problem.

The Least Squares Complex Frequency (LSCF) method is a parametric frequency domain modal identification method originally developed to provide good initial values of the parameters to the MLE with low computational efforts. However, it has been found that it is also able to provide fairly accurate modal parameter estimates and, as a consequence, it can be confidently applied as modal identification technique (Verboven 2002, Zhang et al. 2005b).

For this reason and the previously mentioned drawbacks related to the solution of an optimization problem by iterative algorithms, the MLE is not widely used in practical applications. The interested reader can refer to the literature on this topic for more details (Schoukens and Pintelon 1991, Pintelon et al. 1994). In the following, attention is focused on the LSCF estimator. The main advantage with

its use is in the possibility to get very clear stabilization diagrams (see Sect. 4.9 for more details). This simplifies the identification of the structural modes and provides interesting opportunities for the automation of the modal identification process. However, the LSCF method shows some limitations in the identification of closely spaced modes. Thus, a poly-reference version of the method, the Poly-reference LSCF estimator (also known under the commercial name of PolyMAX), has been introduced to deal with the identification of closely spaced poles. Both the LSCF method and its poly-reference version can be classified as two stage modal identification methods. In fact, the identification of the mode shapes is based on previous estimates of natural frequencies and damping ratios. In particular, as explained next, the identification of the mode shapes is usually carried out according to the LSFD approach once the poles associated to structural modes have been identified in the first stage of analysis.

#### 4.4.3.1 The Least Squares Complex Frequency Method

The LSCF estimator takes advantage of the global character of the structural poles and the common-denominator model to identify the modal parameters. It can be classified as a parametric, frequency domain modal identification procedure. The analysis parameter is represented by the order of the polynomial in the model.

Assume that the numerator polynomial and the common-denominator polynomial are characterized by the same order  $n$ . For a generic couple  $k$  of output channels ( $k = 1, \dots, l \cdot l$ ), the cross-power spectrum at frequency line  $f$  ( $f = 1, \dots, N_f$ ) is modeled as:

$$G_k(\omega_f) = \frac{N_k(\Omega_f, \{\theta\})}{d(\Omega_f, \{\theta\})} \quad (4.113)$$

where:

$$N_k(\Omega_f, \{\theta\}) = \sum_{j=0}^n N_{k,j} \Omega_f^j \quad (4.114)$$

$$d(\Omega_f, \{\theta\}) = \sum_{j=0}^n d_j \Omega_f^j \quad (4.115)$$

are the numerator polynomial and the common-denominator polynomial, respectively. The coefficients  $d_j$  and  $N_{k,j}$  are the unknown, complex-valued parameters  $\{\theta\}$  to be estimated.  $\Omega_f$  is the *generalized transform variable*, evaluated at the frequency line  $f$ . Different choices for  $\Omega_f$  are possible.

In its classical implementation, the LSCF estimator was based on a continuous-time domain model with real-valued coefficients. In that case the generalized transform variable was  $\Omega_f = i\omega_f$ .

Nevertheless, the problem was numerically ill-conditioned, in particular for high order systems, and even the normalization of the frequency axis led to moderate

improvements of the numerical conditioning. A significant improvement of numerical conditioning of continuous-time domain models was obtained through the introduction of orthogonal polynomials—Forsythe and Chebyshev polynomials—(Verboven et al. 2005) as generalized transform variable. Nevertheless, numerical conditioning problems were still present to a certain extent and the coefficients estimated according to the polynomial basis had to be transformed back to the original power polynomial basis in order to extract the modal parameters. In order to overcome these drawbacks, the LSCF estimator is currently based on a common-denominator model in the discrete-time domain, and the generalized transform variable has the following formulation in the  $z$ -domain:

$$\Omega_f = e^{i\omega_f \Delta t} = z_f. \quad (4.116)$$

This complex polynomial basis function ensures good numerical conditioning. As a consequence, only the  $z$ -domain formulation is considered in the following. From (4.116) it follows that:

$$\Omega_f^j = e^{(i\omega_f \Delta t)j} = z_f^j \quad (4.117)$$

The estimation of the coefficients  $\{\theta\}$  requires the application of a constraint in the solution of the least squares problem. In fact, multiplication of numerator and denominator by a scalar  $a \neq 0$  yields an equivalent scalar matrix fraction description:

$$G_k(\omega_f) = \frac{N_k(\Omega_f, \{\theta\})}{d(\Omega_f, \{\theta\})} = \frac{a \cdot N_k(\Omega_f, \{\theta\})}{a \cdot d(\Omega_f, \{\theta\})}. \quad (4.118)$$

Possible strategies to remove the parameter redundancy consist in setting one of the denominator coefficients equals to 1 (the effect of different choices for the restrained coefficient is discussed in Sect. 4.9) or in imposing that the vector of the parameters  $\{\theta\}$  (or eventually the vector holding only the denominator coefficients) has norm 1.

In the following derivations the highest order coefficient of the denominator is constrained to be equal to 1:

$$d_n = 1 \quad (4.119)$$

since this choice simplifies the identification of the structural poles (Sect. 4.9).

The polynomial coefficients are obtained as a solution of a linear least squares problem. In order to obtain equations that are linear in the parameters, the following approximation is considered:

$$\varepsilon_k(\omega_f, \{\theta\}) = N_k(\Omega_f, \{\theta\}) - \hat{G}_k(\omega_f) d(\Omega_f, \{\theta\}) \approx 0 \quad (4.120)$$

where  $\hat{G}_k(\omega_f)$  is the measured spectrum for the k-th couple of output channels, evaluated at the frequency line f. The unknown polynomial coefficients are obtained through the minimization of the following equation error:

$$\ell(\{\theta\})_{LS} = \sum_{k=1}^{l-l} \sum_{f=1}^{N_f} |N_k(\Omega_f, \{\theta\}) - \hat{G}_k(\omega_f) d(\Omega_f, \{\theta\})|^2. \quad (4.121)$$

Since (4.120) is linear in the unknown parameters  $\{\theta\}$ , it can be rewritten as follows, taking into account that a common-denominator model has been adopted:

$$\{\varepsilon\} = [J]\{\theta\} = \begin{bmatrix} [\Gamma_1] & [0] & \dots & [0] & [\Upsilon_1] \\ [0] & [\Gamma_2] & \ddots & [0] & [\Upsilon_2] \\ \vdots & \vdots & \ddots & \vdots & \vdots \\ [0] & [0] & \dots & [\Gamma_{l-l}] & [\Upsilon_{l-l}] \end{bmatrix} \begin{Bmatrix} \{\theta_{N_1}\} \\ \{\theta_{N_2}\} \\ \vdots \\ \{\theta_{N_{l-l}}\} \\ \{\theta_d\} \end{Bmatrix} \approx \{0\} \quad (4.122)$$

where:

$$\{\varepsilon\} = \begin{Bmatrix} \{\varepsilon_1\} \\ \vdots \\ \{\varepsilon_k\} \\ \vdots \\ \{\varepsilon_{l-l}\} \end{Bmatrix}, \quad \{\varepsilon_k\} = \begin{Bmatrix} \varepsilon_k(\omega_1) \\ \varepsilon_k(\omega_2) \\ \vdots \\ \varepsilon_k(\omega_{N_f}) \end{Bmatrix} \quad (4.123)$$

$$\{\theta_{N_k}\} = \begin{Bmatrix} N_{k,0} \\ N_{k,1} \\ \dots \\ N_{k,n} \end{Bmatrix} \quad (4.124)$$

$$\{\theta_d\} = \begin{Bmatrix} d_0 \\ d_1 \\ \dots \\ d_n \end{Bmatrix} \quad (4.125)$$

$$[\Gamma_k] = \begin{Bmatrix} \{\Gamma_k(\omega_1)\}^T \\ \{\Gamma_k(\omega_2)\}^T \\ \dots \\ \{\Gamma_k(\omega_{N_f})\}^T \end{Bmatrix} = \begin{bmatrix} z^0(\omega_1) & z^1(\omega_1) & \dots & z^n(\omega_1) \\ z^0(\omega_2) & z^1(\omega_2) & \dots & z^n(\omega_2) \\ \dots & \dots & \dots & \dots \\ z^0(\omega_{N_f}) & z^1(\omega_{N_f}) & \dots & z^n(\omega_{N_f}) \end{bmatrix} \quad (4.126)$$

$$[\Upsilon_k] = \begin{Bmatrix} \{\Upsilon_k(\omega_1)\}^T \\ \{\Upsilon_k(\omega_2)\}^T \\ \vdots \\ \{\Upsilon_k(\omega_{N_f})\}^T \end{Bmatrix} = \begin{bmatrix} -\hat{G}_k(\omega_1)z^0(\omega_1) & \dots & -\hat{G}_k(\omega_1)z^n(\omega_1) \\ \vdots & \dots & \vdots \\ -\hat{G}_k(\omega_{N_f})z^0(\omega_{N_f}) & \dots & -\hat{G}_k(\omega_{N_f})z^n(\omega_{N_f}) \end{bmatrix} \quad (4.127)$$

The unknown parameters can be estimated directly from the Jacobian matrix  $[J]$ . However, a significant reduction in computational time and memory requirements can be achieved through the formulation of normal equations. The normal matrix:

$$[J]^H[J] = \begin{bmatrix} [\Gamma_1]^H[\Gamma_1] & [0] & \dots & [\Gamma_1]^H[\Upsilon_1] \\ [0] & [\Gamma_2]^H[\Gamma_2] & \dots & [\Gamma_2]^H[\Upsilon_2] \\ \vdots & \vdots & \ddots & \vdots \\ [\Upsilon_1]^H[\Gamma_1] & [\Upsilon_2]^H[\Gamma_2] & \dots & \sum_{k=1}^{l,l} [\Upsilon_k]^H[\Upsilon_k] \end{bmatrix} \quad (4.128)$$

consists of submatrices that are structured (Toeplitz) matrices (a *Toeplitz matrix* is a matrix in which each diagonal is characterized by the repetition of the same element). If the following submatrices are defined:

$$[R_k] = [\Gamma_k]^H[\Gamma_k] \quad (4.129)$$

$$[S_k] = [\Gamma_k]^H[\Upsilon_k] \quad (4.130)$$

$$[T_k] = [\Upsilon_k]^H[\Upsilon_k] \quad (4.131)$$

the normal equations can be written in this form:

$$[J]^H[J]\{\theta\} = \begin{bmatrix} [R_1] & [0] & \dots & [S_1] \\ [0] & [R_2] & \dots & [S_2] \\ \vdots & \vdots & \ddots & \vdots \\ [S_1]^H & [S_2]^H & \dots & \sum_{k=1}^{l,l} [T_k] \end{bmatrix} \begin{Bmatrix} \{\theta_{N_1}\} \\ \{\theta_{N_2}\} \\ \vdots \\ \{\theta_{N_l}\} \\ \{\theta_d\} \end{Bmatrix} \approx \{0\}. \quad (4.132)$$

Since the parameter constraint has been applied to the denominator coefficients  $\{\theta_d\}$  only, the numerator coefficients can be eliminated from the normal equations by substitution of:

$$\{\theta_{N_k}\} = -[R_k]^{-1}[S_k]\{\theta_d\} \quad (4.133)$$

into (4.132); this results in the so-called *reduced normal equations*:

$$\left[ \sum_{k=1}^{l-l} \left( [T_k] - [S_k]^H [R_k]^{-1} [S_k] \right) \right] \{ \theta_d \} = [M] \{ \theta_d \} \approx \{ 0 \}. \quad (4.134)$$

A significant reduction in the dimension of the problem has been obtained, since the square  $(n+1) \times (n+1)$  matrix  $[M]$  is much smaller than the normal matrix  $[J]^H [J]$ . Under the constraint given by (4.119), the least squares solution is obtained as:

$$\{ \theta_d \} = \begin{bmatrix} -[M_{(1:n, 1:n)}]^{-1} [M_{(1:n, n+1)}] \\ 1 \end{bmatrix} \quad (4.135)$$

where  $[M_{(1:n, 1:n)}]$  is the submatrix made by the first  $n$  rows and  $n$  columns of  $[M]$ , while  $[M_{(1:n, n+1)}]$  is the submatrix made by the first  $n$  rows and the last column of  $[M]$ . Once the coefficients  $\{ \theta_d \}$  have been computed, the poles in the  $z$ -domain are obtained as the roots of the denominator polynomial. Taking into account the relation between the poles in the  $z$ -domain and those in the Laplace domain:

$$z_r = e^{\lambda_r \Delta t} \Rightarrow \lambda_r = \frac{\ln(z_r)}{\Delta t} \quad (4.136)$$

the natural frequency, the damped modal frequency, and the damping ratio of the  $r$ -th mode can be computed as follows:

$$f_r = \frac{|\lambda_r|}{2\pi} \quad (4.137)$$

$$f_{d,r} = \frac{\text{Im}(\lambda_r)}{2\pi} \quad (4.138)$$

$$\xi_r = -\frac{\text{Re}(\lambda_r)}{|\lambda_r|}. \quad (4.139)$$

Once the denominator coefficients  $\{ \theta_d \}$  are known, the numerator coefficients can be obtained from (4.133); the mode shapes can be theoretically estimated from those polynomial coefficients. However, the numerator coefficients are actually computed only if the LSCF estimator is used to determine the starting value for the MLE. In practical applications mode shapes are, instead, obtained from the modal model as a solution of a second least squares problem. The reason under this two-stage approach is that the common-denominator model does not force rank-one residue matrices on the measurements, while it is known from modal analysis theory that the residue matrix is of rank one.

Once the structural modes are identified, the corresponding poles are passed to the LSFD estimator for the identification of the residue matrices and, as a consequence, the mode shapes associated to the selected physical poles. Since the poles are known from the previous stage, the modal model is linear in the parameters (the residues), which can be obtained as a solution of a linear least squares problem.

The residue matrices can be computed by minimizing the following functions:

$$g_k(R_{k,j}) = \sum_{f=1}^{N_f} \left( \hat{G}_k(\omega_f) - \sum_{j=1}^{N_m} \left( \frac{R_{k,j}}{i\omega_f - \lambda_j} + \frac{R_{k,j}^*}{i\omega_f - \lambda_j^*} \right) \right)^2 \quad (4.140)$$

with respect to  $R_{k,j}$  ( $k = 1, \dots, l \cdot l$ ) in a least squares sense. In general, two additional terms, the upper (UR) and lower (LR) residual terms, can be considered (Peeters and Van der Auweraer 2005). They are introduced to approximate the effects of out-of-band modes (below the lower bound and above the upper bound of the analyzed frequency range). However, their use is restricted to continuous-time fraction polynomial models (Verboven 2002).

The minimization of  $g_k$  implies that its partial derivatives with respect to the unknown residual coefficients  $R_{k,j}$  are zero:

$$\frac{\partial g_k}{\partial R_{k,j}} = 2 \sum_{f=1}^{N_f} \left( \hat{G}_k(\omega_f) - \sum_{j=1}^{N_m} \left( \frac{R_{k,j}}{i\omega_f - \lambda_j} + \frac{R_{k,j}^*}{i\omega_f - \lambda_j^*} \right) \right) \left( -\frac{1}{i\omega_f - \lambda_j} \right) = 0 \quad (4.141)$$

with  $k = 1, \dots, l \cdot l$  and  $j = 1, \dots, 2N_m$ , where  $N_m$  denotes the number of identified physical modes. The obtained equations can be expressed in matrix form as follows:

$$[\Lambda_\Lambda] \{R_k\} = \{G_\Lambda\} \quad (4.142)$$

where:

$$[\Lambda_\Lambda] = \sum_{f=1}^{N_f} \{\Lambda(\omega_f)\} \{\Lambda(\omega_f)\}^T \quad (4.143)$$

$$\{G_\Lambda\} = \sum_{f=1}^{N_f} \hat{G}_k(\omega_f) \{\Lambda(\omega_f)\} \quad (4.144)$$

$$\{\Lambda(\omega_f)\} = \begin{Bmatrix} \frac{1}{i\omega_f - \lambda_1} \\ \vdots \\ \frac{1}{i\omega_f - \lambda_j} \\ \vdots \\ \frac{1}{i\omega_f - \lambda_{N_m}} \\ \frac{1}{i\omega_f - \lambda_1^*} \\ \vdots \\ \frac{1}{i\omega_f - \lambda_j^*} \\ \vdots \\ \frac{1}{i\omega_f - \lambda_{N_m}^*} \end{Bmatrix} \quad (4.145)$$

$$\{R_k\} = \begin{Bmatrix} R_{k,1} \\ \vdots \\ R_{k,j} \\ \vdots \\ R_{k,N_m} \\ R_{k,1}^* \\ \vdots \\ R_{k,j}^* \\ \vdots \\ R_{k,N_m}^* \end{Bmatrix}. \quad (4.146)$$

As a consequence, since the physical poles are known, the residues can be determined as follows:

$$\{R_k\} = [\Lambda_\Lambda]^{-1} \{G_\Lambda\}, \quad k = 1, \dots, l \cdot l. \quad (4.147)$$

The  $l \times l$  residue matrix  $[R_j]$  corresponding to the  $j$ -th mode is easily constructed by taking the elements of the  $\{R_k\}$  vectors corresponding to  $\lambda_j$  for  $k = 1, \dots, l \cdot l$ . Once the  $[R_j]$  matrices ( $j = 1, \dots, N_m$ ) have been determined, the mode shapes  $\{\phi_j\}$  are obtained by SVD of the residue matrices:

$$[R_j] = [U][\Sigma][V]^T \quad (4.148)$$

In fact, assuming that  $\text{rank}([R_j]) = 1$ , the first column of  $[U]$  is an estimate of the mode shape  $\{\phi_j\}$  of the  $j$ -th mode.

#### 4.4.3.2 The Poly-Reference Least Squares Complex Frequency Method

The poly-reference version of the LSCF estimator is based on an RMFD. The development of the p-LSCF method was motivated by some inherent limitations of the LSCF estimator based on the common-denominator model. In particular, they concern the identification of closely spaced modes and the reduction of the quality of fit when the polynomial model is converted to a modal model (Peeters and Van der Auweraer 2005). In fact, closely spaced poles might erroneously show up as a single pole in LSCF, in particular at low values of the model order. The reduction of the quality of fit is instead related to the fact that the common-denominator model does not force the residue matrices to be rank-one. This extra freedom leads to an “artificial” enhancement of the quality of fit, since the model does not fulfill the modal analysis theory in terms of rank of the residue matrices.

The p-LSCF method is herein illustrated with reference to one-sided spectra, but positive power spectra are analyzed in the same way by replacing  $[G_{YY}(\omega_f)]$  with  $[S_{YY}^+(\omega_f)]$  (or their respective estimates), and  $\langle \hat{G}_o(\omega_f) \rangle$  with  $\langle \hat{S}_o^+(\omega_f) \rangle$ . A comparison between the results obtained from the application of the method to positive power spectra and one-sided spectra is reported in Sect. 4.9. In p-LSCF the PSD matrix at each frequency line  $f$  ( $f = 1, \dots, N_f$ ) is modeled by the RMFD (Cauberghe 2004):

$$[G_{YY}(\omega_f)] = [B(\Omega_f, [\theta])] [A(\Omega_f, [\theta])]^{-1} \quad (4.149)$$

where  $[\theta]$  is the matrix of the unknown parameters. For every output channel  $o$  ( $o = 1, \dots, l$ ),  $\langle B_o(\Omega_f, [\theta]) \rangle$  is the numerator matrix polynomial:

$$\langle B_o(\Omega_f, [\theta]) \rangle = \sum_{j=1}^n \langle B_{o,j} \rangle \Omega_f^j \quad (4.150)$$

and  $[A(\Omega_f, [\theta])]$  is the denominator matrix polynomial:

$$[A(\Omega_f, [\theta])] = \sum_{j=0}^n [A_j] \Omega_f^j. \quad (4.151)$$

The  $1 \times l$  matrices  $\langle B_{o,j} \rangle$  and the  $l \times l$  matrices  $[A_j]$  are the unknown parameters to be estimated. The polynomial coefficients can be collected in a single complex-valued matrix as follows:

$$[\theta] = \begin{bmatrix} [\beta_1] \\ \vdots \\ [\beta_l] \\ [\alpha] \end{bmatrix} \quad (4.152)$$

where:

$$[\beta_o] = \begin{bmatrix} \langle B_{o,0} \rangle \\ \vdots \\ \langle B_{o,n} \rangle \end{bmatrix} \quad (4.153)$$

$$[\alpha] = \begin{bmatrix} [A_0] \\ \dots \\ [A_n] \end{bmatrix} \quad (4.154)$$

and  $n$  is the model order. As in the case of the common-denominator model, the polynomial basis function can be expressed in the continuous Laplace domain ( $\Omega_f = i\omega_f$ ) or in the discrete  $z$ -domain. As already mentioned in the illustration of the LSCF method, the  $z$ -domain formulation (4.116) is recommended to improve numerical conditioning.

The following error formulation:

$$\langle E_o(\omega_f, [\theta]) \rangle = \langle B_o(\Omega_f, [\theta]) \rangle - \langle \hat{G}_o(\omega_f) \rangle [A(\Omega_f, [\theta])] \quad (4.155)$$

is introduced to obtain a linear least squares problem. This is defined by minimizing the following cost function:

$$\ell([\theta]) = \sum_{o=1}^l \sum_{f=1}^{N_f} \text{tr} \left( \langle E_o(\omega_f, [\theta]) \rangle^H \langle E_o(\omega_f, [\theta]) \rangle \right). \quad (4.156)$$

The minimization of the cost function given by (4.156) corresponds to the solution of the following matrix equation:

$$[J][\theta] = [0] \quad (4.157)$$

where the Jacobian matrix  $[J]$  is given by:

$$[J] = \begin{bmatrix} [\Gamma_1] & [0] & \dots & [0] & [Y_1] \\ [0] & [\Gamma_2] & \dots & [0] & [Y_2] \\ \vdots & \vdots & \ddots & \vdots & \vdots \\ [0] & [0] & \dots & [\Gamma_l] & [Y_l] \end{bmatrix} \quad (4.158)$$

with:

$$[\Gamma_o] = \begin{bmatrix} \langle 1 & z_1 & \dots & z_1^n \rangle \\ \langle 1 & z_2 & \dots & z_2^n \rangle \\ \dots \\ \langle 1 & z_{N_f} & \dots & z_{N_f}^n \rangle \end{bmatrix} \quad (4.159)$$

$$[\Upsilon_o] = \begin{bmatrix} -\langle 1 \ z_1 \ \dots \ z_1^n \rangle \otimes \langle \hat{G}_o(\omega_1) \rangle \\ -\langle 1 \ z_2 \ \dots \ z_2^n \rangle \otimes \langle \hat{G}_o(\omega_2) \rangle \\ -\langle 1 \ z_{N_f} \ \dots \ z_{N_f}^n \rangle \otimes \langle \hat{G}_o(\omega_{N_f}) \rangle \end{bmatrix}. \quad (4.160)$$

$\otimes$  denotes the Kronecker product. The matrices  $[\Gamma_o]$  and  $[\Upsilon_o]$  have dimensions  $N_f \times (n+1)$  and  $N_f \times (n+1) \cdot l$ , respectively.

It is possible to show that (Cauberghe 2004):

$$\ell([\theta]) = \sum_{o=1}^l \sum_{f=1}^{N_f} \text{tr} \left( \langle E_o(\omega_f, [\theta]) \rangle^H \langle E_o(\omega_f, [\theta]) \rangle \right) = \text{tr} \left( [\theta]^H [J]^H [J] [\theta] \right) \quad (4.161)$$

and, on the analogy with the LSCF estimator, it is possible to reduce the dimensions of the matrix equation through the definition of the normal equations:

$$[J]^H [J] [\theta] = \begin{bmatrix} [R_1] & \dots & [0] & [S_1] \\ \vdots & \ddots & \vdots & \vdots \\ [0] & \dots & [R_l] & [S_l] \\ [S_1]^H & \dots & [S_l]^H & \sum_{o=1}^l [T_o] \end{bmatrix} \begin{bmatrix} [\beta_1] \\ \vdots \\ [\beta_l] \\ [\alpha] \end{bmatrix} = [0] \quad (4.162)$$

with:

$$[R_o] = [\Gamma_o]^H [\Gamma_o] \quad (4.163)$$

$$[S_o] = [\Gamma_o]^H [\Upsilon_o] \quad (4.164)$$

$$[T_o] = [\Upsilon_o]^H [\Upsilon_o]. \quad (4.165)$$

$[R_o]$ ,  $[S_o]$  and  $[T_o]$  have dimensions  $(n+1) \times (n+1)$ ,  $(n+1) \times (n+1) \cdot l$  and  $(n+1) \cdot l \times (n+1) \cdot l$ , respectively. The  $[\beta_o]$  coefficients can be eliminated from (4.162) taking into account that:

$$[\beta_o] = -[R_o]^{-1} [S_o] [\alpha]. \quad (4.166)$$

As a final result, the reduced normal equations are obtained:

$$\sum_{o=1}^l ([T_o] - [S_o]^H [R_o]^{-1} [S_o]) [\alpha] = [M] [\alpha] = [0] \quad (4.167)$$

where  $[M]$  is a square  $(n+1) \cdot l \times (n+1) \cdot l$  matrix.

On the analogy with the LSCF method, the parameter redundancy is removed by setting one of the denominator coefficients equal to the identity matrix. If the

highest order coefficient is constrained to be equal to the identity matrix of dimensions  $l \times l$ :

$$[A_n] = [I_l] \quad (4.168)$$

the least squares solution is given by:

$$[\alpha] = \begin{bmatrix} -[M_{(1:nl, 1:nl)}]^{-1} [M_{(1:nl, (nl+1):(n+1)l)}] \\ [I_l] \end{bmatrix}. \quad (4.169)$$

The matrix  $[M_{(1:nl, 1:nl)}]$  is the submatrix of  $[M]$  made by its first  $n \cdot l$  rows and columns; the matrix  $[M_{(1:nl, (nl+1):(n+1)l)}]$  is the submatrix of  $[M]$  made by its first  $n \cdot l$  rows and its last  $n \cdot l$  columns. Once the  $[\alpha]$  coefficients have been determined, the  $[\beta_o]$  coefficients can be computed by substitution of  $[\alpha]$  into (4.166).

The roots of the denominator polynomial  $[A(\Omega_f, [\theta])]$  are the eigenvalues of the following companion matrix:

$$[A] = \begin{bmatrix} -[A_0]^{-1}[A_n] & -[A_0]^{-1}[A_{n-1}] & \dots & -[A_0]^{-1}[A_2] & -[A_0]^{-1}[A_1] \\ [I] & [0] & \dots & [0] & [0] \\ \vdots & \vdots & \ddots & \vdots & \vdots \\ [0] & [0] & \dots & [I] & [0] \end{bmatrix} \quad (4.170)$$

The companion matrix is a square  $n \cdot l \times n \cdot l$  matrix and it models a dynamic system with  $(n \cdot l)/2$  modes. Its eigenvalues  $\zeta_r$  have to be converted into the poles expressed in the Laplace domain as per (4.136). Equations (4.137)–(4.139) provide the natural frequency, the damped modal frequency, and the damping ratio of the  $r$ -th mode, respectively.

Once the poles associated to physical modes have been selected, the LSFD estimator is used to get the corresponding mode shapes. The residue matrices can be computed by minimizing the scatter between the experimentally estimated PSD matrix and the modeled one (De Troyer et al. 2009a):

$$[g([R_j])] = \sum_{f=1}^{N_f} \left( [\hat{G}_{YY}(\omega_f)] - \sum_{j=1}^{N_m} \left( \frac{[R_j]}{i\omega_f - \lambda_j} + \frac{[R_j]^*}{i\omega_f - \lambda_j^*} \right) \right)^2. \quad (4.171)$$

The minimization of  $[g([R_j])]$  implies that its partial derivatives with respect to the unknown residues are zero. The obtained equations can be expressed in matrix form as follows:

$$[\Lambda_\Lambda][R] = [G_\Lambda] \quad (4.172)$$

where:

$$[\Lambda_\Lambda] = \sum_{f=1}^{N_f} \left( \begin{bmatrix} \frac{[I_f]}{(i\omega_f - \lambda_1)(i\omega_f - \lambda_1)} & \frac{[I_f]}{(i\omega_f - \lambda_1^*)(i\omega_f - \lambda_1)} & \cdots & \frac{[I_f]}{(i\omega_f - \lambda_{N_m})(i\omega_f - \lambda_1)} & \frac{[I_f]}{(i\omega_f - \lambda_{N_m}^*)(i\omega_f - \lambda_1)} \\ \vdots & \vdots & \ddots & \vdots & \vdots \\ \frac{[I_f]}{(i\omega_f - \lambda_1)(i\omega_f - \lambda_{N_m}^*)} & \frac{[I_f]}{(i\omega_f - \lambda_1^*)(i\omega_f - \lambda_{N_m}^*)} & \cdots & \frac{[I_f]}{(i\omega_f - \lambda_{N_m})(i\omega_f - \lambda_{N_m}^*)} & \frac{[I_f]}{(i\omega_f - \lambda_{N_m}^*)(i\omega_f - \lambda_{N_m}^*)} \end{bmatrix} \right) \quad (4.173)$$

$$[R] = \begin{bmatrix} [R_1] \\ [R_1]^* \\ \vdots \\ [R_{N_m}] \\ [R_{N_m}]^* \end{bmatrix} \quad (4.174)$$

$$[G_\Lambda] = \sum_{f=1}^{N_f} \left( \begin{bmatrix} \frac{[\hat{G}_{YY}(\omega_f)]}{(i\omega_f - \lambda_1)} \\ \frac{[\hat{G}_{YY}(\omega_f)]}{(i\omega_f - \lambda_1^*)} \\ \vdots \\ \frac{[\hat{G}_{YY}(\omega_f)]}{(i\omega_f - \lambda_{N_m})} \\ \frac{[\hat{G}_{YY}(\omega_f)]}{(i\omega_f - \lambda_{N_m}^*)} \end{bmatrix} \right). \quad (4.175)$$

The mode shape of the  $j$ -th mode can be finally estimated once the corresponding  $l \times l$  residue matrix  $[R]$  has been computed from (4.172) (Sect. 4.4.3.1).

## 4.5 Time Domain Methods

### 4.5.1 NExT-Type Procedures

A number of modal identification techniques, initially developed in the deterministic framework of traditional input–output modal analysis, have been extended to output-only modal analysis recognizing that the correlation functions of random responses can be expressed as a sum of decaying sinusoids (4.15) holding the information about the modal parameters. As a consequence, correlation functions of the random responses of the structure under natural excitation have replaced the experimental estimates of IRFs in the application of such modal analysis techniques in the output-only case. For this reason, this class of OMA methods is traditionally referred to as NExT.

The three main methods in this class are:

- The LSCE method,
- The ITD method,
- The ERA method (Juang and Pappa 1985, Juang 1994).

In this section, only the LSCE and the ITD methods are presented. In fact, ERA relies on the system realization theory and it is not herein illustrated because of its similarities with subspace methods. The reader can refer to Sect. 4.5.3.1 for output-only modal identification based on correlation functions and state-space model.

NExT-type methods were very popular at the beginning of OMA. LSCE and ITD have also experienced some enhancements over the years, for instance in order to deal with closely spaced modes (Olsen and Brincker 2013) and spurious harmonics (Mohanty 2005). Due to their historical relevance, they are herein illustrated in their most relevant aspects. However, these methods have been progressively abandoned in favor of the more robust subspace methods. The interested reader can refer to the literature for more details (Allemang and Brown 1998, Vold et al. 1982, Ibrahim and Mikulcik 1977, Mohanty 2005, Olsen and Brincker 2013).

The LSCE method is the time-domain counterpart of the LSCF estimator. Thus, it is basically a curve-fitting algorithm aimed at the extraction of the modal parameters from correlation functions. From (4.15) the generic correlation function can be rewritten as follows in discrete-time and for  $k \geq 0$ :

$$R_{ij}(k\Delta t) = \sum_{r=1}^{N_m} \left( C_{ij,r} e^{\lambda_r k \Delta t} + C_{ij,r}^* e^{\lambda_r^* k \Delta t} \right) \quad (4.176)$$

where  $C_{ij,r}$  is the element  $ij$  of the residue matrix associated to the  $r$ -th mode (the notation for the residues has been slightly modified in this section with respect to the rest of the chapter for the sake of clarity). Taking into account that the poles appear in complex conjugate pairs and considering all the poles in sequence, (4.176) can be rewritten as:

$$R_{ij}(k\Delta t) = \sum_{r=1}^n \bar{C}_{ij,r} e^{\bar{\lambda}_r k \Delta t} \quad (4.177)$$

where  $\bar{C}_{ij,r}$  is the constant associated to the  $r$ -th pole  $\bar{\lambda}_r$  and the sum is extended to  $n = 2N_m$  terms. Moreover, since the poles are in complex conjugate pairs, there exists a polynomial of order  $n$  of which  $z_r = e^{\bar{\lambda}_r \Delta t}$  ( $r = 1, \dots, n$ ) are roots:

$$\beta_0 z_r^0 + \beta_1 z_r^1 + \dots + \beta_{n-1} z_r^{n-1} + z_r^n = 0 \quad (4.178)$$

Equation (4.178) is also known as *Prony's equation*. The highest order coefficient  $\beta_n$  is set equal to 1.

In order to determine the polynomial coefficients  $\beta_k$ , assuming that a number of samples  $q$  larger than  $2n$  are available, (4.177) can be written for the full dataset as follows:

$$\begin{aligned} R_{ij}(k\Delta t)|_{k=0} &= \bar{C}_{ij,1} + \bar{C}_{ij,2} + \dots + \bar{C}_{ij,n} \\ R_{ij}(k\Delta t)|_{k=1} &= \bar{C}_{ij,1}z_1^1 + \bar{C}_{ij,2}z_2^1 + \dots + \bar{C}_{ij,n}z_n^1 \\ &\vdots \\ R_{ij}(k\Delta t)|_{k=q} &= \bar{C}_{ij,1}z_1^q + \bar{C}_{ij,2}z_2^q + \dots + \bar{C}_{ij,n}z_n^q \end{aligned} \quad (4.179)$$

Multiplying the correlation at time instant  $k$  by the coefficient  $\beta_k$ :

$$\begin{aligned} \beta_0 R_{ij}(k\Delta t)|_{k=0} &= \beta_0 \bar{C}_{ij,1} + \beta_0 \bar{C}_{ij,2} + \dots + \beta_0 \bar{C}_{ij,n} \\ \beta_1 R_{ij}(k\Delta t)|_{k=1} &= \beta_1 \bar{C}_{ij,1}z_1^1 + \beta_1 \bar{C}_{ij,2}z_2^1 + \dots + \beta_1 \bar{C}_{ij,n}z_n^1 \\ &\vdots \\ \beta_q R_{ij}(k\Delta t)|_{k=q} &= \beta_q \bar{C}_{ij,1}z_1^q + \beta_q \bar{C}_{ij,2}z_2^q + \dots + \beta_q \bar{C}_{ij,n}z_n^q \end{aligned} \quad (4.180)$$

and summing up these values, the following equation is obtained:

$$\sum_{k=0}^q \beta_k R_{ij}(k\Delta t) = \sum_{r=1}^n \left( \bar{C}_{ij,r} \sum_{k=0}^q \beta_k z_r^k \right). \quad (4.181)$$

It is convenient to set  $q = n = 2N_m$ . Taking into account (4.178) and that  $\beta_n = 1$ , the following equation is obtained:

$$\sum_{k=0}^{n-1} \beta_k R_{ij}(k\Delta t) = -R_{ij}(n\Delta t). \quad (4.182)$$

Repeating this process for different sets of samples (for instance, the next set can be made by the samples  $k = 1, \dots, n+1$ ), a set of  $n$  equations in the  $n$  unknown  $\beta_k$  coefficients is obtained:

$$[R_{ij}] \{\beta\} = -\left\{ \tilde{R}_{ij} \right\} \quad (4.183)$$

where:

$$[R_{ij}] = \begin{bmatrix} R_{ij}(k\Delta t)|_{k=0} & R_{ij}(k\Delta t)|_{k=1} & \dots & R_{ij}(k\Delta t)|_{k=n-1} \\ R_{ij}(k\Delta t)|_{k=1} & \ddots & \ddots & R_{ij}(k\Delta t)|_{k=n} \\ \vdots & \ddots & \ddots & \vdots \\ R_{ij}(k\Delta t)|_{k=n-1} & R_{ij}(k\Delta t)|_{k=n} & \dots & R_{ij}(k\Delta t)|_{k=2n-2} \end{bmatrix} \quad (4.184)$$

is the Hankel matrix (a *Hankel matrix* is a matrix that is constant along its anti-diagonals) holding the values of the correlation function,

$$\{\beta\} = \begin{Bmatrix} \beta_0 \\ \beta_1 \\ \vdots \\ \beta_{n-1} \end{Bmatrix} \quad (4.185)$$

is the vector of the unknown  $\beta_k$  coefficients, and:

$$\left\{ \tilde{R}_{ij} \right\} = \begin{Bmatrix} R_{ij}(n\Delta t) \\ R_{ij}((n+1)\Delta t) \\ \vdots \\ R_{ij}((2n-1)\Delta t) \end{Bmatrix}. \quad (4.186)$$

$[R_{ij}]$ ,  $\{\beta\}$  and  $\left\{ \tilde{R}_{ij} \right\}$  have dimensions  $n \times n$ ,  $n \times 1$  and  $n \times 1$ , respectively. The unknown coefficients are given by:

$$\{\beta\} = -[R_{ij}]^{-1} \left\{ \tilde{R}_{ij} \right\}. \quad (4.187)$$

They are also the coefficients of the Prony's equation (4.178), whose roots  $z_r = e^{\lambda_r \Delta t}$  provide the natural frequency, the damped modal frequency, and the damping ratio ((4.137)–(4.139)) after the conversion into the continuous Laplace domain (4.136).

The above procedure uses a single correlation function. However, since the  $\{\beta\}$  coefficients are global quantities related to the modal parameters, the correlation between any couple of response time series has to provide the same polynomial coefficients (Mohanty 2005). As a consequence, repeating the above procedure for any couple of response time histories leads to the following overdetermined set of equations:

$$\begin{bmatrix} [R_{11}] \\ [R_{12}] \\ \vdots \\ [R_{ll}] \end{bmatrix} \{\beta\} = - \begin{Bmatrix} \left\{ \tilde{R}_{11} \right\} \\ \left\{ \tilde{R}_{12} \right\} \\ \vdots \\ \left\{ \tilde{R}_{ll} \right\} \end{Bmatrix} \quad (4.188)$$

which can be solved in a least squares sense by pseudo-inverse techniques (Chap. 2).

Once the physical poles have been identified, they can be inserted into (4.177) to determine the constants  $\bar{C}_{ij,r}$  from the following set of equations:

$$\begin{bmatrix} z_1^0 & z_2^0 & \dots & z_n^0 \\ z_1^1 & z_2^1 & \dots & z_n^1 \\ \vdots & \vdots & \dots & \vdots \\ z_1^{n-1} & z_2^{n-1} & \dots & z_n^{n-1} \end{bmatrix} \begin{Bmatrix} \bar{C}_{ij,1} \\ \bar{C}_{ij,2} \\ \vdots \\ \bar{C}_{ij,n} \end{Bmatrix} = \begin{Bmatrix} R_{ij}(k\Delta t)|_{k=0} \\ R_{ij}(k\Delta t)|_{k=1} \\ \vdots \\ R_{ij}(k\Delta t)|_{k=n-1} \end{Bmatrix}. \quad (4.189)$$

Thus, the LSCE method is a two-stage method for OMA, where mode shapes are estimated only in a second stage of analysis following the identification of the physical poles. On the analogy with the LSCF estimator, there exists also a poly-reference version of the algorithm, which considers all the measurement channels as references, computes the matrix coefficients  $[\beta_1], \dots, [\beta_n]$  by least squares, and extracts the poles as a solution of a generalized eigenvalue problem. The interested reader can refer to the literature (Heylen et al. 1998, Vold et al. 1982) for more details.

The ITD method is a global modal identification procedure based on processing of all the measured correlation functions at once. Taking into account that the generic correlation function can be decomposed as a sum of complex exponentials and arranging the measured correlation functions in a block Hankel matrix:

$$[H_{0|n-1}] = \begin{bmatrix} [\hat{R}_{yy}(0)] & [\hat{R}_{yy}(1)] & \dots & [\hat{R}_{yy}(n-1)] \\ [\hat{R}_{yy}(1)] & \ddots & \ddots & [\hat{R}_{yy}(n)] \\ \vdots & \ddots & \ddots & \vdots \\ [\hat{R}_{yy}(n-1)] & [\hat{R}_{yy}(n)] & \dots & [\hat{R}_{yy}(2n-2)] \end{bmatrix} \quad (4.190)$$

the following decomposition can be considered:

$$[H_{0|n-1}] = [\Psi][\Lambda] \quad (4.191)$$

where  $[\Psi]$  contains the information about the mode shapes, and  $[\Lambda]$  holds the information about the poles.

A second set of equations is obtained by a time-shift  $\Delta t$  of all the entries in the  $[H_{0|n-1}]$  matrix. The second block Hankel matrix is related to  $[\Lambda]$  as follows:

$$[H_{1|n}] = [\bar{\Psi}][\Lambda]. \quad (4.192)$$

The relation between the matrices  $[\Psi]$  and  $[\bar{\Psi}]$  is expressed by the *system matrix*  $[A]$  as:

$$[A][\Psi] = [\bar{\Psi}]. \quad (4.193)$$

Substitution of (4.193) into (4.192) yields:

$$[H_{1|n}] = [A][\Psi][\Lambda] \quad (4.194)$$

and, taking into account (4.191), the following equation is obtained:

$$[A][H_{0|n-1}] = [H_{1|n}] \quad (4.195)$$

which provides the system matrix  $[A]$  from the measured data contained in the matrices  $[H_{0|n-1}]$  and  $[H_{1|n}]$ :

$$[A] = [H_{1|n}][H_{0|n-1}]^+. \quad (4.196)$$

The modal parameters are finally estimated by the eigenvalue decomposition of the system matrix. Its eigenvalues are the system poles in the  $z$ -domain. The natural frequency, the damped modal frequency, and the damping ratio are obtained from (4.137), (4.138), and (4.139), respectively, once the eigenvalues have been converted into the continuous Laplace domain (4.136). The eigenvector of the system matrix corresponding to a certain eigenvalue is finally used to obtain an estimate of the mode shape for that mode. It is worth pointing out that the ITD method is a low order method. As a consequence, the number of measurement channels  $l$  limits the number of identifiable poles (and therefore modes).

### 4.5.2 AR- and ARMA-Type Methods

The use of ARMA models for output-only modal identification has been attempted in the past, but they never became popular in this field due to a number of drawbacks (convergence problems, excessive computational time). Nevertheless, for their historical relevance, the main concepts under the application of AR and ARMA models to OMA are herein briefly summarized.

In Sect. 4.2.3 it has been mentioned that an ARMAV( $p, p$ ) model:

$$\{y_k\} + [\alpha_1]\{y_{k-1}\} + \dots + [\alpha_p]\{y_{k-p}\} = \{e_k\} + [\gamma_1]\{e_{k-1}\} + \dots + [\gamma_p]\{e_{k-p}\}. \quad (4.197)$$

is an equivalent representation of a dynamic system with  $n = p \cdot l$  poles in the presence of noise (namely, low signal-to-noise ratio; in the absence of noise, a covariance equivalent model is an ARMAV( $p, p - 1$ ) model; Andersen 1997, Andersen et al. 1996). It can be used to describe a linear, time-invariant structure vibrating under unknown input forces, which can be modeled as a zero-mean Gaussian white noise process. Since the order  $p$  of the ARMA model is related to the order  $n$  of the system, the poles of the structure are included in the model only if  $pl \geq n$ . Thus, a preliminary estimate of the model order and, therefore, of the number of modes in the investigated frequency range is needed. In the case  $pl > n$ , additional nonphysical poles appear next to the physical poles and have to be distinguished (Peeters 2000). The poles are extracted from the AR matrix coefficients, while the MA parameters ensure that the statistical description of the data is optimal.

PEM is a data-driven method for the estimation of an ARMA model. A detailed description of the method and an extensive discussion about its application for the identification of the modal parameters of civil engineering structures can be found elsewhere (Ljung 1999, Andersen 1997). The ARMAV model is fitted to the measured time signals by minimizing the *output prediction error*:

$$\{e(t_k, [\alpha_i], [\gamma_i])\} = \{y(t_k)\} - \{\hat{y}(t_k | [Y^{k-1}], [\alpha_i], [\gamma_i])\} \quad (4.198)$$

given by the difference between the measured time signals and the predicted output of the ARMAV model, which depends on the model parameters  $[\alpha_i]$  and  $[\gamma_i]$  and on

the past data  $[Y^{k-1}]$  up to  $t_{k-1}$ . Unfortunately, the minimization of the prediction error requires a nonlinear optimization procedure. Since in practical applications a large number of parameters have to be estimated, this may lead to problems with computational time and convergence. An optimization scheme able to reduce the set of parameters to be estimated has been therefore proposed (Brincker and Andersen 1999a). It basically carries out a translation of the ARMA model in state-space form, defines a reduced set of parameters in the modal domain and then goes back to the ARMA domain to perform the optimization according to PEM. However, in the presence of good quality data this optimization scheme does not significantly improve the modal parameter estimates with respect to the stochastic state-space model (Brincker and Andersen 1999b). Thus, even if ARMA models can be potentially applied in the field of OMA, limited applications of PEM can be found in the literature as a result of the highly nonlinear parameter estimation problem. Since the nonlinearity is associated to the MA terms and the information about the poles is in the AR coefficients, alternative strategies have been developed where the MA coefficients are not estimated.

A first strategy completely omits the MA part, and the application of PEM to the following AR model:

$$\{y_k\} + [\alpha_1]\{y_{k-1}\} + \dots + [\alpha_p]\{y_{k-p}\} = \{e_k\} \quad (4.199)$$

leads to a linear least squares problem, which can be easily solved. However, as mentioned in Sect. 4.2.3, an AR model of order  $p$  is not an equivalent representation of a vibrating structure with  $p$  poles, and the use of the AR model is justified only if its order goes to infinity. Unfortunately, this causes the introduction of a lot of spurious poles that have to be distinguished from the physical ones.

The IV method represents an attempt to overcome the limitations associated to the estimation of the AR terms only. This result is obtained through the formulation of a linear problem for the identification of the AR parameters, but an ARMA model is retained as underlying structure. The method starts recognizing that the ARMAV( $p, p$ ) model of (4.197) is adequate for modal parameter estimation if, when fitting the measured data  $\{y_k\}$ , it extracts the maximum of information from them and returns residuals  $\{e_k\}$  uncorrelated with the past data:

$$E[\{e_k\}\{y_{k-i}\}^T] = [0] \quad \forall i > 0. \quad (4.200)$$

Since  $\{e_{k-p}\}$  is the oldest term in the MA part of (4.197), post-multiplying both sides of (4.197) by  $\{y_{k-p-i}\}^T$  ( $i > 0$ ) and taking the expectation yield the following equation:

$$\begin{aligned} E[\{y_k\}\{y_{k-p-i}\}^T] + [\alpha_1]E[\{y_{k-1}\}\{y_{k-p-i}\}^T] \\ + \dots + [\alpha_p]E[\{y_{k-p}\}\{y_{k-p-i}\}^T] = [0] \quad \forall i > 0 \end{aligned} \quad (4.201)$$

where the equality follows from (4.200). The assumption of stationarity implies:

$$E[\{y_k\}\{y_{k-i}\}^T] = E[\{y_{k+i}\}\{y_k\}^T] = [R_i] \quad \forall i > 0 \quad (4.202)$$

so that the fundamental equation of the IV method can be expressed in terms of the output correlations  $[R_i]$  as:

$$[R_{p+i}] + [\alpha_1][R_{p+i-1}] + \dots + [\alpha_p][R_i] = [0] \quad \forall i > 0. \quad (4.203)$$

Equation (4.203) can be rewritten as:

$$[\alpha_1][R_{p+i-1}] + \dots + [\alpha_p][R_i] = -[R_{p+i}] \quad \forall i > 0 \quad (4.204)$$

pointing out the similarity with the (poly-reference) LSCE method. This is a further example of how different algorithms can be traced back to a common mathematical background, as discussed in Sect. 4.2.5.

If the output correlations are replaced by their estimates  $[\hat{R}_i]$  and (4.204) is written for all the available time lags  $i$ , the AR parameters  $[\alpha_1], \dots, [\alpha_p]$  can be obtained as a least squares solution of an overdetermined set of equations. Natural frequencies, damping ratios, and mode shapes are finally computed from the results of the eigenvalue decomposition of the companion matrix of the AR coefficients, as described in Sect. 4.2.3.

### 4.5.3 Stochastic Subspace Identification

#### 4.5.3.1 Covariance-Driven Stochastic Subspace Identification

The Covariance-driven Stochastic Subspace Identification (Cov-SSI) method addresses the stochastic realization problem, that is to say the problem of identifying a stochastic state-space model from output-only data. The origin of the method can be traced back to the system realization theory for deterministic (input–output) cases and the concept of minimal realization developed by Ho and Kalman (Ho and Kalman 1966).

An extensive discussion about the system realization theory can be found elsewhere (Juang 1994). Here just some basic concepts are reported. As mentioned in Sect. 4.2.3, a minimal realization is the state-space model with the smallest state-space dimension among all the realizable systems characterized by the same input–output relation. To construct such a model, it is important to check whether or not all the system states of interest can be excited (controlled) and/or observed (Juang 1994).

By definition, a state of a system is controllable if it can be reached from any initial state of the system in a finite time interval by some control actions; in a similar way, a state of the system is observable if the knowledge of input and output over a finite time interval completely determines the state.

It is possible to show (Juang 1994) that, if a certain condition about the rank of two specific matrices is fulfilled, the system is observable and controllable.

Such matrices are the so-called observability and controllability matrices and they will be introduced next in this section.

A system of order  $n$  is observable/controllable if and only if the observability/controllability matrix is of rank  $n$ . The solution of the realization problem consists in determining a minimal realization of order  $n$  of the state-space matrices from the measured data. As clarified next in this chapter, in practical applications the actual order of the system is unknown and its determination is always affected by a certain degree of uncertainty due to noise effects. As a consequence, even if a minimal realization of a system of order  $n$  can be theoretically identified from the measured data and used to extract the modal parameters, the determination of the correct order of the system is usually a very complex task. A conservative approach to identify all the structural modes in the data consists in the overestimation of the order of the system. This causes the appearance of additional nonphysical poles next to the physical poles, and specific criteria and tools to sort the structural poles are needed (refer to Sect. 4.9 for more details).

The Cov-SSI method can be classified as a time-domain, parametric, covariance-driven procedure for OMA. It starts from the computation of output correlations:

$$[\hat{R}_i] = \frac{1}{N-i} [Y_{(1:N-i)}] [Y_{(i:N)}]^T \quad (4.205)$$

where  $[Y_{(1:N-i)}]$  is obtained from the  $l \times N$  data matrix  $[Y]$  by removal of the last  $i$  samples, while  $[Y_{(i:N)}]$  is obtained from  $[Y]$  by removal of the first  $i$  samples;  $[\hat{R}_i]$  denotes the unbiased estimate of the correlation matrix at time lag  $i$  based on a finite number of data. The estimated correlations at different time lags are gathered into the following block Toeplitz matrix:

$$[T_{1|i}] = \begin{bmatrix} [\hat{R}_i] & [\hat{R}_{i-1}] & \dots & [\hat{R}_1] \\ [\hat{R}_{i+1}] & [\hat{R}_i] & \ddots & [\hat{R}_2] \\ \vdots & \vdots & \ddots & \vdots \\ [\hat{R}_{2i-1}] & [\hat{R}_{2i-2}] & \dots & [\hat{R}_i] \end{bmatrix} \quad (4.206)$$

Each correlation matrix has dimensions  $l \times l$ ; thus, the block Toeplitz matrix has dimensions  $li \times li$ . For the identification of a system of order  $n$ , the number of block rows  $i$  has to fulfill the following condition:

$$li \geq n \quad (4.207)$$

In practical applications the actual order of the system is obviously unknown. However, an estimate of the number of modes in the frequency range of interest can be obtained in a number of ways, for instance as the number of peaks in the trace of the PSD matrix or in the singular value plots given by the SVD of the PSD matrix (see Sects. 4.4.1 and 4.4.2).

Assuming that the order of the system has been estimated and taking into account that the number of outputs  $l$  is a constant of the identification problem, a value for  $i$  larger than or equal to  $n/l$  can be set. The adopted value for  $i$  is basically a user's choice and it is definitely based on a physically insight of the problem.

Applying the factorization property given by (4.51) to the block Toeplitz matrix:

$$[T_{1|i}] = \begin{bmatrix} [C] \\ [C][A] \\ \vdots \\ [C][A]^{i-1} \end{bmatrix} \begin{bmatrix} [A]^{i-1}[G] & \cdots & [A][G] & [G] \end{bmatrix} = [O_i][\Gamma_i] \quad (4.208)$$

the *observability matrix*:

$$[O_i] = \begin{bmatrix} [C] \\ [C][A] \\ \vdots \\ [C][A]^{i-1} \end{bmatrix} \quad (4.209)$$

and the *reversed controllability matrix*:

$$[\Gamma_i] = \begin{bmatrix} [A]^{i-1}[G] & \cdots & [A][G] & [G] \end{bmatrix} \quad (4.210)$$

are obtained.  $[O_i]$  and  $[\Gamma_i]$  have dimensions  $li \times n$  and  $n \times li$ , respectively. If the condition of (4.207) is fulfilled and the system is observable and controllable, the rank of the block Toeplitz matrix equals  $n$ . In fact, it is a product of a matrix with  $n$  columns— $[O_i]$ —and a matrix with  $n$  rows— $[\Gamma_i]$ .

The SVD of the block Toeplitz matrix:

$$[T_{1|i}] = [U][\Sigma][V]^T = [[U_1] \quad [U_2]] \begin{bmatrix} [\Sigma_1] & [0] \\ [0] & [0] \end{bmatrix} \begin{bmatrix} [V_1]^T \\ [V_2]^T \end{bmatrix} \quad (4.211)$$

provides its rank, which equals the number of nonzero singular values (Sect. 2.3.1). If the zero singular values and the corresponding singular vectors are omitted, (4.208) and (4.211) yield:

$$[T_{1|i}] = [O_i][\Gamma_i] = [U_1][\Sigma_1][V_1]^T \quad (4.212)$$

where the matrices  $[U_1]$  and  $[V_1]^T$  have dimensions  $li \times n$  and  $n \times li$ , respectively, and the  $n \times n$  diagonal matrix  $[\Sigma_1]$  holds the positive singular values arranged in descending order. The matrices  $[O_i]$  and  $[\Gamma_i]$  can be computed by splitting the SVD in two parts as follows:

$$[O_i] = [U_1][\Sigma_1]^{1/2}[T] \quad (4.213)$$

$$[\Gamma_i] = [T]^{-1}[\Sigma_1]^{1/2}[V_1]^T \quad (4.214)$$

where  $[T]$  is a nonsingular matrix which plays the role of a similarity transformation applied to the state-space model (Sect. 4.2.2); since the choice of  $[T]$  simply determines one of the infinite equivalent realizations of the state-space model, it can be set equal to the identity matrix:

$$[T] = [I] \quad (4.215)$$

Taking into account the definitions of observability matrix (4.209) and controllability matrix (4.210), the output influence matrix  $[C]$  and the next state-output covariance matrix  $[G]$  can be easily obtained as the first  $l$  rows of  $[O_i]$  and the last  $l$  columns of  $[\Gamma_i]$ , respectively.

The state matrix  $[A]$  can be computed according to different approaches. The first is based on the decomposition property of the one-lag shifted Toeplitz matrix:

$$[T_{2|i+1}] = \begin{bmatrix} [\hat{R}_{i+1}] & [\hat{R}_i] & \dots & [\hat{R}_2] \\ [\hat{R}_{i+2}] & [\hat{R}_{i+1}] & \ddots & [\hat{R}_3] \\ \vdots & \vdots & \ddots & \vdots \\ [\hat{R}_{2i}] & [\hat{R}_{2i-1}] & \dots & [\hat{R}_{i+1}] \end{bmatrix} = [O_i][A][\Gamma_i] \quad (4.216)$$

Introducing (4.213) and (4.214) into (4.216), taking into account (4.215) and solving for  $[A]$ , the following expression for the state matrix is obtained:

$$[A] = [O_i]^+ [T_{2|i+1}] [\Gamma_i]^+ = [\Sigma_1]^{-1/2} [U_1]^T [T_{2|i+1}] [V_1] [\Sigma_1]^{-1/2}. \quad (4.217)$$

This variant of the Cov-SSI algorithm is basically equivalent to the NExT-ERA method.

As an alternative, the state matrix  $[A]$  can be estimated by exploiting the shift structure of the observability matrix. Pre- and post-multiplying the matrix  $[T_{1|i}]$  by the invertible weighting matrices  $[W_1]$  and  $[W_2]$ , computing the SVD of the weighted Toeplitz matrix and omitting the zero singular values yield the following expression for the observability matrix (Yi and Yun 2004):

$$[O_i] = [W_1]^{-1} [U_1] [\Sigma_1]^{1/2} \quad (4.218)$$

and the state matrix is given by:

$$[A] = [O_i^\uparrow]^+ [O_i^\downarrow] \quad (4.219)$$

where  $[O_i^\uparrow]$  and  $[O_i^\downarrow]$  are obtained from the matrix  $[O_i]$  by removal of the last and the first  $l$  rows, respectively.

Depending on the adopted weighting matrices, the following two variants of Cov-SSI can be considered: Balanced Realization (BR) and Canonical Variate Analysis (CVA).

The BR Cov-SSI uses identity matrices as weights:

$$[W_1] = [W_2] = [I] \quad (4.220)$$

In a balanced realization the controllability grammian— $[\Gamma_i]$   $[\Gamma_i]^T$ —and the observability grammian— $[O_i]^T [O_i]$ —are equal and diagonal (taking into account that  $[U_1]$  and  $[V_1]$  are orthonormal matrices):

$$\begin{aligned} [O_i]^T [O_i] &= [\Sigma_1]^{1/2} [U_1]^T [U_1] [\Sigma_1]^{1/2} = [\Sigma_1] = [\Sigma_1]^{1/2} [V_1]^T [V_1] [\Sigma_1]^{1/2} \\ &= [\Gamma_i] [\Gamma_i]^T \end{aligned} \quad (4.221)$$

and this implies that the realized system is controllable as well as observable (Juang 1994). A balanced realization means that the signal transfers from the input to the state and from the state to the output are similar and balanced (Juang 1994).

In the CVA variant of Cov-SSI the Cholesky factorization (Chap. 2) of the following matrices:

$$\left[ T_{0|i-1}^+ \right] = \begin{bmatrix} [\hat{R}_0] & [\hat{R}_1]^T & \dots & [\hat{R}_{i-1}]^T \\ [\hat{R}_1] & [\hat{R}_0] & \ddots & [\hat{R}_{i-2}]^T \\ \vdots & \ddots & \ddots & \vdots \\ [\hat{R}_{i-1}] & [\hat{R}_{i-2}] & \dots & [\hat{R}_0] \end{bmatrix} = [L^+] [L^+]^T \quad (4.222)$$

$$\left[ T_{0|i-1}^- \right] = \begin{bmatrix} [\hat{R}_0] & [\hat{R}_1] & \dots & [\hat{R}_{i-1}] \\ [\hat{R}_1]^T & [\hat{R}_0] & \ddots & [\hat{R}_{i-2}] \\ \vdots & \ddots & \ddots & \vdots \\ [\hat{R}_{i-1}]^T & [\hat{R}_{i-2}]^T & \dots & [\hat{R}_0] \end{bmatrix} = [L^-] [L^-]^T \quad (4.223)$$

provides the weights (Hermans and Van Der Auweraer 1999):

$$[W_1] = [L^+]^{-1}, \quad [W_2] = [L^-]^{-1} \quad (4.224)$$

In CVA Cov-SSI the singular values of the weighted Toeplitz matrix  $[W_1][T_{1|i}][W_2]$  can be interpreted as the cosines of the angles, the so-called canonical angles, between two subspaces (Hermans and Van Der Auweraer 1999). The CVA weighting can be physically interpreted as a weighting that leads to balanced modes in terms of energy. As a consequence, it enhances the possibility to identify those modes that are less excited in operational conditions.

Once the matrices  $[A]$  and  $[C]$  have been estimated, the modal parameters can be extracted. The (complex conjugate pairs of) poles in discrete-time are in the diagonal matrix  $[M]$  obtained from the eigenvalue decomposition of the state matrix (4.77). After the conversion of the poles corresponding to physical modes from discrete-time to continuous-time (4.136), the natural frequencies, the damped modal frequencies,

and the damping ratios can be estimated according to (4.137), (4.138), and (4.139), respectively. The mode shape of the  $r$ -th mode is estimated from the eigenvector  $\{\psi_r\}$  of  $[A]$  corresponding to the selected pole  $z_r$  according to (4.79).

About the transformation from continuous-time to discrete-time and vice versa, it is worth noting that the restriction of the Laplace variable to purely imaginary values corresponds to a restriction to values on the unit circle in discrete-time (Verboven 2002). Moreover, the transformation from discrete-time to continuous-time is not unique (Juang 1994). Any couple of frequencies differing by a multiple of  $2\pi/\Delta t$  is indistinguishable when observed at the sampled times. As a consequence,  $\Delta t$  must be sufficiently short or a filter has to be adopted in order to prevent that the frequencies beyond the Nyquist frequency are mirrored at a lower frequency in the realization (aliasing).

The output correlations and the identified state-space matrices are estimates of the corresponding true quantities based on a finite number of samples (for this reason, they should be denoted with  $\hat{\cdot}$ :  $[\hat{A}]$ ,  $[\hat{C}]$ ,  $[\hat{G}] \dots$ ). The presence of noise can determine some errors in the estimates. Typical noise sources are:

- modeling inaccuracies (for example, the system that generated the data cannot be exactly modeled as a stochastic state-space model),
- measurement noise (due to sensors and measurement hardware),
- computational noise (due to the finite precision),
- the finite number of data points (leading to estimates of the output correlations).

As a consequence of noise and the finite number of samples, also the factorization property of the Toeplitz matrix (4.208) does not hold exactly. If, in principle, the order  $n$  of the system can be obtained as the number of nonzero singular values of the block Toeplitz matrix  $[T_{1|i}]$ , the presence of noise makes all singular values different from zero. Thus, the rank of  $[T_{1|i}]$  is “approximately”  $n$ , and the truncation of the smallest singular values leads to a certain error in the estimation of the state-space matrices. A rule of thumbs for the evaluation of the order  $n$  of the system suggests to look at the gap between two subsequent singular values. The model order is identified in correspondence of the maximum value of this gap. However, this criterion cannot be slavishly applied, since clear gaps are often absent in the case of real records of the structural response. As a consequence, as previously mentioned, a usual practice consists in overestimating the model order to a certain extent and in sorting out the physical poles by appropriate tools and criteria. They are illustrated in Sect. 4.9.

An assessment of the quality of the identified state-space model is possible through the comparison of the synthesized spectra with those directly estimated from the measurements. A closed-form expression for the spectrum of a discrete-time stochastic state-space model is as follows (Peeters 2000):

$$[S_{YY}(z)] = [C](z[I] - [A])^{-1}[G] + [R_0] + [G]^T \left( z^{-1}[I] - [A]^T \right)^{-1} [C]^T \Big|_{z=e^{i\omega\Delta t}} . \quad (4.225)$$

### 4.5.3.2 Data-Driven Stochastic Subspace Identification

DD-SSI algorithms have become very popular in the system identification community in recent years. Such techniques are very attractive for a number of reasons. They rely on an elegant mathematical framework and robust linear algebra tools to identify the state-space matrices from the raw data. As a result, in comparison with other data driven algorithms such as PEM, nonlinear optimization problems are avoided. In fact, the identification problem is linearized, that is to say it is reduced to a simple least squares problem. Moreover, the use of well-known tools from numerical linear algebra, such as SVD and LQ decomposition, leads to a numerically very efficient implementation.

An innovative aspect of DD-SSI consists in the identification of the state sequence before the estimation of the state-space matrices. A number of theorems show that the states can directly be calculated from measurements through some geometric operations (Van Overschee and De Moor 1996). These are the so-called orthogonal and oblique projections. In the context of OMA, only orthogonal projections are used. The concept of projection can be easily understood if the rows of a matrix are interpreted as a basis for a vector space. Therefore, it is possible to define the operator  $[\Pi_E]$ , which projects the row space of a matrix on the row space of a reference matrix  $[E]$ :

$$[\Pi_E] = [E]^T \left( [E][E]^T \right)^+ [E]. \quad (4.226)$$

The orthogonal projection of the row space of a generic matrix  $[F]$  on the row space of  $[E]$  is:

$$[F]/[E] = [F][\Pi_E] = [F][E]^T \left( [E][E]^T \right)^+ [E]. \quad (4.227)$$

More details about projections and their role in DD-SSI can be found elsewhere (Van Overschee and De Moor 1996). The key idea, which has to be remarked here, is that the Kalman filter state estimates can be obtained as a linear combination of the rows of certain block Hankel matrices holding the raw data. As discussed in Sect. 4.2.2, the role of the Kalman filter is to produce an optimal prediction of the state vector  $\{s_k\}$  from observations of the outputs up to the time instant  $k - 1$ . The Kalman filter state sequence  $[\hat{s}_i]$ , therefore, collects all the state estimates obtained from the output data at the previous  $i$  time instants. Each column of  $[\hat{s}_i]$  represents one of these state estimates. For instance, assuming that the filter is started at  $j$  different time instants, so that the Kalman filter state sequence is:

$$[\hat{s}_i] = [\{\hat{s}_i\} \quad \{\hat{s}_{i+1}\} \quad \dots \quad \{\hat{s}_{i+j-1}\}] \quad (4.228)$$

the  $(q + 1)$ -th column  $\{\hat{s}_{i+q}\}$  of  $[\hat{s}_i]$  represents the state estimate based on the following  $i$  output values:  $\{y_q\}, \dots, \{y_{i+q-1}\}$  (Van Overschee and De Moor 1996).

The DD-SSI algorithm starts from a block Hankel matrix constructed directly from the measurement data. It has  $2i$  block rows and  $j$  columns (for the statistical proof of the method, the following assumption is made:  $j \rightarrow \infty$ ; thus,  $j$  must be rather large). The value of  $i$  is determined in agreement with (4.207). The block Hankel matrix has dimension  $2i \times j$  and it can be partitioned into the two sub-matrices of the past— $[Y_p]$ —and future— $[Y_f]$ —outputs as follows:

$$\left[ H_{0|2i-1} \right] = \frac{1}{\sqrt{j}} \begin{bmatrix} \{y_0\} & \{y_1\} & \dots & \{y_{j-1}\} \\ \{y_1\} & \ddots & \ddots & \{y_j\} \\ \vdots & \ddots & \ddots & \vdots \\ \{y_{i-1}\} & \{y_i\} & \dots & \{y_{i+j-2}\} \\ \{y_i\} & \{y_{i+1}\} & \dots & \{y_{i+j-1}\} \\ \{y_{i+1}\} & \ddots & \ddots & \{y_{i+j}\} \\ \vdots & \ddots & \ddots & \vdots \\ \{y_{2i-1}\} & \{y_{2i}\} & \dots & \{y_{2i+j-2}\} \end{bmatrix} = \begin{bmatrix} [Y_{0|i-1}] \\ [Y_{i|2i-1}] \end{bmatrix} = \begin{bmatrix} [Y_p] \\ [Y_f] \end{bmatrix}. \quad (4.229)$$

The sub-matrices  $[Y_p]$  and  $[Y_f]$  have dimensions  $li \times j$ . The output data are scaled by the factor  $1/\sqrt{j}$  to be consistent with the definition of correlation (Chap. 2). In fact, it is possible to show that, under the assumptions of ergodicity and  $j \rightarrow \infty$ , the block Toeplitz matrix of correlations can be computed from the block Hankel matrices of output data as follows:

$$[T_{1|i}] \approx \frac{1}{j} [Y_f] [Y_p]^T. \quad (4.230)$$

In practical applications the number of columns  $j$  is taken equal to  $N - 2i + 1$ , so all given data samples are used. Adding one block row to the past outputs and omitting the first block row of the future outputs yield another division of the Hankel matrix:

$$\left[ H_{0|2i-1} \right] = \begin{bmatrix} [Y_{0|i-1}] \\ [Y_{i|i}] \\ [Y_{i+1|2i-1}] \end{bmatrix} = \begin{bmatrix} [Y_{0|i}] \\ [Y_{i+1|2i-1}] \end{bmatrix} = \begin{bmatrix} [Y_p^+] \\ [Y_f^-] \end{bmatrix}. \quad (4.231)$$

where  $[Y_p^+]$  is the block Hankel matrix of the past outputs with one block row added, and  $[Y_f^-]$  is the block Hankel matrix of the future outputs with the first block row removed. The identification of the Kalman filter state sequences and, as a consequence, of the state-space matrices is based on the orthogonal projection of the row space of the future outputs on the row space of the past outputs. The definition of this projection:

$$[P_i] = [Y_f] / [Y_p] = [Y_f] [Y_p]^T \left( [Y_p] [Y_p]^T \right)^+ [Y_p]. \quad (4.232)$$

points out that correlations and projections are closely related. In fact,  $[Y_f][Y_p]^T$  and  $[Y_p][Y_p]^T$  are basically block Toeplitz matrices holding output correlations. The orthogonal projection of (4.232) can be efficiently computed by the LQ factorization of the block Hankel matrix of the outputs  $[H_{0|2i-1}]$ :

$$[H_{0|2i-1}] = [L][Q] \quad (4.233)$$

so that the Hankel matrix is expressed as the product of a lower triangular matrix  $[L]$ :

$$[L] = \begin{array}{ccc} & li & l & l(i-1) \\ & \leftrightarrow & \leftrightarrow & \leftrightarrow \\ \begin{matrix} li \\ l \\ l(i-1) \end{matrix} & \uparrow & \left[ \begin{matrix} [L_{11}] & [0] & [0] \\ [L_{21}] & [L_{22}] & [0] \\ [L_{31}] & [L_{32}] & [L_{33}] \end{matrix} \right] & \end{array} \quad (4.234)$$

and an orthonormal matrix  $[Q]$ :

$$[Q] = \begin{array}{c} j \\ \leftrightarrow \\ \left[ \begin{matrix} [Q_1]^T \\ [Q_2]^T \\ [Q_3]^T \end{matrix} \right] \end{array}. \quad (4.235)$$

The projections  $[P_i]$  and  $[P_{i-1}]$  of the row space of the future outputs on the row space of the past outputs can be obtained from the LQ decomposition as follows:

$$[P_i] = [Y_f] / [Y_p] = \left[ \begin{matrix} [L_{21}] \\ [L_{31}] \end{matrix} \right] [Q_1]^T \quad (4.236)$$

$$[P_{i-1}] = [Y_f^-] / [Y_p^+] = \left[ \begin{matrix} [L_{31}] & [L_{32}] \end{matrix} \right] \left[ \begin{matrix} [Q_1]^T \\ [Q_2]^T \end{matrix} \right]. \quad (4.237)$$

Moreover, the output sequence  $[Y_{i|i}]$  (4.231) can be expressed as:

$$[Y_{i|i}] = \left[ \begin{matrix} [L_{21}] & [L_{22}] \end{matrix} \right] \left[ \begin{matrix} [Q_1]^T \\ [Q_2]^T \end{matrix} \right]. \quad (4.238)$$

Assuming that the system is controllable and observable (so that all its modes are excited by the process noise and can be identified) and the condition expressed by (4.207) is satisfied, the main theorem of DD-SSI states that the projection matrix  $[P_i]$  can be factorized into the product of the observability matrix  $[O_i]$  and the Kalman filter state sequence  $[\hat{S}_i]$  (Van Overschee and De Moor 1996):

$$[P_i] = [O_i] [\hat{S}_i] = \begin{bmatrix} [C] \\ [C][A] \\ \vdots \\ [C][A]^{i-1} \end{bmatrix} \begin{bmatrix} \{\hat{s}_i\} & \{\hat{s}_{i+1}\} & \cdots & \{\hat{s}_{i+j-1}\} \end{bmatrix}. \quad (4.239)$$

The factorization of the projection matrix into the product of a matrix with  $n$  columns— $[O_i]$ —and a matrix with  $n$  rows— $[\hat{S}_i]$ —implies that  $\text{rank}([P_i]) = n$ . Estimating the rank of  $[P_i]$  by SVD and retaining only the nonzero singular values:

$$[P_i] = [[U_1][U_2]] \begin{bmatrix} [\Sigma_1] & [0] \\ [0] & [0] \end{bmatrix} \begin{bmatrix} [V_1]^T \\ [V_2]^T \end{bmatrix} = [U_1][\Sigma_1][V_1]^T \quad (4.240)$$

the observability matrix and the Kalman filter state sequence can be computed as:

$$[O_i] = [U_1][\Sigma_1]^{1/2}[T] \quad (4.241)$$

$$[\hat{S}_i] = [O_i]^+ [P_i] \quad (4.242)$$

where the similarity transformation  $[T]$  can be set equal to the identity matrix.

A factorization similar to (4.239) can be applied to  $[P_{i-1}]$ , obtaining:

$$[P_{i-1}] = [O_i^\uparrow] [\hat{S}_{i+1}]. \quad (4.243)$$

Since  $[O_i^\uparrow]$  can be directly obtained from  $[O_i]$  by deleting the last 1 rows, while  $[P_{i-1}]$  has been obtained from the LQ decomposition of the Hankel matrix of the output data, the Kalman state sequence  $[\hat{S}_{i+1}]$  can be computed from (4.243) as follows:

$$[\hat{S}_{i+1}] = [O_i^\uparrow]^+ [P_{i-1}]. \quad (4.244)$$

The state-space matrices can be now derived according to three different approaches. They differ for the capability to ensure the positive realness of covariance sequences. In simple words, the first two algorithms that are going to be illustrated provide asymptotically unbiased estimates (if  $i \rightarrow \infty$ ) of the noise covariances  $[Q^{ww}]$ ,  $[R^{vv}]$  and  $[S^{vw}]$  (4.43) and of the matrices  $[G]$  and  $[R_0]$  but they do not ensure the positive realness. This can lead to a synthesized spectrum matrix which is not positive definite at all frequencies. Since for a positive definite matrix all its diagonal entries are positive (Golub and Van Loan 1996), the synthesized spectrum might become negative at certain frequencies and this is obviously meaningless. Moreover, when the covariance sequence is not positive real, an innovation model cannot be computed. When the positive realness of covariance sequences is of interest, the third algorithm has to be adopted which, however, is not asymptotically unbiased. More details about positive realness and its implications can be found elsewhere (Van Overschee and De Moor 1996). It is

worth pointing out that also the Cov-SSI algorithm does not ensure the positive realness of the identified covariance sequence and, as a consequence, a forward innovation model cannot be obtained.

The first algorithm uses the state sequences to estimate the state-space matrices. In fact, once the Kalman filter state sequences  $[\hat{S}_i]$  and  $[\hat{S}_{i+1}]$  have been estimated according to (4.242) and (4.244), the matrices  $[A]$  and  $[C]$  can be computed from the following overdetermined set of linear equations, obtained by stacking the state-space models for the time instants from  $i$  up to  $i+j-1$ :

$$\begin{bmatrix} [\hat{S}_{i+1}] \\ [Y_{i|i}] \end{bmatrix} = \begin{bmatrix} [A] \\ [C] \end{bmatrix} [\hat{S}_i] + \begin{bmatrix} [\rho_w] \\ [\rho_v] \end{bmatrix}. \quad (4.245)$$

Since the Kalman filter residuals  $[\rho_w]$  and  $[\rho_v]$  are uncorrelated with the states  $[\hat{S}_i]$  (see also (4.46) and (4.47)), this set of equations can be solved in a least squares sense. In fact, taking into account that the least squares residuals are orthogonal and, therefore, uncorrelated with the regressors  $[\hat{S}_i]$ , asymptotically unbiased least squares estimate of  $[A]$  and  $[C]$  are obtained as follows (Van Overschee and De Moor 1993):

$$\begin{bmatrix} [A] \\ [C] \end{bmatrix} = \begin{bmatrix} [\hat{S}_{i+1}] \\ [Y_{i|i}] \end{bmatrix} [\hat{S}_i]^+. \quad (4.246)$$

It is worth noting that all quantities on the right side of (4.246) can be expressed in terms of the LQ factors. As a result of their orthonormality, the Q factors cancel out in (4.246). A significant data reduction can be therefore obtained by expressing the right-side quantities in (4.246) in terms of the L factors only.

The matrix  $[G]$  corresponds to the last  $l$  columns of the reversed controllability matrix, which can be computed as follows:

$$[\Gamma_i] = [O_i]^+ [T_{1|i}] \quad (4.247)$$

while  $[R_0]$  is obtained as the autocorrelation of  $[Y_{i|i}]$ :

$$[R_0] = \frac{1}{j} [Y_{i|i}] [Y_{i|i}]^T. \quad (4.248)$$

The second algorithm takes advantage of the shift structure of the observability matrix, which implies that:

$$[O_i^\dagger] [A] = [O_i^\dagger]. \quad (4.249)$$

As a consequence, the discrete state matrix can be computed in agreement with (4.219). Alternatively, it can be computed by SVD of the concatenated matrix  $\begin{bmatrix} [O_i^\downarrow] & -[O_i^\uparrow] \end{bmatrix}$ :

$$\begin{bmatrix} [O_i^\downarrow] & -[O_i^\uparrow] \end{bmatrix} = [U][\Sigma][V]^T \quad (4.250)$$

where the matrix  $[V]$  can be then partitioned as follows:

$$[V] = \begin{array}{c|cc} & \overset{n}{\leftrightarrow} & \overset{n}{\leftrightarrow} \\ \begin{matrix} n \\ \uparrow \\ n \end{matrix} & \begin{bmatrix} [V_{11}] & [V_{12}] \\ [V_{21}] & [V_{22}] \end{bmatrix} & \begin{matrix} n \\ \uparrow \\ n \end{matrix} \end{array}. \quad (4.251)$$

The matrix  $[A]$  is finally given by (Van Overschee and De Moor 1996):

$$[A] = [V_{22}][V_{12}]^{-1} \quad (4.252)$$

while the matrix  $[C]$  is directly obtained from the first  $l$  rows of  $[O_i]$ . The matrices  $[G]$  and  $[R_0]$  are obtained as for the previous algorithm.

The third algorithm computes  $[A]$  and  $[C]$  by least squares in agreement with (4.245) and (4.246), as in the case of the first algorithm, but the matrices  $[G]$  and  $[R_0]$  are obtained by a different procedure. The covariances of the process and measurement noise are obtained from the residuals as follows:

$$\frac{1}{j} \begin{bmatrix} [\rho_w] \\ [\rho_v] \end{bmatrix} \begin{bmatrix} [\rho_w]^T & [\rho_v]^T \end{bmatrix} = \begin{bmatrix} [Q_i^{ww}] & [S_i^{wv}] \\ [S_i^{wv}]^T & [R_i^{vv}] \end{bmatrix} \quad (4.253)$$

where the subscript  $_i$  indicates that they are nonsteady state covariance matrices of the nonsteady state Kalman filter equation (see also Sect. 4.2.2):

$$[\Sigma_{i+1}] = [A][\Sigma_i][A]^T + [Q_i^{ww}] \quad (4.254)$$

$$[G] = [A][\Sigma_i][C]^T + [S_i^{wv}] \quad (4.255)$$

$$[R_0] = [C][\Sigma_i][C]^T + [R_i^{vv}]. \quad (4.256)$$

Since the Kalman filter converges when  $i \rightarrow \infty$ , the following approximations:

$$[Q^{ww}] = [Q_i^{ww}], \quad [S^{wv}] = [S_i^{wv}], \quad [R^{vv}] = [R_i^{vv}]. \quad (4.257)$$

introduce a bias when  $i$  is finite but they ensure the positive realness of the covariance sequences, since the matrix  $\begin{bmatrix} [Q^{ww}] & [S^{ww}] \\ [S^{wv}]^T & [R^{vv}] \end{bmatrix}$  is positive definite by construction and this condition leads to positive real covariance sequences (Van Overschee and De Moor 1996). Once the matrices  $[A]$ ,  $[C]$ ,  $[Q^{ww}]$ ,  $[R^{vv}]$  and  $[S^{wv}]$  are known, the matrices  $[G]$  and  $[R_0]$  can be obtained from (4.48)–(4.50). Solution of the Riccati equation (4.67), together with (4.68), provides the Kalman gain and, as a consequence, the forward innovation model is finally obtained (Van Overschee and De Moor 1996).

Once the matrices  $[A]$  and  $[C]$  have been determined according to one of the previous algorithms, the modal parameters can be obtained from the eigenvalue decomposition of the discrete state matrix as discussed in the previous sections ((4.77), (4.79), (4.137), (4.138), (4.139)), after the conversion of the eigenvalues from discrete-time to continuous time (4.136). Since the modal parameter estimates depend on  $[A]$  and  $[C]$  only, they are not affected by eventual bias on the matrices  $[G]$  and  $[R_0]$ . When also these last two matrices are estimated, the spectrum matrix of the model can be computed from (4.225).

It is worth emphasizing that, due to the finite data length, the identified state-space model (and therefore the matrices  $[A]$ ,  $[C]$ ,  $[G]$  and  $[R_0]$ ) is just an estimate of the model that actually generated the data. On the analogy with the Cov-SSI method, the order of the system can be obtained as the rank of the projection matrix  $[P_i]$ , if the number of block rows has been set in agreement with (4.207). Since none of the singular values will exactly be zero as a result of the presence of noise, the rank of the matrix can only approximately be determined in correspondence with the maximum gap between two subsequent singular values (which are arranged in descending order). In practical applications, since a clear drop in the sequence of singular values is often not detectable, the order of the system is overestimated to a certain extent and specific tools and criteria are used to identify the physical poles (Sect. 4.9).

On the analogy with Cov-SSI, some variants of DD-SSI can be obtained through the application of some weights to the projection matrix  $[P_i]$  before SVD. The weighting matrices  $[W_1]$  and  $[W_2]$  have dimensions  $i_i \times i_i$  and  $j \times j$ , respectively, and they obey some conditions. In particular,  $[W_1]$  is of full rank, while  $[W_2]$  is such that:

$$\text{rank}([Y_p]) = \text{rank}([Y_p][W_2]). \quad (4.258)$$

The variants of DD-SSI and the corresponding weighting matrices are:

- the Unweighted Principal Component (UPC) algorithm:  $[W_1] = [I_{ii}]$ ,  $[W_2] = [I_j]$  (where the subscripts  $i$  and  $j$  denote the dimensions of the identity matrix);
- the principal component (PC) algorithm:  $[W_1] = [I_{ii}]$ ,  $[W_2] = [Y_p]^T \left( \frac{1}{j} [Y_p] [Y_p]^T \right)^{-1/2} [Y_p]$ ;
- the CVA:  $[W_1] = \left( \frac{1}{j} [Y_f] [Y_f]^T \right)^{-1/2}$ ,  $[W_2] = [I_j]$ .

In the case of CVA DD-SSI the singular values of the weighted projection matrix  $[W_1][P_i][W_2]$  can be interpreted as the cosines of the principal angles between two subspaces, the row space of the past outputs  $[Y_p]$  and the row space of the future outputs  $[Y_f]$  (see Van Overschee and De Moor 1996 for more details).

As a practical rule, UPC DD-SSI should be used in the presence of modes of equal strength and data with a good signal-to-noise ratio; on the contrary, CVA DD-SSI should be used in the presence of noisy data and modes characterized by widely different strength. The PC variant can be considered as a compromise between UPC and CVA. Even if these three variants have different physical explanations, a number of computer simulations and practical applications have demonstrated that there are no significant accuracy differences among them in the field of OMA (Zhang et al. 2005b).

The above discussion about Cov-SSI and DD-SSI is certainly not comprehensive, but, in agreement with the objectives of this book, it provides the main concepts for the implementation of those algorithms for OMA applications. The interested reader can refer to the literature for an extensive discussion about SSI methods and their variants (Van Overschee and De Moor 1996, Aoki 1987, Katayama 2005).

#### 4.5.4 Second Order Blind Identification

A recent proposal in the field of OMA concerns the possibility to apply Blind Source Separation (BSS) techniques to identify the modal parameters. BSS techniques allow extracting a set of signals, the so-called *sources*, from observations of their mixtures (Ans et al. 1985), based on fairly general assumptions about the sources and the mixing process.

Applicability of BSS techniques to OMA has been investigated in detail in a number of fairly recent publications (Kerschen et al. 2007, Poncelet et al. 2007, Zhou and Chelidze 2007, McNeill and Zimmerman 2008). In the context of OMA, such techniques can be referred to as time domain methods. Moreover, since no model is fitted to the data, they can be classified as nonparametric methods. Even if BSS techniques, which are based only on a statistical treatment of data, show promising performance in the field of output-only modal identification of civil structures, some limitations can be identified. They are related to the basic assumptions under different BSS techniques and their compatibility with the dynamic systems of interest. These aspects are discussed in this section right after a short introduction about BSS.

BSS techniques can be classified as linear or nonlinear, depending on the type of combination of the sources. Moreover, linear simultaneous (static) mixing and convolutive mixing can be considered. Even if the convolution product of the IRF of a structure with the external forcing vector gives the dynamic response of the structure itself, the problem of extraction of the sources from convolutive mixtures is not completely solved yet. For this reason, the possibility to interpret

the dynamic response of a structure as a static mixture of sources has been investigated for modal identification purposes (Kerschen et al. 2007).

Assuming that the dynamic response of a structure can be modeled as a linear and static mixture of sources, it can be expressed in matrix form as follows (Poncelet et al. 2007):

$$\{y(t)\} = [A]\{s(t)\} \quad (4.259)$$

where  $\{s(t)\}$  are the source signals and  $[A]$  is now referred to as the *mixing matrix*. BSS techniques aim at recovering the mixing matrix  $[A]$  and the sources  $\{s(t)\}$  from their observed mixtures  $\{y(t)\}$ , based on general assumptions about the sources themselves.

The applicability of BSS to vibration data is obvious if the modal expansion of the dynamic response of the structure (4.102) is compared to (4.259). Such a comparison shows that there is a one-to-one relationship between mixing matrix and sources on one hand and modal matrix and modal coordinates on the other hand. Thus, under given assumptions, the modal coordinates may act as virtual sources regardless of the number and type of the physical excitation forces (Kerschen et al. 2007, Poncelet et al. 2007). No mathematical model is assumed to describe the process that produced the measured data. The mixing model is the only assumption, confirming that BSS techniques can be referred to as nonparametric procedures for modal identification.

The above-mentioned concepts and the moderate complexity of BSS justify the increasing application of these statistical signal-processing techniques in the field of OMA. In the case of static mixing, two approaches can be identified: the first is based on higher-order statistics, if the sources are statistically independent and no more than one source is Gaussian (Comon 1994); the second relies on second-order statistics, if the sources are uncorrelated (Belouchrani et al. 1997). In both cases separation is affected by some indeterminacies related to the order of the sources (any permutation of the sources is also a solution of the blind identification problem) and their amplitude.

Early use of BSS for modal identification can be found in a number of publications (Feeny and Kappagantu 1998, Kerschen and Golmival 2002) focused on the relation between proper orthogonal modes provided by a Principal Component Analysis (PCA) and normal modes. Applicability of PCA to real case studies has been limited by the need for information about the mass matrix (Kerschen et al. 2007). Chelidze and Zhou (Chelidze and Zhou 2006) investigated this issue, developing a new multivariate data analysis method (the so-called smooth orthogonal decomposition). Additional details about applicability of PCA in structural dynamics can be found in the literature (Kerschen et al. 2005).

Independent Component Analysis (ICA) appears much more suitable than PCA to vibration data processing for modal identification purposes (Kerschen et al. 2007). The main assumptions of ICA for the solution of the blind identification problem are the mutual independence (so that the joint probability density of the sources can be factorized into the product of their marginal densities) and non-Gaussianity of the sources (only one source with Gaussian distribution can

be tolerated; Even and Moisan 2005). Under these assumptions, the solution of an optimization problem based on a given cost function provides the sources. In particular, ICA is based on the maximization of non-Gaussianity of the sources. Moreover, as many other BSS algorithms, it includes some preprocessing steps. In particular, centering (removal of mean values from measurements) and whitening (basically, a PCA) are carried out in order to reduce the noise level and improve convergence.

The main drawbacks of ICA are related to the use of high-order statistics, whose estimation is computational demanding and difficult in the presence of a scarcity of data, and to some limitations strictly related to modal identification. In fact, ICA works well only in the case of weakly damped systems, characterized by damping ratios lower than 1 % (Kerschen et al. 2007). These reasons make ICA unattractive for modal identification purposes.

Methods based on second-order statistics of the observed signals assume that the sources are uncorrelated for all delays and have different spectra. Among these, the Algorithm for Multiple Unknown Signal Extraction (AMUSE) (Tong et al. 1991) and the Second Order Blind Identification (SOBI) algorithm are based on a similar theoretical background. In fact, they exploit the information contained in covariance matrices. However, while SOBI jointly diagonalizes several time-shifted covariance matrices, AMUSE relies on the EVD of the covariance matrix eventually at one time lag only. Thus, SOBI overcomes the shortcoming of AMUSE related to an eventually inappropriate choice of the time lag. This can result in two similar eigenvalues and makes unfeasible the identification of the corresponding sources. It has been shown that SOBI is also much more robust to noise than AMUSE (Zhou and Chelidze 2007).

When SOBI is applied to vibration data, the real-valued mixing matrix implies real-valued mode shape estimates. This can be a drawback of the method in the presence of complex modes. An evolution of SOBI able to deal with complex modes is the Blind Modal Identification (BMID) algorithm (McNeill and Zimmerman 2008).

In this section attention is focused on SOBI, with an illustration of the main steps of the algorithm and its theoretical assumptions in agreement with relevant publications available in the literature (Belouchrani et al. 1997, Poncelet et al. 2007, Zhou and Chelidze 2007). In fact, normal modes are typically identified from modal identification tests of civil structures, so SOBI can be profitably applied in most cases.

On the analogy with other BSS techniques, the measured response is assumed to be a linear mixture of the sources (the modal coordinates), as expressed by (4.259). If some (additive) noise  $\{n(t)\}$  is present in the measured response, (4.259) can be rewritten as follows:

$$\{y(t)\} = [A]\{s(t)\} + \{n(t)\}. \quad (4.260)$$

The  $l$  recorded time histories are, therefore, modeled as a linear combination of  $N_m$  sources plus noise. As a consequence, if there are  $N_m$  modes in the frequency

range under investigation, they can be identified only if  $\text{rank}([A]) = N_m$ . Since the mixing matrix has dimensions  $l \times N_m$ , this implies that the number of measurement channels has to be equal or larger than the number of active modes:  $l \geq N_m$ . Moreover, since the columns of the mixing matrix represent estimates of the mode shapes of the structure under test, a careful selection of sensor locations is needed so that the observed mode shape vectors are linearly independent and the rank of  $[A]$  is preserved. Taking into account the previously mentioned limitations, SOBI can be classified as a low order method for OMA. The issues related to the identifiability of a limited number of modes can be mitigated through the repeated application of band-pass filtering until the entire frequency range of interest is investigated. However, this procedure leads to a major increase in the time of analysis.

Assuming that the sources are stationary, uncorrelated, and scaled to have unit variance, their covariance matrix is the identity matrix:

$$[R_{ss}(0)] = E\left[\{s(t)\}\{s(t)\}^T\right] = [I]. \quad (4.261)$$

The additive noise is assumed to be a temporally and spatially white stationary random process, with:

$$E[\{n(t)\}] = \{0\} \quad (4.262)$$

$$E\left[\{n(t)\}\{n(t)\}^T\right] = \sigma^2[I] \quad (4.263)$$

If the added noise is also independent of the source signals, this implies:

$$E\left[\{n(t)\}\{s(t)\}^T\right] = [0]. \quad (4.264)$$

The first step of the algorithm consists of whitening the signal part  $\{x(t)\} = [A]\{s(t)\}$  of the observed data. This is achieved by applying a linear transformation to  $\{x(t)\}$  such that the whitened data  $\{z(t)\}$  are uncorrelated and have unit variance:

$$\{z(t)\} = [W]\{x(t)\} \Rightarrow [R_{zz}(0)] = E\left[\{z(t)\}\{z(t)\}^T\right] = [I]. \quad (4.265)$$

The matrix  $[W]$  defining this transformation is referred to as the *whitening matrix*. From (4.265) and (4.261) it is easy to recognize that:

$$[R_{zz}(0)] = [W][A]E\left[\{s(t)\}\{s(t)\}^T\right][A]^T[W]^T = [W][A][A]^T[W]^T = [I]. \quad (4.266)$$

Thus, if  $[W]$  is a whitening matrix,  $[A'] = [W][A]$  is an  $N_m \times N_m$  unitary matrix. As a consequence, the mixing matrix can be factored as the product of the inverse of the whitening matrix and a unitary matrix (to be determined).

Whitening of the measured response  $\{y(t)\}$  also obeys a linear model:

$$[W]\{y(t)\} = [W]([A]\{s(t)\} + \{n(t)\}) = [A'][s(t)] + [W]\{n(t)\}. \quad (4.267)$$

From the covariance matrix of the observed mixture:

$$[R_{yy}(0)] = E\left[\{y(t)\}\{y(t)\}^T\right] = [A][A]^T + \sigma^2[I] \quad (4.268)$$

the following equation is obtained:

$$[A][A]^T = [R_{yy}(0)] - \sigma^2[I]. \quad (4.269)$$

Combining (4.267) with (4.269) and taking into account (4.261), (4.263), and (4.264), it is possible to show that the whitening matrix  $[W]$  can be derived from the covariance matrix  $[R_{yy}(0)]$ , provided that the noise covariance is known or can be estimated:

$$[W][R_{yy}(0)][W]^T = [W][A][A]^T[W]^T + [W]\sigma^2[W]^T. \quad (4.270)$$

From a practical point of view, once the measured data have been centralized by removal of the mean value from each component of  $\{y(t)\}$ , whitening is obtained via PCA as follows.

First of all, the eigenvalue decomposition of  $[R_{yy}(0)]$  is computed:

$$[R_{yy}(0)] = E\left[\{y(t)\}\{y(t)\}^T\right] = [E][D][E]^T \quad (4.271)$$

where  $[E]$  is the orthogonal matrix of eigenvectors and  $[D]$  is the diagonal matrix of eigenvalues. If only the  $N_m$  largest eigenvalues  $d_1, \dots, d_{N_m}$  and the corresponding eigenvectors  $\{e_1, \dots, e_{N_m}\}$  of  $[R_{yy}(0)]$  are retained, the average of the remaining  $l - N_m$  eigenvalues provide an estimate  $\hat{\sigma}^2$  of the noise variance, under the assumption of white noise (Belouchrani et al. 1997). The whitened signals are then computed from the largest eigenvalues and the corresponding eigenvectors as:

$$\{z(t)\} = ([D_{N_m}] - \hat{\sigma}^2[I_{N_m}])^{-1/2}[E_{N_m}]^T\{y(t)\} = [W]\{y(t)\} \quad (4.272)$$

where  $[D_{N_m}]$  is the submatrix of  $[D]$  holding only the  $N_m$  largest eigenvalues,  $[E_{N_m}]$  is the submatrix of  $[E]$  collecting the eigenvectors corresponding to the  $N_m$  largest eigenvalues of  $[R_{yy}(0)]$  and the whitening matrix is given by:

$$[W] = ([D_{N_m}] - \hat{\sigma}^2[I_{N_m}])^{-1/2}[E_{N_m}]^T. \quad (4.273)$$

Taking into account (4.272), p time-shifted covariance matrices have to be computed:

$$[R_{zz}(\tau_k)] \quad k = 1, \dots, p. \quad (4.274)$$

In order to estimate the sources and the mixing matrix, an approximate joint diagonalization of those  $p$  time-shifted covariance matrices is carried out according to the Joint Approximate Diagonalization (JAD) technique (Belouchrani et al. 1997). The objective of JAD is to find the unitary matrix  $[\tilde{A}']$  that approximately diagonalizes the time-shifted covariance matrices. An optimization problem is defined with respect to the matrix  $[\tilde{A}']$  which minimizes the sum of the off-diagonal terms of  $[\tilde{A}']^T [R_{zz}(\tau_k)] [\tilde{A}']$  ( $k = 1, \dots, p$ ) for the  $p$  time-shifted covariance matrices:

$$\min_{[\tilde{A}']} \sum_{k=1}^p \text{off}\left([\tilde{A}']^T [R_{zz}(\tau_k)] [\tilde{A}']\right) \quad (4.275)$$

The solution to the minimization problem is pursued by means of a numerical algorithm based on the Jacobi rotation technique (Cardoso and Souloumiac 1996). Two parameters have to be set: the number  $p$  of time-shifted covariance matrices to be jointly diagonalized, and the threshold  $t$  used to stop JAD. About the threshold  $t$ , the problem of its setting has been analyzed by Cardoso and Souloumiac (Cardoso and Souloumiac 1996), showing that very small values for  $t$  have no sense because the diagonality criterion is approximate itself. Thus, it is usually unnecessary to push the accuracy of the rotation matrix to the machine precision. A value equal to its square root can be recommended. About the number  $p$  of time-shifted covariance matrices, the diagonalization performance improves when  $p$  increases and it seems to rapidly converge (Belouchrani et al. 1997). Once the matrix  $[\tilde{A}']$  has been obtained, the de-mixing matrix  $[U]$  and the mixing matrix  $[A]$  can be computed:

$$[U] = [\tilde{A}']^T [W] \quad (4.276)$$

$$[A] = [W]^+ [\tilde{A}'] \quad (4.277)$$

The resulting sources are shift-uncorrelated because the matrices  $[R_{ss}(\tau_k)]$  are nearly diagonal. They are obtained as follows:

$$\{s(t)\} = [U]\{y(t)\}. \quad (4.278)$$

The mode shapes of the structure are obtained from the columns of the mixing matrix. The technique for the estimation of natural frequencies and damping ratios depends on the type of data used for modal identification. In the literature SOBI has been applied to free responses, impulse responses, and responses to random excitation (Zhou and Chelidze 2007, McNeill and Zimmerman 2008, Poncelet et al. 2007). In the first two cases, the estimation of natural frequencies and damping

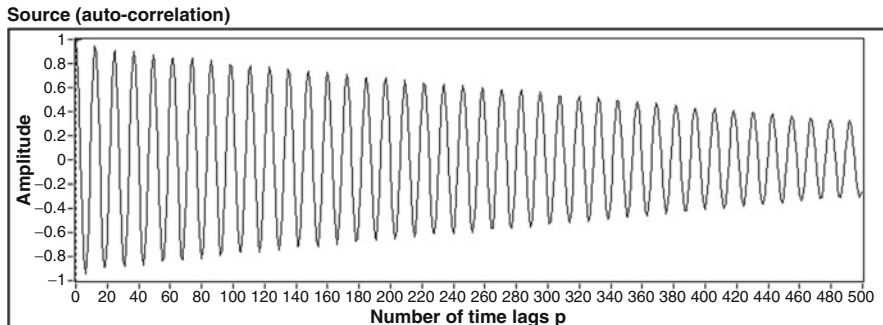


**Fig. 4.5** Sample auto-correlation of a source

ratios from the obtained sources is straightforward. In fact, taking into account that the free vibration response can be expressed as a sum of exponentially decaying sinusoids, fitting this expression to the data permits the estimation of the modal parameters (refer to McNeill and Zimmerman 2008 for more details). In the case of response to random excitation, if the estimation of natural frequencies from the identified sources is again straightforward, this is not the case of damping ratios, whose estimation requires the knowledge of the applied random excitation (Poncelet et al. 2007). However, the extension of SOBI to the analysis of random responses for the estimation of modal parameters including damping is immediate by taking into account that also the correlations of random responses can be expressed as a sum of decaying sinusoids. This is the same basic assumption of the NExT-type procedures. Thus, for random responses there is no need to recover the sources, since natural frequencies and damping ratios can be directly estimated from their correlations  $R_{ss}(\tau_k)$  (Fig. 4.5) as obtained from JAD. A simplified approach to the estimation of the modal properties by SOBI in the case of random response can be outlined as follows:

- Compute the whitening matrix  $[W]$  from the centralized dataset according to (4.271) and (4.273); since the number of modes is not known a-priori and the criterion for proper selection of the number  $N_m$  of eigenvalues to be retained is still debated, it is possible to set  $N_m = l$ ; since  $l$  sources are extracted from the data but the number of modes is likely lower than  $l$ , the sources associated to the actual structural modes have to be selected based, for instance, on the error in fitting the correlations  $R_{ss}(\tau_k)$  by exponentially damped harmonic functions; this approach has been originally proposed by Poncelet et al. (Poncelet et al. 2007) for the analysis of impulse responses;
- Compute  $\{z(t)\} = [W]\{y(t)\}$ ;
- Compute the time-shifted covariance matrices  $[R_{zz}(\tau_k)]$  and select  $p$  of them to apply JAD;

- The JAD of the p time-shifted covariance matrices  $[R_{zz}(\tau_k)]$  with  $k = 1, \dots, p$  provides the unitary matrix  $[\tilde{A}']$ , which permits the computation of the mixing matrix  $[A]$  according to (4.277), and the autocorrelations of the sources  $R_{ss}(\tau_k)$ ;
- Natural frequencies and damping ratios are estimated from the correlations of the sources  $R_{ss}(\tau_k)$ ; regression on zero-crossing times and logarithmic decrement (as with EFDD) or other SDOF estimators can be used; the use of SDOF curve fitting estimators permits the computation of the fitting error and, as a result, a quantitative selection of the correlations associated to actual structural modes in the case noise rejection has not been previously carried out in the computation of the whitening matrix; the selection of the number of time lags p now plays a primary role in the process, since it is not responsible only for the matrix  $[\tilde{A}']$  but it also defines the length of the correlation functions  $R_{ss}(\tau_k)$ ; thus, taking into account the physics of the problem, p has to be set as a function of the period of the fundamental mode so that a sufficient number of cycles are present in the auto-correlation of the source associated to the fundamental mode;
- The mode shapes are obtained from the columns of the mixing matrix corresponding to the source correlations selected in the previous step of analysis.

It is interesting to note that, unlike other two-stage modal identification methods, SOBI provides the mixing matrix and, therefore, the mode shapes first, while natural frequencies and damping ratios are estimated in a second stage through post-processing of the obtained sources. Finally, it is worth pointing out that only source signals having different spectral shape can be recovered by JAD (Belouchrani et al. 1997). This means that SOBI can identify distinct modes but it shows serious limitations in the presence of repeated modes.

---

## 4.6 Other Methods for OMA

Several different methods for OMA have appeared in the literature over the years. Most of them are just variants of the previously described algorithms, aiming at improving specific aspects or overcoming some drawbacks inherent in those procedures. However, additional original tools and methods for OMA have also been proposed. For instance, examples of wavelet analysis for output-only modal identification of natural frequencies and damping ratios only (Ruzzene et al. 1997, Gouttebroze and Lardies 2001) or also of mode shapes (Lardies and Gouttebroze 2002, Han et al. 2005) are available. Other researchers have instead proposed the use of cepstral analysis for OMA (Hanson et al. 2007). Even if wavelet and cepstral analysis show some advantages, they are not widely used. The interested reader can refer to the literature for more details. Other techniques for OMA that have been systematized over the years and are currently in use are based on transmissibility functions and the RD signature.

### 4.6.1 Transmissibility Functions

The use of transmissibility functions for OMA was first proposed in 2007 (Devriendt and Guillaume 2007). The method has been progressively refined and improved over the years: the basic concepts are herein reported.

The *transmissibility function* is defined as a sort of FRF and, as such, it can be estimated in a nonparametric preprocessing step. However, transmissibility functions are computed from variables of the same type instead of conjugate variables (i.e.: motion response and force input) as in classical FRFs. The transmissibility function between the output  $i$  and a reference output  $j$  is given by the ratio of their Fourier transforms:

$$T_{ij}(\omega) = \frac{Y_i(\omega)}{Y_j(\omega)}. \quad (4.279)$$

In practice it is estimated from the spectra as:

$$T_{ij}(\omega) = \frac{S_{Y_i Y_j}(\omega)}{S_{Y_j Y_j}(\omega)}. \quad (4.280)$$

Since the reference output is present in all transmissibility functions, it has to be carefully selected so that it carries the maximum amount of information about the structural modes.

Starting from the definition of transmissibility function and taking into account the modal model or, equivalently, the common denominator model, it is possible to show that the transmissibility does not depend on the coloring of the unknown forces, which can be arbitrary, but it only depends on the location and amplitude of the unknown forces. Moreover, the poles of the transmissibility functions are not the system poles, which are canceled out by taking the ratio between the response spectra. Thus, the peaks in the magnitude of transmissibility functions do not coincide with the structural resonances. However, an opportune combination of transmissibility functions obtained under different loading conditions makes possible the identification of the system poles. In fact, the transmissibility functions approach a constant value when converging to a pole of the system (Devriendt and Guillaume 2007):

$$\lim_{\omega \rightarrow \omega_n} T_{ij}(\omega) = \frac{\phi_{i,n}}{\phi_{j,n}}. \quad (4.281)$$

As shown by (4.281), such a value is directly related to the mode shape components at the measurement locations  $i$  and  $j$ . Moreover, since the limit is independent of the input, transmissibility functions pertaining to the same responses but computed from two tests characterized by different loading conditions  $a$  and  $b$

exactly cross each other in correspondence with the structural resonances. As a consequence, their difference is zero at a structural resonance:

$$\lim_{\omega \rightarrow \omega_n} \left( T_{ij}^a(\omega) - T_{ij}^b(\omega) \right) = \frac{\phi_{i,n}}{\phi_{j,n}} - \frac{\phi_{i,n}}{\phi_{j,n}} = 0. \quad (4.282)$$

This implies that the poles of the system are also poles of the following rational function, given by the inverse of the difference between transmissibility functions associated to the same responses but computed for different loading conditions:

$$\frac{1}{\Delta T_{ij}^{ab}(\omega)} = \frac{1}{T_{ij}^a(\omega) - T_{ij}^b(\omega)}. \quad (4.283)$$

The application of parametric frequency domain estimators based on the common denominator model to (4.283) provides the structural poles. The mode shapes are estimated in a second stage from the residues (Devriendt et al. 2010).

The functions given by (4.283) might contain additional poles not related to the structure. However, the poles of the system can be easily distinguished from the additional mathematical poles by using a SVD (Devriendt and Guillaume 2008).

Even if the method is still under development, the main advantage consists in its robustness even in the presence of spurious harmonics. In fact, the method seems to be able to provide unbiased estimates of the modal parameters even in the case of spurious harmonics close to the structural resonances (Devriendt et al. 2009), thus overcoming a relevant limitation of standard OMA methods (see also Chap. 5). Nor prior knowledge about the frequency of the spurious harmonic neither filtering/interpolation are required. The only requirement affects the loading conditions, which must differ for location, number, or amplitude of the applied forces.

#### 4.6.2 The Random Decrement Technique

The Random Decrement (RD) technique is a simple method for the estimation of functions that can be interpreted as free decays and, therefore, processed by covariance-driven identification methods. Thus, it represents a preliminary signal processing step for OMA rather than an autonomous OMA method. However, it is discussed here because it represents an alternative method for the estimation of correlation functions that is often applied in combination with some of the previously discussed OMA methods.

The RD technique was developed in the late 1960s at NASA (Cole 1968, Cole 1973) as a method to characterize stochastic time series. It was soon extended to modal identification of structures (Ibrahim 1977). The theoretical basis of the method has been later systematized and extended by other researchers (Vandiver et al. 1982, Asmussen et al. 1999).

The RD technique provides an estimate of the so-called RD signature. Under the assumption of ergodic stochastic processes, the cross-RD signature is estimated

from two time series  $y_1(t)$  and  $y_2(t)$  by averaging  $N_b$  segments of the time series  $y_1(t)$  associated to the  $N_b$  triggering points where the time series  $y_2(t)$  satisfies at the time instants  $t_n$  the triggering condition  $C_{y_2}(t_n)$ :

$$\hat{D}_{y_1 y_2}(\tau) = \frac{1}{N_b} \sum_{n=1}^{N_b} y_1(t_n + \tau) | C_{y_2}(t_n). \quad (4.284)$$

Up to  $M$  data points before and  $M$  points after the trig points ( $\tau = m\Delta t$ ,  $-M \leq m \leq M$ ) are used in the computation of the signature, where  $M$  is user-defined. The number  $N_b$  of averages depends on the length of the time series and the adopted triggering condition. Different triggering conditions  $C_{y_2}(t_n)$  can be applied:

- Level crossing:  $y_2(t_n) = \bar{y}_2$ ,
- Slope crossing:  $\dot{y}_2(t_n) = \bar{\dot{y}}_2$ ,
- Positive value:  $y_2(t_n) > 0$ ,
- Positive slope:  $\dot{y}_2(t_n) > 0$ ,

and any combination of the previous conditions (for instance, zero crossing condition with positive slope:  $y_2(t_n) = 0 \wedge \dot{y}_2(t_n) > 0$ ). When the triggering condition is applied to the same time series, whose data segments are averaged in (4.284), the auto-RD signature is estimated:

$$\hat{D}_{y_1 y_1}(\tau) = \frac{1}{N_b} \sum_{n=1}^{N_b} y_1(t_n + \tau) | C_{y_1}(t_n). \quad (4.285)$$

When the condition affects both level and slope, it has been shown (Brincker et al. 1992) that the RD signature estimate is a linear combination of the correlation function and its derivative:

$$D_{y_1 y_2}(\tau) = \frac{R_{y_1 y_2}(\tau)}{\sigma_{y_2}^2} \bar{y}_2 + \frac{\dot{R}_{y_1 y_2}(\tau)}{\sigma_{\dot{y}_2}^2} \bar{\dot{y}}_2 \quad (4.286)$$

where  $\sigma_{y_2}^2$  is the variance of the triggering process  $y_2(t)$  and  $\sigma_{\dot{y}_2}^2$  is the variance of the derivative  $\dot{y}_2(t)$  of the triggering process. The triggering condition can be selected in order to obtain an RD-signature, which is proportional only to the correlation function or its derivative. In particular, conditions applied only to the triggering process (i.e. level crossing, positive value) lead to an RD-signature proportional to the correlation function only, while the application of triggering conditions only to the derivative of the triggering process (i.e. slope crossing, positive slope) yields an RD signature proportional to the derivative of the correlation function.

A relevant application of the RD signature concerns the investigations about the amplitude dependence of modal damping ratios by appropriately varying the triggering condition. The interested reader can refer to the literature (Tamura and Suganuma 1996) for more details.

## 4.7 Some Remarks About OMA Methods

The theoretical background of a number of output-only modal identification procedures has been analyzed in the previous sections, discussing in detail those aspects related to the software implementation of selected algorithms. Far from being a comprehensive discussion about OMA techniques, the analysis of the individual methods in their most relevant aspects provides an overview of the advantages and drawbacks, from a practical point of view, related to the use of different analysis procedures. Relevant results of a comparative analysis of the previously illustrated OMA methods are summarized in this section, also to explain the larger attention devoted to some methods with respect to the others. The following considerations have also guided the selection of the procedures implemented into the software accompanying this book and used for the applications proposed at the end of this chapter. Even if the test engineer typically has a favorite OMA method of his own, selected according to criteria related to the simplicity or accuracy of the method itself, the concurrent use of different OMA techniques is always recommended for successful modal parameter identification. In fact, the comparison of the estimates provided by different OMA methods ensures the reliability of the modal identification results.

Even if developed since a long time and widely applied to civil engineering structures, NExT-type procedures have been progressively abandoned in favor of the more robust subspace methods. When NExT-type procedures appeared, they represented a significant enhancement in the field of output-only modal analysis with respect to the classical Peak Picking technique. In fact, they improved the accuracy of data analysis, especially in the presence of closely spaced modes, and allowed the extraction of actual mode shapes instead of ODSs. Notwithstanding their historical relevance, they show some limitations with respect to the subspace methods. The ITD method, for instance, suffers the lack of noise truncating mechanisms, thus leading to several spurious poles. Moreover, high order modes require filtering procedures to be extracted and this leads to the repeated application of the procedure to the same dataset, resulting in a time consuming process.

ARMA models aim at modeling the dynamics of both the structural system and the noise. Since also noise is modeled, lots of additional spurious poles, not related to the dynamics of the system under test, appear. This makes the selection of the system poles difficult, and the presence of noise can affect the modal parameter estimates as well. For instance, the lack of a noise truncating mechanism in the IV method is reflected in less accurate mode shape estimates with respect to subspace methods; moreover, higher order models are required to obtain good modal parameter estimates (Peeters 2000). When PEM is considered, the advantage of an optimal statistical description of data due to the presence of the MA matrix polynomial is paid by the need to solve a highly nonlinear optimization problem. Since the application of PEM does not improve too

much the modal parameter estimates (Brincker and Andersen 1999b), subspace methods, characterized by lower computational time and no convergence problems, are preferred.

Subspace methods have noise truncating mechanisms based on SVD. Since the identification problem is solved by means of linear algebra tools, nonlinear optimization problems are avoided. This results also in a lower computational burden. In the presence of noise or poorly excited modes, weighting matrices can be applied to improve the performance of the estimators. Both Cov-SSI and DD-SSI perform equally well in terms of quality of the modal parameter estimates; however, DD-SSI can be implemented in a way that positive realness of the covariance sequences is ensured. All the above-mentioned characteristics have made SSI methods very popular in the modal analysis community.

The availability of nonparametric frequency domain OMA procedures in the equipment of the modal analyst is also recommended. They can be profitably used for a quick check and analysis of data in the field. In fact, they are less computational demanding with respect to subspace methods and give reasonable estimates of the modal parameters. The use of FDD is recommended because of its less restrictive assumptions with respect to BFD. Moreover, due to the simplicity of nonparametric frequency domain methods, they can be used to get a first insight into the identification problem and, as a result, to guide the setting of the analysis parameters in subspace algorithms.

Other methods such as LSCF (and its poly-reference version) and SOBI are becoming more and more popular because they simplify the identification of the structural modes and provide interesting opportunities for the automation of the modal identification process (Chap. 6).

Whatever is the adopted OMA method, modal identification tests often require processing of a large amount of data. However, a certain degree of redundancy or overdetermination is always present in the data. As a consequence, techniques for the reduction of the amount of data to processed can profitably be applied in order to keep the computational time within reasonable values. Filtering and decimation are usually used to reject unnecessary information and to limit the frequency band under investigation. Selected reference channels (Peeters 2000) are also sometimes adopted in order to reduce data redundancy. They have to be carefully chosen to avoid that some modes are lost together with the redundant information. The use of reference channels can lead to problems of missing modes mainly in the presence of repeated roots and a too small number of reference channels, or in the case of local modes, which do not appear in the selected reference channels. An approach to the selection of the best reference channels is based on the computation of the correlation coefficients of the measured data:

$$\rho_{y_i y_j}^2 = \frac{R_{y_i y_j}^2(0)}{R_{y_i y_i}(0) R_{y_j y_j}(0)} \quad (4.287)$$

and on the construction of the following matrix:

$$\begin{bmatrix} \rho_{y_i y_j} \end{bmatrix} = \begin{bmatrix} 1 & \rho_{y_1 y_2} & \rho_{y_1 y_3} & \dots & \rho_{y_1 y_l} \\ \rho_{y_2 y_1} & 1 & \rho_{y_2 y_3} & \dots & \vdots \\ \rho_{y_3 y_1} & \rho_{y_3 y_2} & \ddots & \dots & \vdots \\ \vdots & \dots & \dots & \ddots & \vdots \\ \rho_{y_l y_1} & \dots & \dots & \dots & 1 \end{bmatrix}. \quad (4.288)$$

For each channel, the following index can be computed:

$$M_i = \sum_{j=1}^l \left| \rho_{y_i y_j} \right| \quad j \neq i, \quad i = 1, \dots, l \quad (4.289)$$

and the reference channels are finally selected as those characterized by the largest values of the  $M_i$  index.

The use of reference channels leads to an appreciable reduction of computational efforts and response time. In the previous sections about OMA methods all measurement channels have been taken as references. When only some channels are selected as references, slight changes to the previously described algorithms are required in order to take into account that the number  $r$  of reference channels is lower than the total number of measurement channels. The interested reader can refer to the literature for reference-based versions of some of the OMA procedures discussed in this chapter (see, for instance, Peeters and De Roeck 1999 for the reference-based version of SSI algorithms).

Another interesting aspect, which is beyond the scope of the present book, concerns the possibility to estimate the uncertainty bounds of the modal parameter estimates from a single output-only modal identification test. This information plays a primary role in a variety of applications, ranging from the analysis of the influence of selected parameters on the vibration response to SHM. Moreover, the information about the uncertainty bounds can support the discrimination between physical and spurious poles, since the latter are usually characterized by larger variance. The interested reader can refer to the literature for more details (Reynders et al. 2008, Pintelon et al. 2007, De Troyer et al. 2009a, De Troyer et al. 2009b).

---

## 4.8 Post-Processing of Modal Parameter Estimates

### 4.8.1 Analysis of Mode Shape Estimates

Most of the OMA methods provide their results in the form of complex eigenvalues and complex eigenvectors. Since the mode shape estimates are in the form of complex vectors, a distinction between normal modes, characterized by real-valued mode shape vectors, and complex modes is needed.

In particular, it is worth realizing if complex mode shape estimates actually represent the dynamics of the structure under investigation or they are the result of other factors.

In the case of normal (real) modes, the displacements at the various DOFs reach their maximum at the same time and pass through the equilibrium position at the same time. This is not the case of complex modes, where both the maximum values and the null values of modal displacements are attained at different time instants for the various DOFs (Chopra 2000). As a result, while the phase angles are all  $0^\circ$  or  $180^\circ$  for normal modes, both amplitude and phase characterize the motion of the different DOFs in the case of complex modes.

Complex modes may originate for a number of reasons, such as gyroscopic effects, aerodynamic effects, nonlinearities, and nonproportional damping (Ewins 2000, Chopra 2000).

Close modes sometimes show significant complexity, too (Ewins 2000). In this regard it is worth noting that two modes characterized by some frequency separation (that is to say, the difference between the respective natural frequencies) may be close or not depending on the value of damping: the larger the damping, the closer the modes. As a measure of separation of two modes, the *modal overlap factor* (MOF) (Srikantha Phani and Woodhouse 2007) can be computed:

$$MOF_n = \frac{f_n \xi_n}{f_n - f_{n-1}} \quad (4.290)$$

where  $f_n$  and  $f_{n-1}$  represent the natural frequencies of the two modes under consideration, while  $\xi_n$  is the damping ratio associated to the n-th mode.

Even if in the majority of cases the identified modes are normal, it is important to recognize those situations where complex modes have to be expected and properly estimated.

Complex modes are often obtained from modal tests as a result of measurement noise (poor signal-to-noise ratio). However, the degree of complexity is usually moderate. Even if slight complexities can be encountered in practical applications and a complex-to-real conversion of mode shapes can be carried out with negligible errors, the evaluation of specific indicators can provide a quantitative measure of the degree of complexity of the estimated mode shapes.

The simplest method to assess modal complexity consists in plotting the components of the i-th eigenvector in the complex plane, thus obtaining the so-called *complexity plot* (Fig. 4.6). It permits the evaluation of the degree of complexity by a simple visual inspection. A method based on complexity plots for the quantitative assessment of the degree of complexity of the estimated mode shapes is described elsewhere (Ewins 2000). Other indexes measuring the mode shape complexity are the *Modal Phase Collinearity* (MPC) and the *Mean Phase Deviation* (MPD).

If a structure is proportionally damped, the mode shape components for a certain mode lie on a straight line in the complex plane (Fig. 4.6a).

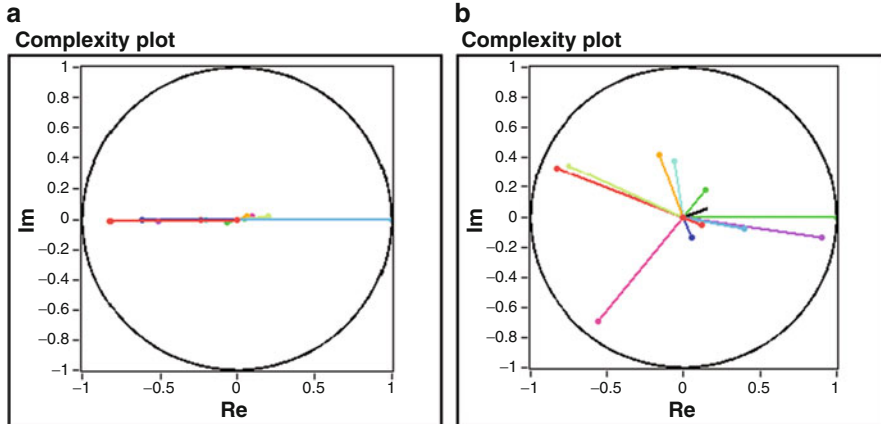


**Fig. 4.6** Complexity plots for normal (a) and complex (b) modes

Deviations from this behavior can be quantified by the MPC for nearly real normal modes (Pappa et al. 1992). It can be computed by subtracting the mean value of the r-th mode shape vector components to each of them:

$$\tilde{\phi}_{i,r} = \phi_{i,r} - \frac{\sum_{k=1}^l \phi_{k,r}}{l} \quad i = 1, \dots, l. \quad (4.291)$$

The MPC of the r-th mode shape is then given by:

$$MPC_r = \frac{\left\| \operatorname{Re}\left(\{\tilde{\phi}_r\}\right) \right\|^2 + \left( \operatorname{Re}\left(\{\tilde{\phi}_r\}^T\right) \operatorname{Im}\left(\{\tilde{\phi}_r\}\right) \right) \left( 2(\varepsilon_{MPC}^2 + 1) \sin^2(\theta_{MPC}) - 1 \right) / \varepsilon_{MPC}}{\left\| \operatorname{Re}\left(\{\tilde{\phi}_r\}\right) \right\|^2 + \left\| \operatorname{Im}\left(\{\tilde{\phi}_r\}\right) \right\|^2} \quad (4.292)$$

where:

$$\varepsilon_{MPC} = \frac{\left\| \operatorname{Im}\left(\{\tilde{\phi}_r\}\right) \right\|^2 - \left\| \operatorname{Re}\left(\{\tilde{\phi}_r\}\right) \right\|^2}{2 \left( \operatorname{Re}\left(\{\tilde{\phi}_r\}^T\right) \operatorname{Im}\left(\{\tilde{\phi}_r\}\right) \right)} \quad (4.293)$$

$$\theta_{MPC} = \arctan \left( |\varepsilon_{MPC}| + \operatorname{sgn}(\varepsilon_{MPC}) \sqrt{1 + \varepsilon_{MPC}^2} \right) \quad (4.294)$$

$\|\cdot\|$  and  $\operatorname{sgn}(\cdot)$  denote the L<sub>2</sub> norm and the signum function, respectively. MPC values are dimensionless and bounded between 0 and 1. For real modes, the index approaches unity, while its value is low in the case of a complex mode.

If normal modes are expected, a low value of MPC may indicate nonstructural modes.

As an alternative, the degree of complexity can be quantified by computing the MPD. A simple expression for MPD (Heylen et al. 1998) starts from the computation of the following index for the r-th mode shape vector:

$$MP_r = \frac{\sum_{k=1}^l \varphi_{k,r}}{l} \quad (4.295)$$

with:

$$\begin{aligned} \varphi_{k,r} &= \arctan \left( \frac{\operatorname{Re}(\phi_{k,r})}{\operatorname{Im}(\phi_{k,r})} \right) && \text{if } \arctan \left( \frac{\operatorname{Re}(\phi_{k,r})}{\operatorname{Im}(\phi_{k,r})} \right) \geq 0 \\ \varphi_{k,r} &= \arctan \left( \frac{\operatorname{Re}(\phi_{k,r})}{\operatorname{Im}(\phi_{k,r})} \right) + \pi && \text{if } \arctan \left( \frac{\operatorname{Re}(\phi_{k,r})}{\operatorname{Im}(\phi_{k,r})} \right) < 0. \end{aligned} \quad (4.296)$$

Then, the MPD index is computed as follows:

$$MPD_r = \sqrt{\frac{\sum_{k=1}^l (\varphi_{k,r} - MP_r)^2}{l}}. \quad (4.297)$$

In the case of normal mode shapes, the value of MPD is zero. An improvement of the MPD index for those cases where there are mode shape components with a large imaginary part but a small real part can be found in the literature (Reynders et al. 2012).

Taking into account the previous discussion and that OMA provides only un-scaled mode shapes, there is the need for simple approaches to scaling and complex-to-real conversion of the estimated mode shape vectors.

The need for complex-to-real conversion of the estimated mode shapes stems from one of the typical applications of modal data, the comparison between the experimental values of the modal properties and those obtained from numerical models. In fact, the latter are usually obtained from undamped models and, as a consequence, the mode shapes are real-valued. Whenever normal modes are expected from the modal test, the simplest approach to carry out the complex-to-real conversion consists in analyzing the phase of each mode shape component and setting it equal to  $0^\circ$  or  $180^\circ$  depending on its initial value. If the phase angle lies in the first or in the fourth quadrant it is set equal to  $0^\circ$ ; it is set equal to  $180^\circ$  if it lies in the second or in the third quadrant. To be rigorous, this approach should be applied only in the case of nearly normal modes, when the phase angles differ

no more than  $\pm 10^\circ$  from  $0^\circ$  to  $180^\circ$ . However, it is frequently extended to all phase angles (Ewins 2000).

The mode shape vectors obtained from the different OMA methods are often rescaled so that the magnitude of the largest modal displacement is equal to 1. A simple procedure to obtain normalized, real mode shapes starting from the experimental results is the following:

- starting from the complex-valued components of the  $r$ -th experimental mode shape, find the component  $\phi_{r,\max}$  characterized by the largest modulus;
- divide every component of the experimental vector by  $\phi_{r,\max}$ ;
- carry out the complex-to-real conversion as previously illustrated;
- return the normalized mode shape vector in terms of amplitude and phase; alternatively, return the modal displacement with sign (+ if the phase is  $0^\circ$ , – if it is  $180^\circ$ ).

The experimentally identified mode shapes have to be graphically displayed, because the visual inspection of the estimated mode shapes represents the simplest method for a preliminary check of the modal identification results. Two approaches exist for the graphical display of mode shape estimates. The static display provides a picture of the mode shape, eventually superimposed to the undeformed configuration of the structure (Fig. 4.7). This is the display format used in reports.

Taking into account the measurement directions of the sensors installed on the structure and their positions, the deformed shape is obtained by assigning to each measured point in each measured direction a displacement proportional to the corresponding component of the mode shape vector. The scaling constant is set in a way that the various modal displacements are appreciable but not too large, otherwise the basic geometry of the structure might appear heavily altered. The sign of the mode shape component determines if the measured point is moving in-phase (+) or out-of-phase (–) with respect to the reference direction of the sensor.

The static display is able to represent only real modes. As a consequence, a preliminary complex-to-real conversion of the estimated mode shapes is necessary. The visual inspection of complex mode shapes by static plots can be, therefore, misleading. Fortunately, normal or nearly normal modes are typically encountered in practical applications. Plotting animated mode shapes overcomes the limitations of static display. Animated plots simulate the swing of the structure according to the selected mode shape, so they can effectively represent also the complex modes.

One of the main drawbacks inherent in the visual inspection of the identified mode shapes is related to the fact that the identified model is incomplete, since measurements are carried out in a few points. The number of measurement points is typically much lower (by some order of magnitudes) than the number of DOFs adopted, for instance, in numerical models. Since there are several unmeasured DOFs during tests, in the grid of points adopted to represent the geometry of the structure some of them will always be characterized by null modal displacements.

This effect, caused by the finite number of measurement channels, has to be taken into account in the visual inspection of mode shapes. In fact, those points probably exhibit some displacements, which are not represented in the plots.

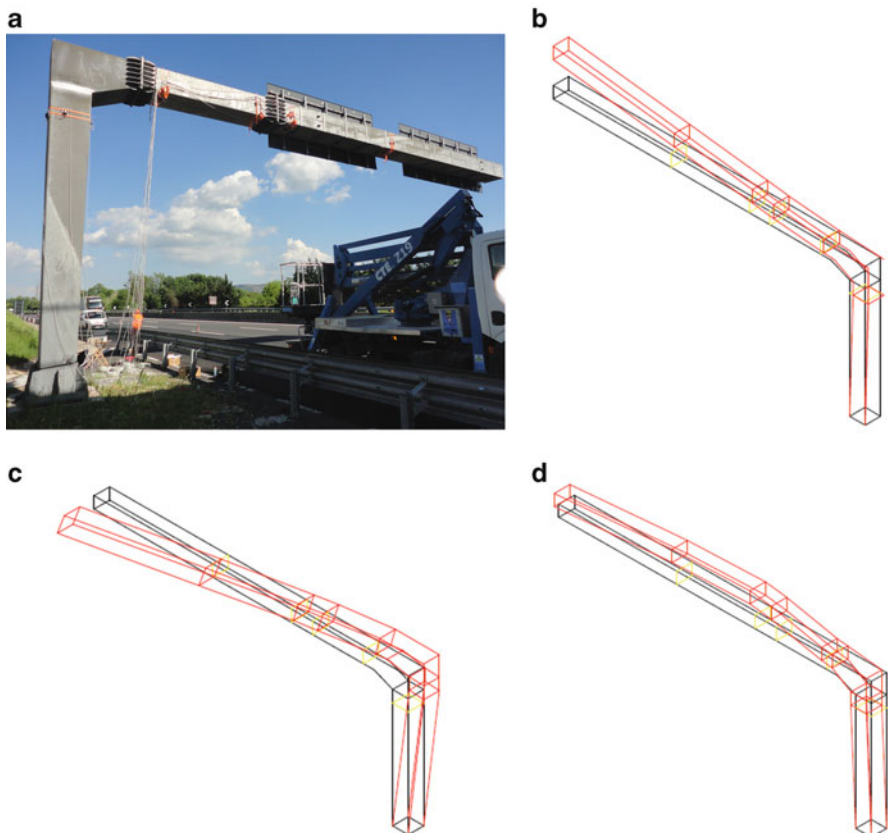


**Fig. 4.7** Steel structure for road sign (a) and static display of some of its experimentally estimated mode shapes (b–d)

Neglecting the effect of incomplete measurements can lead to misleading results in the interpretation of the experimental mode shapes. In some cases interpolation of modal displacements or consideration of some constraints (for instance, the presence of rigid diaphragms) can compensate the lack of information about some modal displacements in the experimental estimates.

However, erroneous plots are obtained if, for instance, the assumption of constrained DOFs is not verified or interpolation of modal displacements is applied in the case of a structure characterized by the presence of joints or abrupt changes in its section. In summary, an effective display of the identified mode shapes is always the result of a good choice of the sensor layout and the installation of a sufficient number of sensors to ensure the observability of the modes of interest (see also Chap. 3).

In the extreme case, when the adopted sensor layout is too coarse with respect to the geometric complexity of the structure under test, there are problems not only in

displaying the deformation patterns but also in the analysis of the deformed shapes. In fact, an insufficient number of sensors leads to the well-known problem of spatial aliasing (Ewins 2000) with the related problems of distinction of the various modes, which appear very similar each other. An effective tool to assess (ex post) the quality of the adopted sensor layout is introduced in Sect. 4.8.2.2.

## 4.8.2 Quality Checks and Comparisons

### 4.8.2.1 Natural Frequencies

Validation of modal identification results mainly relies on consistency checks obtained by comparing the experimental estimates provided by different OMA methods. If the experimental estimates provided by the different methods are in good agreement each other, they can eventually be compared with the results of numerical models of the structure under investigation. Comparisons and correlations between experimental and numerical estimates of the modal properties represent the primary tools to verify numerical models. A *verified model* is a model that includes all the necessary features to provide an acceptable representation of the actual dynamic behavior of the structure. A verified model can eventually undergo some adjustments to make its dynamic properties closer to the experimental values. The calibration of a numerical model based on experimental estimates of the modal properties is referred to as *model updating*. This is one of the main applications of modal testing. Even if most of the necessary tools to compare numerical and experimental results are discussed in this section, the interested reader can refer to the literature (Friswell and Mottershead 1995, Mottershead et al. 2011, Ewins 2000) for an extensive discussion about model updating techniques, which are beyond the scope of the present book.

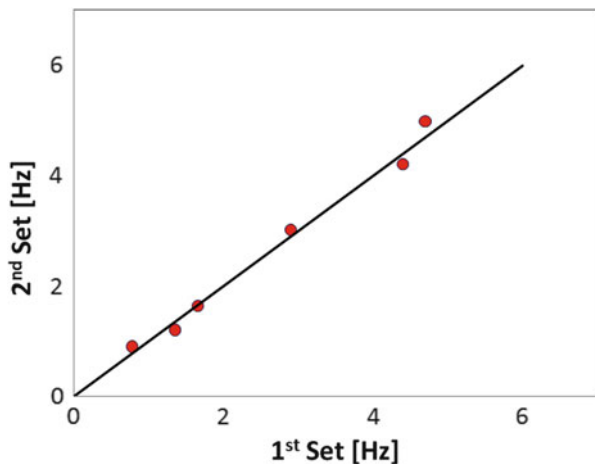
Natural frequencies can be compared by a simple tabulation, quantifying the relative scatter, expressed in percent, as follows:

$$\Delta f_n = \frac{f_{2,n} - f_{1,n}}{f_{1,n}} \cdot 100 \quad (4.298)$$

where  $f_{1,n}$  and  $f_{2,n}$  are the two values of the natural frequency for the n-th mode under comparison;  $f_{1,n}$  and  $f_{2,n}$  can be either experimental estimates, obtained from two different OMA methods, or represent the numerical and the experimental estimate of the experimental frequency of the n-th mode, respectively.

An alternative approach to compare two sets of natural frequency estimates consists of plotting the natural frequencies in the second set against the natural frequencies of the first set in a Cartesian plane (Fig. 4.8). The first set holds the reference natural frequency estimates (for instance, those provided by a certain OMA method, or average values of the estimates obtained from different methods) while the second set holds the values of the natural frequencies that have to be compared with the corresponding estimates in the first dataset. The natural frequencies in the second set can be experimental estimates obtained from a

**Fig. 4.8** Comparison of natural frequencies



different OMA method or the values predicted by a numerical model. In the ideal case of very good correlation between the two sets of natural frequencies, the points lie very close to the line passing through the origin of the axes with  $45^\circ$  slope. However, mainly in the case of the comparison between numerically predicted and experimentally estimated natural frequencies, it may happen that the points lie along a different line or they are fairly scattered with respect to the  $45^\circ$  line. Depending on how the points are distributed, it is possible to determine the reasons for the deviations. For instance, about the comparison between numerically predicted natural frequencies and the corresponding experimental estimates, if the numerical model is representative of the actual behavior of the structure, only small and randomly distributed deviations of the points from the  $45^\circ$  line are expected. When the points lie close to a line with slope different from  $45^\circ$ , the deviation can be addressed to erroneous setting of the material properties in the numerical model. If the points are widely scattered with respect to the  $45^\circ$  line, the model is unfit to represent the experimental data and a new model has to be set. Finally, if the deviations are small but all or nearly all the points lie on one side of the  $45^\circ$  line, they suggest the presence of a systematic error (Ewins 2000). Similar considerations can be done in the analysis of the experimental results provided by different methods.

In both cases of tabulation and graphical representation, a correct mode pairing plays a critical role in determining the results and effectiveness of the comparisons. It is not sufficient to compare two sets of ordered frequencies since there is no guarantee of one-to-one correspondence between the modes in the first set and those in the second set. For a correct mode pairing the information about the mode shapes has also to be taken into account, in order to ensure that the two natural frequency estimates under comparison are representative of the same mode. An incorrect mode pairing can lead to misleading results. The evaluation of the correlation between couples of mode shapes is based on the tools discussed in the next section.

### 4.8.2.2 Mode Shapes

Classical books about experimental modal analysis suggest the comparison of mode shapes through their graphical representation according to one of the methods discussed in Sect. 4.8.1; plots in the Cartesian plane similar to that discussed in Sect. 4.8.2.1 to compare natural frequencies can also be used. Even if those methods can provide a certain amount of information, for instance about poor numerical modeling (Ewins 2000), they suffer problems in the presence of some scaling errors in the data and they are inadequate to compare complex-valued mode shapes. This can lead to major errors in the analysis of results and mode pairing. A more effective comparison of mode shapes, able to deal also with complex modes, is based on some numerical indexes. The MAC (Allemang and Brown 1982) represents the most popular index to quantify the correlation between mode shapes, but it also shows some limitations. For this reason, a number of other indexes have been developed over the years. The use of MAC and other indexes to evaluate the correlation between couples of mode shapes is discussed in this section, pointing out the respective advantages and limitations. In particular, the role of those indexes in proper mode pairing, in the assessment of the quality of the adopted sensor layout and in the verification of numerical models is illustrated.

Given the two mode shape vectors under comparison, for instance the experimentally estimated mode shape  $\{\phi_n^e\}$  and the numerically predicted mode shape  $\{\phi_n^a\}$  of the n-th mode of the investigated structure, in the most general case of complex-valued vectors the MAC is computed as follows:

$$MAC(\{\phi_n^a\}, \{\phi_n^e\}) = \frac{\left| \{\phi_n^a\}^H \{\phi_n^e\} \right|^2}{\left( \{\phi_n^a\}^H \{\phi_n^a\} \right) \left( \{\phi_n^e\}^H \{\phi_n^e\} \right)}. \quad (4.299)$$

If both vectors are real-valued, as usually happens in the presence of numerically predicted mode shapes, the transpose operator replaces the Hermitian and (4.299) can be rewritten as follows:

$$MAC(\{\phi_n^a\}, \{\phi_n^e\}) = \frac{\left| \{\phi_n^a\}^T \{\phi_n^e\} \right|^2}{\left( \{\phi_n^a\}^T \{\phi_n^a\} \right) \left( \{\phi_n^e\}^T \{\phi_n^e\} \right)}. \quad (4.300)$$

The MAC index is basically a squared, linear regression correlation coefficient and it provides a measure of the consistency (degree of linearity) between the two vectors under comparison. The MAC values are bounded between 0 and 1, representing inconsistent and perfectly consistent correspondence between the two vectors, respectively. Even if the MAC between analytical and experimental mode shapes is generally used for verification and updating of finite element models, it is worth taking into account that it provides only a measure of consistency between the vectors but it does not ensure validity.

For instance, when the experimental mode shapes are measured at few locations, the incomplete information can lead to a MAC value near unity with the corresponding analytical mode shape, but the consistency between the two vectors does not ensure that the analytical mode shape is correct. If more points are measured, the consistency between analytical and experimental mode shapes can decrease to values much lower than 1.

It is also worth pointing out that the MAC is sensitive to large differences between the corresponding components of the vectors under comparison, but it is basically insensitive to small changes and small magnitudes of the modal displacements. Moreover, the MAC is not able to distinguish between random errors and systematic deviations from the reference mode shape components. Notwithstanding the previous limitations, the MAC is by far the most used index for mode shape comparisons.

Taking into account the relative scatter between the natural frequencies (4.298) and the consistency of the mode shape vectors (4.299), an effective mode pairing is possible. The information about the mode shapes plays a primary role for a correct mode pairing above all in the case of closely spaced modes, when proper matching between analytical and experimental mode shapes can be difficult if only the information about the natural frequencies is available.

When the mode shapes under comparison exhibit a consistent, linear relationship, it is possible to compute the *modal scale factor* (MSF) as follows:

$$MSF(\{\phi_n^e\}, \{\phi_n^a\}) = \frac{(\{\phi_n^a\}^H \{\phi_n^e\})}{(\{\phi_n^a\}^H \{\phi_n^a\})} \quad (4.301)$$

if the analytical mode shape is considered as reference, or as:

$$MSF(\{\phi_n^a\}, \{\phi_n^e\}) = \frac{(\{\phi_n^e\}^H \{\phi_n^a\})}{(\{\phi_n^e\}^H \{\phi_n^e\})} \quad (4.302)$$

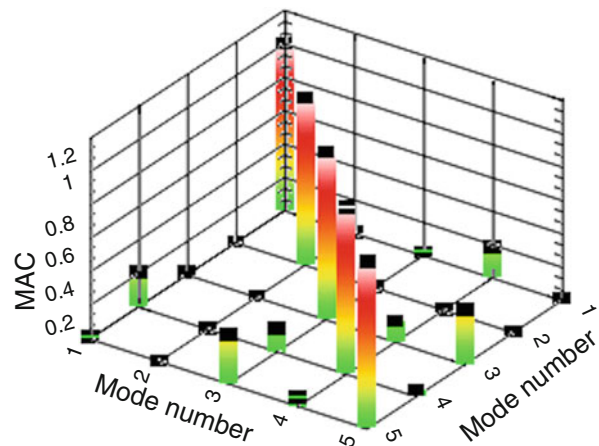
if the experimental mode shape is considered as reference. The MSF does not provide information about the quality of the fit, but it only gives the scale factor between consistent vectors.

An alternative index to assess the mode shape correlation is represented by the *Normalized Modal Difference* (NMD) (Waters 1995, Maia et al. 1997):

$$NMD(\{\phi_n^a\}, \{\phi_n^e\}) = \sqrt{\frac{1 - MAC(\{\phi_n^a\}, \{\phi_n^e\})}{MAC(\{\phi_n^a\}, \{\phi_n^e\})}} \quad (4.303)$$

The NMD basically represents a close estimate of the average difference between the components of the two vectors  $\{\phi_n^a\}$  and  $\{\phi_n^e\}$ . It appears much more sensitive to mode shape differences than the MAC and, therefore, it is sometimes used to better remark the differences between highly correlated mode shapes.

**Fig. 4.9** Graphical representation of MAC matrix



In practical applications, given  $N_m^e$  experimentally identified modes and  $N_m^a$  numerically predicted modes, the  $N_m^e \times N_m^a$  MAC matrix (Fig. 4.9) is computed. Assuming without loss of generality that  $N_m^e = N_m^a$ , if the numerical and experimental mode shape vectors are consistent the MAC matrix will show values close to 1 along its main diagonal, where the MAC is computed for mode shapes corresponding to the same mode, and close to 0 elsewhere, where the MAC is related to two different modes.

When the MAC matrix is different from this ideal case, for instance because of the presence of low MAC values along the main diagonal or of off-diagonal terms characterized by large values of the MAC, a supplement of investigation is needed since these anomalies can be the result of poor modeling, poor analysis of the experimental data, inappropriate choice of the DOFs included in the correlation or incorrect mode pairing.

MAC values between mode shapes corresponding to the same mode are always expected to be slightly lower than 1 in practical applications, due to the unavoidable uncertainties associated to the experimental estimates and the approximations inherent in numerical models. However, when the objective of the comparison is simply a verification of the numerical model, values of MAC in excess of 0.8–0.9 can be accepted as indicators of good consistency, while values less than 0.1–0.2 can be accepted as indicators of poor consistency. These limit values for the MAC must not be regarded in absolute terms, since there are some applications that demand high levels of consistency and some others that can accept lower MAC values, depending on the final use of the verified or updated model.

The MAC index is a measure of the overall consistency between two vectors, but it gives no information about the scatter between corresponding DOFs. When the information about the spatial distribution of the degree of correlation is of interest, extensions of the MAC have to be considered.

The Coordinate Modal Assurance Criterion (COMAC) (Ewins 2000) has been developed to identify the DOFs that yield low MAC values. In the case of

real-valued mode shapes and a set of  $N_m$  couples of paired experimental-numerical mode shapes, the COMAC associated to the r-th DOF can be computed as follows:

$$COMAC_r = \frac{\sum_{j=1}^{N_m} |\phi_{r,j}^a \cdot \phi_{r,j}^e|^2}{\sum_{j=1}^{N_m} (\phi_{r,j}^a)^2 \cdot \sum_{j=1}^{N_m} (\phi_{r,j}^e)^2} \quad (4.304)$$

where  $\phi_{r,j}^a$  and  $\phi_{r,j}^e$  denote the r-th component of the j-th analytical and experimental mode shape, respectively. Thus, the COMAC preserves the information about the individual DOFs. Low values of COMAC indicate poor correlation.

An Enhanced Coordinate Modal Assurance Criterion (ECOMAC) has also been proposed (Hunt 1992) to overcome the potential problems caused by erroneous calibration scaling or definition of the orientation of the sensors. In particular, the erroneous definition of sensor orientations causes the inversion of the sign of the associated components of the experimental mode shapes. Given a set of  $N_m$  couples of paired experimental-numerical mode shapes, the ECOMAC associated to the r-th DOF can be computed as follows:

$$ECOMAC_r = \frac{\sum_{j=1}^{N_m} |\phi_{r,j}^a - \phi_{r,j}^e|}{2N_m}. \quad (4.305)$$

Thus, the ECOMAC basically represents a measure of the average difference between the vector components corresponding to a certain DOF.

The role of the MAC index in the verification of numerical models has been already introduced. However, it can be used also to check the effectiveness of the adopted sensor layout and to assess the consistency between mode shape estimates provided by different OMA methods.

For instance, the effectiveness of sensor layout can be assessed through the computation of the AutoMAC matrix of the experimental mode shape estimates provided by a given OMA method. The entries of this matrix are represented by the values of the MAC obtained when a set of experimental mode shapes are correlated with themselves. Thus, the AutoMAC matrix is a symmetric matrix characterized by values all equal to 1 along the main diagonal. When the off-diagonal terms are all close to 0, the adopted sensor layout is effective in distinguishing the different modes; on the contrary, the presence of large off-diagonal terms means that similar mode shape vectors have been obtained for distinct modes. This requires a supplement of investigation to define the reasons of the correlation. It could be due to the fact that the orthogonality condition of the modes with respect to the mass matrix cannot be translated into a perfectly diagonal AutoMAC matrix. However, it is frequently an indicator of problems, such as spatial aliasing or spurious modes erroneously included into the set of identified physical modes. Including additional

sensors and eventually changing the measurement positions to enhance the observability of the different modes can solve the problems related to spatial aliasing and poor discrimination of the modes.

The consistency between mode shape estimates provided by different OMA methods can be assessed by the construction of the CrossMAC matrix. It is basically a MAC matrix but both the sets of vectors under comparison are made by experimental mode shape estimates. The two sets of experimental mode shapes have been obtained from the application of different OMA techniques. If the two set of mode shape estimates are consistent, a CrossMAC matrix characterized by values very close to 1 along the main diagonal and close to 0 elsewhere is obtained, provided that the AutoMAC matrices of the two sets of experimental mode shapes are approximately diagonal (absence of large off-diagonal terms).

---

## 4.9 Stabilization Diagrams for Parametric OMA Methods

An appropriate parameter setting in parametric OMA methods requires some prior knowledge about the order of the model to identify all modes in the analyzed frequency range. As a consequence, the number of modes has to be estimated in advance based on a physical insight or from the peaks in the output power spectra or in the singular value plots obtained by SVD of the output PSD matrix at all discrete frequency values.

More formal procedures are based on the comparison of models characterized by different orders according to some predefined criteria, which can eventually include penalties to avoid overfit (Ljung 1999). In the case of SSI methods it has also been shown that the order of the model can theoretically be determined from the experimental data as the rank of the Toeplitz matrix of correlations (Sect. 4.5.3.1) or of the projection matrix (Sect. 4.5.3.2) provided that the condition expressed by (4.207) is fulfilled. Unfortunately, due to noise and modeling inaccuracies, it often happens that no clear gap is visible in the sequence of the singular values of those matrices, thus resulting in serious problems for the determination of the correct model order. This is due to the fact that the factorization properties given by (4.208) and (4.239) do not exactly hold in the case of a finite number of data points. However, in the case of experimental/operational modal analysis the final objective is the identification of accurate and reliable modal parameter estimates rather than a good model as such. As a consequence, in practical applications a conservative approach is adopted based on the overspecification of the order of the model, which is set large enough to ensure the identification of all physical modes.

The amount of overspecification mainly depends on the characteristics of the analyzed dataset. In any case overmodeling introduces spurious poles, which have to be separated from the physical poles. This makes the modal parameter estimation more complicated. Spurious modes can be:

- noise modes: they are represented, for instance, by poles of the excitation system and, as such, they are due to physical reasons;

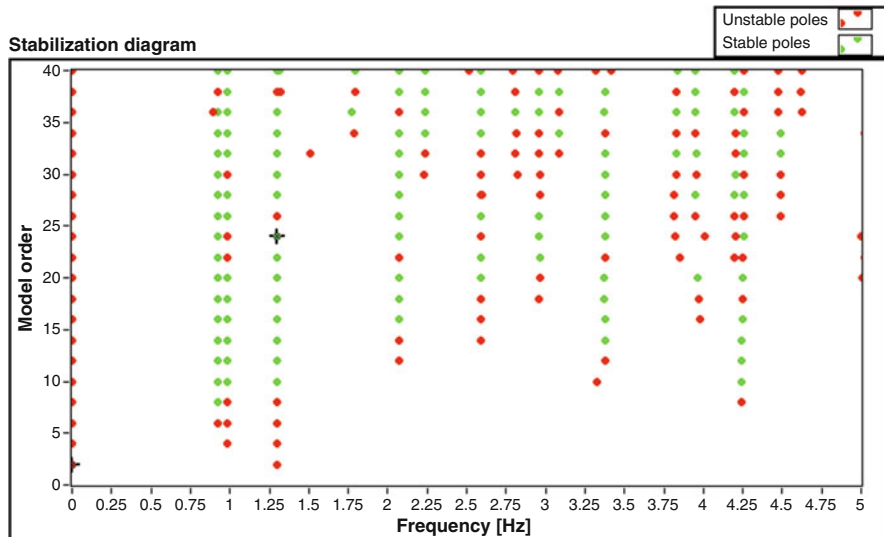


**Fig. 4.10** Stabilization diagram

- mathematical modes: they are created by the model in addition to the physical poles to ensure the mathematical description of the measured data, which are inevitably affected by slight imperfections (measurement noise, computational noise, modeling inaccuracies); thus, they are the result of the overestimation of the order of the model.

The separation of the physical poles from the spurious mathematical ones can take advantage of the construction of the so-called *stabilization diagram* (Fig. 4.10). It shows the poles obtained for different model orders as a function of their frequency. By tracking the evolution of the poles for increasing model orders, the physical modes can be identified from alignments of stable poles, since the spurious mathematical poles tend to be more scattered and typically do not stabilize. The alignments of stable poles can start at lower or higher values of the model order, depending on the level of excitation of the modes.

The construction of the stabilization diagram is based on the comparison of the poles associated to a given model order with those obtained from a one-order lower model. Only the poles that fulfill assigned user-defined stabilization criteria are labeled as stable. Typical stability requirements are expressed by the following inequalities:

$$\left( \frac{|f(n) - f(n+1)|}{f(n)} \right) < 0.01 \quad (4.306)$$

$$\left( \frac{|\xi(n) - \xi(n+1)|}{\xi(n)} \right) < 0.05 \quad (4.307)$$

$$\left[ 1 - MAC(\{\phi(n)\}, \{\phi(n+1)\}) \right] < 0.02. \quad (4.308)$$

In other words, (4.306) implies that the scatter between the estimates of the natural frequency at two subsequent model orders has to be lower than 1 % for a pole to be labeled as stable. Similar conditions on damping ratios and mode shapes are expressed by (4.307) and (4.308), respectively.

If all the conditions expressed by the previous inequalities are satisfied, the pole is labeled as stable. In the case of two stage methods, when the information about mode shapes is not available, the stabilization criteria apply to natural frequency and damping ratio estimates, only. It is worth pointing out that the relative criteria to assess the stability of the poles have to be used with caution. In fact, they can be particularly severe in the case of lightly damped modes, when the damping ratios are small and their percentage variations can be larger than the preset limit.

After the identification of the alignments of stable poles, eventual noise modes can be discarded according to physical criteria based on the expected damping ratio or the expected properties and aspect of the mode shapes.

It is worth pointing out that a bias of the modes can sometimes occur at low orders of the model. The estimates are biased since the poles represent a combination of different modes. This phenomenon is denoted by the splitting of a certain alignment of stable poles in the stabilization diagram into two separate columns from a certain model order. Thus, only if the maximum model order in the stabilization diagram has been set large enough, the bias of the modes can be identified. In this case, the modal parameters have to be estimated from the two alignments of poles generated after the splitting.

In the case of SSI methods, the stabilization diagram can be efficiently constructed once the factorization property given by (4.208) for Cov-SSI or (4.239) for DD-SSI has been computed for the maximum order of the model. In fact, models of lower order can be directly obtained by excluding an increasing number of singular values and vectors in the computation of  $[O_i]$  and  $[\Gamma_i]$  or  $[\hat{S}_i]$  (Peeters 2000). Moreover, the poles in complex conjugate pairs allow plotting the stabilization diagram considering only those characterized by positive imaginary component (and, therefore, positive damped frequency). As a result, the state-space model provides modal parameters for a number of modes equal to half of its order (Magalhaes and Cunha 2011).

In the case of OMA methods based on least squares estimators (LSCE, LSCF, and their poly-reference versions), coefficient constraint and basis function have a relevant influence on the discrimination between physical and mathematical modes. In fact, an appropriate choice of the constraint applied to the coefficients with respect to the adopted basis function can force the mathematical poles to be unstable (positive real part, negative damping) while the physical modes are stable (negative real part, positive damping). As a result, the distinction between

mathematical and physical poles is simplified, because it is based on the sign of damping. Mathematical poles are forced to be unstable by adopting the following combinations of coefficient constraint and basis function (Cauberghe et al. 2005):

- the lowest-order coefficient is unitary and the basis function is  $z^{-1}$ ;
- the highest-order coefficient is unitary and the basis function is  $z$ .

When the adopted basis function is  $z^{-1}$ , the denominator coefficients in the LSCF method are computed as follows:

$$\{\theta_d\} = \left[ \begin{array}{c} 1 \\ -[M_{(2:n+1, 2:n+1)}]^{-1} [M_{(2:n+1, 1)}] \end{array} \right] \quad (4.309)$$

where  $[M_{(2:n+1, 2:n+1)}]$  is the submatrix made by the last  $n$  rows and  $n$  columns of  $[M]$  (4.134), while  $[M_{(2:n+1, 1)}]$  is the submatrix made by the last  $n$  rows and the first column of  $[M]$ . In the case of the p-LSCF method, instead, the denominator coefficients are computed as follows:

$$[\alpha] = \left[ \begin{array}{c} [I_l] \\ -[M_{(l+1:(n+1)l, l+1:(n+1)l)}]^{-1} [M_{(l+1:(n+1)l, 1:l)}] \end{array} \right] \quad (4.310)$$

where  $[M_{(l+1:(n+1)l, l+1:(n+1)l)}]$  is the submatrix made by the last  $nl$  rows and  $nl$  columns of  $[M]$  (4.167), while  $[M_{(l+1:(n+1)l, 1:l)}]$  is the submatrix made by the last  $nl$  rows and the first  $l$  columns of  $[M]$ . In this last case, the roots of the denominator polynomial are the eigenvalues of the following companion matrix:

$$[A] = \begin{bmatrix} -[A_n]^{-1}[A_{n-1}] & -[A_n]^{-1}[A_{n-2}] & \cdots & -[A_n]^{-1}[A_1] & -[A_n]^{-1}[A_0] \\ [I] & [0] & \cdots & [0] & [0] \\ \vdots & \vdots & \ddots & \vdots & \vdots \\ [0] & [0] & \cdots & [I] & [0] \end{bmatrix}. \quad (4.311)$$

In Sect. 4.4.3.2, the procedure for mode shape estimation in the context of the p-LSCF method has been discussed. Another approach consists in the conversion of the RMFD model into a state-space model (Magalhaes and Cunha 2011). In this case, the model coefficients have to be rearranged into the output influence matrix as follows:

$$[C] = \left[ \begin{array}{cccc} [B_{n-1}] - [B_n][A_n]^{-1}[A_{n-1}] & \cdots & [B_0] - [B_n][A_n]^{-1}[A_0] \end{array} \right] \quad (4.312)$$

where:

$$[B_j] = \begin{bmatrix} \langle B_{1,j} \rangle \\ \vdots \\ \langle B_{o,j} \rangle \\ \vdots \\ \langle B_{l,j} \rangle \end{bmatrix}. \quad (4.313)$$

The theoretical derivations can be found elsewhere (Reynders 2009). Once the matrices  $[A]$  and  $[C]$  are known from (4.311) and (4.313), the modal parameters are obtained as described in Sect. 4.5.3.1.

The combination coefficient constraint-basis function has an influence on damping ratio estimates only in the case of discrete-time models. The superior quality of the stabilization diagram, that simplifies its interpretation, explains why discrete-time models are preferred over continuous-time models.

Some authors (Peeters and Van der Auweraer 2005, Cauberghe 2004) suggest the application of p-LSCF in combination with positive power spectra instead of one-sided spectra, because this yields very clear stabilization diagrams. The improvement in the quality of stabilization can be appreciated by comparing the plots shown in Fig. 4.11. They represent the stabilization diagrams obtained from the application of p-LSCF to one-sided spectra (Fig. 4.11a) and positive power spectra (Fig. 4.11b) estimated from the same dataset. However, the accuracy of mode shape estimates might be negatively affected when positive power spectra are used. For this reason, the comparison of the mode shape estimates obtained from the application of p-LSCF to positive power spectra with those obtained from one-sided spectra is recommended.

## 4.10 Applications

### 4.10.1 Basic Frequency Domain

*Task.* Develop software for output-only modal identification based on the Basic Frequency Domain (Peak Picking) method. Alternatively, install and use the software in “Chapter 4/BFD”. Use the data in “Sample record 12 channels – sampling frequency 10 Hz.txt” in the folder “Chapter 2/Correlation” of the disk accompanying the book. Data in the file are organized in columns: time is in the first column; data are in the next 12 columns. Assume that the data have been collected on a framed structure made by three floors and that four sensors per floor have been installed according to the layout shown in Fig. 4.12. Assume that the time series in the file are ordered for increasing sensor number (excluding the column of time, the first column holds the data from sensor #1, the second column holds the data from sensor #2, and so on; the last column holds the data from sensor #12).

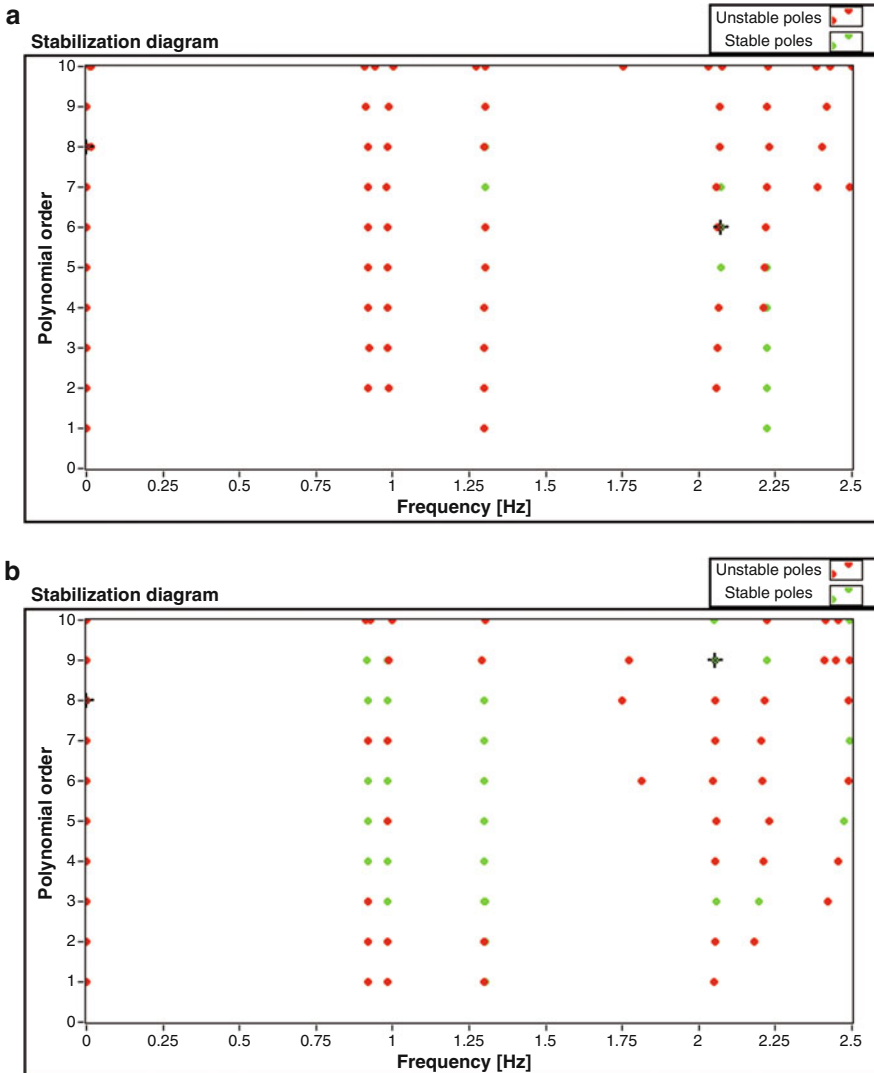
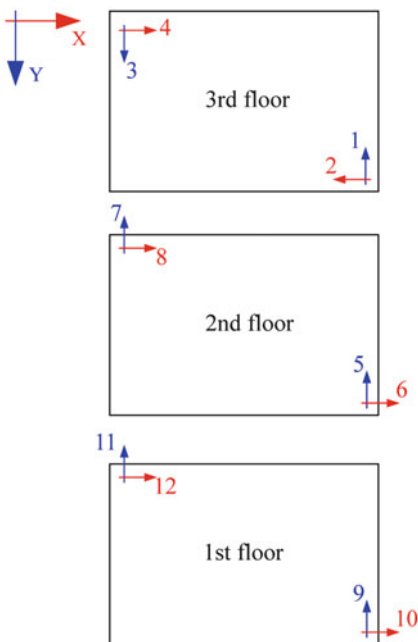


**Fig. 4.11** Stabilization diagram obtained from the application of p-LSCF to one-sided spectra (a) and positive power spectra (b)

*Suggestions.* Starting from the sample code for computation of power spectra developed in Chap. 2, develop software for output-only modal identification based on the BFD (Peak Picking) method. It should be able to carry out the following operations (adoption of state machine architecture or event structure is recommended):

- At start-up, load the data and set the main analysis parameters (window, number of segments, decimation factor, overlap);
- Compute the PSD matrix and show its trace in a plot to identify the peaks that can be recognized as possible structural modes (possible structural modes can be eventually identified also as recurrent peaks in the auto-power spectra);

**Fig. 4.12** Sensor layout for applications



- After having identified the peak frequencies, select a reference channel and compute its auto-power spectrum and the cross-power spectra with all the remaining channels;
- Show the spectra in terms of amplitude and phase and the coherence functions;
- Collect the values of amplitude, phase, and coherence at the previously identified peak frequencies; take advantage of the coherence plots to identify structural modes and to define the nature (bending, torsion) of the mode; if certain peaks are missing in the auto-power spectrum of the reference channel, repeat the previous steps with a different choice of the reference channel in order to identify also those modes;
- Normalize the mode shape vectors so that the component with maximum amplitude is equal to 1;
- Create a report of modal identification results in terms of natural frequencies and mode shapes.

It is worth pointing out that the accuracy of natural frequency estimates depends on the frequency resolution; thus, long records of the structural response to ambient vibrations are recommended to compute spectra characterized by a large number of averages and a fine frequency resolution (in the order of 0.01 Hz).

Use the BFD method to identify at least the three fundamental modes of the structure. Create a report with the identified natural frequencies and mode shape estimates; plot the mode shapes considering the floors as rigid diaphragms. Compute the AutoMAC matrix (Sect. 4.8.2.2).

**Table 4.1** Mode shape estimate for the first mode (0.92 Hz—channel #2 as reference)

Amplitude	Phase	Normalized mode shape
6.31E-06	-0.02	-0.114
5.49E-05	0.00	-0.990
2.11E-05	-0.03	-0.380
5.54E-05	3.14	1.000
4.44E-06	-0.03	-0.080
4.19E-05	-3.14	0.756
1.10E-05	3.11	0.198
4.24E-05	3.14	0.764
3.36E-06	0.00	-0.061
1.82E-05	-3.13	0.329
5.27E-06	3.12	0.095
1.90E-05	-3.13	0.343

**Table 4.2** Mode shape estimate for the second mode (0.98 Hz—channel #1 as reference)

Amplitude	Phase	Normalized mode shape
7.42E-0.5	0.00	-0.828
6.54E-06	-0.27	-0.073
8.96E-05	-3.12	1.000
1.85E-05	3.05	0.207
4.60E-05	0.00	-0.513
6.01E-06	2.92	0.067
5.52E-05	0.01	-0.616
9.03E-06	2.99	0.101
1.86E-05	-0.02	-0.207
1.64E-06	2.80	0.018
2.12E-05	0.00	-0.236
4.21E-06	3.02	0.047

Results obtained by the Authors of this book by applying the BFD method are reported in Tables 4.1, 4.2, and 4.3 as reference. The identified mode shapes are also shown in Fig. 4.13, based on the assumption of rigid diaphragms. Real-valued normalized mode shapes were constructed as discussed in Sect. 4.8.1. Channel #2 was selected as reference for the identification of the first and the third mode, while channel #1 was the reference for the identification of the second mode.

*Sample software.* Sample software to carry out output-only modal identification based on the BFD method can be found in “Chapter 4/BFD” of the disk accompanying the book.

**Table 4.3** Mode shape estimate for the second mode (1.30 Hz—channel #2 as reference)

Amplitude	Phase	Normalized mode shape
4.62E-05	-3.13	1.000
8.58E-06	0.00	-0.186
4.17E-05	-3.12	0.903
6.43E-07	2.88	0.014
2.79E-05	-3.13	0.603
5.36E-06	3.14	0.116
2.49E-05	0.02	-0.539
1.32E-06	0.09	-0.029
1.01E-05	-3.13	0.218
2.16E-06	-3.14	0.047
8.91E-06	0.02	-0.193
7.27E-07	0.03	-0.016

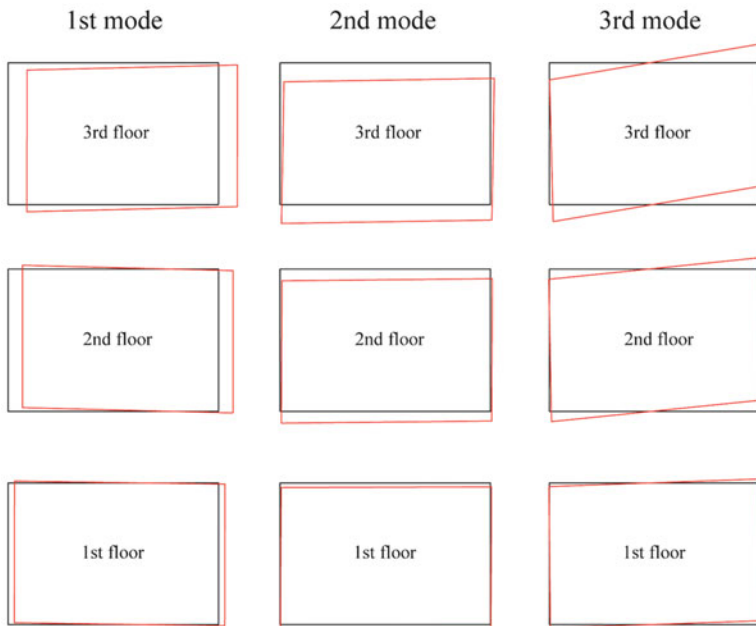


**Fig. 4.13** Plots of the identified mode shapes

#### 4.10.2 Frequency Domain Decomposition

*Task.* Develop software for output-only modal identification based on the FDD method. Alternatively, install and use the software in “Chapter 4/FDD”. Repeat the identification of the fundamental modes of the structure of Sect. 4.10.1. Operational response data are in “Sample record 12 channels – sampling frequency 10 Hz.txt” in

the folder “Chapter 2/Correlation” of the disk accompanying the book. Organization of data in the file has been described in Sect. 4.10.1. Sensor layout is shown in Fig. 4.12.

*Suggestions.* The previously developed software for Peak Picking can be easily extended to carry out output-only modal identification according to the FDD method. Here is the list of the main tasks in software development:

- At start-up, load the data and set the main analysis parameters (window, number of segments, decimation factor, overlap);
- Compute the PSD matrix, organizing the data into an array of  $l \times l$  square matrices; each matrix holds the values of the power spectra at a certain frequency line in the form of complex values;
- At each frequency line compute the SVD of the complex-valued PSD matrix; concatenation of the vectors of the singular values obtained at the various discrete frequencies yields the singular value plots;
- Plot all the singular values as a function of frequency in the same plot; create and use cursors to identify the peaks corresponding to structural modes; the peak frequency can be considered an estimate of the natural frequency (for lightly damped systems) as in the case of the BFD method; the peaks are usually selected in the first singular value plot, unless repeated modes are present;
- Collect the singular vectors associated to the selected singular values at the various frequencies; normalize these vectors so that the component characterized by the largest amplitude is set equal to 1; with a few exceptions for closely spaced modes (Sect. 4.4.2), the singular vectors at the peak frequencies are good mode shape estimates;
- Create a report of modal identification results in terms of natural frequencies and mode shapes.

It is worth noting that also in the case of FDD the accuracy of natural frequency estimates depends on the frequency resolution; thus, long records of the structural response to ambient vibrations are recommended to obtain high quality singular value plots as a result of spectra characterized by a large number of averages and a fine frequency resolution (in the order of 0.01 Hz). Natural frequency estimates independent of the frequency resolution and damping estimates can be obtained by the EFDD method. In this case, the following additional steps have to be included in the previous list before reporting:

- For each peak frequency, compare the singular vector associated to the selected peak frequency with the singular vectors at the nearby frequencies; retain all the singular values in the vicinity of the peak whose singular vectors yield a MAC (4.109) with the singular vector associated to the peak frequency larger than a user-defined MAC Rejection Level (usually, 0.8); the selected singular values belong to the SDOF Bell function of the considered mode;
- Compute the IFT of the SDOF Bell functions to obtain the approximated SDOF correlation functions (Sect. 4.4.2);
- For each correlation function, select the portion characterized by large amplitude (removing the tails where the influence of noise is relevant, and eventually neglecting also the first cycle) and estimate the damping ratio by the logarithmic

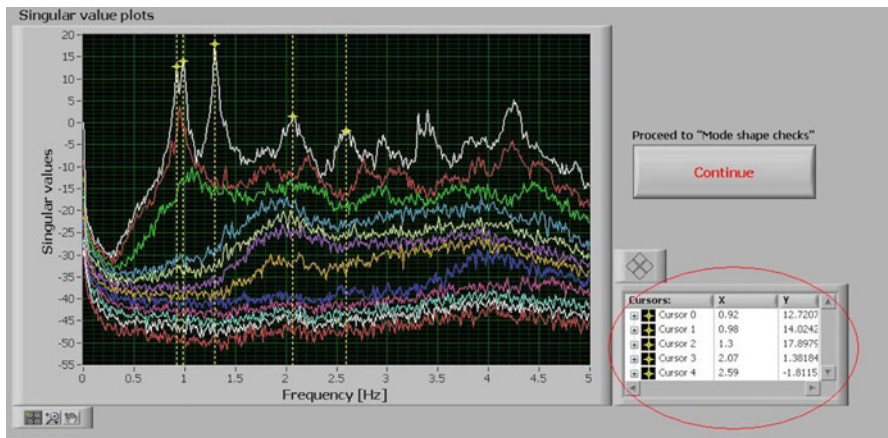


**Fig. 4.14** Singular value plots and cursor legend (in the oval)

decrement technique; get an estimate of the damped frequency independent of the frequency resolution from the number of zero crossing points in the selected interval; use the estimates of damped frequency and damping ratio to compute the natural frequency (4.110).

Use the FDD method to identify the three fundamental modes of the structure. Cursors can be added by right-clicking on the cursor legend (marked by the oval in Fig. 4.14) and selecting “Create Cursor – Single-Plot”; cursors are attached to one of the singular value plots by right-clicking on the cursor legend and selecting “Snap To” and the number of the plot.

Since the fundamental modes are normal, real-valued mode shapes can be easily recovered from the (normalized) complex-valued singular vectors (Sect. 4.8.1). Compute the AutoMAC (Sect. 4.8.2.2). Compare the obtained results with the corresponding natural frequency and mode shape estimates obtained from BFD (Sect. 4.10.1). Report the results of the comparison in a table showing, for each mode, the frequency scatter between the natural frequency estimates (4.298) and the CrossMAC (Sect. 4.8.2.2) between corresponding mode shapes. Use COMAC (4.304) or ECOMAC (4.305) to identify the DOFs causing the major differences in the mode shape estimates provided by the two methods.

*Sample software.* Sample software to carry out output-only modal identification based on the FDD method can be found in “Chapter 4/FDD” of the disk accompanying the book.

### 4.10.3 Least Squares Complex Frequency

*Task.* Develop software for output-only modal identification based on the LSCF method. Alternatively, install and use the software in “Chapter 4/LSCF”. Repeat the identification of the fundamental modes of the structure of Sect. 4.10.1.

Operational response data are in “Sample record 12 channels – sampling frequency 10 Hz.txt” in the folder “Chapter 2/Correlation” of the disk accompanying the book. Organization of data in the file has been described in Sect. 4.10.1. Sensor layout is shown in Fig. 4.12.

*Suggestions.* The previously developed software for Peak Picking can be extended to carry out output-only modal identification according to the LSCF method. Here is the list of the main tasks in software development:

- At start-up, load the data and set the main analysis parameters (window, number of segments, decimation factor, overlap, maximum polynomial order for the construction of the stabilization diagram);
- Compute the PSD matrix;
- Select the  $z$ -domain basis function:  $z_f$  (4.116) or  $z_f^{-1}$ ;
- Assuming that  $z_f$  has been adopted as basis function (in the case of  $z_f^{-1}$  the implementation steps are the same; the only difference is in the coefficient constraint and, therefore, in the formulation for computation of the denominator coefficients; refer to Sect. 4.9 for more details), compute  $z_f^j$  ( $j = 0, \dots, n$ , where  $n$  denotes the polynomial order) at all discrete frequency lines and build the matrices  $[\Gamma_k]$  (4.126) and  $[\Upsilon_k]$  (4.127) for  $k = 1, \dots, l \times l$ ;
- Compute the matrices  $[R_k]$  (4.129),  $[S_k]$  (4.130), and  $[T_k]$  (4.131) for  $k = 1, \dots, l \times l$ ;
- Compute the  $(n+1) \times (n+1)$  matrix  $[M]$  as follows:

$$[M] = \sum_{k=1}^{l \times l} \left( [T_k] - [S_k]^H [R_k]^{-1} [S_k] \right) \quad (4.314)$$

- Compute  $\{\theta_d\}$  (4.135);
- Use “Polynomial Roots.vi” under “Mathematics – Polynomial” in the Functions Palette to compute the roots  $z_r$ ;
- Convert the poles from discrete time to continuous time (4.136);
- Remove the unstable poles (Sect. 4.9);
- Compute natural frequencies (4.137) and damping ratios (4.139) from the remaining poles;
- Repeat the last eight steps for different model orders and plot the stabilization diagram reporting the poles as a function of frequency for different model orders (Sect. 4.9);
- Identify the alignments of stable poles in the stabilization diagram, which correspond to structural modes; select a pole for each identified structural mode;
- Use the selected poles (holding the information about natural frequencies and damping ratios) to compute the residues according to the LSFD method (4.147); rearrange the vector  $\{R_k\}$  into the  $l \times l$  residue matrices  $[R_j]$ ;
- Compute the SVDs of the residue matrices  $[R_j]$  (4.148); for each SVD the first singular vector yields a mode shape estimate;

- Normalize the mode shape vectors so that the component with maximum amplitude is equal to 1;
- Create a report of modal identification results in terms of natural frequencies and mode shapes.

Appropriately replacing the equations (Sect. 4.4.3.2), the p-LSCF method can be implemented in a similar way.

Use the LSCF method to identify the three fundamental modes of the structure. Since they are normal modes, real-valued mode shapes can be easily recovered from the (normalized) complex-valued singular vectors (Sect. 4.8.1). Compute the AutoMAC matrix (Sect. 4.8.2.2). Compare the obtained results with those provided by FDD or BFD. In particular, compute the scatters between corresponding natural frequency estimates (4.298) and the CrossMAC matrix (Sect. 4.8.2.2).

*Sample software.* Sample software to carry out output-only modal identification based on the LSCF method can be found in “Chapter 4/LSCF” of the disk accompanying the book.

#### 4.10.4 Stochastic Subspace Identification

*Task.* Develop software for output-only modal identification based on the Cov-SSI method. Alternatively, install and use the software in “Chapter 4/Cov-SSI”. Repeat the identification of the fundamental modes of the structure of Sect. 4.10.1. Operational response data are in “Sample record 12 channels – sampling frequency 10 Hz. txt” in the folder “Chapter 2/Correlation” of the disk accompanying the book. Organization of data in the file has been described in Sect. 4.10.1. Sensor layout is shown in Fig. 4.12.

*Suggestions.* The software implementation of the Cov-SSI algorithm for output-only modal identification is based on the following steps:

- At start-up, load the data and eventually set the filter parameters and the decimation factor;
- Compute the PSD matrix and show its trace in a plot to estimate the number of structural modes in the frequency range under investigation; set the number of block rows accordingly; the condition expressed by (4.207) must be fulfilled; the product  $l \times i$  defines the limit value of the maximum model order that can be adopted in the construction of the stabilization diagram; however, the maximum model order in the stabilization plot is usually much lower than  $l \times i$ , and it is defined so that only a subset of the singular values and vectors of the block Toeplitz matrix of correlations ((4.206), (4.211), and (4.212)) is retained;
- Compute the SVD of the block Toeplitz matrix of correlations ((4.206), (4.211), and (4.212)) and define the maximum model order in the construction of the stabilization diagram (Sect. 4.9);
- From the retained subset of singular values and vectors of the block Toeplitz matrix of correlations compute the observability matrix  $[O_i]$  (4.213) and the reversed controllability matrix  $[\Gamma_i]$  (4.214); the first  $l$  rows of  $[O_i]$  and the last

$l$  rows of  $[\Gamma_i]$  yield the output influence matrix  $[C]$  and the next state-output covariance matrix  $[G]$ , respectively;

- Compute the state matrix  $[A]$  from (4.216) and (4.217); alternatively, it can be computed according to (4.218) and (4.219), with the weights given by (4.220) or (4.224);
- The poles in discrete time are obtained by the eigenvalue decomposition of  $[A]$  (4.77); they have to be converted from discrete time to continuous time (4.136) in order to compute natural frequency (4.137) and damping ratio (4.139) from each pole; the corresponding mode shapes are obtained from the eigenvectors of  $[A]$  according to (4.79);
- Repeat the last three steps for different model orders and plot the stabilization diagram reporting the poles as a function of frequency for different model orders (Sect. 4.9); in this case, also the information about the mode shapes (4.308) is used for the construction of the stabilization diagram;
- Identify the alignments of stable poles in the stabilization diagram, which correspond to structural modes; select a pole for each identified structural mode;
- Normalize the mode shape vector associated to each pole so that the component with maximum amplitude is equal to 1;
- Create a report of modal identification results in terms of natural frequencies and mode shapes.

DD-SSI can be implemented in a similar way according to the following list of steps:

- The first two steps are the same of Cov-SSI; the only difference is that the block Toeplitz matrix of correlation is replaced by the block Hankel matrix of raw data (4.229);
- Compute the LQ factorization of the block Hankel matrix of the outputs and the projections  $[P_i]$  and  $[P_{i-1}]$  ((4.234), (4.235), (4.236), and (4.237));
- Compute the SVD of  $[P_i]$  (4.240) and define the maximum model order in the construction of the stabilization diagram;
- From the retained subset of singular values and vectors of  $[P_i]$  compute the observability matrix  $[O_i]$  (4.241) and the Kalman filter state sequence  $[\hat{S}_i]$  (4.242);
- Compute  $[\hat{S}_{i+1}]$  from (4.244);
- Compute the state matrix  $[A]$  and the output influence matrix  $[C]$  from (4.246); alternatively, the state matrix can be computed directly from the observability matrix according to (4.219) or (4.252), while the first  $l$  rows of  $[O_i]$  yield the output influence matrix;
- The poles in discrete time are obtained by the eigenvalue decomposition of  $[A]$  (4.77); they have to be converted from discrete time to continuous time (4.136) in order to compute natural frequency (4.137) and damping ratio (4.139) from each pole; the corresponding mode shapes are obtained from the eigenvectors of  $[A]$  according to (4.79);
- Repeat the last four steps for different model orders and plot the stabilization diagram reporting the poles as a function of frequency for different model orders (Sect. 4.9); in this case, also the information about the mode shapes (4.308) is used for the construction of the stabilization diagram;

- Proceed as in the case of Cov-SSI (last three steps) to select the parameters of the structural modes and create a report of modal identification results.

Use the Cov-SSI method to identify the three fundamental modes of the structure. Since they are normal modes, real-valued mode shapes can be easily recovered from the (normalized) complex-valued singular vectors (Sect. 4.8.1). Compute the AutoMAC matrix (Sect. 4.8.2.2). Compare the obtained results with those provided by FDD and LSCF. In particular, compute the scatters between corresponding natural frequency and damping ratio (LSCF/Cov-SSI only) estimates, and the CrossMAC matrices (Sect. 4.8.2.2) with the mode shape estimates provided by LSCF and FDD.

*Sample software.* Sample software to carry out output-only modal identification based on the Cov-SSI method can be found in “Chapter 4/Cov-SSI” of the disk accompanying the book.

#### 4.10.5 Second Order Blind Identification

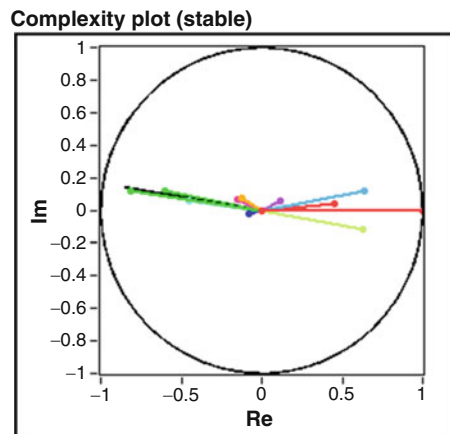
*Task.* Install and use the software in “Chapter 4/SOBI” for output-only modal identification according to the SOBI method. Identify the modes of the structure of Sect. 4.10.1 in the range 0–5 Hz. Compare the results provided by SOBI with those obtained from Cov-SSI or any other method yielding complex-valued mode shape estimates. Operational response data are in “Sample record 12 channels – sampling frequency 10 Hz.txt” in the folder “Chapter 2/Correlation” of the disk accompanying the book. Organization of data in the file has been described in Sect. 4.10.1. Sensor layout is shown in Fig. 4.12.

*Suggestions.* When SOBI is used for output-only modal identification, mode shapes are directly obtained from the mixing matrix (Sect. 4.5.4). Natural frequencies and damping ratios can be estimated from the auto-correlations of the sources as follows:

- for each correlation function, select the portion characterized by large amplitude (removing the tails where the influence of noise is relevant, and eventually neglecting also the first cycle);
- get an estimate of the damping ratio by the logarithmic decrement technique;
- get an estimate of the damped frequency independent of the frequency resolution from the number of zero crossing points in the selected interval;
- use the estimates of damped frequency and damping ratio to compute the natural frequency (4.110).

Use the Cov-SSI method to identify also the higher modes of the structure. Among them, the mode at 2.59 Hz shows appreciable imaginary parts in the mode shape components (Fig. 4.15). Comparison of the modal parameter estimates provided by Cov-SSI with those obtained from SOBI results in a good agreement for the fundamental modes. The mode at 2.07 Hz cannot be properly identified by SOBI. About the mode at 2.59 Hz, SOBI yields a mode shape estimate characterized by a CrossMAC with the corresponding estimate by Cov-SSI that is

**Fig. 4.15** Complexity plot of the mode at 2.59 Hz (mode shape estimate obtained from Cov-SSI)



slightly lower than the CrossMAC values obtained for the fundamental modes. The difference can be addressed to the fact that SOBI forces the mode shape estimates to be real-valued.

*Sample software.* Sample software to carry out output-only modal identification based on the SOBI method can be found in “Chapter 4/SOBI” of the disk accompanying the book.

#### 4.10.6 Influence of Sensor Layout

*Task.* Remove channels #3, #7, and #11 from the dataset in “Sample record 12 channels – sampling frequency 10 Hz.txt” in the folder “Chapter 2/Correlation” of the disk accompanying the book and update the sensor layout shown in Fig. 4.12. Repeat the identification of the modes of the structure of Sect. 4.10.1 by a method of your choice among the previous ones. Compare the AutoMAC matrices before and after the removal of the above-mentioned channels.

*Suggestions.* Even if both translations and torsions are still observable after sensor removal, the presence of large off-diagonal elements in the AutoMAC matrix highlights that the new layout is less effective than the previous one in distinguishing some of the modes.

---

## References

- Allemang RJ, Brown DL (1982) A correlation coefficient for modal vector analysis. In: Proc 1st international modal analysis conference, November 8–10, 1982, Orlando, FL
- Allemang RJ, Brown DL (1998) A unified matrix polynomial approach to modal identification. J Sound Vib 211(3):301–322
- Andersen P (1997) Identification of civil engineering structures using vector ARMA models, Ph.D. thesis. University of Aalborg, Aalborg

- Andersen P, Brincker R (1999) Estimation of modal parameters and their uncertainties. In: Proc XVII international modal analysis conference, February 8–11, 1999, Kissimmee, FL
- Andersen P, Brincker R, Kirkegaard PH (1996) Theory of covariance equivalent ARMAV models of civil engineering structures. In: Proc XIV international modal analysis conference, February 12–15, 1996, Dearborn, MI
- Ans B, Héault J, Jutten C (1985) Adaptive neural architectures: detection of primitives. In: Proc COGNITIVA'85, June 4–7, 1985, Paris
- Aoki M (1987) State space modeling of time series. Springer, Berlin
- Asmussen JC, Brincker R, Ibrahim SR (1999) Statistical theory of the vector random decrement technique. *J Sound Vib* 226(2):329–344
- Bartlett MS (1946) The theoretical specification and sampling properties of autocorrelated time-series. *J R Stat Soc* 8(1):27–41, Supplement
- Belouchrani A, Abed-Meraim K, Cardoso JF, Moulines E (1997) A blind source separation technique using second-order statistics. *IEEE Trans Signal Process* 45:434–444
- Bendat JS, Piersol AG (2000) Random data: analysis and measurement procedures, 3rd edn. Wiley, New York, NY
- Brincker R, Andersen P (1999) ARMA models in modal space. In: Proc XVII international modal analysis conference, February 8–11, 1999, Kissimmee, FL
- Brincker R, Andersen P (1999) Ambient response modal analysis for large structures. In: Proc 6th Int Congr on Sound and Vib, July 5–8, 1999, Copenhagen
- Brincker R, Zhang L (2009) Frequency domain decomposition revisited. In: Proc 3rd international operational modal analysis conference, May 4–6, 2009, Portonovo
- Brincker R, Krenk S, Kirkegaard PH, Rytter A (1992) Identification of dynamical properties from correlation function estimates. *Bygningsstatistiske Meddelelser* 63(1):1–38
- Brincker R, Zhang L, Andersen P (2001) Modal identification of output-only systems using frequency domain decomposition. *Smart Mat Struct* 10:441–445
- Cardoso JF, Souloumiac A (1996) Jacobi angles for simultaneous diagonalization. *SIAM J Matrix Anal Appl* 17:161–164
- Cauberghe B (2004) Applied frequency-domain system identification in the field of experimental and operational modal analysis, Ph.D. thesis. Vrije Universiteit Brussels, Brussels
- Cauberghe B, Guillaume P, Verboven P, Vanlanduit S, Parloo E (2005) On the influence of the parameter constraint on the stability of the poles and the discrimination capabilities of the stabilisation diagrams. *Mech Syst Signal Process* 19:989–1014
- Chelidze D, Zhou W (2006) Smooth orthogonal decomposition-based vibration mode identification. *J Sound Vib* 292:461–473
- Chopra AK (2000) Dynamics of structures – theory and applications to earthquake engineering, 2nd edn. Prentice Hall, Upper Saddle River, NJ
- Cole HA (1968) On-the-line analysis of random vibrations. In: Proc AIAA/ASME 9th structures, structural dynamics and materials Conf, April 1–3, 1968, Palm Springs, CA
- Cole HA (1973) On-line failure detection and damping measurement of aerospace structures by random decrement signatures. NASA contractor report CR22-05
- Comon P (1994) Independent component analysis, a new concept? *Signal Process* 36:287–314
- De Troyer T, Guillaume P, Steenackers G (2009a) Fast variance calculation of polyreference least-squares frequency-domain estimates. *Mech Syst Signal Process* 23:1423–1433
- De Troyer T, Guillaume P, Pintelon R, Vanlanduit S (2009b) Fast calculation of confidence intervals on parameter estimates of least-squares frequency-domain estimators. *Mech Syst Signal Process* 23:261–273
- Devriendt C, Guillaume P (2007) The use of transmissibility measurements in output-only modal analysis. *Mech Syst Signal Process* 21(7):2689–2696
- Devriendt C, Guillaume P (2008) Identification of modal parameters from transmissibility measurements. *J Sound Vib* 314:343–356
- Devriendt C, De Sitter G, Vanlanduit S, Guillaume P (2009) Operational modal analysis in the presence of harmonic excitations by the use of transmissibility measurements. *Mech Syst Signal Process* 23:621–635

- Devriendt C, Steenackers G, De Sitter G, Guillaume P (2010) From operating deflection shapes towards mode shapes using transmissibility measurements. *Mech Syst Signal Process* 24:665–677
- Even J, Moisan E (2005) Blind source separation using order statistics. *Signal Process* 85:1744–1758
- Ewins DJ (2000) *Modal testing: theory, practice and application*, 2nd edn. Research Studies Press Ltd., Baldock
- Feeny BF, Kappagantu R (1998) On the physical interpretation of proper orthogonal modes in vibrations. *J Sound Vib* 211:607–616
- Felber AJ (1993) Development of a hybrid bridge evaluation system, Ph.D. thesis. University of British Columbia, Vancouver
- Franklin GF, Powell JD, Workman ML (2006) *Digital control of dynamic systems*, 3rd edn. Ellis-Kagle Press, Half Moon Bay, CA
- Friswell MI, Mottershead JE (1995) *Finite element model updating in structural dynamics*. Kluwer Academic Publishers, Dordrecht
- Gade S, Møller NB, Herlufsen H, Konstantin-Hansen H (2005) Frequency domain techniques for operational modal analysis. In: Proc 1st international operational modal analysis conference, April 26–27, 2005, Copenhagen
- Golub GH, Van Loan CF (1996) *Matrix computations*, 3rd edn. The Johns Hopkins University Press, Baltimore, MD
- Gouttebroze S, Lardies J (2001) On using the wavelet transform in modal analysis. *Mech Res Comm* 28(5):561–569
- Han J-G, Ren W-X, Xu X-X (2005) Wavelet-based modal parameter identification through operational measurements. In: Proc 1st international operational modal analysis conference, April 26–27, 2005, Copenhagen
- Hanson D, Randall RB, Antoni J, Thompson DJ, Waters TP, Ford RAJ (2007) Cyclostationarity and the cepstrum for operational modal analysis of mimo systems – Part I: modal parameter identification. *Mech Syst Signal Process* 21(6):2441–2458
- Herlufsen H, Andersen P, Gade S, Møller N (2005) Identification techniques for operational modal analysis – an overview and practical experiences. In: Proc 1st international operational modal analysis conference, April 26–27, 2005, Copenhagen
- Hermans L, Van Der Auweraer H (1999) Modal testing and analysis of structures under operational conditions: industrial applications. *Mech Syst Signal Process* 13(2):193–216
- Heylen W, Lammens S, Sas P (1998) *Modal analysis theory and testing*. Katholieke Universiteit Leuven, Leuven
- Ho BL, Kalman RE (1966) Effective construction of linear state-variable models from input/output data. *Regelungstechnik* 14:545–548
- Hunt DL (1992) Application of an enhanced coordinate modal assurance criterion (ECOMAC). In: Proc 10th international modal analysis conference, February 3–7, 1992, San Diego, CA
- Ibrahim SR (1977) Random decrement technique for modal identification of structures. *J Spacecraft Rockets* 14(11):696–700
- Ibrahim SR, Mikulcik EC (1977) A method for direct identification of vibration parameters from the free response. *Shock Vib Bul* 47:183–198
- Ibrahim SR, Brincker R, Asmussen JC (1996) Modal parameter identification from responses of general unknown random inputs. In: Proc 14th international modal analysis conference, February 12–15, 1996, Dearborn, MI
- Jacobsen N-J, Andersen P, Brincker R (2008) Applications of frequency domain curve-fitting in the EFDD technique. In: Proc 26th international modal analysis conference, February 4–7, 2008, Orlando, FL
- James GH, Carne TG, Lauffer JP, Nord AR (1992) Modal testing using natural excitation. In: Proc 10th international modal analysis conference, February 3–7, 1992, San Diego, CA
- James GH, Carne TG, Lauffer JP (1995) The natural excitation technique (next) for modal parameter extraction from operating structures. *J Anal Exp Modal Anal* 10(4):260–277

- Juang J-N (1994) Applied system identification. PTR Prentice Hall, Englewood Cliffs, NJ
- Juang J-N, Pappa RS (1985) An eigensystem realization algorithm for modal parameter identification and model reduction. *AIAA J Guid Contr Dynam* 8:620–627
- Kailath T (1980) Linear systems. Prentice Hall, Englewood Cliffs, NJ
- Katayama T (2005) Subspace methods for system identification. Springer, London
- Kerschen G, Golinval JC (2002) Physical interpretation of the proper orthogonal modes using the singular value decomposition. *J Sound Vib* 249:849–865
- Kerschen G, Golinval JC, Vakakis AF, Bergman LA (2005) The method of proper orthogonal decomposition for dynamical characterization and order reduction of mechanical systems: an overview. *Nonlin Dynam* 41:147–170
- Kerschen G, Poncelet F, Golinval JC (2007) Physical interpretation of independent component analysis in structural dynamics. *Mech Syst Signal Process* 21:1561–1575
- Lardies J, Gouttebroze S (2002) Identification of modal parameters using the wavelet transform. *Int J Mech Sci* 44:2263–2283
- Ljung L (1999) System identification: theory for the user, 2nd edn. Prentice Hall, Upper Saddle River, NJ
- Magalhaes F, Cunha A (2011) Explaining operational modal analysis with data from an arch bridge. *Mech Syst Signal Process* 25:1431–1450
- Maia NMM, Silva JMM, He J, Lieven NAJ, Lin RM, Skingle GW, To W-M, Urgueira APV (1997) Theoretical and experimental modal analysis. Research Studies Press, Taunton
- McNeill SI, Zimmerman DC (2008) A framework for blind modal identification using joint approximate diagonalization. *Mech Syst Signal Process* 22:1526–1548
- Mohanty P (2005) Operational modal analysis in the presence of harmonic excitations, Ph.D. thesis. Technische Universiteit Delft, Delft
- Mottershead JE, Link M, Friswell MI (2011) The sensitivity method in finite element model updating: a tutorial. *Mech Syst Signal Process* 25(7):2275–2296
- Olsen P, Brincker R (2013) Using random response input in Ibrahim Time Domain. In: Proc XXXI International Modal Analysis Conference, February 11–14, 2013, Garden Grove, CA
- Pandit SM (1991) Modal and spectrum analysis: data dependent systems in state space. Wiley, New York, NY
- Pandit SM, Wu SM (1983) Time series and system analysis with applications. Wiley, New York, NY
- Pappa RS, Elliott KB, Schenk A (1992) A consistent mode indicator for the eigensystem realization algorithm. NASA Report TM-107607
- Peeters B (2000) System identification and damage detection in civil engineering, Ph.D. thesis. Katholieke Universiteit Leuven, Leuven
- Peeters B, De Roeck G (1999) Reference-based stochastic subspace identification for output-only modal analysis. *Mech Syst Signal Process* 13(6):855–878
- Peeters B, Van der Auweraer H (2005) PolyMAX: a revolution in operational modal analysis. In: Proc 1st international operational modal analysis conference, April 26–27, 2005, Copenhagen
- Pintelon R, Guillaume P, Rolain Y, Schoukens J, Van Hamme H (1994) Parametric identification of transfer functions in the frequency domain – a survey. *IEEE Trans Automat Contr* 39(11):2245–2260
- Pintelon R, Guillaume P, Schoukens J (2007) Uncertainty calculation in (operational) modal analysis. *Mech Syst Signal Process* 21:2359–2373
- Poncelet F, Golinval JC, Kerschen G, Verhelst D (2007) Output-only modal analysis using blind source separation techniques. *Mech Syst Signal Process* 21:2335–2358
- Rainieri C, Fabbrocino G, Cosenza E (2010) Some remarks on experimental estimation of damping for seismic design of civil constructions. *Shock Vib* 17:383–395
- Reynders E (2009) System identification and modal analysis in structural mechanics, Ph.D. thesis. Katholieke Universiteit Leuven, Leuven
- Reynders E, Houbrechts J, De Roeck G (2012) Fully automated (operational) modal analysis. *Mech Syst Signal Process* 29:228–250

- Reynders E, Pintelon R, De Roeck G (2008) Uncertainty bounds on modal parameters obtained from stochastic subspace identification. *Mech Syst Signal Process* 22:948–969
- Richardson M, Schwarz B (2003) Modal parameter estimation from operating data. *Sound Vib* 302:1–8
- Rodrigues J, Brincker R, Andersen P (2004) Improvement of frequency domain output-only modal identification from the application of the random decrement technique. In: Proc XXII international modal analysis conference, January 26–29, 2004, Dearborn, MI
- Ruzzene M, Fasana A, Garibaldi L, Piombo B (1997) Natural frequencies and dampings identification using wavelet transform: application to real data. *Mech Syst Signal Process* 11(2):207–218
- Schoukens J, Pintelon R (1991) Identification of linear systems: a practical guide to accurate modeling. Pergamon Press, London
- Shih CY, Tsuei YG, Allemand RJ, Brown DL (1988) Complex mode indication function and its applications to spatial domain parameter estimation. *Mech Syst Signal Process* 2(4):367–377
- Srikantha Phani A, Woodhouse J (2007) Viscous damping identification in linear vibration. *J Sound Vib* 303:475–500
- Tamura Y, Suganuma S-Y (1996) Evaluation of amplitude-dependent damping and natural frequency of buildings during strong winds. *J Wind Eng Ind Aerodyn* 59:115–130
- Tong L, Liu RW, Soon VC, Huang YF (1991) Indeterminacy and identifiability of blind identification. *IEEE Trans Circ Syst* 38:499–509
- Van Overschee P, De Moor B (1993) Subspace algorithm for the stochastic identification problem. *Automatica* 29(3):649–660
- Van Overschee P, De Moor B (1996) Subspace identification for linear systems: theory - implementation – applications. Kluwer Academic Publishers, Dordrecht
- Vandiver JK, Dunwoody AB, Campbell RB, Cook MF (1982) A mathematical basis for the random decrement vibration signature analysis technique. *J Mech Des* 104(2):307–313
- Verboven P (2002) Frequency-domain system identification for modal analysis, Ph.D. thesis. Vrije Universiteit Brussels, Brussels
- Verboven P, Guillaume P, Cauberghe B, Vanlanduit S, Parloo E (2005) A comparison of frequency-domain transfer function model estimator formulations for structural dynamics modeling. *J Sound Vib* 279(3–5):775–798
- Vold H, Kundrat J, Rocklin T, Russell R (1982) A multi-input modal estimation algorithm for mini-computers. *SAE Trans* 91(1):815–821
- Waters TP (1995). Finite element model updating using measured frequency response functions, Ph.D. thesis. University of Bristol, Bristol
- Yi J-H, Yun C-B (2004) Comparative study on modal identification methods using output-only information. *Struct Eng Mech* 17(3–4):445–466
- Zhang L, Wang T, Tamura Y (2005) A frequency-spatial domain decomposition (FSDD) technique for operational modal analysis. In: Proc 1st international operational modal analysis conference, April 26–27, 2005, Copenhagen
- Zhang L, Brincker R, Andersen P (2005) An overview of operational modal analysis: major development and issues. In: Proc 1st international operational modal analysis conference, April 26–27, 2005, Copenhagen
- Zhou W, Chelidze D (2007) Blind source separation based vibration mode identification. *Mech Syst Signal Process* 21:3072–3087

## 5.1 Assessing the Adequacy of the Measurement Chain

The first case study illustrates a possible approach to assess the adequacy of the measurement chain band for an application to historical buildings and in particular to the output-only modal identification of a masonry star vault.

The “star vault,” also known as Lecce’s edge vault, is typical of the local culture in the city of Lecce, Southern Italy (Marseglia 2013). It is the most common structural element in several historical buildings. The vaulted surface is generated defining some reference lines in agreement with the available area and height and moving them along the generating lines. The star vault is “groined” because it is composed of orthogonally intersecting barrel vaults. In particular, the four barrel groins do not meet at the crown but are moved backwards leaving at the center a surface with double curvature similar to a star (Fig. 5.1). The complexity of the star vault is associated to the “lines of discontinuity” between the groins and the double curvature.

Some experimental and numerical investigations on a star vault belonging to an historical building (Caserma Cimarrusti, formerly known as Convento dei Carmelitani Scalzi) in the old city center of Lecce have been carried out in the past by the Italian research groups of the University of Salento and the University of Molise. The objective of the research was the reduction of the modeling uncertainties, related to the material properties and the degree of constraint induced by the nearby vaults in the building (Fig. 5.2), via nondestructive techniques. Thus, modal identification tests in operational conditions were carried out in order to reduce such uncertainties and support the setting of a reliable numerical model.

In this framework, dynamic identification tests in operational conditions can be considered as effective tools to enhance the knowledge about the dynamic behavior of the structure under investigation with limited interference. The relevant role of experimental modal analysis in the characterization of the dynamic behavior of historical structures is widely recognized in the literature and by the most advanced design codes and guidelines for interventions on historical structures

**Fig. 5.1** Star vault:  
schematic illustration (a)  
and in operation after sensor  
installation (b)

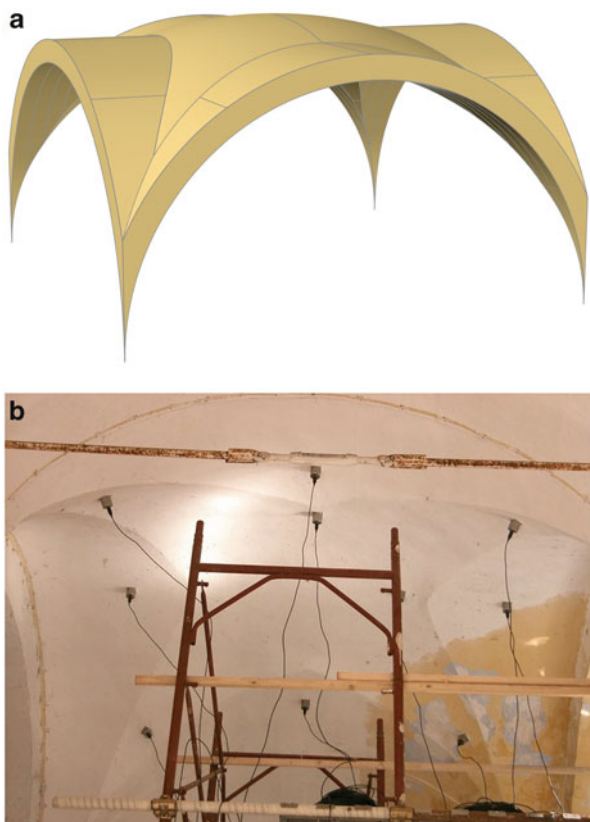


**Fig. 5.2** Series of star  
vaults in a building in Lecce  
(Southern Italy)



(see, for instance, Gentile and Saisi 2007, Ministero dei Beni e delle Attività Culturali 2010). In particular, output-only modal analysis techniques are recommended over input–output techniques, since artificial excitation often leads to problems in test execution and input control while the environmental loads are always present. In addition, tests are cheap and fast and imply a minimum interference with the normal use of the structure. The identified modal parameters are representative of the structural behavior in operational conditions and they can be used to verify or update FE models; moreover, changes in the modal parameters over time can be correlated to structural damage (Doebling et al. 1996).

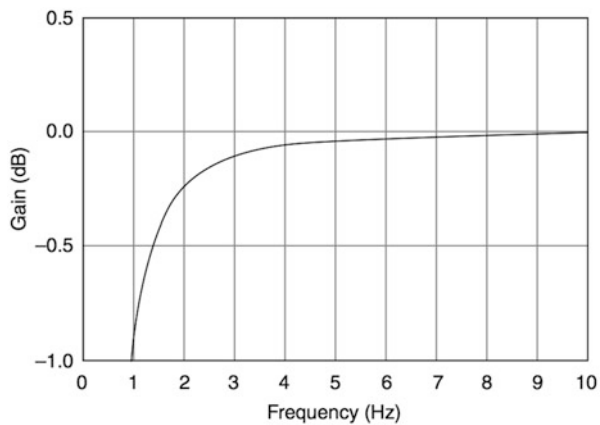
In this section, attention is focused on the opportunities offered by appropriately conceived FE models for the assessment of the adequacy of a measurement chain for a given application, the modal identification of a masonry star vault in operational conditions. A discussion about the correlation between the numerical model of the vault and the experimental results can be found elsewhere (Conte et al. 2011).

The problem of input control is one of the reasons that induce to prefer OMA to traditional experimental modal analysis for applications to historical masonry structures. In fact, these are usually fairly massive and, therefore, it is difficult to excite them. Moreover, they can also be affected by static deficiencies that prevent the application of significant dynamic loads. The main issue in the application of OMA to historical masonry structures is generally related to the low amplitude of vibrations, which requires the installation of a high-performance measurement chain. As discussed in Chap. 3, programmable hardware can be used to develop a customized data acquisition system for dynamic tests. However, a careful selection of the hardware is of paramount relevance for the successful measure of the ambient vibration response of the structure under investigation. Numerical models and sensitivity analyses with respect to different modeling assumptions can support the assessment of the adequacy of a measurement chain for a specific OMA application.

In the case of the star vault under test, a preliminary numerical model has been set according to the results of a number of in-situ investigations for the assessment of geometry and the characterization of material properties (surveys, nondestructive tests, limited destructive tests). Attention has been focused on the “masonry cell” made by the star vault, the boundary arches (representing the connection between consecutive vaults) and the masonry piers supporting the vault itself. The masonry piers have been modeled as fixed at the base. Dead loads have been applied taking into account the contributions of filler at the vault extrados, plaster and floor. No live loads have been applied in compliance with the state of the structure at time of testing.

The main issue in setting the numerical model was related to the definition of the boundary conditions, since the “masonry cell” is not isolated (Fig. 5.2). Modeling the interactions with the nearby macroelements usually requires a calibration process to validate the adopted assumptions. However, in the preliminary stage of test planning, a simplified numerical model of the vault, omitting the interactions, can support the assessment of the adequacy of the bandwidth of the adopted measurement hardware. Such an assessment is based on the comparison between the bandwidth of the measurement system (sensors and data acquisition hardware) and the minimum and/or maximum expected value of the natural frequency of the structure under test. In the present case, the fairly large value of the AC cut-off

**Fig. 5.3** AC cut-off frequency response of the data acquisition hardware



frequency response of the adopted data acquisition system required the preliminary evaluation of a lower bound for the expected value of the fundamental natural frequency of the vault. Neglecting the constraints due to the nearby vaults and taking into account all masses referring to the considered vault due to finishing materials (filler of vault extrados, screed, floor), the numerical model was expected to be representative of the real structure in terms of mass distribution but it was characterized by a lower stiffness. The adopted approach to model setting and the consideration of the range of variability of the material properties made possible the evaluation of the limit for the underestimation of the structural stiffness and, as a consequence, the estimation of the minimum expected value of the fundamental frequency of the vault that resulted about 3.51 Hz.

The selected measurement chain consisted of ten seismic, ceramic shear, high-sensitivity IEPE accelerometers with the following characteristics:

- bandwidth from 0.1 to 200 Hz,
- 10 V/g sensitivity,
- $\pm 0.5$  g full scale range.

The data acquisition modules were characterized by a 24-bit sigma-delta ADC with a dynamic range of 102 dB and an on-board anti-aliasing filter. The connection between accelerometers and recorder was made by RG-58/U coaxial cables. For their characteristics (resolution, sensitivity, dynamic range, and so on), ADC and sensors could be considered adequate to measure the dynamic response of the vault even in the presence of low-amplitude vibrations such as those due to ambient noise (see also Chap. 3). The sole possible limitation could be related to the bandwidth of the measurement system with respect to that of the vault.

The comparison between the expected minimum value of the fundamental natural frequency of the vault (3.51 Hz) and the AC cut-off frequency response of the data acquisition hardware (Fig. 5.3) shows a moderate attenuation (about  $-0.1$  dB). In any case, the first natural frequency is realistically higher than the numerically estimated limit value. This ensures the adequacy of the bandwidth of the selected data acquisition system for the present application. Since the lower bound of the frequency range of the accelerometers used for the present application

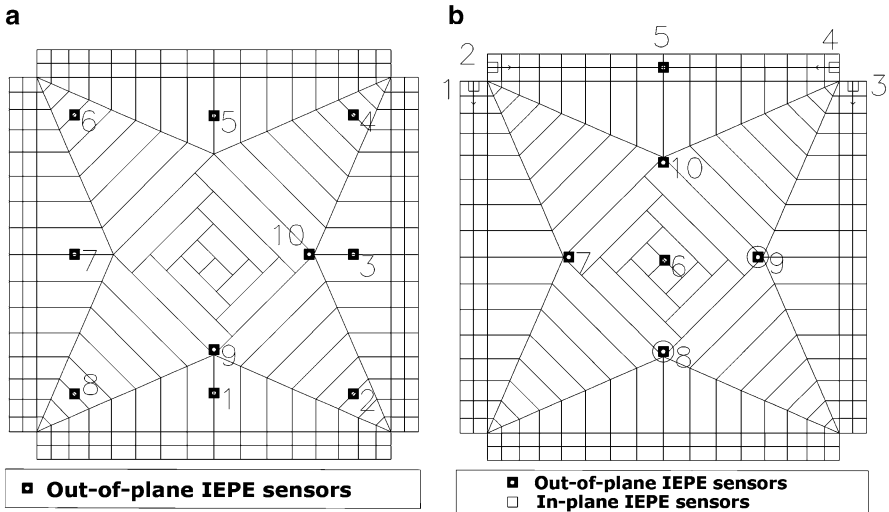


**Fig. 5.4** Sensor layouts: setup A (a) and setup B (b)

is much lower than 0.5 Hz, no further limitations came from the sensors. As a final result, the bandwidth of the measurement chain was expected to be adequate for the present application and able to properly resolve the response signals.

The dynamic response of the vault has been measured by ten accelerometers placed at the intrados (setup A) and, in a second stage, also on two column heads (setup B). The two layouts are shown in Fig. 5.4. Sensors have been installed according to a regular mesh covering as much as possible all portions of the vault. The accelerometers have been placed in contact with the vault surface through a small anchor plate. Sensors have been screwed on the plates and mounted orthogonally to the vault surface. In the second test layout four sensors were installed parallel to the main directions of the columns, in order to observe also the behavior of the piers the vault stands on.

Data have been acquired by means of the above mentioned measurement system based on programmable hardware. The procedure for its development and the software for data acquisition have already been discussed in Chap. 3.

The analysis of the collected datasets according to some of the OMA methods described in Chap. 4 has shown that the fundamental natural frequency of the vault was about 4.3 Hz (Conte et al. 2011), proving the ability of the described approach to provide a reliable assessment of the adequacy of the measurement system.

## 5.2 Damping Estimation

The accurate experimental estimation of damping is still an open problem. Modal frequencies and mode shapes can be confidently and quite easily measured by means of dynamic tests on civil structures, while damping ratio estimates are

usually characterized by large error bounds. In this section the main issues concerning the experimental identification of modal damping ratios are discussed and methods to obtain sufficiently reliable and accurate estimates are summarized. Most of them have been identified from an extensive literature aimed at finding best practice criteria for modal parameter and, in particular, damping estimation.

The effect of damping on the dynamic behavior of structures has been analyzed by many researchers over the years but, despite of the large amount of literature available on the subject, the definition of a well-established formulation to represent damping forces is still debated (Woodhouse 1998). Several damping mechanisms can be found on a given structure. They can be generally classified as (Lagomarsino 1993):

- Damping intrinsic to the structural material;
- Damping due to friction in the structural joints and between structural and nonstructural elements;
- Energy dissipated in the foundation soil;
- Aerodynamic damping;
- Damping introduced by passive and active dissipation systems.

Damping is associated to the energy dissipation of the structure during motion and, therefore, it limits the magnitude of forced vibrations in a structure. In this perspective, the specific damping capacity of a structure can be defined as the percentage of the total energy of vibration lost in a cycle, given by the ratio between the energy lost in a cycle and the corresponding maximum stored energy.

The different damping mechanisms acting on a structure are usually represented by a unique model, the equivalent viscous damping (also known as structural damping) model. It is defined in a way that it takes into account all dissipation sources in a structure. However, damping in structures usually consists of one or a combination of the following damping mechanisms: viscous damping, hysteretic damping, friction (or Coulomb) damping, and aerodynamic (or atmospheric) damping. A concise discussion about the different damping mechanisms can be found elsewhere (Rainieri et al. 2010a). Reviewing the different damping models can help to better understand the behavior of the equivalent viscous damping and the main factors influencing its magnitude.

Much of the energy dissipated in vibrating structures is due to friction. However, real structures usually exhibit at least a combination of hysteretic damping and friction damping (proportional to the amplitude of motion). Aerodynamic damping may arise as a result of the drag and lift forces on an object in air. Such forces are proportional to the square of the velocity of the object with respect to the air stream. In summary, real structures typically show a combination of linear (that is to say, damping independent of the amplitude of motion) and nonlinear (namely, amplitude-dependent) damping mechanisms. As a consequence, there is not a single way to mathematically describe all vibrating structures. In the engineering practice, due to the difficulty of defining the true damping characteristics of typical structural systems, the equivalent viscous damping model is usually adopted, because it leads to linear equations of motion. Even when viscous damping may be not active, such model is generally assumed, and a distinction between existence

of pure viscous damping and assumption of equivalent viscous damping is rarely found in the literature.

It is well known that damping exhibits an increase with amplitude of motion in full-scale data sets. This effect can be addressed to the use of the equivalent viscous damping model to represent all the different damping mechanisms. In fact, this model is nonideal under a wide range of amplitudes of motion and, if it is assumed, actual structures may exhibit a damping that changes with amplitude. Thus, a model for total damping with respect to the amplitude of motion has been proposed for buildings (see, for instance, Jeary 1986). Assuming that frictional losses give a large contribution to the energy dissipation in structures, at low levels of motion there are no significant slipping phenomena in the structure. Once a sufficient number of interfaces are activated, they dissipate energy in proportion to their relative displacements, so that a linear increase in damping can be assumed. At high amplitudes of motion, all interfaces have been activated and friction forces become constant even for increasing amplitudes, thus defining the maximum level of damping that cannot be exceeded unless damage occurs within the structure. In fact, in large amplitude regime, damping ratios can increase only if there are additional sources of damping forces, such as those associated to damage to secondary elements. In the absence of damage, higher damping ratios cannot be expected for structures vibrating within their elastic limit. When the amplitude exceeds this limit, the contribution of hysteretic damping may become predominant. The justification of the nonlinear model of damping behavior with vibration amplitude goes back to the principles of fracture mechanics (refer to Jeary 1997 for more details).

When ambient vibration tests are carried out, the (unknown) spectral distribution of the input, noise in the signal and, eventually, the errors caused by windowing in spectral analysis are responsible for the large variability of damping estimates. Measurement noise affects the quality of fit in curve fitting procedures and, as a consequence, the reliability of damping estimates. The use of the Hanning window in spectrum computation, instead, yields a bias error with respect to the true damping value. However, fine frequency spacing and high number of averages can minimize this effect (Chap. 2; refer also to Brincker et al. 2003 for more details). Thus, reliable damping estimates in frequency domain can be obtained only from long records of the structural response, in order to compute spectra characterized by a high number of averages and a fine frequency resolution. This recommendation applies also to the EFDD method (Chap. 4).

The effect of frequency resolution on modal damping ratios estimated by the EFDD method has been extensively investigated (see, for instance, Tamura et al. 2005), showing that the damping ratio estimates for all modes decrease when the frequency resolution improves, and they converge for a frequency resolution equal to 0.01 Hz or better. Moreover, the error in damping estimation is kept low by inverse Fourier transforming the identified SDOF Bell functions and by fitting the data related only to the first few cycles of the obtained approximate SDOF correlation functions for the considered modes. Particular attention is needed in the case of closely spaced modes, when damping estimates by EFDD might

be inaccurate. In fact, partial identification of SDOF Bell functions, beating phenomena and errors due to windowing can significantly affect the estimates.

SSI methods yield more accurate damping estimates in the presence of closely spaced modes. This is crucial above all for very flexible structures, characterized by low natural frequencies and damping ratios and by several close modes. SSI methods are used to get modal parameter estimates even in the presence of limited amounts of data, since no averages are required. However, it is worth noting that, in principle, an unbiased estimate of modal parameters can be obtained only by means of infinite records. Nevertheless, SSI methods provide reliable estimates of natural frequencies even in the case of short records. Even if record length seems to be less critical for this class of methods, long durations yield more stable and reliable modal parameter and, in particular, damping ratio estimates. A numerical study (Pridham and Wilson 2003) has shown that at least 4,000 data points are necessary for a reasonable identification of system frequencies lower than 1 Hz and damping ratios lower than 1 %. In addition, a sensitivity analysis is recommended to take into account the effect of the number of block rows on the modal estimates provided by SSI methods (Rainieri et al. 2010a).

The roles of the number of block rows in the determination of the order of the system (4.207) and of the stabilization diagram in the discrimination between physical and spurious modes have been discussed in the previous chapter. Attention is herein focused on the influence of the number of block rows on the quality of the stabilization diagram.

Equation (4.207) provides a lower bound for the setting of the number of block rows. However, the engineering practice has shown that, if the system has a low fundamental frequency with respect to the sampling frequency and the number of block rows is set much too low, only a few samples of that modal response are included in the block matrix. As a result, the corresponding modal parameters are not well identified. For this reason, the number of block rows should be set as large as possible, but this might cause an unacceptable increase in computational time and memory usage (Reynders and De Roeck 2008). As an alternative, the number of block rows can be set in agreement with the following equation (Reynders and De Roeck 2008):

$$i \geq \frac{f_s}{2f_0} \quad (5.1)$$

where  $f_s$  is the sampling frequency and  $f_0$  is the lowest frequency of interest. Equation (5.1) is more effective than (4.207) in the case of very flexible structures since it provides a higher lower bound for the number of block rows. However, when  $f_0$  increases, (5.1) also gives a low limit value for  $i$ . Since both (4.207) and (5.1) do not suggest optimal settings of  $i$ , the identification of the range of values of  $i$  that enhance the quality of the stabilization diagram and, therefore, simplify the identification of the structural modes is recommended. Such values depend on several factors (the structure under test, the quality of measurements, etc.). A sensitivity analysis can support their identification.

Some remarks about the role of the condition number in inverse problems can benefit also the analysis of the influence of the number of block rows on the quality of the stabilization diagram.

As mentioned in Chap. 2, the condition number tracks the transition from invertible to noninvertible matrices. A matrix is noninvertible when the condition number approaches infinity, while it is ill conditioned when the condition number is very large. In this case the effect of numerical inaccuracies on the solution may be relevant, and errors in the data are magnified during the inversion. Since the small singular values in ill-conditioned problems magnify the errors, retaining only the largest singular values can limit error magnification. In the context of SSI methods for OMA, the selection of the smallest singular value to be considered in the analysis is associated to the selection of the order of the system from the SVD of the block Toeplitz matrix of correlations ((4.211) and (4.212)) or the projection matrix (4.240). This is a key step in view of the estimation of the state-space matrices.

As already mentioned in Chap. 4, clear jumps in the sequence of singular values and, therefore, the order of the system can be hardly identified in real applications. As a consequence, modal identification is usually based on setting a sufficiently large value for  $i$  and on the construction of the stabilization diagram, whose maximum model order is selected in a conservative way (and it is typically much lower than the product  $l \times i$ ). Sensitivity analyses where the maximum model order in the construction of the stabilization diagram is kept constant and the number of block rows varies in a given range are equivalent to changing the condition number. Thus, it is possible to identify a range of values of the number of block rows that ensure numerical stability and enhance the quality of the stabilization diagram.

Figure 5.5 is helpful to clarify this aspect of the discussion. The sequences of retained singular values and the corresponding stabilization diagrams obtained from application of Cov-SSI to a real dataset (Rainieri et al. 2010b) are shown for different settings of the number of block rows and constant maximum model order (equal to 60). The number of channels in the dataset was equal to 8 ( $l = 8$ ) and the number of modes in the investigated frequency range was equal to 4 ( $n = 2N_m = 8$  was the theoretical order of the system); a sensitivity analysis has been carried out by changing the number of block rows between 10 ( $l \times i = 80$  was the maximum allowable model order in the construction of the stabilization diagram) and 200 ( $l \times i = 1,600$ ). As the number of block rows increases, the effect of inconsistencies due to measurement noise is more and more reduced. Since the maximum model order is set to a constant value, an increase in the number of block rows yields an increase in the magnitude of the smallest retained singular value and the rejection of a larger amount of noise or inconsistent information. On the other hand, the singular values associated to modal information are always retained, due to the conservative approach adopted in setting the maximum model order (much higher than the estimated order of the system). Since an increase in the number of block rows yields a decrease of the condition number, another consequence is the asymptotic transition from an ill conditioned to a well-posed inverse problem. However, if the number of block rows is set much too high, the mathematical poles are pushed towards the alignments of physical poles (Fig. 5.5e, f). In the

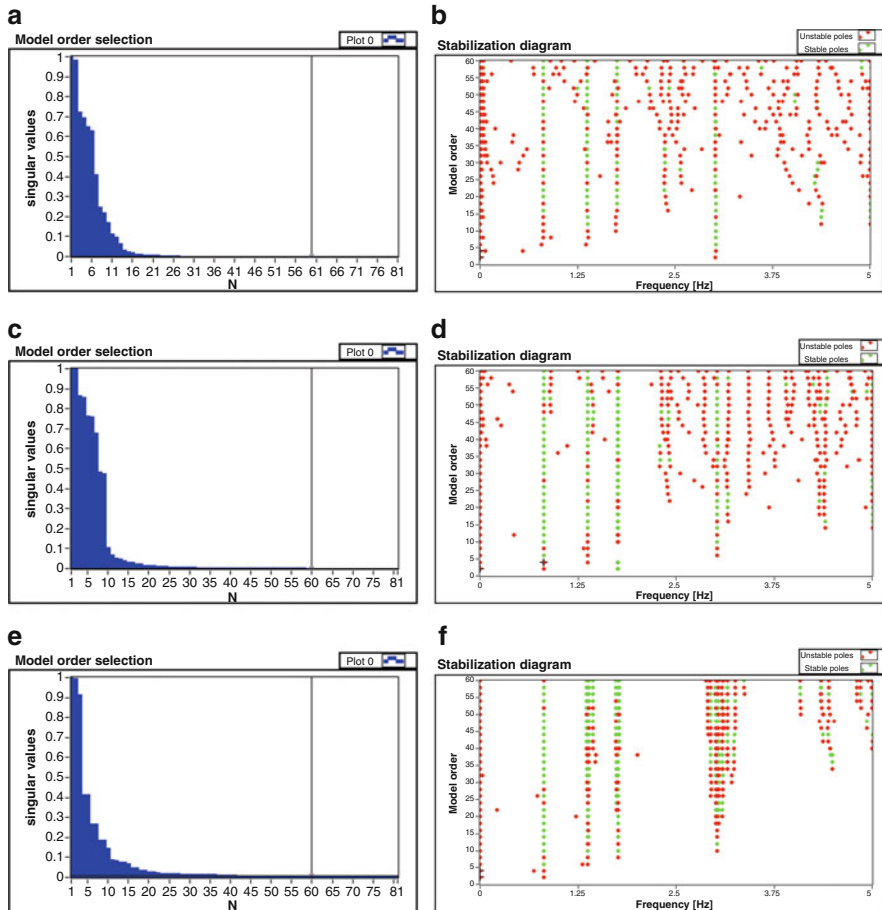


**Fig. 5.5** Evolution of the stabilization diagram: low value of  $i$  (a, b), optimized value of  $i$  (c, d), high value of  $i$  (e, f)

outermost case, physical and mathematical poles are grouped together in small regions nearby the actual structural resonances. Likely modal properties (sometimes very similar to the actual modal properties of the system) are often associated to these mathematical poles, which can eventually form additional alignments of stable poles. Thus, the identification of the poles associated to structural modes by stabilization and physical criteria becomes very complicated or even virtually impossible, and a slight bias in the modal parameter estimates can be observed (Rainieri et al. 2010b).

The enhancement of the quality of the stabilization diagram is the result of more stable estimates of the modal parameters at different model orders. If the variability of the modal parameter estimates at different model order is kept low by an appropriate setting of the number of block rows, the physical poles are more

prone to fit the stabilization criteria, with the related benefits in terms of quality of stabilization and consistency of modal parameter estimates. In particular, from the analysis of the modal parameter estimates obtained at different model orders it is possible to observe (Rainieri et al. 2010b) that the variance of the estimates first decreases when the number of block rows increases, because of noise rejection, and then it increases when the number of block rows is set much too high. The selection of the groups (clusters) of poles associated to the structural modes and their analysis can provide a measure of the level of uncertainty associated to the modal parameter estimates. This information plays a primary role in a number of applications of OMA (Reynders et al. 2008, Rainieri et al. 2010b). In conclusion, the value of the number of block rows can be set in a way able to minimize the variance of the modal parameter estimates obtained at different model orders for the physical modes of interest. This is relevant above all for damping ratios, whose estimates are usually the most scattered.

---

### 5.3 Correlation Between Numerical and Experimental Modal Property Estimates

This section deals with the role of ambient vibration tests and correlation between numerical and experimental estimates of the modal properties in the tuning of selected parameters of the numerical model. This topic is discussed with reference to a real case study. It shows how OMA can contribute to the indirect noninvasive assessment of relevant structures belonging to the architectural heritage of a Country.

The analysis and modeling of historical structures is usually very challenging from the scientific and technical viewpoint due to their unique structural configurations, the large modeling uncertainties and the need of keeping destructive investigations very limited. In this framework the results of output-only modal identification tests can support the rational validation of the numerical model; moreover, the tuning of selected parameters makes possible the setting of a representative model of the structural behavior in operational conditions. It is worth noting that model updating is one of the typical applications of modal identification results. However, illustration of model updating techniques and their application to the present case study would require a dedicated chapter that is beyond the scope of the book. The interested reader can refer to the literature for extensive discussions about model updating and tutorials for applications (Friswell and Mottershead 1995, Ewins 2000, Mottershead et al. 2011).

On the contrary, the present explanatory application basically aims at remarking the potential of OMA in the structural and dynamic assessment of historical structures. This topic is discussed with reference to the case study of the Tower of the Nations (Fig. 5.6), a structure belonging to the modern Italian architectural heritage. It is located within the Mostra D’Oltremare urban park in Naples (the interested reader can refer to Rainieri et al. 2013 for a more complete discussion about the refinement of the numerical model of the Tower based on the results of output-only modal identification tests). The background of the output-only modal

**Fig. 5.6** The Tower of the Nations (Naples, Italy),  
(© Elsevier Ltd. 2013),  
reprinted with permission



identification tests can be traced back to the structural assessment activities aimed at the evaluation of the seismic capacity of the Tower of the Nations before the design of restoration and seismic upgrading interventions. The valuable characteristics of the Tower required the execution of limited destructive investigations. Thus, ambient vibration tests have been carried out to effectively complement the structural assessment with the information about the dynamic properties. They provided reference values of the modal parameters useful for the validation of the numerical model. It is worth pointing out that the present application refers to the investigation of structures subjected to frequent but weak ground motions, so that they are expected to show an elastic response with a relevant role of the participating mass ratios (PMRs) in the characterization of the seismic response. Moreover, attention has mainly been focused on the appropriate modeling of the stiffness properties of the structure, taking also into account the influence of interacting structural and nonstructural members on the dynamic response in operational conditions.

About the applicability of the obtained results in the assessment of the seismic performance of the structure, it is well known that earthquakes cause a lengthening of the period: the stronger the motion, the larger the effect. In serviceability conditions, frequent ground motions are associated to minor lengthening effects.

They are often in the same order of magnitude of the variations induced by environmental factors and operational loads (Rainieri et al. 2011, Hu et al. 2012), or of the increase of the natural period with the vibration amplitude (Gentile and Saisi 2013). For this application, model refinement accounting for the uncertainties in the modal parameter estimates was out of the scope of the work. On the other hand, the small variations of the modal properties induced by increasing levels of vibration in structures vibrating within their elastic limit lead to recognize the validity of the proposed methodological approach, even in the absence of correction factors (Ministero dei Beni e delle Attività Culturali 2010) accounting for the effect of vibration amplitude on the modal parameter estimates in serviceability conditions. With the exception of very stiff structures, a very small increase in the natural period leads to an unchanged or slightly reduced magnitude of the seismic acceleration and the associated forces, as pointed out by the shape of the response spectrum adopted in conventional seismic analyses (Consiglio Superiore dei Lavori Pubblici 2008). An approach based on modal parameter estimates in operational conditions is conservative also when the dissipative forces are considered. In fact, despite of the fairly large uncertainty bounds usually affecting damping estimates, a clear trend for its magnitude with the amplitude of vibrations can be identified (Jeary 1997). In particular, frequent earthquakes cause an increase in the magnitude of damping with respect to the operational conditions as a consequence of the activation of a number of damping mechanisms and, in particular, of the interaction (friction) between structural and nonstructural members in buildings and tower-like structures (Rainieri et al. 2010a). The original aspect of the present application lies in the evaluation of the correlation between numerical and experimental estimates of the modal properties and in tuning of selected model parameters by a process able to pursue the goal of setting a representative model of the structure for seismic assessment purposes in the linear regime. As discussed below, this result has been obtained by tuning selected parameters of the numerical model of the Tower in a way able to minimize the scatter with the experimental data and, at the same time, to enhance as much as possible the accuracy of response spectrum and seismic time-history linear analyses.

### 5.3.1 Preliminary Geometric and Structural Survey

The present example is intended as a basic guide for the rational and systematic nondestructive assessment of the dynamic behavior of architectural heritage structures taking into account the results of OMA tests. The adopted methodological approach is also in agreement with well-established principles for seismic assessment of historical structures (Ministero dei Beni e delle Attività Culturali 2010).

The assessment of the Tower of the Nations started from the collection and analysis of a number of sources of information, and in-situ survey and investigations aimed at:

- Completely defining the geometric characteristics of both structural and nonstructural elements;
- Defining the structural scheme and detailing;
- Evaluating the mechanical characteristics of concrete and steel.

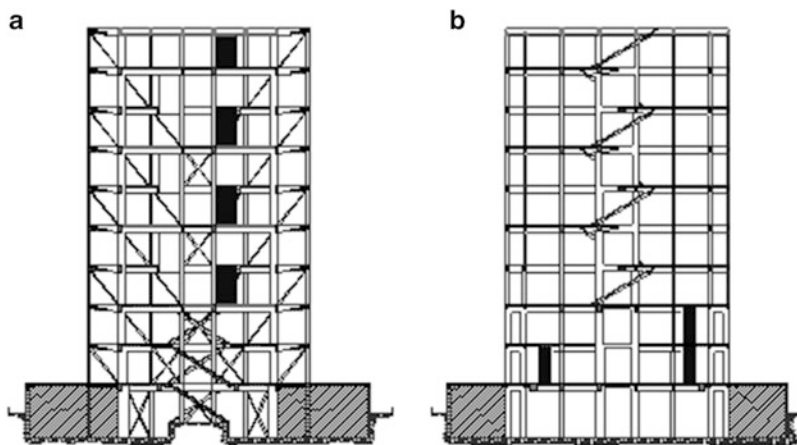


**Fig. 5.7** The Tower of the Nations: longitudinal (a) and transverse (b) sections, (© Elsevier Ltd. 2013), reprinted with permission

In particular, they consisted in the careful review of structural drawings, visual inspections and survey, and execution of destructive and nondestructive tests to assess mechanical properties of materials and structural detailing of members (CEN 2005), such as longitudinal and transverse reinforcement. These preliminary activities play a relevant role in determining the reliability and accuracy of the numerical evaluations of the structural response to dead loads and earthquakes. The analysis of complementary sources of information (structural design drawings, visual inspections, geometric survey, nondestructive tests) is definitely crucial in the rational setting of the numerical model of the structure. However, the model can still be affected by relevant uncertainties, and this requires rational methods to validate or reject some modeling assumptions. In this context dynamic tests can definitely support the setting of a reliable numerical model, representative of the actual dynamic behavior of the structure under test. The main results of in-situ survey of the Tower and inspection of structural drawings are herein summarized in order to clarify the most relevant aspects related to the rational definition of its numerical model.

The Tower of the Nations is an r.c. building characterized by two blind and two completely see-through parallel façades (Fig. 5.6), with elevator shafts and stairs located in the center of the building. Apart from the first, the second, the third and the tenth level, the others are characterized by alternate floors, which cover just a half of the imprint area of the building. The structural system is very attractive and original. Even if the structure was designed to bear gravity loads only, it is very interesting also from the seismic point of view. Two couples of frames with r.c. diagonals and tuff masonry walls within the fields of the frames increase the stiffness in the longitudinal direction (Fig. 5.7a). In the transverse direction (Fig. 5.7b) the structural system is even more complex due to the presence of r.c. walls and alternate floors. Some walls, characterized by a small thickness, link the two frames that represent the exterior

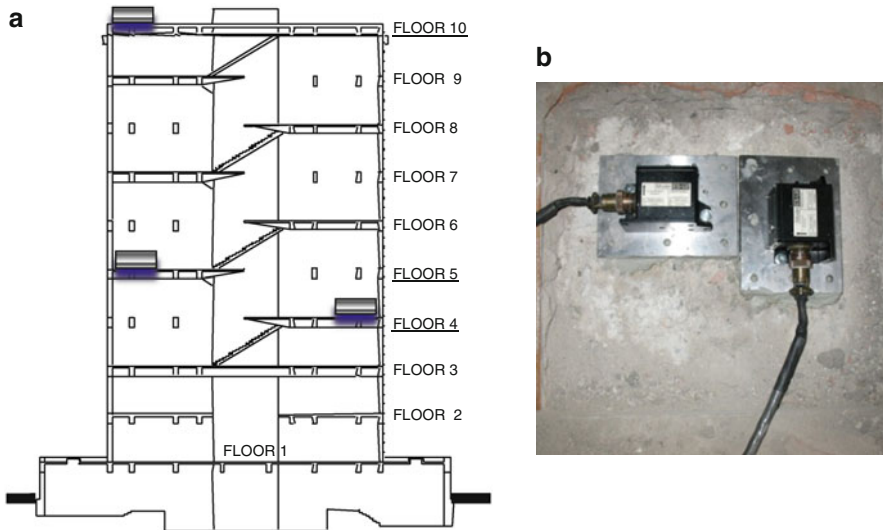


**Fig. 5.8** Instrumented floors (a) and sensors in operation (b), (© Elsevier Ltd. 2013), reprinted with permission

systems; some others, having larger dimensions, are located near the elevator at the center of the building. The structure has a central body (the Tower) with a nearly square shape ( $23.10\text{ m} \times 23.60\text{ m}$ ), which does not change in elevation. At the first level there is also a basement along the whole perimeter with an extension of 6.0 m outside the edge of the Tower. Short deep beams make the link between basement and Tower. This is characterized by a height of 41.0 m with respect to the ground level and of 43.7 m from the foundation level.

The mechanical properties of the concrete have been estimated through a combination of destructive and nondestructive tests (CEN 2005). A relevant uncertainty affected the experimental evaluation of the mechanical properties of concrete, including the elastic modulus (Rainieri et al. 2013). Because of these and other uncertainties in setting the numerical model of the Tower, dynamic tests in operational conditions have been carried out. The results have been used to validate the modeling assumptions and to tune some model parameters, as discussed in the next sections.

### 5.3.2 Output-Only Modal Identification

The ambient vibration response of the Tower has been measured at the fourth and the fifth level of the building and at the roof (Fig. 5.8a). The roof and the fifth level have been instrumented in two corners. At each corner two force balance accelerometers, measuring in two orthogonal directions (Fig. 5.8b), have been placed. Another couple of accelerometers has been placed at the fourth level.

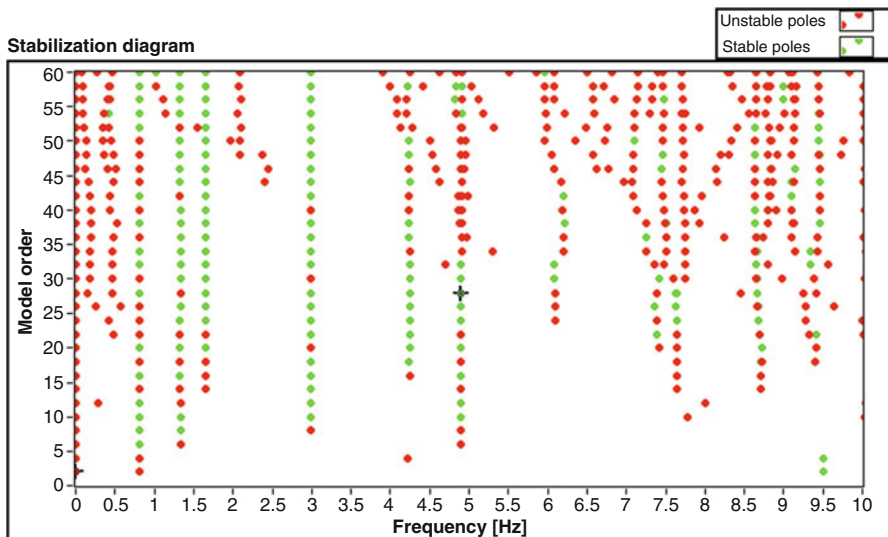


**Fig. 5.9** Stabilization diagram (Cov-SSI), (© Elsevier Ltd. 2013), reprinted with permission

The ten accelerometers have been placed directly in contact with the concrete slab and parallel to the main directions of the building, in order to get both translational and torsional modes.

A bandwidth of about 200 Hz (starting from DC) and a high dynamic range (140 dB) characterized the sensors. The full-scale range was  $\pm 0.25$  g, and the sensitivity was equal to 10 V/g in single-ended configuration. A 24-bit DSP, an analog anti-aliasing filter and a high dynamic range ( $>114$  dB at 200 sps) were the main characteristics of the adopted digital recorder. Ten 24AWG cables, characterized by individually shielded twisted pairs, linked accelerometers and recorder. The collected measurements were originally sampled at 100 Hz. They have been decimated by a factor of 5 before processing. The record duration was about half an hour.

After the preliminary validation and pretreatment of data (offset removal, filtering, etc.), they have been processed according to the EFDD, Cov-SSI and DD-SSI methods. Hanning window and 66 % overlap have been used for spectrum computation and modal identification in frequency domain. A frequency resolution of 0.01 Hz has been adopted.

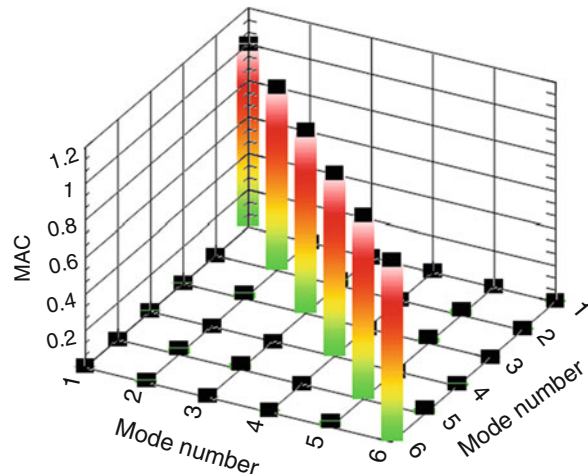
Figure 5.9 reports the stabilization diagram obtained from the analysis of the collected data through Cov-SSI. It shows the alignments of stable poles corresponding to the identified structural modes. In particular, the first six modes of the Tower can be straightforwardly identified. The structure is characterized by well-separated modes. The last two modes (in particular, the fifth) were weakly excited. This circumstance slightly affected the quality of the estimates (above all damping).

The modal identification results (average values) are reported in Table 5.1. Very consistent modal identification results have been obtained from the different OMA methods, also in terms of mode shape estimates as pointed out by CrossMAC values higher than 0.99.

**Table 5.1** Results of output-only modal identification (average values), (© Elsevier Ltd. 2013), reprinted with permission

Mode #	Type	Natural frequency (Hz)	Damping ratio (%)
I	Translation (open side)	0.80	0.4
II	Translation (blind side)	1.33	1.2
III	Torsion	1.66	0.6
IV	Translation (open side)	2.96	1.7
V	Translation (blind side)	4.23	$\approx 5$
VI	Torsion	4.90	$\approx 1$

**Fig. 5.10** AutoMAC matrix, (© Elsevier Ltd. 2013), reprinted with permission



The first and the fourth mode are translational in the X direction (parallel to the open side of the building—Fig. 5.6); the second and the fifth mode are translational in the Y direction (parallel to the blind side); finally, the third and the sixth mode are torsional. Taking into account the geometry of the structure, test results have confirmed that the tuff masonry walls and the diagonal braces increase the stiffness of the structure along the Y direction (blind side) with respect to the X direction (open side).

The influence of tuff masonry walls on the dynamics of the structure is also remarked by the damping values. Weak excitation limited the reliability of damping estimates for the higher modes. However, focusing the attention on the three fundamental modes, it is possible to note that the second mode shows a higher damping with respect to the others. This circumstance can be probably addressed to the contribution of the friction that arises between masonry infills and the surrounding r.c. frames along the blind side. The first and the third mode, conversely, show similar damping values, slightly higher for the third mode than for the first.

In Fig. 5.10 a 3D histogram of the AutoMAC matrix is reported. It confirms the effectiveness of the experimental setup to distinguish the different modes, as

demonstrated by values equal to 1 along the main diagonal and close to 0 elsewhere. Another validation of the obtained mode shapes has been carried out through the complexity plots. As shown in Fig. 5.11, all modes are normal or nearly normal. Slight imaginary components can be observed only in the mode shape of the fifth mode. They can be probably related to noise effects and weak excitation.

### 5.3.3 Finite Element Modeling

The numerical characterization of the dynamic response of the Tower was based on the implementation of a number of FE models. Modal analyses have been carried out through the SAP2000® software (Computers and Structures 2006). The model of the building represented in detail, under different assumptions, the geometric and mechanic characteristics of the structural elements and the mass distribution on plain and along height. Position and geometry of the structural and nonstructural elements at each floor have been defined according to the results of in-situ investigations and original drawings. One-dimensional structural elements (columns, beams, braces) have been modeled by “beam” elements while two-dimensional structural elements (r.c. walls, stairs) have been modeled by “shell” elements. Nonstructural walls made of tuff masonry have been modeled by shell elements as well. This assumption leads to overall stiffness characteristics that are similar to the uncracked shear stiffness evaluated according to relevant behavioral models (Fardis 1996). Finally, at each floor, 0.05 m thick shell elements have been used to model the floors. The structure is assumed fixed at the base, so no soil-structure interaction has been considered.

The masses have been directly associated to the structural elements according to the specific mass of the material (concrete) and the geometric dimensions of the cross section. In a similar way, a uniform area mass has been assigned to floors and stairs. This mass has been evaluated according to the section geometry. No live loads have been applied, in accordance with the state of the structure at time of testing. As regards tuff masonry walls, a linear mass has been externally applied to the beams they stand on.

Correlation with the experimental results has been assessed by defining a number of model classes through the combination of the following modeling assumptions:

- Absence vs. presence of tuff masonry walls;
- Absence vs. presence of the basement structure;
- Shell elements vs. rigid diaphragms to model floors.

The relevant uncertainties in the numerical modeling of the structure required a rational assessment of the effectiveness of these different modeling assumptions. In particular, the evaluation of the correlation with the results of the dynamic test was aimed at the assessment of the influence of curtain walls on the dynamic behavior of the structure, the characterization of the level of interaction between the Tower and the surrounding basement, and the assessment of the sensitivity to different assumptions about the in-plane stiffness of the floors.

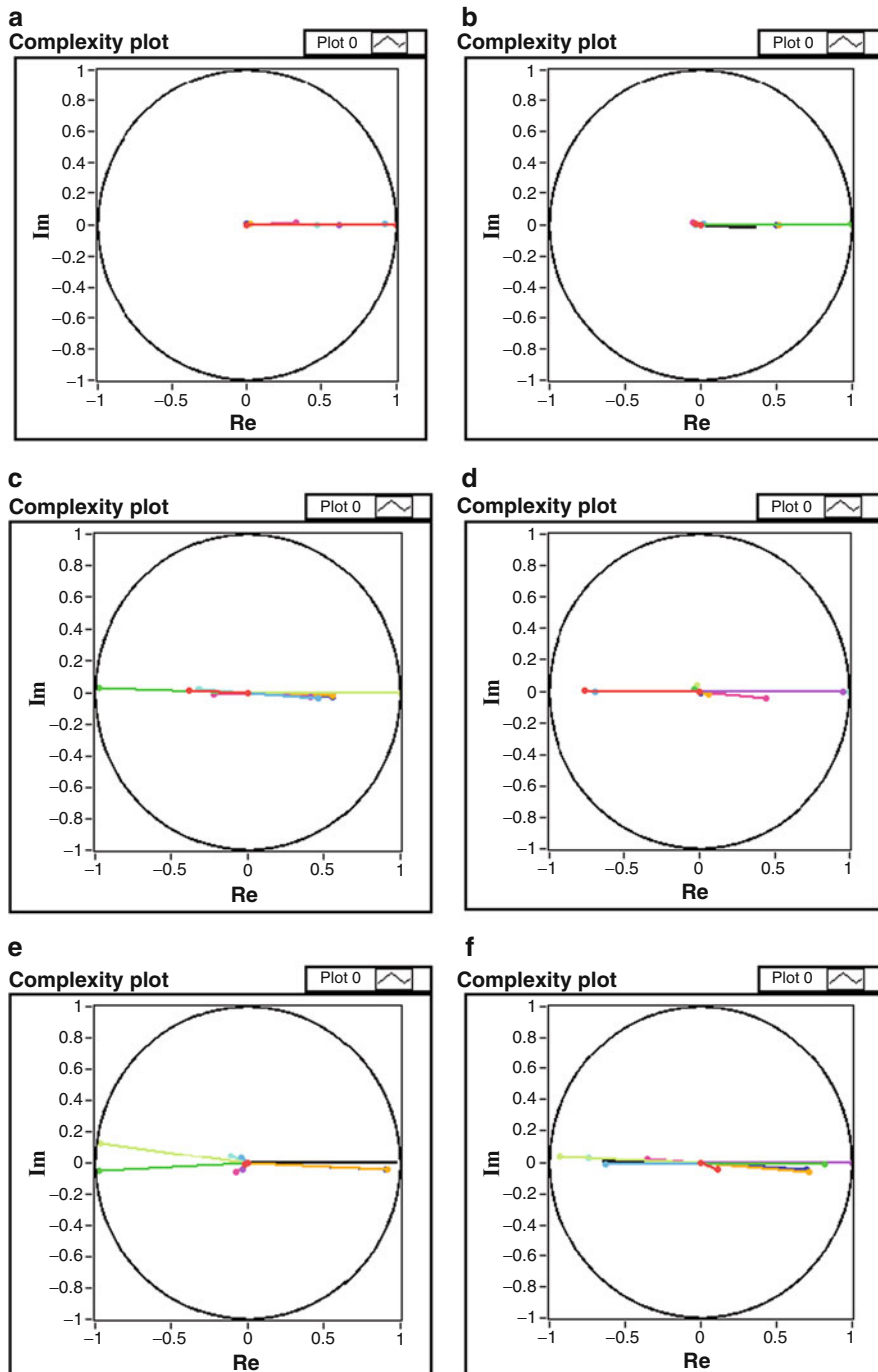


**Fig. 5.11** Complexity plots: mode I (a), II (b), III (c), IV (d), V (e), VI (f). (© Elsevier Ltd. 2013), reprinted with permission

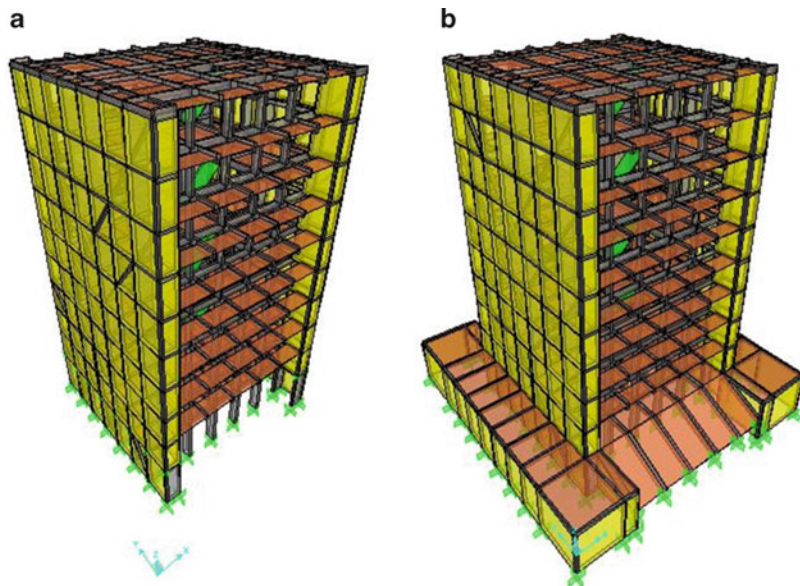


**Fig. 5.12** Numerical models of the Tower under: simplified (a) and complete modeling of the basement (b), (© Elsevier Ltd. 2013), reprinted with permission

As the role of tuff masonry walls is concerned, the correlation with the model characterized by absence of curtain walls has been evaluated mainly because this represents a traditional assumption in structural design. However, as expected, under low levels of excitation the dynamic response of the structure is definitely influenced by the presence of the masonry infills, as pointed out also by the results of the modal identification tests in operational conditions. This circumstance has been confirmed by the poor correlation between experimental and numerical results obtained for the model without walls. As a consequence, this case will be no more discussed hereinafter.

About the basement structure, the main source of uncertainty was related to the specific link (short deep beams) with the inner Tower and the related level of restraint offered to this. A simplified approach has been considered first. It was based on the assumption that the basement can be considered as a translational restraint along the perimeter of the first level of the Tower (Fig. 5.12a). This assumption takes into account the high transverse stiffness of the basement, due to the presence of perimeter r.c. walls and r.c. stairs for the access to the Tower, and its reduced height with respect to the Tower, resulting in a low contribution in terms of participating mass. On the other hand, because of the low level of vibrations in operational conditions, an additional model based on the assumption of full interaction between the Tower and the basement has been considered (Fig. 5.12b). This condition mainly affects the values of natural frequencies, in particular at higher modes.

Floors have been alternatively modeled by shell elements or diaphragms. At the upper levels, characterized by the alternate floors, the diaphragm has been applied only to the portion of structure characterized by the presence of the floor. The influence on the modal properties of the structure has been evaluated, in order to assess from a quantitative point of view the effects of the different assumptions. Slightly better results were expected in the case of floors modeled by shell elements. In fact, due to the role of masonry infills at low levels of excitation and the alternate floors, the adoption of rigid diaphragms at the various levels was not rigorous. However, as discussed below, the application of diaphragms to the half portions of floors at the upper levels also yields a fairly reliable model, characterized by good correlation with the experimental results.

The combination of the above mentioned modeling assumptions has led to definition of the following four classes of models:

- Floor = Diaphragm – With basement,
- Floor = Shell – With basement,
- Floor = Diaphragm – Without basement,
- Floor = Shell – Without basement.

Within each class, the elastic modulus of concrete and the shear modulus (obviously correlated to the elastic modulus) of tuff masonry were the parameters to be tuned. The elastic modulus of concrete has been taken in the range  $(E_{c,min}, E_{c,max}) = [13,000, 30,000]$  MPa in accordance with the large uncertainties in the definition of the mechanical properties of concrete by compressive tests. The shear modulus of tuff masonry has been, instead, taken in the range  $(G_{t,min}, G_{t,max}) = [300, 420]$  MPa in agreement with the range of values provided by the Italian seismic code for existing structures (Consiglio Superiore dei Lavori Pubblici 2008). The corresponding values for the elastic modulus of tuff masonry are  $(E_{t,min}, E_{t,max}) = [900, 1,260]$  MPa.

A fine increment for the values of elastic modules has been adopted and all possible combinations of values of elastic modules of tuff masonry and concrete have been processed, resulting in a total number of 2,132 models. These have been automatically generated and analyzed starting from a basic model for each class by means of software developed on purpose in LabVIEW environment.

As a result, sensitivities of the different model classes to changes in the material properties have been assessed. Typical response surfaces in terms of natural frequencies of the first six modes with respect to the values of elastic modules of concrete and tuff masonry are reported in Fig. 5.13. As expected, the natural frequencies of the first and the fourth mode were mainly influenced by the elastic modulus of concrete. On the contrary, a larger influence of the shear modulus of tuff masonry can be observed for the remaining modes.

### 5.3.4 Tuning of Selected Model Parameters

The validation of the modeling assumptions and the tuning of the model parameters have taken advantage of the sensitivity analyses carried out for each class of models and of the evaluation of correlations with the experimental results. In particular,

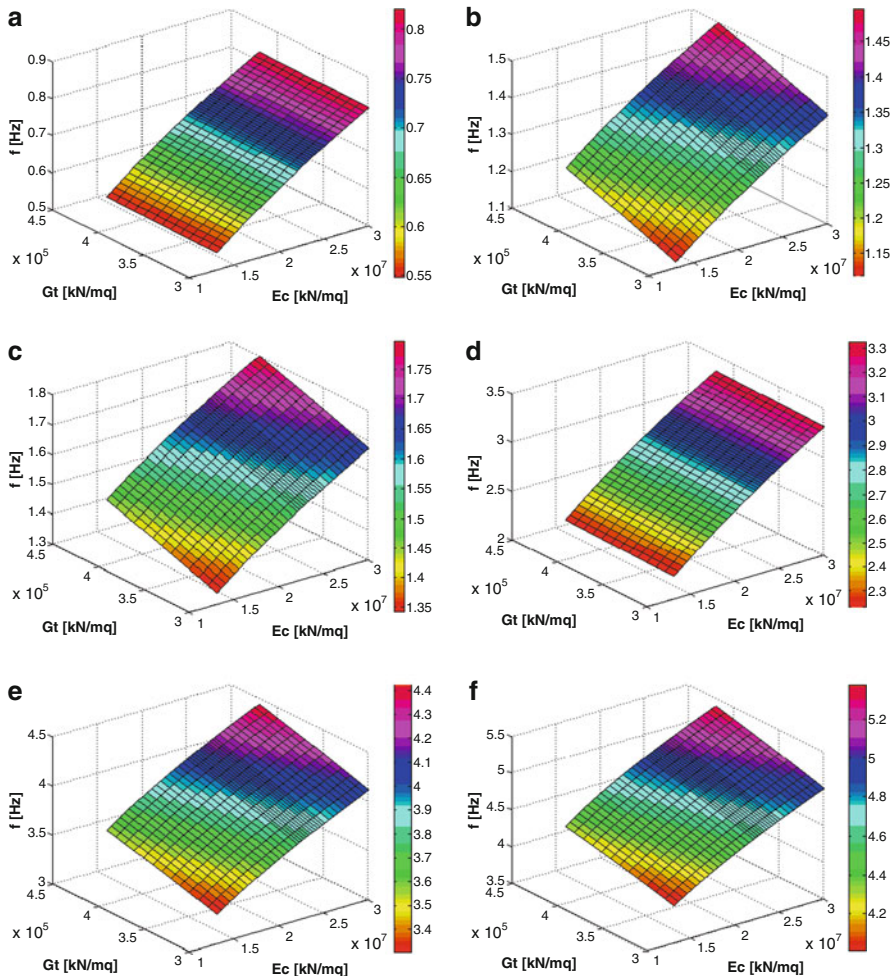


**Fig. 5.13** Sensitivity of natural frequencies to changes in the elastic modulus of materials (Floor = Shell – With basement): mode I (a), II (b), III (c), IV (d), V (e), VI (f), (© Elsevier Ltd. 2013), reprinted with permission

correlations have been evaluated as discussed in Chap. 4, while the systematic tuning of the parameters of the FE model has required the minimization of a user-defined objective function accounting for the correlation between numerical and experimental estimates of the modal properties. In the literature it is possible to find several objective functions accounting for deviations between numerical and experimental results. Widely used objective functions are defined in terms of the cumulative scatter between analytical and experimental values of natural frequencies only:

$$J_f = \sum_{i=1}^{N_m} |\Delta f_i| \quad (5.2)$$

where the scatter between the numerical and the experimental estimate of the natural frequency of the  $i$ -th mode is computed according to 4.298; alternatively, they can take into account also the mode shape correlation expressed by the MAC or the NMD (see also Chap. 4):

$$J_{f,\{\phi\}} = \sum_{i=1}^{N_m} [w_1 \cdot |\Delta f_i| + w_2 \cdot MAC(\{\phi_i^e\}, \{\phi_i^a\})] \quad (5.3)$$

$$J_{f,\{\phi\}} = \sum_{i=1}^{N_m} [w_1 \cdot |\Delta f_i| + w_2 \cdot NMD(\{\phi_i^e\}, \{\phi_i^a\})] \quad (5.4)$$

where  $w_1$  and  $w_2$  are optional weighting factors, which can be adopted when the dynamic properties are measured with different accuracy (Jaishi and Ren 2005). In the present case, the model parameter tuning was aimed at setting a refined model able to reproduce as close as possible the actual dynamic behavior of the structure and, at the same time, enhance the accuracy of response spectrum and seismic time-history linear analyses. Thus, checks not only of the mode shapes but also of the values of the PMRs (in particular those associated to the less correlated modes) throughout the model refinement process were necessary to properly fit the requirements of seismic analyses.

The PMR of a mode provides a measure of how important that mode is for computing the response of the modeled structure to the ground acceleration loads in each of the three global directions defined into the model. Thus it is useful for determining the accuracy of response spectrum analyses and seismic time-history analyses. International seismic codes (CEN 2003) require that response spectrum analyses are carried out combining, according to appropriate rules, all the modes characterized by a PMR larger than 5 % or, alternatively, a number of modes characterized by a total PMR larger than 85 %. This rule provides also a guide to select the number of modes to be taken into account in model refinement. The values of the PMRs obviously depend on the modeling assumptions and can vary from one model to another. Nevertheless, they represent global parameters, which can be estimated with adequate accuracy if the model to be optimized already shows a good correlation with the experimental data at the beginning of the tuning.

The PMR depends on the mode shapes of the structure and its mass distribution. The latter can usually be estimated with high accuracy. Thus, if the model also shows a good correlation with the experimental mode shapes, the values of the PMRs provided by the model can be considered fairly reliable. This is also the case of the herein considered four model classes. Thus, in the presence of a fairly accurate model, it is possible to take advantage of the information about the PMRs to drive the refinement process towards a solution characterized by maximum accuracy in terms of prediction capability of the structural response to an input ground motion.

Whenever the experimentally identified modes are not enough in number to fulfill code provisions, the experimental results represent a constraint in the model refinement. In the present case the values of the PMRs (Table 5.2) have pointed out

**Table 5.2** PMRs of sample models for each class, (© Elsevier Ltd. 2013), reprinted with permission

	Mode #	PMR X dir.	PMR Y dir.	Total PMR – X dir.	Sum PMR – Y dir.	PMR Z rotation	Total PMR Z rotation
<b>Floor = Shell – With basement</b>							
I	6.02E–01	8.53E–07	6.02E–01	8.53E–07	2.54E–01	2.54E–01	
II	7.36E–07	6.38E–01	6.02E–01	6.38E–01	2.47E–01	5.01E–01	
III	1.49E–08	1.18E–03	6.02E–01	6.39E–01	1.10E–01	6.11E–01	
IV	1.73E–01	3.35E–06	7.75E–01	6.39E–01	7.35E–02	6.84E–01	
V	3.16E–06	1.59E–01	7.75E–01	7.98E–01	6.54E–02	7.50E–01	
VI	4.53E–08	1.30E–05	7.75E–01	7.98E–01	2.32E–02	7.73E–01	
<b>Floor = Diaphragm – With basement</b>							
I	5.94E–01	2.95E–06	5.94E–01	2.95E–06	2.51E–01	2.51E–01	
II	2.00E–06	6.29E–01	5.94E–01	6.29E–01	2.40E–01	4.91E–01	
III	3.25E–08	1.75E–03	5.94E–01	6.31E–01	1.12E–01	6.03E–01	
IV	1.77E–01	3.68E–06	7.71E–01	6.31E–01	7.53E–02	6.78E–01	
V	5.24E–06	1.60E–01	7.71E–01	7.91E–01	6.56E–02	7.44E–01	
VI	2.21E–08	3.57E–05	7.71E–01	7.91E–01	2.41E–02	7.68E–01	
<b>Floor = Shell – Without basement</b>							
I	6.52E–01	8.12E–07	6.52E–01	8.12E–07	2.81E–01	2.81E–01	
II	7.30E–07	7.07E–01	6.52E–01	7.07E–01	2.80E–01	5.60E–01	
III	3.40E–08	1.31E–03	6.52E–01	7.09E–01	1.25E–01	6.86E–01	
IV	1.69E–01	3.37E–06	8.20E–01	7.09E–01	7.32E–02	7.59E–01	
V	3.00E–06	1.43E–01	8.20E–01	8.52E–01	5.99E–02	8.19E–01	
VI	1.30E–10	1.25E–05	8.20E–01	8.52E–01	2.12E–02	8.40E–01	
<b>Floor = Diaphragm – Without basement</b>							
I	6.81E–01	4.32E–06	6.81E–01	4.3E–06	2.93E–01	2.93E–01	
II	2.34E–06	7.47E–01	6.81E–01	7.47E–01	2.90E–01	5.83E–01	
III	4.26E–08	2.15E–03	6.81E–01	7.50E–01	1.36E–01	7.19E–01	
IV	1.78E–01	6.72E–06	8.59E–01	7.50E–01	7.71E–02	7.96E–01	
V	7.14E–06	1.56E–01	8.59E–01	9.05E–01	6.47E–02	8.61E–01	
VI	4.49E–10	5.99E–01	8.59E–01	9.05E–01	2.44E–02	8.85E–01	

**Table 5.3** Frequency scatter after parameter tuning according to (5.2) and (5.5), (© Elsevier Ltd. 2013), reprinted with permission

J	Solution	$\Delta f_1$	$\Delta f_2$	$\Delta f_3$	$\Delta f_4$	$\Delta f_5$	$\Delta f_6$	Total scatter
Equation (5.2)	Floor = Diaphragm – Without basement ( $E_c = 22,500$ MPa; $G_t = 310$ MPa)	3.08	0.01	2.45	11.56	0.08	1.99	19.17
	Floor = Shell – Without basement ( $E_c = 19,500$ MPa; $G_t = 390$ MPa)	10.66	0.68	1.50	0.91	2.98	0.59	17.31
	Floor = Diaphragm – With basement ( $E_c = 24,250$ MPa; $G_t = 300$ MPa)	6.05	0.03	2.25	4.07	3.43	0.008	15.83
	Floor = Shell – With basement ( $E_c = 24,000$ MPa; $G_t = 360$ MPa)	8.03	2.11	0.008	0.65	4.86	0.12	15.78
Equation (5.5)	Floor = Diaphragm – Without basement ( $E_c = 24,000$ MPa; $G_t = 300$ MPa)	0.04	1.08	1.40	14.96	0.61	2.75	20.84
	Floor = Shell – Without basement ( $E_c = 24,750$ MPa; $G_t = 300$ MPa)	0.24	0.75	1.35	12.04	3.41	0.46	18.27
	Floor = Diaphragm – With basement ( $E_c = 27,500$ MPa; $G_t = 300$ MPa)	0.13	3.64	1.33	10.51	0.25	3.29	19.15
	Floor = Shell – With basement ( $E_c = 28,500$ MPa; $G_t = 300$ MPa)	0.30	2.90	0.79	8.77	4.33	0.40	17.49

that, in almost all cases, six modes are not sufficient to get a total PMR larger than 85 %; however, higher modes after the fifth were generally characterized by PMRs lower than 5 %. This confirmed that the response of the Tower to input ground motions mostly depends on the first five or six modes. Thus, the experimentally identified modes were sufficient for the objectives of the analysis.

For each class of models the solution provided by the minimization of the above mentioned objective functions was locally unique but, in almost all cases, the maximum error affected the fundamental mode of the structure (Table 5.3). This was also characterized by a high PMR and, therefore, contributed significantly to the structural response to an input ground motion. In order to maximize the overall correlation with the experimental estimates of the modal parameters and minimize the error on the fundamental modes, characterized by the largest PMRs, an alternative objective function has been formulated. The information about the PMRs has

**Table 5.4** Mode shape correlation (NMD) of models characterized by different assumptions for the basement and model parameters tuned by minimization of the function in (5.5), (© Elsevier Ltd. 2013), reprinted with permission

Solution	Mode I	Mode II	Mode III	Mode IV	Mode V	Mode VI
Floor = Shell – Without basement ( $E_c = 24,750 \text{ MPa}$ ; $G_t = 300 \text{ MPa}$ )	0.242	0.076	0.319	0.306	0.140	0.352
Floor = Shell – With basement ( $E_c = 28,500 \text{ MPa}$ ; $G_t = 300 \text{ MPa}$ )	0.207	0.060	0.309	0.285	0.126	0.347

been directly included into the objective function as a weighting factor for the frequency scatters, thus obtaining the following expression:

$$J_{f,PMR} = \sum_{i=1}^{N_m} (|\Delta f_i| \cdot PMR_i) \quad (5.5)$$

where:

$$PMR_i = \frac{\left( \{\phi_i^a\}^T [M] \{I\} \right)^2}{\left( \{\phi_i^a\}^T [M] \{\phi_i^a\} \right)} \quad (5.6)$$

is the PMR of the  $i$ -th mode and  $\{I\}$  the influence vector (Chopra 2000). By this choice of the objective function, a larger error on the less contributing modes does not bias the overall calibration. The model parameters minimizing the objective function in (5.5) for the four model classes are reported in Table 5.3, together with the frequency scatters.

The objective function of (5.5) implicitly takes into account the information about the mode shapes through the PMRs. It provides a solution that is not simply the one minimizing the cumulative scatter with the experimental results. In fact, at the same time it gives the best results in terms of response spectrum and seismic time-history analyses, maximizing the correlation for the modes characterized by large PMRs and allowing larger errors in the case of modes providing minor contributions to the overall seismic response of the structure.

The best correlation with the experimental data has been obtained by modeling the floors by shell elements, taking into account the full interaction with the basement, and considering the following values of the updating parameters:  $E_c = 28,500 \text{ MPa}$ ,  $G_t = 300 \text{ MPa}$ . Taking into account the state of conservation of the structure, realistic values of the elastic properties of materials have been obtained. On the other hand, further checks of the solutions provided by (5.5) in terms of mode shape correlation have shown that the mode shapes obtained when the basement is explicitly modeled are also better correlated to the experimental data than those obtained when the effect of the basement is taken into account in a simplified way. The differences are highlighted by the NMD values shown in Table 5.4.

In summary, the present example provides an overview about the opportunities of OMA for the enhancement of the knowledge about the dynamic behavior of structures. The results put in evidence the relevant contribution of OMA to the minimization of the impact of structural assessment on architectural heritage structures.

The present application has also remarked the importance of proper consideration of the physics of the problem and of the objectives of the analysis for an effective tuning of the model parameters. In this perspective, the present application has pointed out, first of all, the importance of curtain walls on the dynamic response of the structure, at least for low levels of excitation.

The sensitivity analyses have also shown that the two different assumptions for modeling of floors were nearly equivalent, but the actual response of the structure was better reproduced by the use of shell elements, keeping the other modeling assumptions constant. Finally, in spite of its dimensions and the particular link with the body of the Tower, the basement has a not negligible influence on the global dynamic behavior of the structure, in particular when also the higher modes are considered.

---

## 5.4 Mass Normalized Mode Shapes

A major limitation of OMA pertains to the estimation of mode shapes. Since the input is unmeasured, the mode shapes cannot be mass normalized. Only unscaled mode shapes can be estimated because the scaling factors depend on the unknown excitation (Parloo et al. 2005). The missing information about the scaling factors can restrict the use of the modal parameter estimates in those application domains requiring mass normalized mode shapes, such as structural response simulation, load estimation (Parloo et al. 2003), some damage detection techniques (Pandey and Biswas 1994, Parloo et al. 2004). From a general point of view, the knowledge of the scaling factors of the mode shapes is critical whenever an FRF matrix has to be assembled from the estimated modal parameters (see also Chap. 4). For this reason, methods for the experimental estimation of mass normalized mode shapes by OMA procedures have recently been developed. They are based on the modification of the dynamic behavior of the structure under test by changing its mass or stiffness. The results of output-only modal identification of both the original and the modified structure are finally used to estimate the scaling factors.

The most popular methods for the estimation of scaling factors and mass normalized mode shapes belong to the class of the mass-change methods. These methods have been extensively validated by tests in the laboratory and on real structures (see, for instance, Parloo et al. 2005, Lopez-Aenlle et al. 2010). They consist in attaching masses to the points of the structure where the mode shapes of the unmodified structure have been estimated in a previous stage.

The number, magnitude and location of the masses is defined by the modal analyst and, as discussed below, this choice, together with the accuracy of modal parameter estimates, is responsible for the accuracy of the estimated scaling factors.

Moreover, since the mass-change methods use the modal parameters of both the original and the modified structure, they require extensive tests and a careful design of the experimental program. Lumped masses are typically used, so that the mass-change matrix  $[\Delta M]$  is diagonal.

Stiffness-change methods are a possible alternative to mass-change methods. As the mass-change methods, they use the modal parameters of both the original and the modified structure, but in this case the dynamic response of the structure is modified by changing its stiffness. Stiffness changes are obtained by connecting devices, such as cables or bars, at points of the structure where the mode shapes of the unmodified structure have been estimated in a previous stage. Combined mass-stiffness-change methods have also been developed (Khatibi et al. 2009), obtaining promising results. However, changing the stiffness of real civil structures is generally expensive and often impractical. This is the reason why attention is herein focused on the mass-change methods and, in particular, on best practice criteria to obtain accurate estimates of the scaling factors.

Equation (5.7) shows the relation between scaled and unscaled mode shape vectors:

$$\{\psi_j\} = \alpha_j \{\phi_j\} \quad (5.7)$$

where  $\alpha_j$  is the scaling factor for the  $j$ -th mode shape. Equation (5.7) highlights that the value of the scaling factor depends on the normalization used for the unscaled mode shape. Mode shapes normalized in a way that the largest element in each vector is equal to 1 are herein considered.

Omitting the theory behind each formulation (references are provided for the interested reader), well-established expressions for the estimation of the scaling factors by the mass-change approach are reported below.

Those fulfilling the structural-dynamic-modification theory are usually referred to as *exact equations*, to remark the difference with the so-called *approximated equations*, which do not properly take into account the change of the mode shapes when the structure is modified (Lopez-Aenlle et al. 2012). All the proposed formulations to estimate the scaling factor of a certain mode depend only on the modal parameters of that mode. Thus, it is eventually possible to optimize the estimation of the scaling factor of individual modes at the expenses of an increase in number and time of testing.

The original idea of the mass-change method can be traced back to Parloo et al. (2002). Using a first-order approximation for the sensitivity of the natural frequencies of lightly damped structures to mass changes, they derived a closed-form expression for the estimation of the scaling factors:

$$\alpha_j = \sqrt{\frac{2(\omega_{j,0} - \omega_{j,m})}{\omega_{j,0}\{\phi_{j,0}\}^T [\Delta M] \{\phi_{j,0}\}}} \quad (5.8)$$

where  $\omega_{j,0}$  and  $\omega_{j,m}$  represent the natural frequency of the  $j$ -th mode of the original and the modified structure, respectively, and  $\{\phi_{j,0}\}$  is the  $j$ -th (unscaled) mode

shape of the original structure. The validity of this formulation is restricted to small changes of the modal properties as a result of the mass change.

Alternative formulations able to take into account the changes in mode shapes and permitting relatively large modifications have been proposed by Bernal (2004) and Lopez-Aenlle et al. (2010). If mode shape estimates of both the original and the modified structure are available, the following matrix can be computed:

$$[\hat{B}] = [\hat{\Phi}_0]^+ [\hat{\Phi}_m] \quad (5.9)$$

where  $[\hat{\Phi}_0]$  and  $[\hat{\Phi}_m]$  are the matrices collecting (in columns) the estimates of the mode shapes of the original and the modified structure, respectively. The terms on the main diagonal of  $[\hat{B}]$  are close to one while the off-diagonal terms are close to zero, except for closely spaced modes (Lopez-Aenlle et al. 2012). The terms on the main diagonal are usually fairly accurate even in the presence of modal truncation effects, while poor accuracy characterizes the off-diagonal terms (Lopez-Aenlle et al. 2012). If only the diagonal terms  $\hat{B}_{jj}$  of  $[\hat{B}]$  are considered, the scaling factor of the j-th mode can be computed as:

$$\alpha_j = \sqrt{\frac{(\omega_{j,0}^2 - \omega_{j,m}^2)B_{jj}}{\omega_{j,m}^2\{\phi_{j,0}\}^T[\Delta M]\{\phi_{j,m}\}}} \quad (5.10)$$

where  $\{\phi_{j,m}\}$  is the j-th (unscaled) mode shape of the modified structure. This expression was originally obtained by Bernal (2004) as a result of the projection of the mode shapes of the modified system on the basis of the original structure. The expression proposed by Lopez-Aenlle et al. (2010) is a special case of the formulation given by (5.10) where  $\hat{B}_{jj}$  is assumed to be equal to one:

$$\alpha_j = \sqrt{\frac{(\omega_{j,0}^2 - \omega_{j,m}^2)}{\omega_{j,m}^2\{\phi_{j,0}\}^T[\Delta M]\{\phi_{j,m}\}}}. \quad (5.11)$$

Equations (5.8), (5.10) and (5.11) point out the primary role of output-only modal parameter identification in the accurate estimation of scaling factors. The uncertainties associated to natural frequency and mode shape estimates must be as low as possible (best practices to carry out a good modal identification have been discussed throughout this book).

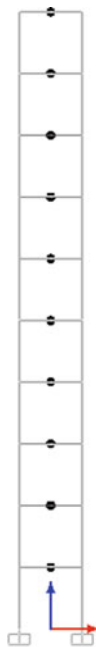
However, the uncertainties in the estimation of scaling factors depend not only on the accuracy of modal parameter estimates but also on the adopted mass-change strategy. Different choices for the number, magnitude and location of the masses lead to different changes in the dynamic behavior of the structure. Thus, the mass-change strategy has to be carefully designed and analyzed before applying the mass-change method for the estimation of the scaling factors. Previous experiences reported in the literature provide the following guidelines for a successful estimation of scaling

factors by mass-change methods (Lopez-Aenlle et al. 2010, Lopez-Aenlle et al. 2012, Parloo et al. 2005):

- The mass change should not be too large: a mass change of about 5 % of the total mass of the structure is recommended; however, depending on the specific structure under investigation and the number and location of masses, the adopted mass change can be slightly higher or lower than the above mentioned recommended value; as a general rule, the applied mass change has to produce frequency shifts of about 1.5–2 %; a larger frequency shift can be recommended for the fundamental modes of very flexible structures; on the other hand, it is worth pointing out that the mass change has to be applied in a way able to minimize the modification of mode shapes: thus, for a given total mass change, small mass changes, proportional to the mass matrix of the original structure, are recommended for the DOFs considered in the tests; taking into account that the added masses are usually represented by large concrete blocks when the mass-change methods are applied to civil structures, maintaining the masses as small as possible reduces also the possibility of local changes in stiffness caused by the blocks and, therefore, the estimation errors;
- The importance of attaching as many masses as possible also depends on the possibility to simultaneously estimate the scaling factors for several modes; even if the expressions for the scaling factors depend on the modal parameters of the mode of interest only, the availability of a large number of small masses allows the optimization of the mass location for the simultaneous estimation of the scaling factors of a number of modes, thus reducing the time of testing; however, it is worth pointing out that a certain location of the masses can be optimum for certain modes but it can yield inaccurate estimates of the scaling factors for the remaining modes; thus, multiple modal tests are recommended because a different mass layout can significantly improve the accuracy of the estimates of the scaling factors of selected modes;
- The masses have to be placed in points characterized by large modal displacements, since very small frequency shifts are obtained when the masses are located near nodal points of the mode shapes considered in the normalization; as a consequence, the number and location of masses have to take into account the distributions of modal displacements, eventually changing the measured DOFs and the location of masses to enhance the accuracy of the scaling factor estimates of selected modes.

The importance of mass location for the accurate identification of scaling factors can be understood through a simple example. Consider a one-bay ten-story r.c. shear-type frame, with square columns characterized by a 30 cm × 30 cm cross section. Columns and beams are 3 m long. Assume lumped masses of 7,500 kg associated to the ten DOFs of the structure and constant damping (1 %) for all modes. The numerical model of this simple structure (Fig. 5.14) can be used for a simulated application of the mass-change method. The responses of the original and the modified structure to a Gaussian white noise can be simulated and analyzed by OMA methods to estimate the scaling factors. The obtained results can be compared to the reference values provided by the model.

**Fig. 5.14** The r.c. frame for the application of the mass-change method



Assume that only five masses are available. The objective of this example is the analysis of the variations of the scaling factor estimates for two different configurations of the attached masses, one of which has been optimized for the estimation of the scaling factors of the three fundamental modes of the structure.

For this explanatory application, assume that all modes of the structure have been identified and the modal displacements have been initially measured at all the ten DOFs. The optimum location of the masses can be defined from the analysis of modal displacements. The contribution of a unit mass located at the  $j$ -th DOF to shift the natural frequency of the  $k$ -th mode is expressed by the square of the related component of the unscaled mode shape vector of the  $k$ -th mode of the original structure (Lopez-Aenlle et al. 2010). The squared modal displacements are reported in Table 5.5 for all the DOFs and modes of the original structure. They have also been normalized making the largest element equal to 100 for each mode. DOFs are numbered from 1 to 10 from bottom up.

The analysis of the squared modal displacements in Table 5.5 shows that the largest frequency shifts for the three fundamental modes of the structure can be obtained by placing the masses at DOFs #10, #9, #7, #3, #2. The results obtained by this configuration of the added masses are compared with those obtained by placing the masses at DOFs #10, #8, #5, #2, #1.

Denote the optimum configuration of the masses as CONFIG#1 and the other as CONFIG#2. In both cases, the added mass is equal to 3 % of the total mass of the structure. In other words, masses of 450 kg are attached to the five DOFs considered in the respective analysis cases.

**Table 5.5** Contribution of unit mass at DOF j to the frequency shift of mode k

Mode	DOF #10	DOF #9	DOF #8	DOF #7	DOF #6	DOF #5	DOF #4	DOF #3	DOF #2	DOF #1
I	100.0	95.6	87.1	75.4	61.5	46.5	31.9	18.9	8.7	2.2
II	100.0	64.3	19.8	0.0	19.8	64.3	100.0	100.0	64.3	19.8
III	87.1	18.9	8.7	75.4	95.6	31.9	2.2	61.5	100.0	46.5
IV	100.0	0.0	100.0	100.0	0.0	100.0	100.0	0.0	100.0	100.0
V	64.3	19.8	100.0	0.0	100.0	19.8	64.3	64.3	19.8	100.0
VI	46.5	61.5	31.9	75.4	18.9	87.1	8.7	95.6	2.2	100.0
VII	31.9	95.6	2.2	75.4	61.5	8.7	100.0	18.9	46.5	87.1
VIII	19.8	100.0	64.3	0.0	64.3	100.0	19.8	19.8	100.0	64.3
IX	8.7	61.5	100.0	75.4	18.9	2.2	46.5	95.6	87.1	31.9
X	2.2	18.9	46.5	75.4	95.6	100.0	87.1	61.5	31.9	8.7

**Table 5.6** Natural frequency estimates for the original and the modified structures

Mode #	Original structure (Hz)	CONFIG#1 (Hz)	CONFIG#2 (Hz)	CONFIG#3 (Hz)
I	0.363	0.357	0.358	0.358
II	1.082	1.063	1.066	1.066
III	1.777	1.743	1.750	1.750

A third case is also considered, where the masses are attached at the DOFs of CONFIG#1 but the magnitude of the mass change is lower than 3 %. This configuration of the masses is denoted as CONFIG#3 and the added masses, characterized by the same magnitude (367 kg) for the various DOFs, produce the same frequency shift obtained by the mass change considered in CONFIG#2.

The analysis of the simulated response to a Gaussian white noise of the original structure and of the modified structures has given the results shown in Table 5.6 in terms of natural frequency estimates. Cov-SSI has been used to analyze the data.

CONFIG#1 yields frequency shifts in the range 1.7–1.9 %, while the frequency shifts corresponding to CONFIG#2 and CONFIG#3 are in the range 1.4–1.5 %. Please, note that the simulated response of the original structure has been analyzed twice in order to obtain the mode shape estimates at the different sets of DOFs considered in CONFIG#1 and CONFIG#3 on one hand, and CONFIG#2 on the other hand. The scaling factors estimated according to (5.8), (5.10) and (5.11) for the three configurations of added masses are reported in Tables 5.7, 5.8 and 5.9.

The obtained results point out that, for a given mass change (3 % of the total mass of the structure), the scaling factors estimated by CONFIG#1 are by far more accurate than those provided by CONFIG#2. Moreover, comparing the results provided by CONFIG#2 and CONFIG#3 shows that the estimates obtained by CONFIG#3 are characterized by similar (or sometimes better) accuracy with those provided by CONFIG#2, despite of the lower mass change (2.4 % instead of 3 %) and the equal frequency shifts for the considered modes.

**Table 5.7** Scaling factors obtained according to (5.10)

Mode #	Model	CONFIG#1	CONFIG#2	CONFIG#3	Scatter (%) #1	Scatter (%) #2	Scatter (%) #3
I	0.005025	0.005020	0.005053	0.005064	-0.11	0.56	0.77
II	0.004913	0.005021	0.005068	0.005090	2.21	3.16	3.60
III	0.005025	0.005123	0.005129	0.005034	1.95	2.07	0.18

**Table 5.8** Scaling factors obtained according to (5.11)

Mode #	Model	CONFIG#1	CONFIG#2	CONFIG#3	Scatter (%) #1	Scatter (%) #2	Scatter (%) #3
I	0.005025	0.005025	0.005056	0.005068	0.00	0.63	0.86
II	0.004913	0.004862	0.005053	0.004934	-1.04	2.86	0.43
III	0.005025	0.005081	0.005132	0.005003	1.12	2.13	-0.43

**Table 5.9** Scaling factors obtained according to (5.8)

Mode #	Model	CONFIG#1	CONFIG#2	CONFIG#3	Scatter (%) #1	Scatter (%) #2	Scatter (%) #3
I	0.005025	0.004959	0.005002	0.005013	-1.31	-0.46	-0.24
II	0.004913	0.004918	0.005008	0.004998	0.10	1.94	1.72
III	0.005025	0.005031	0.005062	0.004964	0.11	0.74	-1.21

The above discussed example points out the importance of carefully choosing the location of the added masses. Whenever the optimization of the mass location for the simultaneous estimation of the scaling factors of multiple modes is not feasible, repeated tests focused on subset of modes or individual modes are recommended to obtain accurate scaling factor estimates.

---

## 5.5 The Excitation System: Identification of Spurious Frequencies

Response spectra sometimes show dominant frequency components that do not represent natural frequencies of the structure under test. On the contrary, they are frequency components of the excitation system and, as such, they are due to physical reasons. Specific strategies and techniques are, therefore, needed to sort out the natural frequencies of the structure under test from spurious frequencies associated to the excitation.

Civil engineering structures are usually excited by broadband input associated to environmental and operational loads (wind, traffic, micro-tremors, etc.). However, the presence of spurious frequency components due to the excitation cannot a-priori be excluded. A careful analysis of response spectra and checks of the nature of the identified peak frequencies are always required for validation of results.

Spurious peaks are sometimes due to the combination of the stochastic broadband input with harmonic components, deterministic in nature. This phenomenon is more frequent in the case of mechanical systems such as in-flight helicopters, running engines (Peeters et al. 2007) and ships in operation (Rosenow et al. 2007). In the case of civil engineering structures, spurious harmonic components superimposed to the stochastic response can be encountered because of the presence of turbines, generators, ventilation equipment and other mechanical components and systems installed on or nearby the structure. The presence of deterministic signals superimposed to the stochastic response makes the output-only identification of the modal parameters more difficult. In fact, the spurious dominant frequencies of the excitation system can wrongly be identified as physical modes. A high dynamic range is also needed to extract weakly excited modes in the presence of such harmonics. Moreover, when these spurious dominant frequency components are very close to the frequencies of structural modes, they negatively affect the accuracy of modal parameter estimates (Jacobsen et al. 2007, Agneni et al. 2012).

A number of criteria and methods are available to identify the presence of spurious harmonics. If auto-spectral densities with high frequency resolution are estimated, spurious harmonics appear as sharp peaks. Their bandwidth and their spectral density depend on the frequency resolution. In fact, a further reduction of the frequency spacing yields a reduction of the bandwidth and a proportional increase in the spectral density, while the bandwidth of actual structural resonances is not affected by the adopted frequency resolution (Bendat and Piersol 2000). This is a very basic method of detection, which is effective only if the frequency spacing of the estimated spectral densities is smaller than the actual bandwidth of structural modes.

The analysis of the Short Time Fourier Transform (Qian and Chen 1996) of the responses, shown in a contour plot, represents a more refined alternative for harmonic detection. In fact, thin straight lines parallel to the time axis usually denote harmonic components at fixed frequency, while thick straight lines parallel to the time axis characterize structural modes (Jacobsen et al. 2007, Herlufsen et al. 2005).

Spurious harmonics due to rotating equipment can also be identified directly in the modal parameter estimation stage. For instance, SSI methods are able to estimate both the harmonic components and the structural modes, even when they are characterized by close frequencies (Jacobsen et al. 2007). Since the spurious harmonics can be seen as virtual modes with zero damping (Modak et al. 2010), an appropriate setting of the valid range of damping ratios can filter out the poles characterized by very low damping, so that they do not appear in the stabilization diagram (Jacobsen et al. 2007). However, this method can be ineffective in the presence of structural modes characterized by very low damping (Modak et al. 2010).

When the FDD method is adopted, the singular values of the PSD matrix at discrete frequencies can act as an indicator of the presence of a spurious harmonic at a given frequency. In fact, when a spurious harmonic is present, a high rank characterizes the PSD matrix because all modes are excited.

The analysis of the probability density function of the measured response in a narrow frequency range around the peak represents an effective way to sort out harmonic and structural modes when EFDD is used for modal identification. Comparing the probability density function of the potential mode, isolated by band-pass filtering, with those of the sine wave and the sine wave in Gaussian noise on one hand and the Gaussian probability density function on the other hand (Chap. 2) can support the discrimination between spurious harmonics and structural resonances (Brincker et al. 2000).

The visual inspection of mode shapes can also support the discrimination between harmonic and structural modes. In fact, whenever the harmonic component is well separated from structural resonances, it yields an ODS that is the combination of several excited modes and the input. This is not the case of spurious harmonics close to structural modes, since the ODS of the harmonic resembles the actual mode shape leading to potential identification mistakes.

Some authors have proposed the use of statistical indexes, such as kurtosis and entropy, as harmonic indicators (Jacobsen et al. 2007, Agneni et al. 2012). The kurtosis index is defined as the fourth central moment of the generic random variable  $x$  normalized with respect to the fourth power of the standard deviation:

$$\kappa = \frac{E[(x_k - \mu_x)^4]}{\sigma_x^4}. \quad (5.12)$$

For Gaussian distributions the kurtosis is equal to 3, while the kurtosis of a sine wave is 1.5. If the excess kurtosis:

$$\bar{\kappa} = \kappa - 3 \quad (5.13)$$

is used instead of the kurtosis defined by (5.12), harmonic signals are identified by values of  $\bar{\kappa}$  equal to  $-1.5$ , while null values characterize Gaussian distributions. As an alternative, if the probability density function of the random process has been estimated (Chap. 2), harmonic signals in a stochastic process can be identified from local minima of the entropy (sometimes referred to as Shannon entropy) in the frequency range under investigation:

$$S = -\sum_{k=1}^K \hat{p}_k \log(\hat{p}_k). \quad (5.14)$$

Harmonic detection is based on the calculation of either entropy or kurtosis as a function of frequency through the application of a running band-pass filter centered at each discrete frequency considered in the analysis. The major drawback with these methods is the relevant influence of filter parameters (frequency range and roll-off rate of the filter) on the detection ability.

When EFDD is used for modal identification, harmonics close to the natural frequency of the structure can be removed by a linear interpolation in order to

reduce their influence on the estimated natural frequencies and damping ratios (Jacobsen et al. 2007). Whenever the harmonic frequencies close to the eigenfrequencies are known, modified NExT-type methods can also be adopted to explicitly take into account the harmonic excitation components in the identification process and enhance the accuracy of modal parameter estimates. If the presence of the harmonic component is not known in advance, accurate modal parameter estimates can be obtained from the transmissibility-based method under the assumption of fully correlated inputs (such as those coming from a dominant discrete source); no filtering or interpolation is needed, but the assumptions of the method require changing loading conditions. They imply more involved test procedures to ensure changes in the location, number or amplitude of the forces. These methods are beyond the scope of the present book because spurious harmonics rarely lead to major problems in output-only modal identification of civil engineering structures; the interested reader can refer to the literature for more details (Mohanty and Rixen 2004, Mohanty and Rixen 2006, Devriendt et al. 2009). Nevertheless, a complete structural and functional assessment of the structure under test is recommended in order to identify possible sources of harmonic excitation and take into account their possible effects on dynamic measurements and test results.

Few studies are reported in the literature about the output-only identification of structural modes in the presence of spurious dominating frequencies due to dynamic interaction with adjacent structures. Oliveira and Navarro (2009) reported this issue, pointing out the critical role of a careful examination of the peaks in the spectra to successfully sort structural and spurious modes.

An integrated approach to the identification of spurious dominating frequencies due to dynamic interaction with adjacent structures has recently been proposed (Rainieri et al. 2012). It is herein described in its main aspects, because it provides an interesting example of how the integrated use of output-only modal analysis techniques can rationally support the identification of spurious frequencies due to interaction with adjacent buildings. These frequencies do not appear as sharp peaks in response spectra. This makes the discrimination between structural resonances and spurious dominant frequencies even more difficult.

The case study analyzed in this section is particularly interesting in this perspective, because it deals with close and interacting structures characterized by similar natural frequencies. Narrowband excitation due to rotating components is also present. The effect of interactions on response spectra is represented by the presence of several peaks in a narrow frequency range; however, only a few of them are actually related to structural modes.

The herein discussed case study refers to an experimental campaign carried out on four buildings belonging to the B1 Block in the area of the Guardia di Finanza Non-Commissioned Officers' School in Coppito (L'Aquila, Italy) under the coordination of the Italian Department of Civil Protection right after the L'Aquila earthquake on April 6-th, 2009. In particular, the results of dynamic tests are presented.



**Fig. 5.15** The B1 Building Block: East side (a), courtyard (b), South side (c), outdoor stairs (d)

The B1 block of buildings covers a rectangular area of 165 m by 66 m and it consists of nine similar r.c. moment frame buildings distributed on three lines. Connection among the different buildings and vertical distribution are ensured by a number of separated r.c. stairs. Indoor stairs are located in the intermediate courtyards; outdoor stairs are located at each building alignment head. Each building and stair structure appeared to be independent of the adjacent ones because of the presence of seismic joints. Attention is herein focused on buildings. Figure 5.15 shows some views of the analyzed block.

Regularity in elevation from a dynamic standpoint was affected by a different arrangement of partitioning walls at the ground level with respect to the upper levels. Notwithstanding an exterior simple structural configuration, very similar among the different buildings in the block, some differences in their dynamic responses were expected.

Since the dynamic tests were carried out a few days after the L'Aquila earthquake mainshock, the different levels of nonstructural damage that affected each building also influenced the dynamic responses. Identification of their modal properties was made even more difficult by the circumstance that the fundamental modes of the different buildings were characterized by quite similar natural

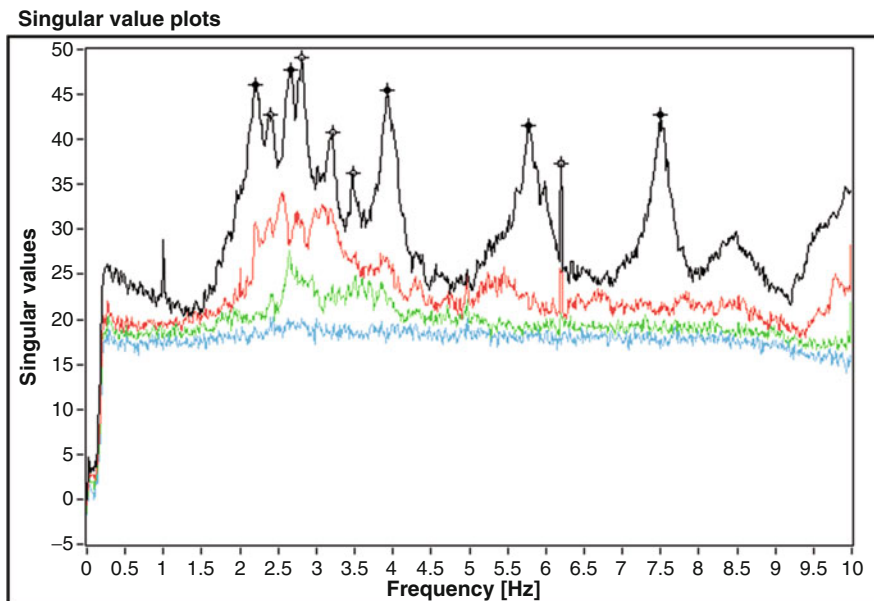


**Fig. 5.16** Sample singular value plots: *filled circles* denote structural modes, *empty circles* denote dominant frequencies due to interactions, the *empty square* denotes a harmonic due to rotating parts, (© Elsevier Ltd. 2012), reprinted with permission

frequencies and, as shown in Fig. 5.16, such frequencies were located in a narrow frequency range between 2 and 4 Hz.

Interaction effects, represented by dominant frequency components in the response spectrum of a building associated to structural resonances of the surrounding structures, were probably related to the solutions adopted for the foundations, which were common to all buildings and stairs in the block.

In addition, as a consequence of ground shaking and of the technological solutions adopted for seismic joints, pounding phenomena between buildings and stairs were not inhibited. The result was a certain degree of interaction among the different buildings and among buildings and stairs (both interior and exterior) so that the natural frequencies of a certain building or stair appeared in the dynamic response in operational conditions of other close buildings in the block. A plane view of the block is reported in Fig. 5.17. In the same picture, numbers 2, 3, 5 and 6 identify the investigated buildings. Their relevant dimensions are 48.7 m by 15.40 m.

Measurements of the dynamic responses of the buildings were carried out to monitor the evolution of the dynamic parameters during aftershocks, as a support to visual inspections for structural damage detection, to refine numerical analyses for capacity assessment, and in view of the installation of a vibration-based SHM system. Thus, the adopted sensor layout was aimed at monitoring the largest number of buildings at the same time with a limited number of available sensors.

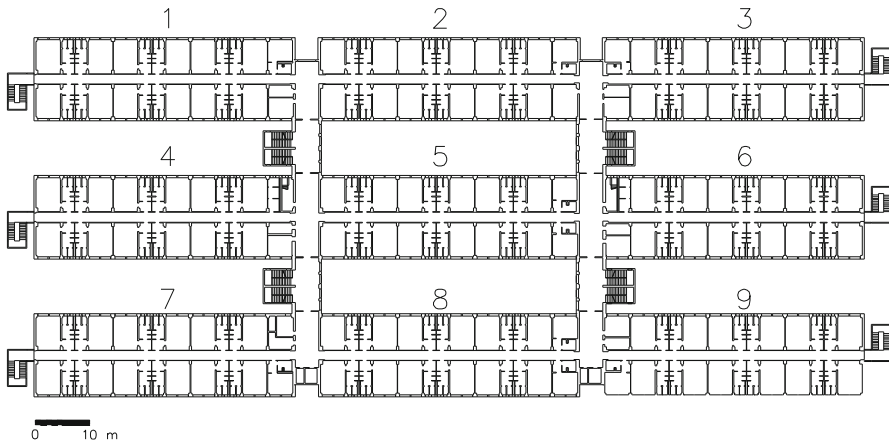


**Fig. 5.17** Plan view of the B1 Block: nine buildings jointed among them and with stairs, (© Elsevier Ltd. 2012), reprinted with permission

The sensor layout had to consider also some operational constraints (limited room accessibility). The final configuration ensured the identification of at least the fundamental bending and torsional modes of the tested buildings. The sensor layout is reported in Fig. 5.18. A tern of sensors in three orthogonal directions has also been installed on the basement in order to measure eventual input at the base of the structure due to ground motion. Even if the whole measurement setup is herein described, only records of the dynamic response of the structures in operational conditions have been considered in the following analyses. Buildings #2 and #3 have been monitored at the upper level and at the intermediate level. Four sensors have been installed in two opposite corners at each level and along two orthogonal directions in order to ensure observability of both translational and tensional modes. Testing of buildings #5 and #6, instead, involved only two couples of sensors placed at the upper level and measuring in two orthogonal directions parallel to the main axes of each building. In the data processing phase it has also been recognized that sensor #3 in the x direction on building #5 was out of order. It has not been used in the analyses. Thus, only three sensors were available for the characterization of the dynamic behavior of building #5. This circumstance increased the complexity of modal identification.

The dynamic responses of buildings #2 and #3 have been measured by means of uniaxial force balance accelerometers, while piezoelectric accelerometers have been installed on buildings #5 and #6. The characteristics of the installed sensors are summarized in Table 5.10. The selected sensors ensured the possibility to properly resolve the dynamic response of the buildings to both the operational loads and eventual input ground motions.

Vibration data have been acquired through a customized 16-bit data acquisition recorder, able to acquire dynamic data from a number of different sensors including force balance and piezoelectric accelerometers. Sensors were installed on steel

**Fig. 5.18** Sensor layouts for building #2 (a), #3 (b), #5 (c), #6 (d), (© Elsevier Ltd. 2012), reprinted with permission

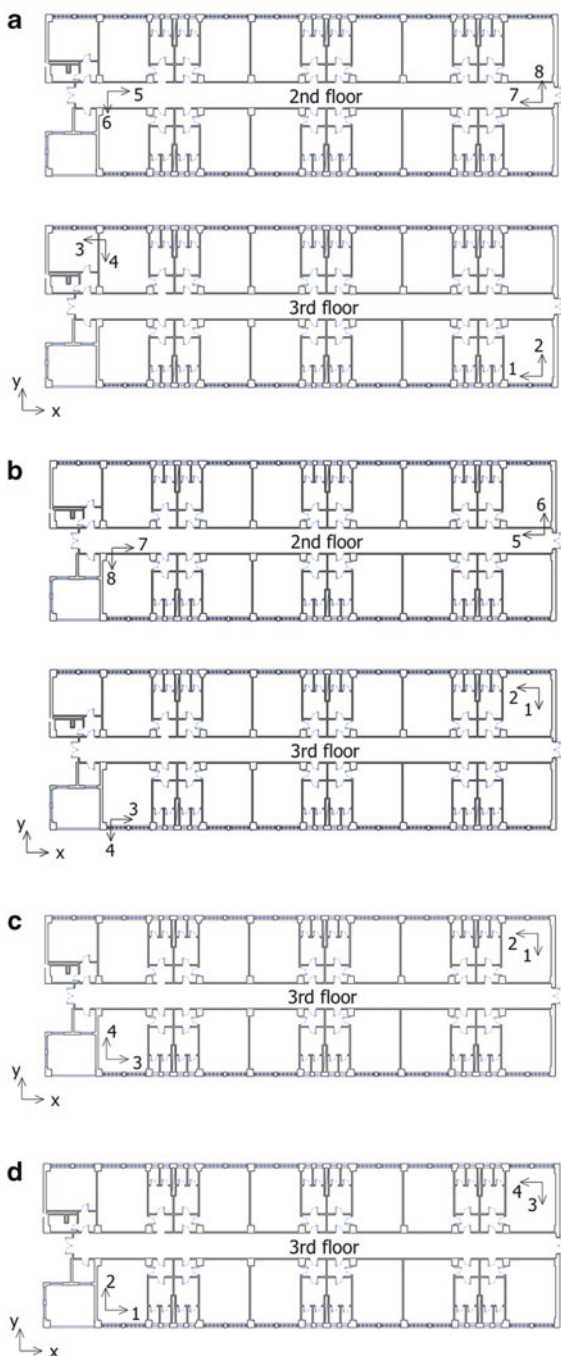


**Table 5.10** Characteristics of the installed sensors, (© Elsevier Ltd. 2012), reprinted with permission

Sensor	Measurement directions	Sensitivity (V/g)	Full-scale range (g)	Resolution (g)	Dynamic range (dB)	Bandwidth (Hz)	Transverse sensitivity (%)	Nonlinearity
Force balance accelerometer	1	20	0.5	—	140	0–200	≤1	<1,000 $\mu\text{g}/\text{g}^2$
IEPE accelerometer	1	10	0.5	0.000001	—	0.1–200	≤5	≤1 %

plates screwed on the floor. Cables were clamped to the structure along the whole path to the data acquisition recorder in order to avoid introduction of measurement noise by triboelectric effects due to cable motion.

Data have simultaneously been acquired from the 27 accelerometers installed over the block of buildings; a sampling frequency equal to 100 Hz was adopted. The dynamic response of the buildings has continuously been monitored for more than two consecutive days. Each stored record was 3,600 s long.

Before processing, the records have been accurately inspected in order to assess data quality. Offsets and spurious trends have been removed. Data have been filtered and decimated to obtain a final sampling rate of 20 Hz. Hanning window and 66 % overlap have been adopted for spectrum computation in view of frequency domain modal parameter estimation. OMA has been carried out according to the following methods: Cov-SSI, EFDD and SOBI. An automated output-only modal identification procedure, named LEONIDA (Rainieri and Fabbrocino 2010), has also been applied. It is a frequency domain algorithm for automated OMA that takes advantage of the information obtained from the SVD of the PSD matrices computed from multiple records to identify the bandwidth of the structural modes before automatically extracting the modal parameters. More details are given in Chap. 6.

The dynamic responses of the buildings have been analyzed from the local and global point of view. The global analysis has put in evidence the similarities. Then, local analyses and consistency checks have made the discrimination between structural resonances and spurious dominating frequencies possible. The selection of candidate modes was based on the analyst's experience following best practice criteria for the various OMA methods. The only exception was represented by the results provided by LEONIDA, which is a fully automated OMA procedure and, as such, it does not require any user intervention. Ranking of the candidate modes resulted from the inspection of a number of features; scores have been assigned according to the list reported in Table 5.11.

A score equal to 1 (−1) has been adopted for values of the parameters usually associated to the presence (absence) of a structural mode; a score equal to 0.5 was, instead, adopted for values of the parameters associated to more uncertain conditions. The maximum achievable total score was 7. A candidate mode has been labeled as structural if the total score was at least equal to 5/7. The minimum value of the total score defining a structural mode and the adopted scores for SOBI take into account that the responses of building #5 and building #6 have been measured by few sensors (only three working sensors for building #5). As already mentioned in Chap. 4, this has consequences on the number of identifiable modes by SOBI. Moreover, this circumstance has limited the possibility to analyze the aspect of mode shapes.

Scoring of candidate modes is detailed in Tables 5.12, 5.13, 5.14, and 5.15. Ranking and identified structural modes (dark bars above threshold) are shown in Fig. 5.19. Realistic damping values were associated to nearly all candidate modes with few exceptions, so their inspection has not been useful to sort the structural modes. For this reason damping has not been selected as a feature for classification. Nevertheless, damping values are reported for the sake of completeness.

**Table 5.11** Scores for mode classification, (© Elsevier Ltd. 2012), reprinted with permission

Feature	Options	Score
EFDD	Presence of peak	1.0
	Absence of peak	-1.0
Cov-SSI	Fully stable poles	1.0
	Partially stable poles	0.5
	Unstable poles	-1.0
SOBI	Well-separated source	1.0
	Not well-separated source	0.5
	Unidentified source	0.0
LEONIDA	Identified mode	1.0
	Unidentified mode	-1.0
Coherence	Higher than 0.98	1.0
	Between 0.8 and 0.98	0.5
	Lower than 0.8	-1.0
Mode complexity	Real valued	1.0
	Slightly complex	0.5
	Complex	-1.0
Mode shape aspect	Physically admissible	1.0
	Not physically admissible	-1.0

**Table 5.12** Building #2: candidate modes and score report, (© Elsevier Ltd. 2012), reprinted with permission

f (Hz)	EFDD	Cov-SSI	SOBI	LEONIDA	Coherence	Mode shape complexity	Mode shape aspect	$\xi$ (%)	Total score
2.18	1.0	-1.0	0	-1.0	0.5	1.0	1.0	5.9	1.5
2.58	1.0	1.0	0.5	1.0	1.0	1.0	1.0	2.2	6.5
2.64	-1.0	1.0	0	-1.0	1.0	-1.0	-1.0	0.2	-2.0
2.88	1.0	1.0	1.0	1.0	0.5	1.0	1.0	2.4	6.5
2.98	-1.0	1.0	0	-1.0	-1.0	-1.0	-1.0	1.3	-4.0
3.52	1.0	1.0	1.0	1.0	1.0	1.0	1.0	1.1	7.0
5.31	1.0	1.0	0.5	1.0	1.0	1.0	1.0	0.9	6.5
7.09	1.0	1.0	0	1.0	1.0	1.0	1.0	0.7	6.0

**Table 5.13** Building #3: candidate modes and score report, (© Elsevier Ltd. 2012), reprinted with permission

f (Hz)	EFDD	Cov-SSI	SOBI	LEONIDA	Coherence	Mode complexity	Mode shape aspect	$\xi$ (%)	Total score
2.18	1.0	-1.0	0	-1.0	-1.0	-1.0	-1.0	2.8	-4.0
2.58	1.0	1.0	1.0	1.0	1.0	1.0	1.0	2.5	7.0
2.88	1.0	0.5	0.5	1.0	1.0	1.0	1.0	1.1	6.0
2.99	1.0	1.0	0	-1.0	0.5	1.0	1.0	2.6	3.5
3.19	1.0	-1.0	0	-1.0	-1.0	-1.0	-1.0	3.7	-4.0
3.52	1.0	1.0	1.0	1.0	1.0	1.0	1.0	1.2	7.0
5.26	1.0	-1.0	1.0	-1.0	-1.0	1.0	-1.0	1.1	-1.0

**Table 5.14** Building #5: candidate modes and score report, (© Elsevier Ltd. 2012), reprinted with permission

f (Hz)	EFDD	Cov-SSI	SOBI	LEONIDA	Coherence	Mode complexity	Mode shape aspect	$\xi$ (%)	Total score
2.20	1.0	1.0	0.5	-1.0	-1.0	-1.0	-1.0	2.7	-1.5
2.41	1.0	1.0	0	-1.0	-1.0	1.0	-1.0	3.2	0.0
2.67	1.0	1.0	1.0	1.0	1.0	1.0	1.0	1.2	7.0
3.15	1.0	1.0	0	1.0	1.0	0.5	1.0	2.5	5.5
3.96	1.0	1.0	1.0	1.0	1.0	1.0	1.0	1.1	7.0

**Table 5.15** Building #6: candidate modes and score report, (© Elsevier Ltd. 2012), reprinted with permission

f (Hz)	EFDD	Cov-SSI	SOBI	LEONIDA	Coherence	Mode complexity	Mode shape aspect	$\xi$ (%)	Total score
2.24	1.0	1.0	0.5	1.0	1.0	1.0	1.0	2.9	6.5
2.41	1.0	1.0	0	-1.0	1.0	1.0	1.0	3.3	4.0
2.67	1.0	1.0	0.5	1.0	1.0	1.0	1.0	1.8	6.5
2.81	1.0	1.0	0.5	1.0	-1.0	0.5	-1.0	1.4	2.0
3.20	1.0	1.0	0	-1.0	-1.0	-1.0	-1.0	3.5	-2.0
3.47	1.0	1.0	0	-1.0	-1.0	-1.0	-1.0	5.3	-2.0
3.96	1.0	1.0	1.0	1.0	1.0	1.0	1.0	1.0	7.0
5.80	1.0	1.0	0.5	1.0	1.0	1.0	1.0	1.5	6.5
7.54	1.0	1.0	0	1.0	1.0	1.0	1.0	0.7	6.0

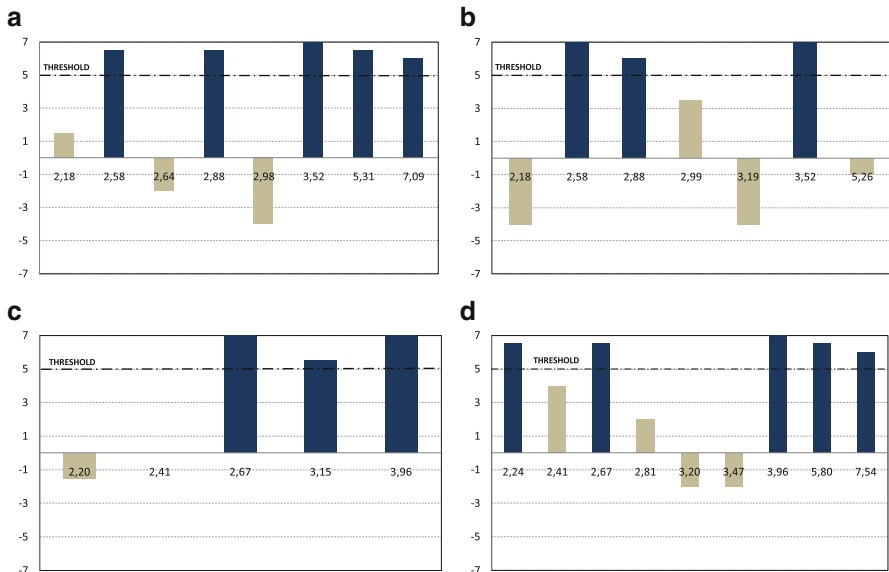


**Fig. 5.19** Score reports and selection of structural modes: building #2 (a), #3 (b), #5 (c), #6 (d), (© Elsevier Ltd. 2012), reprinted with permission

**Table 5.16** Output-only modal identification results, (© Elsevier Ltd. 2012), reprinted with permission

Building #	Mode #	Natural frequency (Hz)	$\xi$ (%)	Type
2	I	2.58	2.2	Translation x
	II	2.88	2.4	Translation y
	III	3.52	1.1	Torsion
	IV	5.31	0.9	Translation x
	V	7.09	0.7	Torsion
3	I	2.58	2.5	Translation x
	II	2.88	1.1	Translation y
	III	3.52	1.2	Torsion
5	I	2.67	1.2	Translation y
	II	3.15	2.5	Mainly translation y (slightly complex)
	III	3.96	1.1	Torsion
6	I	2.24	2.9	Translation x
	II	2.67	1.8	Translation y
	III	3.96	1.0	Torsion
	IV	5.80	1.5	Translation x
	V	7.54	0.7	Torsion

Mode shape complexity and coherence sometimes have also given inconsistent indications. In fact, modes labeled as structural can show slight imaginary components in their shapes as a result of noise effects; on the contrary, real shapes could be associated to spurious frequencies. In a similar way, dominant frequencies not related to structural modes can exhibit large values of coherence between couples of channels. Thus, the use of different OMA procedures and the integrated analysis of different features play a critical role to successfully discriminate structural modes from dominating frequencies associated to dynamic interaction effects. Complete modal identification results are reported in Table 5.16. Their inspection shows that the sequence of modes is slightly different for building #5 with respect to the others. In fact, translational modes in the x direction are missing, while there is an additional bending mode along y. This is probably the result of the very limited number of installed sensors on this building and of the presence of only one working sensor in the x direction. Even if a peak has been identified at 2.20 Hz (Table 5.14), there was a lack of sufficiently coherent information to label it as a structural mode. Another possible reason for the observed differences could be related to the pounding phenomena and damage of partition walls caused by the earthquake that affected that building at a major extent.

Apart from some uncertainties still affecting the results for building #5, the proposed approach has rationally supported the identification of the fundamental modes of the structures under test, successfully discriminating them from frequencies related to dynamic interaction effects. The importance of the integrated approach adopted for output-only modal identification is confirmed by the fact that a single OMA method can lead to wrong results as a result of the possibility of limited

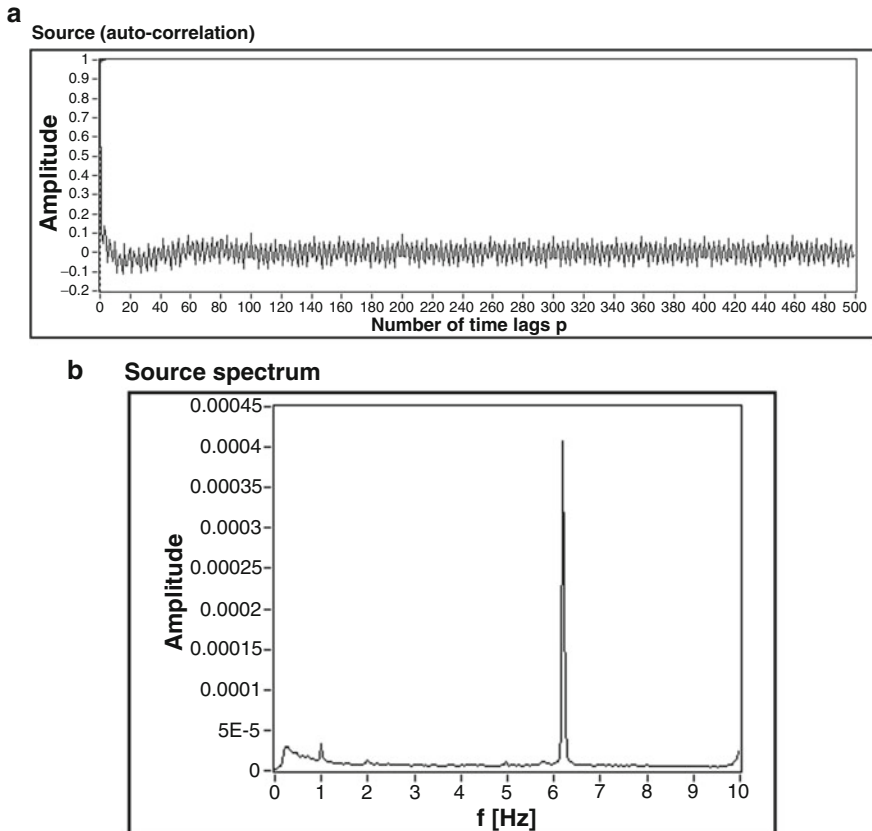


**Fig. 5.20** Spurious harmonic at 6.2 Hz due to rotating parts: source autocorrelation (a) and spectrum (b) obtained from application of the SOBI algorithm, (© Elsevier Ltd. 2012), reprinted with permission

checks. In fact, those based on coherence values and mode shape complexity have been proved to be insufficient in similar conditions. On the contrary, a detailed investigation of the recorded responses through several complementary tools is definitely more effective in the presence of dominant frequencies induced by dynamic interaction effects. Such peak frequencies, similar in the aspect to the actual structural resonances, make the modal identification by a single method particularly complex.

It is also interesting to note the presence of a spurious harmonic at 6.2 Hz in the response spectra (Fig. 5.16). It was due to rotating equipment (the engine of a plumbing) located in the basement of the building. Such harmonic can be clearly identified in Fig. 5.16 as a sharp-pointed resonance. It is far enough from relevant structural modes, so their identification has not been influenced by its presence. Its character of spurious harmonic is remarked by the very low damping ratio ( $\xi = 0.005\%$ ) and by the aspect of the identified source correlation provided by SOBI (Fig. 5.20).

## 5.6 Development of Predictive Correlations

OMA is definitely a valuable and effective tool to enhance the knowledge about the dynamic behavior of structures. Even if model updating is intuitively a natural (and probably the most popular) approach to nondestructive structural investigation and assessment of the dynamic behavior of structures, modal data can also be used to develop empirical models and correlations for the prediction of the dynamic properties of selected classes of homogeneous structures.

An example of such models has already been introduced in Sect. 5.2 to describe the dependence of damping on the amplitude of vibrations (Jeary 1986). This section illustrates how modal parameter estimates obtained from response measurements in operational conditions for homogeneous structures can be processed to develop empirical correlations for the prediction of natural periods as a function of relevant geometric parameters.

The fundamental period of vibration plays a primary role in determining the seismic demand. Recent destructive earthquakes have shown a correlation between the level of seismic damage experienced by a given structure and the closeness between its fundamental vibration period and the predominant period of the soil motion. Thus, seismic risk management in urban areas and the development of damage scenarios can benefit of accurate evaluations of the dynamic characteristics of structures.

A reliable evaluation of the dynamic properties of a structure is relevant for both structural design and seismic performance assessment. The latter is of particular interest in the case of historical structures, where interventions have to be carefully calibrated and very accurate structural models and analyses are necessary.

The estimation of the modal properties and the prediction of the seismic response of a structure usually take advantage of numerical modeling. However, when prescribed regularity conditions are fulfilled so that linear static analyses can be carried out, a complete modal analysis can be avoided. In fact, only the value of the fundamental period is required.

It can be estimated as a function of geometric parameters (usually, the height) by appropriate experimental correlations. In fact, for a given structural typology, the dependence of the fundamental period on mass and stiffness can ultimately be referred to geometric parameters, such as the height and the plan dimensions.

In this section attention is focused on the development of empirical correlations for the prediction of the fundamental periods of masonry towers belonging to the Italian architectural heritage. The development of the predictive correlations is based on the results of OMA tests carried out on several historical masonry towers in Italy.

The effects of recent earthquakes (Umbria-Marche 1997, Molise 2002, L'Aquila 2009, Emilia 2012) on this type of structures have raised the attention on their seismic performance. The large research efforts are also witnessed by the increasing number of dynamic tests carried out on historical masonry towers in Italy and by the development of specific guidelines for their seismic performance assessment (Ministero dei Beni e delle Attività Culturali 2010). Such guidelines recognize

the role of OMA in enhancing the knowledge about the dynamic behavior of historical structures.

The actual seismic response of a structure depends on the evolution of its dynamic properties along the transient base excitation. However, their accurate evaluation at low levels of vibration is also of interest, because the structural behavior in the linear regime and the initial seismic response depend on this set of dynamic properties. The lengthening of the natural period is only a consequence of the input ground motion and its intensity. Thus, an accurate linear model of the structure, representative of its actual behavior, is the fundamental requirement also for nonlinear analyses. Seismic vulnerability assessment (Sepe et al. 2008) and damage detection can also take advantage of accurate estimates of the modal properties in operational conditions. In particular, these are relevant in the context of seismic vulnerability assessment at the large scale, when the knowledge of the dynamic parameters of structures and the underlying soil allows the identification of resonance phenomena (such an approach has been recently adopted for microzonation studies in large cities; see, for instance, Navarro et al. 2004, Panou et al. 2005, Mucciarelli et al. 2008).

All the mentioned applications of modal data explain the large research efforts for the development of empirical correlations for the prediction of the fundamental periods of structures.

In the case of historical towers and similar high-rise structures, their seismic behavior depends on factors such as slenderness, degree of connection between the walls, presence of lower nearby structures acting as horizontal restraints. Since masonry towers are usually characterized by a lower geometric and structural complexity with respect, for instance, to churches, they can be analyzed according to classical structural schemes through accurate and detailed models. Even linear models can provide useful and reliable information about the seismic performance of towers, because they are basically isostatic structures and, therefore, the stress redistribution is very low. The lack of significant energy dissipation is also one of the main reasons why masonry towers are very sensitive to seismic actions. As a consequence, linear dynamic analyses play a primary role in the investigation of the amplification of motion along the structure. This is a critical aspect above all when there are bells in the upper part of the tower. The bell cell, in fact, causes a loss of regularity in elevation. The wide openings for the bells turn the walls into slender and poorly compressed columns. These are usually very vulnerable also in consideration of the amplification of motion from the base to the top of the structure.

A simplified model of masonry towers under seismic loading usually represents the structure as a cantilever beam subjected to the horizontal forces associated to the earthquake. When a linear static analysis is adopted, the total horizontal force depends on the value of the elastic response spectrum. This is evaluated at a period equal to the fundamental natural period of the structure in the considered direction.

The dependence of the seismic action on the fundamental period of the tower requires effective tools for its prediction. The Italian guidelines for intervention

on historical structures (Ministero dei Beni e delle Attività Culturali 2010) recommend the use of fundamental periods of vibration obtained from ambient vibration tests, because the dynamic properties they provide can be referred to as representative of the linear elastic behavior of the structure. The effect of high amplitude vibrations is taken into account through a simplified approach based on the amplification of the period estimated in operational conditions by a factor in the range 1.4–1.75. The amplification factor is introduced for analyses at the ultimate limit state. It accounts for the lengthening of the period induced by increasing levels of damage, cracking and other nonlinear phenomena at high amplitude vibrations.

A large experimental campaign, eventually complemented by an extensive literature review, is the necessary preliminary step for the collection of a sufficiently large database of modal properties and relevant geometric information about historical masonry towers in view of the development of empirical correlations. The herein discussed application started from the experimental campaign, based on ambient vibration tests, aimed at the identification of the fundamental dynamic properties of several historical bell towers in the Molise region (Southern Italy). The results of this experimental campaign are herein summarized for the sake of completeness.

OMA has been used to estimate the fundamental modal parameters of a number of bell towers (Fig. 5.21) belonging to the architectural heritage of the Molise region. The dynamic response of the structures has been measured at different levels by installing a variable number of accelerometers, ranging from 6 to 20, in couples at opposite corners of the towers, so that both translational and torsional modes could be observed. The accelerometers were of the force balance type, with bandwidth ( $-3$  dB) of about 200 Hz (starting from DC) and high dynamic range (more than 140 dB). The full-scale range was 0.5 g and the sensitivity was 20 V/g. The records were 3,600 s long and sampled at 100 Hz. After data validation, filtering and decimation, the ambient vibration response of the bell towers has been analyzed by well-established techniques such as FDD, SSI and SOBI. Data processing in the frequency domain has been carried out adopting Hanning window and 66 % overlap in spectrum computation. Results of modal identification of Molise's bell towers are summarized in Table 5.17.

The identified modal properties have been collected into a database, including also information about geometry, materials, type and number of sensors and so on. The database has been complemented by data collected through an extensive literature review about masonry bell towers located in Italy. As a final result, geometric data and the experimental estimates of the modal properties in operational conditions of a population of 30 Italian masonry bell towers have been stored in the database.

The empirical correlation for the prediction of the fundamental period as a function of geometric data has been obtained by fitting the collected data by an assumed mathematical law. Its parameters have been estimated by a least squares approach (Chap. 2). Following similar studies available in the literature



**Fig. 5.21** The investigated bell towers in the Molise region: Santa Maria delle Rose bell tower in Bonefro (a), S. Pardo bell tower in Larino (b), Santa Maria della Pietà bell tower in Larino (c), Santa Maria Maggiore bell tower in Morrone del Sannio (d), Sant'Alfonso dei Liguori bell tower in Colletorto (e), San Giacomo bell tower in Santa Croce di Maglano (f), Santa Maria delle Rose bell tower in Montorio nei Frentani (g), Santa Maria Assunta bell tower in Provvidenti (h), Santa Maria Assunta bell tower in Ripabottoni (i)

(Lagomarsino 1993), a linear relationship between the fundamental period  $T_1$  and the height  $H$  of the towers has been assumed:

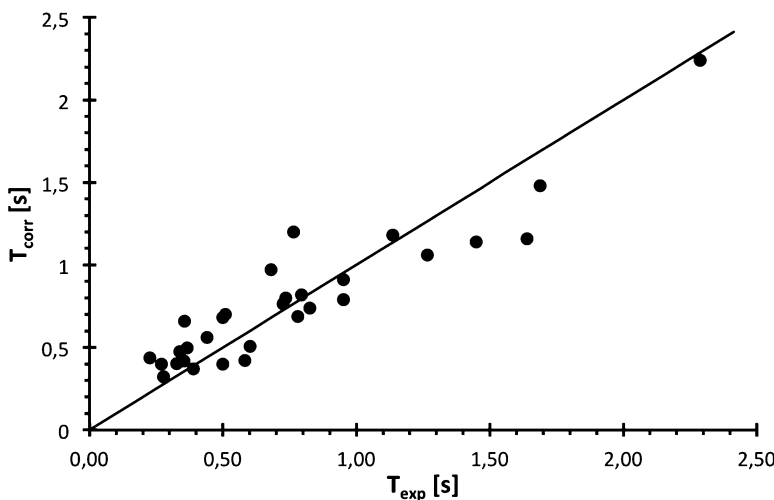
$$T_1 = C \cdot H \quad (5.15)$$

obtaining the following value for the constant:

$$C = 0.02 \quad (5.16)$$

**Table 5.17** Molise's bell towers: output-only modal identification results

Bell tower	$f_1$ (Hz)	$f_2$ (Hz)	$f_3$ (Hz)	$f_4$ (Hz)	$f_5$ (Hz)	$f_6$ (Hz)
Santa Maria delle Rose (Bonefro)	2.96	3.52	6.04	6.96	8.44	—
Santa Maria delle Rose (Montorio nei Frentani)	2.74	3.43	3.80	6.02	7.39	7.70
Santa Maria Maggiore (Morrone del Sannio)	1.96	2.24	4.76	—	—	—
Santa Maria Assunta (Ripabottoni)	2.27	2.68	3.37	3.88	—	—
Santa Maria della Pietà (Larino)	3.61	3.86	4.34	4.75	7.77	8.43
San Giacomo (Santa Croce di Magliano)	3.06	3.44	4.08	—	—	—
San Pardo (Larino)	2.81	3.34	7.00	—	—	—
Sant'Alfonso dei Liguori (Colletorto)	4.44	5.16	6.96	7.68	8.80	—
Santa Maria Assunta (Provvidenti)	2.82	3.40	4.00	—	—	—

**Fig. 5.22** Comparison between experimental and predicted values of the fundamental period of vibration of Italian masonry towers (the *black line* represents the bisector of the plane)

that implies:

$$T_1 = 0.02 \cdot H. \quad (5.17)$$

In Fig. 5.22 the values of the fundamental period predicted according to (5.17) are reported as a function of the corresponding experimental estimates. The analysis of the distribution of the points with respect to the bisector (represented by the black line) points out the good agreement between predicted and experimentally estimated values of the period.

If other formulations for the prediction of the same parameters are available, the  $L_2$  norm of the error between predicted and measured values (Chap. 2) can be evaluated to compare the relative predictive performance.

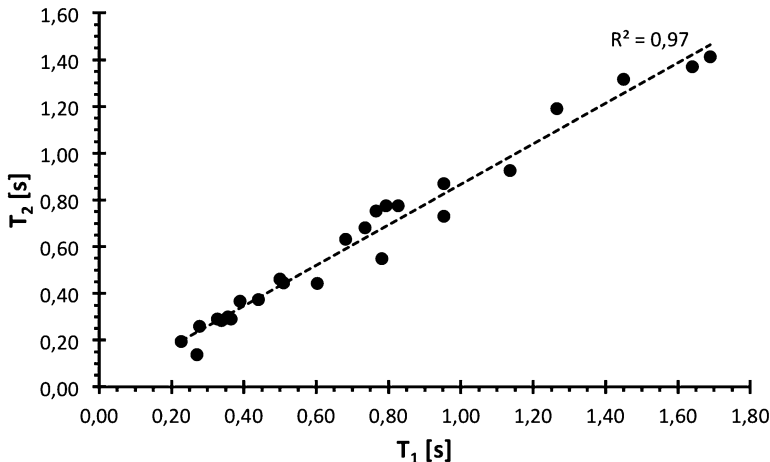


**Fig. 5.23** Correlation between the natural periods of the first two modes for the Italian masonry towers

In the present case the collected data have also made possible the development of correlations for the prediction of the natural period of higher modes as a function of the period of the fundamental mode. In fact, the natural period  $T_2$  of the second mode of Italian masonry towers was found to be related to the natural period  $T_1$  of the first mode as follows:

$$T_2 = 0.86 \cdot T_1. \quad (5.18)$$

In fact, as shown in Fig. 5.23, the collected data show a linear correlation between the two values of the natural period.

Finally, the period of the third (torsional) mode can be estimated from the fundamental period as follows:

$$T_3 = 0.4 \cdot T_1 \quad (5.19)$$

while the periods of the higher bending modes can be estimated from the periods of the corresponding fundamental modes as follows:

$$T_4 = 0.3 \cdot T_1 \quad (5.20)$$

$$T_5 = 0.3 \cdot T_2. \quad (5.21)$$

The correlations expressed by (5.19), (5.20) and (5.21) are based on a more limited number of experimental values (about ten) and they have to be validated against a larger population of samples. Nevertheless, they are in good agreement with similar correlations available in the literature for masonry buildings (Ministerio de Fomento 2002).

In summary, the present and the previous sections in the chapter have presented a number of possible applications of the techniques discussed in this book. Most of the analyzed case studies refer to real experimental tests. They are aimed at giving the reader an overview of the potentialities and limitations of OMA for real life applications. From the analysis of these and eventually other experiences reported in the literature about OMA the reader can get useful hints for design of experiments and data processing.

---

## References

- Agneni A, Coppotelli G, Grappasonni C (2012) A method for the harmonic removal in operational modal analysis of rotating blades. *Mech Syst Signal Process* 27:604–618
- Bendat JS, Piersol AG (2000) Random data: analysis and measurement procedures, 3rd edn. John Wiley & Sons, New York
- Bernal D (2004) Modal scaling from known mass perturbations. *ASCE J Eng Mech* 130(9):1083–1088
- Brincker R, Andersen P, Møller N (2000) An indicator for separation of structural and harmonic modes in output-only modal testing. In: Proc XVIII international modal analysis conference, San Antonio, TX
- Brincker R, Ventura CE, Andersen P (2003) Why output-only modal testing is a desirable tool for a wide range of practical applications. In: Proc XXI international modal analysis conference, Kissimmee, FL
- CEN, European Committee For Standardization (2003) Eurocode 8: design provisions for earthquake resistance of structures, part 1.1: general rules, seismic actions and rules for buildings, Pren 1998-1, Brussels
- CEN, European Committee for Standardization (2005) Eurocode 8: design provisions for earthquake resistance of structures. Part 3: assessment and retrofitting of buildings. Brussels
- Chopra AK (2000) Dynamics of structures – theory and applications to earthquake engineering, 2nd edn. Prentice Hall, Upper Saddle River, NJ
- Computers and Structures (2006) SAP2000® v.11, manual. Computers and Structures Inc, Berkeley, CA
- Consiglio Superiore dei Lavori Pubblici (2008) Nuove Norme Tecniche per le Costruzioni, D.M. Infrastrutture 14/01/2008, published on S.O. n. 30 at the G.U. 04/02/2008 n. 29 (in Italian)
- Conte C, Rainieri C, Aiello MA, Fabbrocino G (2011) On-site assessment of masonry vaults: dynamic tests and numerical analysis. *Geofiz* 28:127–143
- Devriendt C, De Sitter G, Vanlanduit S, Guillaume P (2009) Operational modal analysis in the presence of harmonic excitations by the use of transmissibility measurements. *Mech Syst Signal Process* 23:621–635
- Doebling SW, Farrar CR, Prime MB, Shevitz DW (1996) Damage identification and health monitoring of structural and mechanical systems from changes in their vibration characteristics: a literature review, technical report LA-13070-MS, UC-900. Los Alamos National Laboratory, New Mexico
- Ewins DJ (2000) Modal testing: theory, practice and application, 2nd edn. Research Studies Press Ltd., Baldock
- Fardis MN (1996) Experimental and numerical investigations on the seismic response of RC infilled frames and recommendations for code provisions. ECOEST/PREC8 report no. 6. LNEC, Lisbon
- Friswell MI, Mottershead JE (1995) Finite element model updating in structural dynamics. Kluwer, Dordrecht

- Gentile C, Saisi A (2007) Ambient vibration testing of historic masonry towers for structural identification and damage assessment. *Const Build Mat* 21(6):1311–1321
- Gentile C, Saisi A (2013) Operational modal testing of historic structures at different levels of excitation. *Const Build Mat.* doi: 10.1016/j.conbuildmat.2013.01.013 (in press)
- Herlufsen H, Andersen P, Gade S, Møller N (2005) Identification techniques for operational modal analysis – an overview and practical experiences. In: Proc 1st international operational modal analysis conference, Copenhagen
- Hu W-H, Moutinho C, Caetano E, Magalhães F, Cunha A (2012) Continuous dynamic monitoring of a lively footbridge for serviceability assessment and damage detection. *Mech Syst Signal Process* 33:38–55
- Jacobsen N-J, Andersen P, Brincker R (2007) Eliminating the influence of harmonic components in operational modal analysis. In: Proc XXV international modal analysis conference, Orlando
- Jaishi B, Ren W-X (2005) Structural finite element model updating using ambient vibration test results. *ASCE J Struct Eng* 131(4):617–628
- Jeary AP (1986) Damping in tall buildings – a mechanism and a predictor. *Earthq Eng Struct Dyn* 14:733–750
- Jeary AP (1997) Damping in structures. *J Wind Eng Ind Aerodyn* 72:345–355
- Khatibi MM, Ashory MR, Malekjafarian A (2009) Scaling of mode shapes using mass-stiffness change method. In: Proc 3rd international operational modal analysis conference, Portonovo
- Lagomarsino S (1993) Forecast models for damping and vibration periods of buildings. *J Wind Eng Ind Aerodyn* 48:221–239
- Lopez-Aenlle M, Fernandez P, Brincker R, Fernandez-Canteli A (2010) Scaling-factor estimation using an optimized mass-change strategy. *Mech Syst Signal Process* 24:3061–3074
- Lopez-Aenlle M, Brincker R, Pelayo F, Fernandez-Canteli A (2012) On exact and approximated formulations for scaling-mode shapes in operational modal analysis by mass and stiffness change. *J Sound Vib* 331:622–637
- Marseglia PS (2013) Comportamento sismico di volte in muratura, Ph.D. thesis, University of Salento, Lecce (in Italian)
- Ministero dei Beni e delle Attività Culturali (2010) Linee Guida per la valutazione e riduzione del rischio sismico del patrimonio culturale allineate alle nuove Norme tecniche per le costruzioni (D.M. 14 gennaio 2008), Circolare 26/2010. <http://www.pabaac.beniculturali.it> (in Italian)
- Ministerio de Fomento (2002) Norma de Construcción Sismorresistente. Parte General y Edificación (Spanish Standard, in Spanish)
- Modak SV, Rawal C, Kundra TK (2010) Harmonics elimination algorithm for operational modal analysis using random decrement technique. *Mech Syst Signal Process* 24:922–944
- Mohanty P, Rixen DJ (2004) A modified Ibrahim time domain algorithm for operational modal analysis including harmonic excitation. *J Sound Vib* 275:375–390
- Mohanty P, Rixen DJ (2006) Modified ERA method for operational modal analysis in the presence of harmonic excitations. *Mech Syst Signal Process* 20:114–130
- Mottershead JE, Link M, Friswell MI (2011) The sensitivity method in finite element model updating: a tutorial. *Mech Syst Signal Process* 25(7):2275–2296
- Mucciarelli M, Milutinovic Z, Gosar A, Herak M, Albarello D (2008) Assessment of seismic site amplification and seismic building vulnerability in the Republic of Macedonia, Croatia and Slovenia. In: Proc 14th world conference on earthquake engineering, Beijing
- Navarro M, Vidal F, Feriche M, Enomoto T, Sanchez FJ, Matsuda I (2004) Expected ground-RC building structures resonance phenomena in Granada city (Southern Spain). In: Proc 13rd world conference on earthquake engineering, Vancouver, BC
- Oliveira CS, Navarro M (2009) Fundamental periods of vibration of RC buildings in Portugal from in situ experimental and numerical techniques. *Bull Earthq Eng* 8(3):609–642
- Pandey AK, Biswas M (1994) Damage detection in structures using changes in flexibility. *J Sound Vib* 169(1):3–17
- Panou AA, Theodoulidis N, Hatzidimitriou P, Stylianidis K, Papazachos CB (2005) Ambient noise horizontal-to-vertical spectral ratio in site effects estimation and correlation with seismic

- damage distribution in urban environment: the case of the city of Thessaloniki (Northern Greece). *Soil Dyn Earthq Eng* 25:261–274
- Parloo E, Verboven P, Guillaume P, Van Overmeire M (2002) Sensitivity-based operational mode shape normalization. *Mech Syst Signal Process* 16(5):757–767
- Parloo E, Verboven P, Guillaume P, Van Overmeire M (2003) Force identification by means of in-operation modal models. *J Sound Vib* 262(1):161–173
- Parloo E, Vanlanduit S, Guillaume P, Verboven P (2004) Increased reliability of reference-based damage identification techniques by using output-only data. *J Sound Vib* 270:813–832
- Parloo E, Cauberghe B, Benedettini F, Alaggio R, Guillaume P (2005) Sensitivity-based operational mode shape normalisation: application to a bridge. *Mech Syst Signal Process* 19:43–55
- Peeters B, Cornelis B, Janssens K, Van der Auweraer H (2007) Removing disturbing harmonics in operational modal analysis. In: Proc 2nd international operational modal analysis conference, Copenhagen
- Pridham BA, Wilson JC (2003) A study on errors in correlation-driven stochastic realization using short data sets. *Prob Eng Mech* 18:61–77
- Qian S, Chen D (1996) Joint time-frequency analysis: methods and applications. PTR Prentice Hall, Upper Saddle River, NJ
- Rainieri C, Fabbrocino G (2010) Automated output-only dynamic identification of civil engineering structures. *Mech Syst Signal Process* 24(3):678–695
- Rainieri C, Fabbrocino G, Cosenza E (2010a) Some remarks on experimental estimation of damping for seismic design of civil constructions. *Shock Vib* 17:383–395
- Rainieri C, Fabbrocino G, Cosenza E (2010b) On damping experimental estimation. In: Proc 10th international conference on computational structures technology, Valencia
- Rainieri C, Fabbrocino G, Cosenza E (2011) Integrated seismic early warning and structural health monitoring of critical civil infrastructures in seismically prone areas. *Struct Health Monit* 10:291–308
- Rainieri C, Fabbrocino G, Manfredi G, Dolce M (2012) Robust output-only modal identification and monitoring of buildings in the presence of dynamic interactions for rapid post-earthquake emergency management. *Eng Struct* 34:436–446
- Rainieri C, Fabbrocino G, Verderame GM (2013) Non-destructive characterization and dynamic identification of a modern heritage building for serviceability seismic analyses. *NDT E Int* 60:17–31
- Reynders E, De Roeck G (2008) Reference-based combined deterministic-stochastic subspace identification for experimental and operational modal analysis. *Mech Syst Signal Process* 22:617–637
- Reynders E, Pintelon R, De Roeck G (2008) Uncertainty bounds on modal parameters obtained from stochastic subspace identification. *Mech Syst Signal Process* 22:948–969
- Rosenow SE, Uhlenbrock S, Schlotmann G (2007) Parameter extraction of ship structures in presence of stochastic and harmonic excitations. In: Proc 2nd international operational modal analysis conference, Copenhagen
- Sepe V, Speranza E, Viskovic A (2008) A method for large-scale vulnerability assessment of historic towers. *Struct Cont Health Monit* 15:389–415
- Tamura Y, Yoshida A, Zhang L, Ito T, Nakata S, Sato K (2005) Examples of modal identification of structures in Japan by FDD and MRD techniques. In: Proc 1st international operational modal analysis conference, Copenhagen
- Woodhouse J (1998) Linear damping models for structural vibration. *J Sound Vib* 215(3):547–569

## 6.1 Statement of the Problem

A number of applications, ranging from modal-based damage detection to vibration-based monitoring of tensile loads in cables and rods, require automated procedures for the output-only identification of dynamic parameters. The development of automated OMA procedures is not a trivial task since traditional modal identification requires extensive interaction by a skilled analyst, as discussed in the previous chapters. When automated OMA is integrated within continuously operating structural monitoring systems, computational efforts have also to be carefully assessed.

Most of the automated OMA procedures represent an evolution of traditional (manual) methods, since they rely on the same theoretical concepts. Moreover, the previously discussed requirements of OMA testing related to measurement chain and sensor layout apply also to automated OMA. Thus, in the following sections attention is focused only on the automated extraction of the modal parameters, moving from the theoretical background of OMA methods illustrated in Chap. 4.

The first attempts to automate the modal identification process can be traced back to the end of the last Century and the beginning of the current one (see, for instance, Vanlanduit et al. 2003, Peeters and De Roeck 2001a, Pappa et al. 1997). However, the automation of OMA methods has become a relevant and very active research field after 2005, as confirmed by the large number of papers appeared in the literature in the subsequent years.

The first systematic analyses and classifications of automated OMA procedures are very recent (Rainieri and Fabbrocino 2010, Rainieri et al. 2011a). They have made a clear distinction between *automated modal parameter identification* methods and *automated modal tracking* methods. The former estimate the modal parameters from a single dataset without any prior information about the dynamic properties of the structure under investigation; the latter monitor (track) the evolution of the modal parameters of a structure over time taking advantage of a set of reference modal parameters. This set can come from either an automated or manual modal identification.

In spite of their minor autonomy with respect to fully automated modal parameter identification methods, modal tracking procedures are advantageous for applications requiring short response time and low computational efforts.

In the following sections, after a brief literature review about automated OMA methods, two different automated modal parameter identification methods and an automated modal tracking method are described and applied to a number of case studies. The reported applications show that a reliable and accurate automated identification of the modal parameters is possible. They point out the potential of automated OMA in solving a number of monitoring applications, but also the drawbacks related to the influence of environmental and operational factors on the modal parameter estimates. It is worth noting that the herein described automated OMA methods are the authors' research outcome in the field. Thus, this chapter basically reports a specific viewpoint about the matter; the reason is that a wide consensus in the definition of the "best methods" for automated output-only modal identification has not been reached, yet. Nevertheless, relevant references are reported at the end of the chapter for the reader interested in more details about automated OMA methods proposed by different research groups.

---

## 6.2 Automated OMA in Frequency Domain: LEONIDA

### 6.2.1 Objectives

LEONIDA is a fully automated frequency domain modal parameter identification method based on the SVD of the output PSD matrices, on the analogy with the FDD method. The method has been developed to overcome the limits of many automated OMA algorithms concerning the static definition of thresholds and analysis parameters. In fact, if the values of the analysis parameters are static, they have to be calibrated. Calibration is often time consuming and it must always be carried out at the beginning of a new monitoring application; moreover, a recalibration could be required in the case of monitored structures experiencing some changes in their dynamic properties, so that the previous set of analysis parameters is no more adequate. The development of LEONIDA has also been aimed at simplifying and making as physically intuitive as possible the automated identification of the structural modes. In order to clarify these aspects, a brief review of the available automated OMA procedures before the development of LEONIDA is herein reported.

The available algorithms for automated OMA were based on either control theory or conventional signal processing.

As illustrated in Chap. 4, in classical modal analysis the model order is usually overspecified to get all physical modes in the frequency range of interest. However, the discrimination between physical and mathematical modes requires a lot of interaction with an expert user. It takes advantage of tools, such as the stabilization diagram, to select the physical poles. This selection is not a trivial task. It may be difficult and time consuming depending on the quality of data, the performance of

the estimator and the experience of the user. Since the extensive interaction between tools and user is inappropriate for monitoring purposes, the first attempts to automate OMA introduced selection criteria and clustering tools to separate the physical poles from the others without user interactions. For instance, one of the early approaches to automated modal identification, based on the LSCF method (Vanlanduit et al. 2003), performed the selection of physical poles from a high-order model by means of a number of deterministic and stochastic criteria and a fuzzy clustering approach. However, the algorithm for pole selection was quite complex and demanding from a computational point of view.

A very simple criterion for automated modal parameter identification via SSI was proposed in the same period (Peeters and De Roeck 2001a) and applied to monitor the environmental and damage effects on the dynamic behavior of the Z24 Bridge in Switzerland. It was based on the selection, in the stabilization diagram, of the poles that were at least five times stable. This basic criterion has also been applied to track the effects of changing environmental conditions on the modal parameters of Tamar bridge (Brownjohn and Carden 2007). However, it cannot ensure that the identified poles are physical (Chap. 5).

A more refined automated OMA procedure based on the SSI technique was proposed some years later (Deraemaeker et al. 2008). It was basically a tracking method because an initial set of modal parameters, using stochastic subspace identification and stabilization diagram, had to be identified before launching the procedure.

A fully automated method for extraction of modal parameters by SSI was proposed in the same period (Andersen et al. 2007). It was based on the clear stabilization diagram obtained according to a multipatch subspace approach. Pole extraction was carried out by the graph theory. This algorithm was very fast, so that it could be used as a monitoring routine, but further improvements were needed to increase its reliability and robustness.

A refinement of automated Cov-SSI was achieved some years later (Magalhaes et al. 2009). It was able to ensure an effective identification of closely spaced modes, but it showed poor performance in the identification of weakly excited modes. It was based on the application of an advanced clustering algorithm allowing a reliable identification of structural modes. However, a number of parameters had to be set at startup by time-consuming calibrations. Among the parameters to be set there was the number of block rows of the Toeplitz matrix of correlations, whose value has an influence on the quality of the stabilization diagram and is somehow dependent on the signal-to-noise ratio (Chap. 5). Thus, the quality of signals had to be evaluated in advance and the number of block rows chosen accordingly in order to obtain high-quality stabilization. Other parameters requiring calibration were related to the clustering algorithm (the interested reader can refer to Tan et al. 2006 for a detailed analysis of clustering techniques). The rules to build the hierarchical tree and, in particular, the tree cut level had to be set according to the noise level of signals. A preliminary phase of analysis and manual initialization of the system was, therefore, necessary before each application. As previously mentioned, this approach yields static acceptance criteria that cannot

always ensure an effective tracking of dynamic parameters over time. The need of avoiding tuned and statically set parameters was not fully understood, yet.

Among the methods based on conventional signal processing, the so-called time domain filtering method (Guan et al. 2005) was a tracking procedure based on the application of a band-pass filter to the system response in order to separate the individual modes in the spectrum. The frequency limits of the filter were static and user specified according to the PSD plots of response signals. However, when the excitation is unknown, it might be difficult to identify the regions where certain modes are located according only to power spectrum plots. Moreover, in the case of close modes, it is very difficult, or even impossible, to correctly define such limits so that natural changes in modal frequencies can be tracked. Thus, this method only ensured a rough modal tracking.

The automation of the FDD method (Brincker et al. 2007) marked a fundamental step towards the elimination of any user interaction and the use of automated OMA as modal information engine in SHM systems. It was based on the identification of the modal domain around each identified peak in the singular value plots according to predefined limits for the so-called modal coherence function and modal domain function. The recommended limit value was 0.8 for both the indicators. However, if the limit value for the modal coherence indicator was somehow justified (Brincker et al. 2007) on the basis of the standard deviation of correlation between random vectors and on the number of measurement channels, few comments were reported about the modal domain indicator. Moreover, threshold setting for peak detection still affected the results.

A slightly modified version of this approach was applied to the permanent monitoring of the “Infante D. Henrique” bridge (Magalhaes et al. 2008). A reduced effectiveness of the procedure was observed whenever noise level in spectra increased. Among the parameters to be set there was also the MAC rejection level (Chap. 4). It was set by means of a number of sensitivity tests and time-consuming tuning for the monitored structure. The selection of a very small value (0.4) was recommended. However, it was recognized that this value could be ineffective in the case of small number of sensors and close natural frequencies associated to similar mode shape estimates. Moreover, the need for a time-consuming initialization phase and the related static settings of analysis parameters did not guarantee that they were adequate over the whole monitoring period, in particular in the case of remarkable changes in the structure such as those induced by extreme events.

Automated versions of SOBI and of transmissibility-based OMA were also available. About SOBI, the identification of structural modes was based on the rejection of all modes out of the frequency range of interest and of sources characterized by a fitting error higher than 10 %; the selection of the structural modes from the remaining sources was based on the computation of a confidence factor (Poncelet et al. 2008). However, the effectiveness of the method in the analysis of real measurements was not proved.

The automated transmissibility-based OMA method started from the SVD of a two-column matrix consisting of transmissibility functions evaluated at different

loading conditions. Since all transmissibility functions converge to the same value at the natural frequency of the system, rank-one matrices marked the presence of structural modes. They were identified by analyzing the plot of the inverse of the second singular value, which was characterized by a peak at the natural frequency of a mode. However, peak selection was still carried out through the static definition of a threshold. Moreover, in the presence of measurement noise the approach was not reliable. The use of a smoothing function was proposed to overcome this drawback (Devriendt et al. 2008), but it had to be carefully applied to avoid distortions.

In summary, the available automated OMA methods were affected by some common drawbacks:

- most of them moved from a threshold-based peak detection; as a consequence, a first calibration phase was needed for its appropriate definition; only some of the identified peaks corresponded to actual modes, thus validation criteria were needed; moreover, performance of peak detection algorithms got worse in the presence of measurement noise;
- identification of actual modes was based on a number of statically set parameters; a time-consuming calibration process for each monitored structure was required; the static identification of thresholds and parameters was often inadequate to follow natural changes in modal properties of structures due to damage or environmental effects;
- most of the algorithms were somehow sensitive to noise, and higher or poorly excited modes were not always identified.

Thus, an alternative strategy was needed. In the case of LEONIDA, it was based on the definition of some objective criteria for the identification of mode bandwidth before modal parameter extraction.

It is interesting to note that the distinction between automated modal parameter identification and automated modal tracking and the importance of avoiding the tuning of analysis parameters at startup have recently been recognized and accepted also by other authors (see, for instance, Reynders et al. 2012).

### 6.2.2 Principles and Implementation

The identification of the bandwidth of modes in LEONIDA is based on simple considerations about the structure of the output PSD matrix when it is expressed in pole-residue form (4.13). When multiple roots do not exist, in the proximity of a pole of the structure the matrix is dominated by the corresponding term. Since the residues for a given mode are independent of frequency, the information about the amplitude depends on the denominator, which reaches its maximum. Taking into account that the residues hold the information about the mode shapes and that these can be estimated from the singular vectors of the output PSD matrix (Chap. 4), it is possible to identify the bandwidth of modes by assessing the stability of the singular vectors associated to a certain frequency over a number of subsequent datasets. In particular, at a given frequency line in the bandwidth of a mode, the MAC sequence

computed between the first singular vectors obtained from the analysis of the first and the  $n$ -th block of data, with  $n = 1, \dots, n_{\max}$ :

$$MAC(\{u_1^{t_0}(\omega)\}, \{u_1^{t_0+n\Delta T}(\omega)\}) = \frac{\left| \{u_1^{t_0}(\omega)\}^H \{u_1^{t_0+n\Delta T}(\omega)\} \right|^2}{\left( \{u_1^{t_0}(\omega)\}^H \{u_1^{t_0}(\omega)\} \right) \left( \{u_1^{t_0+n\Delta T}(\omega)\}^H \{u_1^{t_0+n\Delta T}(\omega)\} \right)} \quad (6.1)$$

should be constant and equal to 1 for a stationary and ergodic system. This is approximately true for real datasets due to the unknown input and the presence of noise; thus, specific selection criteria and tolerances must be set. In (6.1) the superscripts denote the starting time ( $t_0$  and  $t_0 + n\Delta T$ ) of the first and the  $n$ -th record, respectively. The records have the same duration  $\Delta T$ , yielding spectra characterized by the same number of averages and frequency resolution. Note that, even if the SVD of the output PSD matrix at resonance gives un-scaled mode shapes (Chap. 4) and the scaling factor can vary from record to record, the algorithm is not sensitive to changes in scaling. In fact, it is based on the analysis of the sequence of MAC values that are not affected by a constant multiplier.

Taking into account the basic principle for the identification of the bandwidth of modes, the algorithm can easily be implemented as follows. As in the classical FDD method, the fundamental data processing tool is represented by the SVD of the output PSD matrix. After the decomposition, the first singular vector at each frequency line is considered. This step is repeated for a number of subsequent records. Afterwards, the MAC between the first singular vectors at the same frequency line (6.1) is computed. Since the MAC index is quite sensitive to noise, appropriate countermeasures for noise reduction have to be considered, as discussed below.

The averaged MAC vs. frequency plot (Fig. 6.1) looks like a coherence function. In the frequency range of a given mode, density of points increases, MAC value is high (close to 1) and a kind of bell can be observed. The identification of the bandwidth of the modes is carried out through the evaluation of some statistical parameters related to the MAC value sequence and its first derivative at each frequency line. Since the error in mode shape estimation is basically related to the error in spectrum estimation and, as such, to the number of averages (Chap. 2; the interested reader can also refer to Bendat and Piersol 2000 for more details), it is maintained at a given level by defining the record duration for each step. Thus, the sequences of MAC values indicating the presence of a mode can be identified by the analysis of their statistical parameters, which are mostly influenced by the presence of a mode rather than by the error in spectrum estimation. Mean and standard deviation are the statistical parameters assumed for mode bandwidth identification. In order to have a good estimation of such parameters, at least ten steps have generally to be taken into account.

Figure 6.2 shows that the MAC function is nearly horizontal only at the frequency lines located within a mode bandwidth. It is possible to assume that

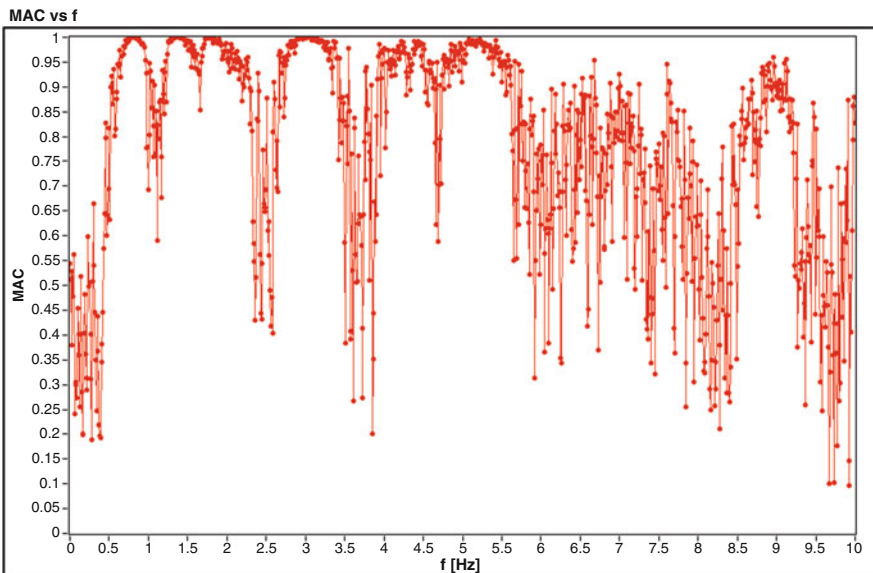


**Fig. 6.1** Sample averaged MAC vs. frequency plot

such a function is horizontal if the reference statistical parameters satisfy some predefined limits; in particular, the MAC value sequence must have an average value higher than 0.95 and a standard deviation lower than 0.01; moreover, the first derivative of the MAC sequence must be, on average, lower than 0.01, with a standard deviation lower than 0.01. These limits are the result of a calibration process, carried out by varying measurement hardware characteristics, level of noise in measurements and number of analysis steps. However, for a better definition of such limits, a given number of steps in the computation of the averaged MAC vs. frequency plot should be used. In fact, a large number of steps would result in a strict and more refined definition of such limits and, thus, in the identification of the bandwidth of modes less sensitive to noise effects.

In the current implementation of the algorithm, frequency resolution and record length are held constant and equal to 0.01 Hz and 10 min for each step, respectively. This duration seems to be the minimum one providing a sufficiently averaged spectrum, thus resulting in a good compromise between accuracy and computational time. However, longer records can result in improved definition of spectra, where most of the noise is averaged out, and, therefore, in more accurate mode shape estimates, thus reducing noise effects on MAC. A large number of averages are also required to reduce the effects of transients, if they are expected; in fact, they can affect mode shape estimation, resulting in a lower value of MAC. Even if the MAC slightly changes due to weakly nonstationary signal effects, it may happen that, due to its variation, the previously defined limits are no more satisfied. As a consequence, in particular in the presence of closely spaced modes, it is possible that a mode is not identified.

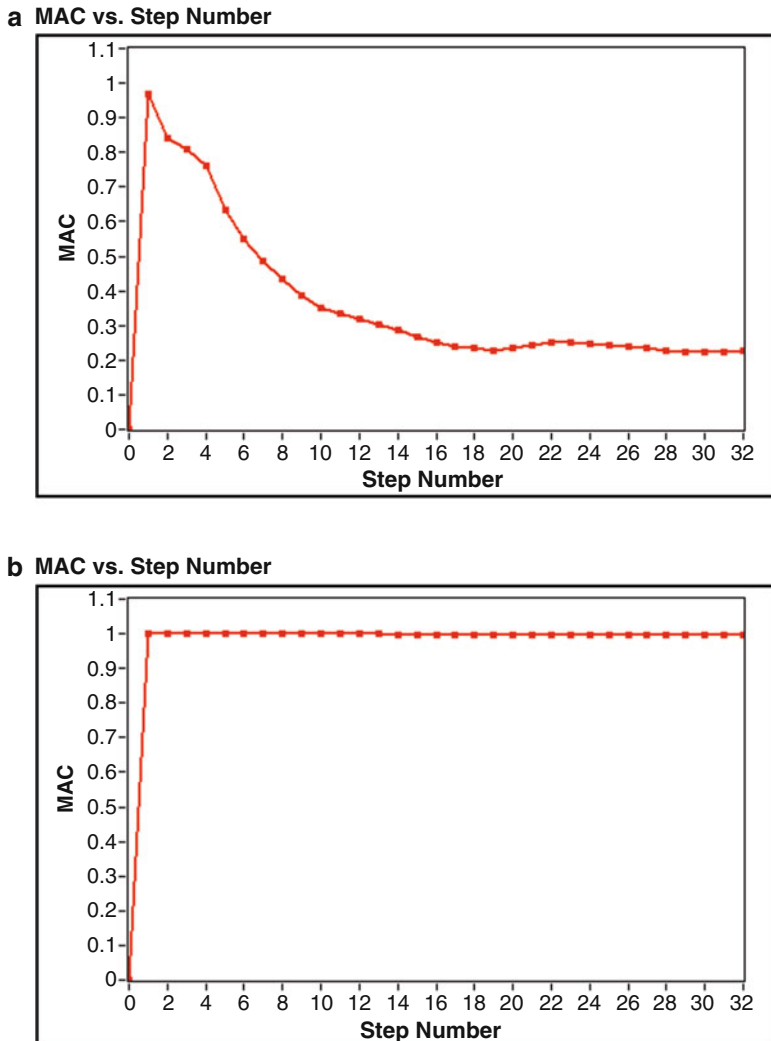


**Fig. 6.2** MAC sequences at different frequency lines: noise domain (a) and mode bandwidth (b), (© Elsevier Ltd. 2010), reprinted with permission

From the analysis of MAC sequences, the bandwidth of a number of modes can be identified. Within each bandwidth, the use of peak detection algorithms over the corresponding portion of the first singular value plot leads to the identification of the natural frequency for that mode. The corresponding singular vector at that frequency line is a good estimate of the mode shape of the structure.

A flowchart of the algorithm is shown in Fig. 6.3. It can be easily implemented in LabVIEW environment by adopting the state machine architecture: in fact,

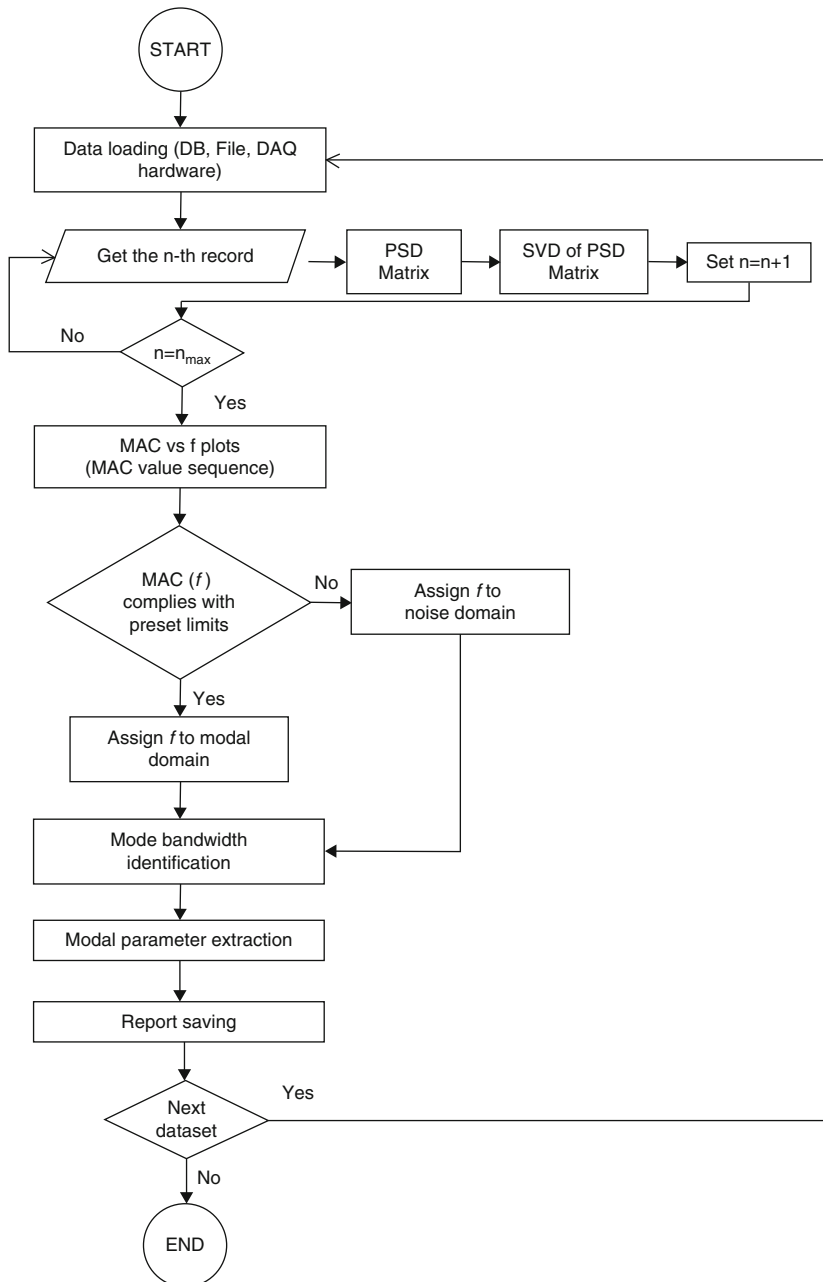
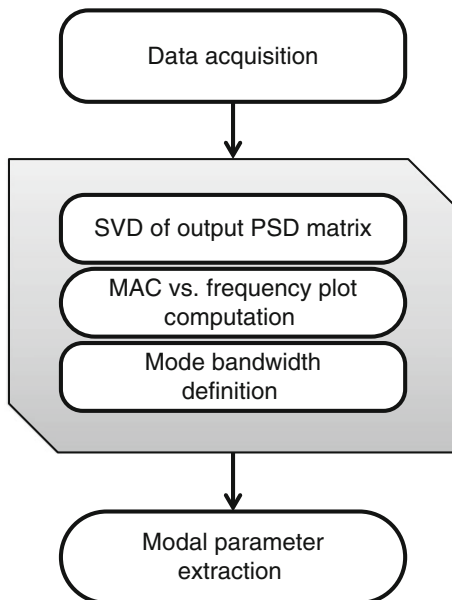


**Fig. 6.3** LEONIDA: Algorithm for automated modal parameter identification, (© Elsevier Ltd. 2010), reprinted with permission

**Fig. 6.4** LEONIDA: State sequence for software implementation



well-defined stages can be identified (Fig. 6.4). The data source can be selected at start-up. For instance, data can be retrieved from file, but also from a remote MySQL database or directly from measurement hardware, thus allowing integration of the software within fully automated SHM systems. If data are retrieved from file, the number of steps cannot be controlled but it depends on the record length. As shown in Section 6.2.4, only 1-h long (or longer) records can assure a sufficiently large number of steps and, therefore, results characterized by high reliability.

In the first stage, the MAC sequences at all discrete frequency lines are computed. Computational time can be optimized adopting parallel recording and data processing procedures. Moreover, a partial overlap between subsequent records can be considered in order to increase the number of steps in the case of data retrieved from file, or to keep the global estimation time low when another data source is adopted.

In the second stage, mode bandwidths are identified according to the previously mentioned limits. At the end of this state, a number of bandwidths are identified by their limit values of frequency.

In the third stage, modal parameters are extracted in a fully automated way by analyzing only the portion of the singular value plots in the given mode bandwidth.

### 6.2.3 Comparison with Other Frequency Domain Algorithms

The original aspects of LEONIDA can be better appreciated if it is compared with other automated OMA procedures based on FDD and proposed by other research groups.

FDD is an efficient and easy to manage OMA technique, but it requires user interaction in its classical implementation (Chap. 4). Its simplicity has made it particularly attractive for the implementation of automated OMA procedures. The first approach to automated output-only modal parameter identification via FDD reported in the literature (Brincker et al. 2007) starts from the identification (through an automated peak picking algorithm) of all peaks in the first singular value plot provided by the SVD of the output PSD matrix. After this preliminary phase, it is necessary to assess the nature of the peaks and associate them to structural modes, noise, or spurious harmonics. The last case can be tackled according to the methods described in Chap. 5.

In order to distinguish structural modes from noise peaks, and different close physical modes, two indicators are defined. First of all, the modal coherence (basically, the MAC index), calculated between the first singular vector at the peak and the first singular vector at adjacent points, is used to distinguish physical modes from noise peaks. If the modal coherence is close to unity, then the first singular value at the neighboring point belongs to the same dominating mode (Brincker et al. 2007). An adjacent point is assumed to hold physical information if the modal coherence exceeds a threshold level. The suggested threshold value for the modal coherence indicator is 0.8.

Once the selection of peaks holding modal information is completed, different closely spaced modes are separated through the so-called modal domain indicator. It consists in the MAC computed between the first singular vectors corresponding to neighboring points in a certain frequency range around a given peak. If its value is high over the whole considered frequency range, only one mode is dominating. All points characterized by a modal domain indicator higher than a user-defined threshold (the recommended value is 0.8) identify the modal domain around the considered peak.

The main steps of this automated FDD method can be, therefore, summarized as follows:

- peak identification;
- check if peak is physical (modal coherence and harmonic indicator);
- if peak is physical, then the corresponding modal domain is defined around it; otherwise, the noise domain is set;
- the identified modal and noise domains are excluded from the search set (initial search set goes from DC to the Nyquist frequency);
- search is stopped when the search set is empty, the peak is below a predefined excitation level or a specified number of modes has been estimated.

Another automated FDD method has been developed afterwards (Magalhaes et al. 2008). It is characterized by a similar approach but it is oriented to simplify some aspects of the previous process. In fact, it is demonstrated that a reliable modal identification can be obtained adopting a suitably low limit value for the modal coherence. However, this threshold must be defined for each monitored structure by means of time-consuming sensitivity tests. Moreover, it has been recognized that the recommended value (0.4) can be ineffective if the number of

sensors is small and similar mode shape vectors for close natural frequencies are obtained from the identification process.

These circumstances clearly show that those methods are characterized by some relevant drawbacks. First of all, the threshold-based peak detection is very sensitive to noise and spurious harmonics, as remarked also by Brincker et al. (2007). If the automated FDD is used as a monitoring routine, the threshold for peak detection has to be defined by means of a time-consuming calibration process based on a number of sensitivity tests carried out on the monitored structure, as suggested by Magalhaes et al. (2008). No specific suggestions exist for a-priori threshold definition in the case of single tests.

It is worth noting that an initialization phase can eventually be accepted for SHM applications, when the time spent to carry out sensitivity analyses for threshold and parameter definition is negligible with respect to the whole observation period. In the case of single tests, instead, there is no other way than a-priori threshold and parameter definition. Criteria for objective identification of physical modes are, therefore, of primary importance to avoid any preliminary initialization and to ensure the versatility of the algorithm for different applications (single modal identification tests, continuous SHM) independently of the structural typology. An attempt to tackle this issue is present in the first method (Brincker et al. 2007). However, if the limit value for the modal coherence indicator is somehow justified on the basis of the standard deviation of the correlation between random vectors and of the number of measurement channels, few comments are reported about the modal domain indicator.

It is also worth noting that the number and position of sensors can influence the correlation between singular vectors in a certain frequency range, where more than one mode could be present. In the presence of a few not optimally located sensors, criteria based on correlation between singular vectors in a certain frequency range may fail. Finally, parameters and thresholds that have been set for a given structure through an initialization phase are not guaranteed to be always adequate even for the structure itself; this is the case, for example, of structures that experience remarkable changes (damages) due to extreme events.

LEONIDA overcomes most of these drawbacks since there is no preliminary threshold-based peak detection. In LEONIDA the logical process is reversed, exploiting the preliminary identification of the bandwidth of the modes. Within each bandwidth, modal parameters are then estimated. In addition, since it is based only on the correlation between singular vectors at the same frequency line, it is virtually insensitive to number and position of sensors. Some tests, in fact, have shown that it is effective provided that the observability of a given mode is ensured by at least two sensors (see, for instance, Rainieri et al. 2012). The definition of criteria for mode separation and the calibration of limits on a number of different datasets, case studies, and measurement chains allow avoiding any initialization phase and ensure the applicability of LEONIDA in different conditions (single tests, continuous monitoring).

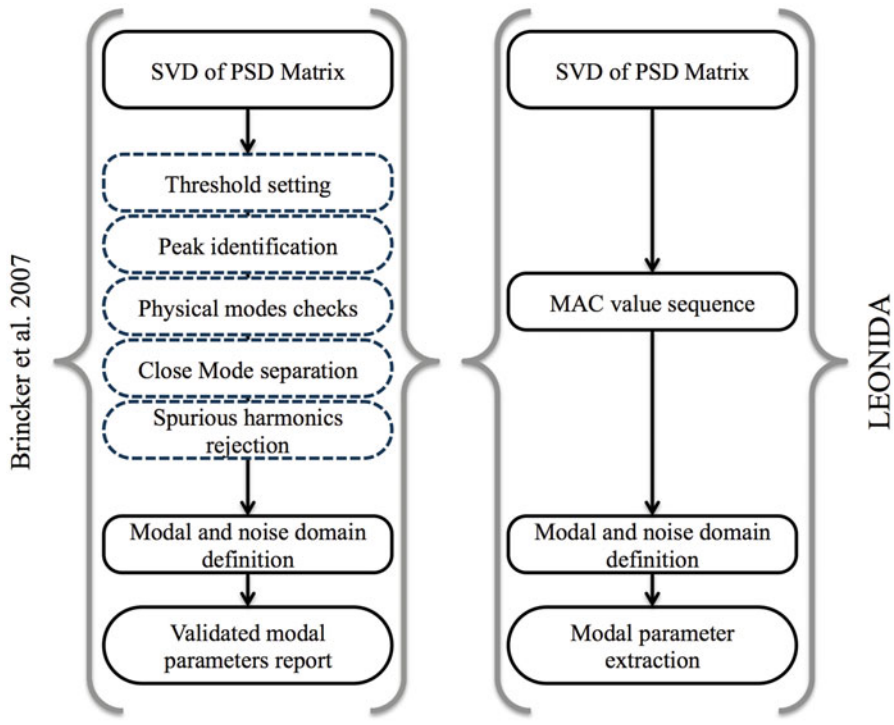


**Fig. 6.5** Innovative features of LEONIDA with respect to previous automated FDD procedures (the *dashed boxes* denote analysis steps that are avoided or implicitly carried out in LEONIDA)

The innovative features of LEONIDA in comparison with the automated FDD method proposed by Brincker et al. (2007) are schematically reported in Fig. 6.5.

It is worth noting that some steps (identified by the dashed line) are omitted or implicitly carried out in LEONIDA. In addition, the same figure shows that LEONIDA follows a reverse logical process, where the estimation of the natural frequency comes after the identification of the bandwidth of modes.

The next section deals with the identification performance of LEONIDA when it is applied to case studies characterized by different degrees of complexity (well-separated modes, closely spaced modes, low SNR). The main issues related to the identification of higher modes and poorly excited modes are also discussed.

#### 6.2.4 Explanatory Applications

The identification performance of LEONIDA has been assessed through its application to case studies characterized by different degrees of complexity. Different record lengths and measurement hardware have been considered. Structure under test,

**Table 6.1** Summary of records and measurement hardware, (© Elsevier Ltd. 2010), reprinted with permission

Structure	Sensors	Data acquisition hardware	Record	Duration (s)
Tower of the Nations (Naples)—r.c.	Epi-sensor FBA ES-U2 (Kinematics Inc.)	K2 (Kinematics Inc.)—24 bit ADC	TdN1 TdN2	1,500 2,400
Bell tower (Montorio)—masonry	Epi-sensor FBA ES-U2 (Kinematics Inc.)	TrioGuard 32—16 bit ADC	Single record	3,600
Bell tower (Montelongo)—r.c.	Epi-sensor FBA ES-U2 (Kinematics Inc.)	TrioGuard 32—16 bit	Single record	3,600
S. Maria del Carmine Bell Tower (Naples)—masonry	Epi-sensor FBA ES-U2 (Kinematics Inc.)	PXI-4472 (NI)—24 bit ADC	Single record	1,800
School of Engineering Main Building (Naples)—r.c.	Epi-sensor FBA ES-U2 (Kinematics Inc.)	K2 (Kinematics Inc.)—24 bit ADC	RC0 RC1 RC2 RC3	1,200 1,200 3,300 3,800

hardware characteristics, and record lengths are summarized for completeness in Table 6.1. Attention has been focused first on the identification of fundamental modes, which are of primary interest for civil engineering structures in seismically prone areas due to the related (typically) large amount of participating mass. Performance in the identification of higher modes and poorly excited modes has also been investigated in view of a more general use.

Results are shown in Table 6.2 and compared with those provided by classical (manual) output-only modal identification. They point out that a reliable and fully automated identification of the fundamental modes by LEONIDA is possible. Furthermore, the algorithm makes possible also the estimation of the bandwidth where the considered mode is dominating (Fig. 6.6). In this sense LEONIDA acts like a source separation technique. Scatters of natural frequencies can be addressed to the finite frequency resolution. About mode bandwidth estimation, the availability of a large amount of data in the case of the School of Engineering Main Building (Rainieri et al. 2011b) has given the opportunity to test the algorithm for different numbers of steps and to investigate the effect of record length on the stability of results. Four records have been considered, with different characteristics and duration. RC0 and RC1 are stationary signals. The first has been recorded during the night, the second in the morning of an ordinary weekday. RC2 and RC3, on the contrary, are weakly nonstationary signals recorded during two important (and crowded) football matches at the nearby stadium (Rainieri et al. 2011b). As shown in Table 6.2, the algorithm has been able to identify the fundamental modes of the structure in all test cases.

**Table 6.2** Comparative assessment of the performance of LEONIDA in the identification of fundamental modes (note that the records of the dynamic response of the Tower of the Nations are different from that considered in Chap. 5: they have been collected several months after the first measurement carried out for model refinement), (© Elsevier Ltd. 2010), reprinted with permission

Structure	Record	Mode	$f_{\text{LEONIDA}}$ (Hz)	$f_{\text{FDD}}$ (Hz)	$f_{\text{Cov-SSI}}$ (Hz)	$f_{\text{SOBI}}$ (Hz)
Tower of the Nations (Naples)	TdN1	I	0.81	0.81	0.81	0.81
		II	1.38	1.38	1.38	1.38
		III	1.66	1.66	1.66	1.66
	TdN2	I	0.81	0.81	0.81	0.81
		II	1.36	1.36	1.36	1.36
		III	1.62	1.63	1.63	1.63
Bell tower (Montelongo)	Single record	I	3.41	3.40	3.41	3.43
		II	4.13	4.13	4.11	4.13
		III	5.06	5.06	5.06	5.06
Bell tower (Montorio)	Single record	I	2.75	2.75	2.75	2.75
		II	3.43	3.43	3.44	3.44
		III	3.84	3.83	3.82	3.82
S. Maria del Carmine	Single record	I	0.70	0.70	0.70	0.70
Bell Tower (Naples)		II	0.76	0.76	0.76	0.76
School of Engineering Main Building (Naples)	RC0	I	0.92	0.92	0.92	0.92
		II	0.98	0.98	0.98	0.98
		III	1.30	1.30	1.30	1.30
	RC1	I	0.92	0.92	0.92	0.92
		II	0.98	0.99	0.99	0.98
		III	1.29	1.30	1.30	1.30
	RC2	I	0.93	0.93	0.93	0.93
		II	1.00	0.99	0.99	1.00
		III	1.31	1.31	1.31	1.31
	RC3	I	0.92	0.93	0.93	0.92
		II	0.99	0.99	0.99	1.00
		III	1.31	1.30	1.30	1.30

Also the extension of mode bandwidths is quite stable in all cases independently of the record length (Table 6.3). However, record length has an effect on the identification performance at higher modes. In fact, some tests have shown that short record lengths yield, as a result of noise, a less clear identification of the bandwidth of higher, poorly excited modes. Thus, tools for rejection of false positives are needed in this case. If higher modes are of interest, longer record durations must be considered. In fact, when the number of steps increases, a number of wrongly identified frequency ranges disappear, while regions where modes are actually located remain stable.

Some specific investigations about the performance of the algorithm in the identification of higher modes and poorly excited modes have been performed. Selected records have been decimated until a final sampling frequency of 20 Hz and the modal identification performance has been assessed in the range 0-10 Hz.

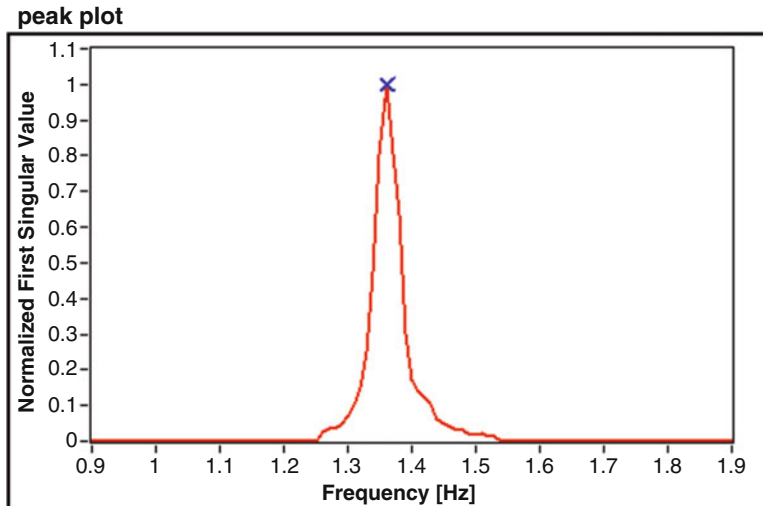


**Fig. 6.6** LEONIDA: Example of identified bandwidth of a mode, (© Elsevier Ltd. 2010), reprinted with permission

**Table 6.3** LEONIDA: identified mode bandwidths for the School of Engineering Main Building, (© Elsevier Ltd. 2010), reprinted with permission

Record	Mode	Bandwidth (Hz)
RC0	I	0.87–0.94
	II	0.96–1.07
	III	1.22–1.36
RC1	I	0.87–0.94
	II	0.97–1.05
	III	1.21–1.51
RC2	I	0.88–0.96
	II	0.98–1.02
	III	1.27–1.34
RC3	I	0.87–0.95
	II	0.97–1.02
	III	1.26–1.37

This frequency range includes the higher modes of the considered test cases. Results are summarized in Table 6.4. They point out that LEONIDA can identify also the higher modes. The only exception is represented by the fifth mode of the Tower of the Nations. It shows that LEONIDA may fail in the presence of poorly excited modes. However, the identification of poorly excited modes is difficult even when an expert user carries out a classical output-only modal analysis.

LEONIDA has also been tested against heavily nonstationary signals, such as those collected by the SHM system of the School of Engineering Main Building on April 6-th, 2009, and related to L'Aquila earthquake. As expected, LEONIDA has not been able to identify any structural mode in this case. However, in view of its

**Table 6.4** LEONIDA: performance in the identification of higher modes, (© Elsevier Ltd. 2010), reprinted with permission

Structure	Mode	$f_{\text{LEONIDA}}$ (Hz)	$f_{\text{FDD}}$ (Hz)	$f_{\text{Cov-SSI}}$ (Hz)	$f_{\text{SOBI}}$ (Hz)
Tower of the Nations (Naples)—record TdN2	I	0.81	0.81	0.81	0.81
	II	1.36	1.36	1.36	1.38
	III	1.62	1.63	1.63	1.63
	IV	3.02	3.02	3.02	3.02
	V	Failure	4.36	4.32	4.36 (not well separated)
	VI	5.17	5.16	5.10	5.22
Bell tower (Montelongo)— single record	I	3.41	3.40	3.41	3.43
	II	4.13	4.13	4.11	4.13
	III	5.06	5.06	5.06	5.06
	IV	5.62	5.62	5.63	5.60
	V	6.35	6.35	6.35	6.33 (not well separated)
	VI	7.42	7.42	7.40	7.40

integration within vibration-based SHM system, it is interesting to analyze how an input ground motion affects the sequence of MAC values. In Fig. 6.7 the MAC vs. frequency plots provided by a weakly nonstationary signal (RC2) and a heavily nonstationary signal (due to the weak ground motion resulting from the propagation of L’Aquila earthquake) are compared. While in the first case it is possible to identify some “bells” around the peaks corresponding to the first three modes of the structure, in the second case the MAC values are lower and no bells around the peaks of the first singular value plot can be identified.

The sequence of MAC values at the frequency of a structural mode (Fig. 6.8) better clarifies the effect of a transient signal. The transient signal associated to the earthquake causes a drop in the MAC vs. step number plot. Thus, the sequence of MAC values does not respect the preset limits and, therefore, the algorithm cannot identify the mode.

In summary, LEONIDA marks a fundamental step in the development of automated OMA procedures, because of the efforts to overcome the typical drawbacks of previous automated modal identification algorithms. In fact, there are no parameters to be calibrated at each new application, and no initialization phase; there is no initial threshold-based peak detection; finally, the algorithm shows good performance also in the case of closely spaced modes and a few, not optimally located sensors. However, long records are needed for an effective identification of higher, weakly excited modes. The problem of model order selection is avoided because LEONIDA is based on a nonparametric frequency domain OMA procedure. The computational load is also fairly low (SVD and computation of the output PSD matrix are the most demanding operations) and the adoption of appropriate implementation strategies can optimize it.

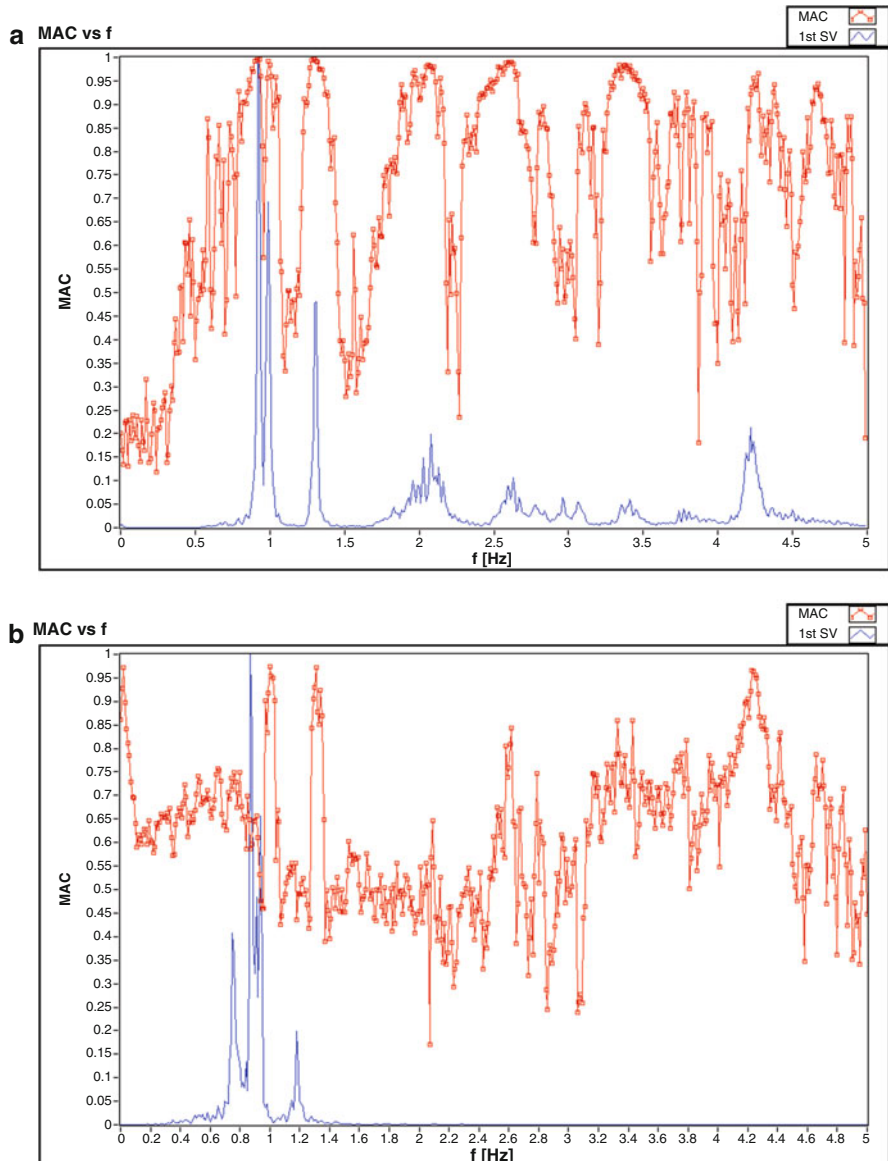


**Fig. 6.7** LEONIDA: MAC vs. frequency plot for the School of Engineering Main Building in operational conditions (a) and in the presence of input ground motion (b), (© Elsevier Ltd. 2010), reprinted with permission

The integration of LEONIDA into a fully automated vibration-based SHM system has also been investigated, obtaining stable and reliable results. More details can be found elsewhere (Rainieri and Fabbrocino 2010).

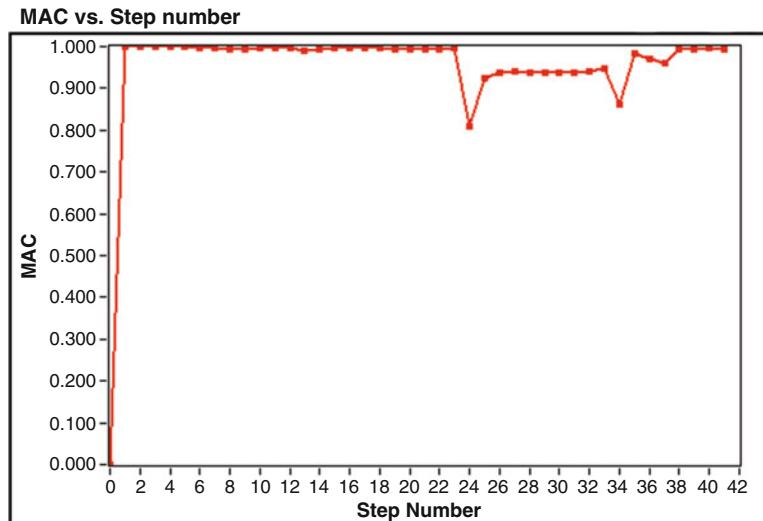


**Fig. 6.8** Effect of input ground motion on the MAC sequence in the bandwidth of a mode, (© Elsevier Ltd. 2010), reprinted with permission

## 6.3 Automated OMA by Hybrid Method: ARES

### 6.3.1 Algorithm

Another more refined automated modal parameter identification method has been recently developed. Even if its performance assessment is still in progress, the description of the algorithm in its most relevant parts can be of interest because of the innovative characteristics of the method. As in the case of LEONIDA, the new algorithm, called ARES (Automated modal paRameter Extraction System), aims at overcoming the typical drawbacks of automated OMA procedures:

- threshold-based peak and physical pole detection;
- need for a preliminary calibration phase at each new application;
- static settings of thresholds and parameters which may be unsuitable to track the natural changes in modal properties of structures due to damage or environmental effects;
- sensitivity to noise, problems of false or missed identification.

Moreover, it aims at providing accurate and reliable estimates of modal damping ratios. Automated OMA algorithms often underestimate this aspect. In fact, they do not provide damping estimates or, whenever they are able to estimate modal damping, they usually yield very scattered results. The fairly large scatter associated to damping estimates, in comparison with that of natural frequency and mode shape estimates, is well documented in the literature. Even if the scatter

can be partially addressed to inherent limitations of the estimators and to the equivalent viscous damping model (Chap. 5; the interested reader can also refer to Rainieri et al. 2010 for more details), adoption of appropriate data processing procedures can minimize the estimation error and enhance robustness and accuracy of modal damping estimates provided by automated OMA procedures.

The core of ARES is the SSI method, but it also includes processing steps from other OMA methods, such as SOBI and FDD; in this sense, it can be considered a hybrid method for automated OMA.

Evaluation and control of the accuracy of modal parameter estimates are critical for a number of applications and, in particular, modal-based damage detection. A number of simulation studies have demonstrated that the modal parameter estimates provided by parametric methods, such as the SSI methods, are by far more accurate than those provided by nonparametric procedures (Peeters and De Roeck 2001b, Reynders et al. 2012). However, the automated interpretation of stabilization diagrams is a very complex activity. In fact, the identification of alignments of stable poles and, therefore, of physical modes is often difficult, since the quality of the stabilization diagram depends on a number of parameters (number of block rows, maximum model order) and thresholds (allowable scatter between the modal properties evaluated at consecutive model orders) whose settings vary from dataset to dataset. This circumstance remarks the relevant role of the analyst's judgment and the difficulty of automation. Thus, a lot of research efforts have been spent on the task of the automated interpretation of stabilization diagrams. Since the poles in a stabilization diagram are labeled as physical if they show similar properties, the use of analysis strategies based on clustering techniques for the identification of physical poles seems the most natural choice. In fact, clustering techniques (Tan et al. 2006) aim at grouping data points based on the characteristics they have. Several studies are reported in the literature about the automatic interpretation of stabilization diagrams by clustering techniques. A (partial) list of references is reported at the end of this chapter for the interested reader (see, for instance, Allemand et al. 2010, Carden and Brownjohn 2008, Chauhan and Tcherniak 2009, Goethals et al. 2004, Magalhaes et al. 2009, Pappa et al. 1997, Reynders et al. 2012, Vanlanduit et al. 2003).

Most of these approaches are based on parameters and threshold that have to be specified by the user. Such parameters are often application-dependent: for instance, the approach proposed by Magalhaes et al. (2009) requires the appropriate setting of the number of block rows, recognizing that it influences the quality of stabilization. Thus, they recommend to spend time for tuning the number of block rows as well as other parameters of the adopted clustering approach that are also dependent on the level of noise in the signals. Other authors, instead, do not consider the problem of setting the value of the number of block rows but they focus the attention on the methods to obtain the maximum of information from the analysis of a given stabilization diagram. However, the resulting approach is often cumbersome because it requires the evaluation of a large number of additional parameters and (hard and soft) validation criteria (see, for instance, Reynders et al. 2012).

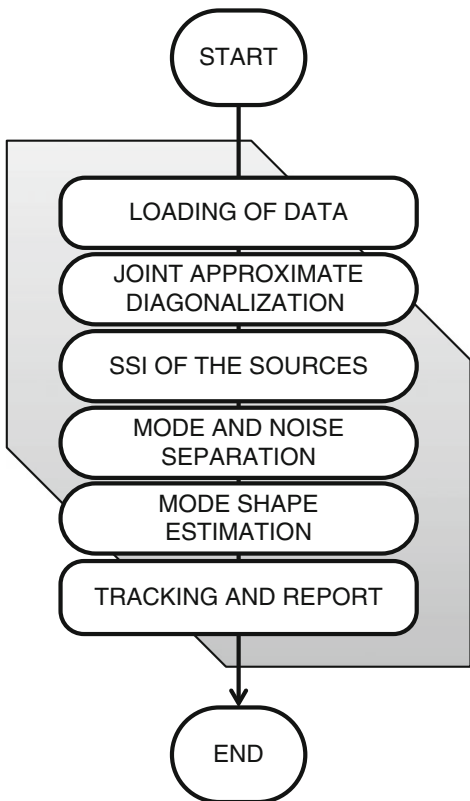
In ARES, SSI is not directly applied to the multivariate time series of the structural response but, after a preprocessing step, it processes the individual source correlations obtained from the JAD of a number of time shifted correlation matrices. The problem of avoiding user interaction in setting the analysis parameters is solved taking into account that ARES is basically insensitive to the settings of  $p$  and  $t$  in JAD (Sect. 4.5.4) and that, for a given maximum model order, the quality of stabilization first improves and then gets worse for increasing values of the number of block rows. Thus, a sensitivity analysis for different values of the number of block rows makes its automated setting possible. In fact, based on the results of the sensitivity analysis, the number of block rows is set in a way able to minimize the variance of the modal parameter estimates at different model orders (see also Chap. 5).

As in the case of other automated OMA methods based on SSI available in the literature, clustering techniques make possible the automatic selection of physical poles in the stabilization diagram. However, the preliminary JAD makes the automatic analysis of the stabilization diagram and extraction of the physical poles easier. In fact, as a result of the JAD, the raw data associated to the measured structural response are transformed into source correlations (Sect. 4.5.4). They can be well-separated (showing the contribution of a single mode to the structural response), not well-separated (showing noise or minor contributions from other modes that are superimposed to the contribution of the main mode) or just noise. Thus, the automated interpretation of the stabilization diagram is simplified because the modal parameters are extracted by applying the SSI method to the individual source correlations instead of the multivariate time series of data. Once the source correlations have been individually analyzed by the SSI method, the physical poles are separated from the spurious ones by means of clustering techniques and mode validation criteria. Their effectiveness is enhanced by the fact that the analyzed stabilization diagrams report information about one mode only at the time. The flowchart of the algorithm is shown in Fig. 6.9.

A state-machine architecture has been adopted for the implementation of ARES, since the following well-established data processing steps can be identified:

- Correlation matrices are computed from the raw data;
- The JAD of  $p$  time-shifted covariance matrices provides the correlations of the sources (both modal and noise sources); a number of analyses involving both real and simulated datasets have shown that the setting of  $p$  has no influence on the estimates, unless it is set much too low ( $p < 100$ ); in this case slight decreases in accuracy can be observed;
- The source correlations are individually analyzed by SSI for the estimation of natural frequencies and damping ratios;
- The obtained poles are grouped into clusters. For each source, the corresponding poles are grouped into clusters according to the hierarchical clustering method. The cluster characterized by the largest number of elements is selected as representative of the mode. This step is repeated for different values of the number of block rows  $i$  ranging in the interval [20, 80] with step  $\Delta i$  equal to 2 (these parameters are theoretically user-selectable but the above mentioned

**Fig. 6.9** ARES: Algorithm for automated modal parameter identification



values are recommended, since they have provided the best results in the majority of applications);

- The obtained natural frequency and damping ratio estimates are subjected to a selection and validation phase. Clusters that do not fulfil the validation checks are removed from the dataset. In particular, the average damping ratio in each cluster has to be in the range 0–5 % and the corresponding coefficient of variation not larger than 10 %. The first limitation is based on an empirical observation about the behavior of civil structures in operational conditions: in fact, they are usually weakly damped. The second limitation recognizes that physical poles are characterized by small standard deviations, while spurious poles show much larger values of this parameter (Reynders et al. 2012). Checks about the physical significance of the estimates are also carried out (for instance, checks of the sign of damping). It is worth pointing out that the validation criteria have to be applied after the hierarchical clustering stage, since they might remove most of the spurious poles and a number of physical poles could be separated and lost as a result of the clustering stage.
- The natural frequency and damping ratio estimates in each cluster are normalized in the range [0, 1] and a k-means clustering algorithm is applied

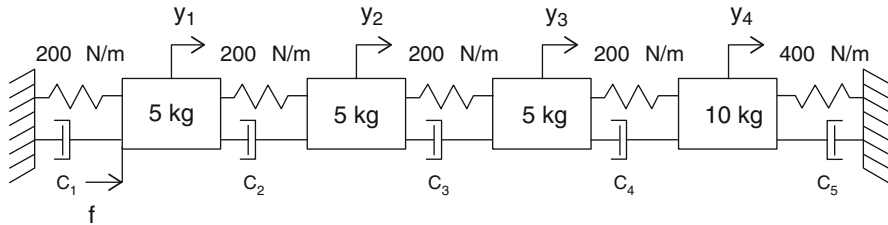


**Fig. 6.10** ARES: The benchmark 4-DOF system

with  $k = 2$  clusters, allowing the presence of empty clusters. This last step removes eventual spurious poles that are still present, thus further refining the precision and accuracy of estimates;

- The final values of natural frequency and damping ratio of the identified modes are selected according to the results of the sensitivity analyses with respect to the number of block rows, for a fixed value of the maximum model order (equal to 16) in the stabilization diagram. The cluster characterized by the minimum variance of the estimates is selected as the one providing the best estimate of the modal parameters for the considered mode;
- Mode shape estimates are finally obtained from SVD of the output PSD matrix at the previously estimated frequency of the mode.

The previous discussion about the sequence of analysis steps in ARES highlights how the source separation makes the discrimination of physical and noise modes easier and more reliable. The sensitivity analysis with respect to the number of block rows and the grouping of the poles in clusters leads to a robust identification of the modal parameters and to a quantification of the precision of the estimates.

### 6.3.2 Validation and Application

The performance of ARES in terms of accuracy and reliability of estimates has been investigated through a statistical analysis of the results obtained from data continuously generated by a simulated 4-DOF system excited by Gaussian white noise.

The mass and stiffness properties of the system are reported in Fig. 6.10. Rayleigh damping is adopted. The modal properties of the system are reported in Table 6.5. The four case studies differ for the assumed values of damping or the SNR.

The system matrices and, therefore, the associated modal parameters have been kept constant in all runs in order to focus the attention only on the uncertainties associated to inherent limitations of the estimator.

The system response to Gaussian white noise has been simulated 10,000 times. The input has been applied at DOF #1. Each simulated dataset consisted of four measurement channels; the total record length was 3,600 s and the sampling frequency was 10 Hz. Gaussian white noise has been added to the system response

**Table 6.5** Modal properties of the simulated 4-DOF system

Mode	$f_r$ (Hz)	Case study #1 (SNR = 5 dB)— $\xi_r$ (%)	Case study #2 (SNR = 15 dB)— $\xi_r$ (%)	Case study #3 (SNR = 5 dB)— $\xi_r$ (%)	Case study #4 (SNR = 5 dB)— $\xi_r$ (%)
I	0.668	1.00	1.00	2.00	2.00
II	1.137	0.88	0.88	1.31	1.76
III	1.526	0.92	0.92	1.09	1.84
IV	1.879	1.00	1.00	1.00	2.00

**Table 6.6** ARES: success rate of automated modal identification in 10,000 runs

Mode	Case study #1—success rate (%)	Case study #2—success rate (%)	Case study #3—success rate (%)	Case study #4—success rate (%)
I	99.79	100.0	99.71	99.87
II	99.96	100.0	99.97	100.0
III	99.95	100.0	99.98	100.0
IV	100.0	100.0	100.0	100.0

in order to simulate the effect of measurement noise. The SNRs are reported in Table 6.5. Each dataset has been then processed using the described algorithm in order to automatically extract the modal parameters of the system.

The analysis of the obtained results has highlighted the reliability of ARES. In fact, a success rate larger than 99 % has been obtained for all modes (Table 6.6). Missed identification of the dynamic properties of one of the modes occurred only in a few runs. This was probably due to a combined effect of weak excitation and low SNR, which affected the quality of separation and stabilization.

The results in terms of natural frequency and damping estimates are summarized in Tables 6.7 and 6.8. Very accurate natural frequency estimates, characterized by low standard deviation  $\sigma$ , have been obtained. The error in natural frequency estimates is much lower than 1 % in the 95 % of the runs for all case studies.

The accuracy of estimates slightly improves when the SNR increases. The estimates are also very precise. In fact, the coefficient of variation  $\gamma_{f,\text{cluster}}$  of the natural frequency estimates in a cluster is much lower than 0.1 % in the 95 % of the runs when the cluster selected by the sensitivity analysis with respect to the number of block rows is considered.

Damping estimates are fairly accurate and characterized by moderate uncertainty ( $\sigma$  lower than 0.2 %). In particular, the variability of estimates slightly increases when the nominal damping values increase. Larger errors are associated to damping estimates with respect to natural frequencies. However, the scatter with respect to the nominal values is lower than 10 and 20 % in the 50 and 95 % of the runs, respectively. The errors slightly decrease when the SNR increases. Damping estimates are also fairly precise (the coefficient of variation  $\gamma_{\xi,\text{cluster}}$  of the damping ratio estimates in a cluster is much lower than 10 % in the 95 % of the runs when the cluster selected by the sensitivity analysis with respect to the

**Table 6.7** ARES: automated modal identification results—natural frequencies

Case study	Mode	$f_{\text{nominal}}$ (Hz)	$f_{\text{av}}$ (Hz)	$\sigma_f$ (Hz)	$\Delta f$ (%) 50th centile	$\Delta f$ (%) 95th centile	$\gamma_{f,\text{cluster}}$ (%) 95th centile
#1	I	0.668	0.668	0.000730	0.072	0.216	0.0254
	II	1.137	1.137	0.000911	0.052	0.156	0.0285
	III	1.526	1.526	0.001157	0.047	0.143	0.0269
	IV	1.879	1.879	0.001568	0.048	0.151	0.0363
#2	I	0.668	0.668	0.000665	0.067	0.196	0.0319
	II	1.137	1.137	0.000879	0.050	0.152	0.0234
	III	1.526	1.526	0.001090	0.047	0.140	0.0232
	IV	1.879	1.879	0.001425	0.047	0.149	0.0296
#3	I	0.668	0.668	0.001275	0.121	0.359	0.0598
	II	1.137	1.137	0.001324	0.070	0.219	0.0509
	III	1.526	1.526	0.001309	0.054	0.166	0.0345
	IV	1.879	1.879	0.001469	0.048	0.148	0.0346
#4	I	0.668	0.668	0.001368	0.117	0.358	0.0729
	II	1.137	1.137	0.001636	0.086	0.278	0.0814
	III	1.526	1.526	0.002054	0.083	0.260	0.0798
	IV	1.879	1.879	0.002825	0.085	0.277	0.0991

**Table 6.8** ARES: automated modal identification results—damping ratios

Case study	Mode	$\xi_{\text{nominal}}$ (%)	$\xi_{\text{av}}$ and (mode, median) (%)	$\sigma_\xi$ (%)	$\Delta\xi$ (%) 50th centile	$\Delta\xi$ (%) 95th centile	$\gamma_{\xi,\text{cluster}}$ (%) 95th centile
#1	I	1.00	1.02 (1.0, 1.02)	0.108	7.2	21.6	7.0
	II	0.88	0.89 (0.9, 0.89)	0.080	6.0	18.0	4.4
	III	0.92	0.93 (0.9, 0.93)	0.072	5.1	15.3	2.5
	IV	1.00	1.01 (1.0, 1.01)	0.075	4.9	14.9	3.1
#2	I	1.00	1.01 (1.0, 1.01)	0.099	6.7	19.4	2.2
	II	0.88	0.88 (0.9, 0.88)	0.075	5.7	16.6	1.6
	III	0.92	0.92 (0.9, 0.92)	0.073	5.3	15.5	1.7
	IV	1.00	1.00 (1.0, 1.00)	0.074	4.7	14.6	2.1
#3	I	2.00	2.03 (2.0, 2.03)	0.179	5.9	17.9	7.7
	II	1.31	1.32 (1.3, 1.32)	0.109	5.4	16.7	5.1
	III	1.09	1.10 (1.1, 1.10)	0.081	4.9	14.7	2.4
	IV	1.00	1.01 (1.0, 1.00)	0.075	4.9	14.9	2.8
#4	I	2.00	2.03 (2.0, 2.02)	0.183	6.0	18.3	6.7
	II	1.76	1.78 (1.8, 1.78)	0.138	5.2	15.6	4.6
	III	1.84	1.85 (1.8, 1.85)	0.129	4.5	13.9	3.0
	IV	2.00	2.02 (2.0, 2.02)	0.143	4.3	14.0	3.6

number of block rows is considered). Sample distributions of the identified damping ratios after 10,000 runs for the four modes are depicted in Fig. 6.11. The mean, mode, and median of the identified damping ratios after 10,000 runs are very close each other and to the nominal values of modal damping ratios (Table 6.8). Taking into account the uncertainty associated to damping estimates, the mode of damping values is given with one decimal place only.

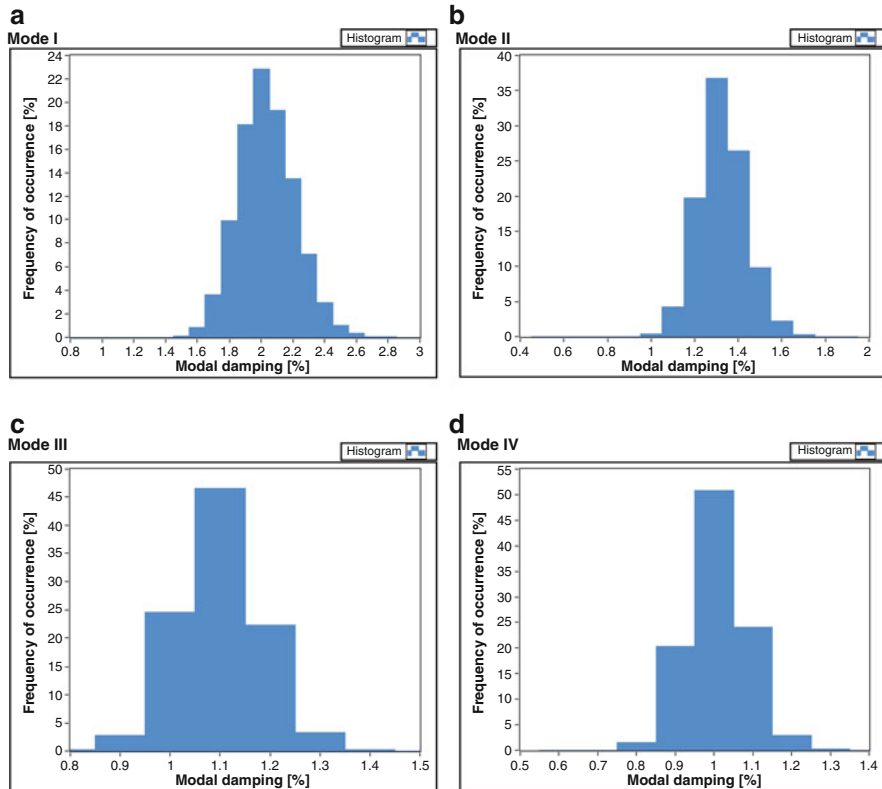


**Fig. 6.11** ARES: Distribution of the identified damping ratios after 10,000 runs (case study #3)—mode I (a), mode II (b), mode III (c), mode IV (d)

Marginal refinements can be obtained by outlier removal, confirming the robustness and accuracy of the algorithm.

The performance of ARES at higher modes has been assessed by the analysis of the RC1 record (Sect. 6.2.4) of the response to ambient vibrations of the School of Engineering Main Building in Naples (Rainieri et al. 2011b).

The 1,200 s long record, consisting of 12 time series originally sampled at 100 Hz, has been decimated ten times before processing, obtaining a final sampling frequency of 10 Hz. The obtained modal identification results are reported in Table 6.9, together with a description of the sources. The results provided by ARES are compared to those provided by LEONIDA. ARES has shown good performance even at higher modes. It has been able to properly identify the content of the sources, separating physical modes and noise. Overall, ARES seems to perform much better than LEONIDA.

Further investigations are in progress to assess the performance of ARES in the case of its integration into continuous vibration-based SHM systems.

**Table 6.9** ARES: performance in the identification of higher modes

Source	Description	ARES [f (Hz), $\xi$ (%)]	LEONIDA [f (Hz)]
I	Well separated	[0.92, 1.25]	0.92
II	Well separated	[0.98, 1.02]	0.98
III	Well separated	[1.30, 0.65]	1.30
IV	Not well separated (modes at 2.07 Hz and 4.20 Hz)	[2.07, 3.52]	2.07
V	Not well separated (mode + noise)	[2.60, 3.12]	2.59
VI	Not well separated	[2.79, 2.05]	Not identified
VII	Not well separated (mode + noise)	[2.94, 1.55]	2.95
VIII	Not well separated (mode + noise)	[3.37, 1.92]	3.40
IX	Well separated	[3.94, 1.64]	Not identified
X	Not well separated	[4.20, 1.65]	Not identified
XI	Well separated	[4.26, 1.17]	4.25
XII	Noise	Noise	–

## 6.4 Automated Modal Tracking: AFDD-T

### 6.4.1 Objectives

The requirements of advanced seismic protection systems for critical structures lead to focus the attention on the reduction of computational efforts and response time of modal extraction engines. LEONIDA definitely represents a solution for automated modal parameter identification. It can also be used as modal information engine in vibration-based monitoring systems, but length of records, amount of computational burden, and response time make it not ideal for a specific class of applications, the continuous monitoring of structures in seismically prone areas. Thus, the availability of an optimized strategy for automated modal tracking for rapid structural health assessment in seismically prone areas is crucial. In the case of structures exposed to seismic risk, the procedures for automated modal tracking have to be accurate and reliable but they also have to be robust and able to provide frequent estimates of dynamic properties.

From a general point of view, both automated modal tracking and automated modal parameter identification algorithms are suitable for modal-based SHM. However, most of the automated OMA procedures are characterized by high response time. On the contrary, an automated modal tracking procedure can be considered effective for vibration-based SHM in seismic areas if it is characterized by low computational burden and it is robust even in the case of short records. In fact, these characteristics allow increasing the number of modal parameter estimates per hour. Moreover, application-dependent data processing parameters have to be avoided in order to effectively follow the natural changes of the modal properties of structures due to damage or environmental effects.

Refinement of these aspects is relevant for the fast evaluation of health conditions of a structure after an earthquake or during a seismic sequence. Statistical treatment of modal parameter estimates and elimination of environmental effects (Hu et al. 2012, Sohn et al. 2003, Worden et al. 2007) can be effective for accurate health assessment purposes. Even in the case of structures subjected to seismic events, a reliable evaluation of the variation of the modal parameters induced by a ground motion cannot avoid the analysis of a sufficiently large population of samples collected in the first few hours after the event. The collection of a sufficient amount of data allows an appropriate consideration of the effect of random errors and slight nonstationarities on the estimates. However, the need for near real-time estimation of the modal parameters after seismic events is above all related to the issues of emergency management. As also demonstrated by recent seismic events occurred in Italy—see for instance the L’Aquila earthquake 2009 data—a sequence of closely repeated in time earthquakes (much less than 1-h lag between two consecutive ground motions) is usual, in particular in the first days after the mainshock. Thus, a near real-time estimation of the modal properties allows the collection of sufficient amount of information about the structure in between two events, when the effects of input ground motions that negatively affect the output-only estimation of the modal parameters are null (Rainieri and Fabbrocino 2010, Rainieri et al. 2011b). The collection of a fairly large amount of data in a short time after the seismic is not a trivial task. Most of the automated OMA procedures are not optimized in this sense. Nevertheless, fast, reliable, and robust modal tracking procedures able to provide frequent modal parameter estimates after the event play a fundamental role for effective vibration-based SHM in seismically prone areas. In this context it is worth mentioning that the prompt post-earthquake health assessment of strategic structures is also crucial to support rescue operations.

#### **6.4.2 Principles and Implementation**

A strategy for effective automated modal tracking in seismically prone areas is herein presented in its most relevant aspects. It takes advantage of the knowledge of the experimental mode shapes and a revised concept of spatial filtering in order to achieve the previously mentioned objectives and target performance. As in the case of LEONIDA, the core of the algorithm is the SVD of the output PSD matrix. The present automated modal tracking strategy, called in the following Automated Frequency Domain Decomposition-Tracking (AFDD-T), can be used in combination with LEONIDA or ARES for fully automated vibration-based SHM of real structures. The monitoring system of the School of Engineering Main Building in Naples represents an example of successful integration of LEONIDA and AFDD-T into continuous vibration-based monitoring systems. The description of the structure and of the installed SHM system is beyond the scope of the book and it can be found elsewhere (Rainieri et al. 2011b).

The main characteristics of the monitoring system are scalability, durability, redundancy, and integration achieved by the use of a remote MySQL database for data storage (Rainieri et al. 2011b).

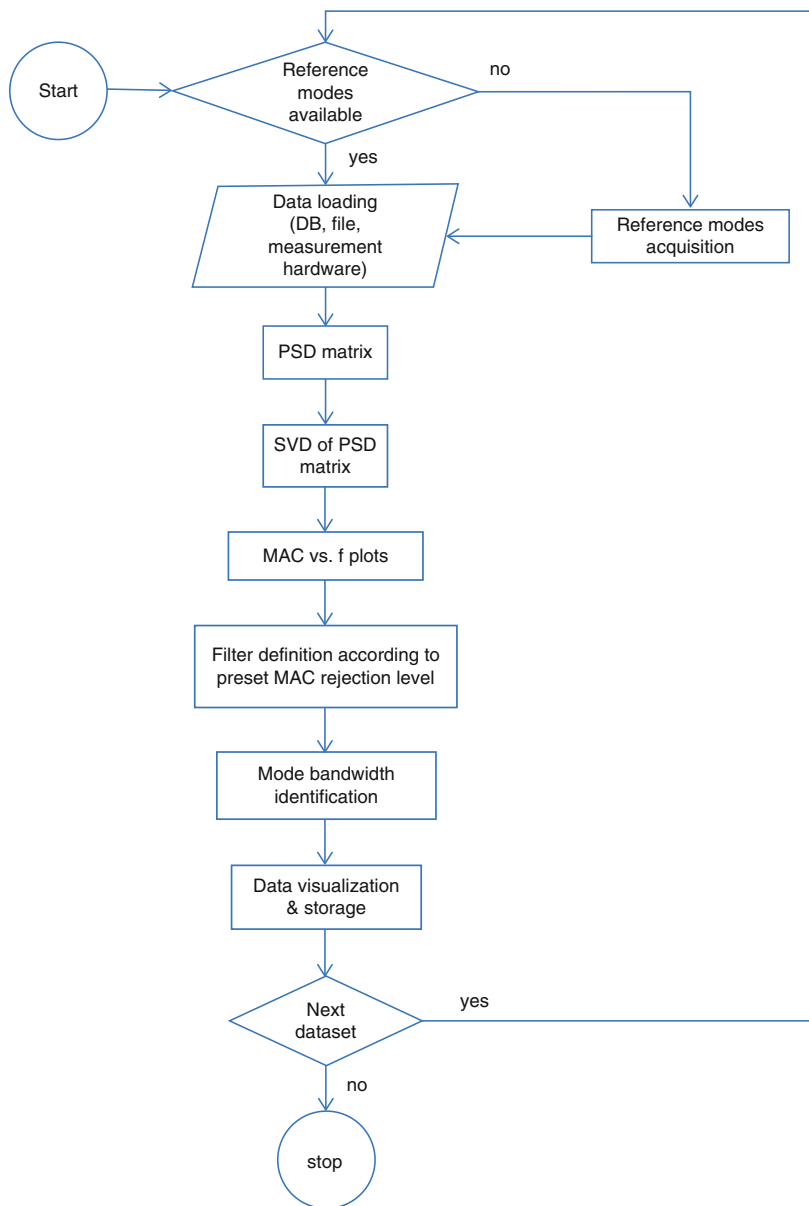
As mentioned in Sect. 6.2, LEONIDA has solved the problem of avoiding threshold-based peak detection over the whole frequency range under investigation and static setting of analysis parameters, thus making possible a fully automated modal parameter identification. However, it requires long records—i.e. 1 h—of the structural response, so it is partially ineffective for SHM applications in seismically prone areas.

An automated FDD-based modal tracking can be carried out according to the flowchart shown in Fig. 6.12, where the information about the mode shapes is used for a spatial filtering of data. In its development, the algorithm has been optimized in order to fit the requirements of seismic protection of structures in terms of balanced performance between accuracy and robustness on one hand, and frequency of estimates on the other. Since AFDD-T takes advantage of prior information about mode shapes, it plays a role only in the context of SHM applications. In spite of its limited autonomy, it can yield reliable modal parameter estimates from records much shorter than those required by automated modal parameter identification methods, such as LEONIDA. This makes possible an automated, reliable, and near real-time tracking of the modal parameters that can provide relevant information about the health state of the structure in between consecutive, close in time ground motions for emergency management purposes.

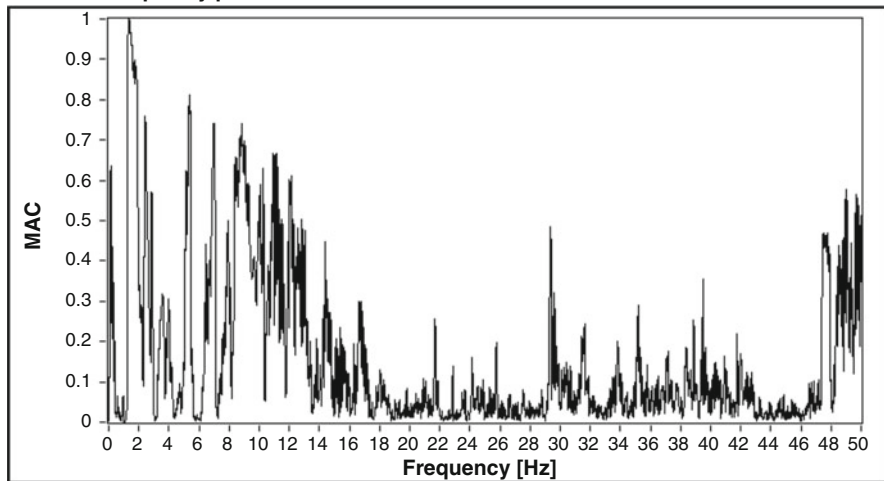
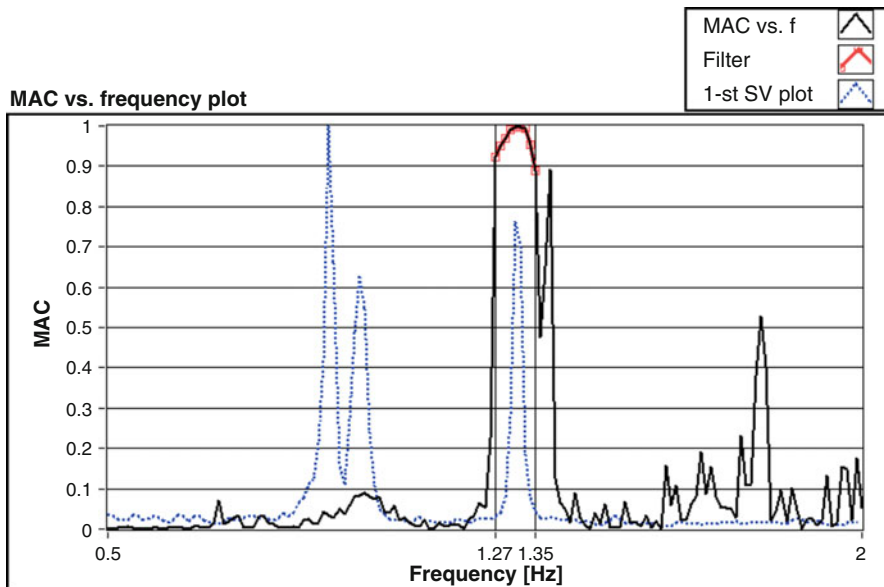
There is a fundamental difference between the use of mode shape estimates for spatial filtering in AFDD-T and traditional applications of this kind of filtering. In fact, instead of considering the product of the mode shapes with the output PSD matrix, as in the case, for instance, of the FSDD method (Sect. 4.4.2), each mode shape vector is used to identify the limits of a bandpass filter for the mode of interest starting from the computation of the MAC with the singular vectors obtained at each frequency line by SVD of the PSD matrix.

The  $k$ -th mode of interest is, therefore, identified by inspecting the MAC vs. frequency plot (Fig. 6.13). The reference mode shape defines a bandpass filter (Fig. 6.14) characterized by an adaptive bandwidth. It is obtained by selecting all points that show a MAC value higher than a user-defined MAC Rejection Level, i.e. 80–90 % of the maximum MAC in the MAC vs. frequency plot. The analysis of the filtered data permits a straightforward identification of the natural frequency.

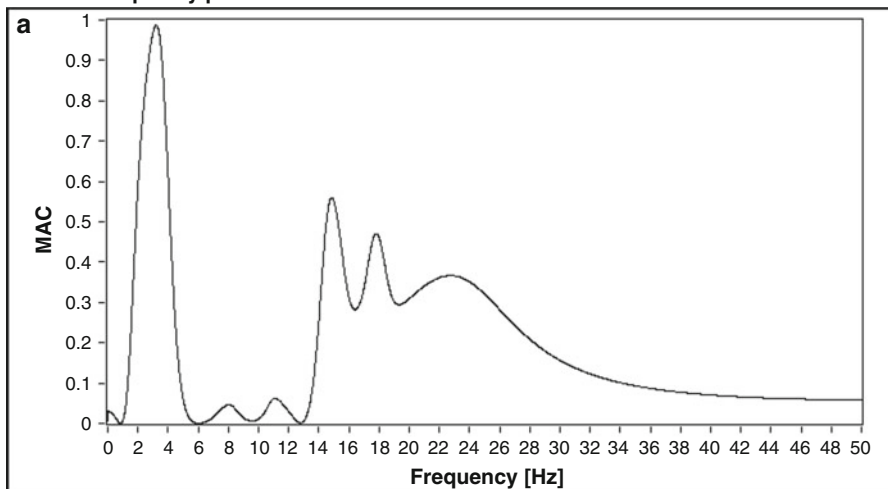
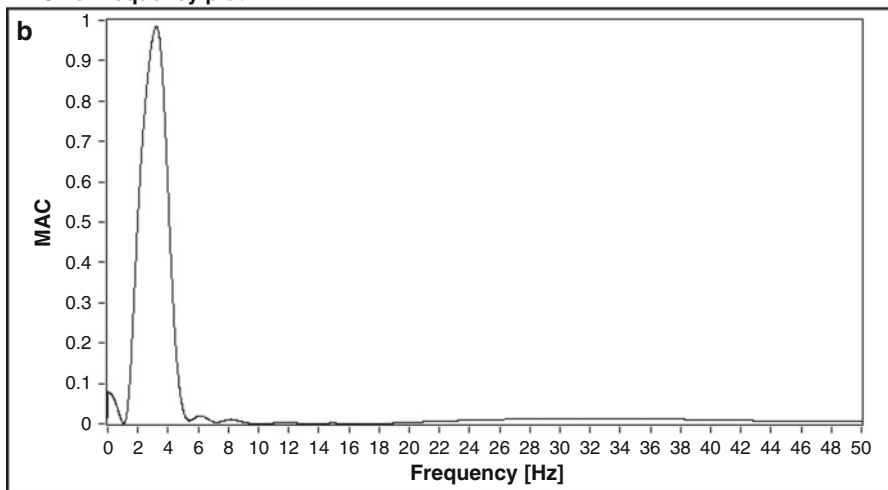
In some cases the dynamic response of the structure to ambient vibrations could be affected by harmonic components superimposed to the stochastic part (Chap. 5). The role of harmonic excitations is different depending on the relative distance between the natural frequencies of interest and the harmonic. Whenever the latter is far from structural modes, the ODS is a combination of several excited modes and the forces acting on the structure; thus, it yields low MAC values with the reference mode shapes. On the contrary, if the harmonic is close to a structural mode, high MAC values could be observed and the modal parameter estimation could be biased. A structural and functional assessment of the monitored building is, therefore, recommended in order to identify eventual spurious harmonic components.



**Fig. 6.12** AFDD-T: Algorithm for automated modal tracking, (© Elsevier Ltd. 2011), reprinted with permission

**MAC vs. frequency plot****Fig. 6.13** AFDD-T: MAC vs. frequency plot, (© Elsevier Ltd. 2011), reprinted with permission**Fig. 6.14** AFDD-T: Automatic selection of the bandwidth of the mode, (© Elsevier Ltd. 2011), reprinted with permission

In such cases, implementation of methods able to identify and remove harmonic components (Chap. 5) can solve the problem at the expenses of an increase in computational efforts and hardware requirements.

**MAC vs. frequency plot****MAC vs. frequency plot**

**Fig. 6.15** AFDD-T: Effect of the number of sensors (simulated data): poor spatial definition (a), improved spatial definition (b), (© Elsevier Ltd. 2011), reprinted with permission

Another relevant issue concerns the definition of the number of sensors that ensures an effective spatial filtering. Figure 6.15 shows that the effectiveness of spatial filtering improves as the number of sensors increases. Results of simulations and real applications have shown that, in the presence of a few sensors, local maxima appear in the MAC vs. frequency plot; however, the absolute maximum is reached in the bandwidth of the considered mode defined by the reference mode shape. Thus, detection of the absolute maximum ensures a reliable automatic setting of the filter and an effective extraction of modal parameters. Only a poor sensor

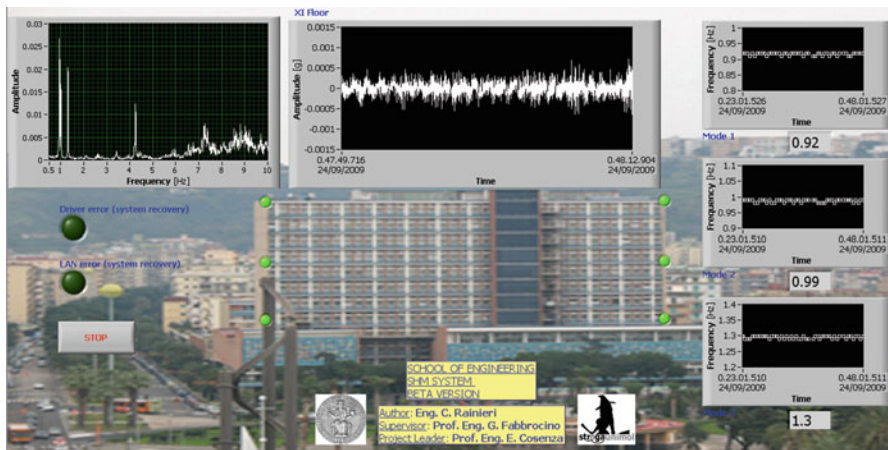


**Fig. 6.16** SHM system of the School of Engineering Main Building: User interface of AFDD-T, (© Elsevier Ltd. 2011), reprinted with permission

placement, unable to put in evidence the differences in the shapes of the structural modes, can seriously affect the reliability of the automated modal tracking (Rainieri et al. 2012). In this case it is possible to observe a decrease in the success rate of identification of the modes characterized by very similar mode shape estimates. On the contrary, if the sensor layout is properly set (off-diagonal terms in the AutoMAC matrix very close to 0), the filtering procedure is effective even in the case of a few sensors and short records. Note that the short duration of time series yields noisy spectra as a result of the little number of averages. The adoption of an appropriate architecture for data processing allows getting a new modal parameter estimate every 3–5 min. This time interval fits the requirements of safety and emergency management in seismically prone areas, allowing the observation of the evolution of the structure in between consecutive events of the seismic sequence.

AFDD-T has been implemented into software running on the local server of the School of Engineering Main Building SHM system and interfaced with its remote MySQL database. The software, working on a on-line basis, has been developed in LabVIEW environment and it is characterized by a graphic interface showing the location of sensors on the structure, the plot of the first singular value (obtained by SVD of the output PSD matrix) vs. frequency, the acceleration waveforms and the results of identification in the form of plots of the natural frequency estimates vs. time (Fig. 6.16).

The software is characterized by a Producer/Consumer architecture (Fig. 6.17). The Producer cycle is used to get data from the database while the Consumer cycle processes these data and shows the output on screen. Parallel cycles extract the dynamic properties (natural frequency and mode shape) for each monitored mode.

The adopted software architecture and a partial overlap among subsequent time series allow collecting a new estimate of the fundamental modal parameters every

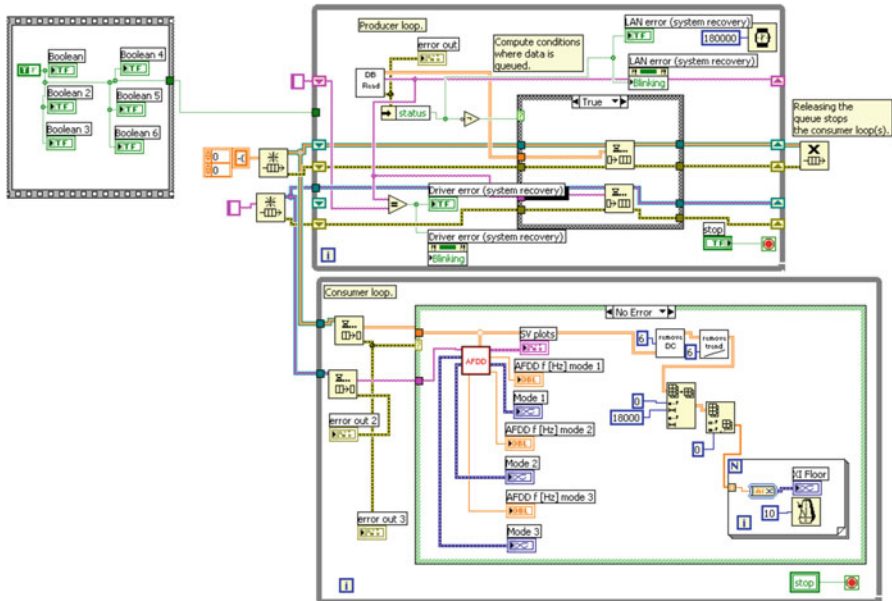


**Fig. 6.17** AFDD-T: Software architecture, (© Elsevier Ltd. 2011), reprinted with permission

3 min. Several error checks ensure software robustness against possible hardware bad functioning conditions. Thus, AFDD-T makes possible an effective tracking of modal parameters and, indirectly, of the health state of the structure (Sohn et al. 2003) in seismically prone areas.

#### 6.4.3 Validation and Application

AFDD-T has been validated against simulated data before its integration in the monitoring system of the School of Engineering Main Building. Simulated data have been obtained by applying a Gaussian white noise as input on a shear-type 15-stories 1-bay r.c. frame, characterized by well-separated modes, and a 3D two stories r.c. frame, characterized by closely spaced modes. The effect of the number of sensors has been assessed first. The obtained results confirm that a reliable modal tracking is possible even in the presence of a few sensors, provided that mode observability is assured. The only effect is the presence of other relative maxima in the MAC vs. frequency plot together with the absolute maximum, as mentioned in the previous section.

Attention has been then focused on the robustness of the procedure. Local stiffness changes have been applied to the structural models in order to simulate damage. The capability of AFDD-T of identifying the modal parameters without updating the reference mode shapes has been evaluated. The obtained results have shown that AFDD-T is able to follow the variation of the natural frequencies with reduced errors (lower than 1 %) even in the case of a few sensors and for quite large stiffness (and, therefore, natural frequency) variations. The robustness with respect to

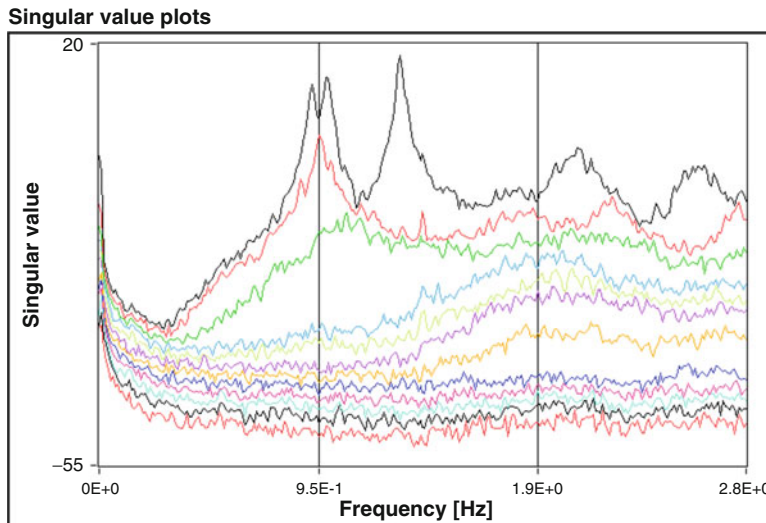


**Fig. 6.18** The School of Engineering Main Building: Singular value plots, (© Elsevier Ltd. 2011), reprinted with permission

moderate changes in the structural mode shapes is crucial for applications of modal tracking for emergency management purposes, when a sequence of closely repeated in time earthquakes can hit the structure and make the automatic update of the reference mode shapes through LEONIDA (or ARES) unpredictable. In the case of closely spaced modes and a few sensors, the use of mode shape estimates obtained by FDD-based algorithms improves the effectiveness of spatial filtering in the presence of noise. More details about the results of simulations for validation of AFDD-T can be found elsewhere (Rainieri et al. 2011a).

AFDD-T has also been tested against real datasets collected by the SHM system of the School of Engineering Main Building in view of its integration into the continuous vibration-based monitoring system. They have been analyzed offline, first. Test results have remarked the superior performance of spatial filtering over traditional filtering. Application of a bandpass filter may suffer some limitations. In fact, the identification of the bandwidth of a mode according only to PSD plots or singular value plots may be difficult. Moreover, static filter limits allow the observation only of limited variations of the natural frequencies, in particular in the presence of closely spaced modes. The School of Engineering Main Building, for instance, is characterized by two closely spaced modes having natural frequencies equal to 0.92 and 0.99 Hz, respectively. However, such values can decrease until 0.89–0.9 Hz for the first mode and 0.95–0.97 Hz for the second mode in summer, while they increase in winter up to 0.94–0.95 and 1.01–1.02 Hz for the first and second mode, respectively. If a limit value equal to 0.95 (Fig. 6.18) is adopted to separate the modes, in agreement with the sample singular value plots obtained from a single output-only modal identification by FDD, the classical

bandpass filter does not provide satisfactory results in terms of effectiveness and reliability of modal parameter tracking. In fact, in the presence of closely spaced modes, damage or environmental effects can easily move the natural frequencies outside the limits of the filter, causing an error in the estimates. On the contrary, AFDD-T sets the limits of the filter at each iteration so that changes in modal parameters can effectively and automatically be tracked.

The performance of AFDD-T in estimating higher modes has been assessed by offline analysis of a number of records of the dynamic response to ambient vibrations of the School of Engineering Main Building collected by its monitoring system. Each record consisted of six measurement channels and was 10-min long.

The first record has been used to carry out a manual identification of the structural modes by FDD. Then, the other records have been used for the automated modal tracking, carried out by adopting as reference mode shapes those provided by the manual modal parameter identification. Some of the higher modes of the structure were not identifiable from the considered dataset, and they have been excluded also from the performance assessment of AFDD-T. This is consistent with the fact that the automated identification of higher, poorly excited modes can fail. Results have shown that AFDD-T is able to carry out an effective modal tracking also at higher modes. Only in the case of poorly excited modes and relevant noise level AFDD-T has provided more scattered data (refer to Rainieri et al. 2011a for more details). However, also a manual identification of the modal properties may be difficult or even unfeasible in similar conditions, when the resonance is almost buried in noise. As the role of the number of sensors is concerned, results of modal tracking confirm that only six sensors, among those installed on the School of Engineering Main Building, are enough to provide a robust and reliable identification of modes if observability is assured. This is relevant for large scale monitoring of strategic structures, because the number of sensors and, therefore, the costs of the monitoring system can be reduced without detrimental influence on the reliability of results. This circumstance permits an optimization of the economic resources assigned to the implementation of structural monitoring systems in the case of a relevant number of structures.

After validation, AFDD-T has been optimized to continuously monitor the fundamental modes of the School of Engineering Main Building, because they are the most relevant from the seismic response standpoint.

An effective automated modal parameter identification and tracking has been obtained by the combination of LEONIDA with AFDD-T (Fig. 6.19) and their integration within the SHM system installed on the structure. LEONIDA provides the reference mode shapes to AFDD-T. Periodically or on demand (i.e. after an extreme event), a new reference can be obtained by LEONIDA and used to confirm the previous one or to replace it.

The herein reported monitoring results clearly point out the potentialities and limitations of automated OMA procedures for vibration-based monitoring. The sequences of natural frequency estimates collected in summer 2008 and in winter

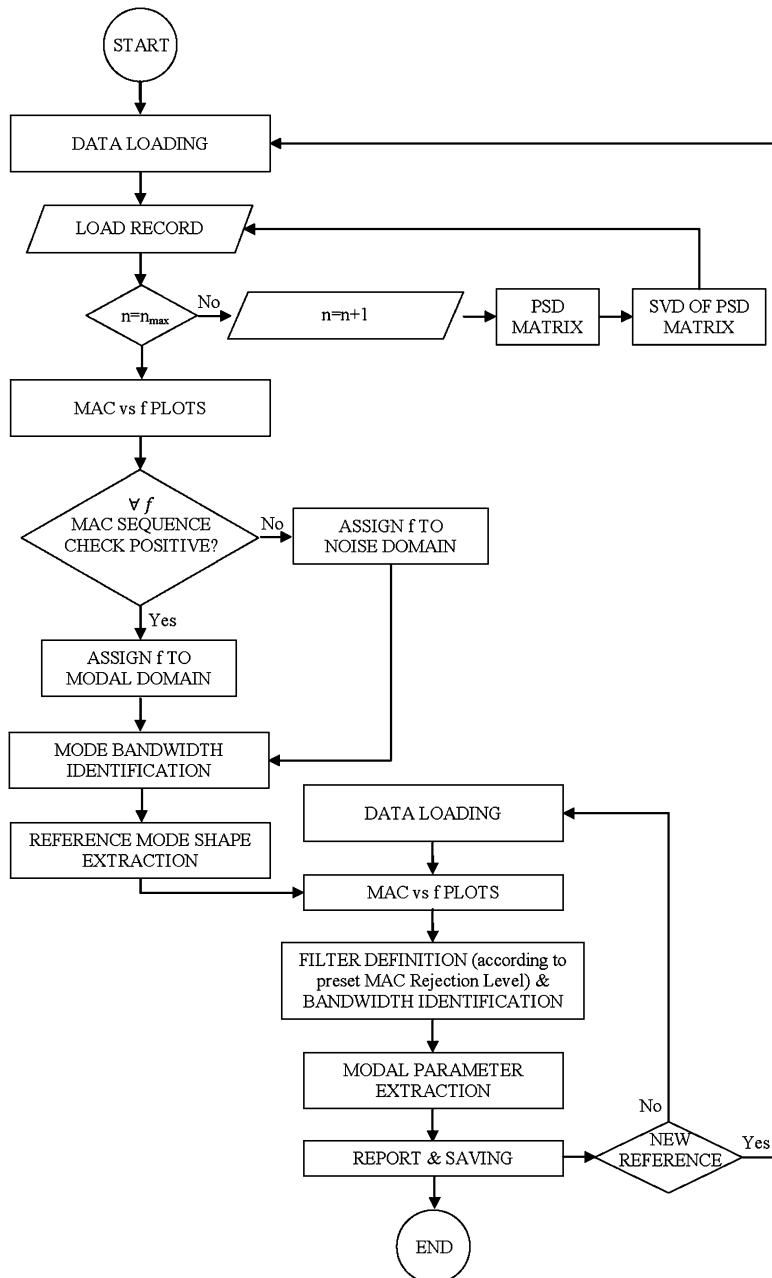


**Fig. 6.19** Integration of LEONIDA and AFDD-T for fully automated vibration-based monitoring

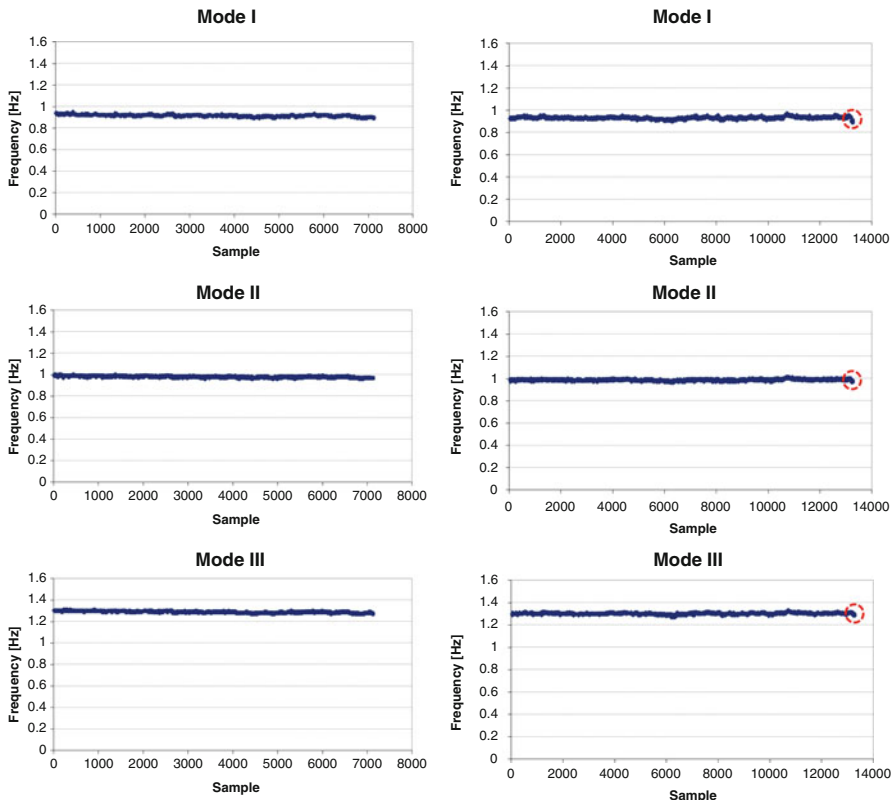


**Fig. 6.20** The School of Engineering Main Building: Monitoring results in summer 2008 (left) and winter 2009 (right); occurrence of L'Aquila earthquake is marked by the circles, (© Elsevier Ltd. 2011), reprinted with permission

2009 are shown in Fig. 6.20. Their analysis has put in evidence some environmental effects on the modal parameter estimates.

The sequence related to winter 2009 also includes the effects of the ground motion induced by the L'Aquila earthquake mainshock, occurred on April 6-th, 2009. It is represented by the sudden drop at the end of the plots.

Statistics are computed on 7,132 samples in the first case (summer 2008) and on 13,265 samples in the second (winter 2009).

In order to better visualize the variations of the natural frequencies over different days, natural frequency estimates related to the same day are also grouped together and plotted over time in Fig. 6.21.

Histograms of data collected in summer 2008 and winter 2009 are shown in Fig. 6.22. In Table 6.10 a synthesis of the results of automated modal parameter tracking in operational conditions is reported. Analysis of data and histograms confirm that the estimates are normally distributed.

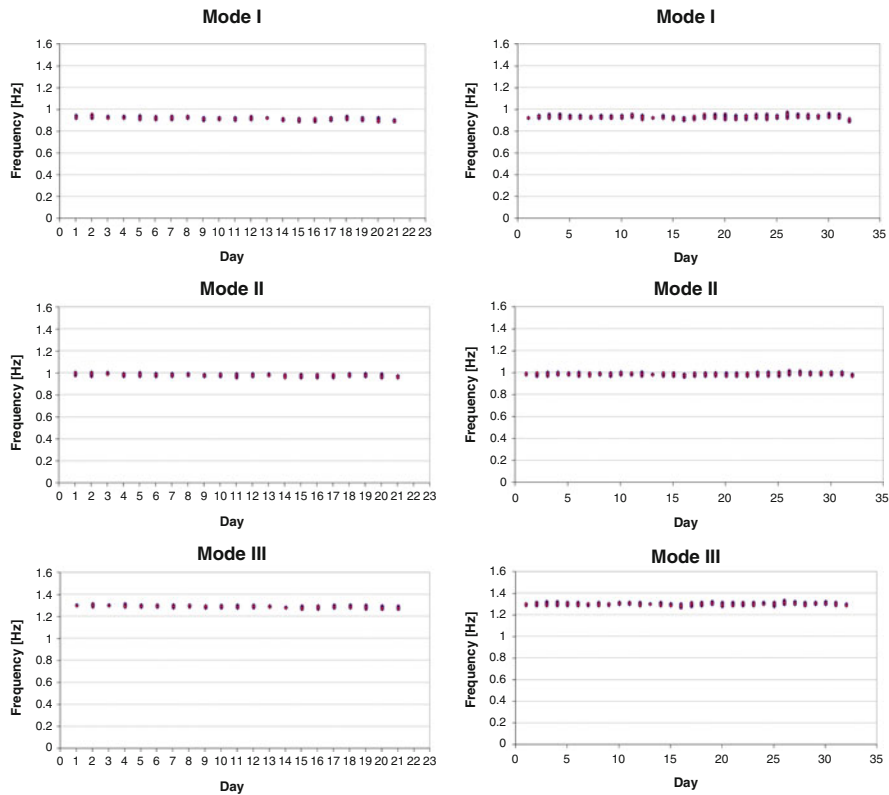


**Fig. 6.21** The School of Engineering Main Building: Monitoring results in summer 2008 (*left*) and winter 2009 (*right*)—aggregated data, (© Elsevier Ltd. 2011), reprinted with permission

The collected data can be useful also for a detailed characterization of the structure in its health state. In particular, the effect of environmental factors can be studied and the estimates can be depurated from these effects before the application of damage detection procedures. This aspect is out of the scope of the book. The interested reader can refer to the wide literature on this topic for more details (see, for instance, Deraemaeker et al. 2008, Magalhaes et al. 2012, Hu et al. 2012). In the context of the present discussion, it is sufficient to observe a moderate influence of temperature on the dynamic characteristics of the monitored structure. In fact, during hot summer time, lower values of natural frequency for the first three modes have been observed (in particular for the first and the third mode) with respect to those observed in winter.

The low values of standard deviation of natural frequencies reported in Table 6.10 confirm that the influence of environmental parameters on this structure is relatively small (standard deviations lower than 0.01 Hz) and relatively uniform for all modes.

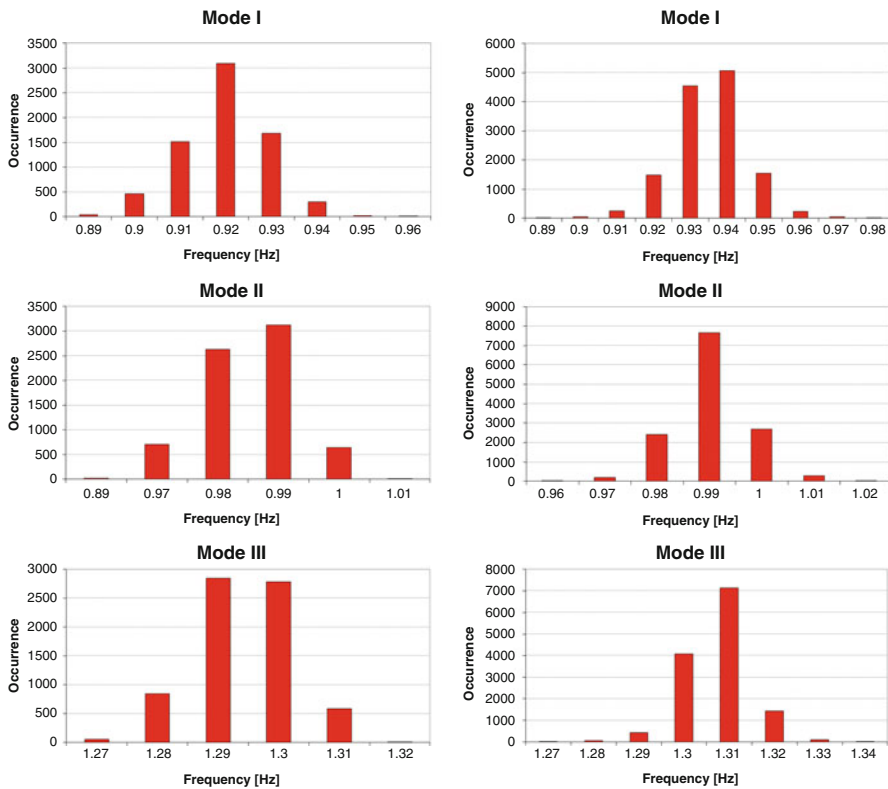


**Fig. 6.22** The School of Engineering Main Building: Distributions of natural frequencies observed in summer 2008 (left) and winter 2009 (right), (© Elsevier Ltd. 2011), reprinted with permission

**Table 6.10** The School of Engineering Main Building: summary of monitoring results, (© Elsevier Ltd. 2011), reprinted with permission

Monitoring period	Mode	$f_n$ (Hz) modal value	$f_n$ (Hz) mean value	$f_n$ (Hz) standard deviation
Summer 2008 (7,130 samples)— average temperature 25.2 °C	I	0.92	0.92	0.0098
	II	0.99	0.99	0.0081
	III	1.29	1.29	0.0084
Winter 2009 (13,265 samples)— average temperature 11.5 °C	I	0.94	0.94	0.0101
	II	0.99	0.99	0.0074
	III	1.31	1.31	0.0075

Environmental effects have provided the opportunity for an extensive check of reliability and robustness of AFDD-T in the case of closely spaced modes. The identification of the region where a certain mode is located before the extraction of the corresponding modal parameters is definitely more effective than threshold-based peak detection followed by bandwidth definition. In fact, it is less influenced by the relative strength of modes.

Thus, AFDD-T is a valuable tool for vibration-based SHM in earthquake prone regions, because it ensures fast analysis of data and robust and effective tracking of modal parameters in the presence of environmental effects, such as those due to temperature, or in the presence of damage.

The record of the structural response to the ground motion induced by the propagation of L'Aquila earthquake has also given the opportunity to analyze the response of AFDD-T in the presence of an input (weak) ground motion. As expected, AFDD-T is not able to identify any structural mode when the transient signal due to an earthquake is present in the analyzed record.

This can be clearly observed in Fig. 6.23, where the dashed circles mark the occurrence of the ground motion. The little decrease of natural frequencies with respect to the corresponding estimates before the event was probably due to a change of the degree of interaction with curtain walls, partitioning walls, and other nonstructural components (Rainieri et al. 2011a, Rainieri et al. 2011b).

It is interesting to note that the estimates of the modal parameters after the quake were independent of the reference mode shapes. In fact, either the original reference mode shapes or the updated mode shapes, identified by LEONIDA from 1-h record in operational conditions after the ground motion, have provided the same results. This circumstance confirms the robustness of AFDD-T.

---

## 6.5 Automated OMA and Vibration-Based Monitoring

This long (and exciting, we hope!) journey through OMA and its applications ends with an outlook on the opportunities of (automated) OMA in the field of vibration-based monitoring. In fact, as mentioned in Chap. 5 and remarked in this chapter, the identification of the modal parameters is often an intermediate step in view of other analyses. Model updating is just one of the possible applications. Others concern damage detection and tensile load estimation. A detailed discussion about these last two topics strictly related to continuous vibration-based SHM is beyond the scope of the book. This section is intended to provide only an overview about them to highlight the wide applicative perspectives of the previously described procedures. Relevant references are reported at the end of the chapter for the interested reader.

Vibration-based SHM is a very active research field. Extensive surveys and dedicated books are available in the literature (Doebling et al. 1996, Sohn et al. 2003, Farrar and Worden 2013). The monitoring process consists in the observation of the structure over long periods of time. Records of the structural response are continuously acquired by appropriate sensors and measurement systems, and damage sensitive feature are extracted from the collected data and analyzed to assess the health conditions of the structure.

From a general point of view, damage is defined as any change of the structure that adversely affects its performance (Sohn et al. 2003). This change can be in the form of stiffness change (for instance, cracking), mass change, connectivity change (for instance, looseness in a bolted joint) or boundary condition change (for instance, bridge scour). An effective SHM system should be able to automatically

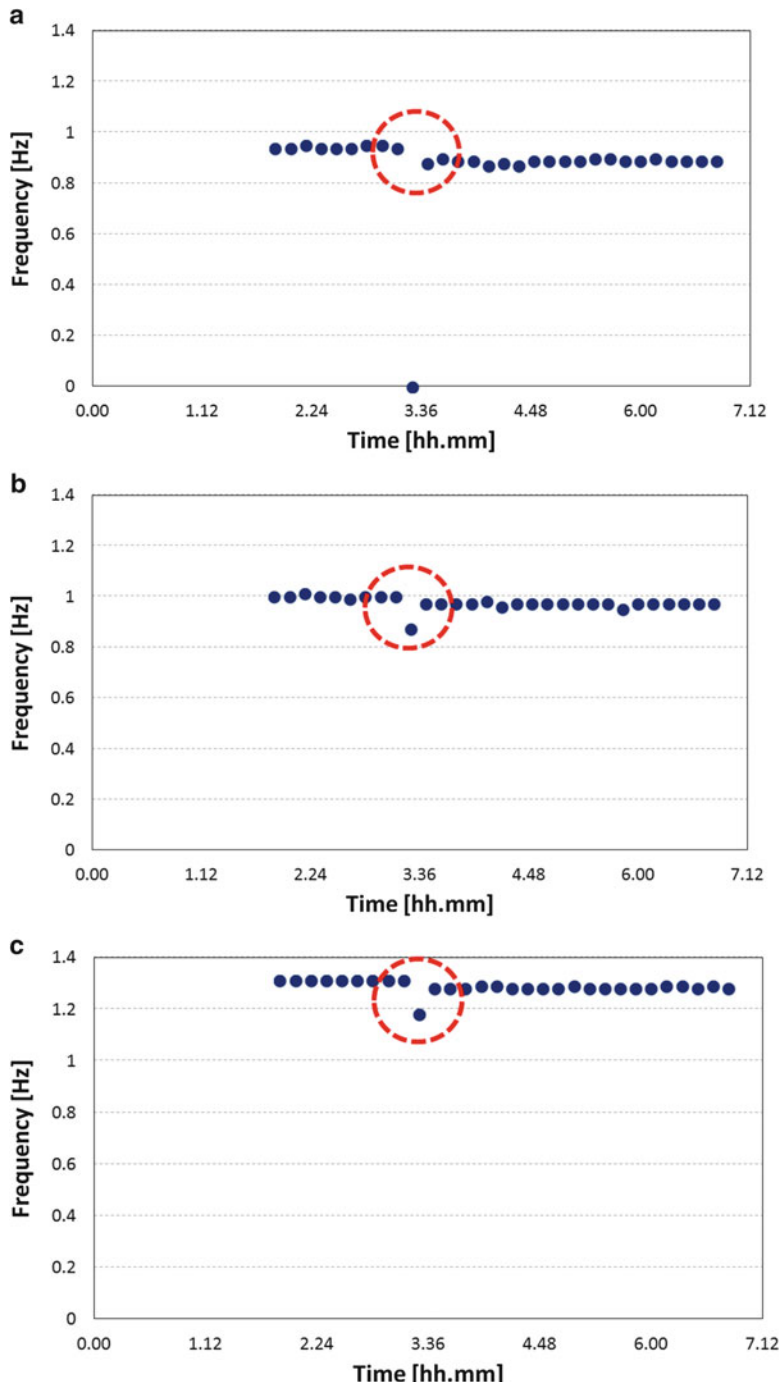


**Fig. 6.23** The School of Engineering Main Building: Monitoring results before and after L'Aquila earthquake (occurring at time 3.32) for mode I (a), mode II (b), and Mode III (c), (© Elsevier Ltd. 2011), reprinted with permission

detect damage at an early stage (Doebling et al. 1996). Five damage detection levels have been defined (Sohn et al. 2003):

- Level 1: identification of damage existence;
- Level 2: localization of damage;
- Level 3: identification of the type of damage;
- Level 4: quantification of damage severity;
- Level 5: prediction of the remaining service life of the structure (prognosis).

Modal-based damage detection starts by recognizing that the modal parameters are functions of the physical parameters (mass, stiffness, and damping). Assuming that damage yields a change in the physical properties of the structure, this is reflected by a change in the modal properties. Thus, it is theoretically possible to identify damage from the analysis of the variations of the modal parameters. A number of damage sensitive features have been, therefore, defined in terms of modal parameters. One of the main drawbacks of modal-based damage detection is related to the sensitivity to environmental and operational conditions that can cause changes in the modal parameters of the same order of magnitude of those induced by damage. As a consequence, the modal parameter estimates have to be depurated from the effects of environmental factors in order to effectively detect damage. Possible approaches to remove environmental effects are those based on regression analysis (a sample application can be found in Magalhaes et al. 2012), when measurements of the environmental parameters are available, and those based on factor analysis (see, for instance, Deraemaeker et al. 2008) to get rid of the variability due to the environment without information about the environmental factors.

Damage sensitive features can be defined in terms of natural frequencies and mode shapes. Natural frequency variations provide the easiest way to detect the presence of damage, because they can be accurately estimated even in the presence of a few sensors. However, the information they provide is limited to Level 1 damage detection. Moreover, their sensitivity to damage is relatively low while they are quite sensitive to environmental effects; thus, early stage damage detection is often difficult. Other features are defined in terms of mode shapes and mode shape curvatures. Mode shapes are less sensitive to environmental conditions, and they provide relevant information for damage location. However, they are typically estimated with lower accuracy with respect to natural frequencies.

Once the damage sensitive features have been purified from the environmental effects, a number of tools can be applied for feature discrimination. They can be broadly classified as supervised and unsupervised learning approaches (Farrar and Worden 2013). The former are applied when data are available for both the undamaged and damaged structure, while the latter are applied when reference data are available only for the structure in healthy state.

This brief review about modal-based damage detection confirms the fundamental role played by automated OMA procedures in the field of SHM and the importance of getting very accurate modal parameter estimates in a fully automated way.

Another interesting application of automated OMA procedures concerns the indirect estimation and monitoring of tensile loads in cables and tie rods. A vibration-based system for tensile load monitoring can easily be developed based on the concepts and procedures illustrated throughout this book.

The tensile load can be obtained from estimates of the dynamic parameters of bending modes of the cable or tie-rod under investigation through the solution of an inverse problem. A number of approaches for tensile load estimation are available in the literature (see, for instance, Tullini and Laudiero 2008, Rebecchi et al. 2013, Wenzel and Pichler 2005, Maes et al. 2013). Their review is out of the scope of this section. However, the fundamental concepts behind some of them are herein reported to show how a tensile load monitoring system can be developed based on automated OMA procedures. Other, eventually more refined approaches for tensile load estimation can obviously replace those herein reported with no loss of generality for the present discussion.

The approach proposed by Rebecchi et al. (2013) can be adopted for the estimation of the tensile load in tie-rods. In the most general case of uncertain boundary conditions, the tensile load can be estimated from measurements of one mode shape of the member in at least five positions. The method starts from the equation governing the dynamic behavior of a beam with uniform section and subjected to a constant axial tensile force:

$$EI \frac{\partial^4 v(x, t)}{\partial x^4} + N \frac{\partial^2 v(x, t)}{\partial x^2} + \rho \frac{\partial^2 v(x, t)}{\partial t^2} = 0 \quad (6.2)$$

where EI represents the bending stiffness,  $\rho$  is the mass per unit length,  $v(x, t)$  is the transverse displacement at abscissa  $x$  and time  $t$ , and  $N$  the tensile force. The partial differential equation of (6.2) can be separated into two ordinary differential equations, providing natural frequencies and mode shapes respectively (Clough and Penzien 1993). In particular, the shapes of the vibrating beam are given by:

$$\phi(x) = C_1 \sin(\alpha x) + C_2 \cos(\alpha x) + C_3 \sinh(\beta x) + C_4 \cosh(\beta x) \quad (6.3)$$

where:

$$\alpha^2 = \frac{N}{2EI} \left( \sqrt{1 + \frac{4\omega_r^2 \rho EI}{N^2}} - 1 \right), \quad \beta^2 = \frac{N}{2EI} \left( \sqrt{1 + \frac{4\omega_r^2 \rho EI}{N^2}} + 1 \right) \quad (6.4)$$

with  $\omega_r$  the natural frequency of the considered mode. The coefficients  $C_1$ ,  $C_2$ ,  $C_3$ , and  $C_4$  are determined from the measured modal displacements in four points of the beam; the last modal displacement is used to compute the tensile load  $N$ . The number of unknowns and, therefore, of measurement points can be reduced if the boundary conditions are known. More details can be found elsewhere (Tullini and Laudiero 2008, Rebecchi et al. 2013).

When the influence of bending stiffness and end constraints is negligible with respect to the tensile load, the problem is reduced to that of the wire. In this case the natural frequencies are given by the following closed-form expression (Lagomarsino and Calderini 2005):

$$f_n = \frac{n}{2L} \sqrt{\frac{N}{\rho}} \quad n = 1, 2, \dots, N_m \quad (6.5)$$

where L is the length of the cable. Thus, the experimental estimation of a single natural frequency is sufficient to estimate the tensile load. A correction factor can eventually be applied to take into account the negligible but not null influence of bending stiffness and support conditions in real cases (Wenzel and Pichler 2005).

When only the rotational stiffness of the supports is negligible with respect to the bending stiffness, the problem becomes that of the prestressed pinned beam. The analytical expression for the natural frequency of the n-th mode is:

$$f_n = \frac{n}{2} \sqrt{\frac{n^2 \pi^2 EI}{\rho L^4} + \frac{N}{\rho L^2}} \quad n = 1, 2, \dots, N_m \quad (6.6)$$

Two natural frequency estimates are required to solve the inverse problem in this case, because there are two unknowns (N and EI). These can be obtained from the following closed form expressions (Lagomarsino and Calderini 2005):

$$N = 4\rho L^2 \left( \frac{j^2 f_i^2}{i^2(j^2 - i^2)} - \frac{i^2 f_j^2}{j^2(j^2 - i^2)} \right) \quad (6.7)$$

$$EI = \frac{4\rho L^4}{\pi^2} \left( \frac{f_j^2}{j^2(j^2 - i^2)} - \frac{f_i^2}{i^2(j^2 - i^2)} \right) \quad (6.8)$$

where  $f_i$  and  $f_j$  are the natural frequency estimates for the i-th and j-th modes respectively, with  $i < j$ .

Taking advantage of programmable hardware and integrating an automated OMA procedure and the appropriate method for tensile load estimation, a continuous vibration-based monitoring of tensile loads can be carried out. A monitoring system for members in traction is herein described. It is based on distributed wireless modules for acceleration measurements and on a centralized data processing system. A small number of piezoelectric accelerometers are installed on each cable. The vibration data related to one or more cables are acquired by the wireless modules and stored into a MySQL database. Each monitored element has an individual table of its own. ARES continuously analyzes the dynamic response of the cables to ambient vibrations, providing the modal parameter estimates for tensile load estimation. The architecture of the system is illustrated in Fig. 6.24. When the number of monitored elements is very large, the data acquisition task can be fragmented among a number of local servers.

The master server acquires time histories of predefined duration from the local servers and carries out the automated identification of the modal parameters. Tensile loads are then estimated according to the most appropriate procedure (depending on the characteristics of the member) among those previously outlined.

A prototype system has been recently installed in Italy (Rainieri and Fabbrocino 2013). It is monitoring the tensile load in one of the cables of a sample steel arch (Fig. 6.25). Interesting preliminary results have been obtained until now, remarking the influence of environmental factors on the dynamic response of structural systems.

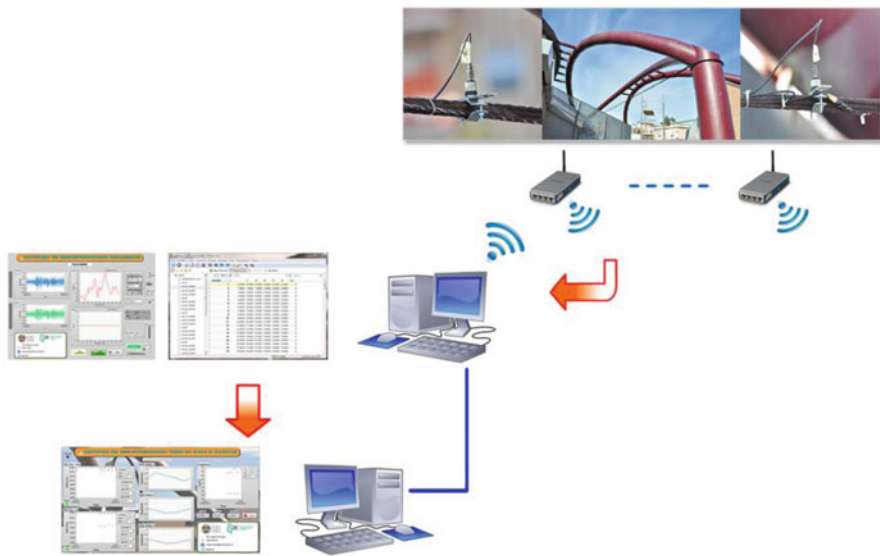


**Fig. 6.24** Architecture of the axial force monitoring system



**Fig. 6.25** Installation of the prototype of monitoring system on one of the cables of a sample steel arch

## References

- Allemand RJ, Brown DL, Phillips AW (2010) Survey of modal techniques applicable to autonomous/semi-autonomous parameter identification. In: Proc international conference on noise and vibration engineering ISMA 2010, Leuven
- Andersen P, Brincker R, Goursat M, Mevel L (2007) Automated modal parameter estimation for operational modal analysis of large systems. In: Proc 2nd international operational modal analysis conference, Copenhagen
- Bendat JS, Piersol AG (2000) Random data: analysis and measurement procedures, 3rd edn. John Wiley & Sons, New York
- Brincker R, Andersen P, Jacobsen NJ (2007) Automated frequency domain decomposition for operational modal analysis. In: Proc 25th SEM international modal analysis conference, Orlando
- Brownjohn JMW, Carden EP (2007) Tracking the effects of changing environmental conditions on the modal parameters of Tamar bridge. In: Proc 3rd international conference on structural health monitoring of intelligent infrastructure, Vancouver
- Carden EP, Brownjohn JMW (2008) Fuzzy clustering of stability diagrams for vibration-based structural health monitoring. *Comp Aid Civil Infrastr Eng* 23:360–372
- Chauhan S, Tcherniak D (2009) Clustering approaches to automatic modal parameter estimation. In: Proc XVII International Modal Analysis Conference, Orlando
- Clough RW, Penzien J (1993) Dynamics of structures, 2nd edn. McGraw-Hill Inc., New York
- Deraemaeker A, Reynders E, De Roeck G, Kullaa J (2008) Vibration-based structural health monitoring using output-only measurements under changing environment. *Mech Syst Signal Process* 22:34–56
- Devriendt C, De Troyer T, De Sitter G, Guillaume P (2008) Automated operational modal analysis using transmissibility functions. In: Proc international conference on noise and vibration engineering ISMA 2008, Leuven
- Doebling SW, Farrar CR, Prime MB, Shevitz DW (1996) Damage identification and health monitoring of structural and mechanical systems from changes in their vibration characteristics: a literature review. Technical report LA-13070-MS, UC-900. Los Alamos National Laboratory, New Mexico
- Farrar CR, Worden K (2013) Structural health monitoring: a machine learning perspective. Wiley, Chichester
- Goethals I, Vanluyten B, De Moor B (2004) Reliable spurious mode rejection using self learning algorithms. In: Proc international conference on noise and vibration engineering ISMA 2004, Leuven
- Guan H, Karbhari VM, Sikorski CS (2005) Time-domain output only modal parameter extraction and its application. In: Proc 1st international operational modal analysis conference, Copenhagen
- Hu W-H, Moutinho C, Caetano E, Magalhaes F, Cunha A (2012) Continuous dynamic monitoring of a lively footbridge for serviceability assessment and damage detection. *Mech Syst Signal Process* 33:38–55
- Lagomarsino S, Calderini C (2005) The dynamical identification of the tensile force in ancient tie-rods. *Eng Struct* 27:846–856
- Maes K, Peeters J, Reynders E, Lombaert G, De Roeck G (2013) Identification of axial forces in beam members by local vibration measurements. *J Sound Vib* 332:5417–5432
- Magalhaes F, Cunha A, Caetano E (2008) Dynamic monitoring of a long span arch bridge. *Eng Struct* 30:3034–3044
- Magalhaes F, Cunha A, Caetano E (2009) Online automatic identification of the modal parameters of a long span arch bridge. *Mech Syst Signal Process* 23:316–329
- Magalhaes F, Cunha A, Caetano E (2012) Vibration based structural health monitoring of an arch bridge: from automated OMA to damage detection. *Mech Syst Signal Process* 28:212–228

- Pappa RS, James III GH, Zimmerman DC (1997) Autonomous modal identification of the Space Shuttle tail rudder. Report NASA TM-112866, National Aeronautics and Space Administration
- Peeters B, De Roeck G (2001a) One-year monitoring of the Z24-bridge: environmental effects versus damage events. *Earthq Eng Struct Dyn* 30:149–171
- Peeters B, De Roeck G (2001b) Stochastic system identification for operational modal analysis: a review. *ASME J Dyn Syst Meas Contr* 123(4):659–667
- Poncelet F, Kerschen G, Golinval JC (2008) In-orbit vibration testing of spacecraft structures. In: Proc international conference on noise and vibration engineering ISMA 2008, Leuven
- Rainieri C, Fabbrocino G (2010) Automated output-only dynamic identification of civil engineering structures. *Mech Syst Signal Process* 24:678–695
- Rainieri C, Fabbrocino G (2013) Vibration data as a tool for continuous monitoring of cable tensile loads. In: Proc 9th international workshop on structural health monitoring, Stanford
- Rainieri C, Fabbrocino G, Cosenza E (2010) Some remarks on experimental estimation of damping for seismic design of civil constructions. *Shock Vib* 17:383–395
- Rainieri C, Fabbrocino G, Cosenza E (2011a) Near real-time tracking of dynamic properties for standalone structural health monitoring systems. *Mech Syst Signal Process* 25:3010–3026
- Rainieri C, Fabbrocino G, Cosenza E (2011b) Integrated seismic early warning and structural health monitoring of critical civil infrastructures in seismically prone areas. *Struct Health Monit* 10:291–308
- Rainieri C, Fabbrocino G, Manfredi G, Dolce M (2012) Robust output-only modal identification and monitoring of buildings in the presence of dynamic interactions for rapid post-earthquake emergency management. *Eng Struct* 34:436–446
- Rebecchi G, Tullini N, Laudiero F (2013) Estimate of the axial force in slender beams with unknown boundary conditions using one flexural mode shape. *J Sound Vib* 332:4122–4135
- Reynders E, Houbrechts J, De Roeck G (2012) Fully automated (operational) modal analysis. *Mech Syst Signal Process* 29:228–250
- Sohn H, Farrar CR, Hemez FM, Shunk DD, Stinemates DW, Nadler BR (2003) A review of structural health monitoring literature: 1996–2001. Technical report LA-13976-MS, UC-900, Los Alamos National Laboratory
- Tan P-N, Steinbach M, Kumar V (2006) Introduction to data mining. Pearson Addison-Wesley, Reading
- Tullini N, Laudiero F (2008) Dynamic identification of beam axial loads using one flexural mode shape. *J Sound Vib* 318:131–147
- Vanlanduit S, Verboven P, Guillaume P, Schoukens J (2003) An automatic frequency domain modal parameter estimation algorithm. *J Sound Vib* 265:647–661
- Wenzel H, Pichler D (2005) Ambient vibration monitoring. Wiley, Chichester
- Worden K, Manson G, Surace C (2007) Aspects of novelty detection. *Key Eng Mater* 347:3–16

---

# Index

## A

- Absolute accuracy, 72  
ADCs. *See* Analog-to-digital converters (ADCs)  
AFDD-T. *See* Automated frequency domain decomposition-tracking (AFDD-T)  
Aliasing, 81, 90  
Analog-to-digital converters (ADCs)  
    conversion time, 72  
    cross talk, 72  
    dynamic range, 71–72  
    nonlinearity, 73  
    offset, 73  
    resolution, 71  
    sampling rate, 72  
Applications, OMA  
    damping estimation  
        aerodynamic damping, 216  
        damping ratio, 215–216  
        energy dissipation, 216  
        fracture mechanics, 217  
        frequency resolution, 217  
        frictional loss, 217  
        modal identification, 219  
        modal parameter estimates, 221  
        modal properties, 220  
        natural frequency, 218  
        noninvertible matrix, 219  
        physical criteria, 220  
        sensitivity analysis, 218  
        stabilization diagram, 218–220  
excitation system  
    bending mode, 255  
    cable motion, 252  
    candidate modes, 252–254  
    characteristics of sensors, 249, 251  
    dynamic responses, 248  
    dynamic tests, 247  
    environmental and operational loads, 243

- frequency domain algorithm, 252  
interaction effects, 248  
kurtosis index, 245  
mode classification, 252–253  
mode shape complexity and coherence, 255  
narrowband excitation, 246  
probability density function, 245  
sensor layouts, 249–250  
short time Fourier transform, 244  
source correlation, 256  
spurious harmonics, 244  
spurious peaks, 244  
stair structure, 247  
structural modes, 252, 254  
transmissibility-based method, 246  
vibration data, 249  
mass normalized mode shapes  
    approximated equations, 238  
    columns and beams, 240  
    frequency shifts, 241–242  
    Gaussian white noise, 240  
    lightly damped structures, 238  
    mass-change methods, 237  
    mass-change strategy, 239  
    modal truncation effects, 239  
    natural frequency estimates, 242  
    r.c. frame, 240–241  
    scaling factors, 237, 242–243  
    squared modal displacements, 241–242  
    stiffness-change methods, 238  
measurement chain assessment  
    AC cut-off frequency response, 213–214  
    data acquisition modules, 214  
    dynamic response, 215  
    FE model, 213  
    low-amplitude vibrations, 214  
    masonry cell, 213  
    modal identification tests, 211

- Applications, OMA (*cont.*)
  - output-only modal analysis technique, 213
  - reduction of modeling uncertainties, 211
  - sensor layouts, 215
  - star vault, 211–212
- numerical and experimental modal property estimates
- ambient vibration tests, 222
  - dynamic response, 237
  - finite element modeling, 228, 230–232
  - frequency scatters, 236
  - geometric and structural survey, 222–225
  - ground acceleration load, 233
  - ground motions, 222
  - mode shape correlation, 233, 236
  - natural frequencies, 232
  - output-only modal identification, 225–229
  - PMRs, 233–234
  - seismic assessment, 223
  - seismic capacity, 222
  - serviceability conditions, 223
  - shell elements, 236
  - structural response, 235
  - Tower of the Nations, 221–222
- predictive correlations
- accelerometers, 259
  - ambient vibration tests, 259
  - bell towers, 259–261
  - bending mode, 262
  - elastic response spectrum, 258
  - Italian masonry towers, 261–262
  - nondestructive structural investigation, 257
  - seismic performance, 257
  - seismic vulnerability, 258
  - torsional mode, 262
- ARES.** *See* Automated modal parameter extraction system (ARES)
- Auto-correlation functions, 55–56
- Automated frequency domain decomposition-tracking (AFDD-T)
- algorithm, 296
  - architecture, 299, 300
  - environmental effects, 306
  - FDD-based algorithms, 301
  - histograms, 304, 306
  - integration, 303
  - L'Aquila earthquake, 307, 308
  - principles and implementation, 294–300
  - r.c. frame, 300
- real-time estimation, 294
- School of Engineering Main Building, 301–306
- statistical treatment, 294
- Automated modal parameter extraction system (ARES)
- algorithm, 288
  - benchmark 4-DOF system, 289, 290
  - clustering techniques, 286
  - modal damping ratios, 285, 291
  - performance, 292–293
  - SNR, 290
  - SSI method, 286, 287
  - stabilization diagram, 286, 287
  - state-machine architecture, 287
  - statistical analysis, 289
- Automated modal parameter identification, 267
- Automated modal tracking methods, 267
- Automated OMA
- AFDD-T
  - algorithm, 296
  - architecture, 299, 300
  - environmental effects, 306
  - FDD-based algorithms, 301
  - histograms, 304, 306
  - integration, 303
  - L'Aquila earthquake, 307, 308
  - principles and implementation, 294–300
  - r.c. frame, 300
  - real-time estimation, 294
  - School of Engineering Main Building, 301–306
  - statistical treatment, 294
- ARES**
- algorithm, 288
  - benchmark 4-DOF system, 289, 290
  - clustering techniques, 286
  - modal damping ratios, 285, 291
  - performance, 292–293
  - SNR, 290
  - SSI method, 286, 287
  - stabilization diagram, 286, 287
  - state-machine architecture, 287
  - statistical analysis, 289
- LEONIDA**
- algorithm, 275
  - applications, 279–285
  - drawbacks, 271
  - FDD method, 270, 276–279
  - integration, 303
  - LabVIEW environment, 274–276
  - LSCF method, 269

MAC sequences, 271–276  
SSI technique, 269  
time domain filtering method, 270  
problem statement, 267–268  
vibration-based monitoring, 307–312  
Auto-power spectral density function, 56  
Autoregressive moving average (ARMA)  
models  
ARMAV, 117  
companion matrix, 119  
IV method, 152–153  
linear time-invariant system, 117  
minimal realization, 118  
observability canonical state-space  
realization, 118  
prediction error, 151–152  
Auto-regressive moving average vector  
(ARMAV) model, 117

**B**

Basic frequency domain (BFD) method,  
127–130, 195–199  
Blind source separation (BSS) techniques  
applicability of, 166  
classification, 166–167  
sources, 166  
static mixtures, 167  
use of, 167–168

**C**

Canonical variate analysis (CVA), 157,  
165–166  
Common-mode rejection ratio (CMRR), 61  
Complex mode indicator function  
(CMIF), 130  
Complex numbers, 23–27, 53  
Coordinate modal assurance criterion  
(COMAC), 189–190  
Correlation functions, 35–38  
Covariance-driven stochastic subspace  
identification (Cov-SSI) method  
BR variant, 157  
canonical angles, 157  
CVA variant of, 157  
Laplace variable, 158  
noise sources, 158  
observability/controllability matrix, 154,  
155  
state-space model, 153  
Toeplitz matrix, 154–156  
Cross-correlation functions, 55

**D**

Damping estimation  
aerodynamic damping, 216  
damping ratio, 215–216  
energy dissipation, 216  
fracture mechanics, 217  
frequency resolution, 217  
frictional loss, 217  
modal identification, 219  
modal parameter estimates, 221  
modal properties, 220  
natural frequency, 218  
noninvertible matrix, 219  
physical criteria, 220  
sensitivity analysis, 218  
stabilization diagram, 218–220  
DAQ Assistant, 97–98  
Data acquisition  
ADCs, 71–73  
aliasing, 81, 90  
anti-aliasing filter, 82  
chi-square goodness-of-fit test, 85  
clipping, 85  
CMRR, 61  
common-mode voltage range, 61  
data pretreatment, 100–101  
data storage, 99–100  
differential measurement system, 60  
file storage, 91–99  
filtering and decimation, 91  
FIR filters, 83  
floating signal sources, 60, 61  
grounded signal sources, 60  
ground-loop current, 61  
hardware selection, 91–99  
IIR filters, 83  
intermittent noise spikes, 85–88  
modal analysis test, 59  
mode shape merging, 90–91  
MySQL database, 99–100  
offsets, 88  
power line pickup, 88  
pseudodifferential systems, 62  
reference sensors, 79  
roving sensors, 78  
sampling frequency, 81  
sensor installation, 75–80  
signal dropouts, 88, 89  
spurious trends, 88–89  
steep learning curve, 70  
transducers  
dynamic range, 67  
force-balance accelerometers, 65

- Data acquisition (*cont.*)  
 offset error, 67  
 Peterson noise curves, 68–69  
 piezoelectric sensors, 62–63  
 sensor resolution, 67  
 sensor self noise, 67  
 settling time, 67  
 wired *vs.* wireless, 73–75
- Data-driven stochastic subspace identification  
 (DD-SSI) method, 117  
 CVA, 166  
 Hankel matrix, 160–161  
 Kalman filter state, 159, 162  
 modal parameter, 165  
 orthogonal and oblique projections, 159  
 principal component algorithm, 165  
 state-space matrices, 162–164  
 UPC algorithm, 165
- Data processing  
 BFD method, 127–130, 195–199  
 FDD method  
   CMIF, 130  
   frequency-spatial domain  
     decomposition, 133  
   k-th mode, 131  
   MAC rejection level, 132  
   modal coordinates, PSD matrix, 131  
   natural frequency estimates, 200  
   output-only modal identification, 199–200  
   SDOF system, 132  
   singular value plots, 131–132, 201  
   singular vectors *vs.* mode shapes, 131  
   spatial filtering, 133  
 frequency domain parametric methods  
   common-denominator model, 134  
   cost function, 134  
   LSCF method (*see* Least squares complex frequency (LSCF) method)  
   LSFD method, 134  
   p-LSCF method (*see* Poly-reference least squares complex frequency (p-LSCF) method)  
 influence of sensor layout, 206  
 mode shape estimates, 179–185  
 OMA (*see* Operational modal analysis (OMA))  
 quality checks and comparisons  
   AutoMAC matrix, 190–191  
   COMAC, 190  
   CrossMAC matrix, 191  
   ECOMAC, 190  
   MAC, 187–189  
   model updating, 185
- mode shapes, 187–191  
 MSF, 188  
 natural frequencies, 185–186  
 NMD, 188  
 verified model, 185
- SOBI, 205–206  
 SSI, 203–205  
 structural dynamics models (*see* Structural dynamics models)  
 time domain methods (*see* Time domain methods)
- Discrete Fourier transform (DFT), 27, 42, 53
- E**
- Eigensystem realization algorithm (ERA), 147  
 Eigenvalue decomposition (EVD), 48  
 Enhanced coordinate modal assurance criterion (ECOMAC), 190  
 Euler's identities, 23–27
- Excitation system  
 bending mode, 255  
 cable motion, 252  
 candidate modes, 252–254  
 characteristics of sensors, 249, 251  
 dynamic responses, 248  
 dynamic tests, 247  
 environmental and operational loads, 243  
 frequency domain algorithm, 252  
 interaction effects, 248  
 kurtosis index, 245  
 mode classification, 252–253  
 mode shape complexity and coherence, 255  
 narrowband excitation, 246  
 probability density function, 245  
 sensor layouts, 249–250  
 short time Fourier Transform, 244  
 source correlation, 256  
 spurious harmonics, 244  
 spurious peaks, 244  
 stair structure, 247  
 structural modes, 252, 254  
 transmissibility-based method, 246  
 vibration data, 249
- Experimental modal analysis (EMA), 1–3
- F**
- Fast Fourier transform (FFT), 27  
 Finite element method (FEM), 2, 228, 230–232  
 Finite impulse response (FIR) filters, 83  
 Forward innovation model, 116  
 Fourier transform

- complex numbers, Euler's identities, 23–27  
DFT, 27, 42, 53  
FFT, 27  
properties, 27
- Fraction polynomial models  
circular correlation function, 122  
common-denominator model, 120  
cross-power spectra, 121  
MFD, 120
- Frequency domain decomposition (FDD)  
method, 103, 199–201  
automation of, 270  
CMIF, 130  
frequency-spatial domain decomposition, 133  
k-th mode, 131  
LEONIDA, 278–279  
MAC rejection level, 132  
modal coordinates, PSD matrix, 131  
SDOF system, 132  
singular value plots, 131–132  
singular vectors *vs.* mode shapes, 131  
spatial filtering, 133  
structural modes, 277  
threshold-based peak detection, 278  
time-consuming sensitivity tests, 277
- Frequency domain parametric methods, 133–135
- Frequency response function (FRF), 6, 106, 107
- G**
- Gaussian noise, 55–56  
Ground-loop current, 61
- I**
- Ibrahim time domain (ITD), 150  
Impulse response function (IRF), 6, 108  
Independent component analysis (ICA), 167–168  
Infinite impulse response (IIR) filters, 83  
Instrumental variable (IV) method, 152–153  
Integrated electronics piezoelectric (IEPE) accelerometers, 63
- J**
- Joint approximate diagonalization (JAD) technique, 171
- L**
- LabVIEW  
event structure, 18–19  
*vs.* other programming languages, 14  
programming in, 12  
software development in, 16–20  
usage, 14
- Least squares complex exponential (LSCE) method, 147
- Least squares complex frequency (LSCF) method  
common-denominator model, 137–138  
generalized transform variable, 135  
Jacobian matrix, 138  
modal identification technique, 134  
natural frequency estimates, 203  
numerator coefficients, 139  
output-only modal identification, 201  
residue matrices, 140–141  
r-th mode, damping ratio, 139  
scalar matrix fraction, 136  
software development, 202  
Toeplitz matrices, 138  
z-domain formulation, 136
- Least squares frequency domain (LSFD) method, 134
- LEONIDA  
algorithm, 275  
applications, 279–285  
drawbacks, 271  
FDD method, 270, 276–279  
integration, 303  
LabVIEW environment, 274–276  
LSCF method, 269  
MAC sequences, 271–276  
SSI technique, 269  
time domain filtering method, 270
- M**
- Matrix fraction description (MFD), 120  
Mean phase deviation (MPD), 180, 182  
Modal assurance criterion (MAC)  
sequences, 271–274  
Modal overlap factor (MOF), 180  
Modal phase collinearity (MPC), 180, 181  
Modal scale factor (MSF), 188  
Mode shape estimates, 179–185  
complexity plot, 180  
MPC, 180, 181  
MPD, 180, 182  
Multi degree of freedom (MDOF) systems, 7  
MySQL database, 99–100

**N**

- Natural excitation techniques (NExT), 103  
 ERA, 147  
 Hankel matrix, 148–149  
 ITD, 150  
 LSCE, 147  
 Prony’s equation, 147  
 system matrix, 150  
 Normalized modal difference (NMD), 188  
 Nyquist frequency, 81

**O**

- Operational deflection shapes (ODSs), 103  
 Operational modal analysis (OMA)  
   advantages and disadvantages, 177–179  
   ambient vibration modal identification, 2  
   applications of  
    data processing, 8  
    input-output testing, 9  
    modal parameters, 9  
    PSD matrix, 8  
    vibration-based damage detection, 9–10  
 broadband excitation, 105  
 classification of, 126–127  
 combined system, 104–105  
 data acquisition, 4  
 definition, 2  
 diagonal matrices, 6  
 EMA, 1–3  
 FDD, 103  
 forward problems, 4  
 frequency response function, 6  
 generalities  
   block diagram, 13–15  
   front panel, 13  
 high order model, 126  
 impulse response function, 6  
 inverse problems, 4  
 LabVIEW (*see* LabVIEW)  
 linearity, 104  
 linear time-invariant system, 4–5  
 low order model, 126  
 MDOF systems, 7  
 modal mass, 6  
 mode shapes, 5  
 natural frequencies, 5  
 NExT, 103  
 noise, 4  
 observability, 104  
 ODS, 103  
 organization of, 10–12  
 physically realizable, 7  
 random decrement technique, 175–176  
 SDOF system, 7

**signal-to-noise ratio, 4**

- software development  
   design patterns, 16  
   event structure, 18–19  
   producer/consumer architecture, 18, 20  
   state machine, 17–18  
   VI hierarchy, 16–17  
 spatial filter, 12  
 SSI, 103  
 stable system, 7  
 stationarity, 104  
 structural health monitoring, 3  
 testing types, 7  
 transmissibility function, 174–175  
 virtual instruments, 13, 15–16  
 Output-only modal identification, 225–229

**P**

- Parametric OMA methods  
   mathematical modes, 192  
   noise modes, 191  
   stabilization diagrams for, 191–195  
 Peak picking method, 127–130, 195–199  
 Poly-reference least squares complex  
   frequency (p-LSCF) method  
   closely spaced modes, 142  
   companion matrix, 145–146  
   cost function, 143  
   error formulation, 143  
   Jacobian matrix, 143–144  
   single complex-valued matrix, 142–143  
 Principal component analysis (PCA), 167  
 Probability density function, 29, 34, 54–55  
 Probability theory, 29–35

**R**

- Random data analysis  
   auto-and cross-correlation functions, 55  
   auto-power spectral density function, 56  
   complex numbers, 23–27, 53  
   condition number  $\kappa$ , 51  
   error norms, 49–52  
   Euler’s identities, 23–27  
   Fourier transform, 23–27  
    DFT, 27, 42, 53  
    FFT, 27  
    properties, 27  
   Gaussian noise, auto-correlation of, 55–56  
   least squares method, 52  
   matrix algebra  
    decomposition method, 46  
    eigenvector, 48  
    EVD, 48

- identity matrix, 46  
Moore–Penrose pseudoinverse, 49  
nonsingular matrix, 47  
null space, 48  
orthogonal, 47  
real-valued/complex valued, 46  
singular matrix, 47  
square matrix, 46–47  
SVD, 49, 51  
symmetric, 47  
trace, 46  
unitary matrix, 47  
sampling interval, 26  
Shannon’s theorem, 26  
SRP (*see* Stationary random processes (SRP))  
statistics, 54  
Random decrement (RD) technique, 175–176
- S**
- Second order blind identification (SOBI)  
auto-correlation, 172  
blind modal identification, 168  
BSS techniques  
applicability of, 166  
classification, 166–167  
sources, 166  
static mixtures, 167  
use of, 167–168  
complexity plot, 205–206  
drawback of, 168  
JAD technique, 171  
natural frequencies and damping ratios, 172  
random response, 172–173  
sample software, 206  
sensor layout, 197, 205  
whitening matrix, 169–170
- Signal-to-noise ratio (SNR), 4, 290  
Single degree of freedom (SDOF) system, 7  
Singular value decomposition (SVD),  
49, 56–57
- Spectral density functions  
coherence function, 41  
coincident, 40  
cross, 39  
Fourier transforms, 38  
Hanning window, 43  
Hermitian matrix, 43  
and OMA, 44–46  
quadrature, 40  
random error, 42–46  
rectangular window, 42
- two-sided, 39  
Welch procedure, 41  
Wiener–Khinchin relations, 40  
Star vault, 211–213  
State-space models  
continuous-time, 111  
covariance equivalent model, 113  
DD-SSI, 117  
direct transmission matrix, 111  
forward innovation model, 116  
Kalman filter, 114–115  
measurement noise, 113  
non-steady state Kalman gain, 115  
observation equation, 109–110  
optimal predictor, 114  
process noise, 113  
realization, 111  
Riccati equation, 115  
state equation, 109–110  
state prediction error, 114  
state vector, 109
- Stationary and ergodic random processes (SERP), 28
- Stationary random processes (SRP)  
bias error, 44  
correlation coefficient, 31  
correlation functions  
auto-and cross-, 36  
DFT, 27  
FFT, 27  
weakly ergodic, 36  
covariance function, 30  
damping ratio, 45, 46  
Gaussian probability, 32  
joint probability, 29  
mean square error, 44  
mean square value, 30  
normalized rms error, 44–45  
probability density function, 29, 34  
probability distribution function, 29  
random/stochastic process, 28  
sample function, 28  
sample record, 28  
SERP, 28
- spectral density functions  
auto-spectral density functions, 40, 41  
Blackman–Tukey procedure, 41  
coherence function, 41  
coincident spectral density function, 40  
cross-spectral density functions, 39, 40  
Gaussian probability density function, 32  
Hanning window, 43  
quadrature spectral density function, 40

- Stationary random processes (SRP) (*cont.*)  
 rectangular window, DFT, 42  
 Welch procedure, 41  
 Wiener–Khinchin relations, 40  
 standard deviation, 30–31  
 statistically independent, 30  
 weakly stationary random processes, 28
- Stochastic subspace identification  
 (SSI), 103, 269
- Cov-SSI method (*see* Covariance-driven Stochastic Subspace Identification (Cov-SSI) method)
- DD-SSI method (*see* Data-driven stochastic subspace identification (DD-SSI) method)
- Structural damping, 216
- Structural dynamics models
- ARMA models
    - ARMAV, 117
    - companion matrix, 119
    - linear time-invariant system, 117
    - minimal realization, 118
    - observability canonical state-space realization, 118
  - fraction polynomial models
    - circular correlation function, 122
    - common-denominator model, 120
    - cross-power spectra, 121
    - MFD, 120
    - positive power spectra, 123
  - frequency response, 105–109
  - FRF, 106, 107
  - impulse response, 105–109
  - IRF, 108
  - MDOF system, 105
  - positive power spectra, 108
  - residue matrix, 107
  - spatial model, 106
  - state-space models (*see* State-space models)
  - time domain modal, 108
  - UMPA, 123–125
  - un-scaled mode shapes, 108

**T**

- Time domain methods, 127  
 ARMA model, 151–153

- Cov-SSI method  
 BR variant, 157  
 canonical angles, 157  
 CVA variant of, 157  
 Laplace variable, 158  
 noise sources, 158  
 observability/controllability matrix, 154, 155  
 state-space model, 153  
 Toeplitz matrix, 154–156
- DD-SSI method  
 CVA, 165–166  
 Hankel matrix, 160–161  
 Kalman filter state, 159, 162  
 modal parameter, 165  
 orthogonal and oblique projections, 159  
 principal component algorithm, 165  
 state-space matrices, 162–164  
 UPC algorithm, 165
- NEXT-type procedures  
 ERA, 147  
 Hankel matrix, 148–149  
 ITD, 150  
 LSCE, 147  
 Prony's equation, 147  
 system matrix, 150
- SOBI algorithm (*see* Second order blind identification (SOBI))
- Transducers  
 dynamic range, 67  
 force-balance accelerometers, 65  
 offset error, 67  
 Peterson noise curves, 68–69  
 piezoelectric sensors, 62–63  
 sensor resolution, 67  
 sensor self noise, 67  
 settling time, 67

**U**

- Unified matrix polynomial approach  
 (UMPA), 123–125
- Unweighted principal component (UPC)  
 algorithm, 165

**V**

- Virtual instruments (VI), 13, 15–16